Titre: Title:	Investigation of the Geomechanical Behavior of Mine Backfill and its Interaction with Rock Walls and Barricades
Auteur: Author:	Pengyu Yang
Date:	2016
Type:	Mémoire ou thèse / Dissertation or Thesis
Référence: Citation:	Yang, P. (2016). Investigation of the Geomechanical Behavior of Mine Backfill and its Interaction with Rock Walls and Barricades [Thèse de doctorat, École Polytechnique de Montréal]. PolyPublie. https://publications.polymtl.ca/2388/

UNIVERSITÉ DE MONTRÉAL

INVESTIGATION OF THE GEOMECHANICAL BEHAVIOR OF MINE BACKFILL AND ITS INTERACTION WITH ROCK WALLS AND BARRICADES

PENGYU YANG

DÉPARTEMENT DE GÉNIES CIVIL, GÉOLOGIQUE ET DES MINES

ÉCOLE POLYTECHNIQUE DE MONTRÉAL

THÈSE PRÉSENTÉE EN VUE DE L'OBTENTION

DU DIPLÔME DE PHILOSOPHIAE DOCTOR

(GÉNIE MINÉRAL)

DÉCEMBRE 2016

UNIVERSITÉ DE MONTRÉAL

ÉCOLE POLYTECHNIQUE DE MONTRÉAL

Cette thèse intitulée :

INVESTIGATION OF THE GEOMECHANICAL BEHAVIOR OF MINE BACKFILL AND ITS INTERACTION WITH ROCK WALLS AND BARRICADES

présentée par : YANG Pengyu

en vue de l'obtention du diplôme de : Philosophiae Doctor

a été dûment acceptée par le jury d'examen constitué de :

M. SIMON Richard, Ph. D., président

M. LI Li, Ph. D., membre et directeur de recherche

M. AUBERTIN Michel, Ph. D., membre et codirecteur de recherche

M. JAMES Michael, Ph. D., membre

M. CHIASSON Paul, Ph. D., membre externe

DEDICATION

To my wife

To my parents

To my homeland

ACKNOWLEDGEMENTS

I am extremely appreciative of the support from my supervisors Prof. Li Li and Prof. Michel Aubertin. This work would not have been possible without their tremendous help in preparing the pre-doctoral report (including literature review and research proposal), articles, and this thesis. Thanks to them for generously sharing their knowledge and ideas. I am also thankful for the opportunities to present my research in various occasions. Over years, I have been deeply influenced by their attitude, insight, preciseness and generosity. I am forever grateful of these. My special thanks go to Prof. Li, who has generously spent a lot of time in discussing various aspects of this project.

I would like to thank Prof. Bruno Bussière and Prof. Richard Simon for their time and evaluation of the pre-doctoral report during the Comprehensive Examination. Prof. Robert Chapuis is acknowledged for his time and help in using SEEP/W. Many thanks also to Prof. Richard Simon, Dr. Michael James and Prof. Paul Chiasson for being the committee members. Prof. Musandji Fuamba is also acknowledged for being the representative of the Directeur d'études supérieures.

My thanks also go to Profs Michael James, Benoit Courcelles, Tikou Belem, Mamert Mbonimpa, Carmen Mihaela Neculita, Isabelle Demers and Gérald J. Zagury for their courses. Chantal Tétreault of Prêt Entre Bibliothèques at Library of Polytechnique Montréal is also acknowledged for helping search various documents.

I also very much appreciate my colleagues and friends for their help, advice and kindness.

Also, I would like to acknowledge the financial support from the following organizations:

Natural Sciences and Engineering Research Council of Canada (NSERC)

Institut de recherche Robert-Sauvé en santé et en sécurité du travail (IRSST)

Fonds de recherche du Québec - Nature et Technologies (FRQNT)

Industrial partners of the Research Institute on Mines and the Environment (RIME UQAT-Polytechnique; rime-irme.ca/).

Finally, special thanks to my lovely wife Wenxi who has gone through everything with me in China and Canada. I also want to thank my great parents and brother, very sincerely, for their love and support.

RÉSUMÉ

Les rejets solides produits par les mines comprennent les rejets de concentrateur (résidus miniers) et les roches stériles. Ces rejets sont usuellement entreposés en surface, ce qui peut engendrer divers risques environnementaux et géotechniques. Une autre option consiste à remblayer les chantiers miniers avec des stériles ou des résidus miniers. Cette pratique permet de réduire les quantités de rejets entreposés en surface, et aussi d'améliorer la stabilité du terrain, de diminuer la dilution et d'augmenter la récupération de minerai.

Le remblayage est utilisé avec diverses méthodes d'exploitation souterraine, pour différentes fonctions. Les préoccupations majeures associées à cette pratique sont la stabilité des structures de support (barricades) peu après le versement du remblai dans le chantier et la stabilité du remblai cimenté exposé après un certain temps après le remblayage. L'état des contraintes dans les chantiers remblayés a été largement étudié au cours des dernières années. Cependant, plusieurs incertitudes existent encore en lien avec des préoccupations majeures, notamment sur le peu de solutions disponibles afin d'évaluer l'évolution des contraintes dans les chantiers, pour concevoir les barricades et le remblai cimenté exposé, ainsi que sur pour estimer la valeur du coefficient de pression des terres K ($= \sigma'_h/\sigma'_v$).

L'objectif principal de ce projet est d'évaluer l'état des contraintes dans le remblai confiné et ses interactions avec les barricades peu après sa mise en place et avec les trois parois latérales pour le remblai exposé à plus long terme. De nouvelles solutions analytiques sont proposées pour évaluer l'évolution du niveau d'eau dans un chantier remblayé d'un remblai hydraulique. Ces solutions sont vérifiées à l'aide de simulations numériques réalisées avec le logiciel d'éléments finis SEEP/W. Ces analyses indiquent que l'eau accumulée sur le remblai hydraulique peut induire des pressions interstitielles plus élevées et ainsi compromettre la sécurité des barricades.

Une solution analytique améliorée est également proposée pour le dimensionnement des barricades en roches stériles pour la rétention du remblai en pâte. Des simulations numériques réalisées avec le logiciel de différences finies FLAC sont utilisées pour analyser les principaux facteurs d'influence et aussi pour valider la nouvelle solution. Les résultats ont permis d'identifier deux mécanismes de rupture de la barricade faites de roches stériles, qui dépendent principalement des propriétés aux interfaces et de la résistance des stériles.

Des simulations ont été effectuées avec FLAC^{3D} pour évaluer la stabilité du remblai cimenté lors d'une exposition verticale. Les résultats montrent que le mode de rupture tend à changer avec l'augmentation de la cohésion du remblai. Une nouvelle solution analytique est ensuite proposée pour estimer la résistance requise du remblai exposé, sur la base d'un mode de rupture plus réaliste. Les résultats des simulations sont utilisés pour valider cette nouvelle solution et évaluer l'effet de divers facteurs, y compris la géométrie du chantier et les propriétés du remblai.

La bonne corrélation entre les solutions analytiques proposées et les résultats numériques indique que ces nouvelles solutions peuvent être utilisées pour la conception des barricades et du remblai minier cimenté exposé.

D'autres analyses numériques ont été réalisées (avec FLAC) afin d'évaluer les rapports des contraintes ($K = \sigma'_h/\sigma'_v$, et le rapport des contraintes principales $K_{ps} = \sigma'_3/\sigma'_1$) dans les remblais pulvérulents placés dans des ouvertures verticales. Les simulations sont effectuées en considérant que les valeurs de l'angle de frottement interne ϕ' et du coefficient de Poisson v du remblai sont indépendantes ou reliées entre elles. Ce dernier cas (avec un lien entre ϕ' et v) est basé sur la définition d'une valeur unique et cohérente du coefficient de pression des terres au repos K_0 pour les simulations menées avec des modèles élasto-plastiques. Les résultats indiquent que les rapports de contraintes ($K_{ps} = K$) le long de la ligne de centre verticale de l'ouverture peuvent être influencées par la relation entre ϕ' et v. Le rapport K_{ps} est toujours proche du coefficient de pression active de Rankine K_a près des parois.

Les principaux résultats sont présentés dans quatre articles de revue qui ont été publiés, acceptés ou soumis. Cette thèse présente également des résultats supplémentaires mis dans des annexes, y compris la relation expérimentale entre l'angle de frottement interne ϕ' et le coefficient de Poisson v (à petites déformations) pour les matériaux granulaires.

ABSTRACT

Solid wastes produced by mines include tailings and waste rock. These wastes are usually stored on the surface, which may raise various environmental and geotechnical risks. Another option is to backfill underground mine stopes with waste rock or tailings. This practice can reduce the surface disposal, and also improve ground stability and ore recovery in mining operations.

Backfill is widely applied in different underground mining methods for various purposes. The associated major concerns are the stability of the support structure (barricades) at very early time and that of the exposed cemented fill at longer time. In recent years, the stress state in backfilled stopes has been extensively investigated. However, there are uncertainties regarding the major concerns including limited solutions for stress evolution in stopes and for design of barricades and exposed backfill, as well as the actual value of earth pressure coefficient K ($= \sigma'_h/\sigma'_v$) in confined fills.

The main objective of this project is to evaluate the stress state within confined backfill and its interactions with barricades at very early time (shortly after the filling) and remaining three sidewalls upon exposure at longer time (typically a few weeks after the filling). New analytical solutions for evaluating the transient seepage are proposed for stopes filled with hydraulic fill. These solutions are verified using simulations conducted with the finite element code SEEP/W. These analyses indicate that ponding, generated on the top of the settled hydraulic fill, can induce higher pore water pressures and jeopardize the barricade safety.

An improved analytical solution is also proposed for sizing waste rock barricades to retain paste fill. Numerical simulations performed with the finite difference code FLAC are used to analyze key influencing factors and also to validate the new solution. The results identify two failure mechanisms for the waste rock barricade, which depend mainly on the interface properties and waste rock strength.

Simulations are conducted with FLAC^{3D} to assess the stability of cemented backfill upon vertical exposure. The results show that the failure mode tends to change as the fill cohesion increases. A new analytical solution is then proposed to estimate the required strength of exposed fill, based on a more realistic failure mode. Simulation results are used to validate this new solution and evaluate the effect of various factors including the stope geometry and fill properties.

The good agreement between the proposed analytical solutions and numerical results indicates that these new solutions can be useful for the design of barricade and exposed cemented mine backfill.

This work also involves numerical analyses (with FLAC) of the stress ratios ($K = \sigma'_h/\sigma'_v$ and the principal stress ratio $K_{ps} = \sigma'_3/\sigma'_1$) in particulate (cohesionless) fills placed in vertical openings. The simulations are conducted using both independent and linked values of the backfill internal friction angle ϕ' and Poisson's ratio v. The latter is based on a unique and consistent value of the at-rest earth pressure coefficient K_0 for simulations performed with an elasto-plastic model. The results indicate that along the centerline of the opening, the stress ratios ($K_{ps} = K$) can be influenced by the relationship between ϕ' and v. The ratio K_{ps} is always close to Rankine's active earth pressure coefficient K_a near the walls.

The main results are presented in four journal manuscripts that have been published, accepted or submitted. This thesis also presents additional results in appendices, including the experimental relationship between the internal friction angle ϕ' and Poisson's ratio v (at small strains) of granular materials.

TABLE OF CONTENTS

LIST OF TABLES

LIST OF FIGURES

LIST OF SYMBOLS AND ABBREVIATIONS

Symbols

B	width of the stope or opening (m)
B_t	equivalent width of the sliding wedge in the presence of a tension crack (m)
C	a constant representing the hydraulic and geometric characteristics of a stope with hydraulic fill and porous barricade (s^{-1})
C_U	coefficient of uniformity
C_M	calibration factor
c	cohesion (kPa)
c'	effective cohesion (kPa)
c_i	cohesion of fill-rock interface (kPa)
c_b	cohesion along the back wall (kPa)
c_s	cohesion along the sidewalls (kPa)
D_{60}, D_{10}	size at which 60% and 10% of particles pass the sieve (mm)
d_{max}	maximum particle size (mm)
E	Young's modulus (MPa or GPa)
E_r	Young's modulus of the rock mass (GPa)
e	void ratio
H	height of the stope or opening (m)
H^*	equivalent height of the wedge (m)
H_d	drift/ barricade height (m)
H_w	pond height in the stope (m)
H_{w0}	initial height of the pond (m)
H_b	height of settled hydraulic fill in the stope (m)

H_t	depth of the tension crack (m)
I_D	density index (%)
K	coefficient of earth pressure
K_a	Rankine's active pressure coefficient
K_p	Rankine's passive pressure coefficient
K_0	coefficient of earth pressure at-rest
$(K_0)_{\phi'}$	coefficient of earth pressure at-rest based on Jaky's equation
$(K_0)_v$	coefficient of earth pressure at-rest defined by the Poisson's ratio
K_{ps}	principal stress ratio
k	hydraulic conductivity (m/s)
k_{sat}	saturated hydraulic conductivity (m/s)
K_n	normal stiffnesses of interface elements (GPa/m)
K_t	shear stiffnesses of interface elements (GPa/m)
L	stope length (m)
L_B	average length of the waste rock barricade (m)
L_{BT}	top length of waste rock barricade (m)
L_{BB}	base length of waste rock barricade (m)
L_d	drift/ barricade width (m)
l	distance of the barricade to the drawpoint (m)
n	porosity
n_s	porosity of the settled hydraulic fill
P	solid weight content of backfill (%)
p_0	surcharge exerted on the backfill top surface (kPa)
Q	total volume of hydraulic fill placed in the stope (m^3)

r_b	adherence ratio along the back wall
r_s	adherence ratio along the sidewalls
S_s	shear force acting along the sidewalls (kN)
S_t	shear force acting along the tension crack (kN)
T	total time needed to drain the pond (s or h)
t	a transient time (s or h)
T_0	tensile strength of cemented backfill
u	pore water pressure (kPa)
u_{base}	pore water pressure at the stope base (kPa)
V	volume (m^3)
W	weight of the sliding wedge (kN)
α	inclination angle of the sliding plane to the horizontal (°)
α_1	upstream slope angle of waste rock barricade on the stope side (°)
α_2	downstream slope angle of waste rock barricade on the drift side (°)
β	inclination angle of the stope to the horizontal (°)
θ_w	volumetric water content
ϕ	internal friction angle (°)
ϕ'	effective internal friction angle (°)
δ	interface friction angle (°)
δ'	effective interface friction angle (°)
δ_c	critical interface friction angle (°)
Ψ	dilation angle (°)
σ_h	horizontal stress (kPa)
σ_v	vertical stress (kPa)

σ'_h	horizontal effective stress (kPa)
σ'_v	vertical effective stress (kPa)
σ_1	major principal stress (kPa)
σ_3	minor principal stress (kPa)
σ'_1	major effective principal stress (kPa)
σ'_3	minor effective principal stress (kPa)
γ	unit weight of the backfill (kN/m^3)
γ_w	unit weight of water (kN/m^3)
γ_b	unit weight of the cemented paste backfill (kN/m^3)
γ_{wr}	unit weight of the waste rock (kN/m^3)
γ_r	unit weight of the rock mass (kN/m^3)
γ_{sat}	unit weight of saturated backfill (kN/m^3)
γ_{sub}	unit weight of submerged backfill (kN/m^3)
v	Poisson's ratio
v_r	Poisson's ratio of rock mass
λ	a parameter for relating the internal friction angle ϕ' and Poisson's ratio v of granular materials

Abbreviations

CHF	cemented hydraulic fill
CRF	cemented rock fill
CPB	cemented paste backfill
FDM	finite difference method
FEM	finite element method
FLAC	Fast Lagrangian Analysis of Continua

FS	factor of safety
FW	footwall
HAR	high aspect ratio
HF	hydraulic fill
HW	hanging wall
LAR	low aspect ratio
MM	Modified Mitchell
PWP	pore water pressure
RF	rock fill
RW	rock wall
UCS	unconfined compressive strength
VCL	vertical center line
WRB	waste rock barricade

LIST OF APPENDICES

CHAPTER 1 INTRODUCTION

Mining is a major component of Canada's economy. However, mining generates substantial amount of solid wastes, mainly in the form of tailings and waste rock. Tailings are crushed rock produced by mineral extraction and are typically disposed as slurry. Waste rock is the coarse grained material excavated to create mine openings; it has no economic value.

Tailings and waste rock are typically stored on the surface in tailings impoundments and waste rock piles. These structures greatly increase the footprints of mining operations and can pose significant environmental and geotechnical issues. As a priority for the mining industry and society, their safe, environmentally responsible, long-term management is a significant challenge (e.g., Aubertin et al. 2002, 2011, 2016). Underground mine stope backfilling with mine wastes can significantly reduce the amount of wastes disposed on the surface. This can be an environmentally friendly and responsible solution for mine waste management.

In recent decades, underground mine stope filling has been increasingly used worldwide and it has become a common practice. Besides the environmental benefits, backfilling's advantages also include improved regional ground stability, ore recovery, ore dilution and ventilation (Thomas 1979; Hassani & Archibald 1998; Potvin et al. 2005; Hambley 2011).

In underground mining, the application of mine backfill largely depends on the mining methods employed. In open stoping, the backfill is commonly used to stabilize the rock mass and help recover the (vertical) rib pillars (secondary stopes); this backfill is usually called "delayed backfill". Cemented backfill is used to recover (horizontal) sill pillars. In cut-and-fill mining, backfill usually serves as a working floor or as a roof for further extraction; it also serves to increase the rock mass stability. When the backfill contains water and/or cement - mostly for rib and sill pillar recovery in open stoping or for the underhand cut-and-fill mining, barricades need to be built in the lower drift (near the drawpoint) to retain the hydraulically transported saturated fill. Several critical issues associated with the design of the backfill and barricades are raised:

- How to design the barricade?
- What is the optimal strength of the backfill exposed vertically on one side or exposed horizontally at the base?

The first theme is mostly related to the backfill behavior at very early time (shortly after the filling), while the second to the behavior of the backfill at longer time (typically a few weeks after filling). The realization of these tasks requires a good understanding of the geomechanical behavior of the backfill and its interactions with the confining structures (i.e., rock walls and barricades). The complex interactions between backfill and confining structures constitute the problems to be investigated, which are briefly presented in the following.

1.1 Definition of the problem

The primary concern related to stope filling is the barricade stability shortly after the placement of backfill. A number of documented failures indicate that the barricade design remains a major challenge (e.g., Bloss & Chen 1998; Yumlu & Guresci 2007). More work is needed to evaluate the critical backfill pressure exerted on the barricade and its design. This requires, in turn, a good understanding of pore water pressures (PWP) and total (and effective) stresses in the backfilled stope and drift where the barricade is built.

Recently, barricades constructed with waste rock has become popular in Canada and elsewhere due to their simple and low-cost construction, compared to the traditional barricades made of bricks, concrete blocks, or reinforced shotcrete. However, solutions developed for traditional barricades are not directly applicable to waste rock barricades. It is thus necessary to develop new methods for sizing such waste rock barricades.

A second crucial issue is the stability of the exposed cemented fill in the primary stope during the subsequent secondary recovery (which usually occurs a few weeks after filling). The failure of the exposed fill can lead to ore dilution or serious instability issues. These can be reduced or avoided by increasing the binder usage (cement, fly ash, slag, pozzolan, etc.); but the associated cost considerably increases. Thus, the question is how to estimate the minimum (optimal) required strength of cemented fill upon vertical exposure. This demands stability analysis of exposed fill with regard to its interactions with the remaining three sidewalls.

Another issue is how the ground stability can be improved by the backfill. This requires a comprehensive understanding of the interactions between the backfill and confining rock walls. The stress state within the backfilled stopes and adjacent rock mass should be correctly evaluated, which can be done by theoretical (closed-form solutions) and numerical analyses. To this end,

analytical solutions are in high demand by mining engineers. Most existing analytical solutions involve a parameter called earth pressure coefficient K ($= \sigma'_h/\sigma'_v$). Its value can largely influence the estimated stress state in backfilled openings, which in turn affects various design aspects of mine backfill and barricade. More work is needed to better understand this aspect (as will be demonstrated below).

1.2 Thesis objectives

The primary objective of this project is to investigate the geomechanical behavior of backfill placed in vertical mine stopes and similar openings. More specifically, the project focuses on the behavior of the backfill at very early time for sizing waste rock barricades, on the behavior of cemented fills at longer time before and after exposure on one side, and on the stress state within the confined fill itself. The following sub-objectives have been specifically addressed:

1) Investigate the evolution of the water table and PWP in stopes with hydraulic fill

- Develop 3D analytical solutions to describe the evolution of the water table and PWPs in the stope;
- Conduct numerical simulations to evaluate the PWPs in stopes and drifts, and to validate the proposed analytical solutions.

2) Sizing of waste rock barricades constructed to retain paste fill during stope filling:

- Propose 3D analytical solutions for sizing waste rock barricades with respect to their global and local stability;
- Perform numerical simulations to identify the failure mechanism and instability criterion of waste rock barricades, and to verify the proposed solutions.

3) Assess the stability of cemented mine backfill upon a vertical exposure:

- Develop improved analytical solutions for estimating the required strength and factor of safety of mine backfill with an open face;
- Conduct numerical simulations (with related values of internal friction angle ϕ' and Poisson's ratio v of the fill) to assess the failure mode and instability criterion of exposed mine backfill, and to validate the proposed analytical solutions;

4) Numerical analysis of stress state in vertical backfilled openings with cohesionless fills:

- Evaluate the earth pressure coefficient K ($= \sigma'_h/\sigma'_v$) in backfilled openings to estimate the stress distribution within fills;
- Investigate the principal stress ratio K_{ps} ($= \sigma'_3/\sigma'_1$) in backfilled openings to evaluate the backfill state;
- Assess the effect of using related and independent backfill parameters ϕ' and v on the stress state and coefficients K and K_{ps}; and
- Analyze the effect of interface elements and their frictional properties on the stress state and coefficients K and K_{ps}.

1.3 Contributions

The main scientific contributions of this research project include the following four articles published in or submitted to peer-reviewed journals:

Article 1:

Yang PY & Li L. (2016) Evolution of water table and pore water pressure in stopes with submerged hydraulic fill. *ASCE International Journal of Geomechanics*. Accepted with changes in October 2016. This article is presented in Chapter 3.

Article 2:

Yang PY, Li L, Aubertin M, Brochu-Baekelmans M & Ouellet S. (2016a) Stability analyses of waste rock barricades designed to retain paste backfill. *ASCE International Journal of Geomechanics*, doi: 10.1061/(ASCE)GM.1943-5622.0000740, 04016079. This article is presented in Chapter 4.

Article 3:

Yang PY, Li L & Aubertin M. (2016b) A new solution to assess the required strength of mine backfill with a vertical exposure. *ASCE International Journal of Geomechanics*. Submitted in September 2016. This article is presented in Chapter 5.

Article 4:

Yang PY, Li L & Aubertin M. (2016c) A comprehensive numerical analysis of stress ratios in vertical backfilled openings. *ASCE International Journal of Geomechanics*. Submitted in November 2016. This article is presented in Chapter 6.

The following three articles have also been published in or to be submitted to peer-reviewed journals in the course of this project:

Yang PY, Li L, Aubertin M & Tiwari A. (2016d) An investigation of the relationships between K_0, ϕ' and v for granular materials. To be submitted. Main results are presented in Appendix A.

Yang PY & Li L. (2015) Investigation of the short-term stress distribution in stopes and drifts backfilled with cemented paste backfill. *International Journal of Mining Science and Technology*, 25(5): 721-728.

Li L & Yang PY. (2015) A numerical evaluation of continuous backfilling in cemented paste backfilled stope through an application of wick drains. *International Journal of Mining Science and Technology*, 25(6): 897-904.

The following two conference papers have also been published in the course of this project:

Yang PY, Brochu-Baekelmans M, Li L & Aubertin M. (2014) An improved solution for sizing barricades made of waste rock to retain cemented paste backfill. In *Proceedings of 67th Canadian Geotechnical Conference*, Regina, SK, Canada.

Yang PY & Li L. (2014) A 3D analytical solution for the short-term stress distribution in backfilled stopes and on barricades. In *Proceedings 67th Canadian Geotechnical Conference*, Regina, SK, Canada.

This project contributes to better addressing major geomechanical challenges encountered in underground stope filling, including the design of support structures (barricades) and exposed cemented backfill. Analytical and numerical solutions presented in this project provide tools to help evaluate the evolution of the water table and PWPs in stopes with hydraulic fill, size waste rock barricades for retaining paste fill, and assess the stability of exposed cemented backfill. These analytical (closed form) solutions can be useful for mining engineers, at least in the preliminary design. Other components of this research also lead to improved assessment of stress state in backfilled openings; this may help increase the productivity and reduce the associated risks in underground mining.

1.4 Content of this thesis

The scope of this research is relatively broad due to the number and complex nature of the issues involved.

The literature review is presented in Chapter 2; it includes review of the state of knowledge on the following themes:

- Underground mining methods employing backfills;
- Classification of mine backfills and their typical geomechanical properties and characteristics;
- Typical barricades used for retaining mine backfill;
- Analytical solutions for stress estimation in backfilled stopes and on barricades;
- Analytical methods to assess the stability of cemented fill with vertical exposure;
- Numerical simulations for evaluating the stress state and stability of backfilled stopes;
- Experimental tests for assessing backfill stress in stopes and barricade drifts.

Chapters 3 to 6 are presented in the form of manuscripts which have been published or submitted to peer-reviewed journals.

Chapter 3 (Article 1) presents 3D analytical solutions for describing the evolution of the water table and pore water pressures (transient seepage) in stopes with submerged hydraulic fill. This corresponds to the condition when a pond is generated on the backfill surface by the self-weight consolidation of the fill particles. The proposed solutions are verified using numerical simulations by modelling the transient seepage as the water table drops in the stope. The main influencing factors on the evolution of the water table and pore water pressures are evaluated and compared for the two approaches.

Chapter 4 (Article 2) presents the development of a more complete 3D analytical solution for sizing trapezoidal barricades made of waste rock to retain cemented paste backfill, considering both global and local stability. The failure mechanism and an explicit instability criterion of the waste rock barricade are identified from numerical simulations conducted with interface elements. The proposed solutions are then calibrated and validated using numerical results for

representative geometrical and mechanical properties of barricades. In this paper, the internal friction angle ϕ' and Poisson's ratio v of waste rock are taken as independent parameters, as is commonly assumed in numerical analyses. Sample calculations are also presented to illustrate the application of this solution.

Chapter 5 (Article 3) presents the development of a new analytical solution for assessing the stability of mine backfill with a vertical exposure, based on a new failure mode observed from numerical simulations and existing experimental tests. An explicit instability criterion for side-exposed backfill is introduced based on numerical results. The validation of the new solution using numerical models is then illustrated for different stope geometries and backfill properties. For numerical simulations presented here, the internal friction angle ϕ' and Poisson's ratio v of backfill are related using the correlation proposed in Appendix A, based on the consideration of a unique and consistent value of K_0.

Chapter 6 (Article 4) contains the main numerical results for evaluating the earth pressure coefficient K and principal stress ratio K_{ps} near the center and walls of openings backfilled with granular (no cohesion) fills. The simulations are conducted with both independent and related values of internal friction angle ϕ' and Poisson's ratio v of the backfill. The effect of various mechanical and geometric characteristics on the stress ratios (K and K_{ps}) is evaluated. The backfill stress state is assessed with the principal stress ratio K_{ps} based on the Mohr-Coulomb criterion. The interface elements are also used to assess the effect of fill-wall contacts and its properties on the stress state of backfill.

Chapter 7 provides a summary and general discussion on the main results of the research. The procedure and validation of numerical modelling are also discussed. Conclusions and recommendations for further studies can be found in Chapter 8.

This thesis also includes an extensive References list and Appendices that present the validation of SEEP/W, FLAC and FLAC^{3D} and complementary results on various aspects of this research.

Besides, the Appendix includes additional results (Appendix A) that proposes a relationship between the internal friction angle ϕ' and Poisson's ratio v (at small strains) for granular materials, based on the two basic approaches for defining the earth pressure coefficient at-rest K_0. This correlation is tested using a number of conventional triaxial compression tests results taken from the literature on granular materials.

CHAPTER 2 LITERATURE REVIEW

This chapter first reviews the major underground mining methods where backfills are commonly used for various engineering purposes. Typical mine backfills, i.e., rockfill, hydraulic fill and paste fill, are then reviewed with respect to their typical physical, hydraulic and mechanical properties. A review of typical barricades used for retaining backfill in place is also presented. This chapter then presents the state of knowledge on the stress state in backfilled stopes and drifts, and the stability design of the barricade and cemented backfill with vertical exposure.

2.1 Mining with backfill

In order to convert a mineral resource to a probable or proven reserve, a preliminary feasibility study needs to be undertaken, which includes selecting mining methods. In practice, the selection of a mining method is largely based on the characteristics of the deposit and rock mass. In some mines, more than one method is used synergistically.

Mining methods are basically divided into surface mining methods (e.g., open-pit mining, strip mining) and underground mining methods (Hartman & Britton 1992; Darling 2011). The latter can include self-supported methods (room-and-pillar mining, sublevel stoping, shrinkage stoping, vertical crater retreat), artificially supported methods (cut-and-fill mining), and caving method (longwall mining, sublevel caving and block caving). Details on these mining methods can be found in the SME Mining Engineering Handbook (Hartman & Britton 1992; Darling 2011).

A number of variants have been created based on basic mining methods to account for the uniqueness of each mineral deposit (Hamrin 2001; Hustrulid & Bullock 2001). This subsection is aimed at summarizing briefly the characteristics of the major mining methods in which backfill can be employed. Emphasis is given here to the type of backfill that can be used and its functions, filling sequences, infrastructures associated with filling, and aspects to consider in backfill design.

2.1.1 Self-supported methods

In self-supported (or naturally supported) methods, ore (or waste rock) pillars are left (and definitely lost for most cases) to stabilize rock walls. These usually apply to low-grade deposits where the increase in ore recovery does not justify the cost of backfill (Potvin et al. 2005).

However, backfill is sometimes used to recover the pillars or secondary stopes following the extraction of the rooms and primary stopes. Such secondary recovery can be classified as artificially supported method due to the use of backfill. Here, the application of backfill in such combined method is included under self-supported method.

2.1.1.1 Room-and-pillar mining

In room-and-pillar (R&P) mining, pillars are left to support the hanging wall and back (roof) as rooms (horizontal openings) are extracted (Bullock 2011). This method is used in subhorizontal mineral deposits with uniform and limited thickness (Hamrin 2001).

In some cases, ore pillars need to be recovered which involves placing cemented or uncemented fill among pillars up to the back of a room. The backfill provides ground support and helps control the back-floor convergence (e.g., Hunt 1988; Roberts et al. 1998; Lane et al. 2001; Tesarik et al. 2009). The filling usually starts from the perimeter pillars towards the center of the filled area. Barricades (or fill fences) are built between perimeter pillars to retain the fill. The associated concerns are the barricade stability and the minimum required fill strength for self-standing during the extraction of ore pillars.

2.1.1.2 Sublevel stoping

Sublevel stoping is used in more than 60% underground mines in North America (Pakalnis & Hughes 2011). It can be applied with competent rock mass and steep (from 50° to 90°) ore bodies. The most commonly used sublevel stoping methods include blasthole stoping, long-hole stoping, shrinkage stoping and vertical crater retreat.

In blasthole stoping, multiple drilling levels (sublevels) are created between main levels. Holes (20-30 m in length) are drilled by top-hammer drills in the sublevel drifts. The blasted ore is mucked from the drawpoints at the stope base (Hamrin 2001; Darling 2011). The long-hole stoping can be regarded as a large-scale variation of blasthole stoping. The longer (up to about 100 m), greater and straighter holes are drilled by in-the-hole (ITH) technique (Hamrin 2001). The multiple drilling levels are thus eliminated.

In shrinkage stoping, the ore is removed upwards with horizontal slices from the stope base. About 35% of blasted ore is first drawn off while the remnant blasted ore provides working floor and support of rock walls for further extraction (temporarily fulfilling some roles of backfill).

When the blasted ore is totally drawn out, the stope may be filled (mostly with waste rock from development) or left open.

Vertical crater retreat (VCR) is a patented mining method developed by INCO and CIL Inc. VCR first involves an undercut to create a horizontal slot. ITH holes are drilled from an upper level to the slot. The ore is then blasted upwards in slices. Only a portion of the blasted ore is mucked at drawpoints; VCR can thus be regarded as a form of shrinkage stoping. Vertical block mining (VBM) can be regarded as a variant of VCR. With VBM, the extraction is usually performed in larger slices (e.g., three or four; Emad et al. 2014, 2015a). Each slice is blasted and mucked out prior to blasting the next lift.

Backfill can be applied in sublevel stoping and its variants. For blasthole stoping, long-hole stoping and shrinkage stoping, backfill can be used to increase ground stability and/or to recover ore pillars. If pillar recovery is unnecessary, stopes can be filled with uncemented fill. It is then possible to increase the ore recovery by reducing the size of pillars. When pillars must be recovered (as is the case of VCR), it is customary to divide the stopes into primary and secondary stopes. The former are filled with cemented backfill (i.e., cemented rock, hydraulic or paste fill) to form man-made rib pillars, while the latter are filled with either uncemented or low cement content backfill or a mix of uncemented (upper part) and cemented (lower part) fill (Fig. 2-1).

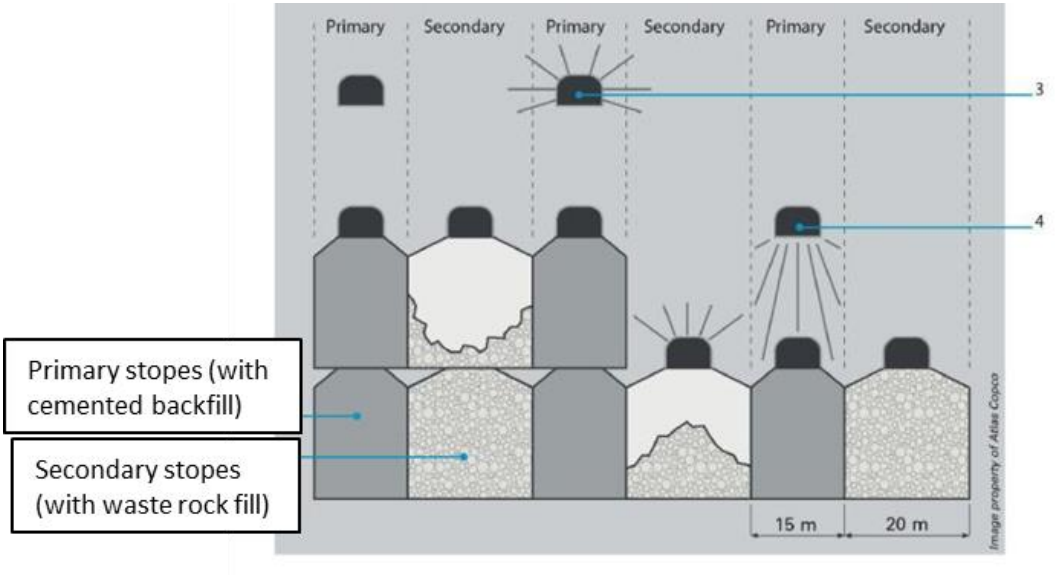

Figure 2-1: Illustration of open stope mining showing the backfilling of primary and secondary stopes (taken from Atlas Copco 2014)

Backfilling may proceed in a checkerboard pattern following the mining sequence. The design of backfill strength is largely dependent on the later extraction, number of exposed faces, stope geometry and stability of rock mass. The cemented fill is required to be self-standing upon excavation of an adjacent secondary stope. A critical issue is how to estimate the minimum required strength of the exposed (unsupported) cemented fill. Current backfill design is mostly based on an analytical solution proposed by Mitchell et al. (1982). Several updates have been made by Zou & Nadarajah (2006), Dirige et al. (2009), Li & Aubertin (2012, 2014), and Li (2014a, 2014b).

Another critical concern is how to design the barricade, built in the drift near the drawpoint, to retain backfill during and after filling. Different types and sizes of barricades can be used based on the backfill type, filling sequence, rising rate, required strength, drainage capacity, and materials available (e.g., Mitchell et al. 1975; Soderberg & Busch 1985; Beer 1986; Kuganathan 2001, 2002a, 2002b; Revell & Sainsbury 2007b; Li & Aubertin 2009c, 2009d, 2011; Li 2013; Yang et al. 2014, 2016a; Rajeev & Sivakugan 2016).

These solutions (analytical and numerical) for assessing the stability of exposed cemented fill and barricade design will be reviewed in Sections 2.4 and 2.5.

2.1.2 Artificially supported methods

In artificially supported methods, the backfill (often combined with pillars) is used to control rock wall stability and mine near-field displacements (Brady & Brown 2004). In most cases, artificially supported mining designates cut-and-fill mining. Strictly, a cut-and-fill mining means a cut followed by immediately filling (Hartman & Britton 1992; Darling 2011). However, rooms or stopes in self-supported method are filled only after the entire stope is extracted; the backfill used is thus called “delayed backfill” (Stephan 2011).

2.1.2.1 Cut-and-fill mining

When the rock mass and ore conditions do not permit the creation of large stopes, mined-out voids have to be filled concurrently with extraction. Cut-and-fill (C&F) mining is designed for such conditions. During extraction, voids are usually filled with cemented or uncemented fill once a slice of ore is mined out. The fills serve as a working floor or roof for further extraction and also stabilize the rock mass. In the former case, the fill strength should be designed to

support machine operation and to minimize ore dilution (Belem & Benzaazoua 2008; Stephan 2011). The use of hydraulic fill and paste fill requires more management (e.g., constructing barricades) at multiple points of drainage. Two main variations of C&F mining are first described based on the rock mass conditions and extraction sequence. Other variations, such as drift-and-fill mining, Avoca mining and postpillar mining, are presented with more details in Yang (2015).

Overhand C&F method (Fig. 2-2a) is used when the condition of ore bodies is fairly good. Usually, uncemented fill (e.g., hydraulic or rock fill) provides a working floor (platform) for the bottom-up ore extraction. A top layer of cemented fill is often used to facilitate the machine operation. In some cases, several extractions are operated simultaneously at different locations. A horizontal sill (or crown) pillar is used to separate extractions in two adjacent levels. To recover the sill pillar, it is necessary to construct an overlying sill mat that is usually made of cemented fill (reinforced with steel bar or not; Bullock & Hustrulid 2001). Such sill mat is critical to the global stability of stope once the sill pillar is removed (e.g., Mitchell 1991; Oulbacha 2014; Sobhi & Li 2015).

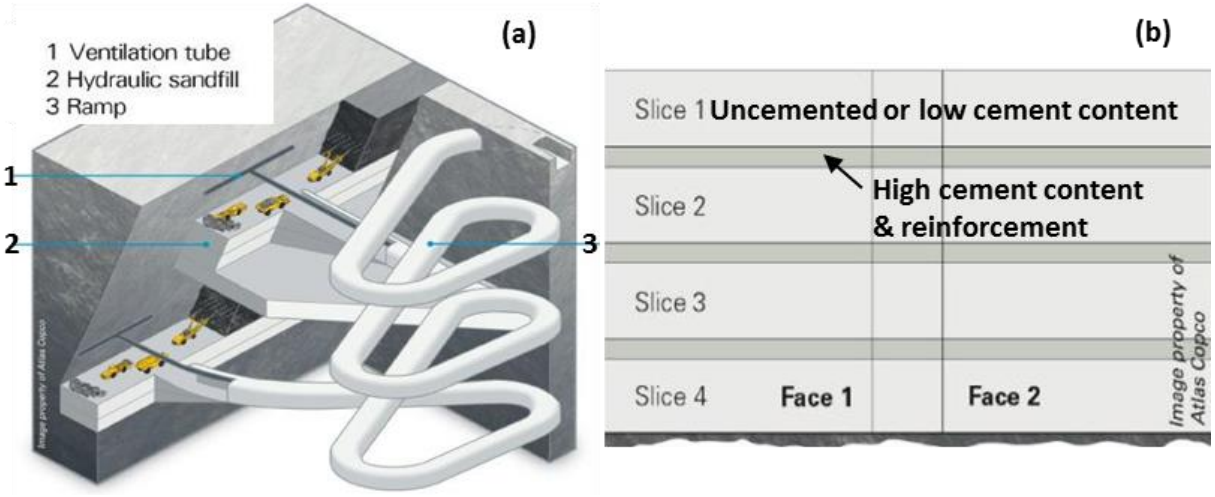

Figure 2-2: Schematic layout for (a) overhand and (b) underhand C&F (side view along the strike) mining (taken from Atlas Copco 2014)

Underhand C&F method may be used when the quality of rock mass and orebody is poor. This method involves a top-down excavation and filling sequence. A sill mat is required at the stope base, while the upper portion is filled with uncemented fill or left unfilled (Fig. 2-2b). Another option is to fill the whole stope with cemented backfill (similar to a thick sill mat). With both options, the sill mat serves as a working roof for miners when excavating the underlying stopes.

2.1.2.2 Other variations of cut-and-fill mining

There are several other variations of cut-and-fill mining methods, such as the drift-and-fill mining method (Fig. 2-3a), Avoca mining method (Fig. 2-3b), and postpillar mining method (Fig. 2-3c). In general, cemented or/and uncemented backfill can be used for overhand mining, while cemented backfill must be used for underhand mining if sill pillars are recovered.

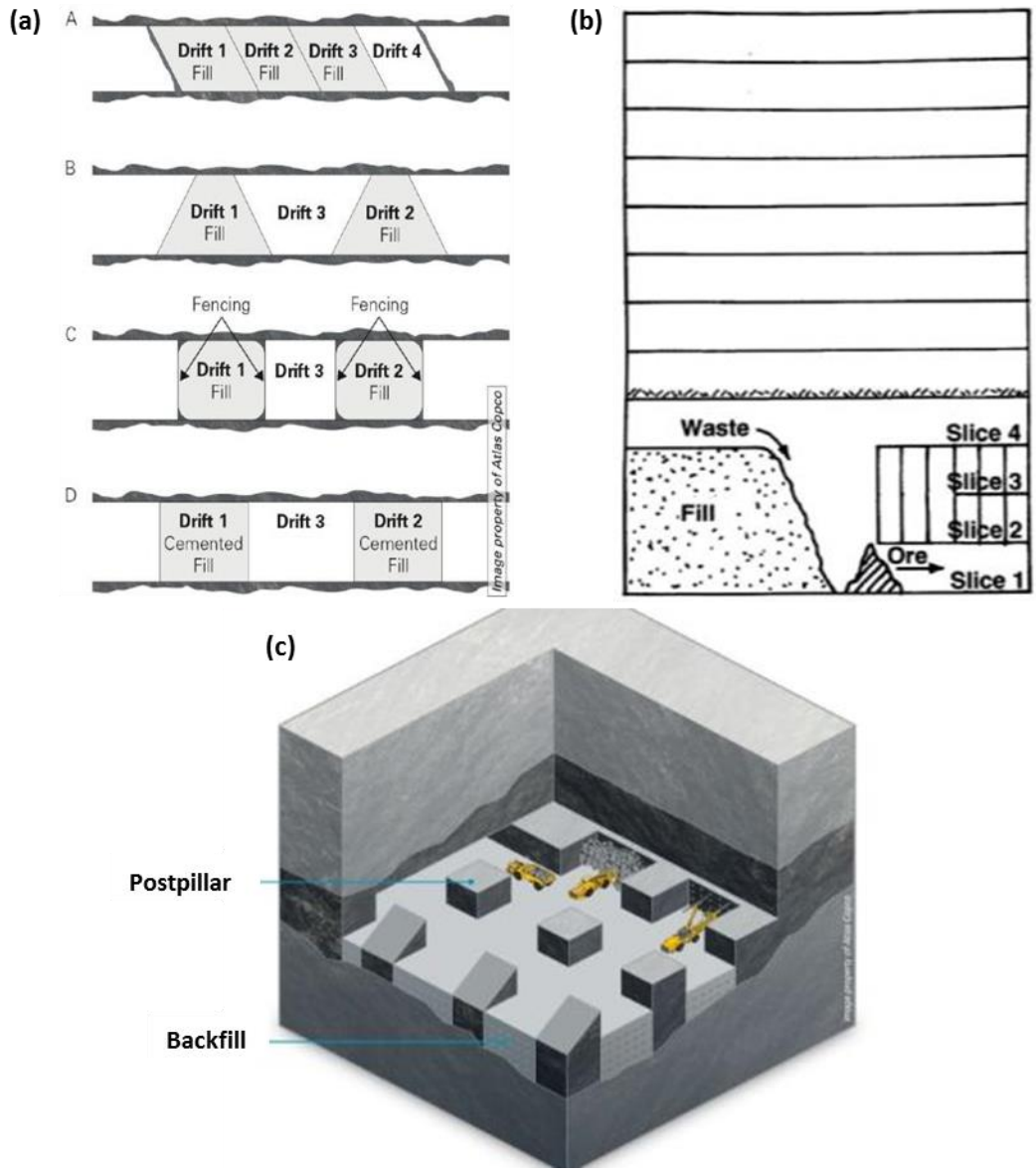

Figure 2-3: Variations of cut-and-fill mining methods: (a) drift-and-fill mining; (b) Avoca mining; (c) postpillar mining (a and c are taken from Atlas Copco 2014; b is taken from Bullock & Hustrulid 2001)

2.1.3 Caving methods

Caving mining methods include sublevel caving, block caving and longwall mining method (Hartman & Britton 1992; Darling 2011). Backfill can be used in the last one but rarely used in the first two ones. The longwall mining is commonly used for tabular and horizontal mineral deposits (e.g., coal seam, potash and trona). During ore extraction, the working area is protected by a hydraulic shield that moves in the direction of extraction.

Usually, the hanging wall behind the working area is allowed to cave to fill the mined-out voids. These voids should be filled when the subsidence is prohibited (e.g., extraction under infrastructures). Backfill is placed or injected into cavity zones behind shields to stabilize the hanging wall and rock mass in some Polish coal mines (Palarski 1994, 2014). Similar mechanized mining technique with backfilling system has been applied in many Chinese coal mines (e.g., Zhang et al. 2012, 2016).

2.1.4 Remarks

The major underground mining methods employing backfill have been briefly reviewed. A variety of mining backfill can be used to satisfy various mining requirements. First of all, it is seen that the selection (types and mechanical properties) of backfill is determined by its functions and engineering goals that are, in turn, largely dependent on the adopted mining methods. Furthermore, the application of backfill can vary from mine to mine even with the same mining method. In all cases, it will be seen in the next section (Section 2.2) that mine backfilling is a complex and integrated process, including fill preparation, transportation, placement, water management, exposures and barricade design. Each individual part deserves carefully engineered design to ensure a successful mining operation. This requires a comprehensive understanding of the geomechanical behavior of the backfill placed in stopes and its interaction with the confining structures (rock walls and barricades).

2.2 Types of mine backfills

The history of backfilling underground mined-out voids probably dates back to the beginning of mining several centuries ago (Potvin et al. 2005). In recent decades, the practice of mine filling has increased significantly worldwide. In general, mine backfill plays the role of ensuring

stability of regional ground around stopes, increasing ore recovery and minimizing ore dilution (Peele 1941; Thomas 1979; Singh & Hedley 1980; Hassani & Archibald 1998; Jung & Biswas 2002; Potvin et al. 2005; Hambley 2011). The surface disposal of mine wastes (i.e., waste rock and tailings) can be reduced by backfilling, which can help prevent the production of acid mine drainage (Aubertin et al. 2002, 2011, 2016; Bussière 2007; Benzaazoua et al. 2008).

A variety of mining backfills have been developed to meet various engineering goals for different mining methods. In general, the most commonly used types of mine backfills can be divided into rockfill, hydraulic fill and paste fill. In this subsection, typical mine backfills are briefly reviewed in terms of typical physical, hydraulic and mechanical properties. Note that the geochemical and microstructural properties of mine backfills (particularly for paste backfill) are not discussed here as they are considered beyond the scope of this work.

2.2.1 Rockfill

Waste rock from mining development or surface quarry has been used to fill underground stopes for a quite long time (e.g., Yu 1989; Dismuke & Diment 1996; Farsangi 1996; Kuganathan 2005a; Potvin et al. 2005; Hambley 2011; Liston 2014; Sainsbury & Sainsbury 2014; Emad et al. 2015a, 2015b). Rockfill (RF) usually refers to waste rock transported and placed in underground stopes. Depending on its applications, RF can be modified by optimizing grain size (such as crushing or adding fine-grained materials) and/or by adding binders (Hassani & Archibald 1998; Kuganathan 2005a).

Rockfill is generally utilized to ensure ground stability by means of passive support at the rock walls. RF has a limited ground support capability and a negligible self-standing height in the absence of binder (Hassani & Archibald 1998). Therefore, RF is usually used when side and base exposures are not required. It may be used as a working floor (top exposure) in some cases.

Cemented (or Consolidated) Rockfill (CRF), with a range between 1-8% (solid weight) binders, is capable of assuring not only ground stability but also active support when exposed during extraction of adjacent stopes (Hassani & Archibald 1998; Liston 2014; Emad et al. 2015a). The binder usually consists of Portland cement, slag and fly ash. The application of CRF at Kidd Creek mine and Meikle mine in Canada is presented in Emad et al. (2015a).

2.2.1.1 Physical properties of rockfill

Fig. 2-4 shows the in-situ rockfill material at Ballarat Gold mine (Fig. 2-4a) and emplaced rockfill at Louvicourt mine (Fig. 2-4b). The hydraulic and mechanical behavior of a rockfill is basically dependent on its physical properties.

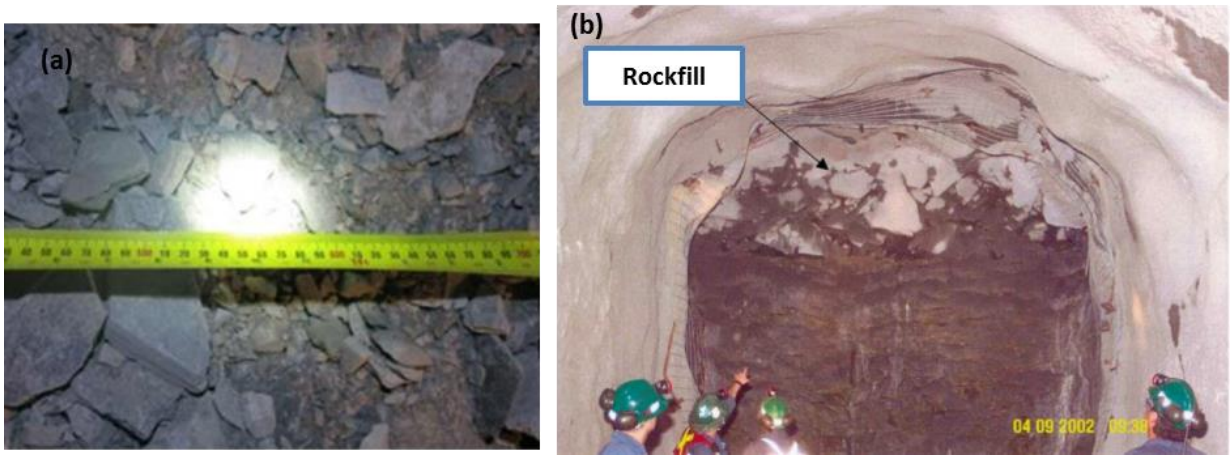

Figure 2-4: In-situ rockfill material (a) at Ballarat Gold mine (Sainsbury & Sainsbury 2014) and (b) at Louvicourt mine (Belem et al. 2013)

The typical angle of repose for RF (waste rock) is close to 37° (± 3°), which may vary with physical characteristics of the waste rock (Farsangi 1996; Aubertin 2013).

The typical particle size used for RF can range from 1 to 100 mm. It should be optimized (graded or modified) to minimize void ratio and maximize in-situ density. Adding binder and fine-grained materials is aimed at increasing the fill strength which can be associated with reduced final void ratio (or porosity). For a given type of rockfill, the fill strength is inversely related with the void ratio (Li & Aubertin 2003).

In concrete industry, it has been empirically found that the most appropriate particle size distribution can be obtained by Talbot grading, which gave the maximum in-situ density. The Talbot grading has been adopted to design the optimal particle size distribution for RF (Kuganathan 2005a). The particle size distribution of different sources of rockfill as well as Talbot grading (with d_{max} = 150 mm) are shown in Fig. 2-5. It is observed that the rock material from quarry may need crushing for CRF production while that from mine development usually has good grading (Kuganathan 2005a). The particle size distribution varies from one operation to another and its optimization remains challenging.

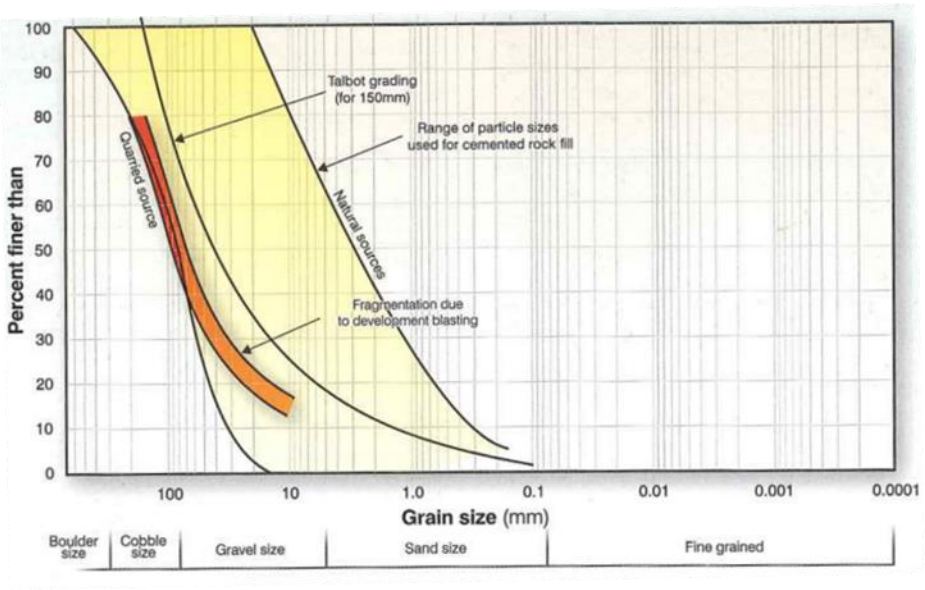

Figure 2-5: Particle size distribution of different sources of rockfill compared with Talbot grading (Potvin et al. 2005)

As RF is placed into a stope by trucks or raises, the different ejection velocity, motion trajectory and settling effects between coarse and fine aggregates produce a fill with different layers (varying from coarse aggregates to fine particles). This is a well-known phenomenon in RF filling operation, called "segregation" (Hassani & Archibald 1998). The degree of segregation depends on the filling method, raise dip and length, aggregate size, stope geometry and free fall height (Yu 1989; Farsangi 1996; Annor 1999). Farsangi (1996) concluded that the key for producing a properly engineered CRF is to minimize the segregation during placement, based on in-situ observations and physical model tests at the Kidd Creek mine. The segregation is also observed in waste rock piles.

2.2.1.2 Mechanical properties of rockfill

RF is cohesionless material. A higher relative density resulting from denser compacting usually causes a higher friction angle. Depending on the relative density, the friction angle of (uncemented) rockfill material may range from 35° to 55° (Kuganathan 2005a). Large-scale tests on waste rock showed that the internal friction angle is in the range of 21° to 62°, with typical values varying between 34° and 45° (Aubertin 2013).

Backfill elastic modulus usually increases with the binder content, as reported by the test results from Pierce et al. (1998). In-situ and laboratory tests done by Yu & Counter (1983) showed that

the elastic modulus of CRF varies from 2.0 to 3.8 GPa. Usually, CRF's elastic modulus is much greater than cemented hydraulic fill and paste fill (Zhu 2002).

Unconfined compressive strength (UCS) tests are the most popular and simple tests to measure the strength of various fills. In general, UCS of RF is close to zero because it is cohesionless material. The UCS of CRF can be much larger by adding binders and fine-grained materials. The in-situ UCS of CRF can go from less than 1MPa to greater than 10 MPa (Hedley 1995; Annor 1999). Laboratory data have shown that the strength of a backfill material is directly proportional to binder content and inversely proportional to porosity (Hedley 1995; Annor 1999). Fig. 2-6 shows some typical unconfined compressive stress-strain curves of CRF with 5% cement (solids weight) performed on specimen from the Ballarat mine in Australia (Sainsbury & Sainsbury 2014). Tests were conducted on 152 mm diameter specimens with height to diameter ratios of 1:1. The axial stress increases somewhat linearly as the strain increases until the peak. At the post-peak stage, the axial stress rapidly decreases with the increase in strain.

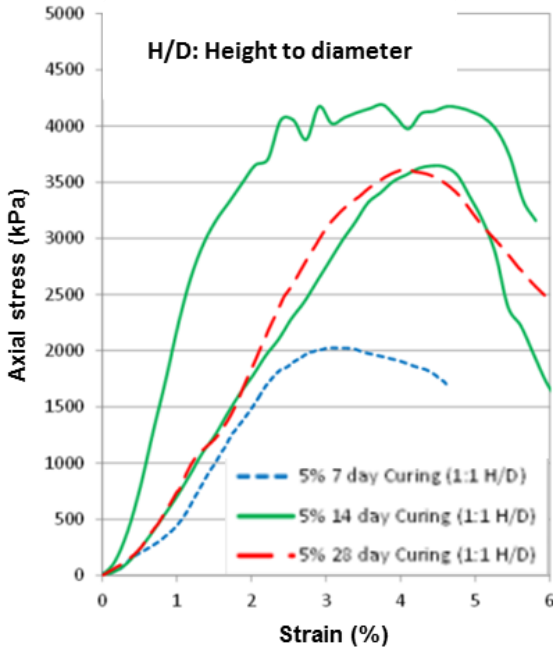

Figure 2-6: Unconfined compressive stress-strain curves of CRF with 5% cement; samples from the Ballarat mine in Australia (Sainsbury & Sainsbury 2014)

2.2.1.3 Hydraulic properties of rockfill

The hydraulic conductivity (also known as coefficient of permeability) represents the average velocity when water flows through the fill mass under constant hydraulic gradient (Potvin et al.

2005). It is affected by particle size distribution, particle shape, void ratio, and so on. It is noted that the hydraulic conductivity mentioned in this work refers to the saturated hydraulic conductivity.

The hydraulic conductivity obtained from infiltration tests on the waste rock pile at Tio mine ranges from 4×10^{-5} to 3×10^{-3} m/s (Lessard 2011). The laboratory column tests conducted by Peregoedova (2012) showed that the hydraulic conductivity of waste rock varies around 10^{-3} m/s. Laboratory and field tests on waste rocks shows that the hydraulic conductivity is usually above 10^{-5} m/s (Aubertin 2013). Since the uncemented rockfill is very similar to waste rock pile, it is reasonably considered that their hydraulic conductivity is in the same range.

2.2.2 Hydraulic fill

Hydraulic fill (HF) has initially been used in some coal mines in US since 1884 (Peele 1941). Its application has quickly spread to different mines around the world (Rahilly 1923; Potvin et al. 2005; Hambley 2011).

HF is defined as low solids content (normally from P = 60% to 75%) slurry, consisting of classified mill tailings and/or natural sand, transported through boreholes and pipelines to underground stopes (Hassani & Archibald 1998; Potvin et al. 2005). HF is typically prepared at solids content around 70% for conventional transportation of settling slurries (Hassani & Archibald 1998; Grice 2001). Due to the hydraulic delivery, it contains a substantial amount of water that drains after placement. Fig. 2-7 shows a schematic diagram of a hydraulic fill stope and a typical stope under filling.

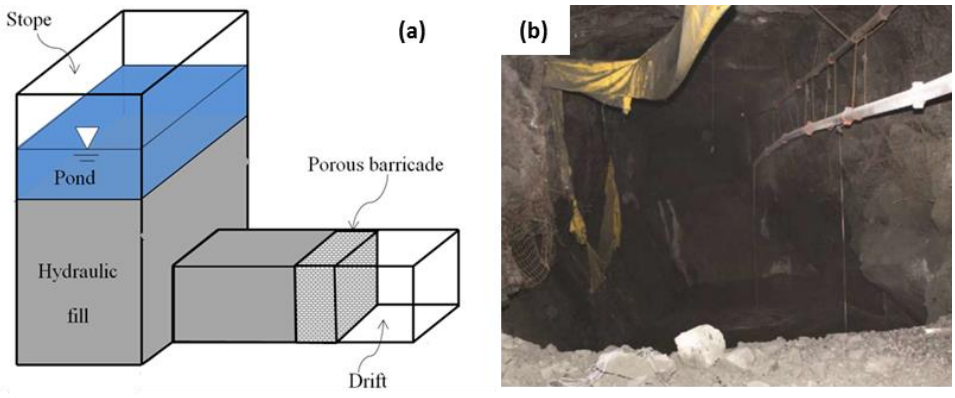

Figure 2-7: (a) Schematic diagram of a hydraulic fill stope with water ponding and a porous barricade (Yang & Li 2016); (b) a stope under filling with CHF (Thompson et al. 2014a)

Based on the source of the fill materials, HF is divided into tailings fill and sandfill. The former uses classified mill tailings, indicating that part of fines have been removed (usually by hydrocyclone) to avoid inadequate drainage, while the latter utilizes sand from natural deposits. In HF, particle size ≤ 10 μm is considered to be the fine fraction. In some cases, two materials are combined. The filtration and dewatering system of HF are detailed in Hassani & Archibald (1998) and Grice (2005).

2.2.2.1 Physical properties of hydraulic fill

For hydraulic fills at 25 Australian mines, Rankine (2005) reported that particles in HF have a relative density ranging from 2.8 to 4.5; the settled fills have a porosity n of 0.37 to 0.48, void ratio e of 0.58 to 0.93 and density index I_D of between 50% and 80%.

Normally, the particle size of HF ranges from 1 to 1000 μm (with an average around 100 μm). Fig. 2-8a shows the particle size distributions of full tailing samples of hard rock from nine Canadian mines. These samples were taken at the mill before deposition in the tailings impoundment (Bussière 2007). Fig. 2-8b shows particle size distributions of typical copper tailings (curve A), cyclone underflow (HF, curve B) and cyclone overflow (fines). The uniformity coefficient C_U defined by the ratio D_{60}/D_{10} can be used to describe the spread of the particle size distribution of HF. The C_U value of full tailing samples can range from 8 to 18 or so (Bussière 2007). For HF, C_U normally varies between 5 and 10 (Kuganathan 2005b), indicating a relatively narrow spread.

The content of fine particles is critical for HF and should be limited to ensure sufficient hydraulic conductivity. For instance, Hassani & Archibald (1998) stated that the content of fines (≤ 10 μm) should normally be less than 20% by weight, while Grice (2001, 2005) stated that fines should be less than 10% by weight. However, it is noted that these limit values may need to be adjusted when applied and should always be used with engineering judgment. In practice, due to the diversity of tailings, infiltration tests on actual fill materials are suggested to determine the mine-specific sizing criteria.

Similar to RF, segregation can occur within HF. Fine particles (including binders) may be driven by the water flow and concentrate in layers, which results in a heterogeneous (anisotropy) mass with strength zoning (Ouellet et al. 1995; Belem et al. 2013; Martic et al. (2014). The low strength layers can become weak and sliding planes if oriented unfavorable or exposed.

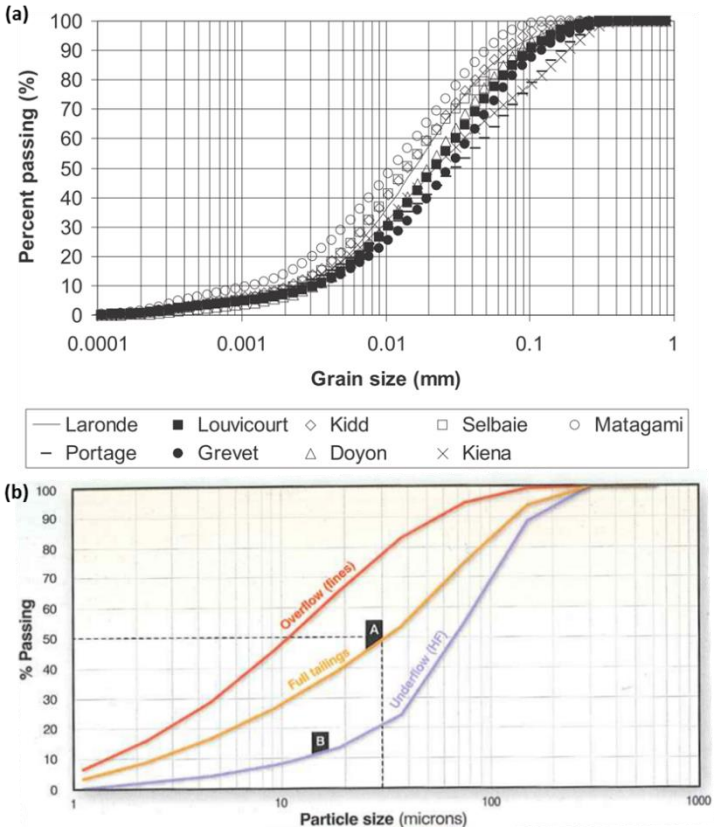

Figure 2-8: Particle size distribution of (a) full tailings sampled at the mill from nine Canadian hard rock mines (Bussière 2007), and (b) full copper tailings, underflow (HF) and overflow (fines) (Potvin et al. 2005)

2.2.2.2 Hydraulic properties of hydraulic fill

The in-situ hydraulic conductivity of uncemented HF usually ranges from 10^{-6} to 10^{-5} m/s (Grice 2001). Rankine (2005) reported that the hydraulic conductivity of Australian hydraulic fills typically ranges from 2.78×10^{-6} to 8.33×10^{-6} m/s.

Before filling, it is necessary to conduct laboratory tests to directly measure the hydraulic conductivity of HF. The constant head infiltration test is widely used to measure the hydraulic conductivity for coarse-grained materials such as HF. The falling head infiltration test is also used for fills with relatively low permeability (Rankine 2005). Alternatively, the hydraulic conductivity of HF can be predicted indirectly from grain size curves by some simple functions based on the well-known Kozeny-Carman equation for granular materials (Aubertin et al. 1996; Mbonimpa et al. 2002; Chapuis & Aubertin 2003). These functions have been used with success for uncemented hydraulic fill or cemented hydraulic fill before the cement hydration starts.

For HF that usually has a high hydraulic conductivity and behaves mostly as sandy material, the dissipation of excess PWPs (associated with self-weight consolidation) is achieved rapidly (during and after filling). A substantial amount of free water then drains out (bleeds) from the barricade. When the drainage through the barricade is not as efficient as that within the fill, a commonly observed phenomenon is the formation of pond (Fig. 2-7a) on the fill top. The water ponding could induce higher PWP and thus endanger the barricade stability (Soderberg & Busch 1985; Yang & Li 2016).

2.2.2.3 Mechanical properties of hydraulic fill

The friction angle of uncemented HF is typically in the range of 35° to 37° and of several cemented hydraulic fills (CHF) varies from about 30º to 48º (Askew et al. 1978; Bloss 1992).

The cohesion of CHF is closely related to the binder type, binder content and curing time. Askew et al. (1978) reported that the cohesion of CHF can climb from 0.1 MPa to 1.5 MPa as the cement content increases from 3 to 17% for 112 days' curing time.

For CHF, Leahy & Cowling (1978) reported a value of 150 MPa for elastic modulus. As shown in Fig. 2-9, the UCS of CHF is positively related to the cement content based on the testing results for several mines in Canada and Australia (Hambley 2011). The mechanical properties of CHF are also largely influenced by segregation, erosion piping, arching effect, etc. The mechanism of erosion piping is reported in Cowling et al. (1988), Grice (1989), Bloss & Chen (1998) and Potvin et al. (2005).

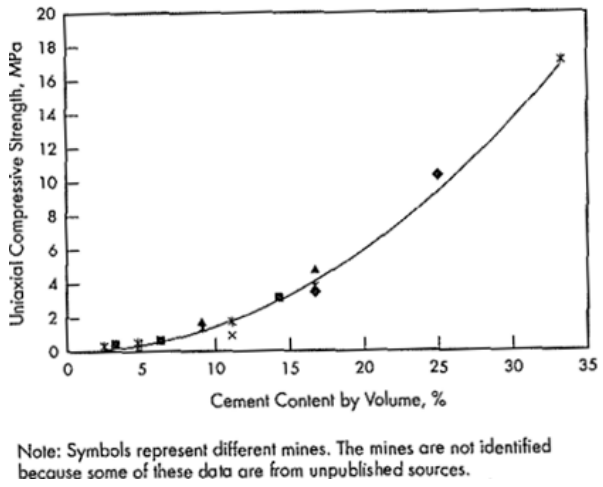

Figure 2-9: UCS of CHF as a function of cement content for several mines in Canada and Australia (Hambley 2011)

2.2.3 Cemented paste backfill

As the tailings become progressively finer due to the improved recovery in mill processing, the disposal of such finer tailings in the form of hydraulic fill is quite limited (Potvin et al. 2005). Cemented paste backfill (CPB) was then developed to solve this problem by using the full tailings as mining backfill (Potvin et al. 2005).

Since the initial use at the Grund mine in Germany in the 1980's, the use of CPB has quickly increased and evolved all over the world. CPB is a high density mixture (75% to 85% solids content) of tailings, binders and water (Hassani & Archibald 1998). The binder can be cement, slag, fly ash, gypsum and so on. For CPB, the particles having size less than 20 μm are usually regarded as fines. There should be a sufficient amount of fines in the fill to produce viscous paste behavior, as shown in Fig. 2-10.

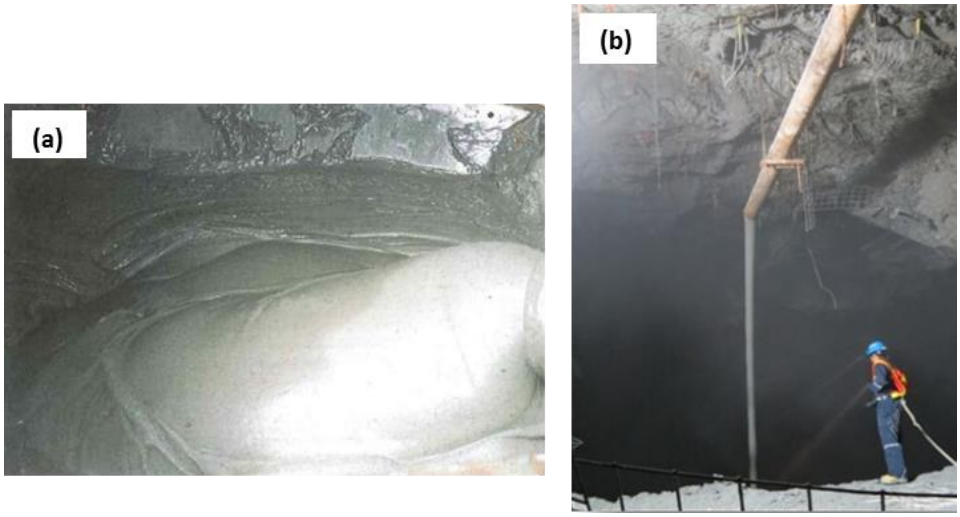

Figure 2-10: Images of (a) lava-like flow of CPB entering a stope (Belem et al. 2013) and (b) a stope under filling with CPB (photo taken at the Goldex mine of Agnico Eagle Mines)

2.2.3.1 Physical properties of CPB

Fig. 2-8a shows the particle size distributions of full tailing samples of hard rock from nine Canadian mines. These samples were taken at the mill before deposition in the tailings impoundment (Bussière 2007). Compared with HF, CPB has a larger uniformity coefficient C_U ranging from 10 to over 20 in some cases due to the use of full tailings (Kuganathan 2005b), which indicates a wider spread and well graded material.

As the content of fines increases, the inter-particle forces dominate in the fill and thereby increasing the viscosity (Potvin et al. 2005). As a rule of thumb, the amount of fines ($\leq$ 20 μm) in CPB should be not less than 15%, by weight (Brackebusch 1994; Potvin et al. 2005). Aref et al. (1992) stated 15% (by weight) fines of minus 45 μm. However, it is again noted that these empirical statements should be used with engineering judgment.

Initially used to measure the workability of concrete, the slump test has been adapted to monitor the paste consistency in the mining industry (Clayton et al. 2003). It is generally believed that the slump of CPB should be less than 230 mm to behave as a non-Newtonian fluid (Potvin et al. 2005). Empirical correlations have been established between slump and yield stress to quickly assess the rheological properties of CPB.

2.2.3.2 Rheological properties of CPB

The transportation of CPB is mainly controlled by its rheological properties. Unlike HF, CPB is classified as a Bingham plastic fluid (similar to fresh concrete; Boger 2002; Potvin et al. 2005; Cooke 2006). For such type of fluid, when an applied shear stress is smaller than its yield shear stress, it has an elastic behavior and the deformation is reversible. Once the applied shear stress exceeds the yield shear stress, the CPB starts to flow as a viscous material with constant (or variable) viscosity.

The yield shear stress is defined as the minimum shear stress to overcome before the fluid is fully mobilized. It is a key parameter for CPB and tailings transportation design. Generally, the yield shear stress of CPB is sensitive to the solids content, water content, content and type of binder, stage of hydration and pore fluid chemistry (Sofra & Boger 2001; Simon & Grabinsky 2013). The correlation between yield shear stress and solids content has been used to predict the pumping energy requirements in pipeline transportation (Sofra & Boger 2001). For CPB, the most commonly used methods for measuring rheological parameters are slump test (e.g., Pashias et al. 1996; Clayton et al. 2003; Boger et al. 2006) and vane tests (e.g., Simon & Grabinsky 2013).

Boger et al. (2006) and Cooke (2006, 2008) indicated that the measured yield stress τ_0 typically ranges from 100 to 800 Pa. Tests performed by Saebimoghaddam (2005) and Simon & Grabinsky (2013) indicated that the yield shear stress of CPB can reach up to 1100 Pa and 1250 Pa, respectively. The viscosity and shear yield stress increase exponentially as the water content of CPB decreases.

2.2.3.3 Hydraulic properties of CPB

Due to the presence of a large amount of fines, the hydraulic conductivity of full tailings in CPB is much lower than that of classified tailings in HF. The hydraulic conductivity of homogenous hard rock tailings and CPB typically ranges from 10^{-8} to 10^{-6} m/s (Aubertin et al. 1996; Bussière 2007; Godbout et al. 2007; Fall et al. 2009).

The falling head infiltration test is usually adopted to directly measure the hydraulic conductivity for materials such as CPB. Besides, the hydraulic conductivity of CPB can be indirectly estimated from practical pedotransfer functions developed for cohesionless materials by Mbonimpa et al. (2002) and Chapuis & Aubertin (2003). Based on the grain size curves, these functions have been used with success for (cemented) paste backfill at early times (i.e., before the cement hydration).

Laboratory tests results have shown that the hydraulic conductivity of CPB is largely affected by many factors such as binder type/proportions, w/c ratio, tailings fineness, sulphate content, the curing time and temperature, stress level and mechanical damage (Godbout et al. 2007; Fall et al. 2009). Larger binder contents and longer curing time can lead to greater reduction in hydraulic conductivity (Belem et al. 2001; Fall et al. 2009). Godbout et al. (2007) and Fall et al. (2009) reported that the largest decrease of the CPB's hydraulic conductivity was observed at the early ages of curing (0-7 days).

CPB has a very low hydraulic conductivity and behaves like a material between a silty and clayey material. The drainage and consolidation process of CPB (comparable to that of clay) takes a much longer time than that of HF. This is why one observes much less water bleeding in stopes backfilled with CPB than with HF. In this case, the geostatic (isostatic) state of CPB can persist at the early time (e.g., Thompson et al. 2012).

2.2.3.4 Mechanical properties of CPB

Similar to CHF, the mechanical properties of CPB are largely decided by the cement content. Hedley (1995) reported that CPB can be very strong, depending on the binder composition, and is capable of developing higher strength compared to CHF.

Fig. 2-11a shows that the UCS of CPB increases as the binder content increases for a given type of binder. It is seen from Fig. 2-11b that the composition of paste mixture plays an important role

on the mechanical properties of CPB (see also Klein & Simon 2006). Experimental data shown in Fig. 2-11 indicate that the CPB shows an elasto-plastic with strain-softening behavior under uniaxial compression (see also Klein & Simon 2006).

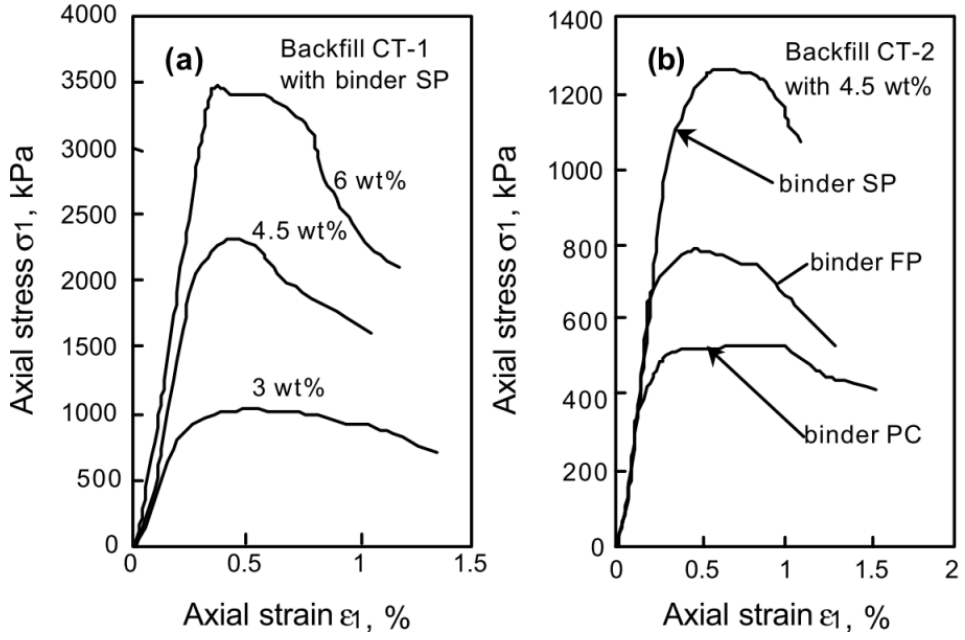

Figure 2-11: Unconfined compressive stress-strain curves of CPB after 112 days of curing for different (a) binder contents and (b) types of binder (Belem et al. 2000)

For CPB, Leahy & Cowling (1978) reported a value of 280 MPa for elastic modulus of CPB. The in-situ tests performed by Barrett & Cowling (1980) showed the elastic modulus of 695 MPa. The elastic modulus of backfill usually increases with the binder content (see Fig. 2-11a).

Laboratory tests conducted with hydration cells revealed that the stress conditions and curing temperature significantly affect the mechanical behaviors of CPB (Helinski et al. 2007; Walske et al. 2016). Walske et al. (2016) reported that the elevated curing temperature could better represent the in-situ curing conditions in terms of the strength development of CPB. Their UCS results showed that the CPB strength increases with the elevated curing temperature and effective stress generation.

2.2.3.5 Rising rate

In practice, a rising rate of 0.2 to 0.4 m/h has been reported depending on the flowrate of the backfill (into stope) and section area of the stope (Thompson et al. 2012). El Mkadmi et al. (2011, 2014) revealed that there is a major influence of the rising rate on the stress state in the stope and

on the pressures acting on barricades. They also indicated that rapid rising rates generate higher PWP and produce larger stresses on the barricade, while slow rising rate, allowing dissipation of excess PWP, leads to increased effective stress and development of arching effect. However, slow rising rate is not favorable because longer waiting time is likely to induce more cost.

2.2.4 Remarks

This subsection recalls the typical physical, hydraulic and mechanical properties of mining backfills. The main properties and behaviors of mining backfills are further summarized in Table 2-1.

Table 2-1: Summary of properties and behaviors of the typical backfills in mine stopes (adapted from Hassani & Archibald 1998)

Properties	Hydraulic Fill	Paste Fill	Rockfill
Placement State	60% to 75% solids (by weight)	75% to 85% solids (by weight)	Dry
Underground Transport System	Borehole/pipeline via gravity	Borehole/pipeline via gravity, can be pumped	Raise, mobile equipment, separate cement system
Binder Application	Cemented or uncemented	Cemented only	Cemented or uncemented
Water to Cement Ratio (w/c)	High w/c ratio, low binder strength	Low to high w/c ratio. Low to high binder strength	Low w/c ratio, high binder strength
Placement Rate	100 to 200 Tonne/hr	50 to 200 Tonne/hr	100 to 400 Tonne/hr
Segregation	Slurry settlement and segregation, low strength development	No segregation	Stockpile and placement segregation, reduced strength and stiffness
Stiffness	Low stiffness	Low or high stiffness	High stiffness if placed correctly
Tight Filling	Cannot tight fill	Easy to tight fill	Difficult to tight fill
Binder Quantity	Requires large quantity of binder	Usually lower quantity of binder required	Moderate binder quantities
Barricades	Expensive	Inexpensive	Not necessary
Water Runoff	Excessive water runoff	Negligible water runoff	No water runoff
Capital Costs	Low capital costs	Higher than for hydraulic fill	Moderate capital costs
Operating Costs	Low distribution costs; lowest cost for an uncemented fill	Lowest cost for a cemented fill	High operating costs

2.3 Barricades

Prior to filling, barricades (also called fill fences or bulkheads) are built in access drifts near drawpoints to prevent in-rush of the initially saturated fills (hydraulic and paste fill), while allowing the drainage of excess water. The barricade usually identifies low pressure and porous structures while the bulkhead usually indicates high pressure and impervious structures (Grice

1998a; Potvin et al. 2005). As drain pipes are commonly used in the impervious structures (i.e., bulkhead), these two terms are sometimes used interchangeably. In this thesis, barricade is used to denote both of them. Usually, the hydraulic conductivity of the barricade should be larger than that of fill to ensure good drainage; otherwise, drainage pipes are used to facilitate the drainage (Potvin et al. 2005). The barricade can take the form of flat or arched with convex towards the stope (Rankine 2005). Fig. 2-12 shows some typical barricades, which are usually made of permeable brick, timber frame, concrete, shorcrete, fibrecrete, or waste rock.

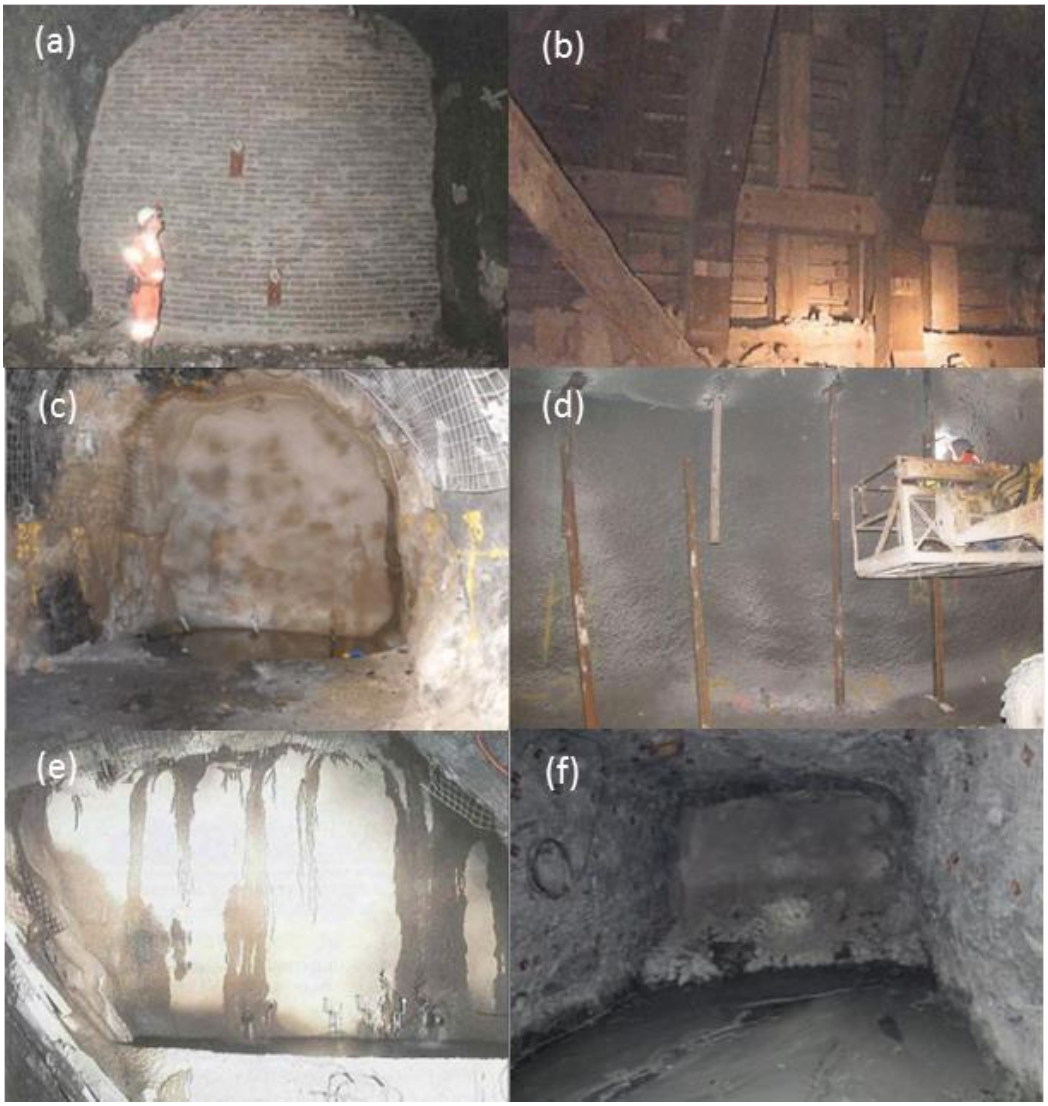

Figure 2-12: Typical barricades made of: (a) arched permeable brick wall ; (b) timber; (c) concrete; (d) shorcrete; (e) fibrecrete; (f) waste rock (a, b & e from Potvin et al. 2005; c & d from Grabinsky 2010; f from personal collection of Li Li)

A number of barricade failures have been reported worldwide (Soderberg & Busch 1985; Bloss & Chen 1998; Grice 1998a, 1998b, 2001; Helinski et al. 2006; Sivakugan et al. 2006a; Revell & Sainsbury 2007a, 2007b; Yumlu & Guresci 2007; Hughes 2008;). Such failures can cause catastrophic results, such as drift flooding, machinery damage and even human casualties. A detailed review of barricade failures can be found in Hughes (2008). Inadequate drainage has been regarded as the main reason for failure in cases of HF. Therefore, a good understanding of the evolution of the PWPs and (total and effective) stresses within HF filled stopes is critical for improving the design of barricades. Yang & Li (2016) have proposed analytical solutions to describe the evolution of the water table and PWP within stopes with submerged HF. This will be presented in Chapter 3.

Barricades are traditionally made of permeable brick walls allowing free drainage (Fig. 2-12a); concrete (Fig. 2-12c) and reinforced shotcrete (Fig. 2-12d) with drain pipes (Sivakugan et al. 2006a; Yumlu & Guresci 2007; Hughes et al. 2010). Alternatively, barricades can be made by waste rock for retaining CPB (Fig. 2-12f). Compared with more traditional methods, the waste rock barricade (WRB) can be easier and faster to implement. It also reduces the surface disposal of mine wastes. Based on Li & Aubertin (2011), Yang et al. (2016a) have proposed an improved analytical solution for designing WRB used to retain CPB (presented in Chapter 4).

2.4 Analytical solutions for the design of backfilled stopes and barricades

Previous sections have shown that evaluating the stress state within backfilled stopes and on barricade is a key issue for their design. This task can be achieved by means of analytical solutions, numerical modelling and in-situ measurements. Each method has its advantages and limitations.

Traditionally, analytical solutions are closed-form expressions that can be solved explicitly by hand calculations. Some mathematical expressions that can be solved by spreadsheet software are also considered as analytical solutions. Many expressions that contain differential or/and integral equations cannot be solved without using numerical tools. But such expressions can be the base of analytical equations. Compared to numerical simulations, analytical solutions are rapid and low cost tools for engineers. Analytical solutions are useful for preliminary designs and the validation of some numerical results. But it is noted that the analytical solutions are more suitable for simple cases, since they are usually based on simplified assumptions with strong limitations.

In the following, existing analytical solutions proposed for estimating the stress state in backfilled stopes and on barricades are presented. Analytical solutions for designing the cemented backfill with a vertical exposure are also presented.

2.4.1 Classical arching status in civil engineering

When a backfill is placed in a confining stiff structure, the backfill tends to settle down under its weight while the confining walls tend to hold the backfill in place by shear resistance. This shear resistance results in a load transfer from the backfill to the abutment. Consequently, the stresses in the backfill are smaller than the overburden stresses. This phenomenon is known as aching effect. It has been firstly analyzed by Janssen (1895) for estimating loads in silos. Marston (1930) made use of the arching theory for calculating the load exercised by backfill on conduits buried in trenches. In this subsection, the classical arching theory and the main assumptions are revisited.

The main general assumptions of arching solutions are summarized as follows:

- The limit equilibrium of a thin horizontal (or inclined or circular) fill element is used to construct the differential equation;
- The backfill is assumed to be at a critical state along walls due to the use of limit equilibrium with the Coulomb criterion;
- It is assumed that there is a sufficient fill movement to mobilize the full shearing strength along the walls;
- It is assumed that vertical stresses distribute uniformly across the stope width and along the drift height;
- The horizontal effective stress σ'_h is related to the vertical effective stress σ'_v through the lateral earth pressure coefficient K, i.e., $\sigma'_h = K\sigma'_v$;
- The earth pressure coefficient K is assumed to be constant within the backfill.

2.4.1.1 Arching solution of Janssen (1895)

Janssen (1895) proposed an arching theory to assess the stress state in silos containing cohesionless fills (Jakobson 1958). The vertical effective stresses σ'_v (kPa) within the fill in a cylindrical silo can be expressed as (cited by Jakobson 1958):

$$\sigma'_v = \frac{\gamma}{K \tan\delta}\frac{A}{U}\left[1 - exp\left(-K\ tan\,\delta\,\frac{U}{A}z\right)\right] \quad (2\text{-}1)$$

where δ (º) is the friction angle of interface between particles and silo walls; U (m) and A (m^2) are the silo's circumference and sectional area; γ (kN/m^3) is the unit weight of fills.

The value of coefficient K is assumed to be constant along the silo. Janssen (1895) did not measure K but its value was calibrated to fit experiments (Pipatpongsa & Ohta 2009).

2.4.1.2 Arching solution of Marston (1930)

In geotechnical engineering, Marston (1930) was the pioneer to adopt the arching theory for estimating the loads of cohesionless backfill on buried conduits in trenches (Fig. 2-13; see also Handy 1985; McCarthy 1988).

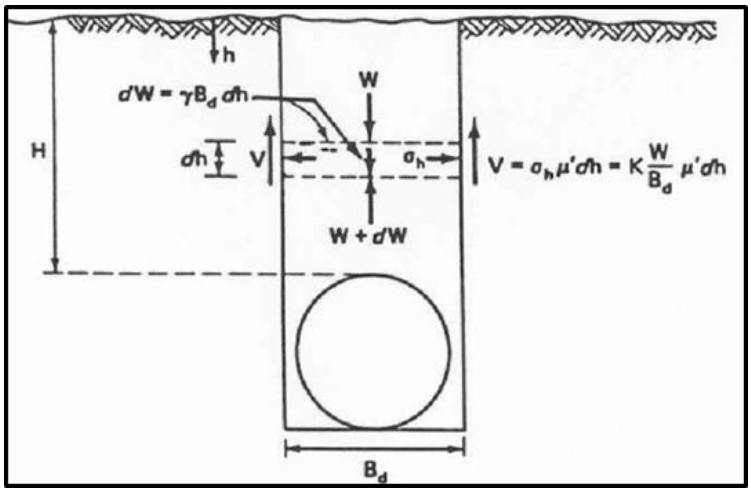

Figure 2-13: The differential element used in the theory of Marston & Anderson (1913; from McCarthy 1988)

Experimental tests (Marston & Anderson 1913; Marston 1930) showed that the loads applied on conduits in the trenches are lower than those calculated by the overburden of fills, due to arching effect between fill and trench walls. Based on the simplified model shown in Fig. 2.13, Marston's solution is given by:

$$\sigma'_v = \frac{B_d\gamma}{2K_a tan\delta}\left[1 - exp\left(-\frac{2K_a tan\delta}{B_d}h\right)\right] \quad (2\text{-}2)$$

where B_d (m) is the width of the trench; K_a is the Rankine's active earth pressure coefficient; δ (º) is the friction angle of fill-wall interfaces [between $1/3\phi'$ and $2/3\phi'$; ϕ' (º) is the internal effective friction angle of the fill].

Marston (1930) suggested Rankine's active earth pressure coefficient K_a in the formulation, but this may be true when the horizontal and vertical stresses are principle stresses (Ladanyi & Hoyaux 1969; Handy 1985). Since there is friction between the fills and trench walls, the use of K_a is not rigorous within the whole trench. Also, fill cohesion was not taken into account in Marston's approach.

2.4.1.3 Terzaghi (1943) solution

Terzaghi (1936a) conducted laboratory experiments to assess the well-known "trap door" problem (Fig. 2-14a), and the arching theory in ideal soils was reported in Terzaghi (1943). To simplify the problem, Terzaghi (1943) assumed vertical sliding surfaces (*ae* and *bf* in Fig. 2-14a) in the sand instead of the true curved sliding surfaces (*ac* and *bd* in Fig. 2-14a). He also stated that the results obtained with vertical sliding surfaces are fairly compatible with the experimental data. Thus, the problem became similar as arching in silos and trenches as mentioned above.

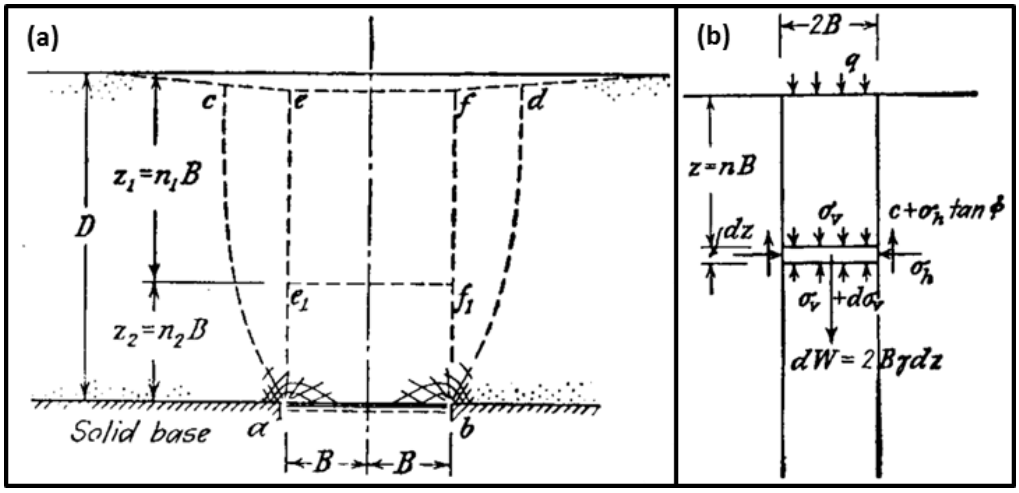

Figure 2-14: (a) Failure caused by the downward movement of the yielding strip (*ab*) at the base of a sand layer; (b) Diagram illustrating assumptions on which computation of pressure in sand between two vertical surfaces of sliding is based (Terzaghi 1943)

Based on the simplified model shown in Fig. 2-14b, Terzaghi (1943) gave the following expression:

$$\sigma'_v = \frac{B\gamma - c}{K\tan\phi'}\left(1 - e^{-K\tan\phi'\frac{z}{B}}\right) + qe^{-K\tan\phi'\frac{z}{B}} \quad (2\text{-}3)$$

where c (kPa) is the fill cohesion; the value of δ is taken as that of ϕ'; q (kPa) is the surface surcharge; z (m) is the depth from the top surface; B (m) is half the width of the opening.

Terzaghi (1943) assumed K as an empirical constant in the soil. Experimental tests performed by Terzaghi (1936b) have indicated that the K value increases from about 1 immediately above the centerline of the yielding strip up to a peak value (≈ 1.5) at an elevation of about $2B$ above the centerline. Although originating from the cohesionless sand, Terzaghi (1943) included the effect of cohesion into his formulations without any explanation. He also stated that the assumption of uniform distribution of vertical stress on horizontal planes can be used for a rough estimate without significant errors.

2.4.2 Stress estimate in backfilled stopes

In mining engineering, traditionally, the vertical ($\sigma'_v = \gamma h$) and horizontal effective stresses ($\sigma'_h = K\sigma'_v$) at any depth h (m) in the backfill are commonly based on the overburden method. In general, the overburden method would lead to an over-conservative design for narrow vertical mine fill stopes where arching effect is well developed. However, the overburden method is applicable to wide vertical stopes with smooth walls where the arching effect could be neglected. In addition, the arching effect may disappear due to blasting, but this aspect hasn't been checked.

Alternatively, the convergence-confinement method utilizes the ground response curves (Fig. 136 in Hoek & Brown 1980) to develop the force-displacement relationships between backfill and rock mass convergence (cited by Aubertin et al. 2003). This method considers the pressure increase within backfill due to wall convergence, in the case of backfill progressively placed during excavation (e.g., C&F mining). But the arching effect along the rock walls is neglected (e.g., Aubertin et al. 2003; James et al. 2004).

As the arching effect results in a significant stress reduction in narrow backfilled stopes, both the overburden method and convergence-confinement method could be overly conservative. In the past few decades, the arching effect in backfilled mine stopes has been intensively studied. In the following, the analytical solutions and their extensions based on classic arching theories will be presented.

2.4.2.1 Arching solutions for backfill placed in stopes

Askew et al. (1978)

Askew et al. (1978) applied Terzaghi's arching solution to minefill stope as follows:

$$\sigma'_v = \frac{B\gamma - c_i}{K \tan \phi'} \left(1 - e^{-K \tan \phi' \frac{z}{B}}\right) \quad (2\text{-}4)$$

where c_i (kPa) is the cohesion of fill-wall interface (not necessarily the fill cohesion).

The intent of Askew et al. (1978) was to develop a procedure for calculating the required cohesion of side-exposed backfill. Eq. 2-4 was used arbitrarily to estimate the backfill stress after exposure. They reported that the value of *K* may vary from point to point due to stress state, anisotropic fill properties and segregation.

Aubertin and co-workers

Aubertin (1999) and Aubertin et al. (2003) modified the Marston solution to assess the stress state in narrow vertical mine stopes backfilled with cohesionless fills. The vertical stress in backfilled stopes can be expressed as:

$$\sigma'_v = \frac{B\gamma}{2\,K \tan \delta} \left[1 - exp\left(-\frac{2K \tan \delta}{B} h\right)\right] \quad (2\text{-}5)$$

where δ (= δ'; º) is the effective friction angle of the fill-wall interface.

The angle δ is taken as the effective friction angle of the backfill ϕ' (e.g., Terzaghi 1943). This is based on the assumption that the failure (yielding) occurs in the fill because the irregular rock surface due to blasting is usually rough and stronger than fill. Depending on the relative movement of stope walls and backfill, the active, passive or at-rest pressure coefficients may be used for *K*.

2.4.2.2 Extension to 3D stopes

The above-mentioned analytical solutions all deal with 2D (plane strain) conditions with two long identical side walls. This may be a good approximation when the structure has a dimension that is much larger than the other two. However, such solutions may be incomplete when the backfilled opening has a limited length or when the walls have different characteristics (Li et al. 2005).

Winch (1999) solution

Winch (1999) extended the Terzaghi solution to investigate the stress distribution in a three-dimensional backfilled stope (rectangular prism). The vertical effective stress σ'_{vT} (kPa) at depth *h* (m) in the fill mass is given by:

$$\sigma'_{vT} = \frac{\frac{B\,L\,\gamma}{R(L+B)} - 2c}{2\,K\tan\phi'}\left[1 - e^{-\frac{2R(B+L)}{BL}K\tan\phi'(h-h_0)}\right] + \sigma'_{v0}e^{-\frac{2R(B+L)}{BL}K\tan\phi'(h-h_0)} \quad (2\text{-}6)$$

where L = stope length (m); h_0 = height of fill (equivalent to a surcharge) at which arching starts to develop (m); σ'_{v0} = vertical normal stress (kPa) at $h = h_0$; R = the proportion of active wall length, as the ratio of active length to total wall length of the stope.

Li et al. (2005) solution

Based on the Marston solution, Li et al. (2005) developed a general 3D solution for estimating earth pressures in vertical narrow backfilled openings with walls having different interface properties (Fig. 2-15). The cohesion of the backfill and fill-wall interface can be taken into account. This general 3D solution can be used to evaluate the stress distribution in backfilled mine stopes and is given by:

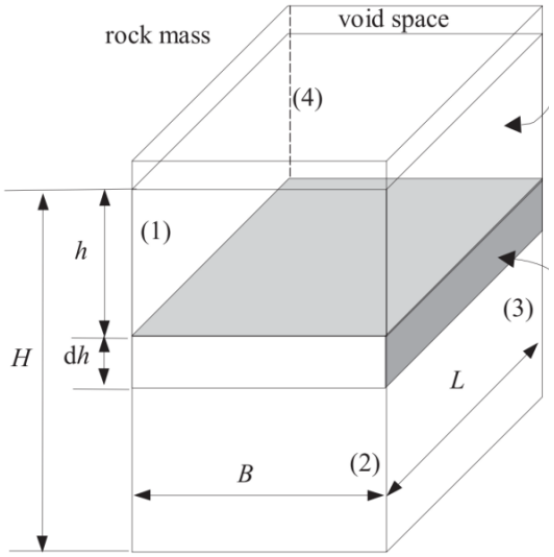

Figure 2-15: A vertical backfilled opening with acting forces on an isolated layer element (Li et al. 2005)

$$\sigma'_{vh} = \frac{\gamma - (\kappa_{13}2B^{-1} + \kappa_{24}L^{-1})}{(\lambda_{13}B^{-1} + \lambda_{24}L^{-1})}\left[1 - exp\left(-h\,(\lambda_{13}B^{-1} + \lambda_{24}L^{-1})\right)\right] \quad (2\text{-}7a)$$

$$\sigma'_{hhi} = K_i\sigma'_{vh} + 2c\tan\alpha_i \quad (2\text{-}7b)$$

$$\text{with } \lambda_{13} = K_1\tan\delta_1 + K_3\tan\delta_3;\ \lambda_{24} = K_2\tan\delta_2 + K_4\tan\delta_4 \quad (2\text{-}7c)$$

$$\kappa_{13} = c_1 + c_3 + 2c\,(\tan\alpha_1\tan\delta_1 + \tan\alpha_3\tan\delta_3) \quad (2\text{-}7d)$$

$$\kappa_{24} = c_2 + c_4 + 2c\,(\tan\alpha_2\tan\delta_2 + \tan\alpha_4\tan\delta_4) \quad (2\text{-}7e)$$

where δ_i and c_i (i = 1-4) are the friction angle (º) and cohesion (kPa) of the ith fill-wall interface; K_i is the earth pressure coefficient when cohesion is zero; its value is expected to be between the at-rest K_0 and active K_a states (for fixed walls); α_i (º) is the fully drained backfill state angle.

The failure is assumed to occur in the fill rather than directly along the fill-wall interface, because the irregular rock surface due to blasting is usually rough and stronger than backfill (hence $\delta_i = \phi'$). Li et al. (2005) showed that the 2D solutions tend to underestimate the arching effect compared to the 3D solutions.

Pirapakaran & Sivagukan (2007a) solution

Based on the Marston solution, Pirapakaran & Sivakugan (2007a) proposed a 3D solution for assessing earth pressures in vertical stopes (rectangular, square or circular) filled with hydraulic fill (HF; no cohesion). It was assumed that the stope walls have inditical properties and behave the same way. The vertical stress can be expressed in the following equation for a rectangular stope:

$$\sigma'_v = \frac{L\gamma}{2K\tan\delta}\left(\frac{B}{B+L}\right)\left[1 - e^{\left(-2\frac{B+L}{BL}K\tan\delta\right)}\right] \quad (2\text{-}8)$$

Eq. 2-8 can be considered as a special case of Li et al (2005) solution when four stope walls are identical and react in the same manner with cohesionless fills. Pirapakaran & Sivakugan (2007a) suggested that the wall movement is very small because the stiffness of rock is about two orders of magnitude larger than that of backfill. Thus, the backfill was assumed to be at-rest state K_0. For HF, they also suggested an interface friction angle equal to 2/3 ϕ' from geotechnical consideration during loose backfilling. Coulthard & Dight (1979) gave a 3D solution similar to Eq. 2-8 but including the backfill cohesion.

2.4.2.3 Extension to inclined stopes

The solutions presented above are only applicable to vertical or subvertical stopes when the stresses on each side have about the same magnitude (e.g., Knutsson 1981). For an inclined silo, Jahns & Brauner (1960, via Knutsson 1981) reported that the deviation from the classical theory is less than 10% if the inclination (to the vertical) is less than 30°. By using the same equation, Knutsson (1981) found that the maximum error is less than 6% for a stope inclined at 23°. However, Li & Aubertin (2009e) suggested that the Aubertin et al. (2003) solution can be applied to assess the vertical and horizontal stresses of an inclined stope with an inclination less than 10°

(to the vertical); a stope inclination of more than 10° would bring a significant difference when compared to the vertical stope. Analytical solutions for inclined stopes are briefly reviewed and discussed.

Blight (1984) solution

Based on the Marston solution, Blight (1984) considered the inclined stope walls and PWP. Firstly, the two inclined fill-wall interfaces are assumed to have the same compressive stress and shear stress as shown in Fig. 2-16. Secondly, it was assumed that the two stope walls are parallel and have the same properties and behave in the same manner. Thirdly, during the placement of backfill and while the fill is draining after placement, the PWP u is represented by the linear relationship $u = u_0 + B'\sigma_z$ (u_0 is the hydrostatic pressure and σ_z is the total stress of backfill), where $B' = 1$ represents the geostatic state of the backfill at short-term condition and $B' = 0$ indicates the hydrostatic state of the backfill at long-term condition when the excess PWP is completely dissipated (i.e., $u = u_0$). This allows the consideration of the dissipation of excess PWP.

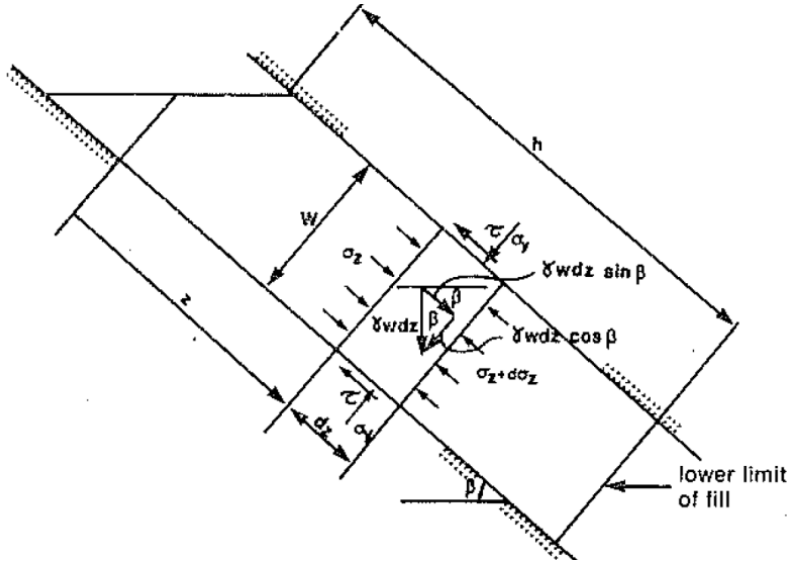

Figure 2-16: Basis for calculating stresses in column of fill (Blight 1984)

Considering the equilibrium of the fill element in the z direction (Fig. 2-16), the distribution of vertical and lateral total stresses in an inclined column of fill is given by:

$$\sigma_z = \frac{w}{2\,K\tan\phi'(1-B')}\left[\gamma\sin\beta - \frac{2}{w}(c' - u_0 K\tan\phi')\right]\left(1 - e^{-\frac{2\,K\tan\phi'(1-B')}{w}z}\right) \quad (2\text{-}9a)$$

$$\sigma_y = K(\sigma_z - u) + u \tag{2-9b}$$

where β (°) is the inclination angle (to the horizontal) of the stope; w (m) is the stope width; c' (kPa) is the effective cohesion of the backfill.

It is noted that the vertical and lateral total stresses defined by Blight (1984) are actually the total stresses in the z direction and the stresses normal to that, respectively. According to Blight (1984), the fill is normally consolidated, so K could be approximated by Jaky's expression $K_0 = (1 - \sin \phi')$ for loose granular soil backfill or by the Reimbert expression $K_0 = (45° - \phi'/2) / (45° + \phi'/2)$. If the shear strength is fully developed, K could be approximated by the expression given by Krynine (1945) for rough vertical walls:

$$K_{Krynine} = \frac{1}{1 + 2\tan^2 \phi'} = \frac{1 - \sin^2 \phi'}{1 + \sin^2 \phi'} \tag{2-10}$$

The non-horizontal differential element, perpendicular to the walls, would result in less accurate stress estimate for backfill close to the surface.

Caceres (2005) solution

Caceres (2005) solution is based on the Marston solution but with inclined stope walls. He assumed that the fill-wall interfaces have the same compressive and shear stresses (Fig. 2-17), and the parallel stope walls have the same properties and behave in the same way (e.g., Blight 1984). The vertical stress of fills in a stope is given by:

$$\sigma'_v = \frac{\gamma B \sin^2 \beta}{2K \tan \phi'} \left[1 - exp\left(-\frac{2K \tan \phi'}{B \sin^2 \beta} h\right)\right] \tag{2-11}$$

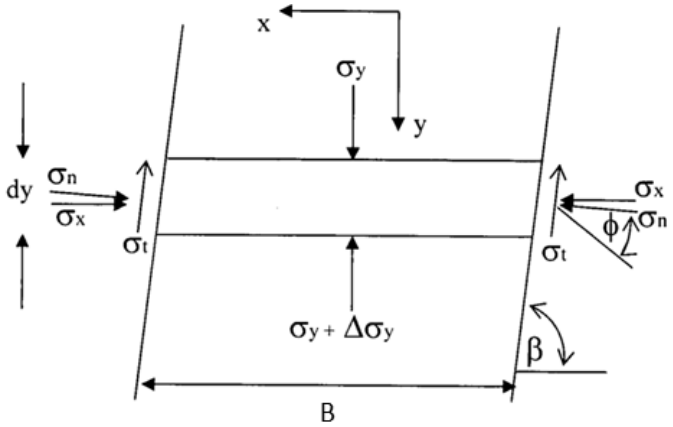

Figure 2-17: Differential element in an inclined stope (adapted from Caceres 2005)

Numerical simulations conducted by Caceres (2005) revealed that the value of K can be represented by a best fitting curve (between K_a and K_0):

$$K = 1.4\ \sin^2\phi' - 2\ \sin\phi' + 1 \tag{2-12}$$

Eq. 2-12 is deemed only valid for cohesionless fill with $\phi' \leq 40°$. Caceres (2005) used Eq. 2-12 to calculate the K value in Eq. 2-11 that is developed for inclined stopes. However, Caceres (2005) did not mention if Eq. 2-12 is based on numerical results obtained with vertical or inclined stopes.

It is worth mentioning that Eq. 2-11 contains some errors. The initial differential equation (the equilibrium of the fill element in y direction; Fig. 2-17) of Caceres (2005) solution was given as follows:

$$B\sigma_y - B\left(\sigma_y + d\sigma_y\right) - \frac{2\sigma_t dy}{\sin\beta} + \gamma B dy = 0 \tag{2-13a}$$

The third term $\frac{2\sigma_t dy}{\sin\beta}$ should be $2\sigma_t dy$ instead and the correct equation should be expressed as follows, as indicated by Ting et al. (2011):

$$B\sigma_y - B\left(\sigma_y + d\sigma_y\right) - 2\sigma_t dy + \gamma B dy = 0 \tag{2-13b}$$

So the corrected Caceres (2005) solution should be expressed as follows:

$$\sigma'_v = \frac{\gamma B \sin\beta}{2K\tan\phi'}\left[1 - exp\left(-\frac{2K\tan\phi'}{B\sin\beta}y\right)\right] \tag{2-14}$$

During the formulation development, $\sigma_t = \sigma_n\ tan\ \phi'$ and $\sigma_n = \sigma_x\ /\ sin\ \beta$ (Fig. 2-17) are used by Caceres to substitute shear stress σ_t with horizontal stress σ_x in Eq. 2-13. The latter equation was subsequently improved by Ting et al. (2011) using more rigorous relationship.

Ting et al. (2011) solution

Using some of the same assumptions as Blight (1984) and Caceres (2005), Ting et al. (2011) proposed an analytical solution to evaluate the pressures in minefill stopes with inclined parallel walls (Fig. 2-18).

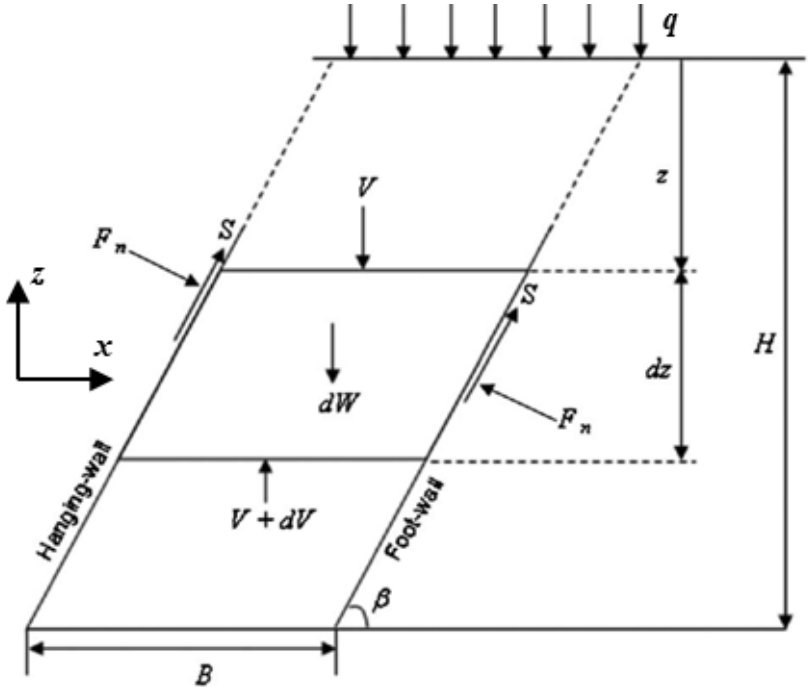

Figure 2-18: Schematic diagram of an inclined stope (Ting et al. 2011)

The shear stresses along the interfaces of the backfill along the hanging wall (HW) and footwall (FW) are taken to be identical. For a cohesive fill with a surcharge q, Ting et al. (2011) solution is expressed as:

$$\sigma'_v = \frac{\gamma B - 2c(1+\sin 2\beta \tan\delta)}{2\,K_\beta \tan\delta}\left[1 - exp\left(-2\,K_\beta \frac{z}{B}\tan\delta\right)\right] + q\ exp\left(-2\,K_\beta \frac{z}{B}\tan\delta\right) \quad (2\text{-}15a)$$

$$K_\beta = \left(\frac{1+K}{2} + \frac{1-K}{2}\cos 2\beta\ + K\ \tan\delta \sin 2\beta\right) \quad (2\text{-}15b)$$

where the interface friction angle δ = 2/3 ϕ'; K_β is the modified earth pressure coefficient for inclined stopes, and the K value is taken as the Jaky's at-rest earth pressure coefficient K_0; c = backfill cohesion (kPa); q = surcharge (kPa).

The initial differential equation of Ting et al. (2011) is essentially the same as that of the corrected Caceres (2005) solution (Eq. 2-13b). As mentioned previously, the relationship between the horizontal stress σ_x and normal stress σ_n along the fill-wall interface (shear surface) is represented more rigorously by Ting et al. (2011) than by Caceres (2005):

$$\sigma_n = \frac{\sigma_z + \sigma_x}{2} + \frac{\sigma_z - \sigma_x}{2}\cos 2\beta + \tau_{zx}\sin 2\beta \quad (2\text{-}16)$$

Ting et al. (2011) reported that the vertical stress decreases as the stope inclination β increases. This reduction is mostly because part of backfill is supported by the FW in inclined stopes. For a stope inclined at 30°, the stresses predicted by Ting et al. solution are significantly less than that predicted by the solution for vertical stopes. Therefore, the solution for vertical stopes is not suggested.

Based on Eq. 2-15b, Sobhi et al. (2016) proposed the following expression to represent the earth pressure coefficient *K* along the centerline of inclined stopes:

$$K_\beta = \frac{1+K_a}{2} + \frac{1-K_a}{2}\cos 2\beta \tag{2-17}$$

Sobhi et al. (2016) showed that Eq. 2-17 agrees well with the *K* value (along the vertical centerline) obtained from numerical simulations for inclinations from 50° to 90°. These numerical simulations were conducted with independent values of internal friction angle ϕ' and Poisson's ratio v of the backfill.

Ting et al. (2014) extended Ting et al. (2011) solution to assess the stress state in minefill stopes with non-parallel inclined walls leaning to the same side. They showed that the stress state in a backfilled stope can significantly vary due to different wall inclinations.

Singh et al. (2011) solution

Singh et al. (2011) proposed a solution for the stresses in an inclined stope using a circular arc element for the principal stresses. For a cohesive fill with surcharge, the major principle stress σ_1 is given by:

$$\sigma'_1 = \frac{\gamma\,\delta\,B\sin^2\alpha\ \operatorname{cosec}\delta - 2c}{2(\sin^2\delta + K\cos^2\delta)\tan\delta}\left[1 - exp\left(-\frac{8(\sin^2\delta + K\cos^2\delta)\tan\delta\sin\delta}{B[2(1+K)\delta-(1-K)\sin 2\delta\cos 2\alpha]\sin^3\alpha}z\right)\right] + \sigma'_0 exp\left(-\frac{8(\sin^2\delta + K\cos^2\delta)\tan\delta\sin\delta}{B[2(1+K)\delta-(1-K)\sin 2\delta\cos 2\alpha]\sin^3\alpha}z\right) \tag{2-18}$$

where σ'_0 (kPa) is the surcharge on the backfill surface; the stope walls are inclined to the horizontal at an angle α (°).

Numerical simulations reported in Li et al. (2003) indicated that the assumption of a uniform horizontal stress distribution across the stope width could be acceptable, but the vertical stress is typically not constant along the width.

Jahanbakhshzadeh et al. (2016a) solution

Jahanbakhshzadeh et al. (2016a) considered the effect of the geometrical factors, such as the horizontal position *l*, vertical position *h* and wall angle *β*, on the stress state in 2D stopes with inclined walls. Based on the solutions of Marston (1930) and Caceres (2005), they proposed the following expressions to estimate the vertical and horizontal stresses:

$$\sigma'_{vh} = \frac{\gamma B \sin\beta}{2K_\beta \tan\phi'}\left[1 - exp\left(-\frac{2K_\beta \tan\phi'}{B\sin\beta}h\right)\right] \quad (2\text{-}19a)$$

$$\sigma'_{hh} = K_\beta \sigma'_{vh} \quad (2\text{-}19b)$$

where K_β is the modified earth pressure coefficient for inclined stopes based on Rankine's earth pressure coefficient K_a; its value is given by

$$K_\beta = K_a \times f_h \times f_w \quad (2\text{-}20)$$

$$\text{with } f_w = 1 + 3\tan\phi\cos\left(\beta - 10^\circ\right)\times\left(1 - l/B\right)^4;\ f_h = \left(1+\cos\beta\right) - \left(h\tan\phi\cos^2\beta/H\right) \quad (2\text{-}21)$$

Jahanbakhshzadeh et al. (2016a) showed that Eq. (2-20) and Eq. (2-17) proposed by Sobhi et al. (2016) are close to each other, but with different trends (curvatures). An alternative closed-form solution based on the Coulomb active earth pressure coefficient was also proposed by Jahanbakhshzadeh et al. (2016b).

Jahanbakhshzadeh et al. (2016c) solution

Jahanbakhshzadeh et al. (2016c) further extended their 2D solution to the following 3D solution by including the third dimension *L* of stopes with inclined walls:

$$\sigma'_{zz} = \frac{\gamma \sin\beta}{2(B^{-1}+L^{-1})K_\beta \tan\phi'}\left[1 - exp\left(-\frac{2(B^{-1}+L^{-1})K_\beta \tan\phi'}{\sin\beta}h\right)\right] \quad (2\text{-}22)$$

The horizontal effective stresses ($\sigma'_{xx} = \sigma'_{yy}$) are estimated from the vertical stresses times the modified earth pressure coefficient K_β (expressed as Eq. 2-17) for inclined stopes.

2.4.2.4 Extension to consider pore water pressures

The above-mentioned solutions (except Blight 1984) consider dry backfill condition where the effect of pore water pressure (PWP) is not involved. However, the effect of water (in terms of

effective stress) can have a significant effect on the state of stress in the cases of hydraulic and paste fill.

Li & Aubertin (2009a) solution

Li & Aubertin (2009a) investigated the effect of water on the stress state in stopes with cohesionless backfill. Their solution was an extension of the Marston solution with considering the PWP under hydrostatic equilibrium state, which differs from that of Blight (1984) which included a parameter (B') to consider the dissipation of excess PWP. Fig. 2-19 shows a backfill stope that is partially submerged.

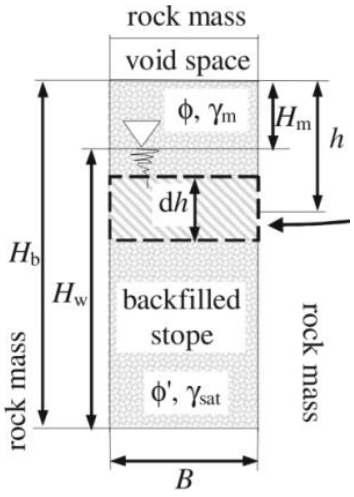

Figure 2-19: A vertical backfilled stope with partially submerged backfill (Li & Aubertin 2009a)

For the area above the water table, Aubertin et al. (2003) solution applies since $\sigma_v = \sigma_v'$ and $\sigma_h = \sigma_h'$ (i.e., u = 0). For the area below the water table ($h > H_m$), the effective stresses can be expressed as:

$$\sigma_v' = \frac{B\gamma_{sub}}{2\,K_s \tan\phi'}\left[1 - e^{\left(-\frac{2\,K_s(h-H_m)}{B}\tan\phi'\right)}\right] + \frac{B\gamma_m}{2\,K\tan\phi}\left[1 - e^{\left(-\frac{2\,K\,H_m}{B}\tan\phi\right)}\right] e^{\left(-\frac{2\,K_s\,(h-H_m)}{B}\tan\phi'\right)} \quad \text{(2-23a)}$$

$$\sigma_h' = K_s\sigma_v' \quad \text{(2-23b)}$$

$$K_s = K_a = \tan^2\left(45 - \frac{\phi'}{2}\right) \quad \text{(2-23c)}$$

where γ_{sub} (kN/m^3) is the submerged unit weight of the backfill defined by $\gamma_{sub} = \gamma_{sat} - \gamma_w$; H_m (m) is wet (drained) fill above the water table; ϕ (º) and γ_m (kN/m^3) are the friction angle and unit weight of the wet fill; ϕ' (º) and γ_{sat} (kN/m^3) are effective friction angle and unit weight of the saturated backfill; K_s is the earth pressure coefficient for the saturated fill, and it is taken as K_a.

Li & Aubertin (2009a) solution indicated that the presence of water may significantly reduce the effective stresses below the water table, while the total stresses may be increased due to the PWP.

Li & Aubertin (2009b) solution

Based on the solutions of Li et al. (2005) and Li & Aubertin (2009a), Li & Aubertin (2009b) proposed a solution for stopes with a 3D geometry, cohesive fill, pore water pressure, and surface load p_0. The model is illustrated in Fig. 2-20. The parameters in this model have the same meaning as the ones in Li & Aubertin (2009a). In addition, the opposite walls are assumed to have the same stresses and the same interface properties.

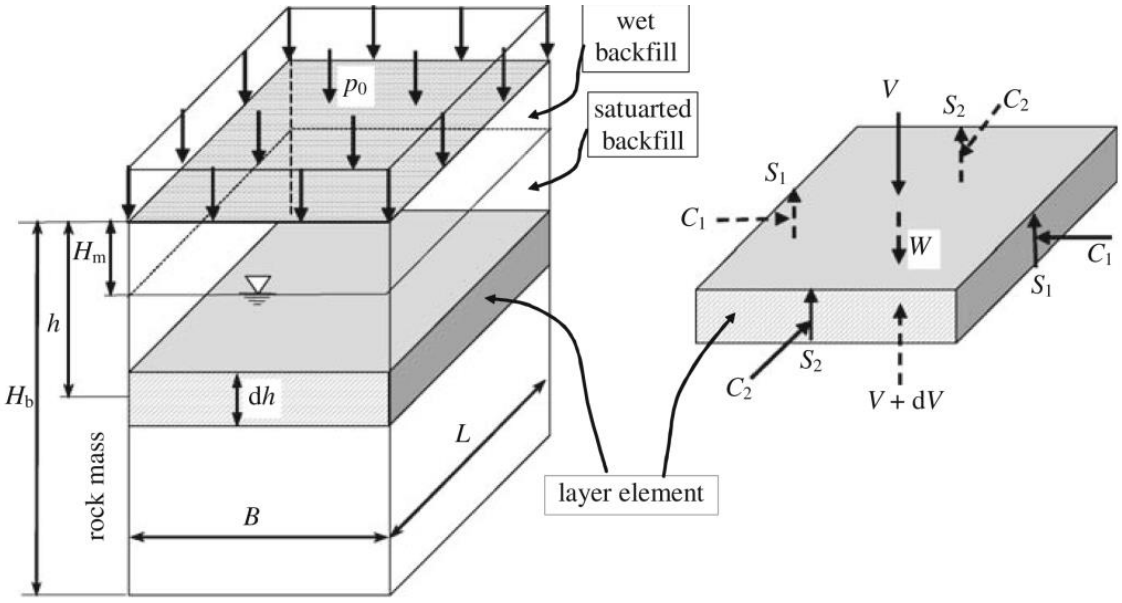

Figure 2-20: A vertical backfilled opening with forces acting on an isolated layer element (Li & Aubertin 2009b)

For the area above the water table, Li & Aubertin (2009b) gave the vertical and horizontal effective stresses at position *h* (m):

$$\sigma'_{vh} = \sigma_{vh} = \frac{\gamma_m - 2c_m(\lambda_{1m}B^{-1} + \lambda_{2m}L^{-1})}{M_m}\left[1 - e^{(-hM_m)}\right] + p_0\, e^{(-h\,M_m)} \quad (2\text{-}24a)$$

$$\sigma'_{h,hi} = \sigma_{h,hi} = K_{im}\sigma_{vh} + 2c_m \tan\alpha_{im} \quad (2\text{-}24b)$$

where $M_m = 2(K_{1m}B^{-1} + K_{2m}L^{-1}) \tan\delta_m$ (2-24c)

$\lambda_{1m} = 1 + 2\tan\delta_m \tan\alpha_{1m}$; $\lambda_{2m} = 1 + 2\tan\delta_m \tan\alpha_{2m}$ (2-24d)

K_{im} is the earth pressure coefficient when cohesion is zero (typically between K_0 and K_a; Li & Aubertin 2009e); and α_{im} is the fully drained backfill state angle.

In practice, 3D problems are effectively treated as 2D models when the length to width ratio (L/B) exceeds a certain value. Li & Aubertin (2009b) indicated that this can be misleading because the difference between the effective stresses at a given depth changes with stope length, and the difference in stresses obtained from the 2D solution and a 3D solution increases as backfill depth increases (for a given length to width ratio L/B).

A non-uniform vertical stress distribution has been used to develop solutions for estimating stresses in backfilled stopes for fully drained and submerged conditions (Li & Aubertin 2008, 2010). Li & Aubertin (2010) showed that the presence of water tends to significantly reduce the effective stresses below the water table, while the total stress is increased by the water pressure. The earth pressure coefficient K in these two solutions is taken as K_a. It is worth mentioning that the actual value of K applied in the existing analytical solutions, presented above, remains uncertain.

2.4.3 Estimation of pore water pressure (PWP) in stopes with HF

Sivakugan and coworkers (Sivakugan et al. 2006b; Sivakugan & Rankine 2006) adopted the method of fragments (Pavlovsky 1956; Harr 1962) to assess the drainage in a 2D stope with hydraulic fill and porous (free-draining) barricade. When the height of the water table is greater than the stope width B (m), Sivakugan et al. (2006b) gave the following expression to estimate the maximum PWP u_{max} (kPa) that occurs at the far end corner of the stope base:

$$u_{\max} = \left[h_L \left(\frac{\alpha\Phi_2 + \Phi_3}{\Phi_1 + \Phi_2 + \Phi_3} \right) + H_d \right] \gamma_w \tag{2-25a}$$

$$\alpha = 0.84 - 0.54\, H_d / B;\ \Phi_1 = H_w / B - 1;\ \Phi_3 = l / H_d - 0.5 \tag{2-25b}$$

where h_L is the head loss within the fill; H_w (m) is the height of water in the stope; H_d (m) is the drift height; l (m) is the distance of barricade from the brow; Φ_1, Φ_2 and Φ_3 are the form factor of different fragments and Φ_2 is obtained from a chart based on numerical simulations (Fig. 5 in Sivakugan et al. 2006b); γ_w (kN/m^3) is the unit weight of water.

In the case of the water table height smaller than the stope width, the maximum PWP is expressed as (Sivakugan & Rankine 2006):

$$u_{\max} = \left[h_L \left(\frac{\alpha \Phi_2 + \Phi_3}{\Phi_2 + \Phi_3} \right) + H_d \right] \gamma_w \tag{2-26a}$$

$$\alpha = -0.7788 \left(\frac{H_w}{B} \right) \left(\frac{H_d}{B} \right) + 0.2473 \left(\frac{H_d}{B} \right) - 0.2193 \left(\frac{H_w}{B} \right) + 1.0689 \tag{2-26b}$$

where Φ_1 and Φ_3 are the same as above; Φ_2 is calculated from a chart based on numerical simulations (Fig. 4 in Sivakugan & Rankine 2006).

It is noted that Eqs. 2-25 & 2-26 are valid for the case of steady-state flow when the height of the water table is constant (known) in the HF filled stope. Also, most existing analytical solutions presented above were proposed for a fully drained (zero PWP; e.g., Askew et al. 1978; Aubertin et al. 2003; Li et al. 2005) or a hydrostatic condition (e.g., Li & Aubertin 2009a, 2009b). These solutions are valid when the fill is fully dry or when a hydraulic equilibrium is reached within the HF filled stope with an impervious barricade.

However, the water table in the HF filled stope draws down with time and can induce changes in PWP and total (effective) stresses. Yang & Li (2016) have developed new analytical solutions (validated using SEEP/W) to represent the evolution of the water table and PWPs within stopes with submerged HF. This will be presented in Chapter 3.

2.4.4 Backfill design for side-exposed backfill

Traditionally, the exposed backfill is designed in such way that it can support the overburden pressure due to self-weight (Mitchell et al. 1982; Pirapakaran & Sivagukan 2007a). The cemented backfill is then considered as a freestanding vertical face without lateral confinement. However, these traditional methods tend to be overly conservative.

Mitchell et al. (1982)

Mitchell et al. (1982) considered the 3D geometry of a cemented fill block with an open face (front face), as shown in Fig. 2-21. In this model, the available shear strength along the sidewalls is due only to the bond cohesion c_s (assumed equal to the fill cohesion c). The strength mobilized

along the back wall is neglected. A sliding plane inclined at an angle α (= 45°+ ϕ'/2 to the horizontal) is assumed.

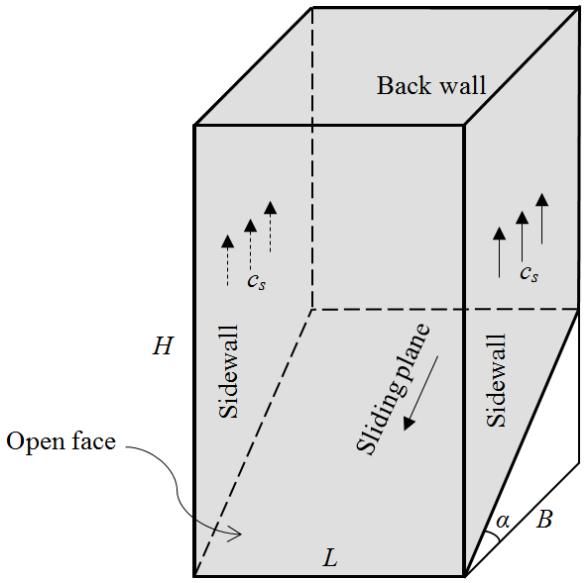

Figure 2-21: Sliding wedge model of the Mitchell et al. solution (adapted from Mitchell et al. 1982)

The factor of safety (FS) of the sliding wedge and the required backfill cohesion c are expressed by:

$$FS = \frac{\tan\phi}{\tan\alpha} + \frac{2cL}{H^*(\gamma L - 2c_s)\sin 2\alpha} \tag{2-27a}$$

$$c = \frac{\gamma H}{2(H/L + \tan\alpha)}, \text{ for FS = 1, } c = c_s \text{ and } H >> B \text{ thus } H^* \approx H \tag{2-27b}$$

where L (m), B (m) and H (m) are the backfill length, width and height, respectively; ϕ (= ϕ', °) is the internal friction angle of the fill; c (= c', kPa) is the backfill cohesion; γ (kN/m^3) is the fill unit weight; H^* (= H – B×tanα/2, m) is the equivalent height of the wedge. This solution will be further reviewed in Chapter 5 (with others presented in the following).

A similar but more sophisticated analysis has been made by Dight & Coulthard (1980) with additional consideration of tension crack (tension-free), closure pressure and surcharge. Fig. 2-22 illustrates that the sliding wedge is defined by the full open face, two side vertical planes, the plane of tension crack, and the base sliding plane. It is also seen that the two side planes pass the

intersection lines between the open face and sidewalls and make an angle θ to the sidewalls towards the back wall. The base sliding plane is similar as that in Mitchell et al. (1982). The use of this solution is however limited due in part to the lack of clear definitions for some key parameters (e.g., angles in Fig. 2-22).

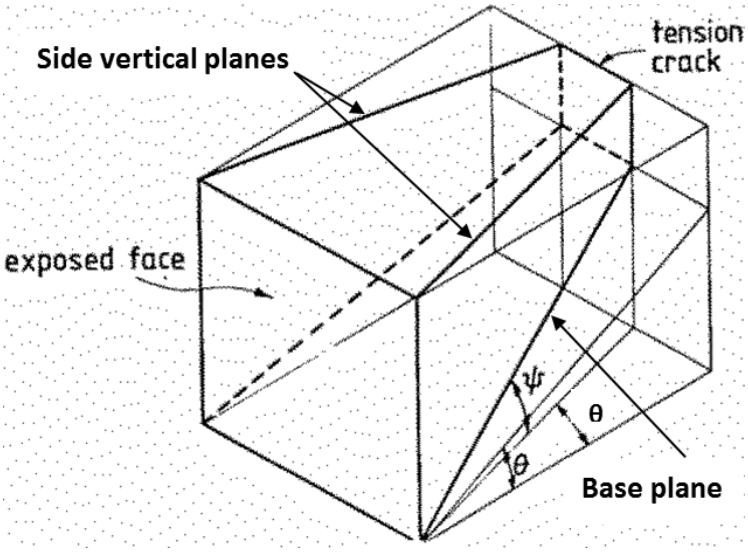

Figure 2-22: Wedge model of Dight & Coulthard (1980) (adapted from Dight & Coulthard 1980)

Modified Mitchell et al. solutions

Li & Aubertin (2012) modified the Mitchell et al. (1982) solution by considering different stope aspect ratios, a smaller bond cohesion along the sidewalls, and the addition of a surcharge p_0 (kPa). The mobilized strength along the back wall and the frictional strength along the sidewalls are neglected. For a high aspect ratio (HAR, $H/B \geq \tan\alpha$, where $\alpha = 45° + \phi'/2$) stope, the sliding plan is limited within the fill body. This leads to the following solution:

$$FS = \frac{\tan\phi'}{\tan\alpha} + \frac{2c}{\left[p_0 + H^*\left(\gamma - 2c_s/L\right)\right]\sin 2\alpha} \tag{2-28a}$$

$$c = \frac{p_0 + \gamma H^*}{\frac{2}{\left(FS - \tan\phi'/\tan\alpha\right)\sin 2\alpha} + \frac{2r_s H^*}{L}} \tag{2-28b}$$

where r_s (= c_s/c; from 0 to 1 where c_s is the fill-sidewall interface cohesion) is the adherence ratio along the sidewalls.

For backfilled stopes with a low aspect ratio (LAR, $H/B < \tan\alpha$, where $\alpha = 45° + \phi'/2$), the potential sliding plan intersects the fill top. The FS and the required backfill cohesion are then given by

$$FS = \frac{\tan\phi'}{\tan\alpha} + \frac{2c}{\left[p_0 + H\left(\gamma/2 - c_s/L\right)\right]\sin 2\alpha} \tag{2-29a}$$

$$c = \frac{p_0 + \gamma H/2}{\frac{2}{\left(FS - \tan\phi'/\tan\alpha\right)\sin 2\alpha} + \frac{r_s H}{L}} \tag{2-29b}$$

Li (2014a) extended the Li & Aubertin (2012) solution by considering the frictional strength along the sidewalls and the bond cohesion along the back wall c_b, which leads to a more generalized solution. For HAR stopes, the FS and the required fill cohesion can be expressed as follows:

$$FS = \frac{\tan\phi'}{\tan\alpha} + \frac{2}{\sin 2\alpha}\left(\frac{p'}{c} - r_b\frac{H - B\tan\alpha}{B} - 2r_s\frac{H^*}{L}\right)^{-1} \tag{2-30a}$$

$$c = p'\left[\frac{2}{(FS - \tan\phi/\tan\alpha)\sin 2\alpha} + r_b\frac{H - B\tan\alpha}{B} + 2r_s\frac{H^*}{L}\right]^{-1} \tag{2-30b}$$

with $$p' = \frac{L}{2K\tan\delta}\left\{\gamma - \frac{1}{B\tan\alpha}\left(\frac{\gamma L}{2K\tan\delta} - p_0\right)\times\left[\exp\left(-\frac{2K\tan\delta}{L}\left(H - B\tan\alpha\right)\right) - \exp\left(-\frac{2K\tan\delta}{L}H\right)\right]\right\} \tag{2-31}$$

where r_b (= c_b/c; from 0 to 1) is the ratio of adherence (c_b) along the back wall to the fill cohesion c; K and δ (°) are the earth pressure coefficient and friction angle along the sidewalls.

For LAR stopes, the Li (2014a) solution is written as:

$$FS = \frac{\tan\phi}{\tan\alpha} + \frac{2}{\sin 2\alpha}\left(\frac{p''}{c} - r_s\frac{H}{L}\right)^{-1} \tag{2-32a}$$

$$c = p''\left[\frac{2}{(FS - \tan\phi/\tan\alpha)\sin 2\alpha} + r_s\frac{H}{L}\right]^{-1} \tag{2-32b}$$

with $$p'' = \frac{L}{2K\tan\delta}\left\{\gamma - \frac{1}{H}\left(\frac{\gamma L}{2K\tan\delta} - p_0\right)\times\left[1 - \exp\left(-\frac{2K\tan\delta}{L}H\right)\right]\right\} \tag{2-33}$$

Numerical results of Li & Aubertin (2014) showed that the shear resistance along sidewalls for the lower block acts in a direction parallel to the sliding plane. Thus, the wedge block is divided into an upper rectangular block and a lower triangular wedge. A modified solution was given in terms of FS and required fill cohesion *c* for HAR stopes:

$$FS = \frac{\tan\phi'}{\tan\alpha} + \frac{c\left(\frac{1}{\cos\alpha} + r_s\frac{H'}{L}\right) + \frac{(\gamma/M - p_1)\left[(1-\exp(-MH'))/MH' - 1\right] + \gamma H'/2}{1 + L/B}}{(p_1 + \gamma H'/2)\sin\alpha} \tag{2-34a}$$

$$c = \frac{D'(p_0 + \gamma(H - H') - G') + \frac{\gamma A' H'}{2}\left(1 + \frac{L}{B}\right)\sin\alpha - \gamma\left(\frac{C'}{M} + \frac{H'}{2}\right)}{B'\left(1 + \frac{L}{B}\right) + D'(H - H')\left(\frac{2r_s}{L} + \frac{r_b}{B}\right)}, \text{ for FS= 1} \tag{2-34b}$$

$$\text{with } H' = B\tan\alpha \quad M = 2K\left(B^{-1} + L^{-1}\right)\tan\delta \tag{2-35a}$$

$$p_1 = p_0 + (H - H')\left[\gamma - c\left(\frac{2r_s}{L} + \frac{r_b}{B}\right)\right] \tag{2-35b}$$

$$G' = \frac{1}{1 + L/B}\left\{\gamma(H - H') + \left(p_0 - \frac{\gamma}{M}\right)\left[1 - \exp\left(-(H - H')M\right)\right]\right\} \tag{2-35c}$$

$$A' = FS - \frac{\tan\phi'}{\tan\alpha} \quad B' = \frac{1}{\cos\alpha} + r_s\frac{H'}{L} \quad C' = \frac{1 - \exp(-MH')}{MH'} - 1 \quad D' = A'\left(1 + \frac{L}{B}\right)\sin\alpha + C' \tag{2-35d}$$

This solution and the Li (2014a) solution may overcome some limitations of the solutions of Mitchell et al. and Li & Aubertin (2012) using more realistic interactions between the fill and rockwalls. The earth pressure coefficient *K* is taken as Rankine's active pressure coefficient K_a. These solutions will also be further reviewed in Chapter 5.

Recent 3D numerical simulations performed by Falaknaz et al. (2016) indicated that these existing analytical solutions of Mitchell et al. (1982) and their modifications cannot well represent the effect of stope geometry on the stability of exposed cemented fill. In the light of these analyses, Yang et al. (2016b) have proposed a new analytical solution, using more realistic failure mode, to better describe the response of cemented fill upon exposure. This will be presented in Chapter 5.

2.4.5 Barricade design

Barricade built in the drift near the stope base is a key structure to retain the backfill. The factor of safety of a barricade depends on the capacity and demand. The demand (load) on a barricade is determined by the pressure exerted by the backfill placed in the stope and drift, while the capacity (resistance) depends on its material, shape, sizes and construction. In this subsection, available analytical solutions for pressure estimation (demand) on the barricade are first presented. The design methods (capacity) for traditional barricades and waste rock barricades are then recalled.

2.4.5.1 Analytical solutions for estimating pressures on barricades

Mitchell et al. (1975) proposed a simple equation to calculate the load on a barricade:

$$F_h = \frac{1}{2}\gamma H^2 L_d K_0 \tag{2-36}$$

where F_h (m) is the horizontal load exerted on the barricade, γ (kN/m^3) is the unit weight of the backfill, H (m) is the total fill height in the stope, and L_d (m) is the drift width. K_0 is the at-rest reaction coefficient.

This solution is based on the overburden pressure without considering the arching effect. To overcome the resulting overestimation, Mitchell (1992) arbitrarily suggested using an active reaction coefficient K_a instead of K_0; but this has not been validated.

By considering the arching effect, Smith & Mitchell (1982) and Mitchell & Roettger (1984) gave an empirical solution to estimate the horizontal stress σ_h (kPa) on a barricade located at a distance l (m) from the brow:

$$\sigma_h = 0.4\gamma H\left(1 - 0.6\frac{l}{L_d}\right) \tag{2-37}$$

This solution assumes that the horizontal stress increases linearly with the backfill height H (m) in the stope; the influence of the barricade height is neglected.

Mitchell et al. (1982) and Mitchell (1983) considered the limit equilibrium of a 3D wedge of backfill in Fig. 2-23. In this figure, L_s (m) is the stope length; H_d (m) is the drift height; W_d (m) is the drift width; w (m) is the weight of the wedge; P_0 (kN) is the surcharge from the above backfill; N (kN) and T (kN) are the normal and shear forces along the sliding plane; c_b (kPa) is the

cohesion between the fill and walls; F_h (kN) is the force provided by a smooth barricade to maintain equilibrium of the wedge.

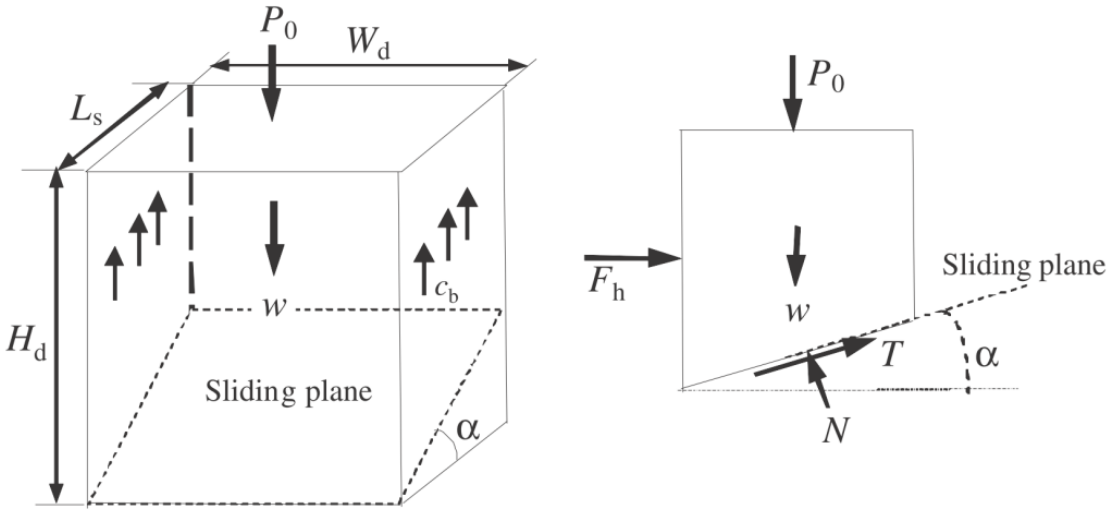

Figure 2-23: Wedge model of Mitchell et al. (1982) (Modified by Li & Aubertin 2009c)

The horizontal load on the barricade is then given by:

$$F_h = \frac{[P_0 + L_s(H_d - L_s \tan\alpha/2)(\gamma W_d - 2c_b)](\sin\alpha - \cos\alpha\tan\phi) - cW_d L_s/\cos\alpha}{\sin\alpha\tan\phi + \cos\alpha} \quad (2\text{-}38)$$

Kuganathan (2002b) proposed the following solution for estimating the horizontal stress σ_h in the drift onto the barricade:

$$\sigma_h = \sigma_0 \exp\left(-\frac{PK_0\tan\phi}{A}l\right) \quad (2\text{-}39)$$

where σ_0 is the horizontal stress at the drawpoint and obtained by using Terzaghi's arching theory; P is the perimeter of the drift; A is the cross section of the barricade.

The above mentioned solutions do not consider the stress transfer between the backfill and stope/drift walls. To account for this, Li & Aubertin (2009c) proposed a 3D analytical solution for fully drained conditions. On Fig. 2-24, l (m) is the distance between the vertical layer element and the drawpoint; σ_{hT0} (kPa) and σ_{hB0} (kPa) are the horizontal normal stresses at the top and base of the drift at the drawpoint, which are calculated using Li et al. (2005) solution.

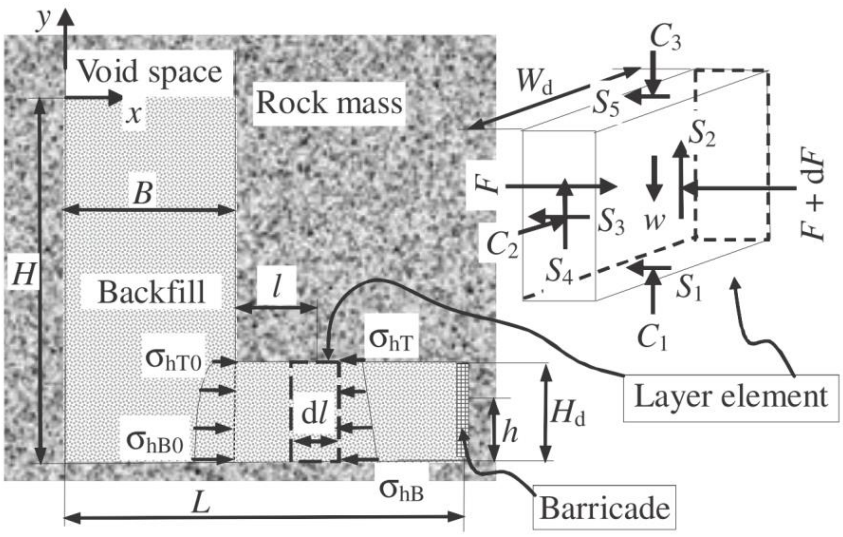

Figure 2-24: Schematic representation of a vertical backfilled stope with a barricade in a fully drained condition (Li & Aubertin 2009c)

The arching theory was applied to the barricade drift. The horizontal stress σ_h (kPa) in the drift axis direction at elevation h (m) is given by:

$$\sigma_h = \left[\frac{h}{H_d}\sigma_{hT0} + \left(1 - \frac{h}{H_d}\right)\sigma_{hB0} \right] \exp\left[-l \frac{2\tan\delta}{K_{dl}} \left(\frac{1}{H_d} + \frac{K_{dt}}{W_d} \right) \right] \tag{2-40}$$

where the earth pressure coefficients K_{dl} or K_{dt} is the ratio of the horizontal stress in the longitudinal or transverse direction over the vertical stress, respectively.

It is noted that the horizontal stress from the top to the base of the drift is assumed uniformly distributed (not the actual distribution in the drift). Li & Aubertin (2009c) showed that their solution corresponds to the stress distribution on a barricade quite well for a fully drained condition based on numerical simulations. They also showed that the load on the barricade is negatively related to the distance of the barricade from brow.

Li & Aubertin (2009d) further extended Li & Aubertin (2009c) solution to account for the pressure generated by submerged fill on the barricade. Their solution applies to submerged conditions after backfill placement where the PWP is equal to a hydrostatic pressure (dissipation of excess PWP is completed). On Fig. 2-25, σ'_{hT0} (kPa) and σ'_{hB0} (kPa) are the effective horizontal stresses at the top and base of the barricade drift at the drawpoint. These values were calculated by Li & Aubertin (2009b) solution.

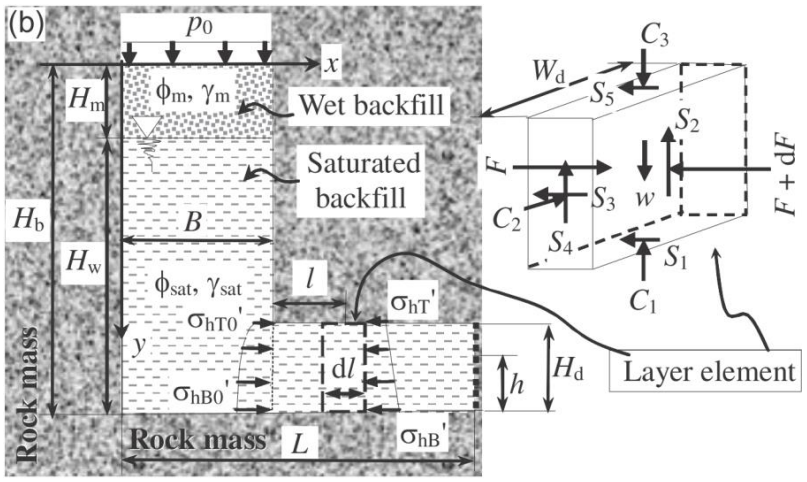

Figure 2-25: Schematic representation of a vertical backfilled stope with a barricade in a submerged condition (Li & Aubertin 2009d)

The effective horizontal stress σ'_h (kPa) in the drift axis direction at elevation h (m) is given by (for $H_b \geq H_d$):

$$\sigma'_h = \left[\frac{h}{H_d} \sigma'_{hT0} + \left(1 - \frac{h}{H_d}\right) \sigma'_{hB0} \right] \exp\left[-l \frac{2 \tan \delta_{sat}}{K_{dl}} \left(\frac{1}{H_d} + \frac{K_{dt}}{W_d} \right) \right] \tag{2-41}$$

For submerged backfill, Li & Aubertin (2009d) observed that effective stresses in barricade drifts are less than those obtained for drained conditions, while total stresses on barricades can be significantly increased by the PWP.

2.4.5.2 Design method for barricade

As mentioned previously, barricades are mainly built with bricks, concrete blocks, shotcrete and fibrecrete. The methods for designing these traditional barricades are mostly based on the flexural failure mechanism (Duffield et al. 2003).

Beer (1986) considered square barricades as simply supported slabs and assumed that the barricade fails with tension cracks developing along the diagonal lines and barricade-rock interface. The following solution was proposed to calculate the maximum load on the barricade:

$$w_p = \frac{24 m_p}{b^2} \tag{2-42a}$$

$$m_p = \sigma_c \frac{t^2}{8} \tag{2-42b}$$

where w_p (MPa) is the ultimate uniformly distributed pressure; m_p (MNm/m) is the ultimate moment capacity per unit length; σ_c (MPa) is the UCS of the mortar; b (m) and t (m) are the width and thickness of the barricade.

Beer (1986) suggested that Eq. 2-42 has an implied safety factor of 1.72 based on the back-analysis of a controlled experiment for barricade failure at the Mont Isa mine. Although originally developed for masonry barricade, this solution has been widely applied to design shotcrete barricades in Australia (Revell & Sainsbury 2007b; Rajeev & Sivakugan 2016). Beer's (1986) solution has been partly validated (with FS = 1.72) using numerical simulations conducted by Revell & Sainsbury (2007b).

Rajeev & Sivakugan (2016) statistically investigated the effect of variability/uncertainties in barricade geometry, material and backfill pressure on the barricade performance. They suggested using a capacity reduction factor in Eq. 2-42 to account for uncertainties of these factors in barricade design. However, the actual value of the reduction factor requires further study.

As an alternative, waste rock barricades are gaining popularity (due to their easy and cost effective construction), particularly in some Canadian mines. Constructing barricades with waste rock from the underground development can also help reduce surface disposal of mine wastes. However, the traditional design methods based on the theory of simply supported slab are not applicable to waste rock barricades.

Considering the limit equilibrium state of the idealized rectangular block, Li & Aubertin (2011) proposed an analytical solution to calculate the length of waste rock barricade (WRB) for fully drained and submerged (partly to fully) conditions. The minimum required length (L_B) of the WRB (for FS = 1) for fully drained backfill is as follows:

$$L_B = \frac{p}{\gamma_{wr}(1+KH_d/L_d)\tan\delta} = \frac{P}{\gamma_{wr}H_d(L_d+KH_d)\tan\delta} \tag{2-43}$$

where p (kPa) is the average backfill pressure on the barricade (this pressure is linearly distributed from top to bottom on the barricade); P ($= pH_dL_d$, kN) is the force exerted on the barricades by the backfill; γ_{wr} (kN/m^3) is the unit weight of waste rock; δ (°) is the friction angle along the interfaces between the waste rock and the drift walls and floor; K (-) is the earth

pressure coefficient within the waste rock along the transversal direction of the drift. L_d and H_d are the width and height of the drift.

For a fully drained condition, the barricade pressure p or load P can be obtained from the solution proposed by Li & Aubertin (2009c). For CPB, the common practice is to estimate the backfill pressures from isostatic stresses based on overburden.

In practice, WRB constructed in drifts have a shape that is close to a trapezoid. The design based on the rectangular block solution may be overly conservative depending on how it is applied in practice. Modified solutions with more representative barricade shape and failure modes have been proposed (and validated using FLAC) by Yang et al. (2014, 2016a) to improve the design of WRB. These will be presented in Chapter 4.

2.4.6 Summary

In the early stage of a project, analytical solutions can offer simple and low-cost tools for a preliminary estimate of the stress state in backfilled openings. It has been shown that arching theories can be well suited for estimating the stress state in narrow backfilled stopes and the loads on barricades if properly applied. These arching solutions differ mainly in the way how the values of earth pressure coefficient K and interface friction angle δ are assumed.

However, it is known that existing analytical solutions to estimate the stresses in stopes have some limitations due to the simplifying assumptions; for instance:

- Most analytical solutions assume a uniformly distributed vertical and horizontal stress across the span of the stope (or drift); this is not valid for most cases (e.g., Drescher 1991; Li & Aubertin 2008, 2010);
- The backfill is assumed to be at a critical state near rock walls so that the shearing strength is fully mobilized, due to the use of limit equilibrium with the Coulomb criterion. This may overestimate the arching effect;
- The contact stress between the fill and walls is expressed as a function of a constant earth pressure coefficient K. However, the actual value of K is unclear even when material properties are known;

- Drainage, water flow and progressive dropdown of the water table in hydraulic backfill are not considered;
- The effect of consolidation (dissipation of excess PWP), strength gain with curing time and cementation (hydration) are neglected;
- The effect of filling rate (sequentially) and excavation sequence are ignored;
- The effect of negative PWP (or suction) is neglected;
- All solutions are developed for regular stope shapes (square, rectangular circular); these may not be applicable to more complex stope geometries.

It is noted that most existing analytical solutions presented above were developed for isolated stopes. These solutions may be satisfactory at the early stage of projects for preliminary estimates. However, they may also encounter many limitations in more complicated conditions. For instance, the extraction in open stoping and underhand C&F mining can induce stress redistribution (or even failure) of backfill in adjacent stopes. Multiple stoping (close to reality) can significantly affect the stress state of fill. Thus, the numerical modelling is a better tool to address design issues in more complicated conditions.

2.5 Numerical simulations for evaluating the stress state and stability of backfilled stopes

Numerical simulations are able to account for complex stope geometries, fill-wall interactions and boundary conditions to simulate more realistic conditions. They can also consider complex processes such as wall convergence, filling sequence, and drainage and consolidation of backfill. Furthermore, numerical methods can incorporate more advanced constitutive models. Hence, they can provide more representative solutions than analytical methods, but they are usually more costly and time consuming.

In the following, numerical simulations conducted to evaluate the stress state in backfilled stopes and drifts are first reviewed. Numerical analyses for assessing the stability of side-exposed cemented fill and earth pressure coefficient in backfilled stopes are then recalled. The review also includes the numerical study of wick drains in backfilled stopes.

2.5.1 Stress state in backfilled stopes

Most numerical analyses presented below consider backfill as an elasto-plastic Mohr-Coulomb material and the rock mass as a linear elastic material (if not specified). In most cases, the commonly used assumption with unrelated Poisson's ratio ν and internal friction angle ϕ' is used for backfill (unless specified). The dilation angle ψ is usually taken as nil. The backfill is usually placed instantaneously or in layers after the completion of the wall convergence. Also, most numerical analyses do not consider interface elements between the fill and rock mass; yielding then occurs within the backfill near the rough and irregular rock face due to production blasting.

2.5.1.1 Vertical backfilled stopes

Askew et al. (1978) conducted simulations, using a 2D finite element method (FEM) code, to verify their analytical solution presented above in Section 2.4.2.1. A good agreement was obtained between the two approaches for the vertical stress along fill depth (except for the stope base). It was shown that the arching is more developed in the cemented fill compared to the uncemented fill. The cohesion used in the cemented case is unknown, but their results tend to indicate that the stress would remain in the same order of magnitude, independently on fill cohesion.

Aubertin et al. (2003) showed simulation results obtained with PHASE 2 (RocScience 2002) to assess the stress state in narrow backfilled stopes. The horizontal and vertical stresses are much greater than the overburden stress around the mid-height of the stope. This is partly caused by the squeeze effect of the inward convergence of the stope walls (Aubertin et al. 2003). In fact, the stress state of fill may be largely affected by the wall convergence depending on the mining methods and geological conditions. In C&F mining, the backfill may be squeezed due to inward wall convergence, which may induce the passive state (Li et al. 2003). Such effect may become more pronounced in deep mining. For isolated stopes in open stoping, the inward convergence has little influence on the (delayed) backfill placed after the occurrence of the convergence.

Aubertin et al. (2003) studied the stress state of a backfilled stope inclined at 45° with PHASE 2. They reported that arching effect of inclined stopes turns out to be less developed compared to that of vertical stopes. They stated that the non-uniform stress distribution is primarily due to the transfer of fill weight to the footwall. So the analytical solutions for vertical stopes are not representative for inclined stopes.

Li et al. (2003) conducted simulations using FLAC (Itasca 2002) to evaluate the stress state in narrow backfilled stopes. Fig. 2-26 shows the stress distribution in a narrow backfilled stope. The arching effect is clearly seen in the stope.

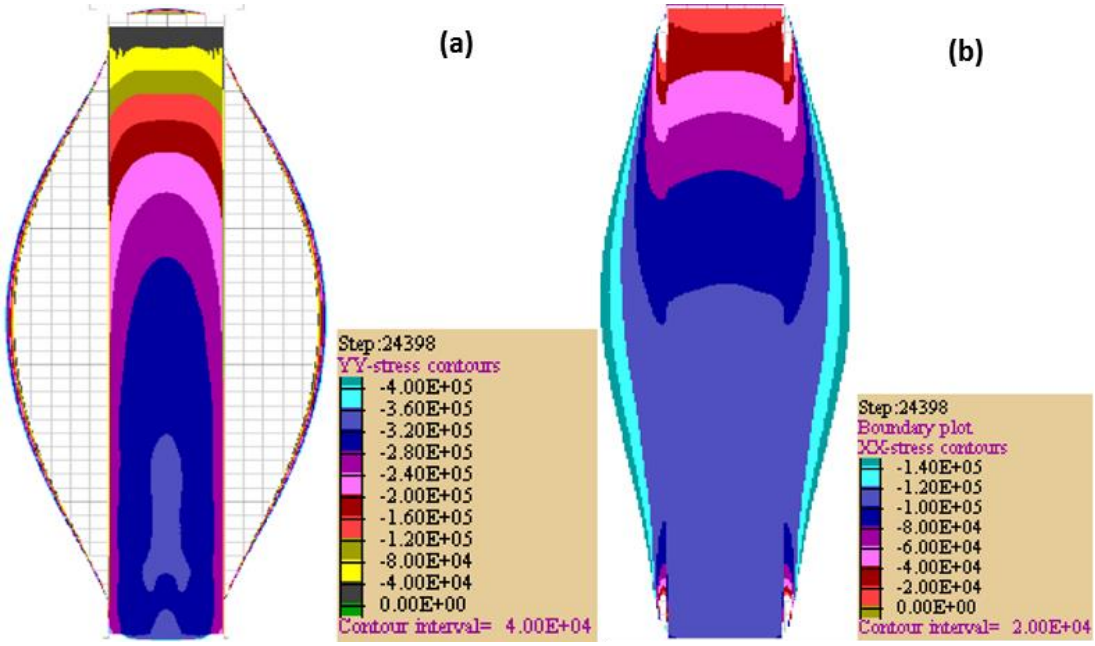

Figure 2-26: Numerical results of the distribution of (a) vertical and (b) horizontal stresses in FLAC (Li et al. 2003)

For a vertical stope, the numerical results of Li et al. (2003) indicated that the horizontal stress is somewhat uniform across the stope width, while the vertical stress is less uniform (e.g., Rankine 2004; Pirapakaran 2008). These results indicate that the uniform distribution of vertical stress postulated in many analytical solutions is not strictly valid.

Li et al. (2003) showed that the value of K ($= \sigma'_h/\sigma'_v$) near the walls (between K_a and K_0) is greater than that at the center (close to K_a). Also, the stress state can be well described with the arching analytical solutions (see Section 2.4.2.2) by assuming the backfill at an active state K_a along the vertical centerline. They also studied the stress state in a backfilled stope inclined at 60°.

Li & Aubertin (2009a) applied the code FLAC to evaluate (and validate) their analytical solutions considering the influence of water on stress state. Fig. 2-27 shows comparisons between the effective and total stresses obtained from the analytical solution and numerical modelling along the vertical centerline (VCL) for submerged backfill. In general, the analytical solution ($K = K_a$) correlated quite well with the numerical results.

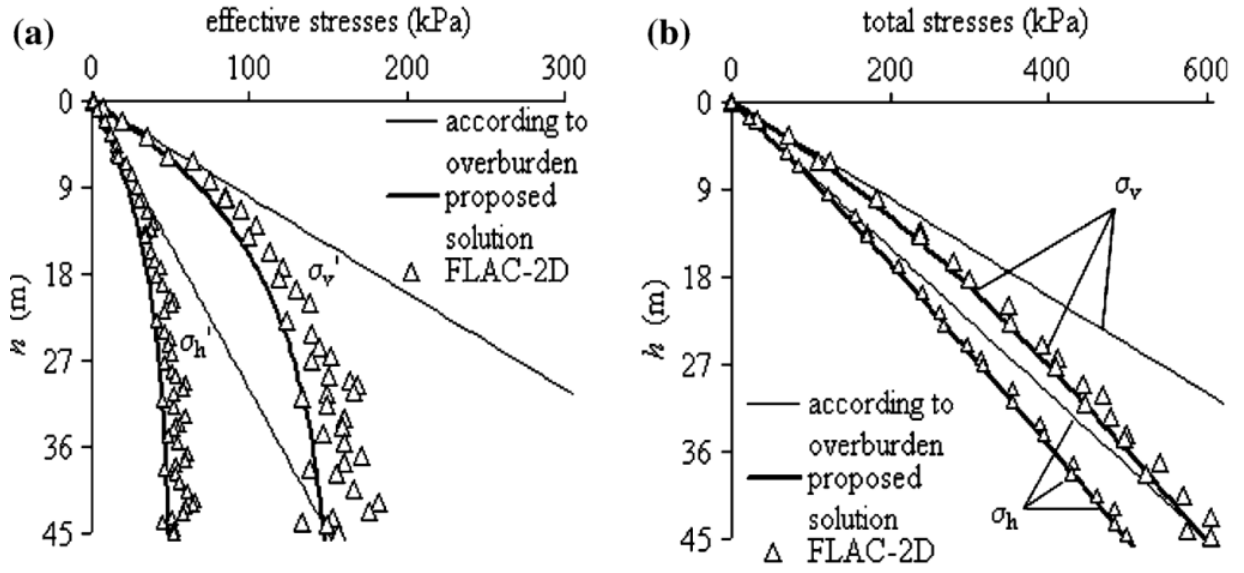

Figure 2-27: Vertical and horizontal effective (a) and total (b) stress along the VCL, obtained from numerical calculations and analytical solution ($K = K_a$) (Li & Aubertin 2009a)

Fahey et al. (2009) performed simulations with PLAXIS (version 8.6) to investigate the influencing factors on arching in vertical backfilled stopes, with dry (drained) and saturated (undrained) fill. Interface elements are included along the walls. The frictional properties of the interface elements are identical to those of the backfill.

Fahey et al. (2009) reported that a positive dilatation angle results in increased horizontal stress and reduced vertical stress, indicating an enhanced arching (see also Li et al. 2007; Pirapakaran 2008; Li & Aubertin 2009e). Conversely, the negative dilation angle would reduce the arching effect. Fahey et al. (2009) pointed out that a zero (even a negative) dilation angle may exist for fill since it is usually placed hydraulically and deposited in a loose state. They also reported that increasing Young's modulus of backfill from 10 MPa to 1 GPa has almost no influence on the stress state (see also Li & Aubertin 2009e).

Numerical results of Fahey et al. (2009) indicated that the horizontal stress increases as Poisson's ratio v increases for the whole range. For $v < 0.4$, the vertical stress reduces as the v value increases. But a reverse relationship is found when the v value varies from 0.4 to 0.499. Essentially, it is noted that Poisson's ratio (compressing) influences the arching effect (stress state) in a somewhat similar manner as the dilation angle.

Fahey et al. (2009) also investigated the influence of hydraulic conductivity *k* of backfill on the stress state. Fig. 2-28 shows the total vertical and horizontal stresses profiles at the end of filling. The results indicated that the greater *k* value tends to produce smaller final total stresses in depth, especially for the total horizontal stress. Hence, consolidation (even partially) during filling may significantly reduce the load on barricade.

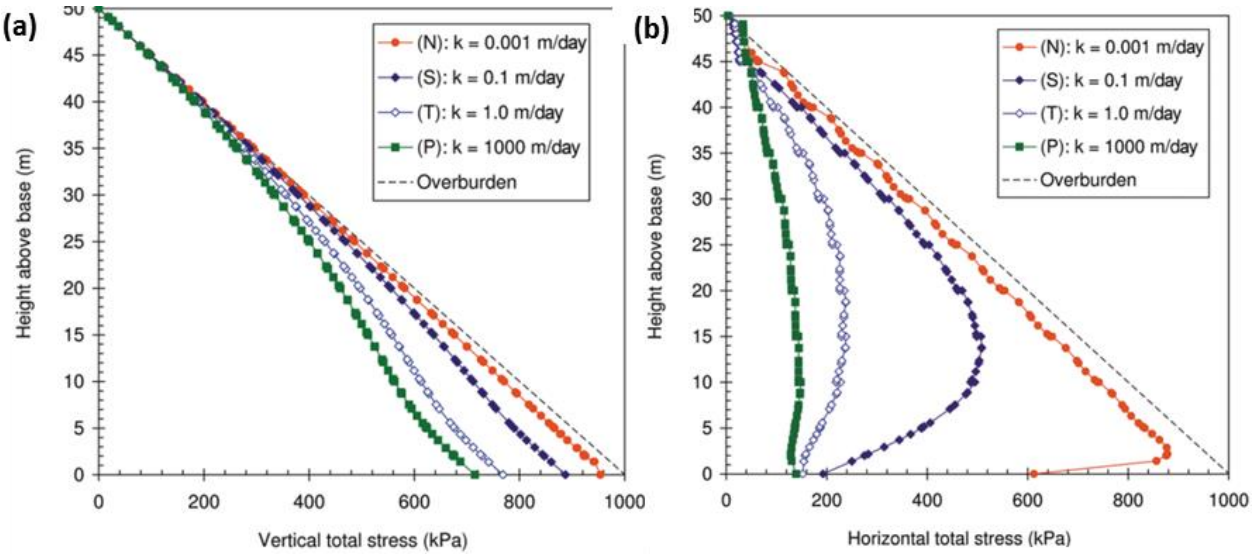

Figure 2-28: Profiles of total (a) vertical and (b) horizontal stresses at the end of filling for different *k* values in a plane strain stope: (Fahey et al. 2009)

In practice, the drift (barricade) width is less than the stope length (along the strike). In the case of plain strain, Fahey et al. (2009) used reduced drawpoint hydraulic conductivity to simulate ("in a crude way") this effect. This reduction in *k* of the drawpoint significantly increases the consolidation time.

Fahey et al. (2009) stated that the final stress state is independent of the filling type (drained or undrained) and backfill permeability. Their results also indicated that the behavior of saturated backfill is affected by the hydraulic conductivity of the backfill (through coefficient of consolidation) relative to the rate of filling.

As mentioned previously, consolidation (and drainage) of CPB can take a fairly long time due to its extreme low permeability. Hence, the evolution of stress state in stopes with CPB largely depends on the consolidation. Based on Terzaghi's 1D consolidation theory, Gibson (1958) has theoretically studied the 1D consolidation in an accreting clay fill under different boundary conditions. In one case shown by Gibson (1958), the backfill is placed at a constant rate on a

permeable base with zero pore pressure on the top of the fill, which can be highly related to the stope filling. The Gibson (1958) solution has been compared to the numerical results reported by Fahey et al. (2010) and Shahsavari & Grabinsky (2014), who considered constant material properties as assumed by Gibson (1958). The drift and barricade were not taken into account and the base drainage was considered through a permeable stope base.

Fahey et al. (2010) performed numerical modelling with the MinTaCo program (Seneviratne et al. 1996). Their results indicated that the Gibson (1958) solution can be used to predict the consolidation of CPB during stope filling at the initial design phase. However, the MinTaCo program was initially developed to model the 1D consolidation and evaporation of surface deposition of slurried tailings. Therefore, the numerical simulations of Fahey et al. (2010) were unable to consider the realistic stope geometry and interactions between fill and walls.

Shahsavari & Grabinsky (2014) stated that the pore pressure on the top of the consolidating CPB layer during filling is not nil, based on in-situ measurements. They numerically studied the 1D consolidation of CPB with a nonzero pore pressure boundary condition on the fill top with FLAC^{3D}. The results indicated that the nonzero pore pressure on top of the consolidating layer tends to induce higher pore pressure. However, an hour interval was maintained between two layers for consolidation.

El Mkadmi et al. (2014) investigated the behavior of backfill within narrow vertical stopes using SIGMA/W. Softer and thin layers of materials were used to represent the interfaces (discussed below in Section 2.5.1.3). They conducted transient analyses, where the initially saturated fill is instantly deposited and followed by progressive drainage at the stope base. The evolutions of total and effective vertical stress along VCL, and PWP along the stope height are shown in Fig. 2-29. Shortly after the filling, the fill is at a geostatic static like heavy fluid (see also Fahey et al. 2009). The effective stress then increases with the dissipation of excess PWP, while the total stress and PWP decreases. El Mkadmi et al. (2014) further reported that after some time, an unsaturated zone (0 to 15 m) in the upper part of the stope appeared. Therefore, the vertical effective stress is positive at this unsaturated zone. This is the first time the unsaturated zone was modeled.

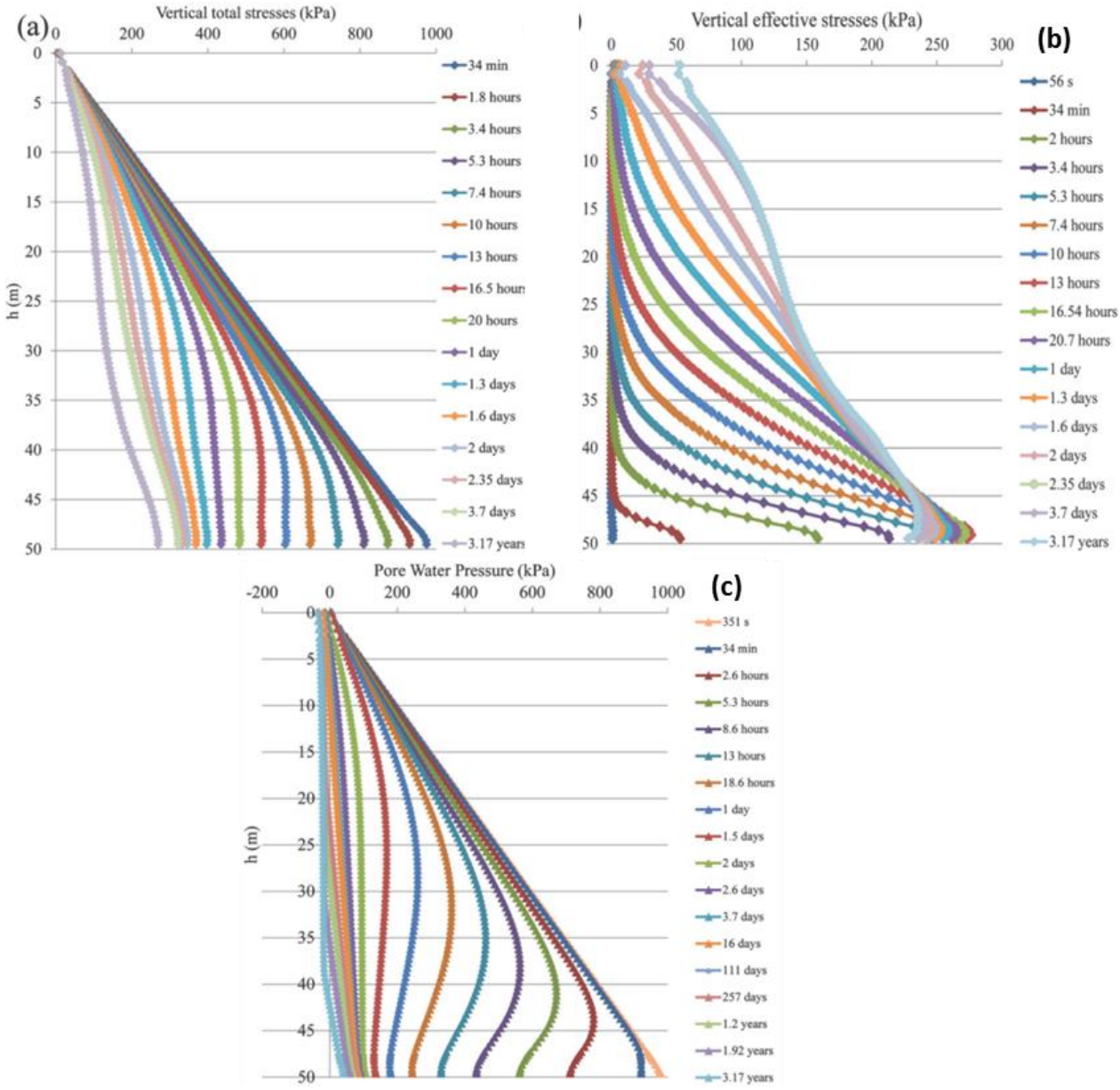

Figure 2-29: Evolution of (a) total vertical stress, (b) effective vertical stress and (c) PWPs (El Mkadmi et al. 2014)

El Mkadmi et al. (2014) modeled sequential filling, involving placing saturated fill in layers on top of previously deposited layer under drainage. The deposition of a new layer would generate excess PWP within itself; meanwhile the lower layers may have a smaller or negative PWP. As the drainage and consolidation take place, the effective stress progressively increases in the new layer.

El Mkadmi et al. (2014) simulated the effect of cementation by evolving the fill properties during filling in the way similarly to experimental results, in terms of cohesion, stiffness, and hydraulic functions. They reported that cohesion due to cementation can significantly speed up the strength gain in backfill. They also stated that the faster filling rate would induce higher total stress in backfill (see also Askew et al. 1978).

Falaknaz et al. (2015a) investigated the response of two adjacent backfilled stopes excavated and filled sequentially using FLAC, for related fill parameters ϕ' and v (see also Falaknaz et al. 2015b). Fig. 2-30 illustrates the stress state in two adjacent stopes obtained at the end of filling the second stope. Although the arching effect develops in both stopes, the stress distributions differ in the two stopes and the stress state in the first stope is also different from that obtained for a single stope. This is due largely to the fact that the backfill stresses of the first stope are altered by the excavation and filling of the adjacent stope. Falaknaz et al. (2015a, 2015b) also analyzed the stress path at different locations of backfilled stopes induced by the excavation and backfilling sequence.

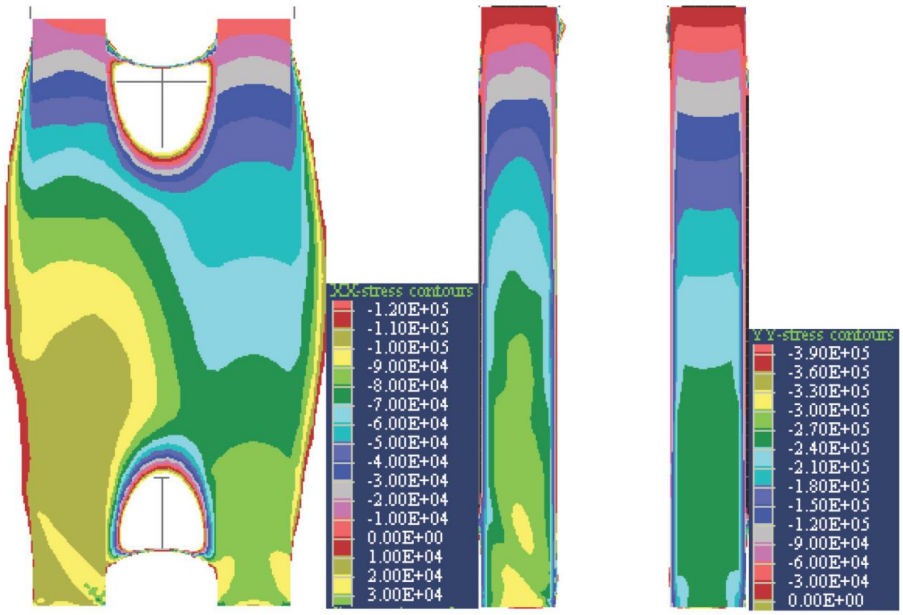

Figure 2-30: Stress (Pa) isocontours in two adjacent backfilled stopes obtained at the end of filling the second stope (right-hand side; Falaknaz et al. 2015a)

Falaknaz et al. (2015b) used an elasto-plastic model for rock mass and their results showed that the stresses are less uniform compared to those obtained with linear elastic rock mass. This indicates that the mechanical behavior of the rock mass has an impact on the stress state of

backfilled stopes, attributed to the differences in the strains of the backfill and displacements of the rock walls.

Falaknaz et al. (2015c) conducted simulations with independent backfill parameters ϕ' and v and their results showed that the way how ϕ' and v are treated (related or not) may affect the stress state in backfilled openings (see also Jahanbakhshzadeh 2016).

2.5.1.2 Inclined backfilled stopes

For convenience, some preliminary numerical modelling of inclined backfilled stopes (Aubertin et al. 2003; Li et al. 2003) have been presented above in the Section 2.5.1.1 together with the simulations for vertical backfilled stopes.

Hassani et al. (2008) performed simulations with FLAC to evaluate the fill-rock interactions in narrow and deep vein mining. The stope walls are inclined at 65°. A strain softening response was used for the rock mass and strain hardening for backfill. The post-peak behaviors of rock mass and backfill were considered. Interface elements were used at fill-rock contact and their friction angle was taken the same as that of backfill. Their results showed that the placement of backfill can mitigate the stress concentrations (due to excavation) and prevent the development of tensile stress in the rock mass.

Hassani et al. (2008) reported that the stress state (and arching) of inclined stope is quite different from that of vertical stope. Their results also showed that the wall inclination could significantly affect the stress distribution in backfill and rock walls. Therefore, the arching solutions developed for vertical openings are not applicable to inclined stopes. Hassani et al. (2008) further reported that a small void left unfilled at the stope top significantly affects the fill-wall interactions throughout the stope.

Li et al. (2007) and Li & Aubertin (2009e) conducted simulations to evaluate the stress state in inclined backfilled stopes using FLAC. The stope is inclined at an angle from 90° (vertical) to 60°. Their results show that the horizontal stress is almost insensitive to the inclination along the stope width and height. The vertical stress decreases significantly along the hanging wall and CL when the stope becomes more inclined from the vertical. These results are confirmed by those presented by Jahanbakhshzadeh (2016), who used numerical simulations to validate his 2D analytical solutions (Eq. 2-19) for inclined stopes using related backfill parameters ϕ' and v.

Fig. 2-31 shows the stress variations with the fill Poisson's ratio in an inclined stope (α = 75°). It is seen that the horizontal stress slightly increases and the vertical stress largely reduces as Poisson's ratio v of backfill increases from 0.2 to 0.4.

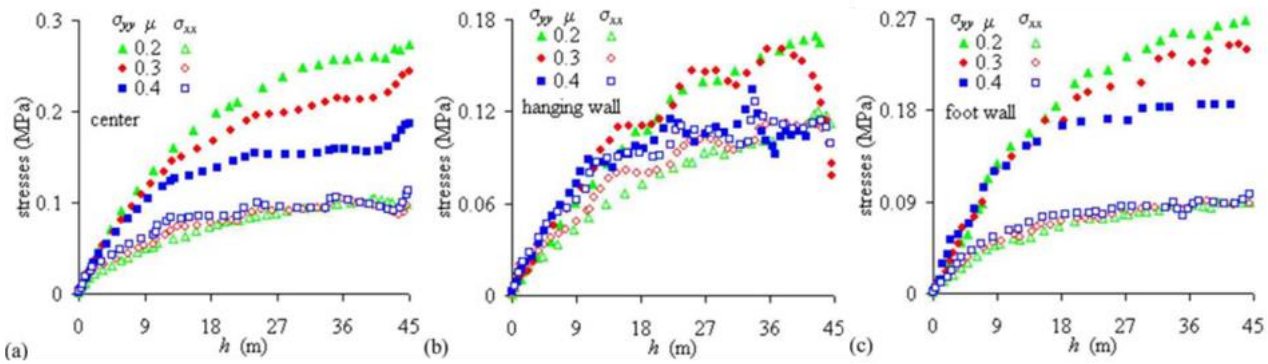

Figure 2-31: Stress variation with backfill Poisson's ratio: along (a) VCL, (b) hanging wall and (c) footwall in FLAC (Li & Aubertin 2009e)

Fig. 2-32 shows the stress variations with the backfill friction angle ϕ' from 10° to 40° in an inclined stope (α = 75°). The results indicated that both stresses decrease with an increased friction angle along the three profiles (see also Jahanbakhshzadeh 2016). They showed that the vertical stress becomes less sensitive to the increase in ϕ' for ϕ' > 20°. This can also be estimated from a few analytical arching solutions introduced in Section 2.4.2 (e.g., Aubertin et al. 2003; Singh et al. 2010), but in a different manner.

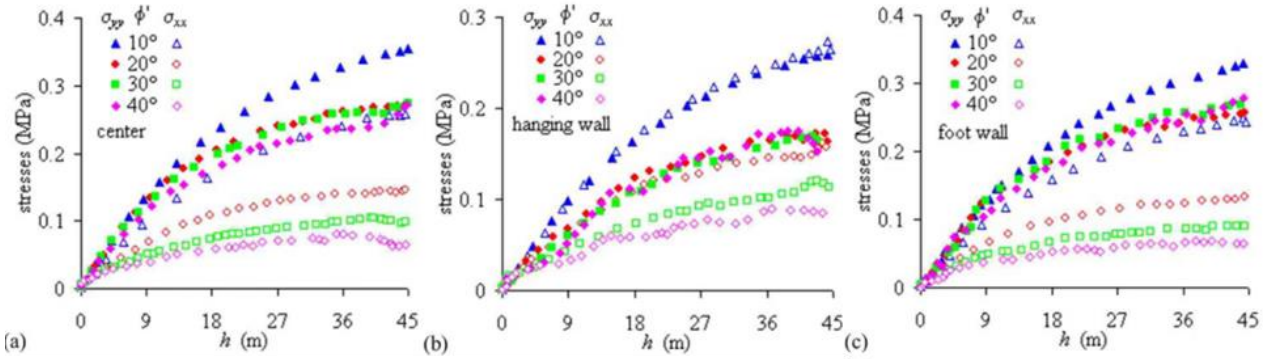

Figure 2-32: Stress variations with the backfill friction angle: along (a) VCL, (b) hanging wall and (c) foot wall in FLAC (from Li & Aubertin 2009e)

The stress can be quite sensitive to the magnitude of the fill cohesion for both a single step (Li et al. 2007) and multistep filling (Li & Aubertin 2009e; see also Jahanbakhshzadeh 2016; Liu et al. 2016a, 2016b). The vertical stress decreases with increased c value along three profiles, but the

stress becomes insensitive to *c* value above 50 kPa. A smaller stope width leads to enhanced arching effect along all three profiles, but such effect is less pronounced near the hanging wall (Li & Aubertin 2009e; Jahanbakhshzadeh 2016). Also, a greater dilatation angle (from 0° to 30°) results in a smaller vertical stress.

Jahanbakhshzadeh et al. (2016c) conducted simulations with FLAC^{3D} in part to validate their 3D analytical solutions (Eq. 2-22) proposed for inclined stopes using related fill parameters ϕ' and v. Their results indicated that increasing the stope length L generally increases the stresses at depth, due to the decreased arching effect. An increase in the angle ϕ' (from 30° to 40°) leads to reduction in horizontal stresses along the four walls.

2.5.1.3 Effect of interface elements

Pirapakaran (2008) introduced interface elements (softer than backfill) between backfill and rock walls in FLAC. El Mkadmi et al. (2014) used two thin layers (softer backfill) to represent the interfaces in SIGMA/W. Their intent was to have the stress state close to that obtained by FLAC without interface elements. In the presence of these elements, the vertical stresses (and displacement) become greater than the cases without interface. Interface elements allow larger movements of backfill, thereby reducing the retaining effect of the rock walls. Inclusion of interfaces seems to have little influence on the horizontal stress.

Liu et al. (2016a, 2016b) conducted simulation using FLAC^{3D} (for 2D models) to analyze the effect of interface elements, between the fill and rock mass, on the stress state along the VCL of backfilled stopes. The backfill parameters ϕ' and v are related.

Numerical results of Liu et al. (2016a) obtained with planar interface elements indicated that both vertical and horizontal stresses are reduced with an increase in the interface shear strength (δ and c_i). This indicates that the arching is mainly controlled by the shear strength of interfaces (not that of the backfill). It is noted that the stresses became unchanged as the interface cohesion increases beyond a certain value (i.e., 25 kPa for the cases considered). They also showed that interface elements are required when the local shear strength is significantly lower than that of the fill.

Liu et al. (2016a) also reported that the vertical and horizontal stresses become nearly insensitive to the normal (K_n) and shear (K_t) stiffness of interface elements as they exceed the values obtained with the method suggested by the FLAC^{3D} manual (Itasca 2013).

Numerical results of Liu et al. (2016b) obtained with nonplanar interface elements showed that stresses in backfilled stopes reduce as the interface roughness rises. This study also showed that interface elements are unnecessary when fill-wall contacts are sufficiently rough (normally the case of stope walls due to blasting).

2.5.2 Stress state in the backfilled drift and onto barricades

Li & Aubertin (2009c) have developed analytical solutions to estimate stresses in drifts when the backfill is in a fully drained (zero PWP) and submerged conditions, presented above in Section 2.4.5.1. To verify these solutions, they conducted numerical simulations with FLAC in plane strain conditions.

Fig. 2-33a shows the numerical and analytical results of normalized horizontal stress at the mid-height of access drift for different barricade positions. On this figure, σ_{hB0} is the horizontal stress at the base of the drawpoint; L is the distance from the barricade to the stope back-wall (Fig. 2-25); B is the stope width; l is the distance between the calculation point and the brow; H_d is the drift height. Within a certain distance (l/H_d < 4 in this case) in the drift, the results indicated a good agreement between the two different methods. The horizontal stress of numerical results in the drift drops to a minimum (constant) value when l/H_d > 4. It is also found that the horizontal stress on barricade becomes insensitive to barricade position for L > 2B in this case.

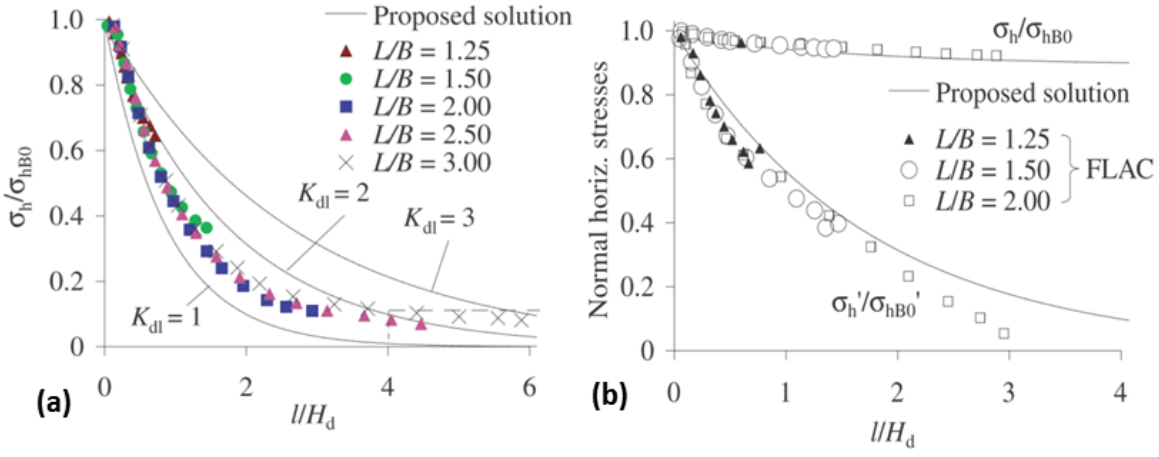

Figure 2-33: Normalized horizontal stress along the access drift (a) for a fully drained and (b) submerged conditions, obtained with numerical and analytical solutions (Li & Aubertin 2009c)

Fig. 2-33b shows numerical and analytical results in submerged conditions for the normalized effective and total horizontal stresses at the mid-height along the access drift. A good agreement

is observed between the two approaches, especially for the total stresses. It is seen that the effective stresses decline with the increased distance, while the total stresses are less sensitive (almost constant) to the distance.

2.5.3 Design of side-exposed backfill

The stability of cemented backfill during adjacent excavation is critical. Fig. 2-34 illustrates the displacement isocontour of the exposed cemented fill of primary stope (along the vertical plane of symmetry) at failure (critical state). A number of numerical analyses have been conducted in 2D and 3D to evaluate the stability of exposed cemented fill. The former may represent the cases of very large exposure length. These analyses are briefly reviewed in the following.

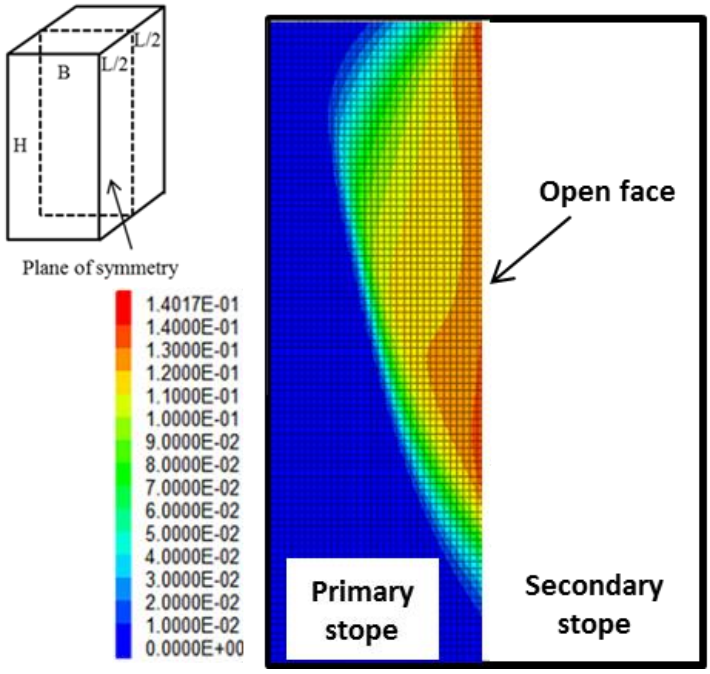

Figure 2-34: Displacement isocontour of the exposed cemented fill in primary stope along the vertical symmetry plane at failure (adapted from Chapter 5)

Cowling & Gonano (1976), Barrett et al. (1978) and Barrett & Cowling (1980) performed 2D and 3D calculations using finite element method (FEM) to assess the stability of cemented rockfill (CRF) and cemented hydraulic fill (CHF) at Mount Isa mine, Australia. It was shown that the fill stability depends on its strength, size of exposure and extraction sequence; the fill is more stable when the open face is close to the fill top than near the base. Barrett et al. (1978) indicated that if redistribution of excess stresses in the fill has not converged within 30 iterations, numerical

instability has usually occurred. The extent of tensile failure and plastic yield are also used to identify the failure.

Cundall et al. (1978) used a 3D explicit FDM code to evaluate the stability of exposed CHF and CRF in deep mining conditions (1200 m). The wall closure is found to be higher with CHF (modulus ratio to rock is 0.002) than with CRF (modulus ratio to rock is 0.1). By evaluating the yield state, it is shown that the stability of CHF is controlled by gravity, while the crushing failure due to wall closure appears in the case of CRF. The effect of fill strength and sequential exposure on fill stability was also studied.

Coulthard & Dight (1980) back-analyzed, using 2D FEM, a major failure of exposed CHF at ZC/NBHC mine, Australia. Their results suggested using a FS of 1.5 for backfill design. Similar 2D simulations conducted by Dight & Coulthard (1980) show the effect of exposure sequence on fill stability. Coulthard (1980) investigated the effect of wall closure on stability of exposed fill with 3D FEM. It was found that a small value (20 mm) of wall closure could stabilize the backfill by limiting the built-up of tensile stress, while a large one (100 mm) is likely to destabilize the exposed fill. A similar approach used by Barrett et al. (1978; see above) is adopted in these analyses to judge the failure.

Bloss (1992) carried out numerical modelling with a FEM code to assess the stress state and stability of CRF and CHF following side exposure at Mount Isa Mines, Australia. His numerical results illustrate the occurrence of arching along the depth, especially near the middle and bottom of the stopes. He also observed that the stability of the cemented backfill and the rock mass is positively related to the binder content, while the stability of exposed cemented fill is negatively related to the exposure width (square stope) for a given stope height. The effect of sequential extraction around a primary backfilled stope on backfill stability was also investigated.

Pierce (1997) assessed the stability of CPB upon vertical exposure (with FLAC^{3D}) at Golden Giant mine, Canada. The effect of fill strength and exposure length on fill stability was investigated. Pierce (2001) evaluated the required strength of CPB upon vertical and horizontal exposures using FLAC^{3D} at Brunswick mine, Canada. He conducted parametric analyses for the stability of exposed CPB to predict optimal binder content. The failure was identified by the extent of displacement and yielding. The required strength determined by the numerical analyses is found to be generally smaller than the backfill strength measured in the lab.

Coulthard (1999) conducted simulations with FLAC^{3D} to study the stability of side-exposed CRF at Mount Isa mine, Australia. His results showed that tensile yield could occur near the fill top and on the open face.

Rankine et al. (2002) studied the stress state within a primary stope filled with CPB during the sequential removal and filling of the surrounding secondary stopes with FLAC^{3D}. Their results show that the vertical stress in the center of backfill in the primary stope generally increases throughout the mining/filling sequence (see also Bloss 1996).

Sainsbury & Urie (2007) used FLAC^{3D} to assess the stability of narrow and inclined CPB filled stopes upon simultaneous horizontal and vertical exposures at Raleigh mine, Australia. A Mohr-Coulomb strain-softening model is used in which the tensile strength and cohesion degrade linearly from their maximum values at zero plastic strain to nil at a critical plastic strain (i.e., 1.5% as suggested by Swan & Brummer 2001). It is shown that the increase in UCS of CPB above a certain value has little effect on fill stability due to increased brittleness and modulus. By evaluating the cohesion and yield state, the exposed CPB could show crushing failure under large wall closure.

Emad et al. (2012, 2014) back-analyzed the failure of exposed CRF under static and dynamic loading conditions at a Canadian mine using FLAC^{3D}. Their results indicate that the exposed fill stable under static condition but it may fail due to blasting. Such failure is indicated by the development of tensile stresses.

Dirige & De Souza (2013) evaluated the stability of exposed CPB with a sillmat in an inclined stope using FLAC^{3D}. The plastic state and extent of displacement are used to identify failure. Results of centrifuge tests show that the failure is initiated by a tension crack starting from the fill top. A sliding plane is also developed upwards to meet the tension crack. Similar failure mode was also observed in centrifuge tests performed on CHF in vertical stopes (e.g., Smith et al. 1983; Mitchell 1986; Dirige & De Souza 2000).

Karim et al. (2013) evaluated (using 3DEC) the stability of three CPB backfilled stopes surrounding an open stope at Kencana mine, Indonesian. The failure of fill is identified by the displacement. Laboratory tests were performed to assess the effect of curing time and binder content on fill strength. Their results show that the pillar (16 m wide, 35 m long and 25 m high) can be mined after 14 days curing for backfill with cement content from 6% to 14%.

Li & Aubertin (2014) analyzed the response of backfill upon removing a rock wall with FLAC^{3D}. Their results suggest that the critical backfill strength can be based on the assessment of the total displacement. An analytical solution, presented above in Section 2.4.4, was proposed (partly) based on these simulations.

Bagde & Mitri (2015) used PHASE 2 to evaluate the stability of exposed CRF. Their results indicate that the fill design should allow for stress concentration in rock mass with high in-situ stress conditions.

Falaknaz et al. (2015d, 2016) analyzed the stress state within the backfill upon vertical exposure using FLAC^{3D}. Their results show that arching is largely decreased and non-negligible stresses exist along the fill-wall interfaces upon exposure. The required strength of the exposed fill is evaluated, based on the total displacement and strength to stress ratio (equivalent to FS). The effect of excavation sequence on fill stability was also investigated. The results indicate that the required strength increases with the increase in the stope length and height, but it is not much influenced by the stope width. It is also shown that the effect of stope geometry on the stability of exposed cemented fill is usually not well reflected by the existing analytical solutions of Mitchell et al. (1982) and their modifications (presented above in Section 2.4.4). There is thus a need to develop a new analytical solution.

Liu et al. (2016c) reproduced the physical box tests performed by Mitchell et al. (1982) using FLAC^{3D}. These tests were conducted in part to validate the well-known Mitchell et al. solution (presented above in Section 2.4.4) for the design of the side-exposed cemented fill under fully drained (long-term) condition. However, good agreement was achieved between the analytical solution and experimental data of Mitchell et al., and numerical results obtained with undrained (short-term) conditions. The box stability tests were performed under a condition close to a short-term undrained condition and the fill strength parameters used in the tests were also obtained under a condition close to the short-term undrained conditions (Liu et al. 2016c). Consequently, the Mitchell et al. solution may place the backfill design in a conservative side; but this limitation is probably somewhat overcome by the use of effective strength and strength gain with curing. It is noted that the failure of exposed cemented fill is evaluated by the yield state and strength-stress ratio.

In numerical simulations, the yield state, shear strength ratio, and the development of displacements and tensile stresses have been commonly used to assess failure of exposed cemented fill. In some cases however, these methods may become limited and somehow subjective. To reduce this subjectivity, Yang et al. (2016a, 2016b) have proposed a novel instability criterion to explicitly judge the onset of instability of waste rock barricades (see Chapter 4) and exposed cemented fills (see Chapter 5) in numerical simulations.

2.5.4 Earth pressure coefficient *K*

As mentioned previously, the backfill was considered as elasto-plastic and governed by the Mohr-Coulomb yield criterion (unless specified).

Li et al. (2003) used FLAC to investigate the stress state in backfilled stopes. Their results indicated that the earth pressure coefficient K ($= \sigma'_h/\sigma'_v$) near the stope walls (between K_a and K_0) is larger than that at the center (close to K_a). Simulated stresses can be well predicted by the arching solutions using $K = K_a$ along the vertical centerline of the stope.

Caceres (2005) conducted simulations with FLAC to study the effect of friction angle of backfill ϕ' on the value of K in the backfilled stope. A constant Poisson's ratio $\nu = 0.25$ was used. The results indicated that the K value agrees well with the Rankine's coefficient K_a when $\phi' \leq 30°$. For $30° < \phi' < 40°$, the K value becomes almost constant and tends to approach Jaky's K_0. Appling curve fitting technique to these numerical results, Caceres (2005) proposed a second order polynomial equation [Eq. (2-12)] to correlate the K value with the friction angle.

Fahey et al. (2009) performed simulations using FEM code PLAXIS. Their results showed that the K value along the VCL of vertical stopes agrees better with K_0 than K_a, for backfill parameters $\nu = 0.2$, $\phi' = 45°$ and $\Psi = 0°$. Fahey et al. (2009) also showed that the positive dilation angle can result in a passive K_p state (need further validation), while the negative one would make a state close to active K_a in some locations.

Sobhi et al. (2014, 2016) conducted simulations using PLAXIS to assess the influence of stope geometry and fill properties on the value of K along the VCL of backfilled stopes. The commonly used assumption with independent ϕ' and ν (= 0.2) was used. Their results indicated that the K value along the VCL of vertical stopes is close to K_a, suggesting that the fill is approaching an active state. These numerical results appear to be partly confirmed by laboratory data

(Pirapakaran & Sivakugan 2007b) and in-situ measurements (Hughes et al. 2010; Thompson et al. 2012; these will be presented in Section 2.6.3).

Numerical simulations conducted by Jahanbakhshzadeh (2016) indicated that the value of K across the width of vertical stopes lies between K_0 and K_a (and somewhat closer to the former). For inclined stopes, he showed that the K value tends to decrease from the hanging wall to the footwall. Thus, the use of a constant K within the whole opening is not representative, especially for openings with inclined walls. These results were obtained with related backfill parameters ϕ' and v.

These numerical results indicate that the actual value of K in backfilled stopes remains unclear. Yang et al. (2016c) have conducted a numerical study to analyze the value of K in backfilled openings (see Chapter 6).

2.5.5 The application of wick drains in stopes backfilled with CPB

A relatively large amount of water is added into CPB to produce a flowable mixture for pipe transportation. The excess PWP generated during the self-weight consolidation of CPB may jeopardize the barricade stability. Consequently, filling is usually performed in two stages: plug pour and final pour, separated by a few days' interval to allow the dissipation of excess PWP (e.g., Thompson et al. 2012, 2013). However, this interval may impair the production and cause pipe clogging. It is thus preferable to maintain a continuous and relatively fast filling by improving drainage and accelerating consolidation in the CPB.

Efforts have been commonly devoted in promoting the characteristics of barricade using porous materials to hold HF (e.g., Sivakugan et al. 2006a) and CPB (e.g., Li & Aubertin 2011; Yang et al. 2016a). Drain pipes are often installed in impervious barricades to accelerate the drainage in stopes with HF (e.g., Bloss & Chen 1982; Potvin et al. 2005) and CPB (e.g., Grabinsky et al. 2007; Thompson et al. 2009; 2011a).

In some other cases, drain pipes are used in stopes to remove the pond, generated on the surface of HF, and to facilitate filling (Neindorf 1983; Soderberg & Busch 1985; Hustrulid & Bullock 2001). As will be shown in the thesis, water ponding may endanger the barricade stability (see Chapter 3). However, the installation of drain pipes in stopes is usually difficult. This is probably why few applications were found in practice, particularly for CPB.

Recently, Li (2013a, 2013b) proposed to use wick drains in stopes to improve drainage and accelerate consolidation of CPB. It is believed that wick drains are easier to install due to its small volume and flexibility compared to regular drains pipes. With wick drains, 2D drainage can occur within backfill. Analytical solutions are available for the vertical and radial drainage around vertical drains (Hansbo 1981; Leo 2004).

Li (2013a, 2013b) performed numerical simulations using SIGMA/W to assess the effect of wick drain on drainage and consolidation of CPB. These models considered only one or two wick drains vertically placed in the stope with instantaneous filling. The drift and barricade were neglected. Fig. 2-35 shows that the maximum PWPs decrease to 200 kPa without wick drain and to 50 kPa with wick drain, 10 days following the filling.

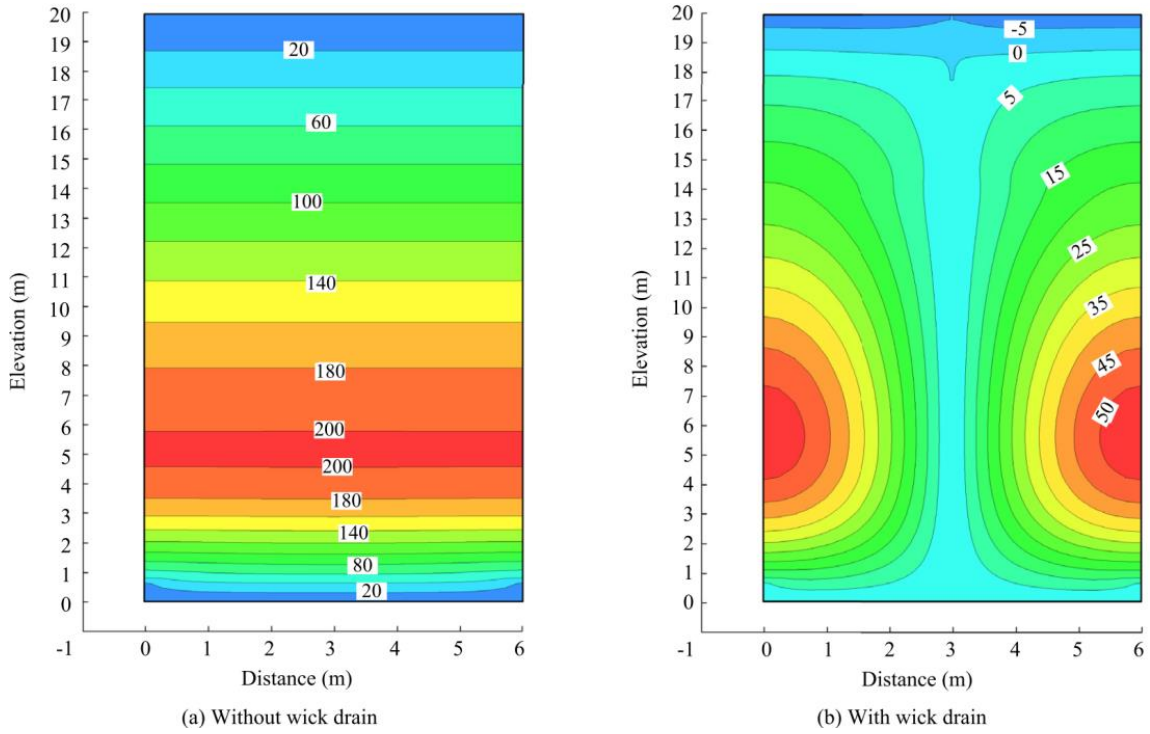

Figure 2-35: Distribution of pore water pressure in CPB; 10 days after filling (Li 2013a)

Li & Yang (2015) conducted numerical simulations with multi-layer filling sequences, more realistic stope geometry, and different configurations of wick drain (see Fig. 2-36). Their results showed that drainage and consolidation can occur during filling, depending on the hydraulic properties and rising rate of CPB. Hence, the complete neglect of the arching effect in CPB may place the barricade design in an over-conservative side. Li & Yang (2015) also showed that a stope can be filled continuously by using wick drains.

These results indicate that the use of wick drains in backfilled stopes is promising to facilitate the filling and production. Nevertheless, this study should be considered as conceptual due to several limitations involved in the numerical modelling discussed by Li & Yang (2015). More details on the application of wick drains can be found in Li (2013a, 2013b) and Li & Yang (2015).

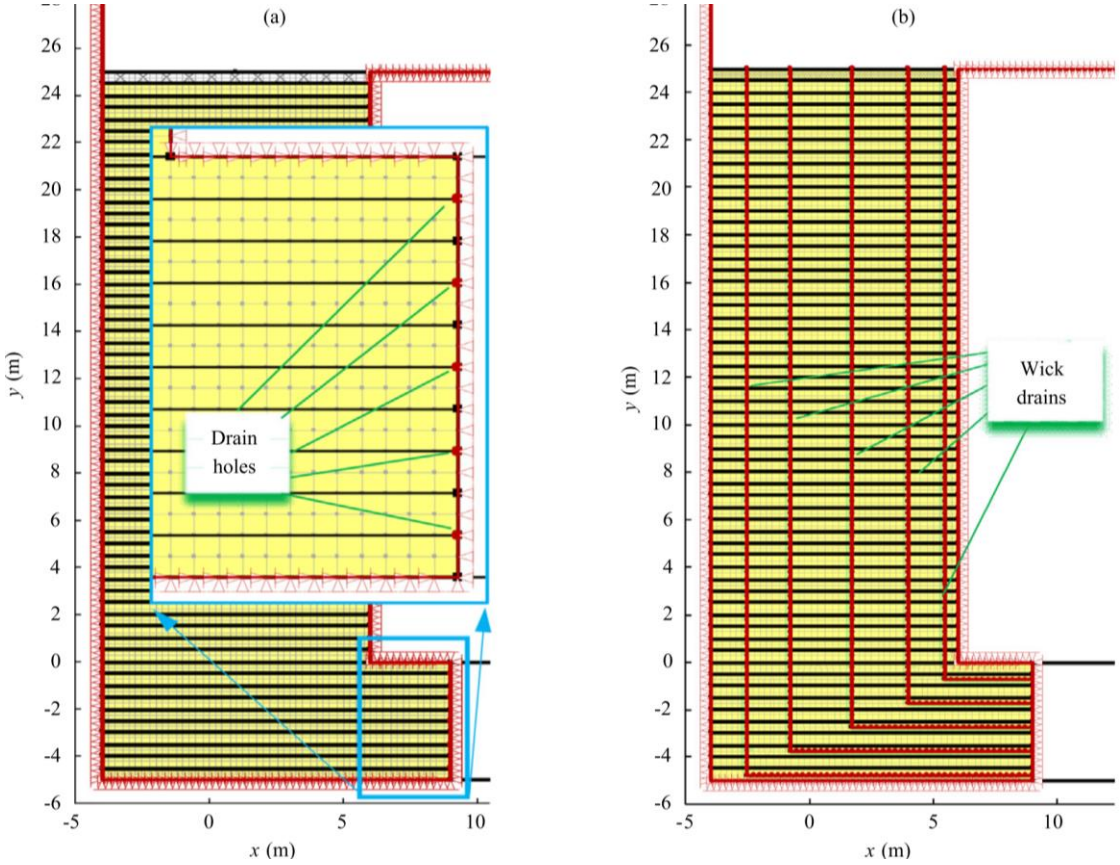

Figure 2-36: GeoStudio models of a backfilled stope: (a) with no wick drain but 5 drain holes on the barricade; (b) with 5 wick drains in the stope and through the barricade (Li & Yang 2015)

2.6 Experimental tests for assessing stresses in backfilled openings and drifts

Laboratory tests and in-situ measurements can provide reliable data that can be compared to analytical and numerical solutions, as long as the measurements are performed in a reliable manner. Thus, experimental data are desirable for engineering applications.

Laboratory tests and in-situ measurements have their advantages and limitations. In laboratory tests, it is easier to control or measure the properties of the materials, model geometries and loading conditions. But these usually suffer from the limited representativeness of field conditions. For field measurements, the complex geometry, material behavior and many

influencing factors may render the interpretation of test results a veritable challenge. Besides, the calibration of instruments for in-situ measurements before and after installation in mining stopes and drifts is very difficult. But this aspect is critical for successful instrumentation and field measurements. Another limitation of most experimental measurements is related to the cost and time.

In the following, some small-scale laboratory tests conducted to study arching effect (dry fills) and consolidation in backfilled openings will be first reviewed. Some in-situ measurements within hydraulic fill (HF) and cemented paste backfill (CPB) will then be presented. It is noted that the geochemical and microstructural properties of CPB have been intensively evaluated, mainly in the laboratory (Benzaazoua et al. 1999, 2002; 2004, 2008; Belem et al. 2001, 2007; Fall & Benzaazoua 2005; Ouellet et al. 2006, 2007, 2008; Fall & Samb 2007, 2008; Fall & Pokharel 2010; Ghirian & Fall 2013, 2014, 2015, 2016). However, these aspects are not discussed here as they are considered beyond the scope of this work.

2.6.1 Laboratory measurements using physical models

2.6.1.1 Vertical stopes

Pirapakaran and co-worker

Pirapakaran and co-worker (Pirapakaran & Sivakugan 2007b; Pirapakaran 2008) designed a 1:100 scaled laboratory apparatus to study the vertical stress distribution in backfilled stopes. Laboratory tests results were used to validate their 3D analytical solutions (Pirapakaran & Sivakugan 2007a; see Section 2.4.2.2) and numerical simulations (see Pirapakaran 2008). Significant arching effects were observed in the backfilled openings in the lab. Pirapakaran (2008) pointed out that the arching effect significantly increases with increased surface roughness.

Sivakugan and co-worker

Sivakugan and co-worker (Sivakugan & Widisinghe 2013; Widisinghe et al. 2013) conducted laboratory tests to investigate the stress state of granular fill using the similar apparatus of Pirapakaran & Sivakugan (2007b). Widisinghe et al. (2013) also performed numerical modelling with FLAC^{3D} for comparison with the experimental results. The analytical and numerical models, based on continuum theory, indicate that the vertical stress tends to become almost constant beyond a certain depth. As a particulate (granular) medium, however, the granular fill exhibits

less arching in laboratory tests. Up to 3B depth, Widisinghe et al. (2013) illustrated that the interlocking of particles (or the formed matrix) between fill grains tends to maintain the continuum behavior. As the filling progresses, the interlocking become less due to higher loads and therefore, the vertical stress increase linearly at the lower part of the stope. It should be noted that this was only based on the interpretation of their experimental results; no interlocking was actually observed. The similar phenomenon can also be observed from the laboratory results of Pirapakaran (2008) and Sivakugan & Widisinghe (2013).

Belem et al. (2016)

Belem et al. (2016) conducted 3-m high column tests (Fig. 2-37) to investigate the self-weight consolidation and strength development of CPB at mine backfill plants. Their results showed that water drainage and settlement induced by self-weight consolidation occur mostly in the first 48-72 h (also depends on the size of column and hydraulic properties of CPB) after the columns are completed filled. The maximum content of water collected (drained through the walls and base) varies from 9% (PLD - partial lateral drainage; middle one in Fig. 2-37) to 26% (a case with FLD - full lateral drained; not shown here) of the initial total water in CPB.

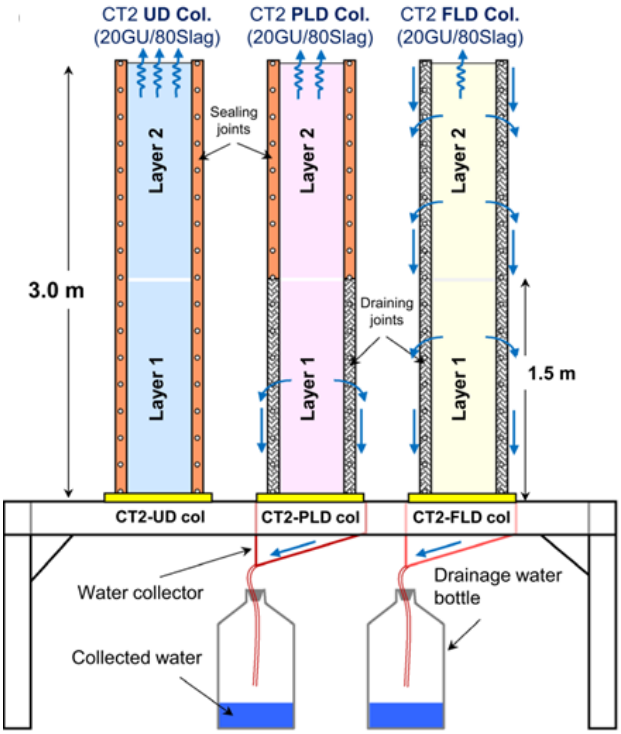

Figure 2-37: Schematic view of the three consolidation columns filled with CPB at a mine backfill plant (Belem et al. 2016)

Belem et al. (2016) reported that the vertical strains lie between 2.5% (UD - undrained column; at left in Fig. 2-37) and 5.5% (FLD - full lateral drained column; at right in Fig. 2-37). Compared to the in-situ volumetric strain range of 3.3 - 5.0% observed, they stated that the in-situ backfilled stopes may behave somewhat similarly to the FLD or the PLD (middle column in Fig. 2-37) conditions. These results suggest that neglecting drainage (during consolidation) through stope walls may not be entirely true for fractured rock mass.

2.6.1.2 Inclined stopes

Ting et al. (2012) modified the laboratory apparatus of Pirapakaran & Sivakugan (2007b) to plane strain conditions to evaluate the vertical stress in inclined stopes filled with granular material. This laboratory apparatus was developed to validate their 2D analytical solution (Ting et al. 2011; see Section 2.4.2.3). The opening had a length (500 mm) to width (100 mm) ratio of 5, to represent a plane strain condition. The height of the stope was 900 mm and the inclination of the stope could be adjusted to 90°, 80°, 75° and 70° (to the horizontal).

The average vertical stress at the stope base increases slightly with the change of stope inclination from 90° to 80° and then, it decreases with the stope inclination varying from 80° to 70°. The average vertical stress peaks at the stope inclination of around 80°, which is inconsistent with the average vertical stress determined by analytical solutions (Ting et al. 2011) and numerical modelling (Li & Aubertin 2009e) of inclined stopes. It is noted that Li & Aubertin (2009e) numerically found the maximum vertical stress near the FW for an inclination of about 70°. The experimental results indicated that the vertical stress near the FW peaks when the stope tilts slightly from the vertical (e.g., less than 20°). Li & Aubertin (2009e) and Ting et al. (2012) both indicated that the variation of vertical stress is insignificant when the inclination angle is between 80° and 90°.

Ting et al. (2012) indicated that the magnitude of stress transferred to the base of stopes largely depends on the wall roughness, aspect ratio and stope inclination.

2.6.2 In-situ measurements

Reported experimental results indicate that samples of in-situ backfill usually show somewhat different properties from lab-prepared samples, with higher shear strength, shear modulus, and lower water content for the same period of curing (Revell 2004; le Roux et al. 2005; Fahey et al.

2011; Thompson et al. 2011b, 2012). These differences may be due to scale effect, different stress state, enhanced field mixing, higher stope temperatures (Grabinsky & Thompson 2009; Fall et al. 2010; Thompson et al. 2014a, 2014b; Walske et al. 2016), wall convergence (Hassani et al. 1998, 2001), drainage and consolidation of backfill (Fahey et al. 2011).

The evolution of the PWP and total/effective stresses in stopes and drifts need to be assessed for a successful application of backfilling. Therefore, it is useful to implement in-situ instrumentation to better understand the backfill response under complex field conditions.

2.6.2.1 Hydraulic fill

US Bureau of Mines

In the early 1960s, a series of field instrumentations were initiated by the US Bureau of Mines. These measurements were performed in mine stopes backfilled with HF.

McNay & Corson (1961) performed some in-situ measurements in some mines of the Coeur d'Alene district in Idaho, USA. The field instrumentation was designed to monitor the in-situ behavior of hydraulic sandfill and evaluate the backfill pressure due to wall displacement. Corson & Wayment (1967) conducted field instrumentation in a subvertical vein stope at the Star mine in Idaho, USA. They investigated the variation of stresses with displacement in a backfilled stope, 3 m wide and 2000 m deep. They reported that the pressures (total stresses) across the vein increased more rapidly than the pressures in the plane along the orebody strike during filling. The closure measured in the stope was approximately 10 cm.

Corson (1971) conducted field instrumentation at the Luck Friday mine in Idaho, USA. Around the instrumented stopes, rockbursts due to the resumed mining would cause increases in backfill pressures. Corson (1971) indicated that large portions of wall loads resulting from rockbursts were transferred to the backfill. The backfill of one trail stope was compacted (with hand-held vibrator and immersion-type vibrator) after filling, and the backfill of the other trial stope was filled naturally. Corson (1971) pointed out that strain rate increased significantly as the rockbursts occurred. The average strain of the compacted fill is less than that of the natural fill.

Askew et al. (1978)

Askew et al. (1978) monitored the pressures of uncemented HF during stope filling at Broken Hill, Australia. Askew et al. (1978) demonstrated a fluctuation of backfill pressures relative to

filling rate. The measured earth pressure coefficient *K* at the center of the stope was 0.58, which correlated well with their numerical results. The measurement indicated total pressures around 20 kPa on the timber barricades when they were completely covered and then, the pressures slightly increase until the end of filling. Askew et al. (1978) attributed these low pressures to the arching effect in the drift.

Knutsson (1981)

Knutsson (1981) conducted in-situ stress measurements in three HF filled stopes (inclined at 23° to the vertical) at the Nasliden mine, Sweden. These stopes are narrow with high length to width ratio (≥ 10). Knutsson (1981) considered the stresses within HF were theoretically the sum of two parts: one due to the self-weight of the backfill and the other due to wall convergence. The former was determined by the silo (arching) theory and the latter by means of soil mechanics (1D compression). But the details of the latter calculation were not given. The stresses calculated in this way correlated fairly well with in-situ measurements. It is noted that Jaky's equation (i.e., $K_0 = 1 - \sin\phi$ where $\phi = 36°$) was used to relate the stress perpendicular to the wall and the vertical stress, although wall convergence occurred for this case.

Thibodeau (1989)

Thibodeau (1989) reported field instrumentation at Levack Mine in Canada. It was found that arching theory and the elastic beam theory could not be applied since the principal stresses measured in the fill were much larger than the maximum stresses calculated using arching equations, attributed to pillar convergence.

2.6.2.2 Cemented paste backfill

Hassani and co-workers

Hassani and co-workers (Hassani et al. 1998, 2001) reported some in-situ measurements for CPB at the Chimo mine, Canada. At the end of first filling (to 13 m), the measured vertical pressure 180 kPa was almost equal to the geostatic pressure 189 kPa. But the lateral stresses were 245 (across the orebody) and 149 kPa (along the orebody), respectively.

The temperature in backfilled stope increased during filling. During the curing period, Hassani et al. (1998, 2001) mentioned that the backfill pressures declined. Hassani et al. (2001) found that the stress along the orebody dropped significantly to zero (tension reaction) due to the opening of

the adjacent stope. As the mining advances in the adjacent stope, their results indicated that both the vertical stress and stress across the orebody rose, but the stress along the orebody hovered around zero and started to increase when the last layer of the orebody was blasted in the adjacent stope.

Hassani et al. (1998) stated that the HW displacement plays an important role in the increased backfill pressure. They also pointed out that CPB was capable of absorbing the energy released by rockburst.

Belem and co-workers

Harvey (2004) and Belem et al. (2004) investigated the evolution of pressures within CPB during placement and consolidation in a trial stope at Doyon Gold mine, Canada. When the filling was resumed, the pressures at the base increased at a rate less than that at the plug/final pour interface, demonstrating the effect of this plug. Belem et al. (2004) mentioned that the third filling step (882 tons CPB added from the 13^{th} day) had little influence on the pressures at the stope floor due to the arching effect. Belem et al. (2004) also pointed out that the pressures during the curing period underwent a slight drop (also observed by Hassani et al. 1998).

Unlike the pressures within the stope, the barricade pressure slightly rose during the curing period. The cause of this increase was not addressed. The barricade pressure peaked around 55 kPa. Following the peak, the barricade pressure fell, showing no pressure increase due to the placement of additional CPB.

le Roux et al. (2005)

le Roux et al. (2005) studied the in-situ performance of CPB at the Golden Giant mine in Ontario, Canada. A self-boring pressure (SBP) meter was used to assess the in-situ strength properties and stress state of CPB after stope filling. The SBP meter was also used at the Bouchard-Herbert mine (Ouellet & Servant 2000).

The SBP results demonstrated that the undrained shear strength of CPB ranges from 435 to 641 kPa and the modulus ranges from 239 to 514 MPa. le Roux et al. (2005) mentioned that the stope was filled after excavation when the destressing of rock walls completed; so the initial stress state of CPB is mainly controlled by its self-weight and later by arching as the CPB gains strength.

le Roux et al. (2005) also conducted laboratory tests on CPB prepared in the lab. The comparison between the in-situ measurements and laboratory results indicated that the lab-prepared CPB has a lower strength (50% - 80%) than the field CPB. Thus, they suggested that design based on the laboratory material may be conservative.

Helinski et al. (2011)

Helinski et al. (2011) conducted in-situ measurements within CPB at the Kanowna Belle (KB) Mine and Savannah Nickel (SN) Mine, Australia.

At the KB mine, a geostatic condition was observed during initial filling. After about 20 h, the deviation of PWP from overburden indicated the development of effective stress. Helinski et al. (2011) attributed this to cement hydration during which the PWP decreases as the volume reduces due to "self-desiccation" (Grabinsky & Simms 2006; Helinski et al. 2007). This may be incomplete because the consolidation within CPB also contributed to the reduction in PWP and hence the increase in effective stress.

At the end of filling, the vertical stress was significantly lower than the overburden pressure, due to arching effect. However, it is worth mentioning that the stresses were measured within a continuum that experiences stiffness change due to consolidation and cement hydration (Take & Valsangkar 2001), hence the total pressure readings can only be treated somewhat as an indication of the true total stress (Helinski et al. 2011). During the one day curing period, the pressures drop slightly.

At the SN mine, the PWP increased at a rate significantly less than that of the overburden stress, demonstrating a significant consolidation during filling. Helinski et al. (2011) attributed the low PWP values to a combination of the high permeability and high stiffness of the material shortly after placement, and the low rising rates. Under such conditions, the CPB behaves somewhat as a typical HF, whose drainage and consolidation can be completed rapidly. The magnitude of PWP is governed by the "steady state" drainage conditions in the fill, which depend on the restriction to flow created at the base of a stope due to a reduced flow area through the stope drawpoint (Cowling et al. 1988; Traves & Isaacs 1991; Yang & Li 2016).

Hasan et al. 2014

Hasan et al. (2014) conducted full-scale monitoring of CPB during and post-filling at the Lanfranchi Nickel mine, Australia. The average rising rate was 0.7 m/h. The stope can be regarded as low and wide.

During initial filling, an almost undrained state was observed. As the filling continued, PWP gradually deviated from total stress, marking the start of consolidation and arching. During the first curing period (13 hours), Hasan et al. (2014) reported a drop of PWP and total stress due to consolidation and hydration. When the filling was resumed, the total stress and PWP again climbed until the second curing period. At this point, the total stress and PWP are much lower than geostatic stress, indicating a continuous arching.

During the second curing period, the total stress started rising following an initial decline while PWPs continuously decreased. The increase of total stress during curing period is against the results of Belem et al. 2004 and Hassani et al. (1998, 2001). However, Hasan et al. (2014) stated that "this anomalous behavior has been observed a number of times and should not be dismissed as instrument malfunction". No detail was given on this response. The pressure increase during curing time is probably due to the temperature increase. However, the increase was not observed during the first curing time and the temperature was not recorded. Hence, the cause of this anomalous response is unclear.

Thompson, Grabinsky and co-workers

A team of University of Toronto has performed a comprehensive monitoring program at three different underground mines: Williams Mine, Kidd Mine and Cayeli Mine.

Grabinsky et al. (2007) measured the backfill pressures in the drift at Williams Mine, Canada. They reported quite low barricade pressures during the plug pour. It was found that the total stresses in the drift fall as the measuring points are farther away from the brow, even evident for the initial filling. This is supported by the analytical solutions of Li & Aubertin (2009c, 2009d) showing that the pressures on barricades are inversely proportional to the distance between the barricade and stope. Thompson et al. (2011a) conducted in-situ measurements during continuously filling a stope at Williams Mine. The geostatic loading was observed for less than five hours. After that, the vertical pressures increased at greater rates than the horizontal pressures.

Thompson et al. (2009) performed field instrumentation at Kidd Mine, Canada. At the end of filling, the horizontal stress deviated significantly from the vertical stress, indicating a well-developed arching in CPB. Fig. 2-38 shows the evolution of total stress acting along the drift towards barricade for four TEPCs. The pressures are close to each other for the first 1.5 days and then varied in different manners. Again, it is seen that the pressures decline with increased distance from the stope brow, indicating arching effect.

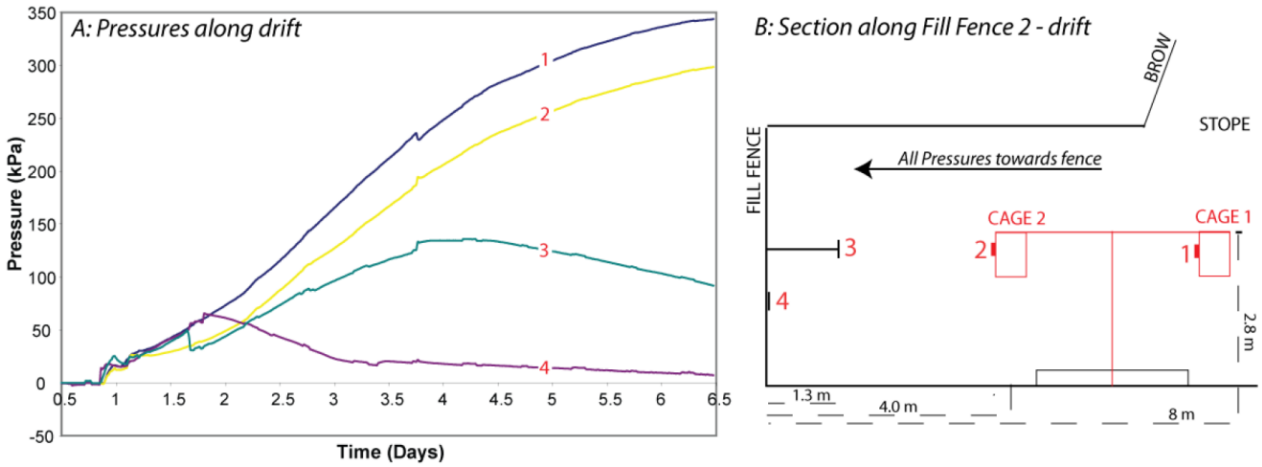

Figure 2-38: (A) Total pressures during the filling for TEPCs on the barricade, in the drift and under the brow as shown in (B) (Thompson et al. 2009)

At Kidd Mine, Thompson et al. (2014a) showed that a positive correlation is found between pressure and temperature (binder hydration). They mentioned a 300 kPa pressure increase due to an 11°C temperature increase at one location. The thermal expansion-induced pressures could constitute 50% and 63% of the vertical and horizontal pressures at the end of the first pour, at a stope. Similar phenomenon was found in CHF.

Thompson et al. (2012) instrumented two stopes (denoted as 685 and 715) at Cayeli Mine, Turkey. For both stopes, three cages were mounted vertically in the center of the stope and two cages were installed under the stope brow. TEPCs and piezometers were also fixed on the 5m high barricades.

The 685 stope was the larger of the two stopes; it was 16 m high with a plan section of 25 m by 12.5 m. The average rising rate was about 0.25 m/h. The binder contents of the plug pour and final pour are 8.5% and 6.5%, respectively. The stope was filled continuously in 2.85 days. The plug pour was completed at 1.8 days.

Thompson et al. (2012) reported that a geostatic loading period was recorded in the plug pour (from 12 to 15 h) and the final pour (20 h). They attributed the longer geostatic loading of the final pour CPB to slower cement hydration due to the lower binder content.

The evolution of total earth pressure (TEP), pore pressure (PP), and temperature for barricade and Cage 3 are depicted in Fig. 2-39 for the initial 5.5 days. The barricade pressure peaked at 47 kPa the end of filling. For Cage 3, the vertical pressures continued climbing at a much greater rate than horizontal pressures after the geostatic loading period. The pore water pressures at the barricade location are significantly lower due to the enhanced drainage around the barricade.

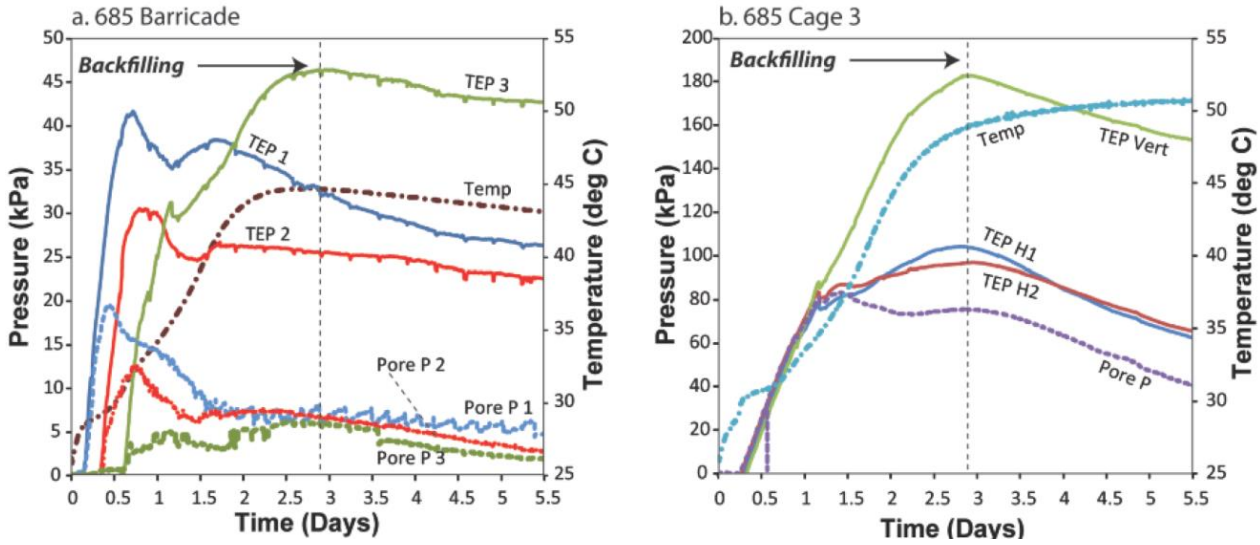

Figure 2-39: TEP, PP and temperature measured at the (a) barricade and (b) Cage 3 in 685 Cayeli Mine stope. TEP orientations H1 and H2 are horizontal and V refers to vertical pressure (Thompson et al. 2011a)

The 715 stope had an undercut area of 10 m and 15 m, with a height of 15 m. The rising rate is between 0.35 and 0.42 m/h. The binder content is 6.5%. The backfilling was completed in two pours separated by a three day's curing period.

The evolution of total earth pressure (TEP), pore pressure (PP), and temperature for barricade and Cage 3 are depicted in Fig. 2-40 for the initial 5.5 days. During the first pour (20 h), Thompson et al. (2012) reported a geostatic loading at all the cages (only Cage 3 is shown). The barricade pressures climbed to 99 kPa. During the curing period, pressures first declined. It is noted that the temperature began rising around 2.5 days, demonstrating the acceleration of cement hydration. Around 12 h after the rising of temperature, total pressures were found to climb at most locations.

This increase agreed quite well with temperature increase and was attributed to thermal expansion of the CPB in a confined volume (Thompson et al. 2009, 2014b). However, the variation of PWPs with the increasing temperature appears to be less regular and was not explained. There was no significant change in pressure at the barricade during the second pour (21 h), emphasizing the contribution of plug to the barricade stability. Thompson et al. (2012) mentioned that the development of effective stress is more rapid in CPB with higher binder content. They also reported that the rising rate is positively related to the rate of pressure increase.

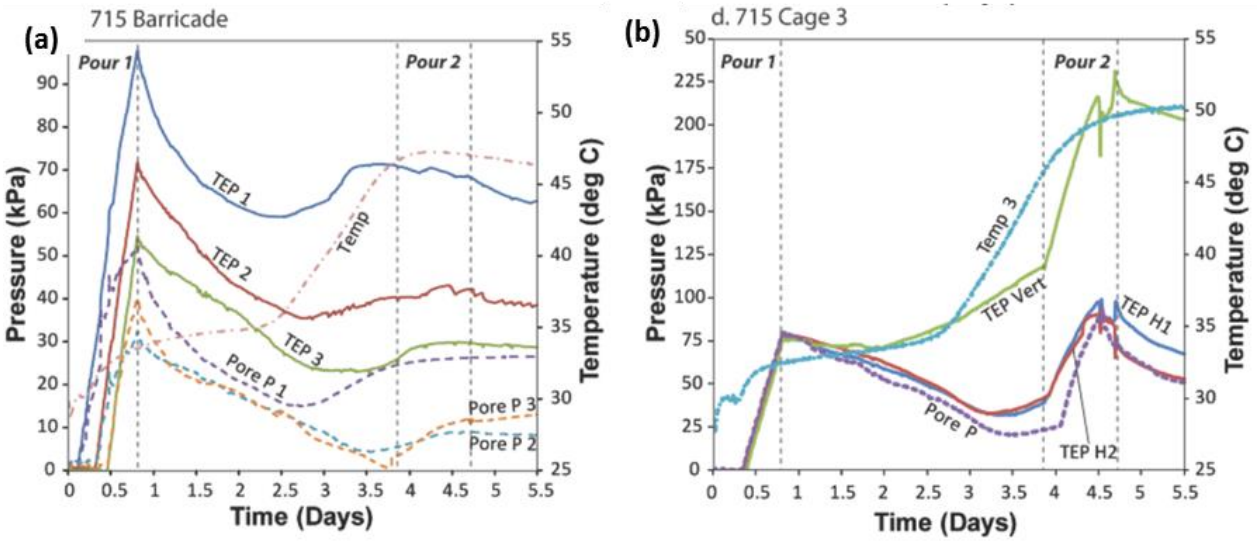

Figure 2-40: TEP, PP and temperature measured at the (a) barricade and (b) Cage 3 in 715 Cayeli Mine stope. TEP orientations H1 and H2 are horizontal and V refers to vertical pressure (Thompson et al. 2011a)

Doherty et al. (2015)

Doherty et al. (2015) conducted instrumentation in three CPB filled stopes at the Raleigh gold mine, Australia. The three stopes are inclined between 20° and 25° (to the vertical), and their geometries are about 17 m high, 18 m long and 3.5 m wide. It was aimed at investigating the effect of the filling sequence, barricade drainage and binder content on the stress state in the backfilled stopes and drifts. Their results indicated that the filling sequence significantly influence the development of PWP and total (effective) stresses of CPB during filling. They also showed that the PWP significantly reduces during the rest time, even for very short rest periods.

The barricade was built with (about) 30 cm-thick shotcrete. Doherty et al. (2015) found that the PWP increases for the barricade with no drain pipe but decreases for the barricade with drain

pipes, near the drawpoint and barricade during rest time. They also reported that the water collected from the drain pipes (on the barricade) is less than 0.1% of the water poured into the stope. Based on the column test results of Belem et al. (2016), it might be inferred that the water may also drains through the (fractured) stope walls and elsewhere.

The stability of cemented backfill upon exposure (subject to dynamic loading conditions) is another concern. The stability of exposed CRF due to blast-induced vibration has been monitored by Emad et al. (2015b) at a nickel mine located in Manitoba, Canada. The results indicate that the CRF is subjected to high vibration levels during blasting and the backfill failure due to blasting can occur near the top of the fill. It was also shown that excessive blast-induced vibrations are the main reason of ore dilution.

2.6.3 Earth pressure coefficient

Thompson et al. (2012) demonstrated that the values of K ($= \sigma'_h/\sigma'_v$) evolve with backfilling, pore pressure dissipation, and curing. However, a consistent pattern is observed if only the hanging cages in the center of the stope are considered.

In the continuously poured trial stope, the lower central portion of the CPB appears to be close to the Rankine's active state while the upper portion appears to be closer to the at-rest state. Hughes et al. (2010) monitored the barricade pressures at the Red Lake mine located in Ontario, Canada. Their results indicated that the value of K during initial placement of CPB is close to Rankine's coefficient K_a. These results are somewhat consistent with the values of K obtained from numerical simulations by Sobhi et al. (2014; 2016; presented above in Section 2.5.4).

In the staged-poured trial stope, however, Thompson et al. (2012) reported that the lower central portion of the stope appears to be close to the at-rest state while the upper portion is higher.

There are still uncertainties on the actual value of K in backfilled stopes. Numerical analyses have been performed by Yang et al. (2016c) to assess the K value in backfilled openings (see Chapter 6).

CHAPTER 3 ARTICLE 1: EVOLUTION OF WATER TABLE AND PORE WATER PRESSURE IN STOPES WITH SUBMERGED HYDRAULIC FILL

Pengyu Yang & Li Li

This article was submitted to ASCE - *International Journal of Geomechanics*, accepted with changes in October 2016.

Abstract: Hydraulic fill is often used to fill large underground voids created during mining operations. It is produced and distributed as a slurry at a pulp density, P of 65-75% (solids content). Consequently, a substantial amount of water needs to drain after placement. Inadequate drainage has been regarded as the main cause of barricade failure for stopes with hydraulic fills. Therefore, a good understanding of the evolution of total and effective stresses within such backfilled stopes is critical for barricade design. Most existing analytical solutions for assessing stresses in stopes were based on Marston's approach by considering a fully drained (without pore water pressure) or hydrostatic state. These conditions are not always representative of the stress state in stopes and behind barricades. When slurried hydraulic fill is placed into a stope, the self-weight consolidation or sedimentation of the fill can take place fairly rapidly. Ponding could first occur on the top of backfill if the drainage through barricades is not sufficient. Drainage through the barricade then allows the water table to descend, changing the pore water pressures with time. In this paper, the authors present analytical solutions for estimating the evolution of the water table and pore water pressures in stopes with submerged hydraulic fills. These solutions are validated using numerical simulations conducted with SEEP/W. The results show that the ponding on the top of the settled fill has a negative impact on the barricade safety. The 2D modelling without considering the reduced drift area tends to underestimate the pore water pressures in stopes and behind barricades, which may render the barricade design non-conservative. Discussion follows on some particular features and limitations of the proposed analytical and numerical solutions.

Keywords: Mine stopes; Hydraulic fill; Drainage; Pore water pressure; Analytical solution; SEEP/W.

3.1 Introduction

The history of backfilling underground mined-out voids (stopes) probably dates back to the beginning of mining several centuries ago (Potvin et al. 2005). In recent decades, the practice of mine backfill has significantly increased worldwide. In general, mine backfill is mainly used to ensure stope stability, increase recovery and minimize dilution (Thomas 1979; Hassani & Archibald 1998). The surface disposal of mine wastes (i.e., waste rock and tailings) can also be reduced by filling underground stopes with these wastes, as an environmentally friendly method (Aubertin et al. 2002, 2016; Bussière 2007; Benzaazoua et al. 2008; Li 2014; Falaknaz et al. 2015; Liu et al. 2016a; Yang et al. 2016a).

A variety of mine backfills have been developed to meet specific engineering goals depending on the mining methods utilized. The most commonly used mine backfills are rockfill (RF), hydraulic fill (HF), and cemented paste backfill (CPB). HF was initially used in some coal mines in the U.S.A. since 1884 and quickly spread around the world (Peele 1941; Potvin et al. 2005). While CPB is gaining popularity, HF remains common (e.g., Martic et al. 2014; Thompson et al. 2014; Liu et al. 2016b). It is defined as slurry with relatively low solids content (normally from 60% to 75%), consisting of classified mill tailings and/or sands (cemented or not), transported through boreholes and pipelines to underground stopes (Hassani & Archibald 1998; Potvin et al. 2005).

Due to the high permeability and the workability requirement for hydraulic delivery (transportation), HF contains a substantial amount of water that drains fast after placement and becomes free water. When the drainage through the barricade is not as efficient as water bleeding, a pond can form on the top surface of the fill, generating high pore water pressures (PWP), threatening the stability of the support structure (barricade). The barricade usually identifies low pressure and porous structures while the bulkhead usually means high pressure and impervious structures (Grice 1998). As drain pipes are usually installed through the impervious structures (i.e., bulkhead), these two terms are sometimes used interchangeably. Here, the term "barricade" is used to represent both of them. The pressure exerted by the backfill on the barricade must be adequately evaluated to ensure a secure barricade design.

Most existing analytical solutions for assessing stresses in backfilled stopes were developed for the case of a fully drained (zero PWP; e.g., Askew et al. 1978; Aubertin et al. 2003; Li et al. 2005) or a hydrostatic state (e.g., Li & Aubertin 2009a, 2009b). These solutions are valid when the

backfill is fully dry or when a hydraulic equilibrium is achieved within the HF retained by an impervious barricade. Alternately, Sivakugan and coworkers (Sivakugan et al. 2006b; Sivakugan & Rankine 2006) made use of the method of fragments to estimate the maximum PWP in a 2D stope with hydraulic fill and a porous barricade. These solutions are valid for the case of steady-state flow when the height of the water table is constant in the backfilled stope. When HF is retained by pervious barricades, the water table in a stope could first rise to form a pond by the decant water, followed by a lowering with time due to the drainage through the barricade; this is usually the case with a porous brick barricade that has a hydraulic conductivity as high as 1 to 3 mm/s (e.g., Rankine 2005; Sivakugan et al. 2006a). It can thus be expected that the water table, PWP, total and effective stresses in the stope evolve with the drainage and water flow through the barricade.

In this paper, a simple solution is first proposed for estimating the initial height of free water above the fill surface generated by the placed HF. Analytical solutions are then proposed for evaluating the evolution of the water table and pore water pressures in the backfilled 3D stope with a free-draining barricade. The proposed solutions are validated using numerical simulations conducted with SEEP/W. Sensibility analysis are performed using typical geometric and hydraulic properties to analyze the key influencing factors.

3.2 Proposed solution

Fig. 3-1 schematically shows a typical backfilled stope with submerged hydraulic fill. A pond above the fill surface is formed by decant water due to the quick drainage and self-weight consolidation of the HF. In this figure, H_w (m) is the pond height and H_b (m) is the height of settled HF in the stope. B (m) is the stope width and L (m) is the stope length. H_d (m) and L_d (m) represent the drift height and width, respectively. The distance of the porous barricade to the stope is denoted by l (m).

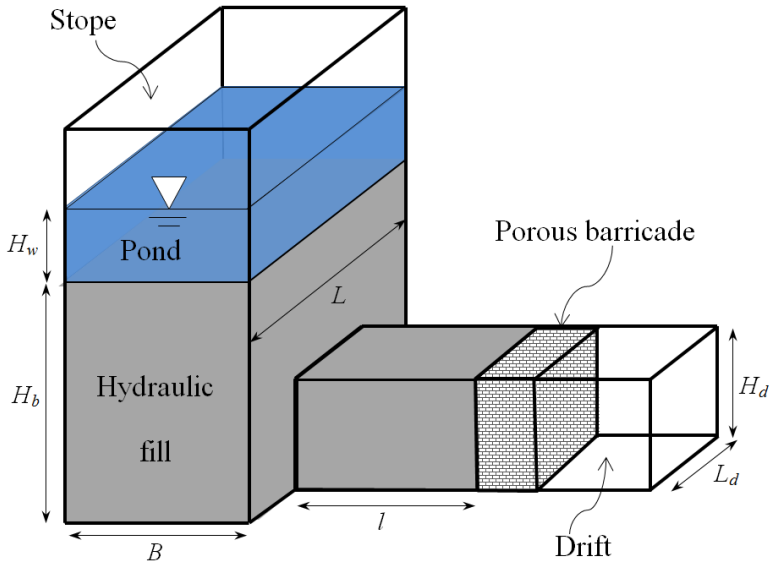

Figure 3-1: Schematic model of a typical backfilled stope with a pond above the fill surface (adapted from Li & Aubertin 2009b)

3.2.1 Initial height of pond H_{w0}

Particles of slurried fills tend to sediment under self-weight to a denser state once placed into a stope. This leads to the generation of excess PWP within fill. The drainage and consolidation accompanied with the dissipation of the excess PWP is a well-known phenomenon, called self-weight sedimentation or consolidation (e.g., Wickland & Wilson 2005; Pedroni 2011; Aubertin 2013; Li et al. 2013; Yang & Li 2015).

Fig. 3-2 illustrates the self-weight sedimentation and generation of a pond above the fill surface in a HF filled stope (the third dimension L and drift are not shown). HF usually has a high hydraulic conductivity and behaves similarly to a sandy material. The self-weight sedimentation can thus take place very fast with bleeding of substantial free water. As shown in Fig. 3-2, the upward drainage could develop within a backfill when the drainage through barricade is not as efficient as the water bleeding, thereby leading to a formation of a pond (with initial height H_{w0}) on the fill top (e.g., Neindorf 1983; Soderberg & Busch 1985; Fourie et al. 1994; Bloss & Chen 1998; Hustrulid & Bullock 2001; Kuganathan 2001; Rankine 2005; Sivakugan et al. 2006a; Helinski & Grice 2007). The pond can accumulate to 10% of the fill height (Kuganathan 2001).

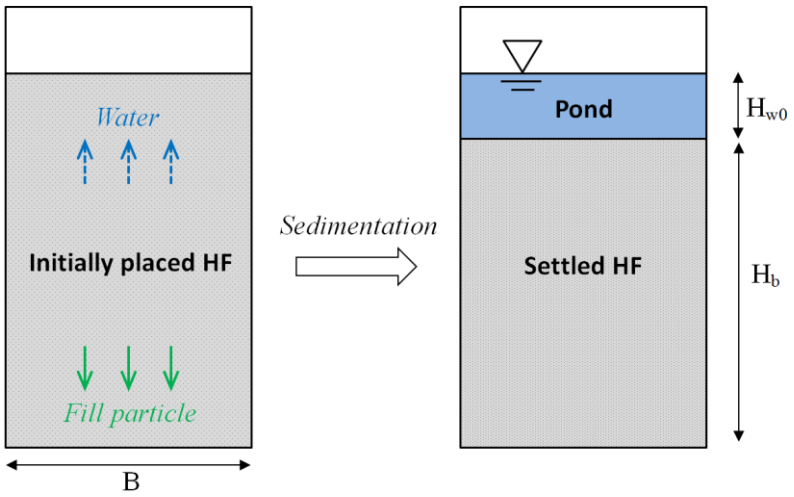

Figure 3-2: Illustration of the generation of a pond above the fill surface in a stope backfilled with hydraulic fill; the cross section shown is taken along the vertical symmetry plane through the drift axis (see Fig. 3-1)

The fill particles tend to sediment to a denser state. By considering the water balance before and after the fill sedimentation (with the detailed formulation presented in Section 3.6 of this chapter), the initial pond height H_{w0} and the settled fill height H_b can be obtained from the following expressions:

$$H_{w0} = Q\frac{\gamma(1-P)-\gamma_w n_s}{\gamma_w BL(1-n_s)} \tag{3.1a}$$

$$H_b = Q\frac{\gamma_w-\gamma(1-P)}{\gamma_w BL(1-n_s)} \tag{3.1b}$$

where Q (m^3) is the total volume of HF placed in the stope; γ (kN/m^3) and γ_w (kN/m^3) are the unit weight of HF and water, respectively; P is the solid weight content (usually from 65% to 75%) of HF, defined by the ratio of the solid weight to the total weight of HF; n_s (%) is the porosity of the settled fill (see below).

The ratio of H_{w0} to H_b is thus given by:

$$\frac{H_{w0}}{H_b} = \frac{\gamma(1-P)-\gamma_w n_s}{\gamma_w-\gamma(1-P)} \tag{3.2}$$

Herget & De Korompay (1978) reported that the values of in-situ n_s of settled HF are 45% and 48%, while Rankine and coworkers (Rankine 2005; Rankine et al. 2006) showed that the n_s value

varies between 37% and 48% (typically 44%) based on laboratory tests performed on hydraulic fills from 25 Australian mines. Eq. (3.1) can thus be used to estimate the initial height of the free water above the settled fill using a typical value of n_s.

3.2.2 Evolution of water table and pore water pressure (PWP) with time

Fig. 3-3 schematically shows the cross section of the water table drawdown and water flow within the HF filled stope. The stope (and drift) base is taken as the datum. It is assumed that the transient seepage takes place once the self-weight sedimentation of fill particles is completed. The height of the water table H and pond height H_w then become functions of time t. The water flow (drainage) is assumed to be one dimensional, i.e., vertical in the stope and horizontal in the drift (Fig. 3-3). This simplification is necessary to render analytical solution possible with a reasonable complexity. It is made by observing the water flow in backfilled stopes, shown in previous investigations (e.g., Bloss & Chen 1998; Ouellet & Servant 1998; Kuganathan 2001; Helinski & Grice 2007). It is further (partly) confirmed by numerical simulations presented later (discussed below). The hydraulic head of the barricade $h_{barricade}$ (m) is taken as zero due to free draining of porous bricks (e.g., Rankine 2005; Sivakugan et al. 2006a). It is also assumed that the head of discharge velocity is negligible compared to the elevation and pressure heads. These assumptions will be further addressed in the Discussion section.

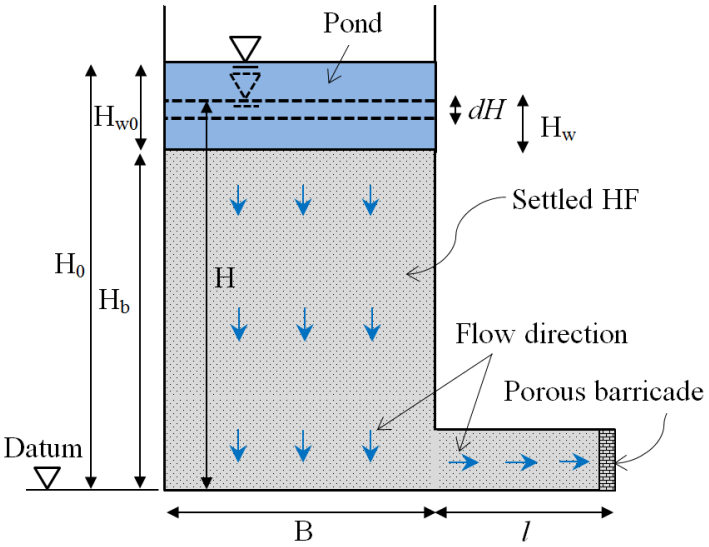

Figure 3-3: Illustration of the water table drawdown in the stope and water flow within hydraulic fill; the cross section is taken along the vertical symmetry plane through the drift axis (see Fig. 3-1)

When considering the water balance during the transient seepage (with the detailed formulation presented in Section 3.7 of this chapter), the PWP at the stope base u_{base} can be given by:

$$u_{base} = \frac{\gamma_w \left(H_b + H_w\right)}{1 + H_b H_d L_d / \left(BLl\right)} \tag{3.3}$$

Eq. (3.3) reduces to the following 2D expression when $L = L_d$:

$$u_{base} = \frac{\gamma_w \left(H_b + H_w\right)}{1 + H_b H_d / \left(Bl\right)} \tag{3.4}$$

By considering the variation of the water table height dH (= dH_w) during a time interval dt (with the detailed formulation presented in Section 3.8 of this chapter), the pond height H_w can be expressed as a function of time t:

$$H_w = \left(H_{w0} + H_b\right)\exp\left(-Ct\right) - H_b \tag{3.5}$$

where the constant $C = (k_{sat} H_d L_d)/(H_b H_d L_d + BLl)$ for 3D condition and $C = (k_{sat} H_d)/(H_b H_d + Bl)$ for 2D conditions; where k_{sat} (m/s) is the saturated hydraulic conductivity of the HF.

One can then obtain the evolution of the water table H in the HF filled stope as follows:

$$H = \left(H_{w0} + H_b\right)\exp\left(-Ct\right) \tag{3.6}$$

The total time T needed to drain the pond is obtained by introducing $H_w = 0$ into Eq. (3.5):

$$T = \frac{1}{C}\ln\left(1 + \frac{H_{w0}}{H_b}\right) \tag{3.7}$$

Eq. (3.6) [or Eq. (3.5)] can be used to describe the evolution of the water table in the stope with submerged HF. The evolution of PWP at the stope base can then be predicted by Eq. (3.3). The total time required for draining the free water above the fill surface is estimated using Eq. (3.7).

3.3 Numerical simulations

3.3.1 Modelling approach

The finite element code SEEP/W (GEO-SLOPE 2010) has been proven to be a good tool for simulating various steady-state and transient problems in unsaturated and saturated mediums

(e.g., Ouellet & Servant 1998; Chapuis & Aubertin 2001; Chapuis et al. 2001; Chapuis 2009). It is thus used here to validate the proposed analytical solutions [Eqs. (3.3) and (3.6)].

The numerical analysis includes modelling the transient seepage within the saturated HF and dropdown of the phreatic surface of the pond. The backfill is modeled as a saturated material and its hydraulic behavior is mainly governed by the saturated hydraulic conductivity k_{sat}. The pond is simulated using "reservoir elements" proposed and validated by Chapuis (2009) in numerical modelling with SEEP/W. The reservoir elements are modeled as unsaturated/saturated material with the hydraulic properties depicted in Fig. 3-4.

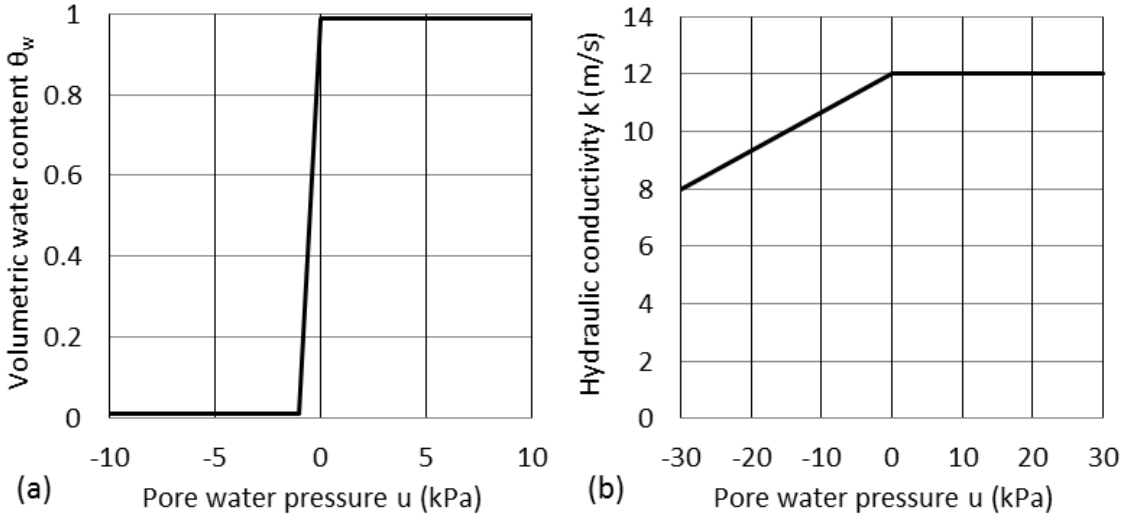

Figure 3-4: Hydraulic functions of reservoir elements used for simulating the pond with SEEP/W: (a) water retention curve; (b) permeability (data taken from Chapuis 2009)

Fig. 3-4 shows the water retention curve [Fig. 3-4(a)] and permeability function [Fig. 3-4(b)] of the reservoir elements used for simulating the pond with SEEP/W (data taken from Chapuis 2009). It is seen that the volumetric water content θ_w [Fig. 3-4(a)] remains constant for both saturated (free water) and residual (void) water contents. As the PWP changes from 0 to -1 kPa, the θ_w value decreases dramatically from 0.99 to 0.01. This behavior can mimic the retaining capacity of a real reservoir (Chapuis 2009). As shown in Fig. 3-4(b), the hydraulic conductivity k of reservoir elements should be much greater than that of the backfills even when the reservoir (pond) is empty. The large k value causes the reservoir elements to easily store and release water with almost unchanged hydraulic head (Chapuis 2009). More details of reservoir elements are provided by Chapuis (2009).

3.3.2 Numerical model

Fig. 3-5 illustrates a typical backfilled stope (plane flow) built with SEEP/W. Quadrilateral elements with edge lengths of 0.1 m are used based on a mesh sensitivity analysis (details of the sensitivity analysis are presented in Appendix D). The time step is also optimized to ensure stable numerical outcomes. The stope and the drift are filled with saturated hydraulic backfill. An initial phreatic surface is set at the top of the pond that is modeled using reservoir elements described above. The porous barricade is simulated using a free-draining surface (PWP = 0) due to the large contrast of the permeability between porous materials (e.g., bricks) and hydraulic fills (e.g., Isaacs & Carter 1982; Ouellet & Servant 1998; Traves & Isaacs 1991; Rankine et al. 2003; Sivakugan et al. 2006a). Other outer boundaries of the model are modeled as impervious. Table 3-1 gives the backfill characteristics used in the simulations. The numerical simulation is solved as a "transient seepage" analysis (GEO-SLOPE 2010).

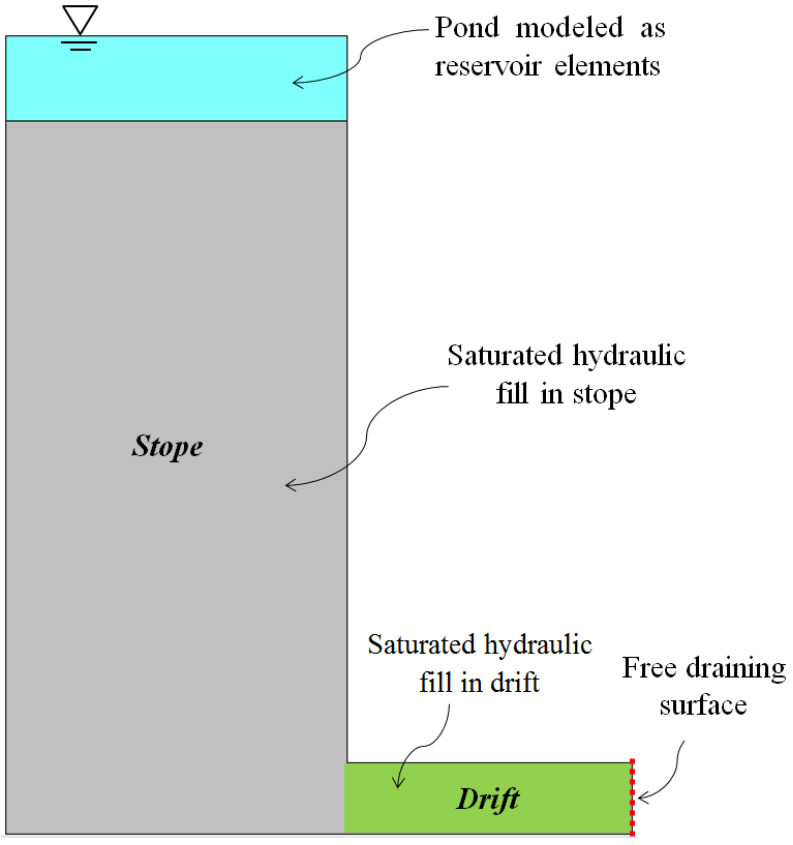

Figure 3-5: A SEEP/W model of a backfilled stope with pond above the fill surface

Table 3-1: The geometric and hydraulic parameters used in the numerical simulations

Case	H_{w0} (m)	H_b (m)	k_{sat} in stope (m/s)	Reduced k_{sat} in drift (m/s)	L/L_d (m)	l (m)
0	6	50	1.85×10^{-5}		1	5
1	Variable	50	1.85×10^{-5}		1	5
2	6	Variable	1.85×10^{-5}		1	5
3	6	50	1.85×10^{-5}		1	Variable
4	6	50	Variable		1	5
5a	6	50	1.85×10^{-5}	Variable	2*	5
5b					5*	
5c					10*	

Note: *the ratio L/L_d is applied in the proposed analytical solution [Eq. (3.6)]; other parameters: B = 6 m, H_d = 5 m and γ_w = 10 kN/m^3.

For a stope with settled fill of H_b of 50 m, an initial height of pond, H_{w0}, is 6 m based on Eq. (3.2) using γ = 20 kN/m^3, γ_w = 10 kN/m^3, P = 75% and n_s = 44%. The value of H_{w0} can vary from 10 m to 20 m when the solids content of the HF is reduced from 73% to 70%. These typical values of H_{w0} are used to investigate the evolution of the water table and PWP in the following.

The in-situ saturated hydraulic conductivity of uncemented HF usually varies between 10^{-6} and 10^{-5} m/s (Grice 2001). A typical range from 2×10^{-6} to 3.5×10^{-5} m/s (e.g., Rankine 2005; Sivakugan et al. 2006a) is used for defining the lower and upper bounds of k_{sat} in Case 4 (Table 3-1). An average k_{sat} value of 1.85×10^{-5} m/s is used in other cases.

In practice, the drift (barricade) width L_d (along the strike of the stope) is smaller than the stope length L. For the plane flow condition, the reduced k_{sat} value (Case 5, Table 3-1) of backfill in the drift is used to represent the restricted flow due to a reduced flow area through the drawpoint. The reduced k_{sat} of drift fill is obtained from the original k_{sat} value divided by the corresponding ratio of L to L_d. This modeling technique is deemed representative of the effect of the third dimension in 2D simulations (e.g., Fahey et al. 2009; Doherty 2015; Doherty & Wood 2016).

3.3.3 Comparisons with proposed analytical solution

Fig. 3-6 illustrates the evolution of the water table H with time t for different values of initial pond height H_{w0}, obtained with the analytical [Eq. (3.6) in 2D] and numerical solutions (Case 1). It is seen that the water table drops down with time in an almost linear manner. The time needed to remove the free water increases from about 100 to 300 h when the value of H_{w0} changes from 6 to 20 m. In all cases, the analytical solutions correlate quite well with the numerical simulations.

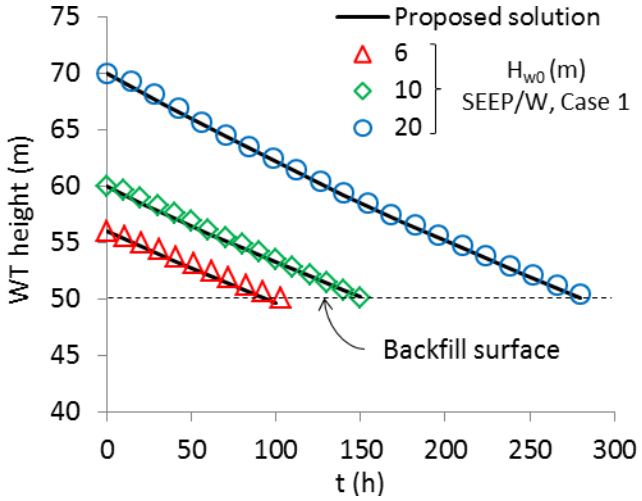

Figure 3-6: Evolution of the water table height H with time t for different values of height H_{w0}, calculated from the analytical [Eq. (3.6) in 2D] and numerical calculations (Case 1, Table 3-1)

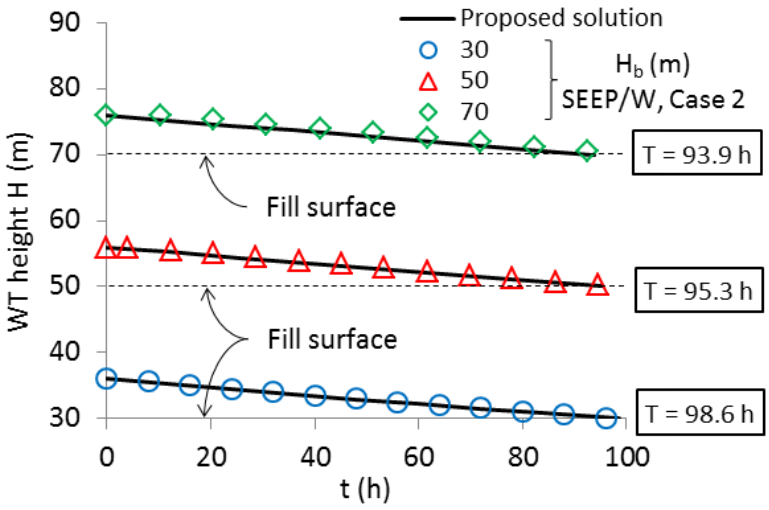

Figure 3-7: Evolution of water table height H with time t for different values of backfill height H_b, obtained with the analytical [Eq. (3.6) in 2D] and numerical calculations (Case 2, Table 3-1)

Fig. 3-7 shows the comparisons of the evolution of the water table H with time t between the analytical [Eq. (3.6) in 2D] and SEEP/W calculations (Case 2), when the settled fill height H_b changes from 30 to 70 m. The results obtained with both methods reveal that the water table draws down almost linearly with time. It is seen that the total time T needed to drain the pond slightly decreases when the value of H_b increases (from 30 to 70 m). Good agreement is obtained between the analytical and the numerical approaches.

Fig. 3-8 illustrates the evolution of the water table H with time t obtained with the analytical solution [Eq. (3.6) in 2D] and numerical simulations (Case 3) when the barricade position l changes from 1 to 10 m. It is observed that the time needed to drain the free water slightly increases from 86 to 105 hours when the l value varies from 1 to 10 m. A good correlation is obtained between the analytical solution and numerical simulations.

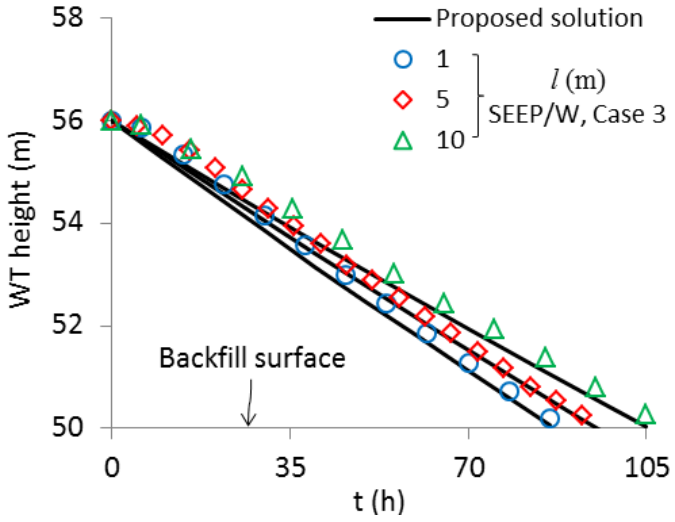

Figure 3-8: Evolution of the water table height H with time t for different values of length l, obtained with the analytical [Eq. (3.6) in 2D] and numerical calculations (Case 3, Table 3-1)

Fig. 3-9 shows the evolution of the water table H with time t for different values of k_{sat}, calculated with the analytical [Eq. (3.6) in 2D] and SEEP/W calculations (Case 4). Again, a good correlation is observed between the analytical solution and numerical calculations. Both indicate a linear relationship between the dropdown of the water table and the draining time. It is also seen that the time needed to fully drain the pond increases significantly when the value of k_{sat} decreases from 3.5×10^{-5} to 2×10^{-6} m/s.

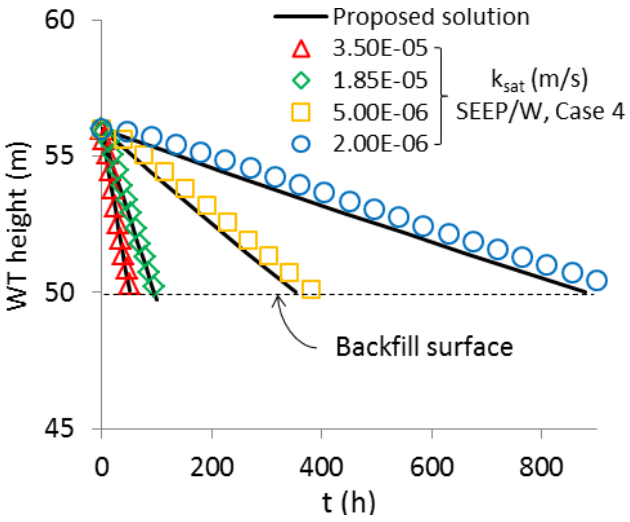

Figure 3-9: Evolution of the water table height H with time t for different values of k_{sat}, predicted by the analytical [Eq. (3.6) in 2D] and numerical calculations (Case 4, Table 3-1)

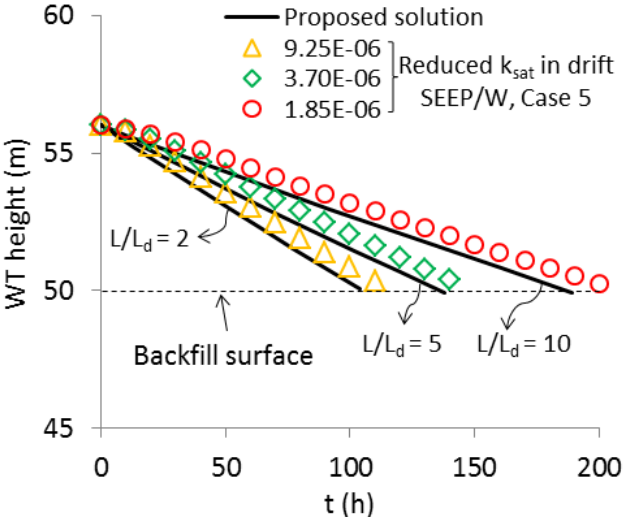

Figure 3-10: Evolutions of the water table height H with t; obtained from Eq. (3.6) (in 3D) with different ratios L/L_d and from numerical results (Case 5, Table 3-1) with values of reduced k_{sat} in the drift

Fig. 3-10 illustrates the evolution of the water table height H with time t, obtained with the proposed analytical solution [Eq. (3.6) in 3D] for different ratios of L to L_d. The numerical results (Case 5) are also plotted using values of reduced k_{sat} of fill in the drift. The good agreement between two approaches indicates that the restricted flow due to the reduced drift width in 3D conditions can be approximated by reducing k_{sat} of drift fill in 2D numerical modelling. When the

reduced k_{sat} value of drift fills decreases from 9.25×10^{-6} to 1.85×10^{-6} m/s, the time required for emptying the pond increases from about 100 to 200 h. This indicates that the reduced drift area in 3D conditions tends to slow down the seepage through the drawpoint.

Fig. 3-11 presents the evolution of the average PWP at the stope base u_{base} obtained from Eq. (3-3) and the PWP from numerical simulations at three locations for Cases 0, 5b and 5c (Table 3-1). The former is calculated with different ratios L/L_d and the latter with values of reduced k_{sat} in the drift. It is seen that the analytical solution predicts a reduction in u_{base} with time associated with the drawdown of the water table (from its initial height to the top surface of the settled fill). A decrease in the simulated PWP along the stope base is observed from Point A (at the stope wall) to Point C (at the drawpoint), probably due to the enhanced drainage near the barricade (e.g., Sivakugan et al. 2006b).

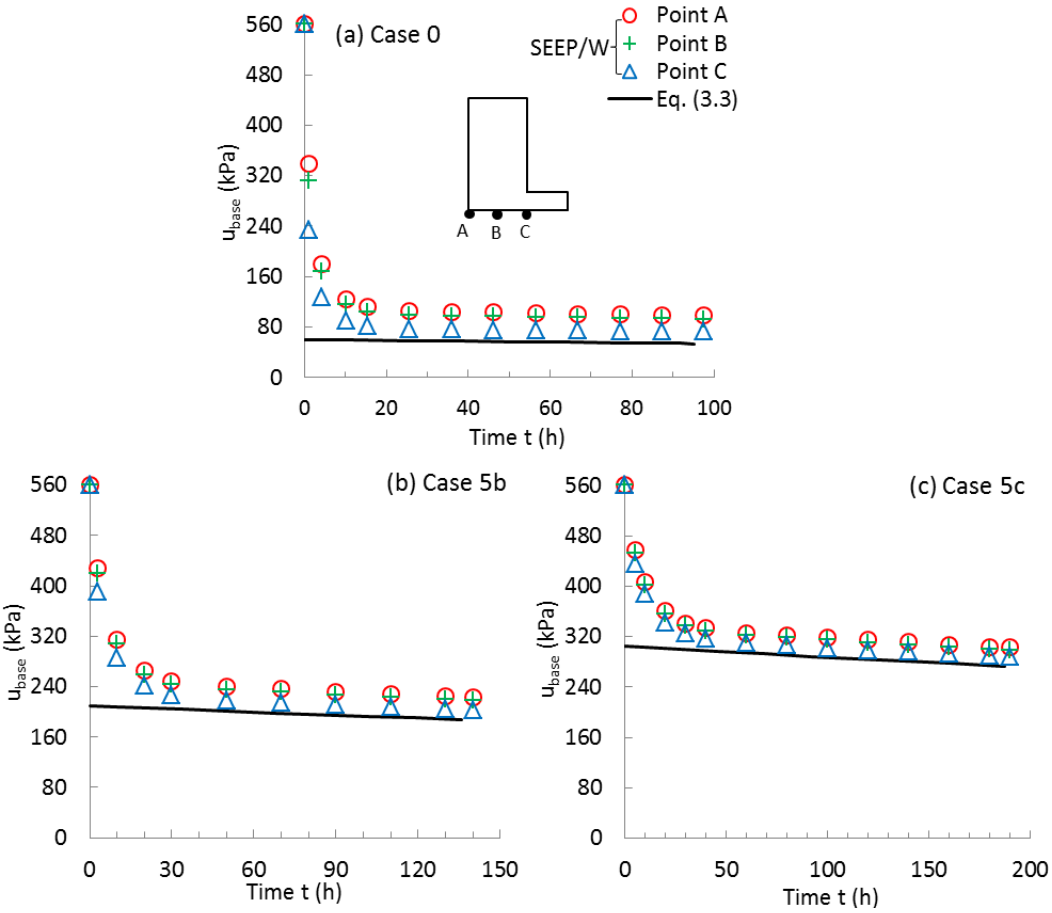

Figure 3-11: Evolution of u_{base} obtained from Eq. (3.3) and numerical simulations for (a) Case 0, (b) Case 5b and (c) Case 5c; Eq. (3.3) is calculated with different ratios L/L_d and numerical results with values of reduced k_{sat} in the drift (see Table 3-1 for details)

Fig. 3-11 also shows that the numerical models start the calculations from a hydrostatic state (with initial u_{base} = 56 m × 10 kN/m^3 = 560 kPa), even though the zero PWP boundary condition is applied along the barricade height. After a short period (about 10 h), the simulated u_{base} (especially at Point C) begin to correlate fairly well with Eq. (3-3) until the pond is fully drained. These indicate that there is a quick transition from an initial hydrostatic state to the (stable) transient seepage, thereby leading to the dramatic drop in the simulated PWPs. Such numerical simulations tend to overestimate the PWPs at the beginning and may place the barricade deign on the over-conservative side, while the analytical solution is deemed more reasonable. The drop in stimulated u_{base} is more dramatic when the stope length is equal to the drift width (Case 0, Table 1), as shown in Fig. 3-11(a). Similar trend has been observed for other cases investigated here.

3.4 Discussion

The good agreement between the proposed analytical solution and numerical modeling indicates that the proposed solution can be useful in estimating the evolution of the water table and PWP within hydraulic fill placed in the stope. However, simplifying assumptions have been made to develop analytical solutions with a reasonable complexity, including the one-dimensional flow in the stope and drift, instantaneous filling, and quick self-weight consolidation.

Fig. 3-12 depicts the vectors of hydraulic velocity when the water table is near the initial height [close to a stable transient state; Fig. 3-12(a)] and top surface of the settled fill [Fig. 3-12(b)], obtained from SEEP/W modelling with uniform k_{sat} value of fill (Case 0, Table 3-1). It is seen that the water flow is vertical in the stope and horizontal in the drift, except near the stope base where the water flow transitions from vertical to horizontal. Somewhat similar numerical results have been reported in the literature (Ouellet & Servant 1998; Sivakugan & Rankine 2006; Helinski & Grice 2007). These previous and new numerical analyses indicate that the assumption of one-dimensional flow made in the theoretical model is deemed representative of relatively high stopes (with limited drift height). For low stopes (especially when the barricade is very near the brow), however, it can be expected that the transition zone with two-dimensional flow (and high PWPs) may affect the transient drainage. Further study is thus required.

Fig. 3-12(b) shows that an unsaturated zone is developed close to the barricade when the water table is near the top surface of the settled backfill. Similar numerical results have been reported by Ouellet & Servant (1998). However, the unsaturated zone is not observed in the numerical

simulations with reduced k_{sat} of drift fill (Case 5b; not shown here). These results indicate that the unsaturated zone is due mostly to the faster drainage through barricade in 2D cases ($L = L_d$), compared to 3D conditions.

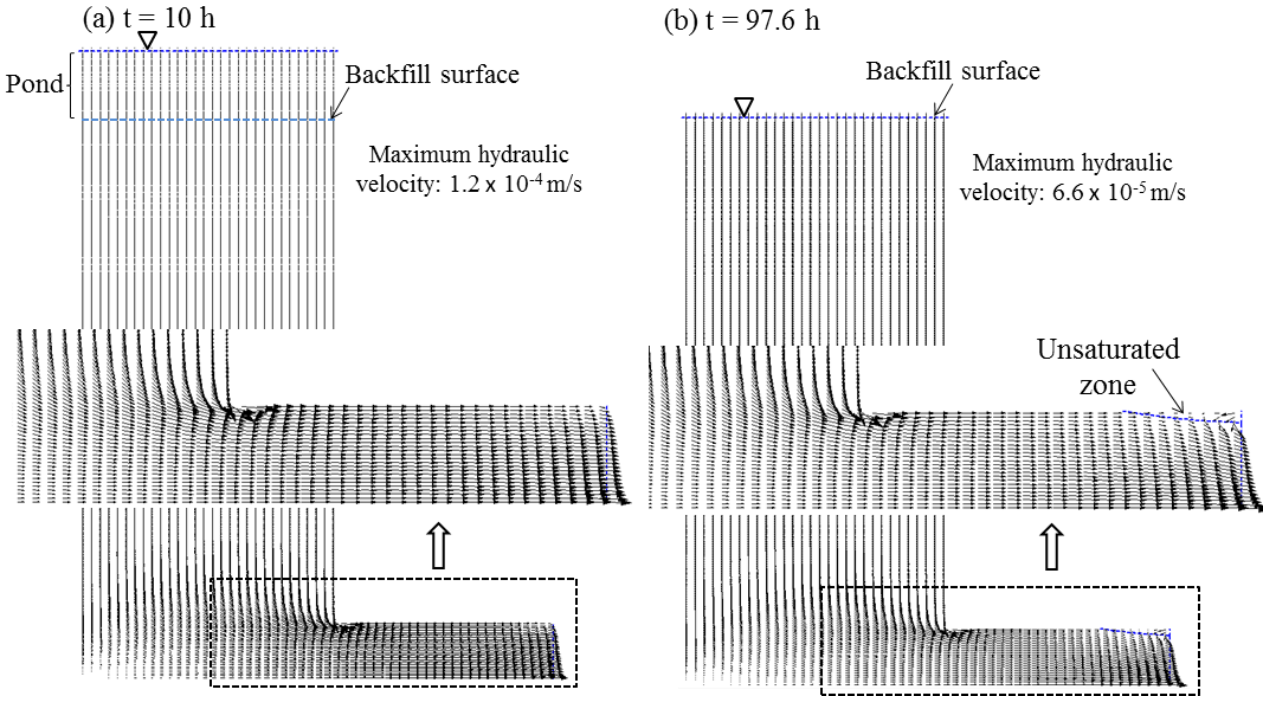

Figure 3-12: Vectors of hydraulic velocity when the water table is near the (a) initial height t = 10 h and (b) settled fill surface t = 97.6 h, obtained from SEEP/W modelling with uniform k_{sat} of backfill (Case 0, Table 3-1)

In the theoretical development, it has been assumed that the hydraulic velocity head is negligible compared to the elevation and pressure heads. This has been confirmed by the very small values of the maximum hydraulic velocity obtained from numerical simulations, as shown in Fig. 3-12. It is also shown that the maximum hydraulic velocity reduces from 1.2×10^{-4} m/s [Fig. 3-12(a)] to 6.6×10^{-5} m/s [Fig. 3-12(b)] as the water table drops from its initial height to the settled fill surface.

Fig. 3-13 illustrates the isocontour of PWP when the water table is near the initial height [close to a stable transient state Fig. 3-13(a)] and settled fill surface [Fig. 3-13(b)], obtained from numerical modelling with uniform k_{sat} value of fill (Case 0, Table 3-1). It is seen that the PWP in the stope increases with depth, but decreases in the drift towards the free-draining barricade. At a given time, the maximum PWP occurs at the far end corner of the stope base, as shown in Sivakugan et al. (2006b). Larger PWPs are seen near the beginning of the drainage which

corresponds to the most dangerous moments for barricade safety. After about 4 days (about 100 hours), the PWP is largely reduced throughout the stope and drift with the water table near the settled fill surface. This indicates that the formation of the pond on top surface of the settled backfill has a negative impact on barricade stability.

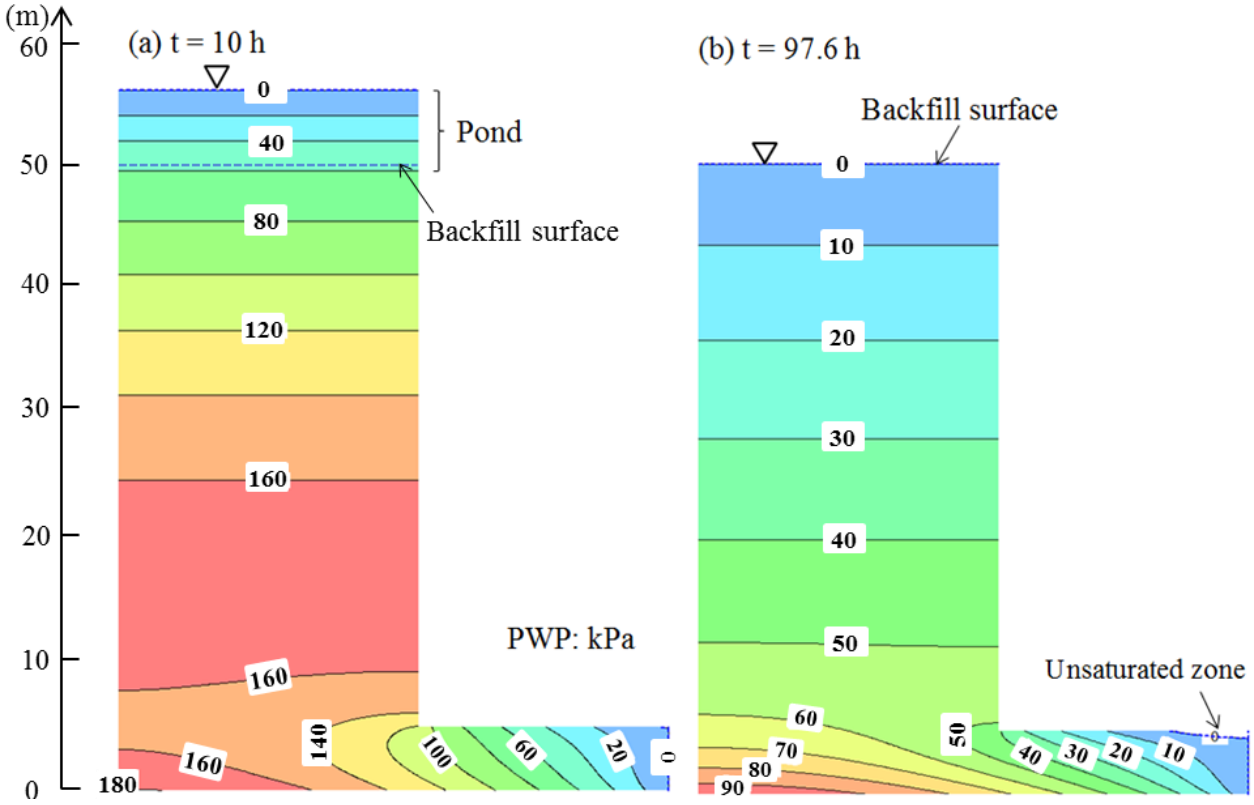

Figure 3-13: Isocontour of pore water pressure for the water table close to a stable transient state when it is near the (a) initial height and (b) settled fill surface, obtained with uniform k_{sat} value of backfill (Case 0, Table 3-1)

Fig. 3-14 shows the isocontour of PWP in cases of the water table near the initial height [Fig. 3-14(a)] and settled fill surface [Fig. 3-14(b)], obtained from numerical modelling with reduced k_{sat} value of fill in the drift (Case 5b, Table 3-1). It is seen that the distribution pattern of PWP is very similar to that observed above in Fig. 3-13 for Case 0 (Table 3-1). However, the values of PWP are much larger than those shown in Fig. 3-13. The difference is caused by the restricted flow due to the reduced k_{sat} of drift fill (or equivalent reduced L_d). It is also seen that the PWP reduces throughout the stope and drift after about 6.25 days (about 150 hours) when the water table is at the settled fill surface. These results explain that the 2D models without considering the restricted

flow through the drawpoint tend to underestimate the PWPs near the barricade. A barricade design based on such solution may not be conservative.

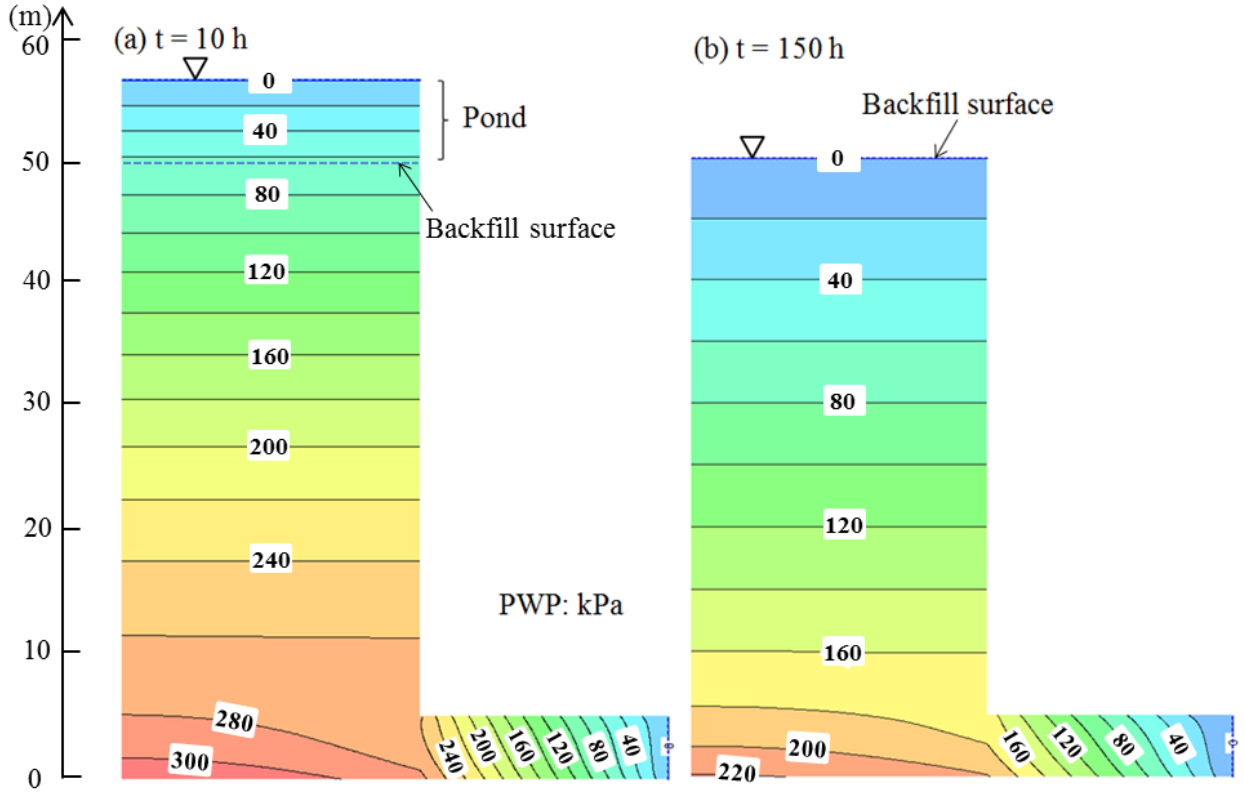

Figure 3-14: Isocontour of pore water pressure for the water table near the (a) initial height and (b) settled fill surface, obtained with reduced k_{sat} of backfill in the drift (Case 5b, Table 3-1)

Fig. 3-15 illustrates the distributions of PWP along the VCL of stope at different times after fill placement, obtained from numerical modelling with uniform k_{sat} (Case 0, Table 3-1) and reduced k_{sat} value in the drift (Case 5b, Table 3-1). At time zero, the results give (initial) hydrostatic states (see also Fig. 3-11). Once the calculation starts, it is first seen that the PWP along the VCL decrease quickly in early hours (about 10 hours) while the water table remains almost unchanged. Such decreases correspond to the quick transition from an initial hydrostatic state to the stable transient seepage as shown in Fig. 3-11. The PWP along the VCL continues to decline with time as the water table drops to the settled fill surface. For a given time, the PWP reduces more severely near the stope bottom due to the improved drainage near the barricade. This phenomenon is more pronounced in the case of equivalent stope and drift length [Fig. 3-15(a)]. It is also seen that for the same time, the PWP of Case 5b [Fig. 3-15(b)] is higher than that of Case 0 [Fig. 3-15(a)], due to the restricted flow caused by the reduced k_{sat} in the drift (or equivalent

reduced L_d). These results show again that the 2D models could result in non-conservative consideration of PWPs behind the barricade, because of the neglect of the reduced flow area in 3D conditions.

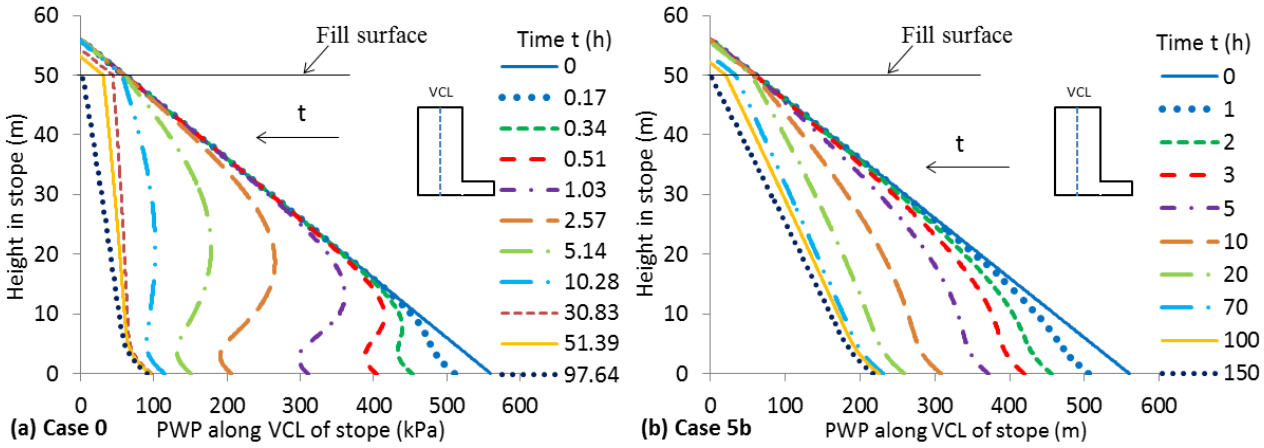

Figure 3-15: Distributions of PWP along the VCL of stope at different times obtained from numerical modelling with (a) uniform k_{sat} (Case 0, Table 3-1) and (b) reduced k_{sat} in the drift (Case 5b, Table 3-1)

Fig. 3-16 presents the evolution of the PWP distribution along the horizontal center line (HCL) of the drift, obtained from numerical modelling with uniform k_{sat} (Case 0, Table 3-1) and reduced k_{sat} value in the drift (Case 5b, Table 3-1). Again, the initial hydrostatic condition is observed for both cases at time zero. The PWP along the HCL declines very fast at the beginning (about 10 hours) as the numerical calculation starts, indicating the intermediate period from an initial static state to transient seepage (as shown in Fig. 3-11). At any given time (except t = 0), the PWPs decrease towards the barricade and drops to zero at the barricade. Fig. 3-16 also shows that for the same time, the PWP of Case 5b [Fig. 3-16(b)] is larger than that of Case 0 [Fig. 3-16(a)], due to the restricted drainage resulting from the reduced k_{sat} in the drift (or equivalent reduced L_d). These results further indicate that the 2D models without considering the reduced drift area could significantly underestimate the PWPs close to the barricade.

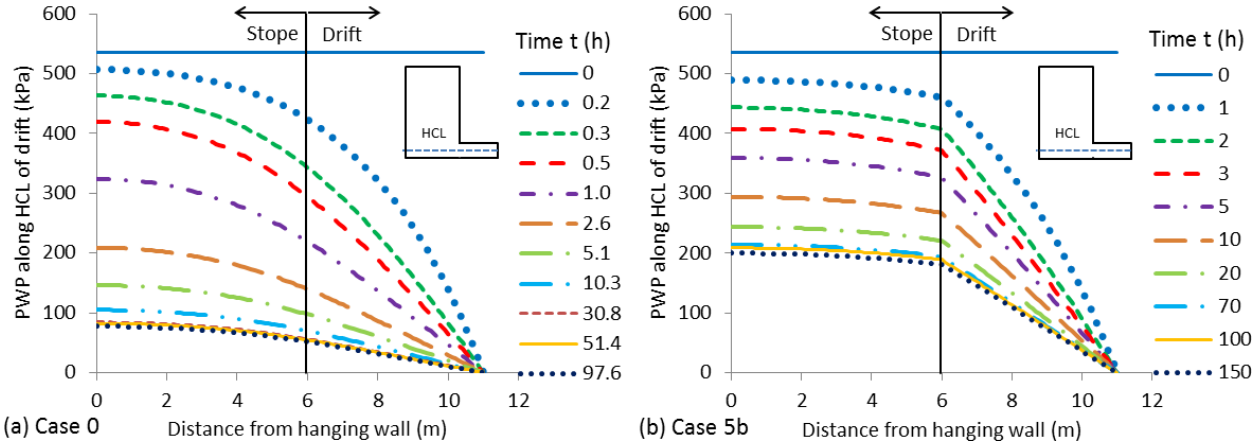

Figure 3-16: Distributions of PWP along the HCL of drift at different times obtained from numerical modelling with (a) uniform k_{sat} (Case 0, Table 3-1) and (b) reduced k_{sat} in the drift (Case 5b, Table 3-1)

Another limitation of the proposed model is related to the instantaneous filling and self-weight consolidation after the fill placement. Numerical simulations conducted by Isaacs and Carter (1982) indicated that the water level increases faster with an increased filling rate. The model with an instantaneous filling ignores the drainage through barricade during filling and sedimentation, resulting in a maximum estimated pond height. The barricade design based on the proposed solutions should be on the conservative side. On the other hand, the proposed model with the assumption of an instantaneous self-weight consolidation of the backfill upon placement may sometimes overestimate the dissipation of excess PWP, especially for high stopes filled quickly with a relatively low permeability backfill. The barricade design based on such model may lead to a more critical scenario for barricade stability. More work is expected to refine the model by considering more realistic filling rate, hydraulic properties of the backfill, and drainage efficiency of the barricade.

It has been shown that the high hydrostatic pressure head due to ponding may endanger the barricade stability in stopes with HF. This justifies the use of drainage pipes (usually suspended along the footwall or hanging wall) in stopes to accelerate the drainage within hydraulic fill (e.g., Neindorf 1983; Soderberg & Busch 1985; Ouellet et al. 1995; Bloss & Chen 1998; Ouellet & Servant 1998; Hustrulid & Bullock 2001). However, attention should be paid to the preferential flowing channels or internal erosion that may be caused by the use of drainage pipes.

The proposed analytical solution and numerical results for describing the evolution of the water table correspond to the case when hydraulic fill is fully submerged (saturated) in the backfilled stope. This is the critical moment for barricade design due to the presence of free water (pond) above the settling or settled fill surface. However, the backfill can become partly unsaturated once the water table is below the fill surface. Then the evolution of the water table (and stresses) could become very different from the saturated condition. Additional work is thus required.

The results presented above indicate that the variations of the water table and PWP with time defined by the proposed relationships [Eqs. (3-3) and (3-6)] are almost linear. This is because that the values of constant C in the exponential terms are very small, due largely to the small k_{sat} value (usually 10^{-6} to 10^{-5} m/s for HF). These relationships can become non-linear as the value of C increases.

3.5 Conclusions

A simple analytical solution is first proposed for estimating the initial height of pond [Eq. (3.1)] generated by the sedimentation of hydraulic fills in a stope. The 3D analytical solutions for describing the evolution of pore water pressures [at the stope base; Eq. (3.3)] and water table [Eq. (3.5) or (3.6)] are also proposed. Eqs. (3.3) and (3.6) are validated using simulations conducted with SEEP/W by modelling the transient seepage as the water table drops in the stope. The effects of various parameters on the evolution of the water table and pore water pressures are analyzed for both approaches. The results show that there is a good agreement between two different approaches. The limitations of the proposed model and analytical solution have been discussed. The analyses presented here pave the way to further development.

The results presented above also reveal that the ponding on the top of the settled fill tends to negatively affect the barricade stability. The 2D modelling without considering the reduced drift area tends to underestimate the pore water pressures in the stopes and near the barricade. A barricade design based on such models may be non-conservative. Additional numerical results indicate that the magnitudes of pore water pressure within hydraulic fill are governed by the drainage conditions that mainly depend on the restricted flow due to a reduced drift area.

3.6 Appendix I: Solution development for initial pond height H_{w0}

The total volume of HF Q (m^3) poured into the stope can be written as (Fig. 3-2):

$$Q = BL\left(H_{w0} + H_b\right) \tag{3.8}$$

The conservation of water mass before and after the sedimentation of hydraulic fill leads to the following expression:

$$\gamma Q\left(1-P\right) = \gamma_w H_b BL n_s + \gamma_w H_{w0} BL \tag{3.9}$$

Rearranging Eqs. (3.8) and (3.9), the initial pond height H_{w0} and the settled fill height H_b in a stope is given by Eq. (3.1).

3.7 Appendix II: Solution development for pore water pressure at the stope base u_{base}

At a transient time t (s), the average hydraulic head h_{top} (m) and h_{base} (m) along the top and base of the settling fill in the stope can be obtained from the Bernoulli's equation (Fig. 3-3):

$$h_{top} = H_b + H_w \tag{3.10a}$$

$$h_{base} = u_{base}/\gamma_w \tag{3.10b}$$

where u_{base} (kPa) is the pore water pressure at the stope base.

The average hydraulic gradient i_{stope} between the top and base of the settling backfill in the stope can then be written as:

$$\begin{aligned} i_{stope} &= \frac{h_{top} - h_{base}}{H_b} = \frac{H_b + H_w - u_{base}/\gamma_w}{H_b} \\ &= 1 + \frac{H_w - u_{base}/\gamma_w}{H_b} \end{aligned} \tag{3.11}$$

The average hydraulic gradient i_{drift} between the drawpoint and barricade in the drift is expressed as:

$$i_{drift} = \frac{h_{base} - h_{barricade}}{l} = \frac{u_{base}/\gamma_w - 0}{l} = \frac{u_{base}}{\gamma_w l} \tag{3.12}$$

The volumetric water flow rates through a horizontal plane very near the stope base and barricade should be equal at any time during the transient seepage. The equation of water balance can be obtained from the Darcy's Law:

$$k_{sat} i_{stope} BL = k_{sat} i_{drift} H_d L_d \tag{3.13}$$

where k_{sat} (m/s) is the saturated hydraulic conductivity of the hydraulic fill.

Introducing Eqs. (3.11) and (3.12) into Eq. (3.13), the pore water pressure at the stope base u_{base} can be expressed by Eq. (3.3).

3.8 Appendix III: Solution development for water table evolution

The variation of height of water table dH (= dH_w; Fig. 3-3) during a time interval dt is given by:

$$dH = dH_w = -v dt = -k_{sat} i_{stope} dt \tag{3.14}$$

where v (m/s) is the discharge velocity of water in the stope and is obtained from the product of k_{sat} and i_{stope} based on the Darcy's Law.

Introducing Eqs. (3.11) and (3.3) into Eq. (3.14), one can obtain the following expression:

$$-\frac{dH_w}{H_w + H_b} = C dt \tag{3.15}$$

where the constant $C = \left(k_{sat} H_d L_d\right)/\left(H_b H_d L_d + BLl\right)$ for 3D conditions and $C = \left(k_{sat} H_d\right)/\left(H_b H_d + Bl\right)$ for 2D conditions.

By considering the initial condition (i.e., $H_w = H_{w0}$ when $t = 0$), the integration of Eq. (3.15) leads to the pond height H_w expressed by Eq. (3.5).

Acknowledgements

The authors would like to acknowledge the financial support from the Natural Sciences and Engineering Research Council of Canada (NSERC 402318), Institut de recherche Robert-Sauvé

en santé et en sécurité du travail (IRSST 2013-0029), Fonds de recherche du Québec – Nature et Technologies (FRQNT 2015-MI-191676), and industrial partners of the Research Institute on Mines and the Environment (RIME UQAT-Polytechnique; http://rime-irme.ca/). GEO-SLOPE and Professor Robert Chapuis are acknowledged for the courtesy of the use of SEEP/W. The anonymous reviewers are gratefully acknowledged for their comments that help improve the quality of the paper.

3.9 References

Askew, J., McCarthy, P. L., Fitzgerald, D. J. (1978). "Backfill research for pillar extraction at ZC/NBHC." *Proc., Mining with backfill: 12th Can. Rock Mechanics Symp.*, CIM, Sudbury, 12, 100-110.

Aubertin M. (2013). "R.M. Hardy Keynote Address: Self-weight consolidation problems related to surface and underground disposal of fine-grained mine wastes." *Proc., 66th Can. Geotech. Conf.*, CGS, Montreal.

Aubertin, M., Bussière, B., and Bernier, L. (2002). Environnement et gestion des rejets miniers (CD-ROM), Presses Internationales Polytechnique, Montréal (in French).

Aubertin, M., Bussière, B., Pabst, T., James, M., and Mbonimpa, M. (2016). "Review of the reclamation techniques for acid-generating mine wastes upon closure of disposal sites." *Proc., Geo-Chicago 2016*, ASCE, 343-358.

Aubertin, M., Li, L., Arnold, S., Belem, T., Bussière, B., Benzaazoua, M., and Simon, R. (2003). "Interaction between backfill and rock mass in narrow stopes." *Proc., Soil and Rock America 2003*, Verlag Glückauf Essen (VGE), Essen, 1, 1157-1164.

Benzaazoua, M., Bussière, B., Demers, I., Aubertin, M., Fried, É., and Blier, A. (2008). "Integrated mine tailings management by combining environmental desulphurization and cemented paste backfill: Application to mine Doyon, Quebec, Canada." *Miner. Eng.*, 21(4), 330-340.

Bloss, M. L., and Chen, J. (1998). "Drainage research at Mount Isa Mines limited 1992-1997." *Proc., 6th Int. Symp. on Mining with Backfill*, M. Bloss, eds., Brisbane, Australia, 98, 111-116.

Bussière, B. (2007). “Colloquium 2004: Hydro-geotechnical properties of hard rock tailings from metal mines and emerging geoenvironmental disposal approaches.” *Can. Geotech. J.*, 44, 1019-1052.

Chapuis, R. P. (2009). “Numerical modeling of reservoirs or pipes in groundwater seepage.” *Comput. Geotech.*, 36(5), 895-901.

Chapuis, R. P., and Aubertin, M. (2001) “Evaluation of saturated and unsaturated seepage through dikes in steady state conditions.” *Can. Geotech. J.*, 38(6), 1321-1328.

Chapuis, R. P., Chenaf, D., Bussière, B., Aubertin, M., and Crespo, R. (2001). “A user's approach to assess numerical codes for saturated and unsaturated seepage conditions.” *Can. Geotech. J.*, 38(5), 1113-1126.

Doherty, J. P. (2015). “A numerical study into factors affecting stress and pore pressure in free draining mine stopes.” *Comput. Geotech.*, 63, 331-341.

Doherty, J. P., and Wood, D. M. (2016). “Back analysis of the Kanowna Belle stope filling case history.” *Comput. Geotech.*, 76, 201-211.

Fahey, M., Helinski, M., and Fourie, A. (2009). “Some aspects of the mechanics of arching in backfilled stopes.” *Can. Geotech. J.*, 46 (11), 1322-1336.

Falaknaz, N., Aubertin, M., and Li, L. (2015). “Numerical analyses of the stress state in two neighboring stopes excavated and backfilled in sequence.” *Int. J. Geomech.*, 15(6), 04015005.

Fourie, A. B., Copeland, A. M., and Barrett, A. J. (1994). “Optimization of the as-placed properties of hydraulic backfill.” *J. South. Afr. Inst. Min. Metall.*, 94(8), 199-210.

GEO-SLOPE. (2010). *Seepage modeling with SEEP/W 2007*, GEO-SLOPE International Ltd. Calgary.

Grice, A. G. (1998). “Stability of hydraulic backfill barricades.” *Proc., 6th Int. Symp. on Mining with Backfill*, Carlton, Australia, 117-120.

Grice, A. G. (2001). “Recent mine fill developments in Australia.” *Proc., 7th Int. Symp. on Mining with Backfill*, Seattle, USA, 351-357.

Hassani, F., and Archibald, J. (1998). *Mine backfill (CD-ROM)*, Canadian Institute of Mine, Metallurgy and Petroleum, Montréal.

Helinski, M., and Grice, A. G. (2007). "Water management in hydraulic fill operations." *Proc., 9th Int. Symp. on Mining with Backfill,* Montréal.

Herget, G., and De Korompay, V. (1978). "In-situ drainage properties of hydraulic backfills." *Proc., Mining with Backfill: 12th Can. Rock Mechanics Symp.*, CIM, 19, 117-123.

Hustrulid, W. A., and Bullock, R. L. (2001). "Underground mining methods: engineering fundamentals and international case studies." *Society for Mining, Metallurgy, and Exploration,* Littleton.

Isaacs, L. T., and Carter, J. P. (1982). "Theoretical study of pore water pressures developed in hydraulic fill in mine stopes." *Research Report No. CE32*, University of Queensland, St. Lucia.

Kuganathan, K. (2001). "Mine backfilling, backfill drainage and bulkhead construction - a safety first approach." *Australia's Mining Monthly*, February, 58-64.

Li, L. (2014). "Generalized solution for mining backfill design." *Int. J. Geomech.*, 14(3), 04014006.

Li, L., Alvarez, I. C., and Aubertin, J. D. (2013). "Self-weight consolidation of a slurried deposition: tests and interpretation." *Int. J. Geotech. Eng.*, 7(2), 205-13.

Li, L., and Aubertin, M. (2009a). "Influence of water pressure on the stress state in backfill with cohesionless Stopes." *Geotech. Geol. Eng.*, 27(1), 1-11.

Li, L., and Aubertin, M. (2009b). "A three-dimensional analysis of the total and effective stresses in submerged backfilled stopes." *Geotech. Geol. Eng.*, 27(4), 559-569.

Li, L., Aubertin, M., and Belem, T. (2005). "Formulation of a three dimensional analytical solution to evaluate stresses in backfilled vertical narrow openings." *Can. Geotech. J.*, 42(6), 1705-1717.

Liu, G., Li, L., Yang, X., and Guo, L. (2016a). "Numerical analysis of stress distribution in backfilled stopes considering interfaces between the backfill and rock walls." *Int. J. Geomech.*, 06016014.

Liu, G. S., Li, L., Yao, M., Landry, D., Malek, F., Yang, X. C., and Guo L. J. (2016d). "An investigation of the uniaxial compressive strength of a cemented hydraulic backfill made of alluvial sand." *Miner.* (submitted in August 2016).

Martic, Z., Gelson, J., Bras, H., Xu, Q., and Brosko, W. (2014). “New perspectives for cemented hydraulic fill with chemical technologies.” *Proc.*, *Mine Fill 2014*, Australian Centre for Geomechanics, Perth.

Neindorf, L. B. (1983). “Fill operating practices at Mount Isa Mines.” *Proc.*, *Mining with Backfill*, Lulea, 179-187.

Ouellet, J., Bussere, B., and Gagnon, G. (1995). “Simulation numérique du remblayage d’un chantier de mine avec du remblai hydraulique cimenté: élaboration du modèle.” *Proc., 3rd Can. Conf. on Computer Applications in the Mineral Industry*, Montréal, 331-339.

Ouellet, J., and Servant, S. (1998). “Numerical simulation of the drainage in a mining stope filled with hydraulic backfill.” *Proc., 6th Int. Symp. on Mining with Backfill*, M. Bloss, eds., Brisbane, Australia, 98, 105-110.

Pedroni, L. (2011). “Étude expérimentale et numérique de la sédimentation et de la consolidation des boues de traitement des eaux acides.” Ph.D. Thesis, Polytechnique Montréal, Montréal (in French).

Peele, I. (1941), *Mining engineers handbook*. John Wiley and Sons Inc., Canada.

Potvin, Y., Thomas, E., and Fourie, A. (2005). *Handbook on mine fill*, Australian Centre for Geomechanics, Perth.

Rankine, K. J. (2005). “An investigation into the drainage characteristics and behaviour of hydraulically placed mine backfill and permeable minefill barricades.” Ph.D. thesis, James Cook Univ., Townsville City.

Rankine, K. J., Rankine, K. S., and Sivakugan, N. (2003). “Three dimensional drainage modelling of hydraulic fill mines.” *Proc. 12th Asian Regional Conf. on Soil Mechanics and Geotechnical Engineering*, Singapore.

Rankine, K. J., Sivakugan, N., and Cowling, R. (2006). “Emplaced geotechnical characteristics of hydraulic fills in a number of Australian mines.” *Geotech. Geol. Eng.*, 24(1), 1-14.

Sivakugan, N., and Rankine, K. S. (2006). “A simple solution for drainage through a 2-dimensional hydraulic fill stope.” *Geotech. Geol. Eng*., 24, 1229-1241.

Sivakugan, N., Rankine, K. J., and Rankine, R. M. (2006a). "Permeability of hydraulic fills and barricade bricks." *Geotech. Geol. Eng*., 24, 661-673.

Sivakugan, N., Rankine, K. J., and Rankine, K. S. (2006b). "Study of drainage through hydraulic fill stopes using method of fragments." *Geotech. Geol. Eng*., 24, 79-89.

Soderberg, R. L., and Busch, R. A. (1985). "Bulkheads and drains for high sandfill stopes." U.S. Department of the Interior, Bureau of Mines.

Thomas, E. G. (1979). *Fill technology in underground metalliferous mines*, International Academic Services Limited, Kingston, Canada.

Thompson, B. D., Hunt, T., Malek, F., Grabinsky, M. W., Bawden, W. F. (2014). "In situ behaviour of cemented hydraulic and paste backfills and the use of instrumentation in optimising efficiency." *Proc. Mine Fill 2014*, Australian Centre for Geomechanics, Perth.

Traves, W. H., and Isaacs, L. T. (1991). "Three-dimensional modelling of fill drainage in mine stopes." *Transactions of the Institution of Mining and Metallurgy*, Section A: Mining Industry, 100, A66-A72.

Wickland, B.E., and Wilson, G. W. (2005). "Self-weight consolidation of mixtures of mine waste rock and tailings." *Can. Geotech. J.*, 42(2), 327-39.

Yang, P. Y., and Li, L. (2015). "Investigation of the short-term stress distribution in stopes and drifts backfilled with cemented paste backfill." *Int. J. Min. Sci. Technol.*, 25(5), 721-728.

Yang, P. Y., Li, L., Aubertin, M., Brochu-Baekelmans, M., and Ouellet, S. (2016a). "Stability analyses of waste rock barricades designed to retain paste backfill." *Int. J. Geomech.*, 04016079. This article is presented in Chapter 4.

CHAPTER 4 ARTICLE 2: STABILITY ANALYSES OF WASTE ROCK BARRICADES DESIGNED TO RETAIN PASTE BACKFILL

Pengyu Yang, Li Li, Michel Aubertin, Marin Brochu-Baekelmans, & Serge Ouellet

This article has been published online in ASCE - *International Journal of Geomechanics* in August 2016.

Abstract: Cemented paste backfill (CPB) is widely applied in underground mines around the world. Prior to stope backfilling, barricades need to be built in drifts near drawpoints to retain the flowable fill. A number of reported barricade failures have shown that the barricade stability is critical to ensure successful and safe application of backfill. The barricades are usually made of high-strength materials like bricks, concrete blocks, or reinforced shotcrete. Alternatively, barricades made of waste rocks are becoming popular due to their simple and low-cost construction. A simple solution was proposed for sizing waste rock barricades (WRB) by considering the limit equilibrium of a 3D-rectangular block. More recently, the authors modified this solution by considering the global stability of trapezoidal barricades, but the local stability was not taken into account. Consequently, the size of the crest can be underestimated, leading to a non-conservative design. In this paper, a more complete solution is proposed, considering both the global and local stabilities of trapezoidal WRB. The analytical solution is calibrated and validated using numerical modeling. The flexibility and validity of the proposed solution is further tested with complementary simulations. Sample calculations are also performed here to show the application of this solution and to illustrate the effect of key influencing factors on barricade design.

Keywords: Mine stopes; Cemented paste backfill; Waste rock barricades; Stability analyses; Analytical solutions; Numerical modeling.

4.1 Introduction

Stope backfilling is a common ground support practice for underground mines (Thomas 1979; Singh & Hedley 1980; Hassani & Archibald 1998; Potvin et al. 2005; Hambley 2011). Using mine waste materials to fill the stopes can also significantly reduce their environmental footprint (Aubertin et al. 2002; Bussière 2007; Benzaazoua et al. 2008). This is particularly the case with cemented paste backfill (CPB), which is a high density mixture (70% to 80% solid content) made with the full tailings and a binder, with some water (Hassani & Archibald 1998; Potvin et al. 2005). In recent years, CPB has been increasingly used in underground mines worldwide. Barricades (or bulkheads) must be built near draw points to retain hydraulically transported saturated backfill. Several documented failures indicate that barricade design is still a major challenge, as these can lead to serious consequences, including flooding of the drifts, damage to equipment, and in extreme cases personnel injury or fatality (e.g., Soderberg & Busch 1985; Bloss & Chen 1998; Grice 1998, 2001; Kuganathan 2001, 2002; Helinski et al. 2006; Sivakugan et al. 2006a, 2006b, 2013; Yumlu & Guresci 2007).

The factor of safety of a barricade depends on the capacity and demand. The capacity (resistance) of a barricade depends on its type, shape, sizes and construction method, whereas the demand (load) is mostly controlled by the pressure applied by the backfill placed in the stope and drift. Traditionally, barricades have been made of permeable bricks allowing easy drainage; concrete blocks and reinforced shotcrete with drainage pipes are also used to construct barricades (Sivakugan et al. 2006b; Yumlu & Guresci 2007; Sivakugan 2008; Grabinsky 2010; Hughes et al. 2010). These types of barricades usually result in relatively high costs and long construction time. Such traditional barricades are also difficult to remove during the ore recovery from secondary stopes. An alternative is to build barricades with waste rocks produced underground. This is an increasingly popular practice in many mines. Compared to more traditional techniques, this type of barricade can be much simpler and faster to build, while the construction material (waste rock) can be readily available at a lower cost when provided by the underground development. Waste rock barricades (WRB) are also somewhat easier to dismantle during ore recovery, and they contribute to a reduction of the environmental footprint of a mining project.

Although there are many advantages to WRB, few solutions are available for designing such barricades. In order to size a WRB, several parameters are needed, including the stress state in the

backfilled stope which in turn influences the pressure distribution in the drift and on the barricade (e.g., Li et al. 2009; Li & Aubertin 2011). This important need justifies the major effort devoted to evaluating the stress state in backfilled stopes in recent years (Aubertin et al. 2003; Li et al. 2003, 2005; Pirapikaran & Sivakugan 2007; Li & Aubertin 2009c; El Mkadmi et al. 2014; Ting et al. 2011, 2012, 2014; Yang & Li 2015); there is also an interest for the corresponding pressures on barricades built near draw points (Mitchell et al. 1975; Kuganathan 2002; Li & Aubertin 2009c, 2009d; Thompson et al. 2009, 2010, 2012; Grabinsky 2010; Li 2013).

Recently, analytical solutions for sizing WRB under fully drained (no pore water pressure) and submerged (hydrostatic water pressure) conditions were proposed (Li et al. 2009; Li & Aubertin 2011). Such solutions have been developed from the limit equilibrium analysis of an idealized rectangular block. These can be used to calculate the minimal required length (and volume) of a WRB. In practice, however, WRB are built with a trapezoidal shape instead of a rectangular block. The design based on the rectangular shape geometry may be overly-conservative, depending on how the contribution of the inclined sides of the WRB is considered (Yang et al. 2014).

In this paper, the original solution proposed by Li & Aubertin (2011) is first briefly recalled. Then, a modified solution is formulated for sizing the WRB by considering a more realistic geometry. Another improvement proposed here is the consideration of both global and local stability of the barricade. The proposed solution specifically addresses the design of trapezoidal WRB constructed to retain CPB during the early hours (i.e., critical period) after deposition. The solution is calibrated and (partly) validated using numerical simulations performed with *FLAC* (Itasca 2011). Sample calculations are performed to show the application of this more complete solution. The effect of key influencing factors on barricade design is illustrated and discussed.

4.2 Original solution

Fig. 4-1 shows a trapezoidal barricade made of waste rock, built near the drawpoint of a backfilled stope. In this figure, H (m) is the backfill height in the stope. H_d (m) and L_d (m) represent the drift height and width, respectively; these also correspond to the barricade height and width. L_{BT} (m) is the top length of WRB and L_{BB} (m), the base length. α_1 (°) is the upstream slope angle of WRB on the stope side; α_1 usually corresponds to the repose angle of waste rock

(typically close to 37°, ± 3°; e.g., Aubertin 2013). α_2 (°) is the downstream slope angle of WRB on the drift side; α_2 can be increased mechanically ($\alpha_2 > \alpha_1$) using pushing equipment.

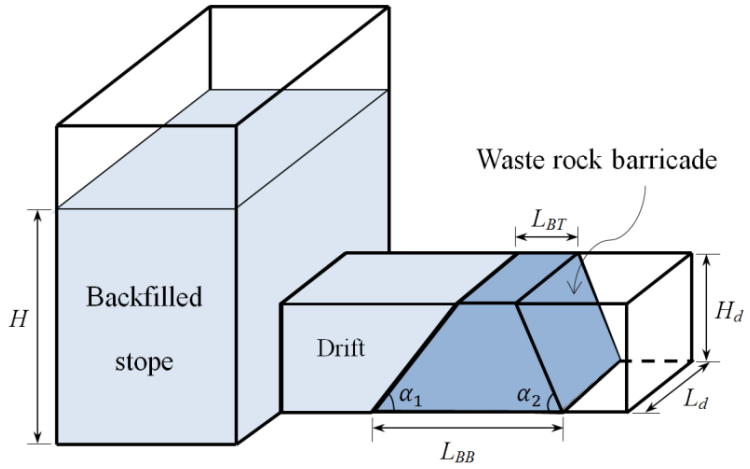

Figure 4-1: Schematic view of a typical backfilled stope with a trapezoidal WRB (adapted from Li & Aubertin 2011)

Li et al. (2009) and Li & Aubertin (2011) developed the initial solution based on an idealized rectangular block. The limit equilibrium analysis of this rectangular block with a volume V (= $L_d \times H_d \times L_B$) gave the minimum required length (L_B) of the WRB (for a factor of safety FS = 1):

$$L_B = \frac{\bar{p} L_d}{\gamma_{wr}(L_d + K H_d)\tan\delta} = \frac{P}{\gamma_{wr} H_d (L_d + K H_d)\tan\delta} \tag{4.1}$$

where $\bar{p}$ ($= \frac{1}{A}\int p dA$, kPa) is an average of the CPB pressure (p, kPa) over the upstream face (A, m^2) of WRB; in the short term, this pressure is assumed to be linearly distributed from the base to the top of the barricade and can be calculated by the iso-geostatic pressure (see Thompson et al. 2012 and El Mkadmi et al. 2014); P (= $\bar{p} \times L_d \times H_d$, kN) is the force exerted on the barricade by CPB; γ_{wr} (kN/m^3) is the unit weight of the waste rock; δ (°) is the friction angle along the interfaces between the WRB and the drift walls and floor; K (-) is the earth pressure coefficient within the waste rock along the transversal direction of the drift.

In practice, engineers would typically consider that length L_B given by Eq. (4.1) represents the WRB length at mid-height. The actual length should then be defined using the slope angle (30° to 45°) on each side. In such case, the required top L_{BT} and base L_{BB} lengths of WRB are given by:

$$L_{BT} = L_B - \frac{H_d}{2}\left(\frac{1}{\tan\alpha_1} + \frac{1}{\tan\alpha_2}\right) \tag{4.2a}$$

$$L_{BB} = L_B + \frac{H_d}{2}\left(\frac{1}{\tan\alpha_1} + \frac{1}{\tan\alpha_2}\right) \tag{4.2b}$$

This solution may give an overly conservative design (Yang et al. 2014). In the following section, a more complete and representative solution is developed, considering more realistic barricade geometry and pressure distribution, based on the analysis of global and local stability.

4.3 Modified formulation

4.3.1 Global stability analysis

Fig. 4-2 depicts a trapezoidal barricade made of waste rock. In this figure, C_T and C_B are the normal compressive forces at the top and base of the WRB, respectively; C_L and S_L are the normal compressive and shear forces acting along the two lateral drift walls, respectively; S_T and S_B are the shear forces at the top and base of the WRB, respectively.

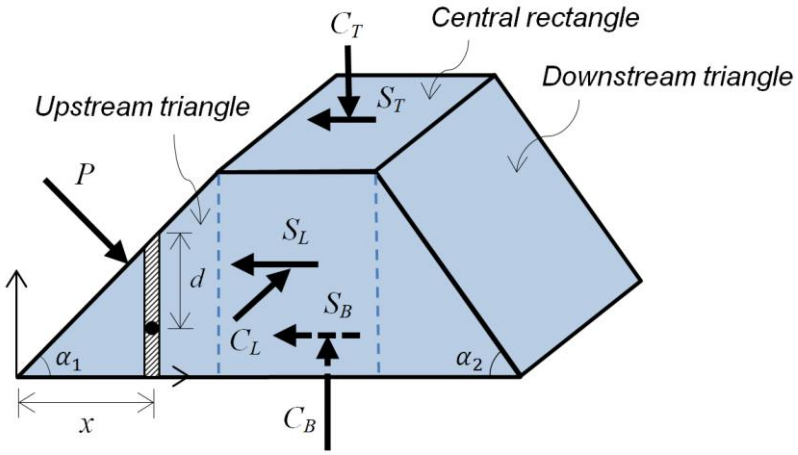

Figure 4-2: Waste rock barricade with various acting forces; symmetric forces acting on the other side (C_L and S_L) of the WRB are not shown here

Numerical simulations and in-situ measurements have shown that the most critical moment for the barricade stability is immediately after the deposition of the saturated CPB, when the pore water pressures in the stope are high (i.e., often close to the overburden stresses due to the weight of the backfill) and the effective stresses are very low (e.g., Thompson et al. 2012; El Mkadmi et al. 2014). In the short term (i.e., before significant drainage), the backfill pressure p and the corresponding force P are expected to act perpendicularly to the upstream face of the barricade (see Fig. 4-2). The horizontal component (P_h) of force P then tends to destabilize the barricade,

while its vertical component (P_v) favors its stability by increasing the normal stress and shear resistance on the floor.

Recently, Yang et al. (2014) modified the solution proposed by Li & Aubertin (2011) by dividing the trapezoidal barricade into a central rectangular part and two triangular portions (see Fig. 4-2). The *FS* can be assessed by considering the limit equilibrium of the barricade. This modified solution is based on several assumptions, including the following (Yang et al. 2014):

1. The effect of pore-water pressures within the WRB is ignored, due to the large contrast (usually 3 orders of magnitude or more) in hydraulic conductivity between the CPB and waste rock.
2. The shear strength between the top of the barricade and the drift roof (back) is neglected, because a void may exist above the barricade, i.e., $C_T = 0$; this conservative assumption was also adopted by Li & Aubertin (2011).
3. Vertical arching due to friction along the barricade vertical side walls is ignored, due to the limited height of drifts (Li & Aubertin 2011); the vertical stress is thus approximated by the overburden.
4. It is postulated that the friction angle along the drift walls is equal to the friction angle between the waste rock and drift floor, δ. When the interfaces are rough, the value of angle δ can be taken as the internal friction angle ϕ' (°) of the waste rock; alternatively, $\delta < \phi'$ should be used if the floor or side walls have a smooth surface (or if these are coated by a fine-grained material layer).
5. The horizontal stress on the two side walls are assumed to be due to the overburden pressure in the waste rock only (without considering the effect of the backfill pressure).

By considering the limit equilibrium of the barricade along the drift axis direction (with the detailed formulation presented in Section 4.9 of this chapter), one can obtain the minimum required top (L_{BT}) and bottom (L_{BB}) lengths (m) of the WRB (Yang et al. 2014):

$$L_{BT} = \frac{\gamma_b\left(H-\frac{H_d}{2}\right)\left(\frac{FS}{tan\,\delta}-\frac{1}{\tan\alpha_1}\right)-\gamma_{wr}\,H_d\left(\frac{1}{2}+K\frac{H_d}{3L_d}\right)\left(\frac{1}{tan\,\alpha_1}+\frac{1}{tan\,\alpha_2}\right)}{\gamma\left(1+K\frac{H_d}{L_d}\right)} \tag{4.3a}$$

$$L_{BB} = L_{BT} + H_d\left(\frac{1}{tan\,\alpha_1}+\frac{1}{tan\,\alpha_2}\right) \tag{4.3b}$$

The corresponding volume of waste rock required to construct the WRB is then given by:

$$V = H_d L_d (L_{BT} + \frac{H_d}{2\,tan\,\alpha_1} + \frac{H_d}{2\,tan\,\alpha_2}) \quad (4.4)$$

Eqs. (4.3) and (4.4) constitute an improved solution for sizing the WRB based on its global stability. As a special case, when FS = 1.0 and $\alpha_1 = \alpha_2 = 90°$, Eqs. (4.3) and (4.4) reduce to the Li & Aubertin (2011) solution. Another special case arises when L_d is very large; the 3D solution [Eq. (4.3a)] then reduces to the following expression that correspond to a 2D (plane strain) condition:

$$L_{BT} = \frac{\gamma_b}{\gamma_{wr}}\left(H - \frac{H_d}{2}\right)\left(\frac{FS}{tan\,\delta} - \frac{1}{\tan\alpha_1}\right) - \frac{H_d}{2}\left(\frac{1}{tan\,\alpha_1} + \frac{1}{tan\,\alpha_2}\right) \quad (4.5)$$

4.3.2 Internal local stability analysis

With Eq. (4.3), very small (or even negative) value can be obtained for the top length L_{BT} (if no constraint is imposed). This is particularly the case for a large interface strength δ. The barricade design based on such solution may lead to internal (local) instability near the upper portion of the WRB (i.e., collapse, sliding or toppling). Hence, there is a need to develop a complementary method to determine the size of the WRB, taking this aspect into account.

Fig. 4-3 shows a model for the local stability analysis of the WRB. This analysis consists of investigating the equilibrium of the potentially unstable upper portion of the WRB having a thickness h (< H_d, m). The approach is the same as for the global stability analysis described above. The friction angle along the potential sliding plane is equal to the internal friction angle ϕ' of the waste rock. Tests on large-scale samples of waste rock indicate that the value of ϕ' typically ranges between 34° and 45° (McLemore et al. 2009; Aubertin 2013) depending on the material density and grain size distribution. The potential sliding plane is assumed to be horizontal here; this aspect will be further discussed below. Also, rotation of the upper portion is not considered here since such rotation could be constrained by the shape of the barricade (wider at the base) and presence of drift roof.

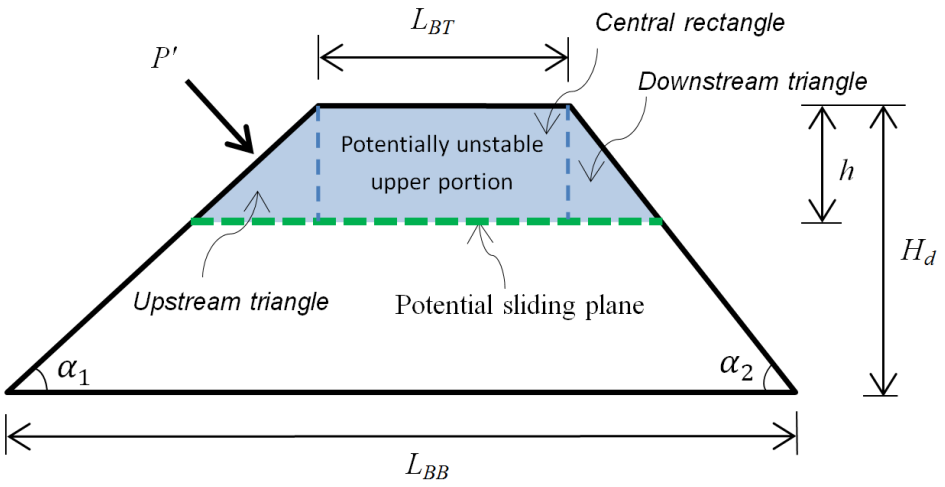

Figure 4-3: A model for internal translation stability analysis of the WRB

By considering the limit equilibrium of the potentially unstable upper portion of the WRB along the drift axis direction (with the detailed formulation presented in Section 4.10 of this chapter), one can obtain the required barricade top length L_{BT} to maintain internal (local) stability:

$$L_{BT} = \frac{\gamma_b\left(H-H_d+\frac{h}{2}\right)\left(\frac{FS}{\tan\phi'}-\frac{1}{\tan\alpha_1}\right)-\gamma_{wr}h\left(\frac{1}{2}+K\frac{h\tan\delta}{3L_d\tan\phi'}\right)\left(\frac{1}{\tan\alpha_1}+\frac{1}{\tan\alpha_2}\right)}{\gamma_{wr}\left(1+K\frac{h\tan\delta}{L_d\tan\phi'}\right)} \tag{4.6}$$

The required top length L_{BT} based on Eq. (4. 6) is related to the position of the critical sliding plane, given by height h. For typical range of the geometric and mechanical characteristics, the required top length L_{BT} monotonously decreases with an increase in h, as illustrated in Fig. 4-4 (calculations made with FS = 1.5, H = 12 m, α_1 = 37°, α_2 = 50°, H_d = L_d = 5 m, δ = ϕ' = 40°, γ_{wr} = γ_b = 19.62 kN/m^3, K = K_a). The most critical position of the sliding plane for the internal stability is naturally at the top of the WRB. Thus, the minimum required L_{BT} is obtained for h = 0.

It can also be noted that when h is equal to H_d in Eq. (4.6), the required length L_{BT} becomes the same as the one determined from the global stability analysis [Eq. (4.3a)] (for ϕ' = δ).

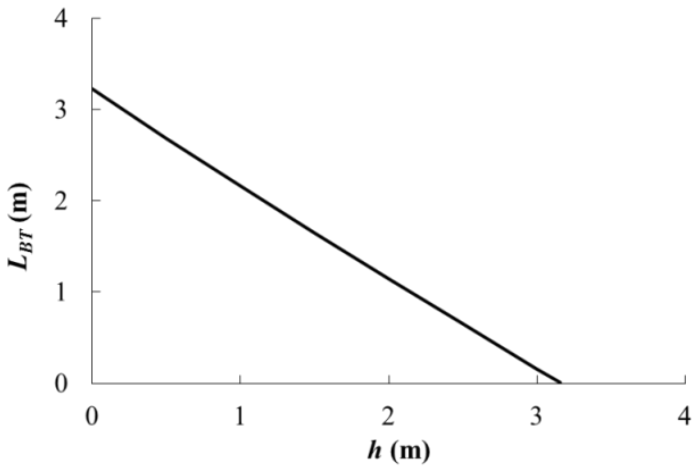

Figure 4-4: Variation of L_{BT} with h for local stability analysis [Eq. (4.6)]

Introducing h = 0 in Eq. (4. 6) gives the minimum required top length of the WRB:

$$L_{BT} = \frac{\gamma_b}{\gamma_{wr}}(H - H_d)\left(\frac{FS}{\tan\phi'} - \frac{1}{\tan\alpha_1}\right) \quad (4.7)$$

One can note that this 3D solution is independent of the drift width L_d. Thus, it can also be considered valid for a 2D (plane-strain) condition.

Eq. (4. 7) also indicates that the required top length L_{BT} is independent of the interface friction angle δ. This is confirmed by the numerical simulations results shown in the next section.

As the angle of the upstream slope must be equal to or smaller than the internal friction angle of the waste rock used for constructing the barricades (i.e., $\alpha_1 \leq \phi'$), the use of Eq. (4.7) can lead to negative values for the required L_{BT} (for FS = 1.0). This means that the barricade would be stable for any top length. Clearly, this does not correspond to a practical (realistic) solution, neither to the numerical modeling results (as will be shown in next section).

To avoid a negative value of the required L_{BT}, a simple modification is proposed by adding a calibration factor C_M in Eq. (4.7), which then becomes:

$$L_{BT} = \frac{\gamma_b}{\gamma_{wr}}(H - H_d)\left(\frac{C_M \times FS}{\tan\phi'} - \frac{1}{\tan\alpha_1}\right) \quad (4.8)$$

Following numerical simulations (shown in next section), this calibration factor C_M can be taken as 1.5. Fig. 4-5 shows the variation of the required L_{BT} [based on Eqs. (4.5) and (4.8) with C_M =1.5] as a function of the interface friction angle δ (with H = 9 m, H_d = 5 m, $\alpha_1 = \alpha_2$ = 37°, ϕ' = 40°, $\gamma_{wr} = \gamma_b$ = 19.62 kN/m^3, $K = K_a$, C_M = 1.5, and FS = 1.0). When δ varies from 15° to 21°

along the rock walls (including drift floor), the WRB stability is mainly dictated by the global stability of the barricade, which moves as a rigid block. As δ increases from 21° to 40° (for the case analyzed here), for a rougher surface along the rock walls, the local stability at near the top of the barricade becomes more critical (i.e., function of ϕ' of the waste rock). L_{BT} then becomes insensitive to the variation of δ once it exceeds a critical value (of about 21° in this case).

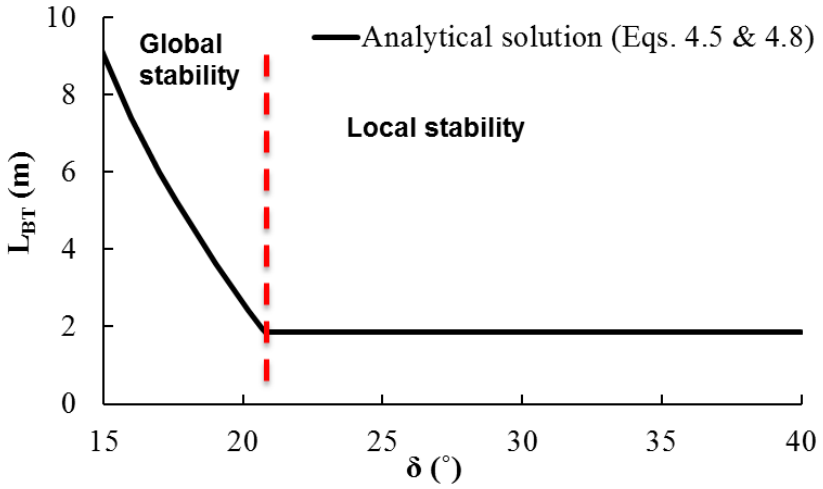

Figure 4-5: Variation of the required top length L_{BT} obtained by Eqs. (4.5) and (4.8) as a function of δ

These results suggest that there is a critical interface friction angle (δ_c) that marks the change in the controlling failure mechanism, from a global (smaller δ) to a local stability of the WRB. In Fig. 4-5, the dash line marks the change of the controlling failure mechanism. This critical interface friction angle can be obtained by equating Eqs. (4.3a) and (4.8), as follows:

$$\delta_c = \tan^{-1}\frac{FS(2H-H_d)\tan\alpha_1}{H_d+2(H-H_d)\left[\frac{C_M\times FS\tan\alpha_1}{\tan\phi'}\left(1+K\frac{H_d}{L_d}\right)-K\frac{H_d}{L_d}\right]+\frac{\gamma_{wr}}{\gamma_b}H_d\left(1+K\frac{2H_d}{3L_d}\right)\left(1+\frac{\tan\alpha_1}{\tan\alpha_2}\right)} \tag{4.9}$$

4.4 Proposed solution

The global and internal (local) stability of the barricades leads to the following equations, based on the above developments:

$$L_{BT} = \frac{\gamma_b\left(H-\frac{H_d}{2}\right)\left(\frac{FS}{\tan\delta}-\frac{1}{\tan\alpha_1}\right)-\gamma_{wr}H_d\left(\frac{1}{2}+K\frac{H_d}{3L_d}\right)\left(\frac{1}{\tan\alpha_1}+\frac{1}{\tan\alpha_2}\right)}{\gamma_{wr}\left(1+K\frac{H_d}{L_d}\right)}, \text{ for } \delta \le \delta_c \tag{4.10a}$$

$$L_{BT} = \frac{\gamma_b}{\gamma_{wr}}(H-H_d)\left(\frac{C_M\times FS}{\tan\phi'}-\frac{1}{\tan\alpha_1}\right), \text{ for } \delta > \delta_c \tag{4.10b}$$

Eqs. (4.10a) and (4.10b) constitute the proposed 3D solution for sizing the required top length of the 3D WRB. The base length of the WBR can be calculated with Eq. (4.3b), whereas the required volume of the WRB is assessed by Eq. (4.4). Sample calculations with the proposed solution [Eq. (4.10)] are illustrated in Section 4.11 of this chapter.

The corresponding 2D (plane-strain) solution can be written as:

$$L_{BT} = \frac{\gamma_b}{\gamma_{wr}}\left(H - \frac{H_d}{2}\right)\left(\frac{FS}{tan\,\delta} - \frac{1}{\tan\alpha_1}\right) - \frac{H_d}{2}\left(\frac{1}{tan\,\alpha_1} + \frac{1}{tan\,\alpha_2}\right), \text{ for } \delta \leq \delta_c \quad (4.11a)$$

$$L_{BT} = \frac{\gamma_b}{\gamma_{wr}}(H - H_d)\left(\frac{C_M \times FS}{\tan\phi'} - \frac{1}{\tan\alpha_1}\right), \text{ for } \delta > \delta_c \quad (4.11b)$$

4.5 Numerical simulations

The two analytical solutions presented above can be used for estimating the required length of WRB for global and local stability. It is important to assess the validity of the proposed solutions using other approaches. As there are no experimental results available to do so (to the authors' knowledge), the analytical solutions are compared with simulations conducted with *FLAC*.

Because the stability analysis of the WRB is a 3D problem, a full validation of the proposed solution requires 3D modeling. In the following subsections, the analytical solution will first be compared with numerical simulations of very wide barricades (i.e., L_d >>) under plane-strain conditions. This corresponds to the worst case scenario (for barricade stability), without the contribution of side walls. The effect of pore water pressure within the WRB is neglected in these simulations. The code *FLAC* was used for this initial assessment of the analytical solutions.

4.5.1 Model Configuration

Numerical modeling with *FLAC* (Itasca 2011) is used in the following to help evaluate the validity of the proposed analytical solutions for the plane-strain condition. The configuration of the WRB model and the material properties are shown in Fig. 4-6. All variables and parameters have been defined in the previous sections.

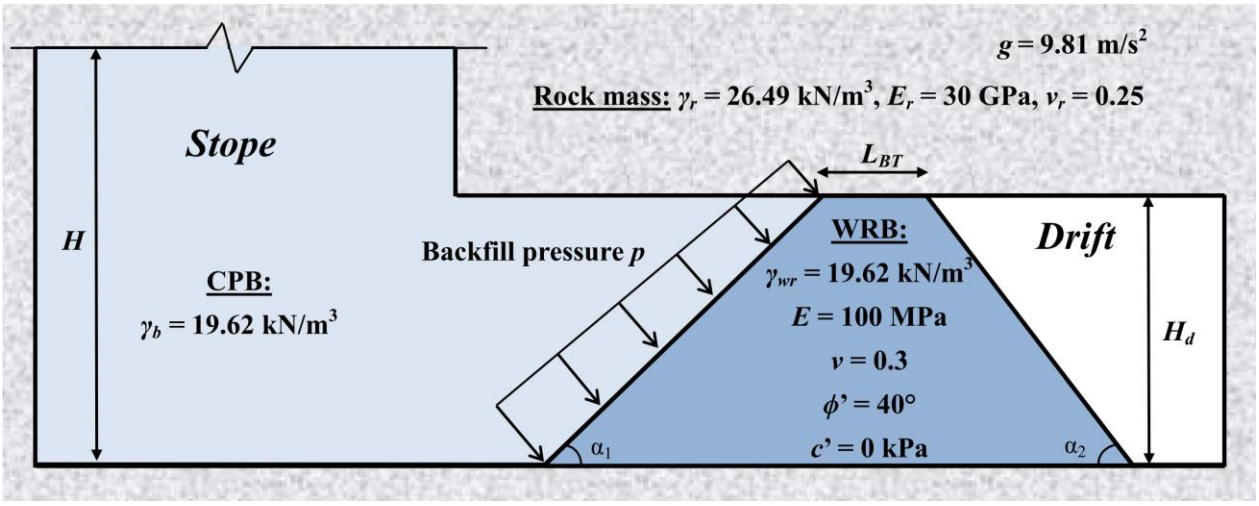

Figure 4-6: Conceptual model of the backfilled stope with a trapezoidal WRB

The height of the barricade (drift) is 5 m. Both upstream α_1 and downstream α_2 slope angles are equal to 37° (i.e., H_d = 5 m and $\alpha_1 = \alpha_2 = 37°$). The rock mass (along the drift floor in this case) is linearly elastic with a unit weight γ_r = 26.49 kN/m^3, a Young's modulus E_r = 30 GPa and a Poisson's ratio ν_r = 0.25. The waste rock is modeled as an elastoplastic material obeying the Mohr-Coulomb criterion; it is characterized by a unit weight γ_{wr} = 19.62 kN/m^3, a Young's modulus E = 100 MPa, a Poisson's ratio ν = 0.3, an effective cohesion c' = 0 kPa and an effective friction angle ϕ' = 40°.

Fig. 4-7 shows a numerical model built with *FLAC*. The rock mass boundary (drift floor) is fixed in the horizontal and vertical directions. As mentioned above, the shear strength along the contact between the barricade top and the back (drift roof) is ignored; neglecting this contribution leads to a conservative design (the barricade top is thus set free). The linearly distributed pressure p perpendicularly applied on the upstream face of the barricade represents the backfill pressure from the stope side. A minimum mesh size 0.1 × 0.1 m (at the barricade top) gives stable numerical results based on the sensitivity study (see details in the sensitivity analysis presented in Appendix E).

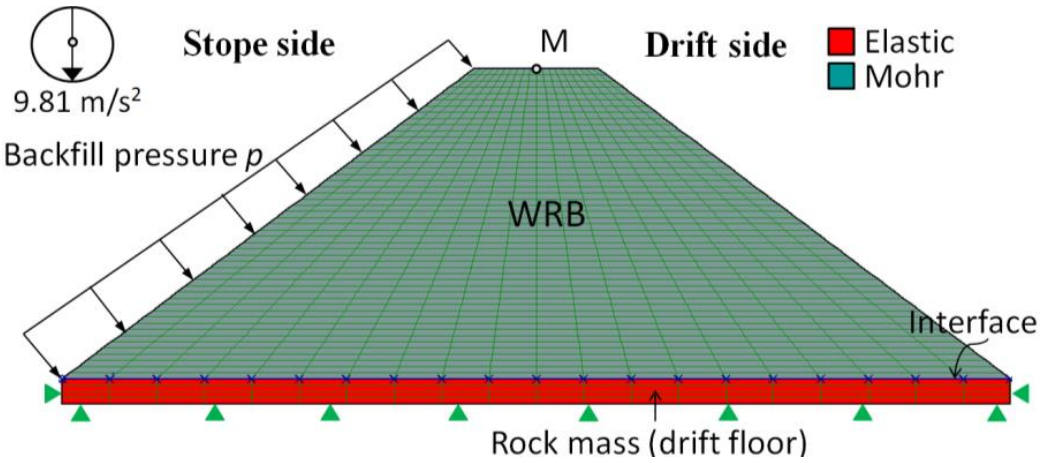

Figure 4-7: WRB model built with *FLAC*, showing the discretization and boundary conditions

Interface elements are used between the waste rock and the drift floor to allow sliding of the barricade when the interface shear strength is exceeded. The stiffness of the interface is determined according to the recommendation given by Itasca (2011). The cohesion and tensile strength of the interface are nil. The interface friction angle δ can vary from a small value (smooth interface) to the internal friction angle ϕ' of waste rock (rough interface).

Each numerical simulation is performed in two steps: i) the addition of the WRB and ii) the application of the backfill pressure (instantaneous filling). The displacements induced within the WRB are set to zero before applying the backfill pressure.

4.5.2 Failure mechanism and sliding criterion

In *FLAC*, the failure (or yielding state) state of material can be displayed by either the yield state or shear strength ratio (equivalent to a *FS*). But these representations may not be reliable for describing the failure of a WRB because the barricade can slip (failure occurs) without showing significant yield or failure zones. This is particularly true when the interface below the barricade (drift floor) is relatively smooth and the interface shear strength is relatively small. In this case, sliding of the whole WRB can take places along the drift floor, as illustrated in Fig. 4-8(a) (case with δ = 20°, H = 9 m, H_d = 5 m, $\alpha_1 = \alpha_2$ = 37°, and ϕ' = 40°); it shows the displacement vectors for the barricade upon applying the fill pressure along the upstream face. Such a small value of δ can occur for a weathered surface or when it is coated by fine-grained material (as if often the case when barricades are close to drawpoints).

When the interface along the base is rougher (i.e., δ close to ϕ'), the top portion of the barricade tends to move sideways, as shown in Fig. 4-8(b) with the horizontal displacements vectors upon the application of the fill pressure along the upstream face (case with δ = 30°, H = 9 m, H_d = 5 m, $\alpha_1 = \alpha_2$ = 37°, ϕ' = 40°).

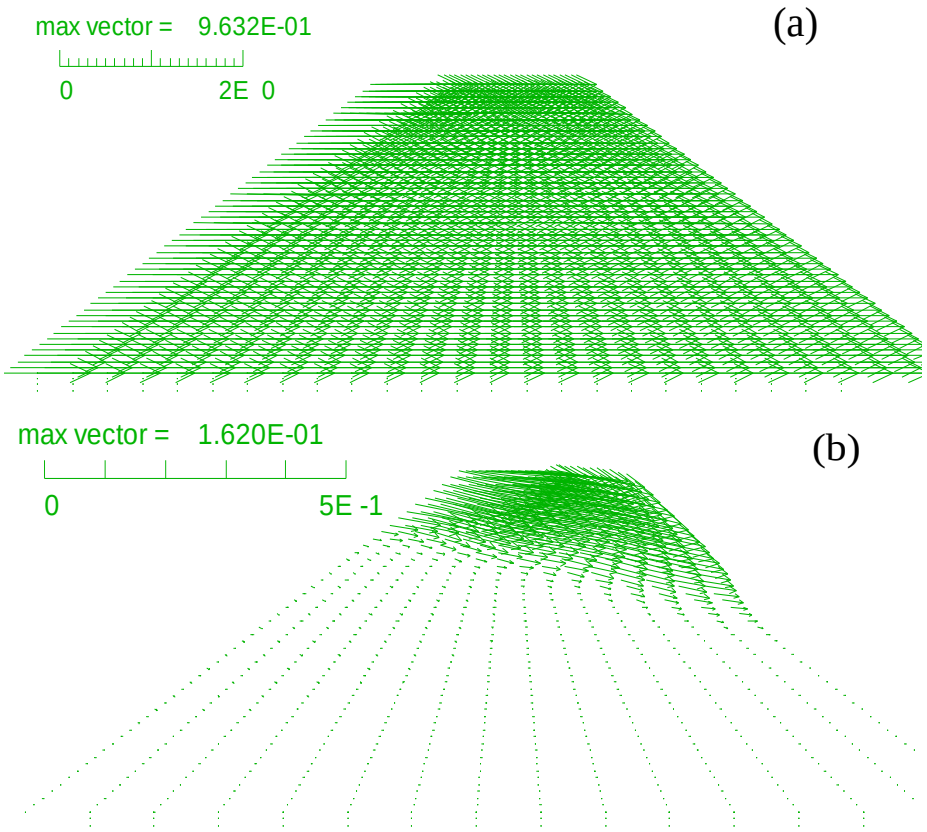

Figure 4-8: Displacement vectors of WRB with (a) a relatively smooth interface (δ = 20°, L_{BT} = 2.5 m), and (b) a rougher interface (δ = 30°, L_{BT} = 1.5 m)

The distributions of displacements, stresses, and yielding state (or shear strength) within the barricade can provide useful information. However, the evaluation of the barricade stability due to global or local sliding based on these observations may be subjective. To reduce this subjectivity, the top horizontal displacement at the center of the barricade (marked by "M" in Fig. 4-7) is monitored. Fig. 4-9 illustrates a typical variation of the horizontal displacement at the top of the barricade (point M) as a function of the barricade top length L_{BT}, obtained with *FLAC* (calculations made for different length L_{BT} with H = 9 m, H_d = 5 m, $\alpha_1 = \alpha_2$ = 37°, δ = 30° and ϕ' = 40°). One can see that the horizontal displacement at the monitoring point M increases slightly, from 2.2 mm to 5.8 mm, when the top length L_{BT} decreases from 3 m to 1.6 m, indicating a stable

state. This displacement dramatically surges to 139 mm when L_{BT} goes from 1.6 m to 1.5 m, indicating a change from a stable to an unstable state.

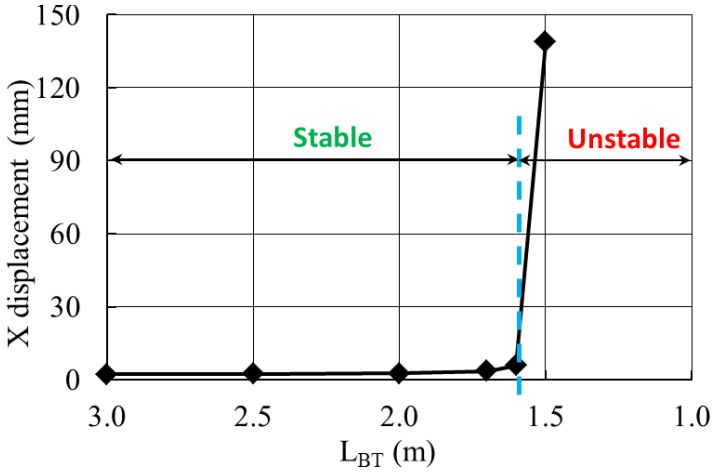

Figure 4-9: Typical variation of the horizontal displacement at point M (see Fig. 4-7) as a function of the barricade top length

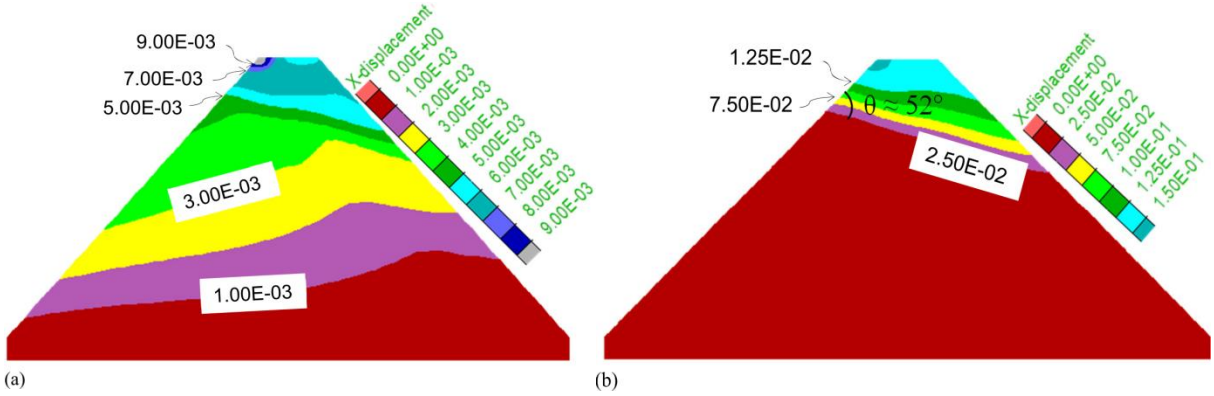

Figure 4-10: Contours of horizontal displacement within the WRB, for L_{BT} equal to (a) 1.6 m and (b) 1.5 m

Fig. 4-10 shows the horizontal displacements iso-contours within the WRB for L_{BT} = 1.6 m [Fig. 4-10(a)] and L_{BT} = 1.5 m [Fig. 4-10(b)], respectively. The calculations were made with H = 9 m, H_d = 5 m, $\alpha_1 = \alpha_2$ = 37°, δ = 30°, ϕ' = 40°. In the former case, the variation of the horizontal displacement across a vertical profile of the WRB is progressive, so the WRB remains intact. The small value of the maximum horizontal displacement at the upstream top (9 mm) indicates that the WRB is stable. When L_{BT} is reduced to 1.5 m, the top portion of WRB moves significantly, with the maximum horizontal displacement at the top exceeding 100 mm [Fig. 4-10(b)]. This provides evidence of sliding near the top along the (inclined) shearing plane within the WRB.

This dramatic increase of the horizontal displacement with a slight decrease of the top length of the barricade is considered as an indicator of local (and global) instability of the WRB. This type of behavior has been observed with various simulations conducted under different conditions (see more details presented in Appendix E).

Figs. 4-8(b) and 4-10(b) indicate that the top portion of the WRB slips along an inclined plane, making an angle θ of about 52° from the upstream slope.

4.5.3 Comparison with the proposed solution

The analytical solution given by Eq. (4.11), for plane strain, is compared with 2D numerical simulations results. Fig. 4-11 shows the variation of the required L_{BT} as a function of the interface friction angle δ obtained from the numerical simulations and proposed solution (calculations made with H = 9 m, H_d = 5 m, $\alpha_1 = \alpha_2$ = 37°, ϕ' = 40°, $\gamma_{wr} = \gamma_b$ = 19.62 kN/m^3, $K = K_a$ and FS = 1.0), for the case shown in Fig. 4-9. It is seen that the application of the Eq. (4.11) with C_M = 1.5 represents well the numerical simulations results.

The good agreement for the global stability of the barricade tends to indicate that Eq. (4.11a) is valid and able to predict the required L_{BT}, as long as the interface friction angle is smaller than the critical interface friction angle, i.e., $\delta \leq \delta_c$. For the internal (local) stability of the barricade, a value of C_M = 1.5 in Eq. (4.11b) leads to a good agreement between the proposed solution and the numerical results, as shown in Fig. 4-11 for $\delta > \delta_c$.

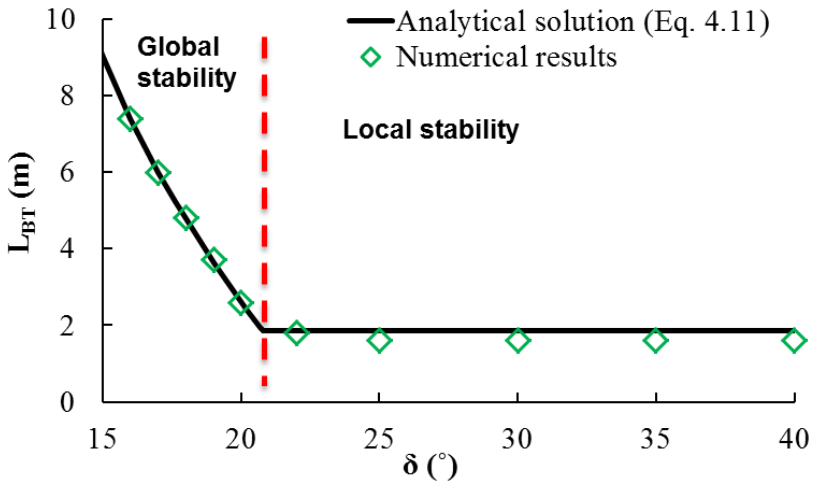

Figure 4-11: Comparison of the required length L_{BT} obtained from the analytical solutions [Eq. (4.11) with C_M = 1.5] and numerical simulations for different values of δ

To further evaluate the validity of the proposed solutions [Eqs. (4.10) and (4.11)], additional numerical calculations were performed with typical geometric parameters and material properties.

Fig. 4-12 shows the variation of the required top length L_{BT} as a function of the interface friction angle δ for different parameters, as obtained from numerical simulations and the proposed solution [Eq. (4.11)]. It can be observed that the proposed analytical solution agrees well with the simulations results.

These results show that when ϕ' increases from 34° to 45°, the upstream (α_1) and downstream (α_2) slope angles have to be increased too, leading to a decrease in the bottom length L_{BB} and an increase in the top length L_{BT}. There is thus an increase in L_{BT} with ϕ' for the global stability analyses [Fig. 4-12(a)]. For local stability, there is a decrease in L_{BT} with an increase in the shear strength of the waste rock [Fig. 4-12(a)]. These numerical features are well captured by the analytical solutions. A good agreement is obtained between these solutions for both the global and internal local stability analyses.

Fig. 4-12(b) shows the variation of L_{BT} obtained by the numerical simulations and proposed solution, when the height of CPB in the stope H varies from 7 to 15 m (the other parameters are also given in the figure). It is seen that L_{BT} increases with H of the CPB in the stope. Again, a good agreement is observed between the proposed solution and numerical simulations.

Fig. 4-12(c) shows the variation of L_{BT} obtained by the simulations and proposed solution when the drift/barricade height (H_d) increases from 3 to 7 m (while other parameters remain constant). The results indicate that thicker barricades are more stable. The values of L_{BT} estimated by the proposed solution correspond well to those obtained by the simulations when the difference in height between the barricade and the CPB is large. The agreement is not as good when the heights of the barricade and CPB are almost the same (with large H_d). Such trend can also be observed in Fig. 4-12(d) when H increases from 10 to 12 m while other parameters (including H_d) remain constant. The values of L_{BT} obtained by the numerical simulations can be slightly higher than that calculated with the proposed solution when H_d and H become close (with large H_d). More work may be needed to improve the analytical solution for this aspect.

In general, the proposed solution [Eq. (4.11)] represents well the results obtained here for the plane-strain condition (for global stability and local stability). It thus provides a useful solution for sizing barricades made of waste rock. Nevertheless, the values of L_{BT} estimated by the

proposed analytical solution can be sometimes smaller than those estimated by numerical simulations as shown in Figs. 4-12c and 4-12d. A *FS* of 1.5 to 2 should be applied in the barricade design with the proposed analytical solution.

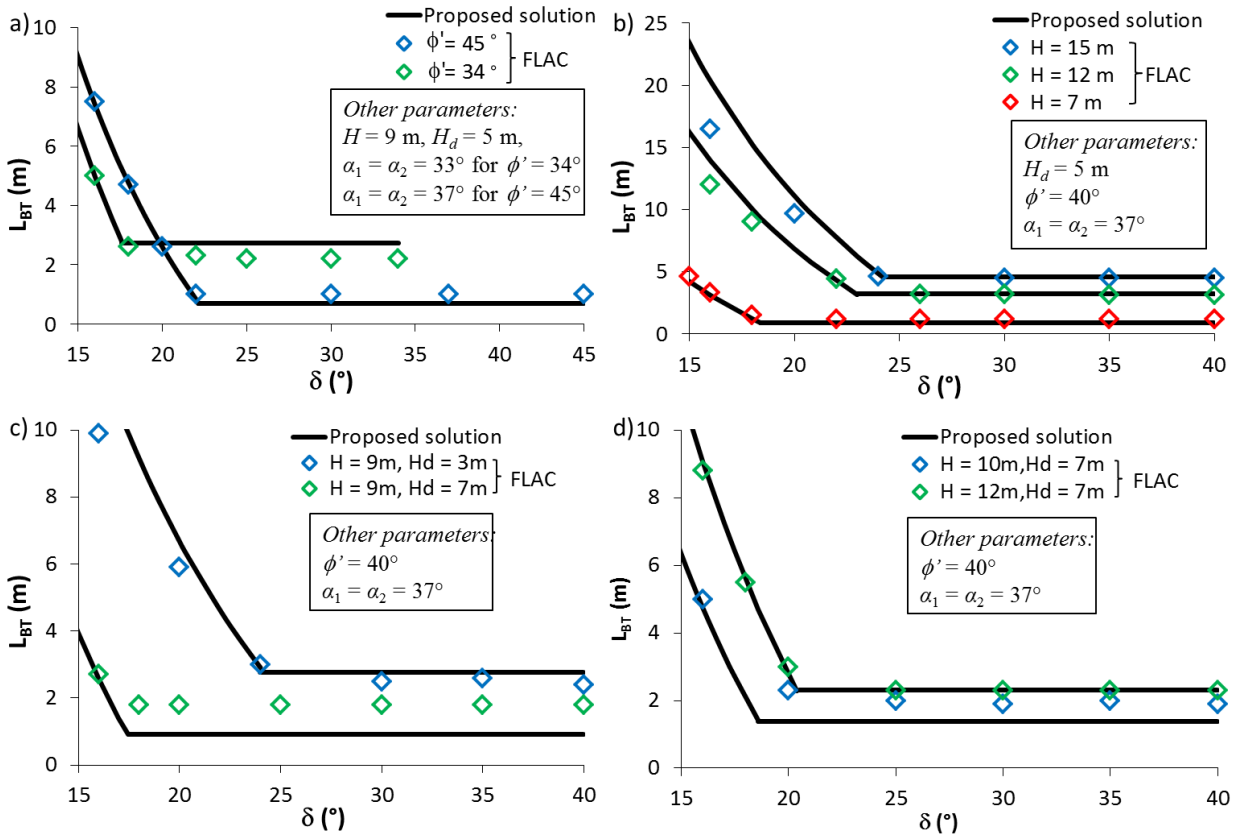

Figure 4-12: Comparison between the analytical solution [Eq. (4.11)] with C_M = 1.5, $\gamma_{wr} = \gamma_b$ = 19.62 kN/m^3, $K = K_a$ and FS = 1.0) and numerical simulations. The calculations give the variation of the required L_{BT} for different values of δ with an increase in (a) waste rock strength ϕ', (b) CPB height H in the stope, (c) barricade height H_d, and (d) CPB height H in the stope

4.6 Parametric analyses

Sample applications of the proposed solution are presented below to show the influence of various parameters on WRB design. Typical values are used for the drift geometry and material properties. The backfill pressure is obtained by considering 10 m high of CPB (unit weight γ_b = 20 kN/m^3). As mentioned above, the most critical period is shortly after the hydraulic deposition of the saturated fill, when the effective stresses are nil and the total backfill pressure can be calculated from the overburden weight.

Fig. 4-13(a-c) show the variation of the required L_{BT} with δ for different values of upstream slope angle α_1 and downstream slope angle α_2 [Fig. 4-13(a)], drift width L_d and height H_d [Fig. 4-13(b)], and internal friction angles ϕ' [Fig. 4-13(c)], calculated with the proposed 3D solution [Eq. (4.10)] using $\gamma_{wr} = \gamma_b = 20$ kN/m^3, $C_M = 1.5$ and $K = K_a$.

Fig. 4-13(a) shows that the required L_{BT} calculated with the proposed 3D solution [Eq. (4.10)] increases significantly with an increase in the upstream slope angle α_1; L_{BT} increases slightly with an increase in the downstream slope angle α_2 (for $\delta \leq \delta_c$) when the barricade design is dictated by the global stability. When local stability governs the barricade design (i.e., $\delta > \delta_c$), the required L_{BT} tends to increase with an increase in α_1, but it is insensitive to α_2.

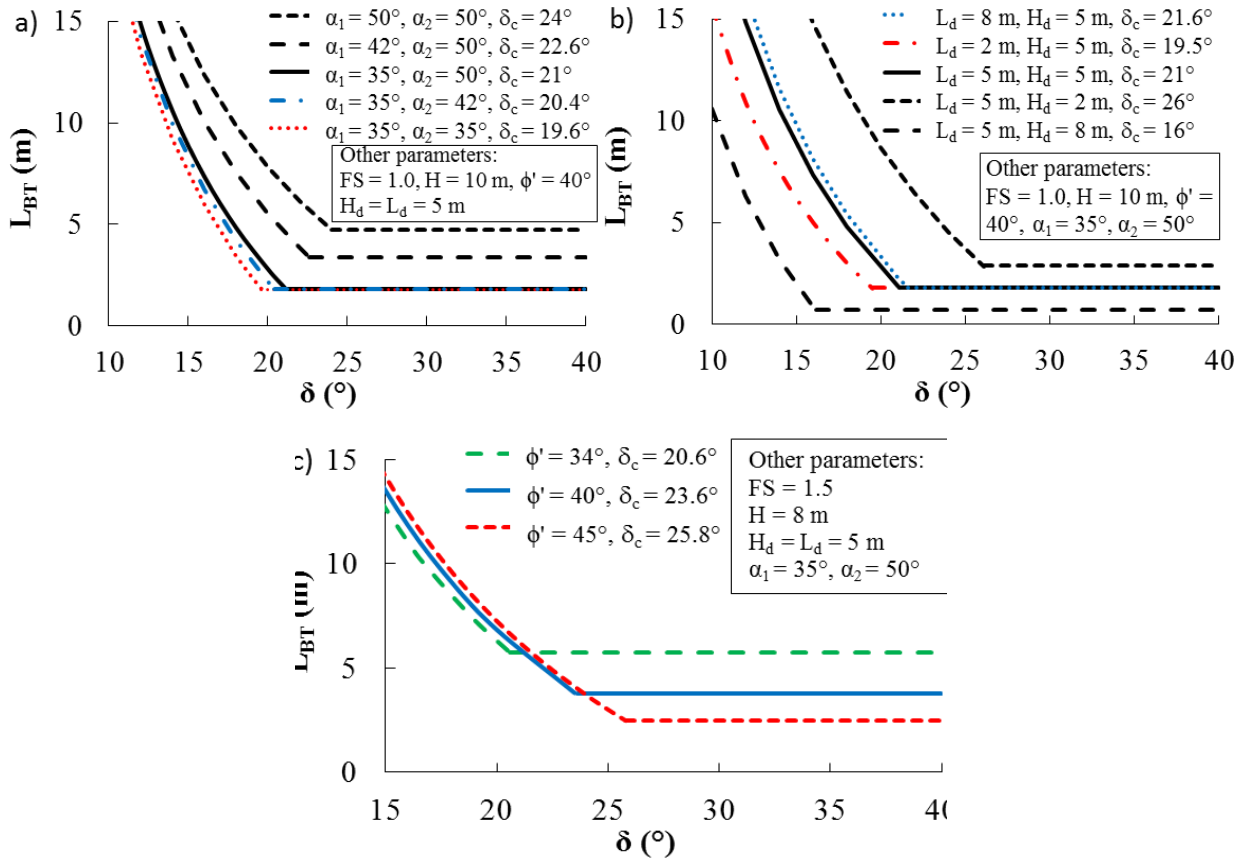

Figure 4-13: Variation of the required L_{BT} with δ for different values of (a) upstream slope angle α_1 and downstream slope angle α_2, (b) drift width L_d and height H_d, and (c) internal friction angles ϕ'

These results indicate that when α_1 increases, the barricade shape becomes closer to rectangular, leading to a decrease in bottom length L_{BB} and a reduction in the resistance (S_B) along the

barricade base. An increase in α_1 also leads to a decreased vertical component of the load P and an increase in its horizontal component. These changes associated with an increased α_1 tend to jeopardize the barricade stability, resulting in a significant increase in L_{BT} (i.e., increasing α_1 is not advisable). When α_2 increases, the barricade shape becomes also closer to a rectangular block, leading to a decreased bottom length L_{BB} and a reduced resistance along the barricade base. But there is no change in other stabilizing factors with an increased α_2. This is why its variation only slightly changes L_{BT}, when controlled by the global stability (when $\delta \leq \delta_c$), but barely the one controlled by the local stability (when $\delta > \delta_c$).

Fig. 4-13(b) shows the variation of the required L_{BT} with different drift width L_d. It is seen that when the barricade design is controlled by global stability (i.e., $\delta \leq \delta_c$), L_{BT} increases with L_d. When the drift is wider, the stabilizing (confining) effect provided by the two side walls becomes weaker, leading to an increased L_{BT}. When the rock walls are very rough ($\delta > \delta_c$), the barricade design is essentially dictated by the local stability near the top of the barricade; L_{BT} is then insensitive to L_d.

Fig. 4-13(b) also shows the variation of the required L_{BT} for different drift height H_d. The solution predicts a reduction of L_{BT} when H_d increases (from 2 to 8 m here). When H_d increases, the contact area and stresses along the floor and side walls of the barricade can increase significantly, leading to a more stable barricade and a decreased L_{BT} for the global stability analyses. The decrease in L_{BT} for local stability is mostly due to a decrease in height difference between the barricade and CPB in the stope.

Fig. 4-13 (c) shows the variation of L_{BT} as a function of δ for different internal friction angles ϕ' of the waste rock. It is seen that L_{BT} tends to increase slightly as ϕ' increases for $\delta \leq \delta_c$ (global stability). This change is mainly due to a decrease in the Rankine's active earth pressure coefficient K_a associated with the decreased ϕ'. When the rock walls are rough (i.e., $\delta > \delta_c$) and the barricade design is dictated by the local stability, the L_{BT} values decrease significantly for a stronger waste rock. As the rock walls are usually rough, it can be expected that the barricade design is mostly dictated by the local stability.

4.7 Discussion

For both the proposed solution and numerical simulations, the backfill pressure on the barricade was calculated from an isostatic stress based on the overburden. This is applicable shortly after the CPB is poured in a stope (e.g., Thompson et al. 2012). In practice, the WRB can be quite pervious so drainage and consolidation of the CPB can take place during the backfilling operation (El Mkadmi et al. 2014). It can be expected that the fill pressures exercised on the WRB are smaller than those calculated with the overburden. This solution is thus conservative from this point of view, particularly for large stopes and slow filling rates.

The proposed solution (and numerical simulations) was developed without considering the effect of water (i.e., pore-water pressure) within the WRB. This assumption is based on the significant contrast in hydraulic conductivity between typical CPB and waste rock in the barricade.

The stresses in the WRB were estimated based on the overburden of the waste rock. Vertical arching (due to a stress transfer along the side walls of the WRB) was neglected. These assumptions are deemed representative, although they may underestimate the barricade size. More work is required to evaluate this aspect.

The interface friction angle δ can be measured by direct shear box tests on a relatively small scale in the laboratory (e.g., Fall & Nasir 2010; Belem et al. 2015). At larger scales, the determination of δ remains challenging as the interfaces between the barricade and rock walls can vary from regular and smooth to very irregular and rough. Thus, the interface friction angle δ depends not only on the contact between the waste rock and planar rock surface, but also on the roughness of rock walls. Work is ongoing on this aspect to better assess the behavior of such interfaces.

The measurement and evaluation of the shear strength of waste rock is another challenge (which is also part of an ongoing project). Leps (1970) showed that typical coarse-grained materials (rockfills) may have a friction angle as high as 55°. Williams (2000) indicated that the friction angle of waste rock can range from 40° to 50°. McLemore et al. (2009) showed that the friction angle of mine waste rock can vary from 20° to 55° (with most results between 35° to 45°). These (and other) results indicate that the use of a friction angle of 40° to 45° can be deemed reasonable in the analyses shown here.

It was shown above that a calibration factor (C_M) of 1.5 leads to a good agreement between the proposed (local) solution and numerical simulations. In some cases however, this C_M value maybe slightly different if the drift is very high [see Figs. 4-12(c) and (d)]. Although the proposed value can be considered representative for most cases, additional work may be required to further investigate the dependency of C_M on other factors such as barricade configuration.

The numerical simulations show that the sliding plane for a local failure is inclined (see Figs. 4-8 and 4-10), not horizontal as assumed in the analytical formulation (Fig. 4-3). This can partly explain the need to add a calibration factor C_M in the solution [Eqs. (4.8) to (4.11)].

The proposed analytical solution was calibrated here and then validated using 2D numerical modeling for plane-strain conditions. The analytical solution for the local stability is independent on the third dimension so it can be considered as validated (at least in part) with the simulations. For global stability, the 2D simulations represent the most conservative case where the contribution of side walls is ignored. A good agreement is obtained between the numerical and analytical solutions without any calibration. 3D numerical modeling is underway to complete the validation of the proposed analytical solution.

4.8 Conclusions

In the early stage of a project, an analytical solution can offer a simple and low-cost tool for the preliminary estimate of the size of a waste rock barricade. An improved and more complete 3D analytical solution is proposed here to define the size of trapezoidal barricades made of waste rock to retain CPB. Both the global and local (internal) stability of the WRB are considered in the solution.

The numerical and analytical results show that the failure mechanism of the WRB depends on the properties of the interface between the rock walls (floor) and waste rock. When the rock walls are smooth covered or heavily weathered, the friction angle (δ) of the interface may be smaller than the critical interface friction angle (δ_c); the global stability then governs the barricade design. When the rock walls are rough, the sizing of WRB usually depends on the local stability. This feature has been demonstrated by the numerical simulations conducted for calibrating and validating the proposed analytical solution.

Good agreements have been obtained between the analytical solution and the numerical simulations for the global stability analyses without any calibration in 2D conditions (most conservative case). Good agreement was also obtained between the proposed analytical solution and the numerical modeling for the local stability analyses. Complementary simulations have shown that the proposed solution predicts quite well the required length of the WRB for a typical range of geometric and mechanical characteristics.

Acknowledgements

The authors would like to acknowledge the financial support from the Natural Sciences and Engineering Research Council of Canada (NSERC 402318), Institut de recherche Robert-Sauvé en santé et en sécurité du travail (IRSST 2013-0029), Fonds de recherche du Québec – Nature et Technologies (FRQNT 2014-MI-183747, 2015-MI-191676), and industrial partners of the Research Institute on Mines and the Environment (RIME UQAT-Polytechnique; http://rime-irme.ca/).

4.9 Appendix I: Solution development for the global stability analysis

Based on assumption (iii), the vertical compression force C_B (see Fig. 4-2) at the base of the WRB is given by:

$$C_B = \gamma_{wr} H_d L_d \frac{L_{BT}+L_{BB}}{2} + P\cos\alpha_1 \tag{4.12}$$

with

$$P = \bar{p} H_d L_d / \sin\alpha_1 \tag{4.13}$$

$$\bar{p} = \gamma_b (H - H_d/2) \tag{4.14}$$

where γ_b (kN/m^3) is the unit weight of saturated backfill.

Using the Coulomb criterion, the shear resistance S_B (see Fig. 4-2) at the base of the barricade is given by:

$$S_B = C_B \tan\delta = H_d L_d (\gamma_{wr} \frac{L_{BT}+L_{BB}}{2} + \gamma_b \frac{H-H_d/2}{\tan\alpha_1}) \tan\delta \tag{4.15}$$

Based on the assumption (v), the horizontal stress on the two side walls can be expressed as:

$$\sigma_h = K\gamma_{wr} d \tag{4.16}$$

where d is the depth (m) of the calculation position from the barricade top surface (see Fig. 4-2); K (-) is the earth pressure coefficient within the waste rock along the transversal direction of the drift (taken conservatively as Rankine's active pressure coefficient K_a, hence minimizing the value of σ_h).

Hence, the compressive C_{LC} and shear S_{LC} forces (with the first subscript L denoting lateral walls and the second subscript C standing for central part) acting on the central part of the barricade can be expressed as:

$$S_{LC} = C_{LC} \tan\delta = \frac{K\gamma_{wr}{H_d}^2 L_{BT}}{2} \tan\delta \tag{4.17}$$

Similarly, the lateral shear resistances acting along the two lateral walls of the triangle portions (S_{LU} and S_{LD}) can be expressed as follows (with subscripts U and D denoting the upstream and downstream triangular portions, respectively):

$$S_{LU} = C_{LU} \tan\delta = K\gamma_{wr} \tan\delta \int_0^{\frac{H_d}{\tan\alpha_1}} \frac{(x\tan\alpha_1)^2}{2} dx = \frac{K\gamma_{wr}{H_d}^3}{6\tan\alpha_1} \tan\delta \tag{4.18}$$

$$S_{LD} = C_{LD} \tan\delta = K\gamma_{wr} \tan\delta \int_0^{\frac{H_d}{\tan\alpha_2}} \frac{(x\tan\alpha_2)^2}{2} dx = \frac{K\gamma_{wr}{H_d}^3}{6\tan\alpha_2} \tan\delta \tag{4.19}$$

where x is the horizontal distance from the toe of the upstream slope to the calculation point (see Fig. 4-2).

The limit equilibrium of the barricade along the drift axis direction leads to the following expression for the factor of safety (FS) against sliding [$S_T = 0$ based on assumption (ii)]:

$$FS = (S_B + 2S_L)/(P\sin\alpha_1) \tag{4.20}$$

where

$$S_L = S_{LC} + S_{LU} + S_{LD} \tag{4.21}$$

Introducing Eqs. (4.13) - (4.15), (4.17) - (4.19) and (4.21) into Eq. (4.20), one can obtain the minimum required top (L_{BT}) and bottom (L_{BB}) lengths of the WRB expressed as Eq. (4.3).

4.10 Appendix II: Solution development for the internal local stability analysis

The pushing force P' (see Fig. 4-3) exerted by the CPB on the upstream slope of the upper portion can be calculated as:

$$P' = \bar{p}' \frac{hL_d}{sin\alpha_1} = \gamma_b \left(H - H_d + \frac{h}{2}\right) \frac{hL_d}{sin\alpha_1} \tag{4.22}$$

where $\bar{p}'$ ($= \frac{1}{A'} \int p' dA'$, kPa) is an average value for the CPB pressure (p', kPa) over the upstream area (A', m^2) of the barricade.

The compression (C_B') and shear (S_B') forces at the base of the upper portion can be expressed as:

$$S_B' = C_B' \tan \phi' = \left(\gamma_{wr} h L_d L_{BT} + \frac{\gamma_{wr} h^2 L_d}{2 \tan \alpha_1} + \frac{\gamma_{wr} h^2 L_d}{2 \tan \alpha_2} + P' \cos \alpha_1\right) \tan \phi' \tag{4.23}$$

The compressive (C_{LC}') and shear (S_{LC}') forces acting along the two lateral walls in the central part of the upper portion are given by

$$S_{LC}' = C_{LC}' \tan \delta = \frac{K \gamma_{wr} h^2 L_{BT}}{2} \tan \delta \tag{4.24}$$

The lateral shear resistances acting on the upstream (S_{LU}') and downstream (S_{LD}') triangle portions of the upper portion can be expressed as follows:

$$S_{LU}' = C_{LU}' \tan \delta = K \gamma_{wr} \tan \delta \int_0^{\frac{h}{\tan \alpha_1}} \frac{h^2}{2} dx = \frac{K \gamma_{wr} h^3}{6 \tan \alpha_1} \tan \delta \tag{4.25}$$

$$S_{LD}' = C_{LD}' \tan \delta = K \gamma_{wr} \tan \delta \int_0^{\frac{h}{\tan \alpha_2}} \frac{h^2}{2} dx = \frac{K \gamma_{wr} h^3}{6 \tan \alpha_2} \tan \delta \tag{4.26}$$

The lateral shear resistance S_L' acting along one lateral wall in contact with the upper portion is given by

$$S_L' = S_{LC}' + S_{LU}' + S_{LD}' = \frac{K \gamma_{wr} h^2}{2} \left(L_{BT} + \frac{h}{3 \tan \alpha_1} + \frac{h}{3 \tan \alpha_2}\right) \tan \delta \tag{4.27}$$

Considering the limit equilibrium of the potentially unstable upper portion of the WRB along the drift axis direction leads to an expression for the *FS*:

$$FS = (S_B' + 2S_L')/(P' \sin \alpha_1) \tag{4.28}$$

Introducing Eqs. (4.22), (4.23) and (4.27) into Eq. (4.28) gives the required barricade top length L_{BT} expressed as Eq. (4.6).

4.11 Appendix III: Sample calculations

The application of the proposed solution is illustrated based on the following cases, using typical geometric and material parameters:

FS = 1.5, C_M = 1.5, H = 8 m, $L_d \times H_d$ = 5 m × 5 m, α_1 = 35°, α_2 = 50°, $\gamma_{wr} = \gamma_b$ = 20 kN/m^3, ϕ' = 37°, $K = K_a = (1-\sin\phi')/(1+\sin\phi') = 0.2486$.

The critical interface friction angle δ_c is calculated from (Eq. 4.9):

$$\delta_c = \tan^{-1}\frac{FS(2H-H_d)\tan\alpha_1}{H_d+2(H-H_d)\left[\frac{C_M\times FS\tan\alpha_1}{\tan\phi'}\left(1+K\frac{H_d}{L_d}\right)-K\frac{H_d}{L_d}\right]+\frac{\gamma_{wr}H_d}{\gamma_b}\left(1+K\frac{2H_d}{3L_d}\right)\left(1+\frac{\tan\alpha_1}{\tan\alpha_2}\right)}$$

$$= \tan^{-1}\frac{1.5(2\times8-5)\,tan\,35^\circ}{5+2(8-5)\left[\frac{1.5\times1.5\times tan\,35^\circ}{tan\,37^\circ}\left(1+0.2486\frac{5}{5}\right)-0.2486\frac{5}{5}\right]+\frac{20\times5}{20}\left(1+0.2486\frac{2\times5}{3\times5}\right)\left(1+\frac{tan\,35^\circ}{tan\,50^\circ}\right)} = 22^\circ$$

Case 1:

If the interface friction angle δ is 16° (< δ_c), the top length of barricade is given by [Eq. (4.10a)]:

$$L_{BT} = \frac{\gamma_b\left(H-\frac{H_d}{2}\right)\left(\frac{FS}{tan\,\delta}-\frac{1}{\tan\alpha_1}\right)-\gamma_{wr}H_d\left(\frac{1}{2}+K\frac{H_d}{3L_d}\right)\left(\frac{1}{tan\,\alpha_1}+\frac{1}{tan\,\alpha_2}\right)}{\gamma\left(1+K\frac{H_d}{L_d}\right)}$$

$$= \frac{20\left(8-\frac{5}{2}\right)\left(\frac{1.5}{tan\,16^\circ}-\frac{1}{tan\,35^\circ}\right)-20\times5\left(\frac{1}{2}+0.2486\times\frac{5}{3\times5}\right)\left(\frac{1}{tan\,35^\circ}+\frac{1}{tan\,50^\circ}\right)}{20\left(1+0.2486\times\frac{5}{5}\right)} = 11.46\,m$$

The volume of barricade is then given by (Eq. 4.4)

$$V = H_dL_d\left(L_{BT}+\frac{H_d}{2\,tan\,\alpha_1}+\frac{H_d}{2\,tan\,\alpha_2}\right) = 5\times5\left(11.46+\frac{5}{2\tan35^\circ}+\frac{5}{2\tan50^\circ}\right) = 428\,m^3$$

Case 2:

If the interface friction angle δ is 35° (> δ_c), the top length of barricade is given by [Eq. (4.10b)]:

$$L_{BT} = \frac{\gamma_b}{\gamma_{wr}}(H-H_d)\left(\frac{C_M\times FS}{\tan\phi'}-\frac{1}{\tan\alpha_1}\right)$$

$$= \frac{20}{20}(8-5)\left(\frac{1.5\times1.5}{\tan37^\circ}-\frac{1}{tan\,35^\circ}\right) = 4.67m$$

The volume of barricade is then given by (Eq. 4.4)

$$V = H_dL_d\left(L_{BT}+\frac{H_d}{2\,tan\,\alpha_1}+\frac{H_d}{2\,tan\,\alpha_2}\right) = 5\times5\left(4.67+\frac{5}{2\tan35^\circ}+\frac{5}{2\tan50^\circ}\right) = 258\,m^3$$

4.12 References

Aubertin, M. (2013). "Waste rock disposal to improve the geotechnical and geochemical stability of piles." *Proc., 23rd World Mining Congress*, CIM, Montreal, Canada.

Aubertin, M., Bussière, B., and Bernier, L. (2002). Environnement et gestion des rejets miniers (CD-ROM), Presses Internationales Polytechnique, Montréal (in French).

Aubertin, M., et al. (2003). "Interaction between backfill and rock mass in narrow stopes." *Proc., Soil and Rock America 2003*, P. J. Culligan, H. H. Einstein, and A. J. Whittle, eds., Vol. 1, Verlag Glückauf Essen (VGE), Essen, Germany, 1157-1164.

Belem, T., et al. (2015). "Comportement mécanique du remblai minier après sa mise en place dans le chantier: étude des interactions remblai-roche." *Presentation, Québec Mines 2015*, Quebec City, Canada (in French).

Benzaazoua, M., Bussière, B., Demers, I., Aubertin, M., Fried, É., and Blier, A. (2008). "Integrated mine tailings management by combining environmental desulphurization and cemented paste backfill: Application to mine Doyon." *Miner. Eng.*, 21(4), 330-340.

Bloss, M. L., and Chen, J. (1998). "Drainage research at Mount Isa Mines limited 1992-1997." *Proc., 6th Int. Symp. on Mining with Backfill*, M. Bloss, eds., Brisbane, Australia, 111-116.

Bussière, B. (2007). "Colloquium 2004: Hydro-geotechnical properties of hard rock tailings from metal mines and emerging geo-environmental disposal approaches". *Can. Geotech. J.*, 44, 1019-1052.

El Mkadmi, N., Aubertin, M., and Li, L. (2014). "Effect of drainage and sequential filling on the behavior of backfill in mine stopes." *Can. Geotech. J.*, 51(1), 1-15.

Fall, M., and Nasir, O. (2010). "Mechanical behaviour of the interface between cemented tailings backfill and retaining structures under shear loads." *Geotech. and Geol. Eng.*, 28(6), 779-790.

Grabinsky, M. W. (2010). "In situ monitoring for ground truthing paste backfill designs." *Proc., Paste 2010*, Toronto, Canada, 85-98.

Grice, A. G. (1998). "Stability of hydraulic backfill barricades." *Proc., 6th Int. Symp. on Mining with Backfill*, M. Bloss, eds., Brisbane, Australia, 117-120.

Grice, A. G. (2001). "Recent mine fill developments in Australia." *Proc., 7th Int. Symp. on Mining with Backfill*, Seattle, USA, 351-357.

Hambley, D. F. (2011). "Backfill mining." *SME Mining Engineering Handbook* (Vol. 1), Darling, P., Eds., SME, 1375-1384.

Hassani, F., and Archibald, J. (1998). *Mine backfill (CD-ROM)*, Canadian Institute of Mine, Metallurgy and Petroleum, Montréal.

Helinski, M., Fourie, A., and Fahey, M. (2006). "Mechanics of early age CPB." *Proc*., *Symp. conducted at the 9th Int. Seminar on Paste and Thickened Tailings*, R. Jewell, S. Lawson, and P. Newman, Eds., Australian Centre for Geomechanics, Limerick, Ireland, 313-322.

Hughes, P. B., Pakalnis, R., Hitch, M., and Corey, G. (2010). "Composite paste barricade performance at Goldcorp Inc. Red Lake Mine, Ontario, Canada". *Int. J. Min, Reclam., Environ.*, 24(2), 138-150.

Itasca. (2011). *FLAC-Fast lagrangian analysis of Continua; User's Guide*, Itasca Consulting Group. Minneapolis.

Kuganathan, K. (2001). "Mine backfilling, backfill drainage and bulkhead construction-a safety first approach." *Australia's Min. Monthly*, February, 58-64.

Kuganathan, K. (2002). "A model to predict bulkhead pressures for safe design of bulkheads." *Proc*., *Filling with Hydraulic Fills Seminar*. Section 6, Australian Centre for Geomechanics, Perth.

Li, L., Aubertin, M., Simon, R., Bussière, B., and Belem, T. (2003). "Modeling arching effects in narrow backfilled stopes with FLAC." *Proc*., *FLAC and Numerical Modeling in Geomech.*, Rotterdam, Netherlands, 211-219.

Li, L., Ouellet, S., and Aubertin, M. (2009). "A method to evaluate the size of backfilled stope barricades made of waste rock." *Proc*., *62nd Can. Geotech. Conf. and 10th Joint CGS/IAH-CNC Groundwater Specialty Conf.*, Halifax, Canada, 497-503.

Li, L., and Aubertin, M. (2009b). "A three-dimensional analysis of the total and effective stresses in submerged backfilled stopes." *Geotech. Geol. Eng.*, 27(4), 559-569.

Li, L., and Aubertin, M. (2009c). "Horizontal pressure on barricades for backfilled stopes. Part I: Fully drained conditions." *Can. Geotech. J.*, 46(1), 37-46.

Li, L., and Aubertin, M. (2009d). "Horizontal pressure on barricades for backfilled stopes. Part II: Submerged conditions." *Can. Geotech. J.*, 46(1), 47-56.

Li, L., and Aubertin, M. (2011). “Limit equilibrium analysis for the design of backfilled stope barricades made of waste rock.” *Can. Geotech. J.*, 48(11), 1713-1728.

Li, L. (2013). “A simple solution to assess pore-water pressure in barricades made of waste rock.” *CIM J.*, 4(1), 53-60.

Leps, T. M. (1970). “Review of Shearing Strength of Rockfill.” *J. Soil Mech. Fdns Div.*, ASCE, Vol. 96, No. SM4, 1159-1170.

McLemore, V. T., et al. (2009). “Literature review of other rock piles: characterization, weathering, and stability.” *New Mexico Bureau of Geol. and Miner. Resources*, Socorro, NM.

Mitchell, R., Smith, J., and Libby, D. (1975). “Bulkhead pressures due to cemented hydraulic mine backfills.” *Can. Geotech. J.*, 12(3), 362-371.

Pirapakaran, K., and Sivakugan, N. (2007). “Arching within hydraulic fill stopes.” *Geotech. Geol. Eng*., 25(1), 25-35.

Potvin, Y., Thomas, E., and Fourie, A. (2005). *Handbook on mine fill*, Australian Centre for Geomechanics, Perth.

Singh, K. H., and Hedley, D. G. F. (1980). “Review of fill mining technology in Canada.” *Proc*., *Conf. on the Application of Rock Mechanics to Cut and Fill Mining*, Lulea: Institution of Mining and Metallurgy, 1-3.

Sivakugan, N., Rankine, K., Lovisa, J., and Hall. W. (2013). “Flow rate computations in hydraulic fill mine stopes.” *Ind. Geotech. J.*, 43(3), 195-202.

Sivakugan, N. (2008). “Geotechnical issues of mining with hydraulic backfills.” *Elect. J. Geotech. Eng.*, Special Volume: Bouquet 08.

Sivakugan, N., Rankine, R. M., Rankine, K. J., and Rankine, K. S. (2006a). “Geotechnical considerations in mine backfilling in Australia.” *J. Cleaner Prod.*, 14(12-13), 1168-1175.

Sivakugan, N., Rankine, K. J., and Rankine, R. M. (2006b). “Permeability of hydraulic fills and barricade bricks.” *Geotech. Geol. Eng*., 24, 661-673.

Soderberg, R. L., and Busch, R. A. (1985). “Bulkheads and drains for high sandfill stopes.” US Department of the Interior, Bureau of Mines.

Thomas, E. G. (1979). *Fill technology in underground metalliferous mines*, International Academic Services Limited, Kingston, Canada.

Thompson, B. D., Grabinsky, M. W., Counter, D. B., and Bawden, W. F. (2009). "In-situ measurements of CPB in long-hole stopes." *Proc., 3rd CANUS Rock Mech. Symp.*, Toronto, M., Diederichs, and G., Grasselli., eds., 199.

Thompson, B. D., Bawden, W. F., Grabinsky, M. W., and Karaoglu, K. (2010). "Monitoring barricade performance in a CPB operation." *Proc., 13th Int. Seminar on Paste and Thickened Tailings*, Toronto, Australian Centre for Geomechanics, 85-98.

Thompson, B. D., M. W. Grabinsky, and W. F. Bawden. (2012). "In-situ measurements of CPB at the Cayeli Mine." *Can. Geotech. J.*, 49, 755-772.

Ting, C.H., Shukla, S.K., Sivakugan, N. (2011). "Arching in soils applied to inclined mine stopes." *Int. J. Geomech*., ASCE, 11(1), 29-35.

Ting, C. H., Sivakugan, N., and Kumar Shukla, S. (2012). "Laboratory simulation of the stresses within inclined stopes." *ASTM Geotech. Test. J.*, 35(2), 280-294.

Ting, C. H., Sivakugan, N., Read, W., and Shukla, S. K. (2014). "Analytical expression for vertical stress within an inclined mine stope with non-parallel walls." *Geotech. Geol. Eng*., 32(2), 577-586.

Williams, D. J. (2000). "Assessment of embankment parameters." *Proc., Slope Stability in Surface Mining*, SME. Denver, CO, 275-284.

Yang, P. Y., and Li, L. (2015). "Investigation of the short-term stress distribution in stopes and drifts backfilled with cemented paste backfill." *Int. J. Min. Sci. Technol.*, 25(5), 721-728.

Yang P. Y., Brochu-Baekelmans, M., Li, L., and Aubertin, M. (2014). "An improved solution for sizing barricades made of waste rock to retain cemented paste backfill." *Proc., 67th Can. Geotech. Conf.*, Regina, Canada.

Yumlu, M., and Guresci, M. (2007). "Paste backfill bulkhead monitoring-A case study from Inmet's Cayeli mine." *Proc., 9th Int. Symp. in Min. with Backfill* (CD-ROM), CIM, Montreal.

CHAPTER 5 ARTICLE 3: A NEW SOLUTION TO ASSESS THE REQUIRED STRENGTH OF MINE BACKFILL WITH A VERTICAL EXPOSURE

Pengyu Yang, Li Li, & Michel Aubertin

This article was submitted to ASCE - *International Journal of Geomechanics* in September 2016.

Abstract: Backfilling is commonly applied to allow pillar recovery in open stope mines. The backfill must then remain self-standing in the primary stope when mining an adjacent secondary stope. The design of exposed fill is often based on a solution proposed by Mitchell and co-workers over 30 years ago. Several modifications of this solution have later been reported. These solutions have been partly validated against a few physical model tests results and they have also been compared with numerical simulations. The analyses have shown that these solutions cannot completely capture the response of the exposed backfill, particularly when the required cohesion of the cemented backfill is relatively large. New simulations results presented here indicate that the sliding plane tends to change from planar at small fill cohesion to spoon-shaped (in 3D) at larger cohesion. In the former case, the failure mechanism is controlled by shear stress along the sliding plane near the base of the stope; this corresponds well to existing analytical models. In the latter case however, failure of the backfill is controlled by both shear (near the base) and tensile (near the top) stresses. This feature is not represented by existing analytical models. In this paper, a new analytical solution is proposed for assessing the stability of exposed cemented backfill with a vertical face. An instability criterion is also introduced for estimating the critical strength of side-exposed backfill. Additional numerical simulations are then conducted with FLAC^{3D} to validate the proposed analytical solution. The results show that the newly developed solution correlates well with the numerical simulations for representative stope geometry and backfill strength. This new solution is thus regarded as an improvement over existing solutions. Further calculations are made to illustrate the effect of key parameters on the stability of side-exposed fill. A discussion follows on the limitations and effect of various influence factors on the design of exposed cemented backfill.

Keywords: Mine stopes; Exposed cemented backfill; Mitchell solution; Stability; Analytical solutions; FLAC^{3D}.

5.1 Introduction

Stope filling is commonly used in underground mines to recover ore pillars with open stoping methods, such as sublevel or longhole stoping, and vertical crater retreat. These can create large-size exposed faces of (unsupported) backfill during pillar removal (e.g., Jones 1972; Libby & Smith 1975; Cundall et al. 1978; Leahy & Cowling 1978; Coulthard & Dight 1980; Barrett & Cowling 1980; Pierce 2001; Sainsbury & Urie 2007; Emad et al. 2012, 2014, 2015b).

It is customary to divide stopes into primary and secondary stopes to create ore pillars. The primary stope is first mined and then filled with cemented fill. During the recovery of a secondary stope, the cemented fill in the primary stope acts as an artificial (rib) pillar that must remain self-standing. Failure of the cemented fill may cause ore dilution, damage equipment or even render the pillar extraction impossible (e.g., Coulthard & Dight 1980). Hence, the stability of the exposed backfill face is critical and its minimum required strength must be correctly determined.

In practice, the exposed backfill is usually designed to support the pressure due to its self-weight (Askew et al. 1978; Mitchell et al. 1982). The cemented fill is then considered as a freestanding vertical prism (1D model) and its required unconfined compressive strength (UCS) must exceed the corresponding vertical stress $\sigma_v = \gamma h$ (γ is the unit weight of the fill; h is the depth from the fill top). This approach suggests a variable fill strength that is linearly proportional to the depth (e.g., Coulthard & Dight 1980). Another design method considers the cemented fill with an open face as a 2D (plane strain) slope with an inclination angle of 90° and a linear sliding plane (e.g., Libby & Smith 1975; Askew et al. 1978; Dight & Coulthard 1980). When the backfill is taken as frictionless, i.e., $\phi = 0$ with UCS = $2c$ (c is the fill cohesion), a limit equilibrium analysis of a 2D wedge leads to the following requirement: UCS $\geq \gamma H/2$ (H is the fill height; Askew et al. 1978; Mitchell et al. 1982).

Typical UCS values of cemented fill vary almost linearly with cement content over the typical range of 3-8% (dry weight; Mitchell et al. 1982).

In practice, both methods mentioned above lead to similar overall binder usage (e.g., Mitchell et al. 1982).

With these two approaches however, the lateral confinement along the remaining sidewalls of the stope is neglected. These traditional approaches are thus deemed overly conservative and may lead to excessive use of binder. This shortcoming has been partly overcome later by the solution proposed by Mitchell et al. (1982). The extensive application of the Mitchell et al. (1982) solution (summarized below) in the industry has led to a significant reduction in cement consumption.

A similar, but a somewhat more elaborate, solution has been proposed by Dight & Coulthard (1980) with the additional consideration of a tension crack, closure pressure and surcharge; its use is however limited due in part to the lack of clear definitions for some key parameters.

Later, the Mitchell et al. (1982) solution has been extended to estimate the critical maximum backfilled stope height with a surcharge (Zou & Nadarajah 2006) and to inclined stopes without any normal stresses along the hanging wall (Dirige et al. 2009). Modifications have also been made by the authors (Li & Aubertin 2012, 2014; Li 2014a) based on assessment of experimental tests and numerical modelling; these latter solutions have been partly validated against Mitchell et al.'s (limited) physical model tests.

Simplified 2D and 3D numerical analyses were also conducted using the finite element method (FEM) to evaluate the stability of side-exposed backfill (e.g., Cowling & Gonano 1976; Barrett et al. 1978; Coulthard & Dight 1980). A few numerical simulations have been performed under 3D conditions using the finite difference code FLAC^{3D} (e.g., Cundall et al. 1978; Pierce 1997, 2001; Coulthard 1999; Li & Aubertin 2014).

Recently, Falaknaz and coworkers (Falaknaz 2014; Falaknaz et al. 2015d; Falaknaz et al. 2016) have performed a series of simulations to analyze the stress state within cemented backfill upon vertical exposure using FLAC^{3D}. Some of the assumptions adopted by Li & Aubertin (2012, 2014) and Li (2014a), in terms of stresses along the back and side walls, have been confirmed by these calculations. However, the comparisons between the numerical results and analytical solutions of Mitchell et al. (1982) and Li & Aubertin (2012, 2014) have indicated that the effect of stope geometry on the required strength (i.e., required cohesion due to cementation) is not always well captured by these solutions. An improved solution is thus needed.

In the following, existing analytical solutions developed to assess the stability of side-exposed mine backfill are first briefly recalled. Results from numerical simulations conducted with

FLAC^{3D} are used to assess the stability of exposed backfill based on a more objective instability (failure) criterion. An improved solution is then proposed for estimating the required strength of side-exposed cemented fill, based on these numerical results and a failure mechanism observed in laboratory tests. The solution is further validated using additional numerical calculations. The effect of key influence factors on the response of exposed backfill are further illustrated and discussed.

5.2 Existing analytical solutions

5.2.1 Mitchell et al. (1982) solution

Mitchell et al. (1982) considered the 3D geometry of a cemented fill block with an open face (front face), as shown in Fig. 5-1. On this figure, L (m), B (m) and H (m) are the backfill length, width and height, respectively. A sliding plane inclined at an angle α (= 45°+ ϕ/2 to the horizontal) is assumed. In this model, the available shear strength along the sidewalls is due only to the bond cohesion c_s (assumed equal to the fill cohesion c). The strength mobilized along the back wall is neglected. These assumptions lead to the following expressions for the factor of safety (FS) of the sliding wedge and the required backfill cohesion c:

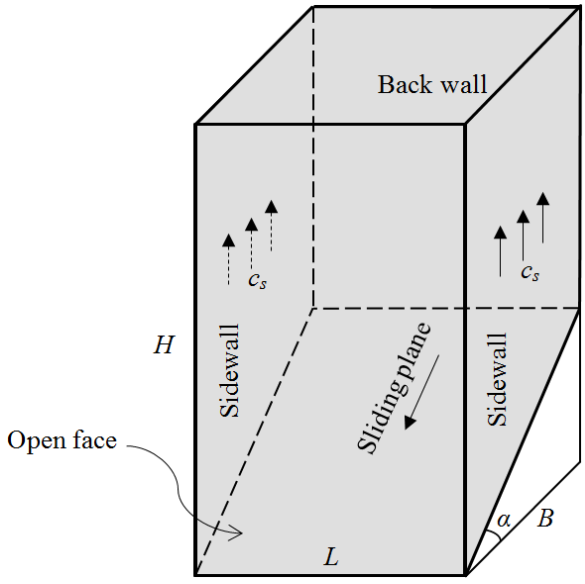

Figure 5-1: Sliding wedge model of the Mitchell et al. solution (adapted from Mitchell et al. 1982)

$$FS = \frac{\tan\phi}{\tan\alpha} + \frac{2cL}{H^*(\gamma L - 2c_s)\sin 2\alpha} \quad (5.1a)$$

$$c = \frac{\gamma H}{2(H/L + \tan\alpha)}, \text{ for FS = 1, } c = c_s \text{ and } H >> B \text{ thus } H^* \approx H \quad (5.1b)$$

where ϕ (= ϕ', °) is the internal friction angle of the fill; c (= c', kPa) is the backfill cohesion; γ (kN/m^3) is the fill unit weight; H^* (= $H - B\tan\alpha/2$, m) is the equivalent height of the wedge.

This solution applies to stopes with a high aspect ratio (HAR, $H/B \geq \tan\alpha$). Its characteristics have been reviewed and discussed by Li & Aubertin (2012, 2014) and Li (2014a), who then proposed the following modifications.

5.2.2 Modified Mitchell (MM) solution

Li & Aubertin (2012) modified the original Mitchell et al. (1982) solution by considering different stope aspect ratios, a smaller bond cohesion along the sidewalls, and the addition of a surcharge p_0 (kPa). Such surcharge may be applied on the fill surface by equipment or due to desiccated (shrinking) backfill that has lost its contact with the walls. Similarly to the original model, the mobilized strength along the back wall and the frictional strength along the sidewalls are neglected. For a HAR stope, the sliding plan is limited within the fill body. This leads to the following MM solution:

$$FS = \frac{\tan\phi'}{\tan\alpha} + \frac{2c}{[p_0 + H^*(\gamma - 2c_s/L)]\sin 2\alpha} \quad (5.2a)$$

$$c = \frac{p_0 + \gamma H^*}{\frac{2}{(FS - \tan\phi'/\tan\alpha)\sin 2\alpha} + \frac{2r_s H^*}{L}} \quad (5.2b)$$

where r_s (= c_s/c; from 0 to 1 where c_s is the fill-sidewall interface cohesion) is the adherence ratio along the sidewalls.

For backfilled stopes with a low aspect ratio (LAR, $H/B < \tan\alpha$), the potential sliding plan intersects the backfill top. The FS and the required backfill cohesion are then given by

$$FS = \frac{\tan\phi'}{\tan\alpha} + \frac{2c}{[p_0 + H(\gamma/2 - c_s/L)]\sin 2\alpha} \quad (5.3a)$$

$$c = \frac{p_0 + \gamma H/2}{\dfrac{2}{(FS - \tan\phi'/\tan\alpha)\sin 2\alpha} + \dfrac{r_s H}{L}} \tag{5.3b}$$

In the presence of a tension crack, Li & Aubertin (2012) assumed that its depth H_t (m) can be defined by the following expression, based on Rankine's active earth pressure theory (e.g., McCarthy 2002; Duncan & Wright 2005):

$$H_t = \frac{2c}{\gamma \tan(45° - \phi'/2)} \tag{5.4}$$

The equivalent width of the sliding wedge B_t is then given by

$$B_t = (H - H_t)/\tan\alpha \tag{5.5}$$

The stability of an exposed backfill face or the required cohesion can then be evaluated by replacing B in Eq. (5.2) with the equivalent wedge width B_t.

The MM solution gives better agreement with the experimental results reported by Mitchell et al. (1982) than the original Mitchell solution. However, the MM solution inherits many of the same limitations as the Mitchell et al. (1982) solution due to very similar assumptions.

5.2.3 Li (2014a) solution

Li (2014a) extended the MM solution by considering the frictional strength along the sidewalls and the bond cohesion along the back wall c_b, leading to a generalized Mitchell et al. solution. For HAR stopes, the FS and the required fill cohesion can then be expressed as follows:

$$FS = \frac{\tan\phi'}{\tan\alpha} + \frac{2}{\sin 2\alpha}\left(\frac{p'}{c} - r_b\frac{H - B\tan\alpha}{B} - 2r_s\frac{H^*}{L}\right)^{-1} \tag{5.6a}$$

$$c = p'\left[\frac{2}{(FS - \tan\phi'/\tan\alpha)\sin 2\alpha} + r_b\frac{H - B\tan\alpha}{B} + 2r_s\frac{H^*}{L}\right]^{-1} \tag{5.6b}$$

with

$$p' = \frac{L}{2K\tan\delta}\left\{\gamma - \frac{1}{B\tan\alpha}\left(\frac{\gamma L}{2K\tan\delta} - p_0\right)\times\left[\exp\left(-\frac{2K\tan\delta}{L}(H - B\tan\alpha)\right) - \exp\left(-\frac{2K\tan\delta}{L}H\right)\right]\right\} \tag{5.7}$$

where r_b (= c_b/c; from 0 to 1) is the adherence ratio along the back wall; the earth pressure coefficient K along the sidewalls is taken as Rankine's active pressure coefficient K_a (see below); the friction angle along the sidewalls δ (°) can range from zero to ϕ'.

For LAR stopes, the Li (2014a) solution is written as:

$$FS = \frac{\tan\phi'}{\tan\alpha} + \frac{2}{\sin 2\alpha}\left(\frac{p''}{c} - r_s\frac{H}{L}\right)^{-1} \tag{5.8a}$$

$$c = p''\left[\frac{2}{(FS - \tan\phi'/\tan\alpha)\sin 2\alpha} + r_s\frac{H}{L}\right]^{-1} \tag{5.8b}$$

$$\text{with } p'' = \frac{L}{2K\tan\delta}\left\{\gamma - \frac{1}{H}\left(\frac{\gamma L}{2K\tan\delta} - p_0\right)\times\left[1 - \exp\left(-\frac{2K\tan\delta}{L}H\right)\right]\right\} \tag{5.9}$$

Eqs. (5.4) and (5.5) are used in the presence of a tension crack. The Li (2014a) solution was shown to better represent the experimental results reported by Mitchell et al. (1982), compared to the original Mitchell et al. and MM solutions.

5.2.4 Li & Aubertin (2014) solution

Preliminary numerical simulations have been presented by Li & Aubertin (2014) using FLAC^{3D} to investigate the behavior of side-exposed cemented fill. These results indicated that the shear resistance along sidewalls for the lower block acts in a direction parallel to the sliding plane. To account for this, the wedge block (Fig. 5-1) is divided into an upper rectangular block and a lower triangular wedge. The bond cohesion along the back wall was also considered. A modified solution was proposed in terms of FS and required backfill cohesion c for HAR stopes:

$$FS = \frac{\tan\phi'}{\tan\alpha} + \frac{c\left(\frac{1}{\cos\alpha} + r_s\frac{H'}{L}\right) + \frac{(\gamma/M - p_1)[(1-\exp(-MH'))/MH' - 1] + \gamma H'/2}{1 + L/B}}{(p_1 + \gamma H'/2)\sin\alpha} \tag{5.10a}$$

$$c = \frac{D'(p_0 + \gamma(H - H') - G') + \frac{\gamma A'H'}{2}\left(1 + \frac{L}{B}\right)\sin\alpha - \gamma\left(\frac{C'}{M} + \frac{H'}{2}\right)}{B'\left(1 + \frac{L}{B}\right) + D'(H - H')\left(\frac{2r_s}{L} + \frac{r_b}{B}\right)}, \text{ for FS= 1} \tag{5.10b}$$

$$\text{with } H' = B\tan\alpha \quad M = 2K\left(B^{-1} + L^{-1}\right)\tan\delta \tag{5.11}$$

$$p_1 = p_0 + (H - H')\left[\gamma - c\left(\frac{2r_s}{L} + \frac{r_b}{B}\right)\right] \quad (5.12)$$

$$G' = \frac{1}{1 + L/B}\left\{\gamma(H - H') + \left(p_0 - \frac{\gamma}{M}\right)\left[1 - \exp\left(-(H - H')M\right)\right]\right\} \quad (5.13)$$

$$A' = FS - \frac{\tan\phi'}{\tan\alpha} \quad B' = \frac{1}{\cos\alpha} + r_s\frac{H'}{L} \quad C' = \frac{1 - \exp(-MH')}{MH'} - 1 \quad D' = A'\left(1 + \frac{L}{B}\right)\sin\alpha + C' \quad (5.14)$$

This solution was shown to better represent the Mitchell et al. (1982) experimental results compared to the original Mitchell solution. This solution and the Li (2014a) solution may overcome some limitations of the original Mitchell et al. and MM solutions by considering more realistic interactions between the fill and rockwalls. The normal stresses along the sidewalls are estimated from the arching solutions (e.g., Aubertin et al. 2003; Li et al. 2003, 2005) developed for confined backfilled in stopes (without exposure). The effect of wall removal on the stress state is thus neglected. The earth pressure coefficient K is taken as Rankine's active pressure coefficient K_a (as is the case for an exposed vertical face of cohesive soil; e.g., Bowles 1984).

These solutions are assessed below using simulations results.

5.3 Numerical simulations

5.3.1 Model configuration

The stability of side-exposed fill is investigated using numerical simulations conducted with the finite difference code FLAC^{3D} (Itasca 2013). Previous investigations have shown that this code (in 2D and 3D) can be used to analyze the stress state in backfilled stopes, with and without an exposed face (Li et al. 2003; Li & Aubertin 2009e, 2014; Falaknaz et al. 2015a, 2015b, 2015c, 2016; Liu et al. 2016c). Fig. 5-2 shows the reference model built with FLAC^{3D} to evaluate the response of a side-exposed cemented fill in a primary stope.

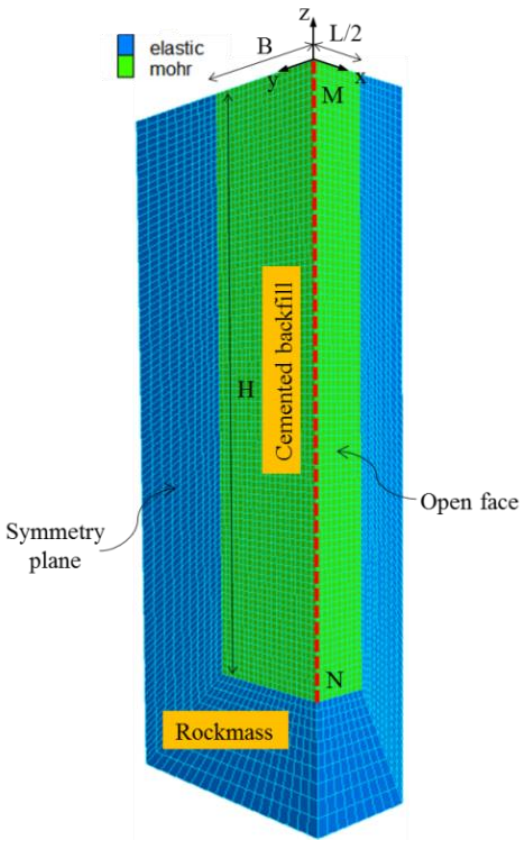

Figure 5-2: The FLAC^{3D} model of exposed backfill in a primary stope; the open face, symmetry plane and discretization are shown

The rock mass is linearly elastic with a unit weight γ_r of 27 kN/m^3, a Young's modulus E_r of 30 GPa and a Poisson's ratio v_r of 0.3. The cemented fill is modeled as an elastoplastic material obeying the Mohr-Coulomb criterion with a tension cut-off. The fill is characterized by a dry unit weight γ of 18 kN/m^3, a dilation angle ψ of 0° (non-associated flow rule) and Young's modulus E of 300 MPa. The values of effective friction angle of fill ϕ' and Poisson's ratio v are related through the following correlation: $v = (1 - \lambda\sin\phi')/(2 - \sin\phi')$ with $\lambda = 1$, based on a unique (consistent) earth pressure coefficient at-rest K_0 (Yang et al. 2016d; see also Eq. (A.9) in Appendix A).

The tensile strength (T_0) of cemented backfill is relatively small in practice. The tensile strength cutoff by default is zero in FLAC^{3D}. This tension cutoff ($T_0 = 0$) is first used to represent the most conservative case. A less conservative and more realistic case considered here is a tension cutoff equals to one tenth of the unconfined compression strength (UCS) (i.e., T_0 = UCS/10; e.g., Mitchell & Wong 1982; Sainsbury & Urie 2007). This value is used in the numerical simulations

performed in this study. It is however only valid for a specific value of ϕ' (around 55°) based on the Mohr-Coulomb criterion; this aspect is further discussed below.

The plane of symmetry $x = 0$ is used in the numerical models (Fig. 5-2). The displacements are free in the y and z directions on this plane, but these are restricted in the x direction. Displacements are restricted in all directions along the outer boundaries of the model, except for the top surface. The cemented fill is represented by quadrilateral elements of 0.5×0.5 m based on the sensitivity analysis of meshes, while the rockmass is modeled by coarser (radial) elements (Fig. 5-2; see details in the sensitivity analysis presented in Appendix F).

There is no interface element between the fill and rockmass; yielding then occurs in the backfill near the irregular (rough) rock surface produced by blasting (Li et al. 2003; Li & Aubertin 2009e; Liu et al. 2016a, 2016b).

The stability analysis of the side-exposed backfill involves two stages: (1) simulating the initial stress state within the backfilled stope and (2) creating the vertical exposure. The stope is first excavated at one step for stage (1). It is then sequentially filled (5 m/layer) after resetting displacements induced by the excavation to zero. The vertical exposure is simulated by freeing the boundary along the open face of the backfill in one step for stage (2). The calculations run until equilibrium or failure occurs. Equilibrium is monitored using the unbalanced forces, displacements and stresses, while failure is evaluated by an instability criterion. The novel instability criterion used here is presented below. These analyses are made using the small strain option of FLAC, which is deemed appropriate to assess the initiation of failure.

5.3.2 Instability criterion for exposed backfill

The distributions of displacements and stresses, yielding (plastic or tensile) state, and shear strength ratio (equivalent to a FS) can be monitored in numerical simulations results. The extent of yielding is commonly used to identify the failure of the exposed backfill (e.g., Barrett et al. 1978; Cundall et al. 1978; Barrett & Cowling 1980; Coulthard 1980; Coulthard & Dight 1980; Sainsbury & Urie 2007; Liu et al. 2016c). Failure can also be evaluated by the yield state, displacement and development of tensile stress (e.g., Pierce 1997, 2001; Coulthard 1999; Emad et al. 2012, 2014; Dirige & De Souza 2013; Karim et al. 2013; Li & Aubertin 2014).) The displacements and shear strength ratio were used by Falaknaz (2014) (also Falaknaz et al. 2016).

In general, these approaches have shown that, in most cases, the stability (or failure) of the exposed backfill can be judged without any ambiguity. In some cases however, this may become more difficult and somewhat subjective. To reduce this subjectivity, an instability criterion is established here based on the monitored total displacement along the vertical centerline of the open face (dotted line MN in Fig. 5-2). This approach is inspired by the instability criterion developed for barricades made of waste rock (Yang et al. 2016a).

Fig. 5-3 shows a typical variation of the total displacement profiles along stope height (line MN), obtained with FLAC^{3D} when the fill cohesion c decreases from 30 to 24 kPa. The maximum total displacement along the monitoring line MN increases slightly, from 3.7 mm to 12.6 mm, as the fill cohesion is reduced from 30 to 25 kPa. These minor displacements along a 45 m high fill body reflect a stable state. Fig. 5-3 also shows that when the exposed fill cohesion goes from 25 to 24 kPa, the maximum total displacement rises dramatically, to about 1 m. This marks the transition from a stable to an unstable state for the fill. Such transition is confirmed by the displacement isocontours along the vertical plane of symmetry in the backfill shown in Fig. 5-4. The large surge of the displacement along the stope height with a slight reduction in the fill cohesion is considered here as an indicator of instability of the exposed cemented backfill. Such behavior has been observed with various simulations conducted under different conditions (see more results presented in Appendix F).

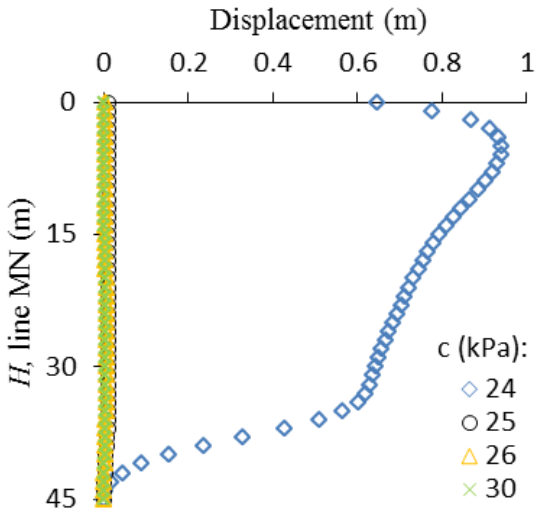

Figure 5-3: Displacement profiles along the stope height (line MN in Fig. 5-2) for different values of fill cohesion c; simulations conducted with H = 45 m, B = 6 m, L = 9 m, ϕ' = 35°, ν = 0.3, γ = 18 kN/m^3 and E = 300 MPa

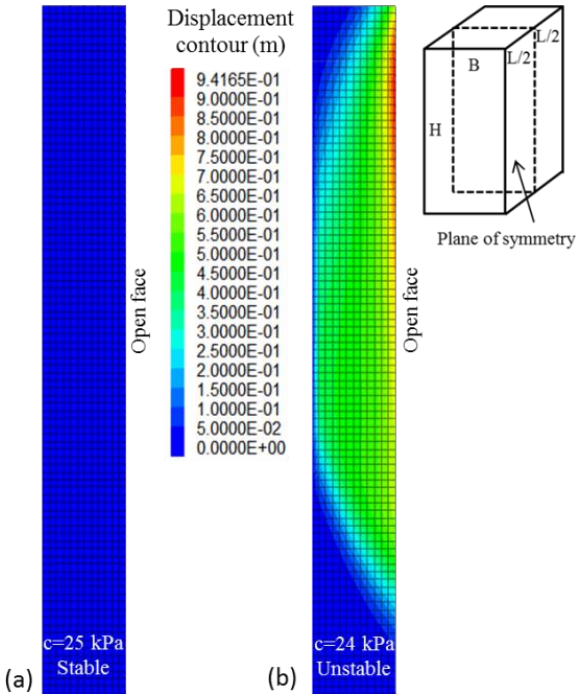

Figure 5-4: Displacements isocontours of the exposed backfill along the vertical plane of symmetry for cohesion c equals to (a) 25 kPa and (b) 24 kPa; simulations conducted with H = 45 m, B = 6 m, L = 9 m, ϕ' = 35°, ν = 0.3, γ = 18 kN/m^3 and E = 300 MPa

5.3.3 Failure mechanism

Analytical solutions were generally developed by considering shearing (slip) of a wedge block along a planar sliding plane as the main failure mechanism (e.g., Mitchell et al. 1982; Li & Aubertin 2012, 2014; Li 2014a, 2014b). This type of failure mechanism was observed during the physical model tests performed by Mitchell et al. (1982) and reproduced by numerical simulations (Liu et al. 2016c). It was noted however that such a failure mode tends to occur when the fill cohesion is relatively low.

Numerical simulations conducted by Bloss et al. (1993) and Coulthard (1999) indicated that failure by shear can develop through the fill body and by tension near the fill top and open face. When the stope geometry requires a large cohesion, Li & Aubertin (2014) and Falaknaz et al. (2016) have shown that the instability is no longer controlled by a sliding wedge block. Instead, the failure surface becomes somewhat spoon-shaped, with tensile stresses near the upper portion of the block. This is further confirmed by the results shown in Fig. 5-4b. Additional numerical results in Fig. 5-5 show the displacement isocontours along the vertical plane of symmetry of the

exposed fill reaches a critical (failure) state when the stope width *B* changes from 10 m to 25 m. These results indicate that the required cohesion is independent of the stope width *B*, due to the tensile stresses near the top of the fill. A new analytical solution is thus needed to take these observations into account.

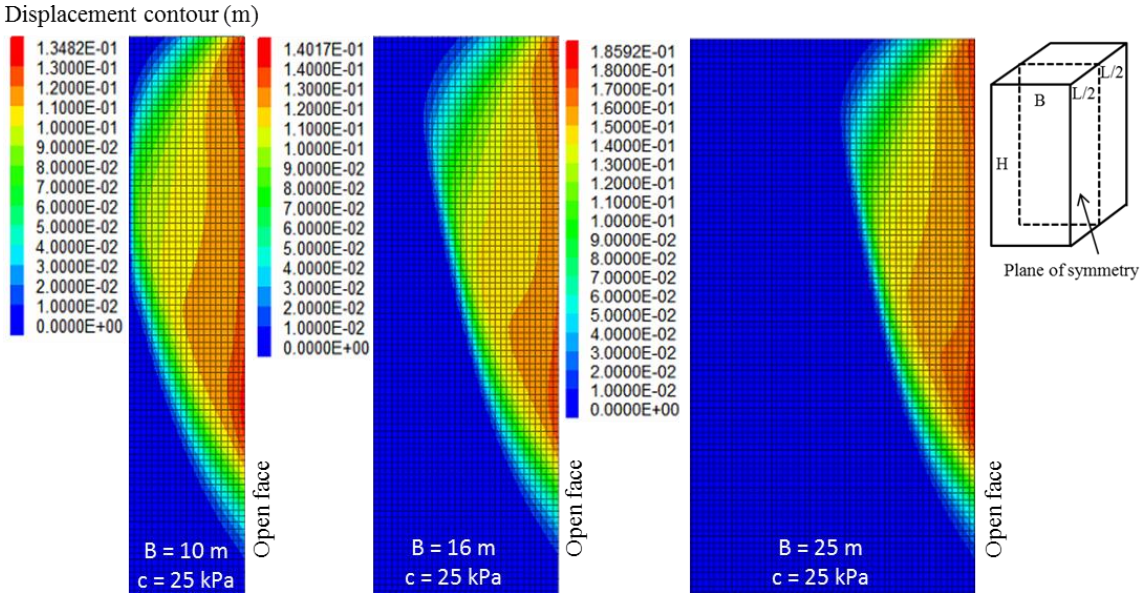

Figure 5-5: Displacements isocontours of the exposed backfill along the vertical plane of symmetry at a critical state when the stope width *B* changes from 10 to 25 m; simulations conducted with H = 45 m, L = 9 m, ϕ' = 35°, ν = 0.3, γ = 18 kN/m^3 and E = 300 MPa

5.4 Proposed solution

Numerical simulations conducted here (and by others) have shown that the shear sliding (failure) surface in backfilled stopes rarely extend to the back wall (unless the stope is very high and narrow) and to the fill top (even for a very low and wide stope) (e.g., Dight & Coulthard 1980; Coulthard 1999; Dirige & De Souza 2013; Emad et al. 2012, 2014; Falaknaz 2014; Falaknaz et al. 2016). These also show that there is a build-up of tensile stress near the top of the exposed backfill. Centrifuge tests results reported by Dirige & De Souza (2000, 2013) also indicate that the failure of side-exposed cemented paste backfill (CPB) involves a tension crack reaching the fill top surface. A curved sliding plane also develops upwards to meet this tension crack. Similar failure modes have been reported following centrifuge tests performed on cemented hydraulic fill (e.g., Smith et al. 1983; Mitchell 1986) and field observations/measurements (e.g., Cowling & Gonano 1976; Coulthard & Dight 1980).

Fig. 5-6 depicts the proposed model which includes a sliding wedge and a vertical potential tension crack originating from the top. On this figure, p_0 (kPa) is the surcharge exerted on the fill top; H_t (m) is the depth of the potential tension crack and B_t (m) is the equivalent width of the sliding wedge [estimated from Eqs. (5.4) and (5.5)]. The sliding plane makes an angle α (= 45° + $\phi'/2$) to the horizontal; W is the weight of the sliding wedge; S_s is the shear forces acting along the sidewalls; S_t is the shear force (due to fill cohesion only) acting along the potential tension crack (disccused below). The frictional strength (normal stress) mobilized along the potential tension crack is neglected.

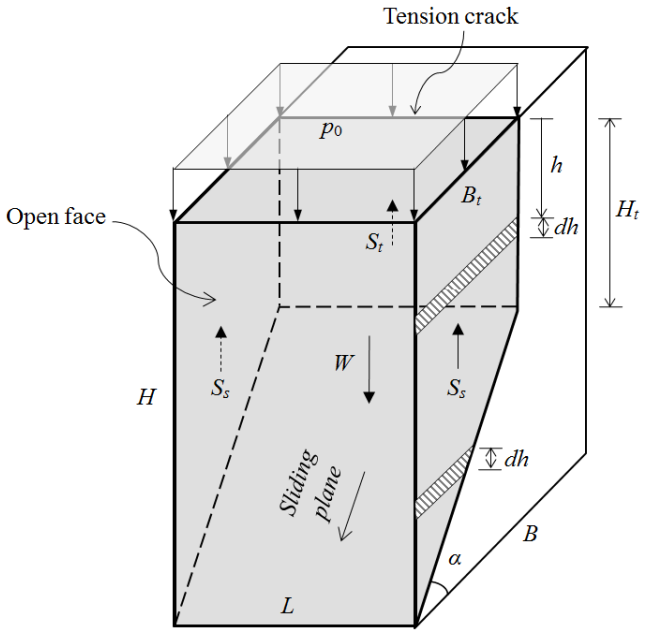

Figure 5-6: The modified wedge model with a vertical potential tension crack showing various acting forces (adapted from Li 2014a)

Based on the limit equilibrium analysis of the sliding wedge (with the detailed formulation presented in Section 5.7 of this chapter), one can obtain the following expressions for the factor of safety FS and required backfill cohesion c:

$$FS = \frac{\tan\phi'}{\tan\alpha} + \frac{2}{\sin 2\alpha}\left(\frac{p}{c} - \frac{H_t}{B_t} - r_s\frac{2H - B_t\tan\alpha}{L}\right)^{-1} \tag{5.15a}$$

$$c = p\left[\frac{2}{(FS - \tan\phi'/\tan\alpha)\sin 2\alpha} + \frac{H_t}{B_t} + r_s\frac{2H - B_t\tan\alpha}{L}\right]^{-1} \tag{5.15b}$$

with

$$p = \frac{L}{2K\tan\delta}\left\{\gamma - \frac{1}{B_t\tan\alpha}\left(\frac{\gamma L}{2K\tan\delta} - p_0\right)\times\left[\exp\left(-\frac{2K\tan\delta}{L}H_t\right) - \exp\left(-\frac{2K\tan\delta}{L}H\right)\right]\right\} \quad (5.16)$$

where H_t and B_t are obtained with Eqs. (5.4) and (5.5), respectively; K is taken as Rankine's active pressure coefficient K_a, as used by Li (2014a) and Li & Aubertin (2014); the other parameters have been defined previously.

5.4.1 Comparison between numerical simulations and analytical solution

Results obtained with the analytical solution given by Eq. (5.15) are compared with simulations results. The elasto-plastic constitutive law with a tension cutoff of zero and UCS/10 is used. The critical backfill cohesion is determined using the instability criterion defined above. Fig. 5-7 shows the required (critical) backfill cohesion c, obtained from the proposed solution and simulations results, as a function of stope geometry. Four other analytical solutions (Mitchell et al. 1982; Li & Aubertin 2012, 2014; Li 2014a) are also plotted for comparison. The stope geometry and material properties are defined in the caption of figures.

The numerical results indicate that the required values of c increase with an increase in stope length L (Fig. 5-7c), and to a much lesser extent with stope height H (Fig. 5-7a). The results are almost insensitive to the stope width B for the case analyzed here (Fig. 5-7b). These observations are very similar to those from the simulations presented by Falaknaz (2014) (also Falaknaz et al. 2016).

For the cases considered here, Figs. 5-7a and 5-7b show that the values of the required cohesion c obtained from numerical simulations are almost the same for a zero tension cutoff and a non-zero tension cutoff (T_0 = UCS/10) when the stope width (B) is between 6 and 25 m and the height (H) varies between 20 and 80 m. Similar results can be observed on Fig. 5-7c for a stope length smaller than 30 m. Significant differences can nevertheless be observed between the required c obtained by the two values of T_0 when the stope is longer than 30 m.

In all cases, results shown in Fig. 5-7 indicate that Eqs. (5.1b) and (5.2b) significantly overestimate the required backfill strength, compared to the results obtained from other (numerical and analytical) approaches.

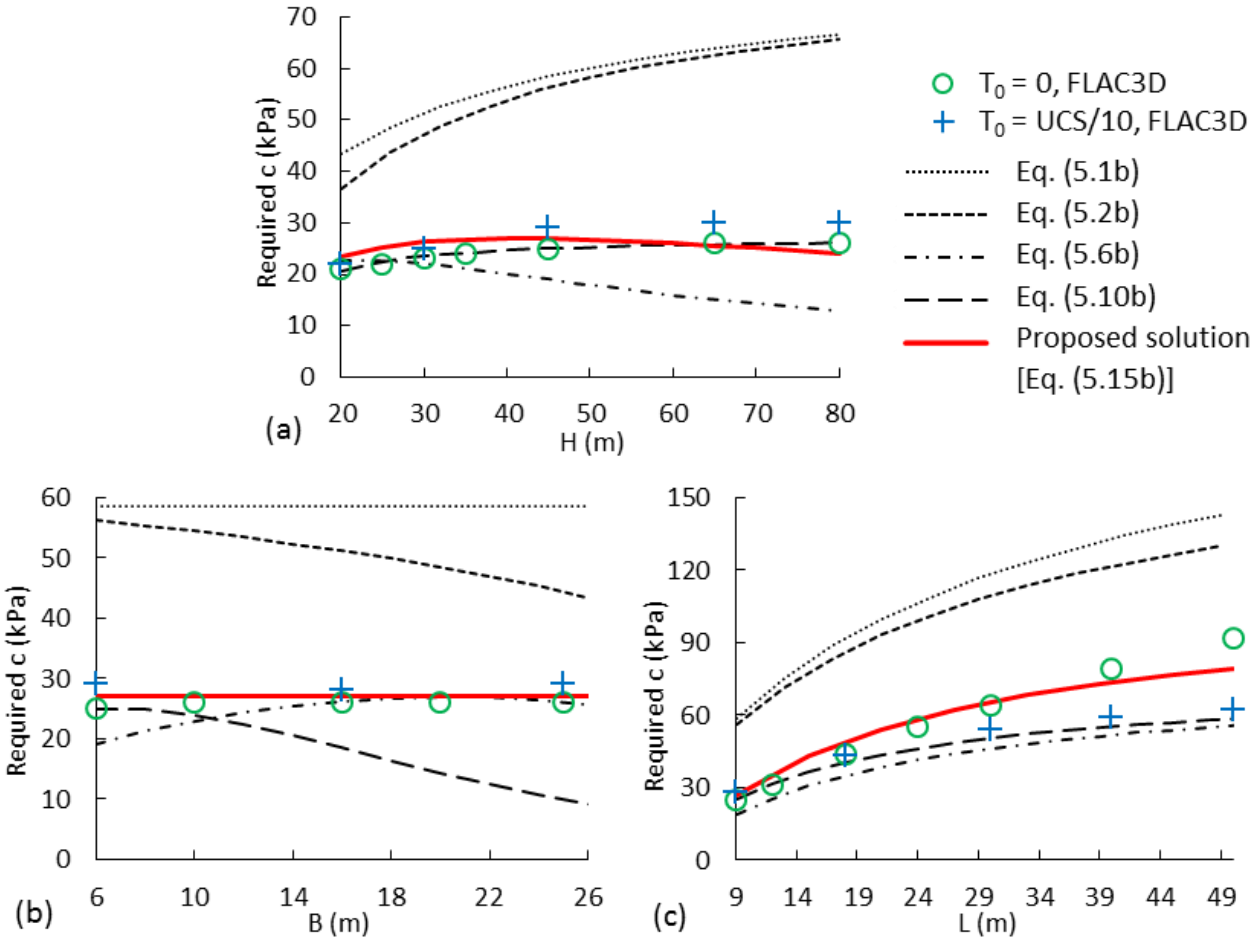

Figure 5-7: Required fill cohesion c obtained from Eq. (5.15b) and four other analytical solutions, and numerical simulations, for different values of stope (a) height H (L = 9 m, B = 6 m), (b) width B (H = 45 m, L = 9 m), and (c) length L (H = 45 m, B = 6 m). Calculations done with Eq. (5.15b) for FS = 1, p_0 = 0, $\phi' = \delta$ = 35°, r_s = 1, γ = 18 kN/m^3; simulations made with ϕ' = 35°, ν = 0.3, γ = 18 kN/m^3, E = 300 MPa, T_0 = 0 and UCS/10

Fig. 5-7a shows that Eq. (5.10b) agrees well with the simulations results, especially for the zero tension cutoff, while Eq. (5.6b) predicts a different tendency, with a decrease in required c with increased exposure height H. As H increases, the required c values predicted by the solution [Eq. (5.15b)] proposed here slightly increase for $H \leq 45$ m and then slightly decrease for $H > 45$ m. Nonetheless, the proposed solution [Eq. (5.15b)] correlates fairly well with the simulations results for both values of tension cutoff, for an exposed height from 20 m to 80 m.

Fig. 5-7b illustrates that, as the stope width B increases, Eq. (5.6b) predicts an initial increase in required c followed by a slight decrease, while the simulated results give constant c value. Eq.

(5.10b) predicts a decrease of c with an increase in B. The proposed solution [Eq. (5.15b)] is seen again to correlate quite well with the numerical results for both values of the tension cutoff.

Fig. 5-7c indicates that Eqs. (5.6b) and (5.10b) lead to good correlations with the numerical results for nonzero tension cutoff with different stope length L; it is not as good for the zero tension cutoff. The proposed solution [Eq. (5.15b)] is able to capture quite well the results obtained by the numerical simulations for both values of T_0.

Additional numerical calculations were performed to further evaluate the proposed solution [Eq. (5.15b)]. Fig. 5-8 shows the comparison of the required backfill strength c obtained from the proposed solution and the simulation results, for different values of backfill internal friction angle ϕ' (and angle along the walls δ). The numerical simulations were conducted with a tension cutoff $T_0 = 0$ and UCS/10. In the simulations, the value of angle ϕ' is related to Poisson's ratio v by the relationship defined above. The minimum value (lower bound) of angle ϕ' is taken as 1° (related $v = 0.496$) because the use of $\phi' = 0$ (and $v = 0.5$) is prohibited in FLAC.

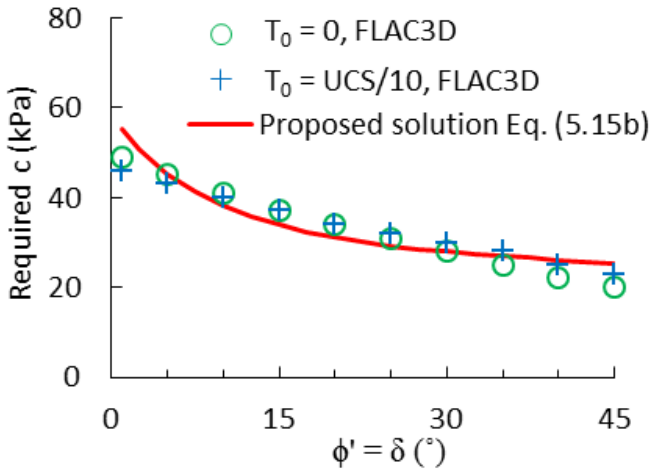

Figure 5-8: Required fill cohesion c obtained from Eq. (5.15b) and from numerical simulations (obtained with a tension cutoff T_0 of zero and UCS/10), for different values of friction angle ϕ'. Calculations made with Eq. (5.15b) for FS = 1, H = 45 m, B = 6 m, L = 9 m, $p_0 = 0$, $\delta = \phi'$, $r_s = 1$, γ = 18 kN/m^3; simulations made with E = 300 MPa and the same backfill unit weight and stope geometry

Fig. 5-8 illustrates that the simulations give a reduction in required c as the ϕ' value increases. Such a decline becomes somewhat less pronounced with the proposed analytical solution for the

typical range of backfill friction angle ϕ' (30° to 40°). Nevertheless, the proposed analytical solution agrees well with the numerical results.

Overall, the proposed analytical solution [Eq. (5.15b)] thus correlates quite well with the numerical results obtained with FLAC^{3D}, for different stope geometries and backfill properties. It thus provides a useful approach for evaluating the required strength of side-exposed mine backfill. The effect of various backfilled stope parameters on the required cohesion and FS is then illustrated in the following.

5.4.2 Parametric analyses

Sample applications of the proposed solution [Eq. (5.15b)] are presented below to illustrate the effect of the various parameters, considering typical stope geometry and material properties (defined in the figures caption).

Fig. 5-9 illustrates the effect of surcharge load p_0 on the required values of c and FS, obtained from Eq. (5.15), when the adherence ratio of the sidewalls r_s increases from 0 to 1. The required c tends to increase (almost) linearly while FS tends to decrease with the surcharge p_0. Increasing the surcharge would thus lead to a decreasing stability for the exposed backfill. The results also indicate that the increased interface cohesion (i.e., large r_s) along the sidewalls tends to stabilize the exposed backfill.

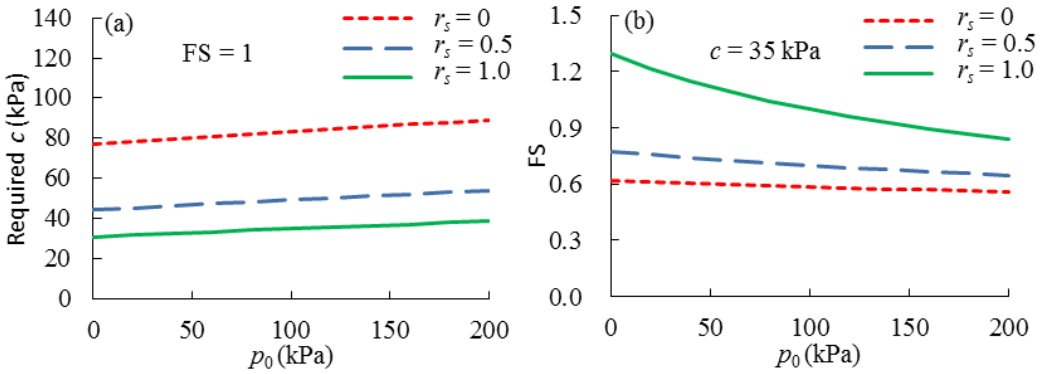

Figure 5-9: (a) Required c (for FS = 1) and (b) minimum FS (for c = 35 kPa) obtained from Eq. (5.15) as a function of surcharge p_0 for different values of r_s; calculations made with H = 50 m, L = 10 m, $\delta = \phi' = 30°$ and $\gamma = 18$ kN/m^3

Fig. 5-10 presents the variation of values of required c and FS as a function of the adherence ratio r_s, obtained from Eq. (5.15), when the internal friction angle of backfill ϕ' varies from 20° to 40°.

The increased adherence ratio leads to a reduction in the required c and then an increase in the FS. It is also seen that a stronger backfill (in terms of ϕ') tends to stabilize the exposed backfill, showing a decrease of the required cohesion or improved backfill stability.

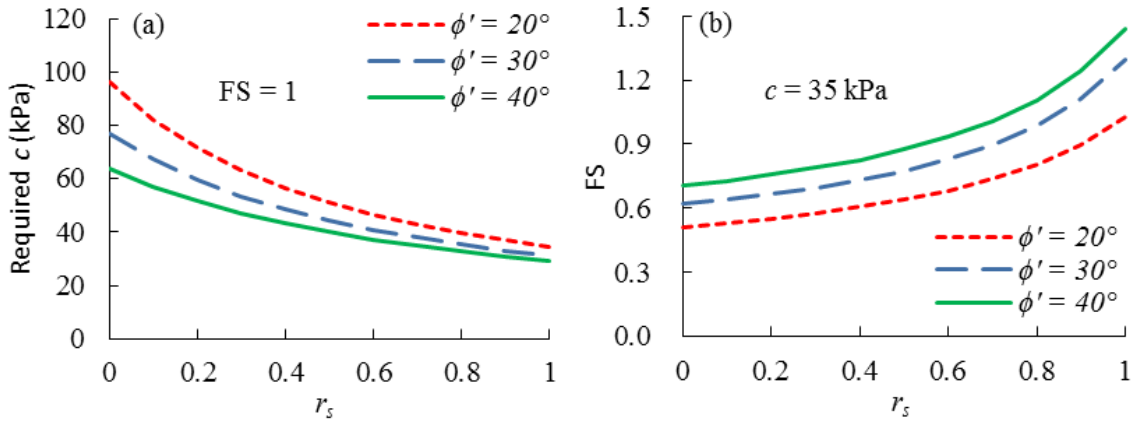

Figure 5-10: (a) Required c (for FS = 1) and (b) FS (for c = 35 kPa) obtained from Eq. (5.15) as a function of adherence ratio r_s for different values of ϕ'. Calculations made with H = 50 m, L = 10 m, p_0 = 0, $\delta = \phi'$ and γ = 18 kN/m^3

Fig. 5-11 shows the variation of values of required c and FS as a function of the adherence ratio r_s, obtained from Eq. (5.15), for different values of interface friction angle δ, i.e., $\phi'/3$, $2\phi'/3$ and ϕ'. Similar trends are observed for the effect of adherence ratio as those shown in Fig. 5-10. The results also indicate that an increase in interface friction angle leads to a decrease in required cohesion and then tends to improve the backfill stability.

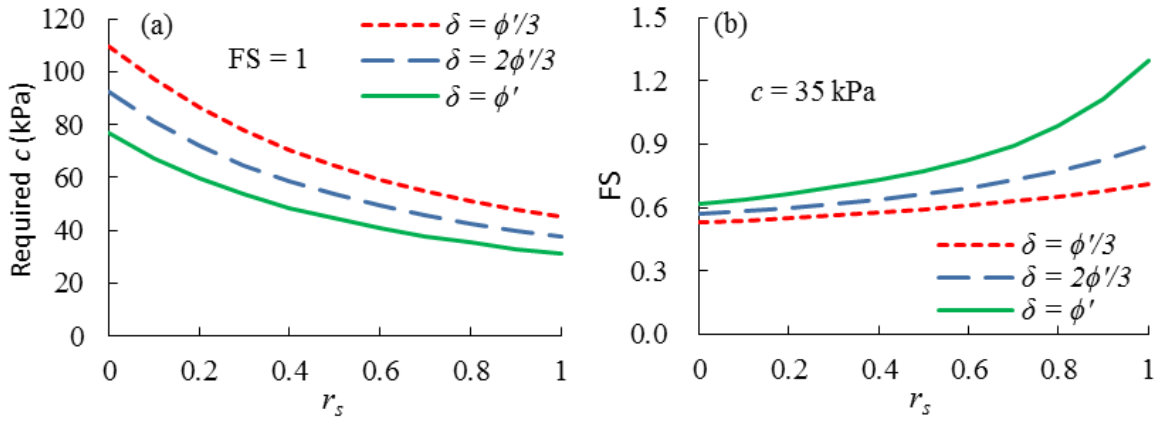

Figure 5-11: (a) Required c (for FS = 1) and (b) FS (for c = 35 kPa) obtained from Eq. (5.15) as a function of adherence ratio r_s for different values of δ. Calculations made with H = 50 m, L = 10 m, p_0 = 0, ϕ' = 30° and γ = 18 kN/m^3

5.5 Discussion

The interactions between the exposed fill and surrounding rockmass (at 3 sides) can be quite complex. Many simplifying assumptions thus have to be used for to develop analytical solutions. The results shown here indicate that the proposed solution may overcome some limitations of the original and modified Mitchell et al. solutions. Despite the good agreement with numerical results, it is noted that the proposed solution relies on a few simplifying assumptions that may not be entirely realistic. For instance, in the case of very high and narrow stopes, the application of Eq. (5.5) may result in a value of B_t that is unrealistic, i.e., larger than the stope width B (see Fig. 5-6). For such situations, the proposed solution should be regarded as empiric. More elaborate models and measurements are required to refine these assumptions.

Also, the failure surface is assumed to pass through the toe of the exposed cemented fill face in the theoretical model. However, results from numerical simulations conducted here indicate that this is not always the case; in some cases, the failure surface can develop somewhat above the toe location.

The consideration of cohesive shear strength along the (potential) tension crack implies that the tension cracking and wedge sliding occur simultaneously at a critical state, rather than tension cracking before wedge sliding. More work is needed to verify this assumption.

Another limitation is related to the planar sliding plane(s) assumed in the proposed model. This shape is quite close to the numerical results when the fill cohesion is low. But when the backfill cohesion is relatively large, the simulations results indicate that the failure surface is curved, with a spoon-shaped region extending from the open face upwards to the fill top. This curved surface is approximated here using a combination of an inclined plane and a vertical planar surface.

Also, numerical results from Falaknaz (2014) (also Falaknaz et al. 2016) indicated that the normal (horizontal) stresses along the sidewalls may change upon exposure, even for a stable cemented backfill. In the analytical model, such stresses are estimated from the arching solution (Li et al. 2005; Li & Aubertin 2009b), without considering such variation. More work is desirable to assess this aspect.

As stated above, interface elements are not used in the numerical models. This approach means that the mechanical properties (strength, stiffness) of the fill-wall interface are controlled by those

of the weakest component, i.e., backfill. In most cases, this approach is reasonable as the stope wall surfaces are usually very irregular and rough, following production blasting. Yielding then mostly takes place near the wall in the fill (Aubertin et al. 2003; Liu et al. 2016b). However, the fill cohesion near the walls (and along the contact) may be reduced, as indicated by some testing results (see below); this possibility was not directly taken into account here. Yielding may also occur along fill-wall contacts in cases of planar and smooth interfaces. Under these conditions, interface elements or a thin layer of softer material can be used in the numerical simulations (e.g., El Mkadmi et al. 2014; Liu et al. 2016a).

Experimental results of direct shear box tests indicated that the δ value of planar and smooth CPB-rock interfaces is very close to ϕ' value of CPB, but the interface cohesion is only a fraction of the fill cohesion (Fall & Nasir 2010; Koupouli et al. 2016). These results indicate that using $\delta = \phi'$ is a realistic assumption. The same results also suggest that a relatively small value should be used for the adherence ratio (r_b and r_s) with the analytical solutions. However, the values of r_b and r_s were taken here as unity for the comparisons with numerical results; as stated above, this is deemed acceptable when yielding develops in the fill, at some distance from the irregular and rough rock surfaces, at least for vertical walls. More work would nonetheless be needed to assess the response of planar and smooth fill-rock wall interfaces, and that of backfill along the hanging wall when the stope is inclined.

The zero tension cutoff corresponds to the most conservative assumption for the tensile strength of cemented fill. This cutoff value $T_0 = 0$ was used in the numerical simulations. However, tensile strength is not nil in practice due to cementation. Laboratory tests conducted by Mitchell & Wong (1982) and Sainsbury & Urie (2007) indicated that this tensile strength is about 0.12 UCS for cement content between 3.3% and 12.5%. Thus, a T_0 value of UCS/10 is deemed representative of cemented fill. This cutoff value was also used in the numerical simulations. It is noted that the ratio of UCS/T_0 = 10 is only valid for a specific value of ϕ' (about 55°) based on the Mohr-Coulomb criterion. More work is needed to well investigate the tensile strength of diverse cemented backfills.

The pore water pressures are neglected in these calculations. This is deemed reasonable since the wall removal usually takes place a few weeks after filling the stopes (e.g., Emad et al. 2015b). It has been shown that positive pore water pressures would be fully dissipated after a few days

following the filling (e.g., Thompson et al. 2012; El Mkadmi et al. 2014). The effect of negative pore water pressure (suction) is neglected here.

Numerical simulations were also conducted for large strain conditions. The stress and displacement given by small and large strain are almost identical when the fill is stable. Once failure occurs, the calculations for small strain cannot converge, while that for large strain give very large displacement after showing bad geometry (twisted meshes).

Previous numerical analyses have shown that the exposed fill may be compressed under deep mining conditions or for large wall closure (e.g., Cundall et al. 1978; Aubertin et al. 2003; Sainsbury & Urie 2007). It was also reported that a small wall closure could limit the build-up of tensile stress and stabilize the backfill, while a larger one may destabilize the exposed fill (e.g., Coulthard 1980; Pierce 1997). These indicate that the stability of exposed fill may also be influenced by wall closure for specific conditions, which are being considered in ongoing work.

5.6 Conclusions

Analytical solutions for predicting the required strength of side-exposed mine backfill have been briefly recalled. New numerical simulations are then conducted with FLAC^{3D} using the elasto-plastic constitutive model with a tensile strength cutoff T_0 of zero and UCS/10, considering the effective friction angle ϕ' and Poisson's ratio ν of the backfill as dependent parameters. An instability criterion has been defined to evaluate more objectively the stability of exposed backfill from the simulation results. These results indicate, among other findings, that the required cohesion of the cemented backfill is mainly dependent on the stope length, and is almost insensitive to the stope width, due to the development of tensile stresses near the backfill top surface.

A new analytical solution is proposed for assessing the stability of exposed cemented fill, considering a more realistic failure mode; the solution is based on a combination of an inclined planar surface and a vertical planar surface. The results indicate that the proposed solution correlates well with the numerical simulations for representative stope geometries and backfill properties. This new solution is thus regarded as an improvement over existing solutions.

5.7 Appendix I: Solution development for the proposed solution

The shear strength acting along the sidewalls τ_s is obtained based on the Mohr-Coulomb criterion:

$$\tau_s = c_s + \sigma_h \tan\delta \tag{5.17}$$

In Eq. (5.17), c_s (= r_s c, $0 \le r_s \le 1$) is the interface cohesion along the sidewalls; σ_h is the horizontal stress along the sidewalls at a depth h (see Fig. 5-6), which is estimated by (Li & Aubertin 2009b):

$$\sigma_h = \frac{\gamma L}{2\tan\delta}\left[1-\exp\left(-2K\tan\delta\frac{h}{L}\right)\right] + Kp_0\exp\left(-2K\tan\delta\frac{h}{L}\right) \tag{5.18}$$

where K is taken as Rankine's active pressure coefficient K_a = (1-sin ϕ')/(1+sin ϕ').

The shear force acting along one fill-sidewall interface S_s is given by (see Fig. 5-6):

$$S_s = \int_0^{H_t} \tau_s B_t dh + \int_{H_t}^{H} \tau_s \frac{H-h}{\tan\alpha} dh \tag{5.19}$$

where B_t is estimated from Eq. (5.5).

Introducing Eqs. (5.17) and (5.18) into Eq. (5.19), one can obtain the expression of S_s as follows:

$$\begin{aligned} S_s = {} & B_t\left(r_s c + \frac{\gamma L}{2}\right)\left(H - \frac{B_t\tan\alpha}{2}\right) - \frac{B_t L}{2}\left(\frac{\gamma L}{2K\tan\delta} - p_0\right) \\ & + \frac{L^2}{4K\tan\alpha\tan\delta}\left(\frac{\gamma L}{2K\tan\delta} - p_0\right)\left[\exp\left(-\frac{2K\tan\delta}{L}H_t\right) - \exp\left(-\frac{2K\tan\delta}{L}H\right)\right] \end{aligned} \tag{5.20}$$

The net weight of sliding wedge W_n is given by:

$$W_n = W + p_0 B_t L - 2S_s - S_t \tag{5.21}$$

where the self-weight of the sliding wedge $W = \gamma B_t L(H - B_t\tan\alpha/2)$; the shear force acting along the potential tension crack $S_t = cH_tL$. H_t is obtained from Eq. (5.4).

The FS of the sliding wedge can then be expressed as:

$$FS = \frac{W_n\cos\alpha\tan\phi' + cLB_t/\cos\alpha}{W_n\sin\alpha} = \frac{\tan\phi'}{\tan\alpha} + \frac{2}{\sin 2\alpha}\frac{cLB_t}{W_n} \tag{5.22}$$

Introducing Eqs. (5.20) and (5.21) into Eq. (5.22), one can obtain the FS of the sliding wedge and the required backfill cohesion *c* expressed as Eqs. (5.15a) and (5.15b), respectively.

Acknowledgements

The authors would like to acknowledge the financial support from the Natural Sciences and Engineering Research Council of Canada (NSERC 402318), Institut de recherche Robert-Sauvé en santé et en sécurité du travail (IRSST 2013-0029), Fonds de recherche du Québec - Nature et Technologies (FRQNT 2015-MI-191676), and the industrial partners of the Research Institute on Mines and Environment (RIME UQAT-Polytechnique; http://rime-irme.ca).

5.8 References

Askew, J., McCarthy, P. L., and Fitzgerald, D. J. (1978). "Backfill research for pillar extraction at ZC/NBHC." *Proc., 12th Can. Rock Mech. Symp.* on *Mining with Backfill*, Sudbury, 100-110.

Barrett, J. R., and Cowling, R. (1980). "Investigations of cemented fill stability in 1100 orebody, Mount Isa Mines, Ltd., Queensland, Australia." *Trans. IMM Sect. A: Min. Ind.*, 89, A118-A128.

Barrett, J. R., Coulthard, M. A., and Dight, P. M. (1978). "Determination of fill stability." *Proc., 12th Can. Rock Mechanics Symp.* on *Mining with Backfill*, Sudbury, 85-91.

Bloss, M. L., Cowling, R., and Meek, J. L. (1993). "A procedure for the design of stable cemented fill exposures." *Proc., Mining with Backfill*, Johannesburg, South African, 3-8.

Bowles, J. E. (1984). *Physical and geotechnical properties of soils*, 2nd ed., McGraw-Hill, New York.

Cundall, P., Shillabeer, J. H., and Herget, G. (1978). "Modelling to predict rock fill stability in transverse pillar extraction." *Proc., 12th Can. Rock Mechanics Symp.* on *Mining with Backfill*, Sudbury, 92-99.

Coulthard, M. A., and Dight, P. M. (1980). "Numerical analysis of failed cemented fill at ZC/NBHC Mine, Broken Hill." *Proc.*, 3rd Australia-New Zealand Geomech. Conf., Wellington, 2-145-2-151.

Coulthard, M. A. (1980). “Numerical analysis of fill pillar stability: three dimensional linearly elastic finite element calculations.” Technical Report. *CSIRO*, Division of Applied Geomechanics.

Coulthard, M. A. (1999). “Applications of numerical modelling in underground mining and construction.” *Geotech. Geol. Eng.*, 17(3-4), 373-385.

Cowling, R., and Gonano, L. P. (1976). “Cemented rockfill practice at Mount Isa Mines Limited.” *Proc., Symp. on Influence of Excavation Design and Ground Support on Underground Mining Efficiency and Costs*, AMIRA, Wollongong.

Dight, P. M., and Coulthard, M. A. (1980). “Numerical analysis of fill pillar stability - two-dimensional analysis of exposures.” Technical Report. *CSIRO*, Division of Applied Geomechanics.

Dirige, A. P. E., and De Souza, E. (2000). “Centrifuge physical modelling of paste fill designs for improved cost performance.” *Proc., the Millennium 2000 CIM Conf.*, Toronto.

Dirige, A. P. E., and De Souza, E. (2013) “Mechanics of failure of paste backfill face exposure during adjacent mining.” *Proc., 23rd World Mining Congress*, Montreal.

Dirige, A. P. E., McNearny, R. L., and Thompson, D. S. (2009). “The effect of stope inclination and wall rock roughness on back-fill free face stability.” *Proc., Rock Engineering in Difficult Conditions, 3rd Canada-US Rock Mechanics Symp*. (CD-ROM), M. Diederichs and G. Grasselli, eds., Toronto.

Duncan, J. M., and Wright, S. G. (2005). *Soil Strength and Slope Stability*, John Wiley & Sons, New York.

El Mkadmi, N., Aubertin, M., and Li, L. (2014). “Effect of drainage and sequential filling on the behavior of backfill in mine stopes.” *Can. Geotech. J.*, 51(1), 1-15.

Emad, M. Z., Mitri, H., and Henning, J. G. (2012). “Effect of blast vibrations on the stability of cemented rockfill.” *Int. J. Min. Reclam. Environ.*, 26(3), 233-243.

Emad, M. Z., Mitri, H., and Kelly, C. (2014). “Effect of blast-induced vibrations on fill failure in vertical block mining with delayed backfill.” *Can. Geotech. J.*, 51(9), 975-983.

Emad, M. Z., Mitri, H., and Kelly, C. (2015b). “In-situ blast vibration monitoring in cemented rockfill stope-a case study.” *Int. J. Min. Reclam. Environ.*, 1-18.

Falaknaz, N. (2014). “Analysis of geomechanical behavior of two adjacent backfilled stopes based on two and three dimensional numerical simulations.” PhD thesis, Polytechnique Montréal, Montréal.

Falaknaz, N., Aubertin, M., and Li, L. (2015a). “Numerical investigation of the geomechanical response of adjacent backfilled stopes.” *Can. Geotech. J.*, 52(10), 1507-1525.

Falaknaz, N., Aubertin, M., and Li, L. (2015b). “Evaluation of the stress state in two adjacent backfilled stopes within an elasto-plastic rock mass.” *Geotech. Geol. Eng.*, 1-24.

Falaknaz, N., Aubertin, M., and Li, L. (2015c). “Numerical analyses of the stress state in two neighboring stopes excavated and backfilled in sequence.” *Int. J. Geomech.*, 15(6), 04015005.

Falaknaz, N., Aubertin, M., and Li, L. (2015d). “On the stability of exposed backfill in mine stopes.” *Proc., 68th Can. Geotech. Conf.*, Quebec City, Canada.

Falaknaz, N., Aubertin, M., and Li, L. (2016). “Stability analyses of backfill in mine stopes with an open face.” *Geotech. Geol. Eng*. (submitted).

Fall, M., and Nasir, O. (2010). “Mechanical behaviour of the interface between cemented tailings backfill and retaining structures under shear loads.” *Geotech. Geol. Eng.*, 28(6), 779-790.

Jones, T. O. (1972). “Pillar recovery in a section of the 650 orebody floor pillar using cemented fill.” *Proc., the Aus. IMM Regional Conf.*

Itasca. (2013). *FLAC3D: Fast lagrangian analysis of continua in 3 dimensions; user’s guide*, version 5.01, Itasca Consulting Group, Inc., Minneapolis.

Karim, R., Simangunsong, G. M., Sulistianto, B., and Lopulalan, A. (2013). “Stability analysis of paste fill as stope wall using analytical method and numerical modelling in the Kencana underground gold mining with long hole stope method.” *Procedia Earth Planet. Sci.*, 6, 474-484.

Koupouli, N. J., Belem, T., Rivard, P., and Effenguet, H. (2016). “Direct shear tests on cemented paste backfill-rock wall and cemented paste backfill-backfill interfaces.” *J. Rock Mech. Geotech. Eng*., 8, 472-479.

Leahy, F. J., and Cowling, R. (1978). "Stope fill developments at Mount Isa." *Proc., 12th Can. Rock Mechanics Symp. on Mining with Backfill*, Sudbury, 21-29.

Li, L. (2014a). "Generalized solution for mining backfill design." *Int. J. Geomech.*, 14(3), 04014006.

Li, L. (2014b). "Analytical solution for determining the required strength of a side-exposed mine backfill containing a plug." *Can. Geotech. J.*, 51(5), 508-519.

Li, L., Aubertin, M., and Belem, T. (2005). "Formulation of a three dimensional analytical solution to evaluate stresses in backfilled vertical narrow openings." *Can. Geotech. J.*, 42(6), 1705-1717.

Li, L., and Aubertin, M. (2009b). "A three-dimensional analysis of the total and effective stresses in submerged backfilled stopes." *Geotech. Geol. Eng.*, 27(4), 559-569.

Li, L., and Aubertin, M. (2009e). "Numerical investigation of the stress state in inclined backfilled stopes." *Int. J. Geomech.*, 9(2), 52-62.

Li, L., and Aubertin, M. (2012). "A modified solution to assess the required strength of exposed backfill in mine stopes." *Can. Geotech. J.*, 49(8), 994-1002.

Li, L., and Aubertin, M. (2014). "An improved method to assess the required strength of cemented backfill in underground stopes with an open face." *Int. J. Min. Sci. Technol.*, 24(4), 549-558.

Li, L., Aubertin, M., Simon, R., Bussière, B., and Belem, T. (2003). "Modelling arching effects in narrow backfilled stopes with FLAC." *Proc., 3rd Int. Symp. on FLAC & FLAC 3D numerical modelling in Geomech.*, Sudbury, 211-219.

Libby, D. J., and Smith, J. D. (1975). "Development of a sub-level mining method with delayed pillar recovery at Sherritts Fox mine, Manitoba: 9F." *IMM Bull. Trans. Aus.*, 84, No. 818, A40-A46.

Liu, G., Li, L., Yang, X., and Guo, L. (2016a). "Numerical analysis of stress distribution in backfilled stopes considering interfaces between the backfill and rock walls." *Int. J. Geomech.*, 06016014.

Liu, G., Li, L., Yang, X., and Guo, L. (2016b). "A numerical analysis of the stress distribution in backfilled stopes considering nonplanar interfaces between the backfill and rock walls." *Int. J. Geotech. Eng.*, 10(3), 271-282.

Liu, G., Li, L., Yang, X., and Guo, L. (2016c). "Numerical modelling of the stability of cemented backfill with a vertical face exposed: a revisit to Mitchell's physical model tests." *Int. J. Min. Sci. Technol.* (available online).

McCarthy, D. F. (2002). *Essentials of soil mechanics and foundations: basic geotechnics*, 6th ed., Prentice Hall, Englewood Cliffs.

Mitchell, R. J. (1986). "Centrifuge model tests on backfill stability." *Can. Geotech. J.*, 23(3), 341-345.

Mitchell, R. J., and Wong, B. C. (1982). "Behaviour of cemented tailings sands." *Can. Geotech. J.*, 19(3), 289-295.

Mitchell, R. J., Olsen, R. S., and Smith, J. D. (1982). "Model studies on cemented tailings used in mine backfill." *Can. Geotech. J.*, 19(1), 14-28.

Pierce, M. E. (1997). "Laboratory and numerical analysis of the strength and deformation behaviour of paste backfill." Master thesis, Queen's University, Kingston.

Pierce, M. E. (2001). "Stability analysis of paste back fill exposes at Brunswick Mine." *Proc., 2nd Int. FLAC Symp.* Lyon, 147-156.

Sainsbury, D. P., and Urie, R. (2007). "Stability analysis of horizontal and vertical paste fill exposures at the Raleigh Mine." *Proc., 9th Int. Symp. on Mining with Backfill*, Montreal.

Smith, J. D., Dejongh, C. L., and Mitchell, R. J. (1983). "Large scale model tests to determine backfill strength requirements for pillar recovery at the Black Mountain Mine." *Proc., Int. Symp. on Mining with Backfill*, Lulea, 413-423.

Thompson, B. D., Grabinsky, M. W., and Bawden. W. F. (2012). "In-situ measurements of CPB at the Cayeli Mine." *Can. Geotech. J.*, 49, 755-772.

Yang, P. Y., Li, L., Aubertin, M., Brochu-Baekelmans, M., and Ouellet, S. (2016a). "Stability analyses of waste rock barricades designed to retain paste backfill." *Int. J. Geomech.*, 04016079. This article is presented in Chapter 4.

Yang, P. Y., Li, L., Aubertin, M., and Tiwari, A. (2016d). "An investigation of the relationships between K_0, ϕ' and v for granular materials." To be submitted. Main results are presented in Appendix A.

Zou, D. H., and Nadarajah, N. (2006). "Optimizing backfill design for ground support and cost saving." *Proc*., 41st US Rock Mechanics Symp.: 50 Years of Rock Mechanics, ARMA, Alexandria.

CHAPTER 6 ARTICLE 4: A COMPREHENSIVE NUMERICAL ANALYSIS OF STRESS RATIOS IN VERTICAL BACKFILLED OPENINGS

Pengyu Yang, Li Li, & Michel Aubertin

This article was submitted to ASCE - *International Journal of Geomechanics* in November 2016.

Abstract: Stresses in backfilled openings depend on the interactions between the backfill and confining walls. Such stresses can be assessed using analytical solutions based on arching theory, which usually include the earth pressure coefficient $K = \sigma'_h/\sigma'_v$, defined as the ratio of the horizontal to vertical effective stresses. The value of this coefficient can significantly affect the estimated stresses in the backfilled openings. Along the centerline of vertical openings, the K value has sometimes been estimated from the at-rest earth pressure coefficient K_0, while others consider that Rankine's active earth pressure coefficient K_a is more appropriate. However, this stress ratio has not been investigated in depth, especially near the walls of openings. Simulations have been conducted using FLAC to evaluate the coefficient K and also the principal stress ratio $K_{ps} = \sigma'_3/\sigma'_1$, defined as the ratio of the minor to the major principal stresses, along the centerline and near the walls. The simulations are conducted using independent and interrelated values of internal friction angle ϕ' and Poisson's ratio ν. The results indicate that along the centerline, stress ratios ($K_{ps} = K$) are close to K_a when the fill Poisson's ratio is below a critical value defined by its internal friction angle ϕ'. Beyond this critical value, stress ratios approaches K_0 based on Poisson's ratio. The ratio K_{ps} near the walls is always close to K_a for both independent and related ϕ' and ν, due probably to the severe shearing of the fill near the rock face. Coefficient K near the walls depends on values of independent ν and ϕ', while K is close to K_0 for interrelated ν and ϕ'. Additional simulations conducted with interface elements along the fill-wall contacts indicate that stress ratios K_{ps} and K along the centerline are insensitive to interface roughness and almost identical to those obtained without interface elements (for both independent and related ϕ' and ν); but they may be different for less rough or smooth interfaces near walls.

Keywords: Backfilled openings (stopes, trenches, silos); Stresses; Earth pressure coefficient; Principal stress ratio; Internal friction angle; Poisson's ratio; Numerical simulations.

6.1 Introduction

The stress state in backfilled openings is largely dependent on the interactions between the backfill and confining structures. The basic methods for evaluating such stresses mainly originated from the arching theory developed for estimating stresses in silos (Janssen 1895). In geotechnical engineering, Marston (1930) adopted arching theory to estimate the loads of backfill on buried conduits in trenches. Later, Terzaghi (1943) modified the arching solution to evaluate the pressures above a yielding strip in cohesive soils (known as trap-door problem). The arching theory has also been applied in mining engineering to assess the stresses in backfilled stopes (e.g., Askew et al. 1978; Aubertin et al. 2003).

For a cohesionless fill, the vertical σ'_v and horizontal σ'_h effective stresses in backfilled openings can be obtained from the following expressions, based on the Marston (1930) solution:

$$\sigma'_v = \frac{B\gamma}{2K\tan\delta'}\left[1-\exp\left(-\frac{2K\tan\delta'}{B}h\right)\right] \tag{6.1a}$$

$$\sigma'_h = K\sigma'_v \tag{6.1b}$$

where K (-) is the earth pressure coefficient, defined as the ratio of the horizontal to the vertical effective stresses (= σ'_h/σ'_v); B (m) is the width of the opening; h (m) is the depth from the fill top; γ (kN/m^3) is the unit weight of backfill; δ' (°) is the effective friction angle of the fill-wall interface. For mine stopes, the value of δ' is often taken as the effective friction angle of the backfill ϕ' (°) as the yielding near the walls tends to occur in the fill due to the rough and stiff rock surfaces (e.g., Aubertin et al. 2003; Li et al. 2003).

Marston's solution has been applied and extended to several cases for estimating the stresses in mine backfilled stopes. These include 2D stopes with inclined walls (Blight 1984; Caceres 2005; Singh et al. 2011; Ting et al. 2011, 2014; Jahanbakhshzadeh 2016), and 3D stopes (Coulthard & Dight 1979; Winch 1999; Li et al. 2005; Pirapakaran & Sivakugan 2007a; Jahanbakhshzadeh 2016). The effect of pore water pressures has also been considered (Li & Aubertin 2009a, 2009b).

Applying these arching solutions requires the knowledge of the earth pressure coefficient K, which can significantly affect the estimated stress state in backfilled openings (e.g., Aubertin et

al. 2003; Li et al. 2003, 2005). However, the actual value of the coefficient K within backfill placed in confining structures (trench, stope, silo, etc.) remains a debated topic.

For isolated mine stopes with delayed backfilling (i.e., backfill placed after the entire stope is mined out), the movement of rock walls is usually considered negligible. Therefore, the K value has sometimes been estimated from the at-rest earth pressure coefficient K_0 along the centerline (e.g., Winch 1999; Helinski 2007; Pirapakaran & Sivakugan 2007a, 2007b; Fahey et al. 2009; Singh et al. 2010, 2011; Ting et al. 2011). However, some numerical simulations have shown that σ'_h/σ'_v is often smaller than K_0 and that the Rankine's active earth pressure coefficient K_a can better represent the stress state along the centerlines of mine backfilled stopes (e.g., Li et al. 2003, 2005; Li & Aubertin 2009a, 2009b; Sobhi et al. 2014, 2016). The latter numerical results have been partly confirmed by laboratory tests results (e.g., Sobhi et al. 2016, using data from Pirapakaran & Sivakugan 2007b) and in-situ measurements (Hughes et al. 2010; Thompson et al. 2012). Numerical simulations conducted by Jahanbakhshzadeh et al. (2016) indicated that the value of K across the width of a vertical stope is between K_0 and K_a (and somewhat closer to the former).

In most previous numerical simulations, the Poisson's ratio ν of the backfill was taken as a constant with a value that is unrelated to the internal friction angle ϕ'. Recently, simulations conducted with interrelated ν and ϕ' values resulted in somewhat different stress states within the backfill (e.g., Falaknaz 2014; Falaknaz et al. 2015a; Jahanbakhshzadeh 2016). The stress ratio can also depend on the relation between ν and ϕ' (e.g., Jahanbakhshzadeh et al. 2016). There is thus a need to assess this stress ratio by considering both independent and interrelated ν and ϕ' values. In addition, the stress ratio near the walls has not been investigated in depth in previous numerical analyses. As the stresses are not uniform across the stope width (Li & Aubertin 2008, 2010; Rajeev et al. 2016), due to the shear stresses between the fill and walls, the use of a constant K within the whole opening is not representative (e.g., Jahanbakhshzadeh 2016). Therefore, it is also deemed necessary to evaluate stress ratios near walls where stresses may be of particular interest for stability analyses.

In the following, the origins of the active (K_a) and at-rest (K_0) earth pressure coefficients are briefly recalled. Attention is paid to the relationship between ν and ϕ', based on unique (and consistent) values for K_0. A series of simulations are then conducted using FLAC, with both

independent and related ϕ' and ν values, to evaluate the effect of various mechanical and geometric characteristics on this stress ratio K in backfilled openings. In addition, the principal stress ratio K_{ps}, defined as the ratio of the minor (σ'_3) to the major (σ'_1) principal stresses is also analyzed. Additional simulations are performed to assess the effect of fill-rock interface and its properties on the stress ratios.

6.2 Active and at-rest earth pressure coefficients

The earth pressure coefficient K has been used to evaluate the pressures on retaining walls and the naturel stress state in soils (e.g., Coulomb 1776; Rankine 1857; Terzaghi 1943; Jaky 1944).

When the horizontal stress behind a frictionless retaining wall is decreased by wall movement to a degree that the soil (fill) reaches a plastic equilibrium (yielding), the soil is said to arrive at an active state. The ratio of the horizontal over the vertical stresses is known as the Rankine's active earth pressure coefficient K_a. For a cohesionless fill with a horizontal surface, the expression of K_a is given by:

$$K_a = \frac{1-\sin\phi'}{1+\sin\phi'} \tag{6.2}$$

When the soil in a semi-infinite region is submitted to a vertical loading that does not produce lateral strain, the soil is said to be at at-rest (e.g., Aysen 2005; Sivakugan & Das 2009) with $K = K_0$. For loose granular materials, the semi-empirical formula proposed by Jaky (1944, 1948) is widely used in practice to evaluate the K_0 value. Jaky's (simplified) equation is expressed as a function of the internal friction angle ϕ':

$$\left(K_0\right)_{\phi'} = 1-\sin\phi' \tag{6.3}$$

Eq. (6.3) has been shown to correlate well with experimental results obtained on sands of various densities (e.g., Al-Hussaini & Townsend 1975; Mesri & Hayat 1993) and on normally consolidated clays (e.g., Brooker & Ireland 1965; Ladd et al. 1977; Mayne & Kulhawy 1982), despite being considered non-rigorous as it relates a yielding strength parameter ϕ' to an at-rest state parameter K_0 (e.g., Michalowski 2005; Talesnick 2012). Eq. (6.3) has also been extended to over-consolidated soils (e.g., Brooker & Ireland 1965; Daramola 1980; Mayne & Kulhawy 1982).

Alternatively, the K_0 value can be obtained more fundamentally from Poisson's ratio v, based on the Hooke's law for a homogeneous, isotropic and linear elastic material (e.g., Bishop 1958; Gould 1970; Morgenstern & Eisenstein 1970; Blight 1986; Bardet 1997; McCarthy 2007; Das 2010; Briaud 2013; Sobhi et al. 2014):

$$\left(K_0\right)_v = \frac{v}{1-v} \tag{6.4}$$

Eqs. (6.3) and (6.4) indicate that the internal friction angle ϕ' and Poisson's ratio v should be, in some ways, related to ensure a unique and consistent value of K_0 with an elasto-plastic model. This has led to the following relationship (Yang et al. 2016d; see also Eq. (A.9) in Appendix A):

$$\nu = \frac{1-\lambda \sin\phi'}{2-\sin\phi'} \tag{6.5}$$

where λ is a material parameter; λ = 1 (e.g., Duncan & Bursey 2013; Falaknaz 2014; Jahanbakhshzadeh 2016) or 0.75 (e.g., Duncan et al. 1991) has generally been used with Eq. (6.5).

In the following, Eq. (6.5) with $\lambda = 1$ is used when the simulations consider related values of ϕ' and v.

6.3 Modelling approach

A number of studies conducted previously by the authors, and others, have shown that the finite difference code FLAC (Itasca 2011) is a useful tool to evaluate the stress state in backfilled openings. Fig. 6-1 illustrates a backfilled opening (under plane strain condition) and the corresponding numerical model built with FLAC. The opening is filled to a height H of 40 m with an open top surface. The relevant parameters are shown on the conceptual model [Fig. 6-1(a)] and the discretization and boundary conditions of the numerical model are shown in Fig. 6-1(b).

In Fig. 6-1(b), the side boundaries of the rockmass are fixed in the horizontal direction, while displacements are fixed in all directions at the base. Sensitivity analyses of different meshes (results not shown here) suggest that the backfill can be modeled by quadrilateral elements of 0.2

× 0.2 m and the rockmass by radial and coarser [Fig. 6-1(b)] meshes to obtain stable numerical results.

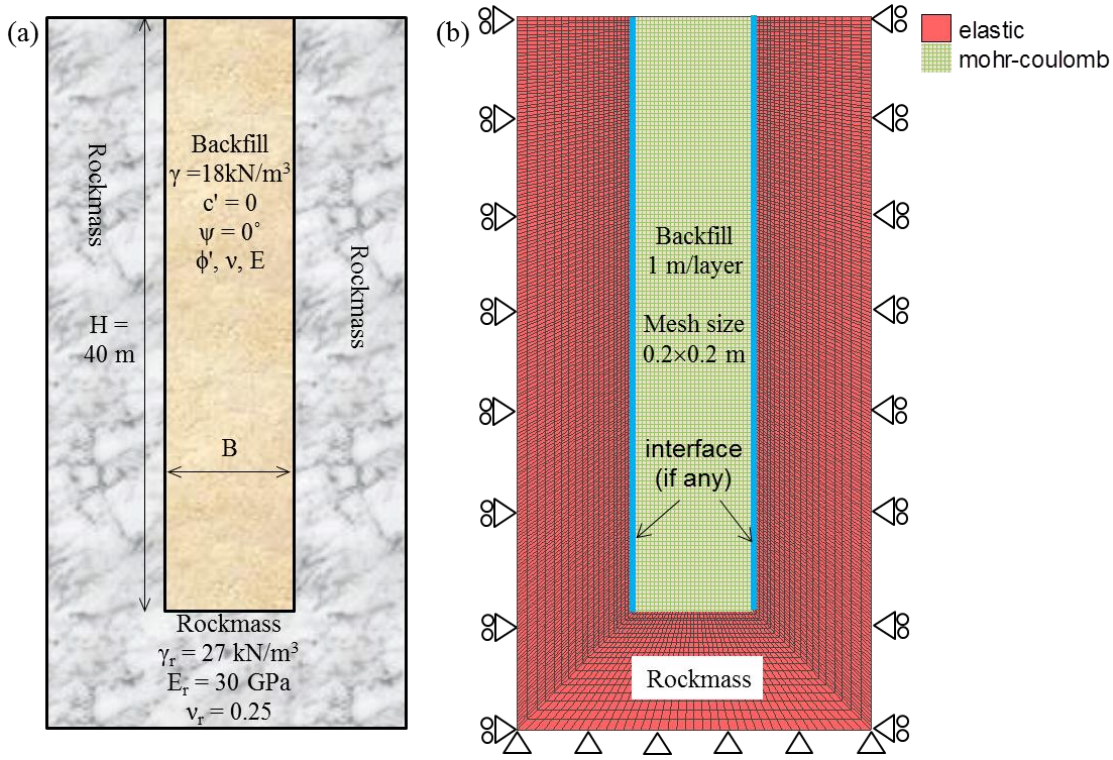

Figure 6-1: Conceptual model (a) and the corresponding FLAC model (b) of a backfilled opening

The opening is first excavated in one step and the induced displacements are set to zero once the system reaches equilibrium. This is valid for delayed filling after complete convergence for very stiff rock walls (e.g., Li et al. 2003; Li & Aubertin 2009e; Falaknaz 2014; Liu et al. 2016b; Jahanbakhshzadeh 2016). Staged filling of the opening is performed in 40 layers with 1 m/layer, which is small enough to minimize the effect of layer thickness on the stress state and stress ratios (results not shown here; see details in the sensitivity analysis presented in Appendix G). The calculations run until reaching an equilibrium state before the addition of a new filling layer.

The rock mass is linearly elastic with a unit weight γ_r = 27 kN/m^3, a Young's modulus E_r = 30 GPa and a Poisson's ratio ν_r = 0.25. The backfill behaves as an elasto-plastic material obeying the Mohr-Coulomb criterion; it is characterized by modulus E (variable), ϕ' (variable), ν (variable), dry unit weight γ = 18 kN/m^3, an effective cohesion c' = 0 kPa (i.e., cohesionless fill), and a dilation angle ψ = 0° (non-associated flow rule). The interfaces between the backfill and the confining walls [Fig. 6-1(b)] are characterized by the effective friction angle δ' and the normal

(K_n) and shear (K_t) stiffnesses (see FLAC Manual of Itasca 2011 for details on their determination). Other parameters are given in detail in Table 6-1 for independent (Cases 0 to 5) and interrelated (Cases 0' to 4') values of ν and ϕ', respectively. For the latter cases, the ν of the backfill is related to its ϕ' through Eq. (6.5) with $\lambda = 1$ (e.g., Falaknaz 2014; Falaknaz et al. 2015a; Jahanbakhshzadeh 2016). Interface elements between the fill and rock-walls are included in Cases 5 and 4', but not in Cases 0 to 4 and 0' to 3'.

Table 6-1: Geometric and mechanical properties of the backfill-stope system used in numerical simulations performed with independent (Cases 0 to 5) and interrelated (Cases 0' to 4') ν and ϕ'

Cases		Figure no.	B (m)	E (MPa)	ϕ' (°)	ν (-)	λ in Eq. 6.5	δ' (°)
Interpendent ϕ' and ν	0	2, 3, 4	8	300	30	0.2	-	-
	1	5	Variable	300	30	0.2	-	-
	2	6	8	Variable	30	0.2	-	-
	3	7, 16	8	300	Variable	0.2	-	-
	4	8	8	300	30	Variable	-	-
	5	13	8	300	30	0.2, 0.3	-	Variable*
Related ϕ' and ν	0'	2, 3, 4, 12	8	300	30	0.333	1	-
	1'	9	Variable	300	30	0.333	1	-
	2'	10	8	Variable	30	0.333	1	-
	3'	11	8	300	Variable		1	-
	4'	14	8	300	Variable		1	Variable*

Note: -, not applicable; *, with interface elements.

6.4 Numerical results and analyses

Fig. 6-2 illustrates the stress contours obtained from FLAC simulations for independent (Case 0 in Table 6-1) and interrelated (Case 0' in Table 6-1) values of ν and ϕ'. The results show that an arching effect develops within the backfill for both cases (with σ'_v smaller than the overburden). A non-uniform distribution across the opening width is observed for both the vertical and horizontal stresses. At a given depth, it is seen that the stresses near the walls are lower than those at the center. These indicate that the values of K along the vertical centerline (VCL) and near rock-walls (RW) could be different in practice.

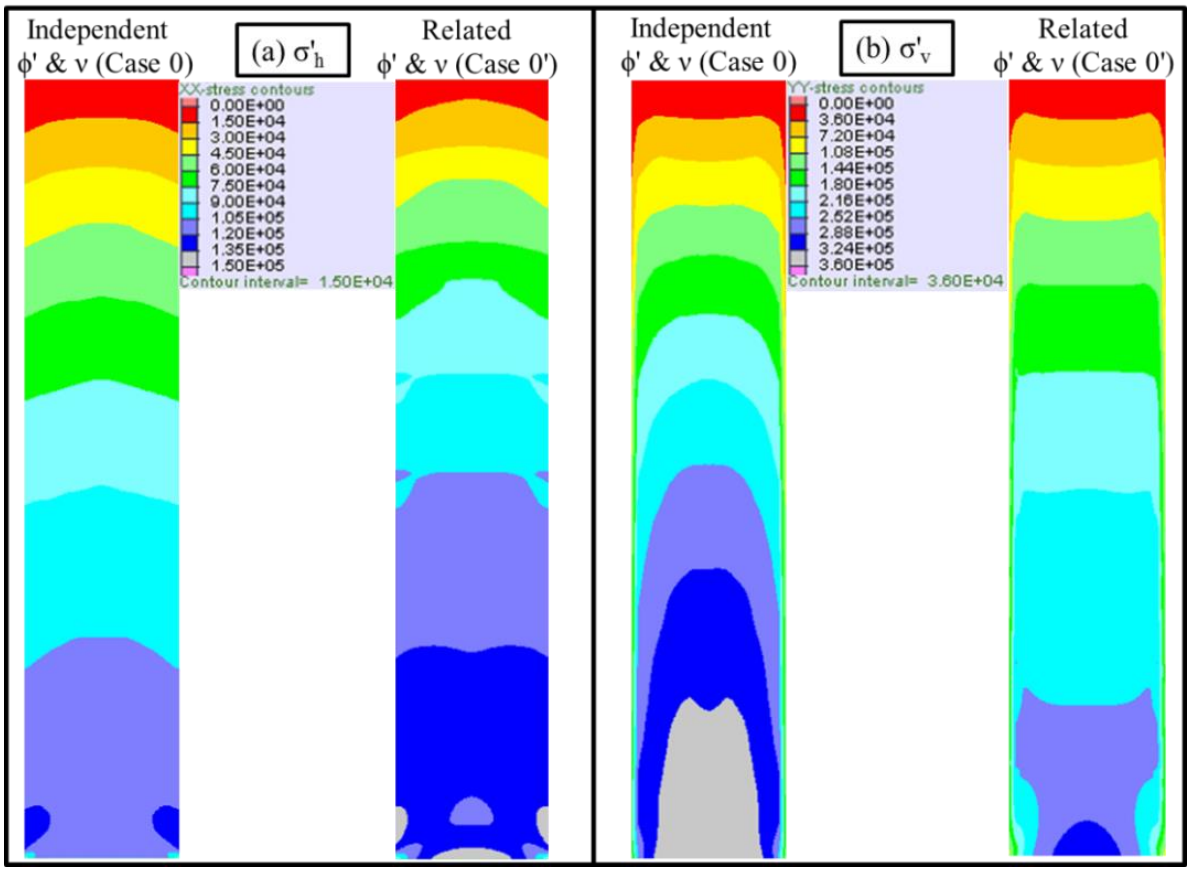

Figure 6-2: Horizontal (a) and vertical (b) stress (in Pa) contours of FLAC simulations conducted for independent (Case 0) and interrelated (Case 0') values of ν and ϕ' (see Table 6-1 for details)

Fig. 6-3(a) presents the stress distributions along the VCL in the backfill for both Case 0 (independent ν and ϕ'; ν = 0.2, ϕ' = 30°) and Case 0' [related ν and ϕ' through Eq. (6.5) with λ = 1; ν = 0.333, ϕ' = 30°], while Fig. 6-3(b) shows the principal (σ'_1 and σ'_3) stresses and horizontal (σ'_h) and vertical (σ'_v) stresses near the RW, respectively. The vertical and horizontal stresses due to overburden (OB) are also plotted, using $\sigma'_v = \gamma h$ and $\sigma'_h = (K_0)_{\phi'}\sigma'_v$. The stresses along the RW correspond to a profile located at a distance of 0.2 m (one element size) from the rock. For both cases, Fig. 6-3 shows that the values of σ'_v and σ'_h are significantly lower than those based on the OB, especially near the base of the backfilled openings.

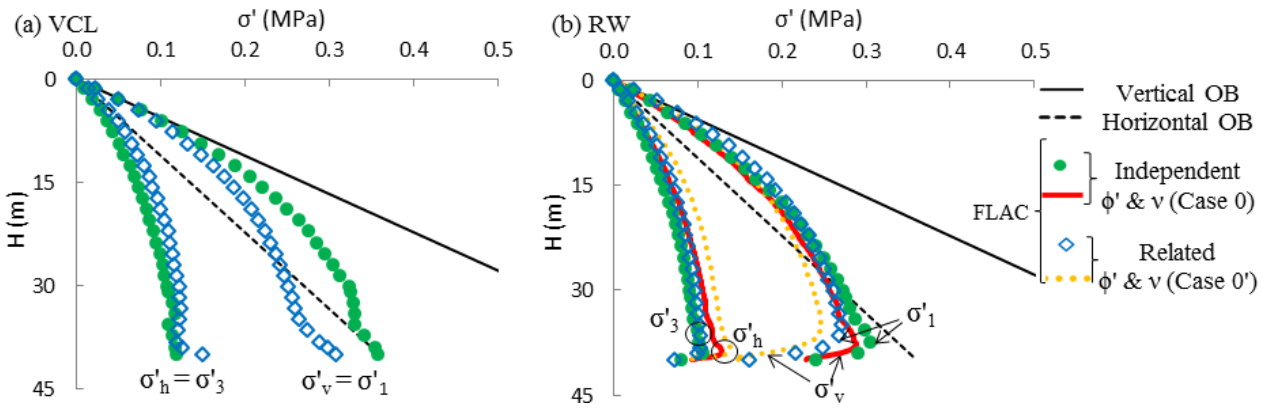

Figure 6-3: Stress distributions (a) along the VCL and (b) near the RW in the backfill for independent (Case 0) and related (Case 0') values of ν and ϕ' (see Table 6-1 for details)

Along the VCL (2D) of the opening, the vertical and horizontal stresses correspond to the major and minor principal stresses, respectively. The principal stress ratio K_{ps} ($= \sigma'_3/\sigma'_1$) is thus equal to the earth pressure coefficient K ($= \sigma'_h/\sigma'_v$).

For ϕ' = 30°, when the value ν increases from 0.2 (Case 0, independent ν and ϕ') to 0.333 [Case 0', with Eq. (6.5) with $\lambda = 1$], Fig. 6-3(a) shows that the vertical principal stress ($\sigma'_v = \sigma'_1$) along the VCL tends to significantly decrease while the horizontal principal stress ($\sigma'_h = \sigma'_3$) slightly increases. Near the RW, the principal stresses and the vertical and horizontal stresses are nearly insensitive to the change of ν, except for near the bottom of the openings, where the major principal stress (σ'_1) and the vertical stress (σ'_v) decrease slightly when ν goes from 0.2 to 0.333 [Fig. 6-3(b)]. These results tend to indicate that the two stress ratios (K_{ps} and K) obtained from the two assumptions differ somewhat. This effect is also illustrated in Fig. 6-4, which shows that the values of K_{ps} and K along the VCL [Fig. 6-4(a)] and near the RW [Fig. 6-4(b)] all increases when ν varies from 0.2 (Case 0) to 0.333 (Case 0'), with a larger variation along the VCL.

In the following sections, the two stress ratios (K_{ps} and K) along the VCL and near the walls will be investigated by considering different cases with independent and interrelated values of ν and ϕ'.

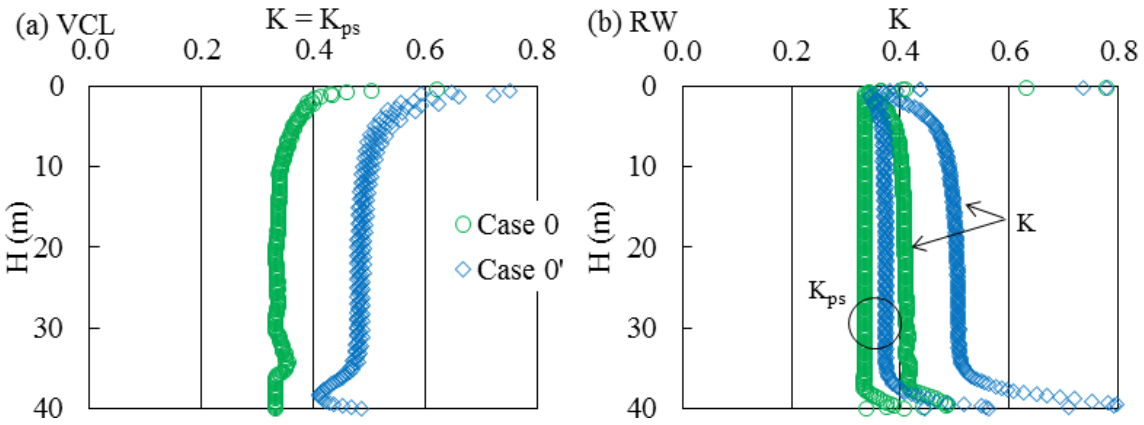

Figure 6-4: Vertical profiles of K and K_{ps} (a) along the VCL and (b) near the RW, for independent (Case 0) and related (Case 0') values of ν and ϕ' (see Table 6-1 for details)

6.4.1 Calculations with independent ϕ' and ν values

In this section, simulation results are presented to illustrate the effect of various parameters for independent values of ν and ϕ'.

Effect of opening width *B*

Fig. 6-5 shows the variations of K_{ps} and K along VCL [Fig. 6-5(a)] and near the RW [Fig. 6-5(b)] of the opening, considering different widths B (disconnected values of ϕ' and ν; Case 1 in Table 6-1). It is seen that the values of K_{ps} along the VCL [Fig. 6-5(a)] and near the RW [Fig. 6-5(b)] are close to Rankine's active earth pressure coefficient K_a [Eq. (6.2)] along most of the depth when B increases from 4 to 20 m, except near the backfill surface (also the base for K_{ps} near the RW). Fig. 6-5(b) shows that the value of K (about 0.4) near the RW is between K_0 and K_a for different widths B (4 to 20 m). An increase in opening width tends to increase the vertical and horizontal (and principal) stresses, due to the reduced arching effect (Li and Aubertin 2009e). The results of Fig. 6-5 nonetheless indicate that the stress ratios (K and K_{ps}) in the backfill are nearly insensitive to the opening width.

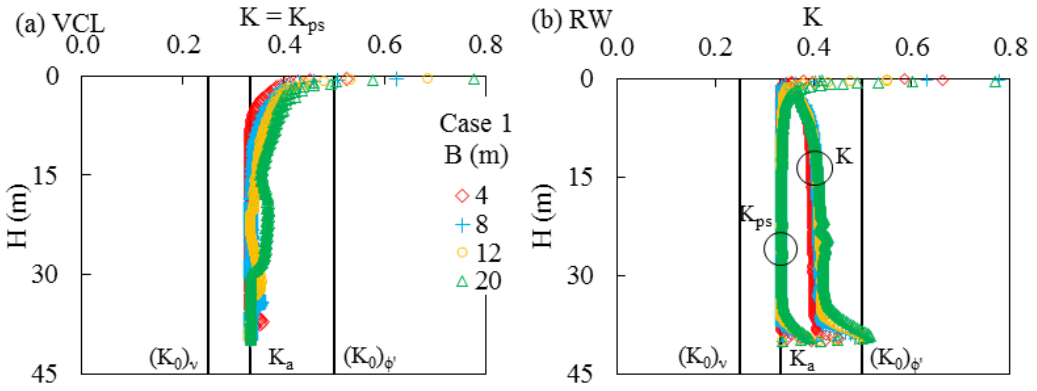

Figure 6-5: Vertical profiles of K and K_{ps} (a) along the VCL and (b) near the RW for different B values for independent values of v and ϕ' (Case 1 in Table 6-1)

Effect of backfill modulus *E*

Fig. 6-6 illustrates the vertical profiles of K_{ps} and K along the VCL [Fig. 6-6(a)] and near the RW [Fig. 6-6(b)] for different values of Young's modulus E (independent v and ϕ'; Case 2 in Table 6-1). When the backfill E varies from 10 MPa to 1 GPa, the values of K_{ps} along the VCL [Fig. 6-6(a)] and near the RW [Fig. 6-6(b)] remain almost constant near K_a, while the K near the RW [Fig. 6-6(b)] is between K_0 and K_a (about 0.4). These indicate that the Young's modulus has little effect on K and K_{ps} (in this range); the stress state in backfilled openings is almost insensitive to backfill modulus (for the given range, 10 MPa to 1GPa).

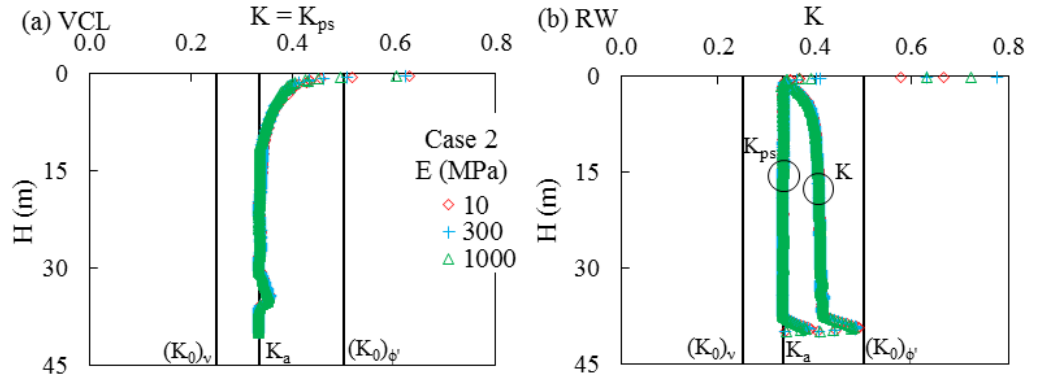

Figure 6-6: Vertical profiles of K and K_{ps} (a) along the VCL and (b) near the RW for different E values for independent values of v and ϕ' (Case 2 in Table 6-1)

Effect of internal friction angle *ϕ'*

Fig. 6-7 presents the variations of the two stress ratios along the VCL [Fig. 6-7(a)] and near the RW [Figs. 6-7(b and c)] for different values of ϕ' with constant v (Case 3 in Table 6-1). As the ϕ'

value goes from 10° to 40°, the K_{ps} (= K) values along the VCL [Fig. 6-7(a)] tend to decrease, but remain close to K_a (to a lesser extent for ϕ' = 40°), except very near the fill top. Near the RW, Fig. 6-7(b) shows that K_{ps} equal K_a. Fig. 6-7(c) shows that the K values near the RW stay close to Jaky's K_0 for ϕ' = 10°. As the ϕ' value increases, the K value tends to diverge from K_0 and move towards K_a; $K \approx K_a$ when ϕ' = 40°. It is also seen that the K value (about 0.4) near the RW is between K_0 and K_a for ϕ' = 30°, as shown above in Case 1 [Fig. 6-5(b)] and Case 2 [Fig. 6-6(b)].

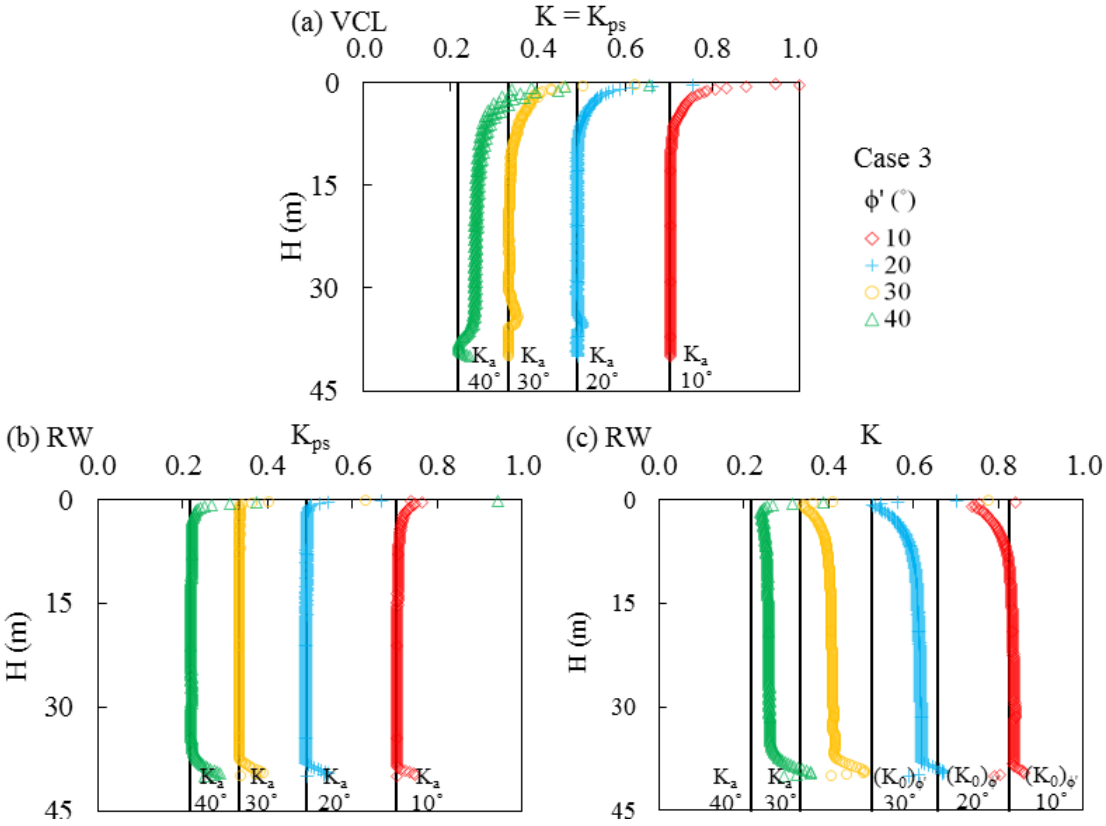

Figure 6-7: Vertical profiles of K and K_{ps} (a) along the VCL and (b and c) near the RW for different ϕ' values with constant ν value (Case 3 in Table 6-1)

Effect of Poisson's ratio ν

Fig. 6-8 illustrates the vertical profiles of stress ratios K and K_{ps} along the VCL [Fig. 6-8(a)] and near the RW [Figs. 6-8(b and c)] for different values of Poisson's ratio ν (constant ϕ' = 30°; Case 4 in Table 6-1). Fig. 6-8(a) shows that the value of K_{ps} (= K) along the VCL remains nearly constant and close to K_a, for a ν value ranging from 0.001 to 0.2, except very near the fill surface; for ν > 0.2, the K value along the VCL becomes a function of Poisson's ratio and close to $(K_0)_\nu$ [Eq. (6.4)], except very near the surface and base of the backfilled opening.

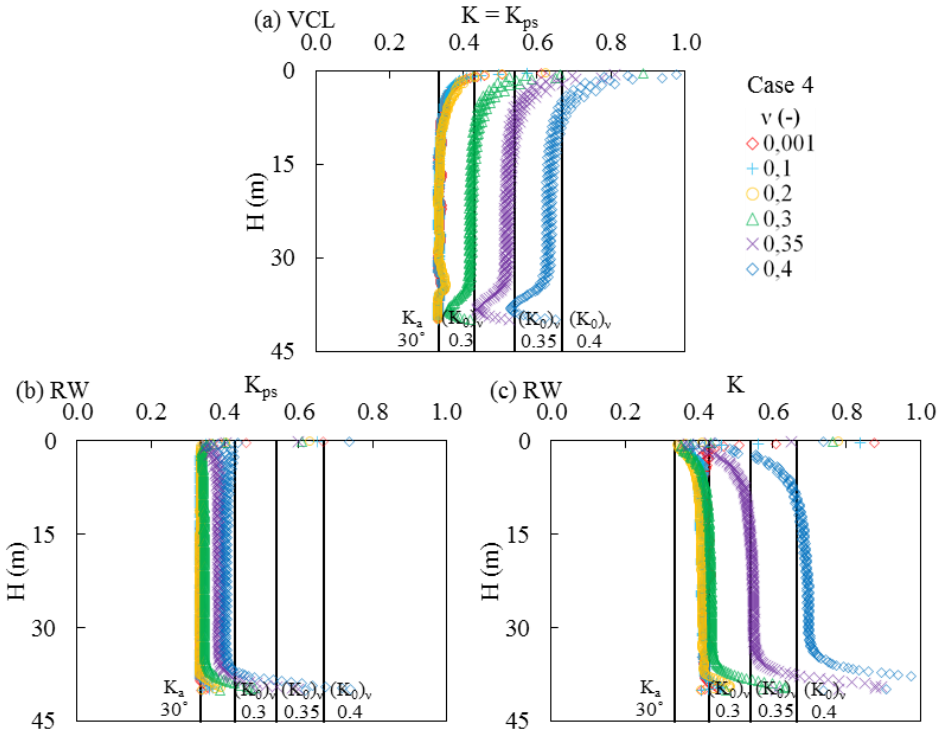

Figure 6-8: Vertical profiles of K and K_{ps} (a) along the VCL and (b and c) near the RW for different ν values when disconnected with ϕ' value (Case 4 in Table 6-1).

Near the RW, Fig. 6-8(b) shows that the K_{ps} values are almost constant and close to K_a for $\nu \leq 0.3$. This is similar to the K_{ps} near the RW in Cases 1 to 3 (with $\nu = 0.2$) presented above. The K_{ps} values slightly increase (still close to K_a) for $\nu > 0.3$. The value of K near the RW shown in Fig. 6-8(c) indicates that it remains nearly constant for $\nu \leq 0.3$ and close to $(K_0)_\nu$ obtained with $\nu = 0.3$. When ν is above 0.3, the K values tend to increase and can be estimated by $(K_0)_\nu$. It is also found that the K value approaches 1.0 when the value of ν is near 0.5; this corresponds to a hydrostatic (isotropic) stress state (results not shown here; see additional results presented in Appendix H).

6.4.2 Calculations with related ϕ' and ν values

The calculations presented above are repeated here for cases where the values of ν and ϕ' are related to each other [through Eq. (6.5) with $\lambda = 1$].

Effect of opening width *B*

Fig. 6-9 illustrates the variations of stress ratios K and K_{ps} along the VCL [Fig. 6-9(a)] and near the RW [Fig. 6-9(b)] as a function of the width B when ϕ' and ν are connected [Eq. (6.5) with $\lambda = 1$; Case 1' in Table 6-1]. Fig. 6-9(a) shows that the values of K_{ps} (= K) along the VCL can be

represented by coefficient K_0 [Eq. (6.3) or (6.4); $(K_0)_v = (K_0)_{\phi'}$], except near the surface and base of the backfill. Fig. 6-9(b) shows that the values of K near the RW are also close to K_0 while those of K_{ps} near the RW are close to K_a. These results also indicate that the stress ratios in backfilled openings are not sensitive to the increase in the opening width.

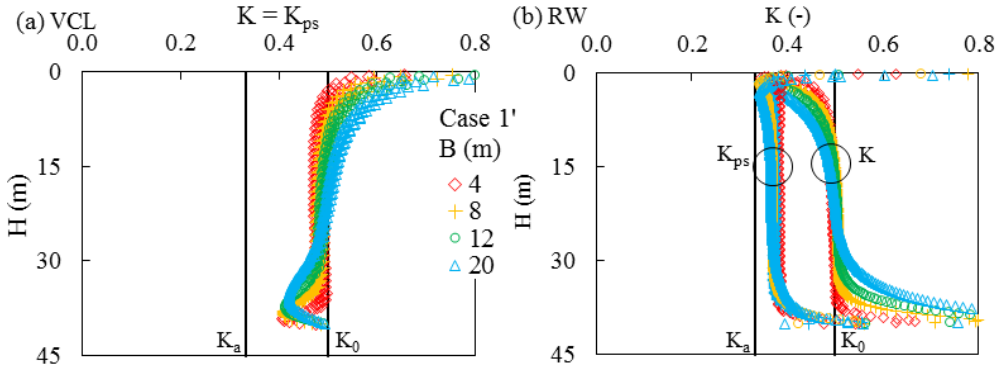

Figure 6-9: Vertical profiles of K and K_{ps} (a) along the VCL and (b) near the RW for different B values for related v and ϕ' values (Case 1' in Table 6-1)

Effect of modulus *E*

Fig. 6-10 presents the vertical profiles of K_{ps} and K along the VCL [Fig. 6-10(a)] and near the RW [Fig. 6-10(b)] as a function of Young's modulus E (related ϕ' and v; Case 2' in Table 6-1). The K values along the VCL [Fig. 6-10(a)] and near the RW [Fig. 6-10(b)] are almost superposed with K_0 when the value of E changes from 10 MPa to 1 GPa. But the K_{ps} near the RW is close to K_a, as shown in Fig. 6-10(b). These results indicate that the Young's modulus has little effect on the earth pressure coefficient. Again, this is because the stresses in backfilled openings are not sensitive to the E value (from 10 MPa to 1 GPa).

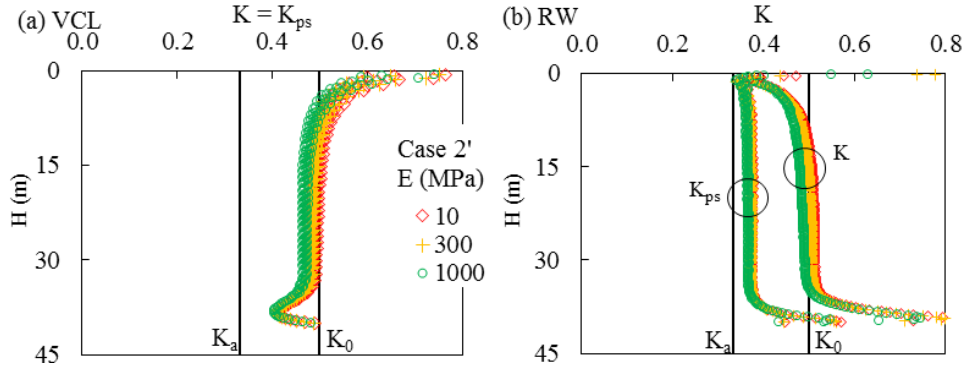

Figure 6-10: Vertical profiles of K and K_{ps} (a) along the VCL and (b) near the RW for different E values for related values of v and ϕ' (Case 2' in Table 6-1)

Effect of ϕ' and v

Fig. 6-11 shows the variations of stress ratios along the VCL [Fig. 6-11(a)] and near the RW [Figs. 6-11(b and c)] (Case 3' in Table 6-1), when ϕ' increases from 10° to 40° [and v goes from 0.452 to 0.263 through Eq. (6.5) with $\lambda = 1$]. The stress ratios ($K_{ps} = K$) along the VCL [Fig. 6-11(a)] is reduced, but correlate quite well with K_0. Fig. 6-11(b) shows that the principal stress ratio K_{ps} near the RW tends to exceed slightly K_a. Fig. 6-11(c) indicates that coefficient K near the RW tends to decrease with the increase in ϕ' (and decrease in v); the value of K agrees very well with K_0.

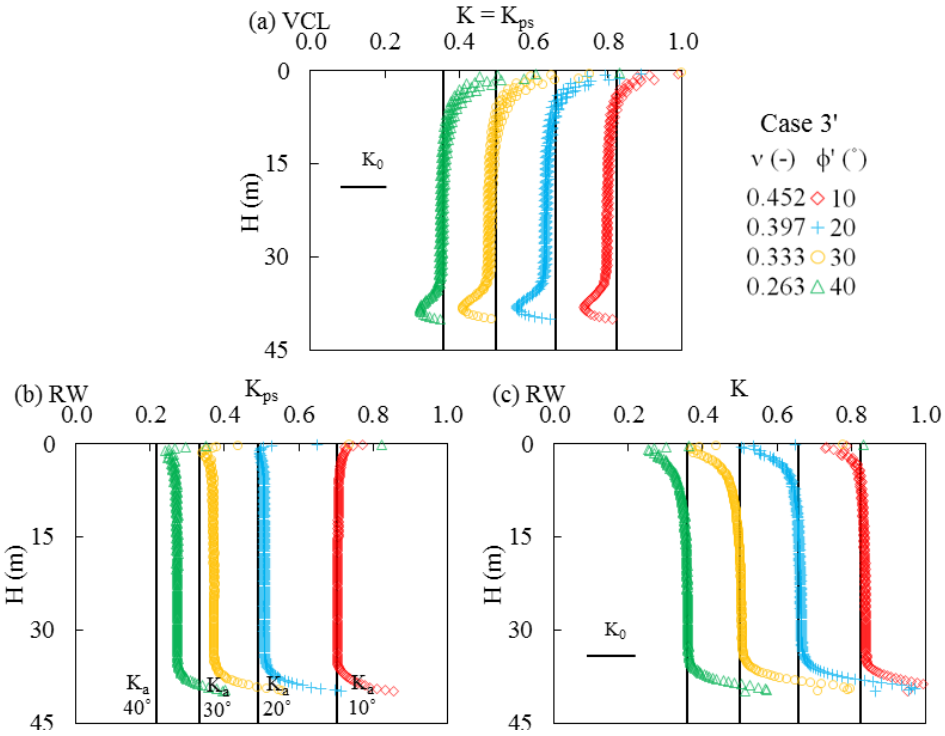

Figure 6-11: Vertical profiles of K and K_{ps} (a) along the VCL and (b and c) near the RW for different ϕ' values related to v values (Case 3' in Table 6-1)

Fig. 6-12 illustrates the distributions of K_{ps} and K across opening width B at different heights (for related v and ϕ'; Case 0' in Table 6-1). Fig. 6-12(a) shows that the values of K_{ps} change gradually from K_0 near the center to a value close to K_a near the walls [see also Fig. 6-14(a) below]; this variation is due to the frictional shearing along the rock walls, which affects the magnitude and orientation of the principal stresses. Fig. 6-12(b) indicates that the values of K remain close to K_0 across the opening width, which is in agreement with the simulations results obtained by Jahanbakhshzadeh et al. (2016).

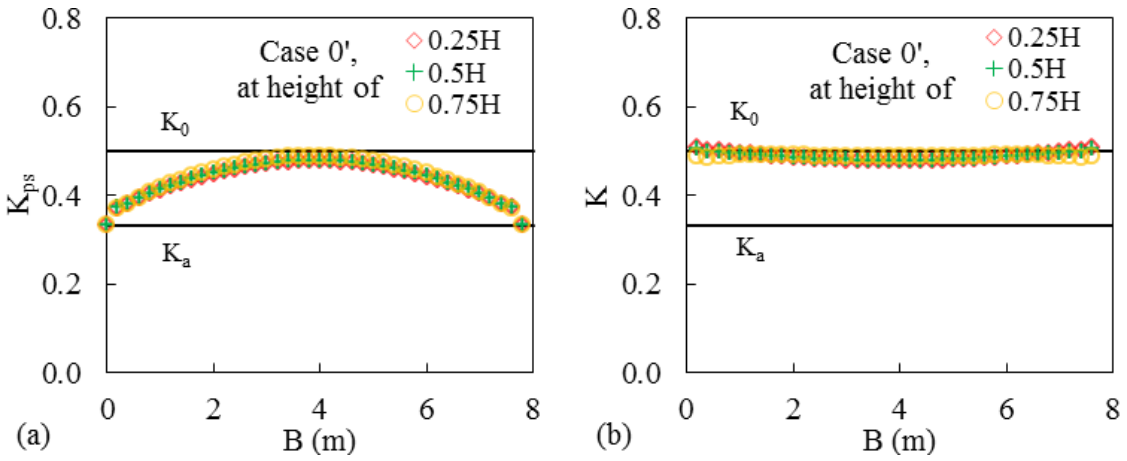

Figure 6-12: Distributions of (a) K_{ps} and (b) K across width B at different heights for related values of ν and ϕ' (Case 0' in Table 6-1)

6.4.3 Modelling with interface elements

The results presented above have been obtained from numerical simulations conducted without interface elements between the fill and rockwalls. Additional simulations are performed to investigate the effect of the interface on the stress ratios in backfilled openings.

The stiffness of the interface elements between the backfill and rockwalls are determined by the approach suggested in the FLAC manual (Itasca 2011) to ensure stable numerical results (e.g., Liu et al. 2016b). The tensile strength and cohesion of the interfaces are nil. The characteristics of fill and interfaces used in simulations conducted with interface elements (Cases 5 and 4') are detailed in Table 6-1. The interface friction angle δ' can vary from zero (frictionless interface) to the value of the backfill internal friction angle ϕ' (rough interfaces). In various civil engineering applications, pressure estimation is often made by assuming $\delta' = 2\phi'/3$ along fill-wall interfaces (e.g., Bowles 1988; Terzaghi et al. 1996). In underground mines, the rough interfaces are commonly encountered in stopes due to production blasting (with $\delta' = \phi'$). The effect of angle δ' on stress ratios (K_{ps} and K) near the center and walls of a vertical backfilled opening is analyzed for both independent and related values of ϕ' and ν.

In the case of independent ϕ' and ν, the numerical results indicate that stress ratios along the VCL are insensitive to δ' value and remains almost the same as these calculations without interface elements [see Figs. (6-5)-(6-8)]. These are not presented here. The stress ratios near the walls may nonetheless be influenced by the value of angle δ'. Fig. 6-13 illustrates the vertical profiles

of principal stress ratios K_{ps} near the walls when ν = 0.2 and 0.3 (for constant ϕ' = 30°), for different values of δ' (Case 5 in Table 6-1). It is seen that for $\delta' = \phi'$, the value of K_{ps} near the walls is close to K_a, which is similar to that obtained from Case 4 without interfaces [Fig. 6-8(b)]. When the δ' value decreases from ϕ' to zero, the value of K_{ps} near the walls remains close to K_a for ν = 0.2 [Fig. 6-13(a)], while it tends to rise and finally approach coefficient $(K_0)_\nu$ in the case of ν = 0.3 [Fig. 6-13(b)].

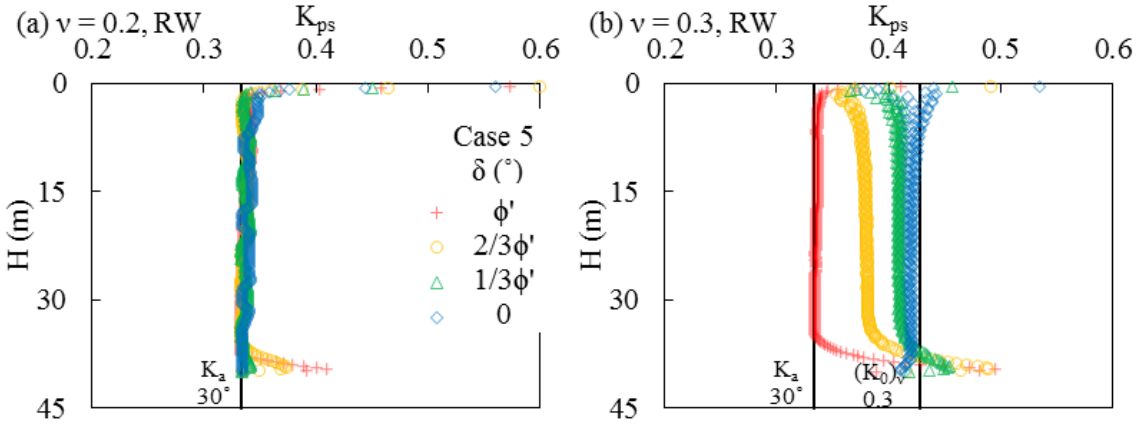

Figure 6-13: Vertical profiles of K_{ps} (= σ'_3/σ'_1) near the walls (RW) as a function of angle δ' for ν = (a) 0.2 and (b) 0.3, obtained with constant values of ϕ' = 30° (Case 5 in Table 6-1)

For related ν and ϕ', the ratio K_{ps} along the VCL and K near the walls are found to be independent of angle δ' and remains almost identical to cases obtained without interface elements (presented above in Figs. (6-9)-(6-11). These are not presented here. However, the ratio K_{ps} near the walls is affected by the δ' value. Fig. 6-14 shows the vertical profiles of principal stress ratios K_{ps} near the RW as a function of ν and ϕ' for different values of δ' (when ϕ' and ν are related; Case 4' in Table 6-1). For $\delta' = \phi'$, Fig. 6-14(a) shows very similar results to these in Fig. 6-11(b) for the simulations without interfaces. The results (not shown) also indicate that the values of K_{ps} vary gradually from K_a near the walls to a value close to K_0 near the center of the opening [very similar to that shown in Fig. 6-12(a)]. As the δ' value decreases from ϕ' to zero, the K_{ps} value near the walls tend to approach coefficient $(K_0)_\nu$ (for the whole range of ϕ' and ν). In the cases of $\delta' = 1/3\phi'$ and $\delta' = 0$, the values of K_{ps} remain close to $(K_0)_\nu$ across the width of the opening.

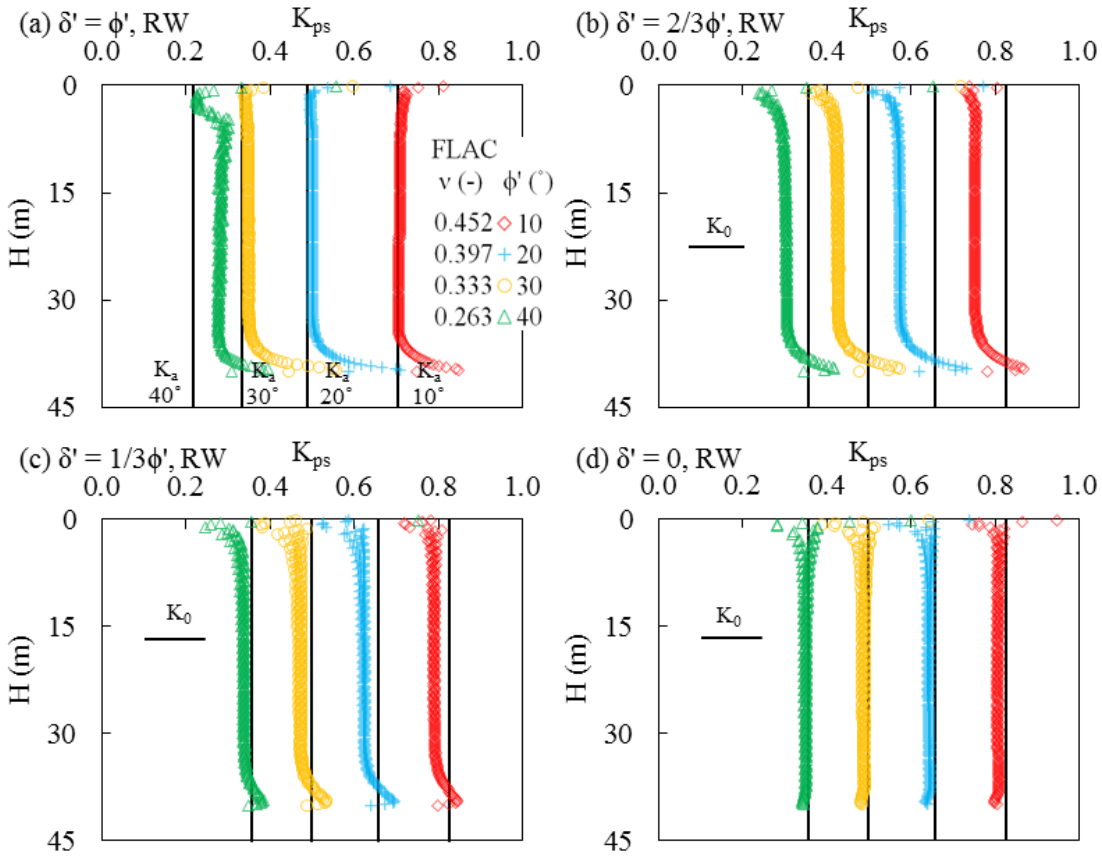

Figure 6-14: Vertical profiles of K_{ps} (= σ'_3/σ'_1) near the walls (RW) as a function of ν for angle $\delta' = \phi'$ (a), $2/3\phi'$ (b), $1/3\phi'$ (c) and 0 (d), obtained with related values of ν and ϕ' (Case 4' in Table 6-1)

It is seen from Figs. 6-13 and 6-14 (and other results not shown here) that the stress ratios obtained with $\delta' = 1/3\phi'$ and $\delta' = 0$ are quite close to each other. It is also found that the principal stress ratio K_{ps} near walls is close to the earth pressure coefficient K once the angle δ' is below $(1/3)\phi'$. This is due to the smaller rotation of the principal stresses with the reduced δ', thereby causing principal stresses to act in the vertical and horizontal directions even near rock walls.

6.5 Discussion

6.5.1 Backfill at an at-rest or active state along the VCL of the opening?

The results presented above indicate that when the value of ν is disconnected from that of ϕ' (= 30°), the stress ratio is very close to Rankine's active earth pressure coefficient K_a for $\nu \leq 0.2$, while it approaches $(K_0)_\nu$ [Eq. (6.4)] for $0.2 < \nu \leq 0.4$. Similar results have been reported for the

case of active state by Sobhi et al. (2014, 2016). For related values of v and ϕ', the stress ratio K (= K_{ps}) along the VCL of the opening agrees very well with the at-rest pressure coefficient K_0.

These results can be explained by analyzing the stress state along the VCL of the opening during filling. With the Mohr-Coulomb elasto-plastic model, the backfill initially behaves as a linear elastic material. Upon placement, the vertical stress along the VCL σ'_v may approach the vertical stress based on the overburden, while the horizontal stress tends to approach $(K_0)_v\sigma'_v$ due to the stiff confining walls and linear elastic behavior of the backfill. For v = 0.2 and ϕ' = 30° (Cases 0, 1 and 2), $(K_0)_v$ = 0.25 and K_a = 0.33. Fig. 6-15 shows the stress states for the backfill along the VCL of the opening on the Mohr-Coulomb plane. The initial stress state based on the linear elastic model is ($0.25\sigma'_v$, σ'_v). Fig. 6-15 illustrates that the corresponding Mohr circle (with a diameter of $0.75\sigma'_v$) exceeds the Mohr-Coulomb yield envelop which defines the maximum diameter as $0.67\sigma'_v$ for an active state. Yielding (plasticity) takes place and the stress state has to change back onto the yield envelop. This explains well the active (yielding) state of the backfill associated with the Rankine's active earth pressure coefficient K_a. It is inferred that the active state appears if the values of ϕ' and v obey the following relationship defined by $(K_0)_v \le K_a$ (see Fig. 6-15):

$$v \le \frac{1-\sin\phi'}{2} \tag{6.6}$$

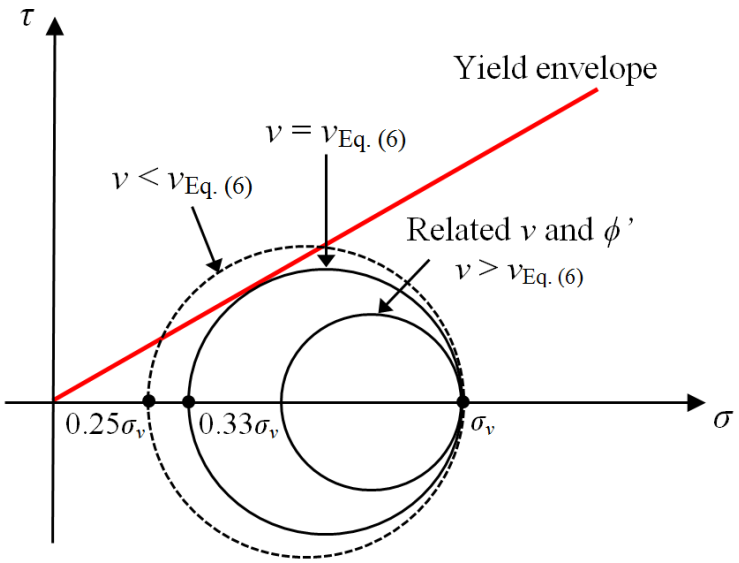

Figure 6-15: Mohr-Coulomb plane showing the stress states for the backfill along the VCL of the opening

When ν and ϕ' are related through Eq. (6.5) with $\lambda = 1$, $\nu = (1 - \sin\phi')/(2 - \sin\phi') > (1 - \sin\phi')/2$. Eq. (6.6) is not met and the Mohr circle is always below the Coulomb yield envelop (see Fig. 6-15). The fill along the VCL is then in an at-rest state (elastic) with K close to $(K_0)_\nu$. This explains well the at-rest state of the backfill when values of ν and ϕ' are related through Eq. (6.5) with $\lambda = 1$ (e.g., Jahanbakhshzadeh et al. 2016).

With a constant ν of 0.2, applying Eq. (6.6) leads to a critical value of $\phi' = 37°$. When $\phi' \leq 37°$, Eq. (6.6) is met and K should approach the Rankine's coefficient K_a. For $\phi' > 37°$, Eq. (6.6) is not satisfied and K should be close to K_0 based on the Poisson's ratio. These can be confirmed by the results illustrated in Fig. 6-16, which shows the vertical profiles of K (= K_{ps}) along the VCL for different values of ϕ' with constant ν (Case 3 in Table 6-1). For a constant $\phi' = 30°$, the backfill along the VCL tends to yield (K_{ps} close to K_a) for $\nu \leq 0.25$ given by Eq. (6.6) [see Fig. 6-8(a)].

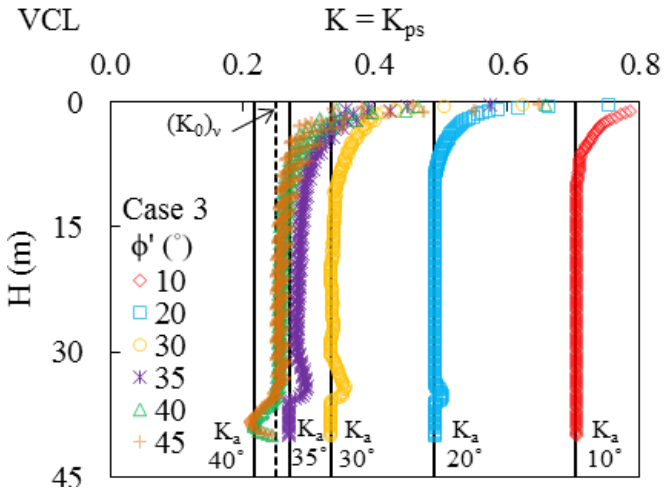

Figure 6-16: Vertical profiles of stress ratios $K_{ps} = K$ along the VCL for different ϕ' values with constant ν value (Case 3 in Table 6-1)

6.5.2 Relationship between ϕ' and ν

Numerical simulations are conducted here with both the commonly used assumption (i.e., independent ϕ' and ν) and the new consideration based on Eq. (6.5) with $\lambda = 1$, to help clarify the discrepancies reported in the literature on the state of backfill in vertical openings. The results presented above show that these two different assumptions can affect the simulated stress state (and stress ratios) in backfilled openings (also see Falaknaz et al. 2015a; Jahanbakhshzadeh 2016). In the light of these analyses, it could be argued that Eq. (6.5) with $\lambda = 1$ (Yang et al.

2016d; see also Eq. (A.9) in Appendix A) should be applied systematically for an elasto-plastic model (in numerical simulations) so a single (unique) value of K_0 is obtained (e.g., Falaknaz et al. 2015a; Liu et al. 2016b; Jahanbakhshzadeh 2016). Additional work is nonetheless ongoing to verify this assumption.

6.5.3 Final remarks

The results presented above indicate that near the opening walls, the K_{ps} value is close to K_a in all simulations conducted with both disconnected and related v and ϕ', for cases without interface elements and for rough walls (i.e., $\delta' = \phi'$). This indicates that the fill is approaching an active state, due in a large part to the severe shearing near the rock face (see also Fig. 6-14). More work is underway to better define the conditions leading to this phenomenon.

The numerical simulations are conducted here with dry cohesionless fill. The effect of pore water pressure and cohesion are thus neglected. The interface cohesion is nil when interface elements are used. The cohesion within the fill and along the interfaces can influence the stress state in backfilled openings (e.g., Li & Aubertin 2009e; Liu et al. 2016a, 2016b; Jahanbakhshzadeh 2016). In-situ measurements of Thompson et al. (2012) have also indicated that the K value may be evolving in the stope during backfilling, with pore pressure generation and dissipation, and cement curing. Additional work is required to evaluate the effect of these factors on stress ratios and fill state.

It should be mentioned that this numerical study is applicable to vertical or subvertical openings with small inclinations (i.e., $\leq 10°$). It is known that the stress state and the resulting earth pressure coefficient can be quite different in inclined openings, as shown by recent investigations (Li & Aubertin 2009e; Jahanbakhshzadeh 2016). Additional work is needed to assess the stress ratios and stress state (and associated mechanisms) in openings with inclined walls.

The results presented here correspond to very long openings, since the effect of the third dimension is not taken into account. It has been shown that the arching effect may be underestimated by 2D (plane strain) models (e.g., Li et al. 2005). More work is required to assess this aspect, to complement the results recently obtained by Jahanbakhshzadeh (2016).

6.6 Conclusions

Numerical analyses conducted with FLAC were used to investigate the dependence of the stress ratios ($K = \sigma'_h/\sigma'_v$ and $K_{ps} = \sigma'_3/\sigma'_1$) on various geometric and mechanical characteristics of backfilled openings, for both independent and related backfill parameters ϕ' and v. The results indicate that the simulated stress ratios and backfill state are mainly controlled by the relationship between the backfill Poisson's ratio v and internal friction angle ϕ'. The values of K and K_{ps} obtained from numerical simulations presented above are summarized in Table 6-2.

Table 6-2: Summary of stress ratios ($K_{ps} = \sigma'_3/\sigma'_1$; $K = \sigma'_h/\sigma'_v$) in backfilled openings obtained from numerical simulations.

Positions in the backfilled opening		**Vertical center line (VCL)**	**Rockwall (RW)**	
Stress ratios		$K_{ps} = K$	K_{ps}	K
Independent ϕ' and v	Without interface	$\approx K_a$ for $v \leq (1 - \sin\phi')/2$	$\approx K_a$	Dependent on ϕ' and v
	With interface $\delta' = \phi'$	$\approx (K_0)_v$ for $v > (1 - \sin\phi')/2$		
Related ϕ' and v	Without interface	$\approx K_0$	$\approx K_a$	$\approx K_0$
	With interface $\delta' = \phi'$			

Note: K_a is estimated from Eq. (6.2); $(K_0)_v$ is obtained from Eq. (6.4); K_0 is obtained from Eqs. (6.3) or (6.4).

For independent v and ϕ', the principal stress ratio K_{ps} (= K) along the VCL is close to Rankine's coefficient K_a when v and ϕ' obey Eq. (6.6) [i.e., $v \leq (1 - \sin\phi')/2$], suggesting that the backfill is approaching an active state. When $v > (1 - \sin\phi')/2$, the K_{ps} (= K) along the VCL is close to the at-rest pressure coefficient K_0 obtained from Eq. (6.4). Near walls, the value of K_{ps} is independent of v and remain very close to K_a, while the value of K (= σ'_h/σ'_v) depend on the values of v and ϕ'.

In the case of interrelated parameters, the ratio K_{ps} (= K) along the VCL correlates quite well with K_0 and the value of K_{ps} near walls appears to be close to K_a. These indicate that the backfill state varies from an at-rest state near the center to an active state close to walls. The K value near walls is close to K_0.

Although two different assumptions were used above, it is deemed highly preferable to use related values of ϕ' and v to ensure a unique (consistent) definition of K_0. The correlation

between ϕ' and v [Eq. (6.5) with λ equal or close to 1; see also Eq. (A.9) in Appendix A] should be applied systematically in numerical analyses with elasto-plastic models.

Additional simulations results obtained with interface elements indicate that the stress ratios (K_{ps} and K) near the center of the backfilled opening are independent of interface roughness and almost identical to those obtained without interfaces for both independent and related parameters. However, these two stress ratios may be different for less rough or smooth interfaces near walls.

Acknowledgements

The authors would like to acknowledge the financial support from the Natural Sciences and Engineering Research Council of Canada (NSERC 402318), Institut de recherche Robert-Sauvé en santé et en sécurité du travail (IRSST 2013-0029), Fonds de recherche du Québec - Nature et Technologies (2015-MI-191676), and industrial partners of the Research Institute on Mines and the Environment (RIME UQAT-Polytechnique; http://rime-irme.ca/).

6.7 References

Al-Hussaini, M., and Townsend, F. (1975). "Stress deformation of sand under K_0 conditions." *Proc., 5th PanAmerican Conf. on Soil Mech. and Found. Eng.*, Vol. 1, Buenos Aires, 129-136.

Askew, J., McCarthy, P. L., and Fitzgerald, D. J. (1978). "Backfill research for pillar extraction at ZC/NBHC." *Proc., 12th Can. Rock Mech. Symp.* on *Mining with Backfill*, Sudbury, 100-110.

Aubertin, M., Li, L., Arnold, S., Belem, T., Bussière, B., Benzaazoua, M., and Simon, R. (2003). "Interaction between backfill and rock mass in narrow stopes." *Proc., Soil and Rock America 2003*, Vol. 1, Verlag Glückauf Essen (VGE), Essen, Germany, 1157-1164.

Aysen, A. (2005). *Soil mechanics: basic concepts and engineering applications*. CRC Press.

Bardet, J. P. (1997). *Experimental soil mechanics*. Prentice Hall, Upper Saddle River.

Bishop, A. W. (1958). "Test requirements for measuring the coefficient of earth pressure at-rest." *Proc., Brussels Conf. on Earth Pressure Problems*, Brussels, Belgium, 2-14.

Blight, G. E. (1984). "Soil mechanics principles in underground mining." *J. Geotech. Eng.*, 110(5), 567-581.

Blight, G. E. (1986). “Pressure exerted by materials stored in silos. Part I: Coarse materials.” *Géotechnique*, 36(1), 33-46.

Bowles, J. E. (1988). *Foundation analysis and design*. McGraw-Hill, New York.

Briaud, J. L. (2013). *Geotechnical engineering: unsaturated and saturated soils.* John Wiley and Sons.

Brooker, E. W., and Ireland, H. O. (1965). “Earth pressures at-rest related to stress history.” *Can. Geotech. J*., 2(1), 1-15.

Caceres, C. (2005). “Effect of backfill on longhole open stoping.” Master Thesis, University of British Columbia, Vancouver.

Coulthard, M.A., and Dight, P.M. (1979). “Numerical analysis of fill pillar stability - two-dimensional calculations of initial stresses.” Technical report, *CSIRO*, Division of Applied Geomechanics.

Coulomb, C. A. (1776). “An attempt to apply the rules of maxima and minima to several problems of stability related to architecture.” *Mémoires de l’Académie Royale des Sciences*, 7, 343-382.

Daramola, O. (1980). “On estimating K_0 for overconsolidated granular soils.” *Géotechnique*, 30(3), 310-313.

Das, B. M. (2010). *Geotechnical engineering handbook*. J. Ross Publishing.

Duncan, J. M., and Bursey, A. (2013). “Soil modulus correlations.” *Proc., Found. Eng. in the Face of Uncertainty: Honoring Fred H. Kulhawy*, ASCE, 321-336.

Duncan, J. M., Williams, G. W., Sehn, A. L., and Seed, R. B. (1991). “Estimation earth pressures due to compaction.” *J. Geotech. Eng.*, 117(12), 1833-1847.

Fahey, M., Helinski, M., and Fourie, A. (2009). “Some aspects of the mechanics of arching in backfilled stopes.” *Can. Geotech. J*.,46, 1322-36.

Falaknaz, N. (2014). “Analysis of the geomechanical behavior of two adjacent backfilled stopes based on two and three dimensional numerical simulations.” PhD thesis. Polytechnique Montréal, Montréal.

Falaknaz, N., Aubertin, M., and Li, L. (2015a). "Numerical investigation of the geomechanical response of adjacent backfilled stopes." *Can. Geotech. J.*, 52(10), 1507-1525.

Gould, J. P. (1970). "Lateral pressures on rigid permanent structures." *Proc.*, Lateral Stresses in the Ground and Design of Earth-Retaining Structures, ASCE, 219-269.

Helinski, M. (2007). "Mechanics of mine backfill." Ph.D. thesis. University of Western Australia, Perth, Australia.

Hughes, P. B., Pakalnis, R., Hitch, M., and Corey, G. (2010). "Composite paste barricade performance at Goldcorp Inc. Red Lake Mine, Ontario, Canada." *Int. J. Min. Reclam. Environ.*, 24(2), 138-150.

Itasca. (2011). *FLAC-Fast lagrangian analysis of Continua; User's Guide*, Itasca Consulting Group. Minneapolis.

Jahanbakhshzadeh, A. (2016). "Analyse du comportement géomécanique des remblais miniers dans des excavations souterraines inclinées." PhD thesis, Polytechnique Montréal, Montréal.

Jahanbakhshzadeh, A., Aubertin, M., and Li, L. (2016). "A new analytical solution for the stress state in inclined backfilled mine stopes." *Geotech. Geol. Eng.*, Submitted in April 2016.

Jaky, J. (1944). "The coefficient of earth pressure at-rest." *Journal of the Society of Hungarian Architects and Engineers*, 78(22), 355-358.

Jaky, J. (1948). "Pressure in silos." *Proc., 2nd Int. Conf. on Soil Mech. and Found. Eng.*, Vol. 1, Rotterdam, 103-107.

Janssen, H. A. (1895). "Versuche uber getreidedruck in silozellen." *Zeitschrift des Vereines Deutscher Ingenieure*, 39(35), 1045-1049.

Ladd, C. C., Foott, R., Ishihara, K., Schlosser, F., and Poulos, H. G. (1977). "Stress-deformation and strength characteristics." *Proc. 9th Int. Conf. on Soil Mech. and Found. Eng.*, Vol. 2, Tokyo, 421-494.

Li, L., Aubertin, M., and Belem, T. (2005). "Formulation of a three dimensional analytical solution to evaluate stresses in backfilled vertical narrow openings." *Can. Geotech. J.*, 42(6), 1705-1717.

Li, L., and Aubertin, M. (2008). "An improved analytical solution to estimate the stress state in subvertical backfilled stopes." *Can. Geotech. J.*, 45(10), 1487-1496.

Li, L., and Aubertin, M. (2009a). "Influence of water pressure on the stress state in backfill with cohesionless stopes." *Geotech. Geol. Eng*., 27(1), 1-11.

Li, L., and Aubertin, M. (2009b) "A three-dimensional analysis of the total and effective stresses in submerged backfilled stopes." *Geotech. Geol. Eng*., 27(4), 559-569.

Li, L., and Aubertin, M. (2009e). "Numerical investigation of the stress state in inclined backfilled stopes." *Int. J. Geomech.*, 9(2), 52-62.

Li, L., and Aubertin, M. (2010). "An analytical solution for the nonlinear distribution of effective and total stresses in vertical backfilled stopes." *Geomech. Geoeng.*, 5(4), 237-245.

Li, L., Aubertin, M., Simon, R., Bussière, B., and Belem, T. (2003). "Modelling arching effects in narrow backfilled stopes with FLAC." *Proc., 3th Int. FLAC Symp.*, Sudbury, Canada, 211-219.

Liu, G., Li, L., Yang, X., and Guo, L. (2016a). "A numerical analysis of the stress distribution in backfilled stopes considering nonplanar interfaces between the backfill and rock walls." *Int. J. Geotech. Eng.*,10(3), 271-282.

Liu, G., Li, L., Yang, X., and Guo, L. (2016b). "Numerical analysis of stress distribution in backfilled stopes considering interfaces between the backfill and rock walls." *Int. J. Geomech.*, 06016014.

Marston, A. (1930). "The theory of external loads on closed conduits in the light of latest experiments." Bulletin 96, Iowa Engineering Experiment Station, Ames, Iowa.

Mayne, P. W., and Kulhawy, F. H. (1982). "K_0-OCR relationships in soil." *Journal of the Geotechnical Engineering Division*, 108(GT6): 851-872.

McCarthy, D. F. (2007). *Essentials of soil mechanics and foundations: basic geotechnics*. 7th edition, Prentice Hall.

Mesri, G., and Hayat, T. M. (1993). "The coefficient of earth pressure at-rest." *Can. Geotech. J.*, 30, 647-666.

Michalowski, R. L. (2005). “Coefficient of earth pressure at-rest.” *J. Geotech. Geoenviron. Eng.*, 131, 1429-1433.

Morgenstern, N. R., and Eisenstein, Z. (1970). “Methods of estimating lateral loads and deformations.” *Proc.*, Lateral Stresses in the Ground and Design of Earth-Retaining Structures. ASCE, 51-102.

Pirapakaran, K., and Sivakugan, N. (2007a). “Arching within hydraulic fill stopes.” *Geotech Geologic Eng*, 25(1), 25-35.

Pirapakaran, K., and Sivakugan, N. (2007b). “A laboratory model to study arching within a hydraulic fill stope.” *Geotech Test J*, 30(6), 496-503.

Rajeev, P., Sumanasekera, P. R., and Sivakugan, N. (2016). “Lateral variation of the vertical stress in underground mine stopes filled with granular backfills.” *Geotech. Geol. Eng*., 34(2), 481-492.

Rankine, W. M. (1857). “On the stability of loose earth.” *Philosophical Transactions of the Royal Society of London*, 147, 9-27.

Singh, S., Sivakugan, N., and Shukla, S. K. (2010). “Can soil arching be insensitive to ϕ?” *Int. J. Geomech.*, 10(3), 124-128.

Singh, S., Shukla, S. K., and Sivakugan, N. (2011). “Arching in inclined and vertical mine stopes.” *Geotech. Geol. Eng*., 29, 685-693.

Sivakugan, N., and Das, B. M. (2009). *Geotechnical engineering: a practical problem solving approach*. J. Ross Publishing.

Sobhi, A. M., Li, L., and Aubertin, M. (2014). “Numerical investigation of the lateral earth pressure coefficient along the VCL of vertical backfilled stopes.” *Proc., 67th Can. Geotech.Conf.*, Regina, SK, Canada.

Sobhi, A. M., Li, L., and Aubertin, M. (2016). “Numerical investigation of the earth pressure coefficient along the center line of backfilled stopes.” *Can. Geotech. J.*, available online.

Talesnick, M. L. (2012). “A different approach and result to the measurement of K_o of granular soils.” *Géotechnique*, 62(11), 1041-1045.

Terzaghi, K. (1943). *Theoretical soil mechanics*. John Weily& Sons, New York.

Terzaghi, K., Peck R. B., and Mesri G. (1996). *Soil mechanics in engineering practice*. John Wiley & Sons.

Thompson, B. D., Grabinsky, M. W., and Bawden, W. F. (2012). "In situ measurements of cemented paste backfill at Cayeli Mine." *Can. Geotech. J.*, 49(7), 755-772.

Ting, C. H, Shukla, S., and Sivakugan, N. (2011). "Arching in soils applied to inclined mine stopes." *Int. J. Geomech*., 29-35.

Ting, C. H, Sivakugan, N., Read, W., and Shukla, S. K. (2014). "Analytical expression for vertical stress within an inclined mine stope with non-parallel walls, *Geotech Geol Eng*., 32, 577-586.

Winch, C. (1999). "Geotechnical characteristics and stability of paste backfill at BHP Cannington Mine." B. E. Hons Thesis, James Cook University, Townsville.

Yang, P. Y., Li, L., Aubertin, M., and Tiwari, A. (2016d). "An investigation of the relationships between K_0, ϕ' and v for granular materials." To be submitted. Main results are presented in Appendix A.

CHAPTER 7 SUMMARY AND DISCUSSION

7.1 Summary of main results

It is recalled that the primary elements (presented above) of this project include:

- A brief review of major underground mining methods employing backfill, mine backfills and barricades.
- A comprehensive review of analytical and numerical analyses of the stress state and stability of backfilled stopes, and stress measurements in backfilled stopes and drifts;
- Analytical and numerical analyses of the evolution of the water table and pore water pressure (PWP) in stopes with hydraulic fill (HF);
- Analytical and numerical analyses of the stability of waste rock barricades;
- Analytical and numerical analyses of the stability of side-exposed cemented fills;
- Numerical study of the earth pressure coefficient K and principal stress ratio K_{ps} in backfilled openings.

The literature review (Chapter 2) indicated that there are many uncertainties and gaps with respect to the understanding of the design of barricades and backfilled mine stopes before and after wall removal. The subsequent Chapters 3 - 6 present the main findings of this research to tackle the main issues raised in Chapter 2. These results are further summarized in the following.

To accomplish the objective of this research, the first step was to investigate the behavior of the backfill at very early time (shortly after the filling). The corresponding stress state (PWP, effective and total stresses) in the backfilled stope and drift is critical for barricade design. The investigation of pore water pressures during transient seepage in stopes with hydraulic fill is presented in Chapter 3, and the stability analysis of a waste rock barricade retaining paste backfill is presented in Chapter 4.

Hydraulic fills (HF) usually contain a substantial amount of water that drains rapidly upon placement, due to its high hydraulic conductivity and the hydraulic delivery method. In some HF filled mine stopes, a pond can first form above the fill surface and the water table is then lowered during drainage, with change in PWPs throughout the stope and drift. These are crucial factors

for barricade stability. Chapter 3 (Article 1) presents analytical solutions to predict the evolution of the water table and PWPs in the stope. These solutions are validated using simulations conducted with SEEP/W. The fill was simulated as a saturated material and the pond was modeled by "reservoir elements" proposed by Chapuis (2009). A free-draining barricade was considered. A simple analytical solution was also developed to estimate the initial height of the pond. Main influencing factors were assessed for the two approaches.

The results indicated that:

- The proposed analytical and numerical results agree well in terms of the evolution of the water table in the stope and PWPs at the stope base;
- The proposed analytical solutions may be used to roughly estimate the total time required to drain the pond;
- The pond formed on the top of the consolidated fill tends to induce high PWPs which can jeopardize the barricade stability;
- The effect of the reduced drift area in 3D conditions on the flow can be mimicked in 2D numerical modelling by reducing hydraulic conductivity k_{sat} of drift fill;
- The reduced drift area in 3D conditions tends to prolong the seepage through the drawpoint. 2D modelling without considering such effect tends to under predict the PWPs at early time in the stope and drift. The barricade design based on such 2D models may be non-conservative; and
- The PWP within HF is mainly controlled by the restricted flow due to the reduced drift area.

An improved analytical solution was proposed in Chapter 4 (Article 2) for designing waste rock barricades to retain paste backfill. Both the global and local stability were considered. This solution was calibrated and validated by simulations using FLAC. "Interface elements" were modeled between the barricade base and drift floor. Both the waste rock and interface elements were simulated as Mohr-Coulomb elastoplastic materials. The backfill pressure on the barricade was obtained from an isostatic stress based on the overburden shortly after placement.

The results of this study indicated that:

- The failure mechanisms, in terms of global sliding and internal local crushing, assumed in the theoretical model were confirmed by numerical results;
- A novel instability criterion, based on monitoring the displacement at the critical point on the barricade, can be used to judge more objectively the onset of instability of the waste rock barricade in numerical modelling;
- The failure mechanism of the waste rock barricade depends on the interface properties at the base. The global stability (sliding) governs the barricade design for relatively smooth rock surface when the interface friction angle δ is smaller than the critical interface friction angle δ_c. Otherwise, the internal local stability (top crushing) controls the barricade size for relatively rough rock faces;
- The proposed analytical solution was calibrated and then validated using 2D numerical modelling in plane strain conditions. The analytical solution for the local stability appears to be independent of the third dimension. For global stability, the 2D simulations correspond to the most conservative case where the contribution of side walls is neglected. A good agreement was obtained between the numerical and analytical solutions (without any calibration);
- The proposed models predict quite well the required barricade size for a typical range of geometric and mechanical characteristics, including the internal effective friction angle of waste rock ϕ' (from 34° to 45°), the backfill (plug) height H (from 7 to 15 m), and the drift/barricade height H_d (from 3 to 7 m).

The second step was to assess the behavior of exposed fill that interacts with the remaining sidewalls at longer time (a few weeks after filling). In open stoping, the stability of cemented fill upon vertical exposure in the primary stope is vital for the safety of production, further ore recovery and dilution. Chapter 5 (Article 3) presents a new analytical solution for predicting the required strength of mine backfill with a vertical exposure, based on a more realistic failure mode observed in numerical simulations and existing experimental tests. A combination of a vertical planar surface (from fill top) and an inclined (from fill base) sliding plane was considered. This solution was validated by simulations conducted using FLAC^{3D}. The cemented backfill was modeled as a Mohr-Coulomb elastoplastic material with a tensile strength cutoff T_0 of zero and

UCS/10. The T_0 value of zero corresponds to the most conservative assumption for the tensile strength of cemented fill. More representative T_0 value of UCS/10 is based on the laboratory data (Mitchell & Wong 1982; Sainsbury & Urie 2007). The internal friction angle ϕ' and Poisson's ratio v of backfill are related using Eq. (A.9) with $\lambda = 1.0$ proposed in Appendix A, based on the uniqueness and consistency of the at-rest earth pressure coefficient K_0.

This part of the project showed that:

- In numerical simulations, the failure of the exposed fill can be assessed explicitly using an instability criterion based on the displacements along the open face;
- The required strength of the cemented fill mainly depends on the stope length L (along the strike) and, to a much lesser extent, on the opening height H;
- The required strength of the cemented backfill is nearly insensitive to the stope width B (from 6 to 25 m; in the direction perpendicular to the exposed face), due to the development of tensile stresses near the top surface of the backfill;
- The required strength of the cemented backfill is reduced as the effective friction angle ϕ' of fill increases;
- There is a good agreement between the proposed analytical solution and numerical simulations for representative stope geometries ($9\text{ m} \leq L \leq 50\text{ m}$, $20\text{ m} \leq H \leq 80\text{ m}$, $6\text{ m} \leq B \leq 25\text{ m}$) and backfill properties ($0° < \phi' \leq 45°$); and
- The stresses and displacements obtained with small and large strains options (in the code FLAC^{3D}) are almost identical when the exposed fill is stable. Once failure occurs, the simulations for small strain cannot converge, while these for large strain yield very large displacements after showing bad geometry (twisted meshes).

Another critical issue was to evaluate the earth pressure coefficient K in cohesionless fills placed in vertical openings. This coefficient K is commonly involved in various aspects of mine backfill design, including the stress estimation in backfilled stopes, on barricades, and along the rock walls for an exposed fill body. The value of K can significantly affect the stress in backfilled openings obtained from analytical solutions.

Chapter 6 (Article 4) presents simulations results obtained with FLAC to evaluate the earth pressure coefficient K ($= \sigma'_h/\sigma'_v$) and principal stress ratio K_{ps} ($= \sigma'_3/\sigma'_1$) in backfilled openings. The simulations were performed with both independent and linked (through Eq. (A.9) with λ = 1.0; see Appendix A) values of internal friction angle ϕ' and Poisson's ratio v of the backfill. The backfill was simulated as a Mohr-Coulomb elastoplastic material. The values of stress ratios (K and K_{ps}) were investigated using various mechanical and geometric properties, including the opening width B (from 4 to 20 m), fill modulus E (from 10 MPa to 1GPa), ϕ' of backfill (from 10° to 40°), and v of backfill (from 0.001 to 0.4).

The results indicated that:

- For independent values of ϕ' and v, the principal stress ratio K_{ps} ($= K$) along the vertical centerline of opening is close to K_a when $v \leq (1 - \sin \phi')/2$, indicating that the fill may approach an active yielding state. For $v > (1 - \sin \phi')/2$, the K_{ps} ($= K$) value along the vertical centerline is close to K_0 [$= v/(1 - v)$]. Near opening walls, K_{ps} remains very close to K_a, while the value of K depends on the values of v and ϕ';

- For linked values of ϕ' and v, the principal stress ratio K_{ps} ($= K$) along the vertical centerline agrees well with K_0, and K_{ps} near the walls appears to be close to K_a. These indicate that the fill varies from an at-rest state to an active state from the center to walls. The value of K near walls is close to K_0;

- K_{ps} near the opening walls is always close to K_a for both independent and linked ϕ' and v. This indicates that the fill is approaching a yielding state, due probably to the high contrast in stiffness between the rock and backfill and severe shearing near the rock face;

- Additional simulations performed with interface elements (along the fill-wall contacts) show that values of K_{ps} and K near the opening center are independent of interface roughness and nearly identical to those obtained without interfaces, for both independent and related ϕ' and v. However, these two stress ratios might be different for less rough or smooth interfaces near the walls.

7.2 Discussion

7.2.1 Validation procedure for numerical modelling

In general, numerical modelling should be conducted in the following steps:

1) Validate the numerical code against reference solutions (e.g., Chapuis et al. 2001; Li & Aubertin 2009f), including sensitivity analysis of the element (mesh) size and domain to ensure stable numerical results;

2) Test the applicability/power of the numerical model against high quality experimental results obtained by laboratory or/and field measurements;

3) Apply the numerical code to analyze the problem to be treated; the sensitivity analysis of the element size and domain is required again for each new problem, always case by case.

Prior to simulating the proposed models, sensibility analyses were conducted to verify the validity and capacity (power/applicability) of the codes with respect to specific problems. The problem of cylindrical hole in an infinite Mohr-Coulomb material in plane strain conditions was used for testing FLAC and FLAC^{3D} (see Appendix C). The simulated results were compared with the analytical solution proposed by Salençon (1969). The variables checked are the mesh size, domain, cohesion, Young's modulus, tensile strength, and third dimension (for FLAC^{3D}). Permeability tests with variable-head were used to validate code SEEP/W, including the assessment of mesh size and time step (presented in Appendix B).

Sensibility analyses were then conducted using these codes (FLAC, FLAC^{3D} or SEEP/W) for each of the proposed models. These results are presented in Appendices D to G. In general, the results indicate that the conditions for numerical modelling are case specific and purpose-oriented in terms of the optimal domain, mesh (or element) size, and thickness of filling layer. For instance, the optimal mesh size of the backfill here is 0.5 × 0.5 m (FLAC^{3D}) for analyzing the stability of side-exposed backfill, while it is 0.008 m in the simulations performed by Liu et al. (2016c) to reproduce the physical tests of Mitchell et al. (1982) using FLAC^{3D}. The optimal mesh size of the backfill is 0.2 × 0.2 m (FLAC) for analyzing the stress ratios in backfilled openings. Also, the optimal thickness of filling layer, to minimize its effect on various outcomes, is 5 m for

assessing the stability of exposed cemented fill and 1 m for evaluating the stress ratios in backfilled openings.

The size of the domain in the numerical simulations depends on the targeted problem. In the numerical analyses of isolated backfilled stopes with or without exposures (Chapters 5 and 6), the effect of wall convergence was not considered. Accordingly, the displacements of rock walls induced by excavation were all set to zero before backfilling. The rock walls then behave as rigid confining walls during filling (due to low pressures exerted by the backfill on the stiff rock walls). In this case, the domain (i.e., size of rock mass) and also excavation sequence do not affect the simulated stress state in the backfill with one open face or all sides confined. However, the dependence of numerical outcomes on the size of the domain and excavation sequence should be checked when the effect of wall convergence is considered, particularly in cut-and-fill mining, multiple stoping and deep mining.

There is no one simple rule for numerical modelling and the validation procedure should be performed for each specific problem to ensure stable, reasonable and reliable outcomes. Experimental results are also needed to test the applicability/power of the numerical models. This part was not done in this study due to the lack of experimental data.

7.2.2 Discussion on main assumptions and limitations

This project presents a numerical analysis that evaluates the stress state and stress ratio in cohesionless backfill placed in underground openings. It also presents new analytical solutions for the evolution of the water table and PWP in stopes with hydraulic fill, for sizing waste rock barricades used to retain paste backfill, and for assessing the stability of side-exposed cemented fills. These analytical (closed form) solutions have been validated (in part) using numerical simulations conducted with various codes. The outcomes can help improve the design of the mine backfill and support structure (barricade). The good agreement between the proposed analytical solutions and numerical results indicates that these solutions can be useful, at least for the preliminary design. However, it should be recalled here that these analyses were based on many simplifying assumptions. The specific assumptions and limitations associated with each sub-objective have been addressed in the “Discussion” of each chapter (Chapters 3 - 6). The main assumptions and limitations are summarized below.

For analyzing the transient seepage in the backfilled stope with hydraulic fill and porous barricade, one-dimensional flow was assumed in the stope and drift, which was partly confirmed by the numerical simulations. The instantaneous filling and quick self-weight consolidation were also assumed in the theoretical development. More work is desirable to refine these assumptions using more realistic filling rate and other types of barricades.

The investigation of the evolution of the water table corresponds to the case when hydraulic fill is fully submerged (saturated) in the backfilled stope. This is the critical time for barricade stability due to the presence of a pond above the fill surface. However, the backfill can become partly unsaturated once the water table is below the fill surface. Then the evolution of stress state could be quite different from the saturated condition. More work is desirable.

The numerical analyses of the stability of waste rock barricades show that the slip surface for a local failure (near the top) is inclined, not horizontal as assumed in the theoretical model. This may partly explain the need of a calibration factor in the solution. Additional work using more realistic slip surface is underway. Also, 3D numerical modeling is ongoing to complete the validation of the proposed analytical solution.

In the theoretical model developed for analyzing the stability of exposed cemented fill, the slip surface was assumed to pass through the toe of the exposed fill face. However, numerical results indicate that this is not always the case. In some cases, the slip surface can form above the toe location. Also, numerical results from Falaknaz et al. (2016) revealed that the horizontal normal stresses along the three remaining sidewalls may be altered upon exposure, even for a stable cemented fill. In the proposed analytical solution, such stresses are calculated from the arching theory (Li et al. 2005; Li & Aubertin 2009b), without considering such variation. More work is required to improve these aspects.

The effect of pore water pressures were neglected in the analyses of stability of waste rock barricade. This is deemed representative due to the significant contrast in permeability between typical paste fill and waste rock. Such assumption is also regarded reasonable in the analyses of stability of exposed cemented fill, since the wall removal usually occurs a few weeks after filling (e.g., Emad et al. 2015b). It has been shown that positive pore water pressures would completely dissipate after a few days following the filling (e.g., Thompson et al. 2012; El Mkadmi et al. 2014).

Another limitation lies in the use of the elastoplastic Mohr-Coulomb model (with or without a tension cut-off) for backfill, as is commonly done. This may not always be representative of backfill behavior. It has been shown that a strain-softening model may better represent the true response of cemented backfill (e.g., Sainsbury & Urie 2007). El Mkadmi et al. (2014) have applied the modified Cam-Clay model to evaluate the sequential filling and consolidation of paste backfill placed in mine stopes. Li et al. (2010) have implemented the $MSDP_u$ (for Mises-Schleicher and Drucker-Prager unified; Aubertin et al. 2000) elastoplasticity criterion into FLAC to assess the stress state near underground backfill openings. These models should be used to better represent the backfill behaviors such as the volume change and tensile stresses.

Interface elements were not used in the numerical analyses of the stability of exposed cemented fill. In most cases, the neglect of the interfaces is reasonable as the rock wall surfaces are usually very irregular and rough, due to blasting. Yielding then mostly takes place near the wall in the fill (Aubertin et al. 2003; Liu et al. 2016b). However, the fill cohesion near the walls (and along the contact) may be reduced, as indicated by some experimental results (Fall & Nasir 2010; Koupouli et al. 2016); this situation was not considered here. Yielding may also occur along fill-wall contacts in cases of planar and smooth interfaces. In these cases, interface elements should be applied in the numerical simulations (e.g., Liu et al. 2016a).

Numerical simulations have been conducted with both the commonly used assumption (i.e., independent ϕ' and ν) and the new consideration based on Eq. (A.9) with $\lambda = 1$ (see Appendix A), to study the state of backfill in vertical openings. The results show that these two different assumptions can differ the simulated stress state (and stress ratios) in backfilled openings (see also Falaknaz et al. 2015a; Jahanbakhshzadeh 2016). The related ϕ' and ν through Eq. (A.9) with λ equal or close to 1 are preferred for an elastoplastic model (in numerical simulations) to ensure a single (unique) value of K_0. The validity of this relationship is partly confirmed by preliminary results on fine-grained materials (sands), but remains to be validated on waste rock and other coarse-grained cohesionless materials as shown in complementary results presented in Appendix A. Additional work is needed to further firmly validate the hypothesis on sands with high quality experimental data. High quality experimental data on waste rock and other cohesionless materials are equally necessary to determine the correlation factor λ.

Another limitation of this study relates to the use of cohesionless fill when analyzing the stress ratios in vertical backfilled openings. The effect of backfill cohesion is thus ignored. The interface cohesion is nil when interface elements were modeled. However, the cohesion within the fill and along the interfaces can affect the stress state in backfilled openings (e.g., Li & Aubertin 2009e; Liu et al. 2016a, 2016b; Jahanbakhshzadeh 2016). In-situ measurements of Thompson et al. (2012) have also indicated that the *K* value may be evolving in the stope during backfilling, with pore pressure generation and dissipation, and cement curing. Additional work is urged to evaluate the effect of these factors on stress ratios and backfill state.

Ideally, laboratory and in-situ measurements should be used to validate the proposed theoretical and numerical models. To the author's knowledge, however, there is no experimental data on the stability of waste rock barricade. A few in-situ data were reported by Hassani et al. (1998, 2001) on the stress variation during the filling of the primary stope and opening of the adjacent stope. Some field observations (e.g., Coulthard & Dight 1980) and laboratory centrifuge tests were performed on the stability of exposed fill (e.g., Smith et al. 1983; Mitchell 1986; Dirige & De Souza 2000, 2013). A few in-situ measurements were made on the earth pressure coefficient in the backfilled stope and drift (Hughes et al. 2010; Thompson et al. 2012). However, these do not provide the required information for validation. More experimental data are desirable to calibrate and validate the analytical and numerical models.

CHAPTER 8 CONCLUSIONS AND RECOMMENDATIONS

8.1 Conclusions

The primary objectives of this project were to assess the stress state in confined backfills and their interactions with the support structures (rock walls and barricades) from very early time (shortly after the filling) upon placement to longer time (a few weeks after the filling) at exposure. Some specific targets have been identified through a broad literature review that covers major underground mining methods with backfill, typical types of mine backfill and barricade, and the stress estimation and design methods of backfilled stopes through theoretical, numerical and experimental analyses. The main conclusions are recalled below.

The self-weight consolidation of hydraulic fill can take place fairly quickly upon placement because of its high permeability. Due to the reduced drift area (equivalent to a reduction of the fill permeability) or the non-efficiency of the barricade draining, a pond can be formed at the fill top surface. The pressure and total stresses exerted on the barricade are closely related to the evolution of the pond. This work fills a gap for barricade design in stopes with hydraulic fill. The theoretical and numerical (with SEEP/W) results show that the ponding may endanger the barricade safety due to high pore water pressure induced. The effect of the reduced drift area (in 3D) on the seepage can be approximated by reducing the fill permeability in the drift in 2D simulation. 2D modelling without considering the effect of the reduced drift area may underestimate the pore water pressure, thereby leading to less conservative barricade design.

The design of waste rock barricade is another challenge for mining engineers. The first theoretical improvement made by considering trapezoidal (more realistic) barricades leads to a large reduction in the minimum required top length of the barricade. This is mostly due to the stabilizing effect of the vertical component of the backfill load exerted on the upstream face of the trapezoidal barricade. However, the results based on such solution showed that the top length of the barricade can sometimes be unrealistic (zero or negative) for large shear strength along the barricade base. Further analyses showed that the local internal stability near the barricade top should be taken into account, thereby leading to a more complete analytical solution. Numerical modelling with FLAC was used to calibrate and validate the analytical solution. The onset of barricade failure was assessed using an instability criterion based on the displacements at the

critical locations on the barricade. Compared to commonly used instability criteria based on the yield state, shear strength ratios (like FS), the extent of displacement and tensile stresses, the proposed criterion allows a more objective judgment on the onset of the instability of the structure. The results indicate that the stability of waste rock barricades is controlled by the frictional strength of the interface along the barricade base. The global sliding and internal local crushing were confirmed by the numerical modelling. The former determines the barricade size for relatively smooth rock surfaces while the latter governs for rough rock faces. The results also show that the required top length of barricade increases with the increase of the fill (plug) height, while it tends to decrease with the increase of barricade/drift height. The good agreement between theoretical and numerical results indicates that the new analytical solutions can help size waste rock barricades.

The stability of cemented fill upon vertical exposure is another important issue closely associated with the safety and economy of mining. Numerical results obtained with FLAC^{3D} indicate that the sliding plane tends to change from planar at small fill cohesion to spoon-shaped (in 3D) at larger cohesion. A new and more objective (compared to those based on shear stress ratio or/and zone state) instability criterion, based on the displacement of the open face, was used to evaluate explicitly the failure of exposed backfill. The results indicate that the required strength of the cemented fill mainly depends on the length L and, to a much lesser extent, on height H of the stope, while it is almost insensitive to the stope width B due to the development of tensile stresses near the fill top surface. The required strength of the cemented fill reduces as the friction angle of fill increases. These numerical results led to a new analytical solution to estimate the minimum require strength of exposed cemented fill. The good agreement between the analytical and numerical calculations indicates that the new solution is an improvement over existing solutions.

The stability of backfilled stopes, sill pillars and sill mats depend on the stresses in the backfilled stopes. Stress estimation using analytical solutions needs the knowledge of earth pressure coefficient K. Numerical analyses performed with FLAC indicate that the stress ratios K_{ps} (= σ'_3/σ'_1) and K (= σ'_h/σ'_v) and the backfill state along the opening centerline are determined by the relationship between the internal friction angle ϕ' and Poisson's ratio v of the backfill and they are independent of interface roughness and almost identical to those obtained without interface elements along the fill-wall contacts. Near the opening walls, the value of K_{ps} is always close to

Rankine's active earth pressure coefficient K_a, due largely to the significant contrast in stiffness between fill and rock and severe shearing near the rock wall.

It is deemed preferable to relate the value of ϕ' to that of ν through Eq. (A.9) with $\lambda = 1$ (see Appendix A) to ensure a unique and consistent definition for the at-rest earth pressure coefficient K_0 in numerical modelling with elastoplastic models. Preliminary results on sands (shown in Appendix A) tend to confirm this hypothesis, while those on waste rock and other coarse rockfill materials point to a correlation with λ different than unity. More experimental data of high quality are required to further confirm this hypothesis.

8.2 Recommendations for further study

Numerical modelling becomes a power means to treat complicated problems. It has been commonly used in many engineering fields. It is important to ensure stable and reliable numerical outcomes. This can be done by following the steps described below:

1) Validate the numerical code against reference solutions, including the sensitivity analysis of the domain and element size to produce stable numerical outcomes;
2) Test the applicability/power of the numerical model against laboratory or/and in-situ measurements of high quality;
3) Apply the numerical code to analyze the problem to be treated; the sensitivity analysis of the domain and element size is also necessary for each new problem.

It is desirable to test the applicability/power of the commonly used Mohr-Coulomb elasto-plastic models (and others) with experimental data.

In addition to the results presented in this project, there are several areas where additional work is recommended, including:

- Numerical analyses presented above are applicable to vertical openings. It has been shown that the stress state and the resultant earth pressure coefficient can be quite different in inclined openings, as shown by recent investigations (Li & Aubertin 2009e; Sobhi et al. 2016; Jahanbakhshzadeh 2016). More work is needed to assess the stress state and stress ratios in openings with inclined walls;

- Emad et al. (2012, 2014) showed that the exposed cemented fill that is stable in static condition may fail under dynamic loads due to blasting. The backfill response under dynamic loading condition requires further study;
- It is also desirable to develop solutions for the evolution of total and effective stresses in the stope backfilled with hydraulic fill;
- More elaborate models and measurements are suggested to refine the assumptions made for analyzing the stability of exposed cemented backfill;
- This study only considers a vertical exposure on one side; it is relatively common to have multiple exposures during the secondary recovery;
- A tensile strength cutoff T_0 of zero and UCS/10 were used for the cemented fill in this study. More tests are required to measure the tensile strength of cemented backfill to better define the response of backfill under tension;
- It is preferable to use more realistic constitutive models to better represent the behavior of backfill in some conditions, such as non-negligible volume change and tensile stresses;
- It is useful to use interface elements between fill-wall contacts to better evaluate the response of exposed cemented fill;
- It is highly recommended to conduct laboratory and/or in-situ measurements to calibrate and validate the analytical and numerical methods;
- It is suggested to relate values of the internal friction angle ϕ' and Poisson's ratio v of the backfill for the uniqueness and consistency of K_0 with elastoplastic models. Direct measurements would be valuable to obtain more accurate and reliable values of ϕ' and v of the backfill;
- Neglecting the effect of cementation, the existing analytical solutions (based on arching theory) developed for fully drained conditions can be used to assess the long-term (drained) stress state of paste fill. The paste fill behaves like a heavy fluid shortly after the placement. During the transient period between the drained and undrained state, drainage and consolidation can take a fairly long time in paste fill due to its extreme low permeability. It

would be useful to develop new analytical solutions to account for the effect of consolidation on the stress state;

- The solutions of Mitchell et al. (1982) and their modifications (Li & Aubertin 2012, 2014; Li 2014a) all assume a uniform fill mass. However, filling of primary stopes is usually performed by a plug followed by a final pour. In most cases, the cement content of plug is higher than that of the final pour. It is thus useful to conduct research on this aspect, to complement the recent work of Li (2014b);
- It is also valuable to investigate the stability of cemented fill upon a horizontal exposure from the base;
- The investigation of backfill stress under unsaturated conditions (suction);
- It would be useful to better define the responses of backfill for complex conditions by considering the irregular (more realistic) stope geometries and realistic mining/filling sequence.

BIBLIOGRAPHY

Annor AB. (1999) A study of the characteristics and behaviour of composite backfill material. *Ph.D. Thesis*, McGill University, Montreal, Canada.

Aref K, Moss A & Durston K. (1992) Design issues for low moisture content backfill. *CIM Montreal*, 270-281.

Askew J, McCarthy PL & Fitzgerald DJ. (1978) Backfill research for pillar extraction at ZC/NBHC. *12th Can. Rock Mech. Symp.* on *Mining with Backfill*, Sudbury, 100-110.

Atlas Copco. (2014) http://multimedia.atlascopco.com/#1407263106031_3 (Accessed on 15 October 2014).

Aubertin M. (1999) Application de la Mécanique des Sols pour l'Analyse du Comportement des Remblais Miniers Souterrains. Short course (unpublished notes), *14e Colloque en Contrôle de Terrain*, Val-d'Or, Association Minière du Québec.

Aubertin M. (2013) Waste rock disposal to improve the geotechnical and geochemical stability of piles. *23rd World Mining Congress*, Montreal, QC, 8p.

Aubertin M, Bussière B & Chapuis RP. (1996) Hydraulic conductivity of homogenized tailings from hard rock mines. *Canadian Geotechnical Journal*, 33, pp. 470-82.

Aubertin M, Bussière B & Bernier L. (2002) *Environnement et Gestion des Rejets Miniers*. [CD-ROM]. Montréal, Quebec: Presses Internationales Polytechnique.

Aubertin M, Bussière B, James M, Mbonimpa M & Chapuis RP. (2011) Vers une mise à jour des critères de stabilité géotechnique pour la conception des ouvrages de retenue de résidus miniers. *Symp. Mines and Environnement*, Rouyn-Noranda, QC, CIM (CD-Rom), 38 p.

Aubertin M, Bussière B, Pabst T, James M & Mbonimpa M. (2016) Review of the reclamation techniques for acid-generating mine wastes upon closure of disposal sites. *Geo-Chicago 2016*, 343-358.

Aubertin M, Li L & Simon R. (2000) A multiaxial stress criterion for short term and long term strength of isotropic rock media. *International Journal of Rock Mechanics and Mining Sciences*, 37, 1169-1193.

Aubertin M, Li L, Arnold S, Belem T, Bussière B, Benzaazoua M & Simon R. (2003) Interaction between backfill and rock mass in narrow Stopes. *SoilRock2003: 12th Panamerican Conference on Soil Mechanics and Geotechnical Engineering and 39th U.S. Rock Mechanics Symposium*, Cambridge, Mass., USA, 1, 1157-1164.

Bagde MN & Mitri HS. (2015) Numerical Analysis of Backfill Face Stability. *Procedia Earth and Planetary Science*, 11, 173-179.

Barrett JR, Coulthard MA & Dight PM. (1978) Determination of fill stability. *12th Can. Rock Mechanics Symp.* on *Mining with Backfill*, Sudbury, 85-91.

Barrett JR & Cowling R. (1980) *Investigations of cemented fill stability in 1100 orebody*. Mount Isa Mines, Ltd., Queensland, Australia, *The IMM Trans Sect A Min Industry*, 89, A118-A128.

Beer G. (1986). Design of brick bulkheads: numerical modelling. *CSIRO Institute of Energy and Earth Resources*, Division of Geomechanics, Long Pocket Laboratories, Project Report 1.

Belem T & Benzaazoua M. (2008) Design and application of underground mine paste backfill technology. *Geotechnical and Geological Engineering*, *26*(2), 147-174.

Belem T, Benzaazoua M & Bussière B. (2000) Mechanical behaviour of cemented paste backfill. *53rd Canadian Geotechnical Conference*, Montreal, 373-380.

Belem T, Bussière B & Benzaazoua M. (2001) The effect of microstructural evolution on the physical properties of paste backfill. In *Proceedings of the Tailings and Mine Waste*, Fort Collins, Colorado, Balkema, Rotterdam, pp. 365-74.

Belem T, El Aatar O, Benzaazoua M, Bussière B & Yilmaz E. (2007) Hydro-geotechnical and geochemical characterization of column consolidated cemented paste backfill. In *Proceedings of the 9th International Symposium in Mining with Backfill* (Vol. 29).

Belem T, El Aatar, O, Bussière B & Benzaazoua M. (2016) Gravity-driven 1-D consolidation of cemented paste backfill in 3-m-high columns. *Innovative Infrastructure Solutions*, 1(1), 37.

Belem T, Harvey A, Simon R & Aubertin M. (2004) Measurement and prediction of internal stresses in an underground opening during its filling with cemented fill. *5th International Symposium on Ground Support*, Perth, Australia. 619-630.

Belem T, Mbonimpa M & Li L. (2013) Note du cours de GML6603 - Remblais miniers. UQAT & Polytechnique Montréal.

Benzaazoua M, Belem T & Bussière B. (2002) Chemical factors that influence the performance of mine sulphidic paste backfill. *Cement and Concrete Research*, 32: 1133-1144.

Benzaazoua M, Bussière B, Demers I, Aubertin M, Fried É & Blier A. (2008) Integrated mine tailings management by combining environmental desulphurization and cemented paste backfill: Application to mine Doyon, Quebec, Canada. *Minerals Engineering*, 21(4), 330-340.

Benzaazoua M, Fall M & Belem T. (2004) A contribution to understanding the hardening process of cemented pastefill. *Minerals Engineering*, 17(2), 141-152.

Benzaazoua M, Ouellet J, Servant S, Newman P & Verburg R. (1999) Cementitious backfill with high sulphur content physical, chemical, and mineralogical characterization. *Cement and Concrete Research*, 29(5), 719-725.

Blight GE. (1984) Soil mechanics principles in underground mining. *Journal of Geotechnical Engineering*, 110(5), 567-581.

Bloss ML. (1992) Prediction of cemented rock fill stability: design procedures and modelling techniques. *Ph.D. Thesis*, University of Queensland, Brisbane, Australia.

Bloss ML. (1996) Evolution of cemented rock fill at Mount Isa mines limited. *Mineral Resources Engineering*, 5(01), 23-42.

Bloss ML & Chen J. (1998) Drainage research at Mount Isa Mines limited 1992-1997. M. Bloss (ed.), *6th International Symposium on Mining with Backfill*, Brisbane, Australia, 111-116.

Boger DV. (2002) *Paste and thickened tailings - A guide*. Jewel et al (eds), ACG, Perth, Australia.

Boger DV, Scales P & Sofra F. (2006) Paste and Thickened Tailings: A Guide (2nd ed.): Rheological concepts. ACG, Perth, 25-37.

Brackebusch FW. (1994) Basics of paste backfill systems. *Mining Engineering*, 46(October), 1175-1178.

Brady BH & Brown ET. (2004) *Rock mechanics: for underground mining*. Springer Science & Business Media.

Bullock RL. (2011) Room-and-pillar mining in hard rock. In *SME Mining Engineering Handbook* (Vol. 1). Darling P. (Ed.), SME, Littleton, 1327-1353.

Bullock RL & Hustrulid WA. (2001) Chapter 3: Planning the underground mine mining methods and applications. In *Underground Mining Methods: Engineering Fundamentals and International Case Studies*, WA. Hustrulid & RL. Bullock (Ed.), SME, Littleton, 29-48.

Bussière B. (2007) Colloquium 2004: Hydro-geotechnical properties of hard rock tailings from metal mines and emerging geoenvironmental disposal approaches. *Canadian Geotechnical Journal*, 44, 1019-1052.

Caceres C. (2005) Effect of backfill on longhole open stoping. *Master Thesis*. University of British Columbia, Vancouver, Canada.

Chapuis RP. (2009) Numerical modeling of reservoirs or pipes in groundwater seepage. *Computers and Geotechnics*, 36(5), 895-901.

Chapuis RP & Aubertin M. (2003) On the use of the Kozeny-Carman equation to predict the hydraulic conductivity of soils. *Canadian Geotechnical Journal*, 40, 616-28.

Chapuis RP, Chenaf D, Bussière B, Aubertin M & Crespo R. (2001) A user's approach to assess numerical codes for saturated and unsaturated seepage conditions. *Canadian Geotechnical Journal*, 38(5), 1113-1126.

Clayton S, Grice TG & Boger DV. (2003) Analysis of the slump test for on-site yield stress measurement of mineral suspensions. *International Journal of Mineral Processing*, 70(1), 3-21.

Cooke R. (2006) Thickened and paste tailings pipeline systems: design procedure - Part 1, Paste 2006, ACG, Perth, Australia.

Cooke R. (2008) Design considerations for paste and thickened tailings pipeline systems, *1st International Oil Sands Tailings Conference*, Edmonton, AB, Canada.

Corson DR. (1971) Field evaluation of hydraulic backfill compaction at the Lucky Friday Mine, Mullan, Idaho. U.S. Bureau of Mines.

Corson DR & Wayment. (1967) Load-displacement measurements in a backfilled stope of a deep vein mine. U.S. Bureau of Mines.

Cowling R & Gonano LP. (1976) Cemented rockfill practice at Mount Isa Mines Limited. *Proc., Symp. on Influence of Excavation Design and Ground Support on Underground Mining Efficiency and Costs*, AMIRA, Wollongong.

Cowling R, Grice AG & Isaacs LT. (1988) Simulation of hydraulic filling of large underground mining excavations. *6th Conference on Numerical Methods in Gcomochanics,* Innsbruck, A.A. Balkema, Rotterdam, 1869-1876.

Coulthard MA. (1980) Numerical analysis of fill pillar stability: three dimensional linearly elastic finite element calculations. Technical Report. *CSIRO,* Division of Applied Geomechanics.

Coulthard MA. (1999) Applications of numerical modelling in underground mining and construction, *Geotechnical and Geological Engineering*, 17(2), 373-385.

Coulthard MA & Dight PM. (1979). Numerical analysis of fill pillar stability - two-dimensional calculations of initial stresses. Technical Report. *CSIRO*, Division of Applied Geomechanics.

Coulthard MA & Dight PM. (1980). Numerical analysis of failed cemented fill at ZC/NBHC Mine, Broken Hill. *3rd Australia-New Zealand Geomech. Conf.*, Wellington, 2-145-2-151.

Cundall P, Shillabeer JH & Herget G. (1978) Modelling to predict rock fill stability in transverse pillar extraction. *12th Can. Rock Mechanics Symp.* on *Mining with Backfill*, Sudbury, 92-99.

Darling P. (2011) *SME Mining Engineering Handbook* (Vol. 1). 3rd ed., SEM.

De Souza E, Archibald JF & Dirige APE. (2003) Economics and Perspectives of Underground Backfill Practices in Canadian Mining. *105th Annual General Meeting of the Canadian Institute of Mining, Metallurgy and Petroleum*. Montreal.

Dight PM & Coulthard MA. (1980) Numerical analysis of fill pillar stability - two-dimensional analysis of exposures. Technical Report. *CSIRO,* Division of Applied Geomechanics.

Dirige APE & De Souza E. (2000) Centrifuge physical modelling of paste fill designs for improved cost performance. *The Millennium 2000 CIM Conf.*, Toronto.

Dirige APE & De Souza E. (2013) *Mechanics of failure of paste backfill face exposure during adjacent mining*. *23rd World Mining Congress*, Montreal.

Dirige APE, McNearny RL & Thompson DS. (2009) The effect of stope inclination and wall rock roughness on back-fill free face stability. *Rock Engineering in Difficult Conditions, 3rd Canada-US Rock Mechanics Symp*., M. Diederichs & G. Grasselli, eds., Toronto.

Dismuke S & Diment T. (1996) The testing, design, construction and implementation of cemented rockfill (CRF) at Polaris, *CIM Bulletin*, 89(1005), 91-97.

Doherty JP, Hasan A, Suazo GH & Fourie A. (2015) Investigation of some controllable factors that impact the stress state in cemented paste backfill. *Canadian Geotechnical Journal*, 52(12), 1901-1912.

Drescher A. (1991) *Analytical methods in bin-load analysis*. Elsevier, Amsterdam.

Duffield WA, Gad E & Bamford W. (2003) Investigation into the structural behavior of mine brick barricades. *AusIMM*, 2 (March/April), 45-50.

EL Mkadmi N, Aubertin M, & Li L. (2011) Numerical analysis of the early response of paste backfill in a vertical stope. *CIM Conference & Exhibition 2011 - Mines without Borders*, Montréal, QC, Canada.

El Mkadmi N, Aubertin M & Li L. (2014) Effect of drainage and sequential filling on the behavior of backfill in mine stopes. *Can. Geotech. J*., 51(1), 1-15.

Emad MZ, Mitri HS & Henning JG. (2012) Effect of blast vibrations on the stability of cemented rockfill. *Int. J. Min. Reclam. Environ.*, 26(3), 233-243.

Emad MZ, Mitri HS & Kelly C. (2014) Effect of blast-induced vibrations on fill failure in vertical block mining with delayed backfill. *Can. Geotech. J*., 51, 1-9.

Emad MZ, Mitri HS & Kelly C. (2015a) State-of-the-art review of backfill practices for sublevel stoping system. *Int. J. Min. Reclam. Environ.*, 29(6), 544-556.

Emad MZ, Mitri HS & Kelly C. (2015b) In-situ blast vibration monitoring in cemented rockfill stope-a case study. *Int. J. Min. Reclam. Environ.*, 1-18.

Fahey M, Helinski M & Fourie A. (2009) Some aspects of the mechanics of arching in backfilled stopes. *Canadian Geotechnical Journal*, 46, 1322-1336.

Fahey M, Helinski M & Fourie A. (2010) Consolidation in accreting sediments: Gibson's solution applied to backfilling of mine stopes. *Géotechnique*, 60(11), 877-882.

Fahey M, Helinski M & Fourie A. (2011) Development of specimen curing procedures that account for the influence of effective stress during curing on the strength of cemented mine backfill. *Geotech. Geolog. Eng.*, 29(5), 709-723.

Fall M & Benzaazoua M. (2005) Modeling the effect of sulphate on strength development of paste backfill and binder mixture optimization. *Cement and Concrete Research,* 35(2), 301-304.

Fall M & Samb S. (2007) Influence of curing temperature on strength, deformation behaviour and pore structure of cemented paste backfill at early ages. *Journal Construction and Building Materials*.

Fall M & Samb S. (2008) Effect of high temperature on strength and microstructural properties of cemented paste backfill. *Journal of Fire Safety*, 44 (44), 642-665.

Fall M, Adrien D, Celestin JC, Pokharel M & Toure M. (2009) Saturated hydraulic conductivity of cemented paste backfill. *Minerals Engineering*, 22(15), 1307-1317.

Fall M & Pokharel M. (2010) Coupled effect of sulphate and temperature on the strength development of cemented backfill tailings: Portland cement paste backfill. *Cement and Concrete Composite*, 32(10), 819-828.

Fall M & Nasir O. (2010) Mechanical behaviour of the interface between cemented tailings backfill and retaining structures under shear loads. *Geotech. Geolog. Eng.*, 28(6), 779-90.

Fall M, Célestin JC, Pokharel M & Touré M. (2010) A contribution to understanding the effects of curing temperature on the mechanical properties of mine cemented tailings backfill. *Engineering Geology*, 114(3), 397-413.

Falaknaz, N. (2014). "Analysis of geomechanical behavior of two adjacent backfilled stopes based on two and three dimensional numerical simulations." *Ph.D. Thesis*, Polytechnique Montréal, Montréal.

Falaknaz N, Aubertin M & Li L. (2015a). Numerical investigation of the geomechanical response of adjacent backfilled stopes. *Can. Geotech. J.*, 52(10), 1507-1525.

Falaknaz N, Aubertin M & Li L. (2015b). Evaluation of the stress state in two adjacent backfilled stopes within an elasto-plastic rock mass. *Geotech. Geol. Eng.*, 1-24.

Falaknaz N, Aubertin M & Li L. (2015c). Numerical analyses of the stress state in two neighboring stopes excavated and backfilled in sequence. *International Journal of Geomechanics*, 15(6), 04015005.

Falaknaz N, Aubertin M & Li L. (2016). Stability analyses of backfill in mine stopes with an open face. *Geotech. Geol. Eng*. (submitted).

Farsangi PN. (1996) Improving cemented rockfill design in open stoping. *Ph.D. Thesis*, McGill University, Montreal, Canada.

Gibson RE. (1958) The progress of consolidation in a clay layer increasing in thickness with time. *Géotechnique*, 8(4), 171-183.

Ghirian A & Fall M. (2013) Coupled thermo-hydro-mechanical-chemical behaviour of cemented paste backfill in column experiments. Part I: physical, hydraulic and thermal processes and characteristics. *Engineering Geology*,164, 195-207.

Ghirian A & Fall M. (2014) Coupled thermo-hydro-mechanical-chemical behaviour of cemented paste backfill in column experiments: Part II: Mechanical, chemical and microstructural processes and characteristics. *Engineering Geology*, 170, 11-23.

Ghirian A & Fall M. (2015) Coupled behavior of cemented paste backfill at early ages. *Geotechnical and Geological Engineering*, 33(5), 1141-1166.

Ghirian A & Fall M. (2016) Long-term coupled behaviour of cemented paste backfill in load cell experiments. *Geomechanics and Geoengineering*, 1-15.

Godbout J, Bussière B, Aubertin M & Belem T. (2007) Evolution of cemented paste backfill saturated hydraulic conductivity at early curing time. *60th Canadian Geotechnical Conference*, Ottawa, Canada.

Grabinsky MW. (2010) In situ monitoring for ground truthing paste backfill designs. *13th International Seminar on Paste and Thickened Tailings*, Toronto, Canada. ACG. 85-98.

Grabinsky MW & Simms P. (2006) Self-desiccation of cemented paste backfill and implications for mine design. *9th International Seminar on Paste and Thickened Tailings*. Edited by R. Jewell, S. Lawson, & P. Newman. ACG, Perth, Australia, 323-332.

Grabinsky MW & Thompson BD. (2009) Thermally induced stresses in cemented paste backfill. *Geotechnical News*, 27(3), 36-40.

Grabinsky M, Bawden WF & Thompson BD. (2007) In situ monitoring of cemented paste backfill in an Alimak stope, *60th Canadian Geotechnical Conference and 8th Joint IAH-CNC and CGS Groundwater Specialty Conference*, Canadian Geotechnical Society and International Association of Hydrogeologists: Canadian National Chapter, Ottawa, 2237-2244.

Grice AG. (1989) Fill research at Mount Isa mines limited. In *Innovations in Mining Backfill Technology*, Hassani et al. (eds), 1989, A.A. Balkema, Rotterdam, 15-22.

Grice AG. (1998a) Stability of hydraulic backfill barricades. *6th International Symposium on Mining with Backfill: Minefill*, Vol. 98, 117-120.

Grice AG. (1998b) Underground mining with backfill. *2nd Annual Summit-Mine Tailings Disposal Systems*, Brisbane.

Grice AG. (2001) Recent mine fill developments in Australia. *7th International Symposium on mining with Backfill*, Seattle, USA, 351-357.

Grice AG. (2005) Introduction to hydraulic fill. In *Handbook on Mine Fill*. ACG, 66-80.

Hambley DF. (2011) Backfill mining. In *SME Mining Engineering Handbook* (Vol. 1). Darling, P. (Ed.), SME, 1375-84.

Hamrin H. (2001) Chapter 1: Underground mining methods and applications. In *Underground Mining Methods: Engineering Fundamentals and International Case Studies.* W.A. Hustrulid & R.L. Bullock (eds.), 3-14. *SME*: Littleton, Colorado.

Handy R. (1985) The arch in soil arching. *Journal of Geotechnical Engineering, ASCE, 3*(111), 302-18.

Hartman HL & Britton SG. (1992) *SME Mining Engineering Handbook*. Vol. 2. 2nd ed., SME: Littleton, Colorado.

Harvey A. (2004) Étude comparative des contraintes triaxiales dans le remblai en pâte selon la portée des chantiers. *Master Thesis*, Polytechnique Montréal, Canada.

Hasan A, Suazo G, Doherty JP & Fourie AB (2014) In situ measurements of cemented paste backfilling in an operating stope at Lanfranchi Mine. *Mine Fill 2014*, Y Potvin & AG Grice (eds), Australian Centre for Geomechanics, Perth, Australia.

Hansbo S. (1981) Consolidation of fine-grained soils by prefabricated drains. *10th ICSMFE*, 3, 677-682.

Harr ME. (1962) Ground Water and Seepage, McGraw Hill.

Hassani F & Archibald J. (1998) Mine backfill. CIM.

Hassani FP, Fotoohi K & Doucet C. (1998) Instrumentation and backfill performance in a narrow vein gold mine. *International Journal of Rock Mechanics and Mining Sciences*, 35(4-5), 392.

Hassani FP, Ouellet J & Servant S. (2001) In situ measurements in a paste backfill: backfill and rock mass response in the context of rockburst. *17th International Mining Congress and Exhibition of Turkey- IMCET 2001*.165-175.

Hassani FR, Mortazavi A & Shabani M. (2008) An investigation of mechanisms involved in backfill-rock mass behaviour in narrow vein mining. *Journal of the South African Institute of Mining and Metallurgy*, 108(8), 463-472.

Hedley DGF. (1995) Final report on the stiff backfill project for M.R.D. Mining Research Directorate, Canadian Rockburst Research Program, Sudbury, Ontario, January.

Helinski M, Fourie A & Fahey M. (2006) Mechanics of early age CPB, In R. Jewell, S. Lawson, & P. Newman (Eds.), *Symposium conducted at the 9th International Seminar on Paste and Thickened Tailings*, ACG, Limerick, Ireland, 313-22.

Helinski M, Fourie A, Fahey M & Ismail M. (2007) Assessment of the self-desiccation process in cemented mine backfills. *Canadian Geotechnical Journal*, 44(10), 1148-1156.

Helinski M, Fahey M & Fourie A. (2011) Behavior of cemented paste backfill in two mine stopes: measurements and modeling. *J. Geotech. Geoenviron. Eng.*,137(2), 171-182.

Hughes PB. (2008) *Performance of paste fill fences at Red Lake Mine*. *Master Thesis*, University of British Columbia, Vancouver, Canada.

Hughes PB, Pakalnis R, Hitch M & Corey G. (2010) Composite paste barricade performance at Goldcorp Inc. Red Lake Mine, Ontario, Canada. *Int. J. Min. Reclam. Environ.*, 24(2), 138-150.

Hunt WG. (1988) The use of consolidated backfill for pillar extraction in room and pillar mining: An integrated design rationale. *Master Thesis*. McGill University, Montreal, Canada.

Hustrulid WA & Bullock RL. (eds.) (2001) *Underground Mining Methods: Engineering Fundamentals and International Case Studies*. SME: Littleton.

Hoek E & Brown ET. (1980) *Underground Excavations in Rock*. Institution of Mining and Metallurgy, London.

Itasca. (2002) *FLAC: Fast Lagrangian Analysis of Continua; User's Guide*. Itasca Consulting Group, Inc., Minneapolis.

Itasca. (2013) *FLAC3D: Fast Lagrangian Analysis of Continua in 3 Dimensions; User's Guide*. version 5.01, Itasca Consulting Group, Inc., Minneapolis.

Jahanbakhshzadeh A. (2016) Analyse du comportement géomécanique des remblais miniers dans des excavations souterraines inclinées. *Ph.D. Thesis*, Polytechnique Montréal, Montréal.

Jahanbakhshzadeh A, Aubertin M & Li L. (2016a) A new semi-analytical solution for the stress distribution in inclined backfilled mine stopes. Submitted to *Journal of Geotechnical and Geological Engineering*.

Jahanbakhshzadeh A, Aubertin M & Li L. (2016b) Evaluation of the earth pressures in inclined backfilled stopes based on the Coulomb active state coefficient. *69th Canadian Geotechnical Conference*, Vancouver, Canada.

Jahanbakhshzadeh A, Aubertin M & Li L. (2016c). Three-dimensional stress state in inclined backfilled stopes obtained from numerical simulations and a new closed-form solution. Submitted to *Canadian Geotechnical Journal*.

Jahns H & Brauner G. (1960) Stowage pressure in steep measures. *3rd International Conference on strata eontroi*, Paris (Saint-Etienne: Edition de l'Industrie Minérale), 151-63.

Jakobson B. (1958) On pressure in silos. *Conference on Earth Pressure Problems*, Brussels, Vol.1, 49-54.

Jaky J. (1944) The coefficient of earth pressure at rest. *Hungarian A nyugalmi nyomas tenyezoje*. J. Soc. Hung. Eng. Arch. (Magyar Mernok es Epitesz-Egylet Kozlonye), 355-358.

James M, Li L & Aubertin M. (2004) Evaluation of the earth pressures in backfilled stopes using limit equilibrium analysis. *57th Canadian Geotechnical Conference*, Quebec City, QC, Canada.

Janssen HA. (1895) Versuche uber getreidedruck in silozellen. *Zeitschrift des Vereines Deutscher Ingenieure*, Berlin, Germany, 39(35), 1045-9.

Jung SJ & Biswas K. (2002) Review of current high density paste fill and its technology, *Mineral Resources Engineering*, 11(2), 165-182.

Karim R, Simangunsong GM, Sulistianto B & Lopulalan A. (2013) Stability analysis of paste fill as stope wall using analytical method and numerical modelling in the Kencana underground gold mining with long hole stope method. *Procedia Earth Planet. Sci.*, 6, 474-484.

Klein K & Simon D. (2006) Effect of specimen composition on the strength development in cemented paste backfill. *Canadian Geotechnical Journal*, 43(3), 310-324.

Knutsson S. (1981) Stresses in the hydraulic backfill from analytical calculations and in situ measurements. *Conference on Application of Rock Mech. to Cut and Fill Mining*, Institution of Mining and Metallurgy, London, 261-268.

Koupouli NJ, Belem T, Rivard P & Effenguet H. (2016) Direct shear tests on cemented paste backfill-rock wall and cemented paste backfill-backfill interfaces. *J. Rock Mech. Geotech. Eng.*, 8, 472-479.

Kuganathan K. (2001) Mine backfilling, backfill drainage and bulkhead construction - a safety first approach, in Australia's Mining Monthly, February, 58-64.

Kuganathan K. (2002a) A model to predict bulkhead pressures for safe design of bulkheads. *Filling with Hydraulic Fills Seminar*. Section 6, ACG, Perth.

Kuganathan K. (2002b) A method to design efficient mine backfill drainage systems to improve safety and stability of backfill bulkheads and fills. *8th AusIMM Underground Operators' Conference "growing our underground operations"*, AusIMM, Carlton, 181-189.

Kuganathan K. (2005a) Rock fill in mine fill. In *Handbook on Mine Fill*. ACG, 101-115.

Kuganathan K. (2005b) Geomechanics of mine fill. In *Handbook on Mine Fill*. ACG, 23-47.

Krynine DP. (1945) Discussion of stability and stiffness of cellular cofferdams by Karl Terzaghi. *Transactions, ASCE*, 110, 1175-1178.

Ladanyi B & Hoyaux B. (1969) A study of the trap-door problem in a granular mass. *Canadian Geotechnical Journal*, 6(1), 1-14.

Lane WL, Yanske TR, Clark LM & Roberts DP. (2001) Chapter 8: Pillar extraction and rock mechanics at the Doe Run Company in Missouri 1991 to 2000. In *Underground Mining Methods: Engineering Fundamentals and International Case Studies*. W. A. Hustrulid & R. L. Bullock, (eds), 95-101. *SME*: Littleton.

le Roux K, Bawden WF & Grabinsky MW. (2005) Field properties of cemented paste backfill at the Golden Giant mine. *Institution of Mining and Metallurgy: Mining Technology,* 114(2), 65-80.

Leahy FJ & Cowling R. (1978) Stope fill developments at Mount Isa. *12th Canadian Rock Mechanics Symposium on Mining with Backfill*, Sudbury, 21-29.

Leo C. (2004) Equal strain consolidation by vertical drains. *Journal of Geotechnical and Geoenvironmental Engineering*, ASCE, 130 (3), 316-327.

Lessard G. (2011) Essais d'infiltration sur la halde à stériles Petit-Pas de la mine Tio, Havre-St-Pierre. *Master Thesis*. Polytechnique Montréal, Canada.

Li L. (2013). A simple solution to assess pore-water pressure in barricades made of waste rock. *CIM Journal*, 4(1), 53-60.

Li L. (2014a). Generalized solution for mining backfill design. *International Journal of Geomechanics*, 14(3), 04014006-1-11.

Li L. (2014b) Analytical solution for determining the required strength of a side-exposed mine backfill containing a plug. *Canadian Geotechnical Journal,* 51(5), 508-519.

Li L. (2013a) A new concept of backfill design - application of wick drains in backfilled stopes. *International Journal of Mining Science and Technology*, 23, 763-770.

Li L. (2013b) Application of wick drains in backfilled stopes for accelerating the drainage. *23rd World Mining Congress* (Paper #163), CIM, Montreal, Canada.

Li L & Aubertin M. (2003). A general relationship between porosity and uniaxial strength of engineering materials. *Canadian Journal of Civil Engineering*, 30(4), 644-658.

Li L & Aubertin M. (2008) An improved analytical solution to estimate the stress state in subvertical backfilled stopes. *Canadian Geotechnical Journal*, 45(10), 1487-1496.

Li L & Aubertin M. (2009a) Influence of water pressure on the stress state in backfill with cohesionless Stopes. *Geotechnical and Geological Engineering*, 27(1), 1-11.

Li L & Aubertin M. (2009b) A three-dimensional analysis of the total and effective stresses in submerged backfilled Stopes. *Geotechnical and Geological Engineering*, 27(4), 559-569.

Li L & Aubertin M. (2009c) Horizontal pressure on barricades for backfilled stopes. Part I: Fully drained conditions, *Canadian Geotechnical Journal*, 46(1), 37-46.

Li L & Aubertin M. (2009d) Horizontal pressure on barricades for backfilled stopes. Part II: Submerged conditions, *Canadian Geotechnical Journal*, 46(1), 47-56.

Li L & Aubertin M. (2009e) Numerical investigation of the stress state in inclined backfilled Stopes. *International Journal of Geomechanics*, 9(2), 52-62.

Li L & Aubertin M. (2009f) An elastoplastic evaluation of the stress state around cylindrical openings based on a closed multiaxial yield surface. *International Journal for Numerical and Analytical Methods in Geomechanics*, 33(2), 193-213.

Li L & Aubertin M. (2010) An analytical solution for the nonlinear distribution of effective and total stresses in vertical backfilled stopes. *Geomechanics and Geoengineering*: An International Journal 5(4), 237-245.

Li L & Aubertin M. (2011) Limit equilibrium analysis for the design of backfilled stope barricades made of waste rock, *Canadian Geotechnical Journal*, 48(11), 1713-1728.

Li L & Aubertin M. (2012) A modified solution to assess the required strength of exposed backfill in mine stopes. *Canadian Geotechnical Journal*, 49(8), 994-1002.

Li L & Aubertin M. (2014) An improved method to assess the required strength of cemented backfill in underground stopes with an open face. *International Journal of Mining Science and Technology*, 24(4), 549-558.

Li L & Yang PY. (2015) A numerical evaluation of continuous backfilling in cemented paste backfilled stope through an application of wickdrains. *International Journal of Mining Science and Technology*, 25(6), 897-904.

Li L, Aubertin M & Belem T. (2005) Formulation of a three dimensional analytical solution to evaluate stresses in backfilled vertical narrow openings. *Canadian Geotechnical Journal*, 42(6), 1705-1717.

Li L, Aubertin M & Shirazi A. (2010) Implementation and application of a new elastoplastic model based on a multiaxial criterion to assess the stress state near underground openings. *International Journal of Geomechanics*, 10(1), 13-21.

Li L Aubertin M, Simon R, Bussière B & Belem T. (2003) Modelling arching effects in narrow backfilled stopes with FLAC. *3th International FLAC Symposium*, Sudbury, 211-219.

Li L, Aubertin M, Shirazi A, Belem T, Simon R. (2007) Stress distribution in inclined backfilled stopes. *9th International Symposium in Mining with Backfill*, Montreal. CIM, 204.

Liston D. (2014) Utilisation of cemented rockfill, cemented hydraulic fill and paste to successfully achieve ore production expansion to 2 Mtpa at Chelopech Mine. *Mine Fill 2014*, Y Potvin & AG Grice (eds), ACG, Perth, Australia.

Liu G, Li L, Yang X & Guo L. (2016a). Numerical analysis of stress distribution in backfilled stopes considering interfaces between the backfill and rock walls. *International Journal of Geomechanics*, 06016014.

Liu G, Li L, Yang X & Guo L. (2016b). A numerical analysis of the stress distribution in backfilled stopes considering nonplanar interfaces between the backfill and rock walls. *International Journal of Geotechnical Engineering*, 10(3), 271-282.

Liu G, Li L, Yang X & Guo L. (2016c). Numerical modelling of the stability of cemented backfill with a vertical face exposed: a revisit to Mitchell's physical model tests. *International Journal of Mining Science and Technology* (available online).

Marston A. (1930) The theory of external loads on closed conduits in the light of latest experiments. *Bulletin 96, Iowa Engineering Experiment Station*, Ames, Iowa.

Marston A & Anderson AO. (1913) The theory of loads on pipes in ditches and tests of cement and clay drain tile and sewer pipe. *Bulletin 31, Iowa Engineering Experiment Station*, Ames, Iowa.

Martic Z, Gelson J, Bras H, Xu Q & Brosko W. (2014) New perspectives for cemented hydraulic fill with chemical technologies. *Mine Fill 2014*, Y Potvin & AG Grice (eds), ACG, Perth, Australia.

Mbonimpa M, Aubertin M, Chapuis RP & Bussière B. (2002) Practical Pedotransfer Functions for Estimating the Saturated Hydraulic Conductivity. *Geotechnical and Geological Engineering*, 20, 235-259.

McCarthy DF. (1988) Essential of soil mechanics and foundations: basic geotechnics. Prentice Hall, Englewwod Cliffs, N.J.

McNay & Corson. (1961) Hydraulic sandfill in deep metal mines. U.S. Bureau of Mines.

Mitchell RJ. (1983). *Earth structures engineering.* Allen & Unwin, Boston, Mass.

Mitchell, RJ. (1986) Centrifuge model tests on backfill stability. *Canadian Geotechnical Journal*, 23(3), 341-345.

Mitchell RJ. (1991) Sill mat evaluation using centrifuge models. *Mining Science and Technology*, 13(3), 301-313.

Mitchell RJ. (1992) Centrifuge model studies of fill pressures on temporary bulkheads. *CIM Bulletin*, 85(960), 48-54.

Mitchell RJ & Roettger J. (1984) Bulkhead pressure measurements in model fill pours. *CIM Bulletin*, 77(868), 50-54.

Mitchell RJ & Wong BC. (1982) Behaviour of cemented tailings sands. *Canadian Geotechnical Journal*, 19(3), 289-295.

Mitchell RJ, Olsen RS & Smith JD. (1982) Model studies on cemented tailings used in mine backfill. *Canadian Geotechnical Journal*, 19(1), 14-28.

Mitchell RJ, Smith J & Libby D. (1975) Bulkhead pressures due to cemented hydraulic mine backfills. *Canadian Geotechnical Journal*, 12(3), 362-371.

Neindorf LB. (1983) Fill operating practices at Mount Isa Mines. *International Symposium on Mining with Backfill*, Lulea, 179-187.

Ouellet J & Servant S. (2000) In-situ mechanical characterization of a paste backfill with a self-boring pressuremeter. *CIM Bulletin*, 93(1042), 110-115.

Ouellet S, Bussière B, Mbonimpa M, Benzaazoua M & Aubertin M. (2006) Reactivity and mineralogical evolution of an underground mine sulphidic cemented paste backfill. *Minerals Engineering*, 19(5), 407-419.

Ouellet S, Bussière B, Aubertin M & Benzaazoua M. (2007) Microstructural evolution of cemented paste backfill: Mercury intrusion porosimetry test results. *Cement and Concrete Research*, 37(12), 1654-1665.

Ouellet S, Bussière B, Aubertin M & Benzaazoua M. (2008) Characterization of cemented paste backfill pore structure using SEM and IA analysis. *Bulletin of Engineering Geology and the Environment*, 67(2), 139-152.

Ouellet J, Bussere B & Gagnon G. (1995) Simulation numérique du remblayage d'un chantier de mine avec du remblai hydraulique cimenté: élaboration du modèle. *3rd Can. Conf. on Computer Applications in the Mineral Industry*, Montréal, 331-339.

Oulbacha Z. (2014) Analyse numérique de la stabilité des piliers-dalles en remblai cimenté: une vérification des modèles de Mitchell. *Master Thesis*, Polytechnique Montréal, Canada.

Palarski J. (1994) Design of backfill as support in Polish coal mines. *Journal of the South African Institute of Mining and Metallurgy*, 94(8), 218-226.

Palarski J. (2014) Filling of voids in coal longwall mining with caving - technical, environmental and safety aspects. *Mine Fill 2014, Y Potvin & AG Grice (eds)*, Australian Centre for Geomechanics, Perth, Australia.

Pakalnis RT & Hughes PB. (2011) Sublevel stoping. In *SME Mining Engineering Handbook* (Vol. 1). Darling, P. (Ed.), SME, 1355-1363.

Pashias N, Boger DV, Summers J & Glenister DJ. (1996) A fifty cent rheometer for yield stress measurement. *Journal of Rheology*, 40(6).

Pavlovsky NN. (1956) Collected Works. Akad Nauk USSR, Lenningrad.

Peele I. (1941) *Mining Engineers' Handbook*. John Wiley and Sons Inc., Canada.

Peregoedova A. (2012) Étude expérimentale des propriétés hydrogéologiques des roches stériles à une échelle intermédiaire de laboratoire. *Master Thesis*, Polytechnique Montréal, Canada.

Pierce ME, Bawden WF & Paynter JT. (1998) Laboratory testing and stability analysis of paste backfill at the Golden Giant Mine. *6th International Symposium on Mining with Backfill*, 159-165.

Pierce ME. (1997) Laboratory and numerical analysis of the strength and deformation behaviour of paste backfill. *Master Thesis*, Queen's University, Kingston, Canada.

Pierce ME. (2001) Stability analysis of paste back fill exposes at Brunswick Mine. *2nd International FLAC Symposium*, Lyon, France, 147-156.

Pipatpongsa T & Ohta H. (2009) Theoretical analyses of arch action and stress distribution due to bin effect in storage silo of granular media. *44th National Conference of Japan Geotechnical Engineerin*g. The Japanese Geotechnical Society, 353-354.

Pirapakaran K. (2008) Load-deformation characteristics of minefills with particular reference to arching and stress developments. *Ph.D. Thesis*, James Cook University, Australia.

Pirapakaran K & Sivakugan N. (2007a) Arching within hydraulic fill stopes. *Geotech. Geologic. Eng.*, 25(1), 25-35.

Pirapakaran K & Sivakugan N. (2007b) A laboratory model to study arching within a hydraulic fill stope. *Geotech. Test. J.*, 30(6), 496-503.

Potvin Y, Thomas E & Fourie A. (2005) *Handbook on mine fill*. ACG, Perth, Australia.

Rahilly HJ. (1923) Mine fires and hydraulic filling. *Trans. AIME*, V102.

Rajeev P & Sivakugan N. (2016) Vulnerability Assessment of Underground Mine Stopes Filled with Granular Backfills. *Geo-Chicago 2016*, 372-381.

Rankine RM. (2004) The geotechnical and static stability analysis of Cannington mine paste backfill. *Ph.D. Thesis*, James Cook University, Townsville, Australia.

Rankine KJ. (2005) An investigation into the drainage characteristics and behaviour of hydraulically placed mine backfill and permeable minefill barricades. *Ph.D. Thesis*. James Cook University, Townsville, Australia.

Rankine RM, Rankine KJ, Sivakugan N, Karunasena W & Bloss ML. (2002) Geotechnical characterisation and stability analysis of BHP Cannington paste backfill. *International Conference on Soil Mechanics and Geotechnical Engineering*, 2, 1241-1244.

Revell MB. (2004) Paste - How strong is it? In *Proceedings of the 8th International Symposium on Mining with Backfill*, Beijing, The Nonferrous Metals Society of China, 286-294.

Revell MB & Sainsbury DP. (2007a). Paste bulkhead failures. *9th International Symposium on Mining with Backfill*, Montréal, QC, Canada.

Revell MB & Sainsbury DP. (2007b). Advancing paste fill bulkhead design using numerical modeling. *9th International Symposium on Mining with Backfill*, Montréal, QC, Canada.

Roberts DP, Lane WL & Yanske TR. (1998) Pillar extraction at the Doe Run Company 1991-1998. In: Bloss M, editor. *6th International Symposium Mining with Backfill*, Victoria, Australia. 227-33.

RocScience (2002) *Phase 2: 2D finite element program for calculating stresses and estimating support around underground excavations*. Toronto, Canada.

Saebimoghaddam A. (2005) Rheological yield stress measurement of mine paste fill material. *Master Thesis*. McGill University, Montreal, Canada.

Sainsbury DP & Urie R. (2007) Stability analysis of horizontal and vertical paste fill exposures at the Raleigh Mine. *9th Int. Symp. on Mining with Backfill*, Montreal.

Sainsbury DP & Sainsbury BL. (2014) Design and implementation of cemented rockfill at the Ballarat Gold Project. In *Mine Fill 2014*, Y Potvin & AG Grice (eds), ACG, Perth, Australia.

Salençon J. (1969) Contraction quasi-statique d'une cavité a symétrie sphérique ou cylindrique dans un milieu elastoplastique. *Annales Des Ponts Et Chaussées*, 4, 231-236.

Shahsavari M & Grabinsky M. (2014) Cemented paste backfill consolidation with deposition-dependent boundary conditions. *67th Canadian Geotechnical Conference*, Regina, Canada.

Simon D & Grabinsky M. (2013) Apparent yield stress measurement in cemented paste backfill. *International Journal of Mining, Reclamation and Environment*. 27(4), 231-256.

Singh KH & Hedley DGF. (1980) Review of fill mining technology in Canada. *In: Proceedings of the Conference on the Application of Rock Mechanics to Cut and Fill Mining*. Lulea: Institution of Mining and Metallurgy, 1-3.

Singh S, Sivakugan N & Shukla SK. (2010). Can soil arching be insensitive to ϕ?. *International Journal of Geomechanics*, 10(3), 124-128.

Singh S, Shukla SK & Sivakugan N. (2011) Arching in inclined and vertical mine stopes. *Geotech. Geol. Eng*., 29, 685-693.

Sivakugan N & Widisinghe S. (2013) Stresses within granular materials contained between vertical walls. *Indian Geotechnical Journal*, 43(1), 30-38.

Sivakugan N & Rankine K. (2006) A simple solution for drainage through a 2-dimensional hydraulic fill stope. *Geotechnical and Geological Engineering*, 24, 1229-1241.

Sivakugan N, Rankine K & Rankine R. (2006a) Permeability of hydraulic fills and barricade bricks, *Geotechnical and Geological Engineering*, 24, 661-73.

Sivakugan N, Rankine KJ & Rankine KS. (2006b) Study of drainage through hydraulic fill stopes using method of fragments. *Geotechnical and Geological Engineering*, 24, 79-89.

Seneviratne N, Fahey M, Newson TA & Fujiyasu Y. (1996) Numerical modelling of consolidation and evaporation of slurried mine tailings. *Int. J. Numer. Analyt. Methods Geomech*. 20(9), 647-671.

Smith JD & Mitchell RJ (1982) Design and control of large hydraulic backfill pours. *CIM Bulletin*, 75(838), 102-111.

Smith JD, Dejongh CL & Mitchell RJ. (1983) Large scale model tests to determine backfill strength requirements for pillar recovery at the Black Mountain Mine. *International Symposium on Mining with Backfill*, Lulea, 413-423.

Sofra F & Boger DV. (2001) Slope prediction for thickened tailings and pastes. In Tailings and Mine Waste '01: 8th International Conference, Fort Collins, Colo., A.A. Balkema, Rotterdam, Netherlands, 75-83.

Stephan G. (2011) Cut-and-fill mining. In *SME Mining Engineering Handbook* (Vol. 1). Darling, P. (Ed.), SME, 1365-1373.

Soderberg RL & Busch RA. (1985) Bulkheads and drains for high sandfill stopes. U.S. Bureau of Mines.

Sobhi MA & Li L. (2015) A numerical study of the stresses in backfilled stopes overlying a sill mat. *13th ISRM International Congress of Rock Mechanics*. ISRM.

Sobhi MA, Li L & Aubertin M. (2014) Numerical investigation of the lateral earth pressure coefficient along the VCL of vertical backfilled stopes. *67th Can. Geotech.Conf.*, Regina, SK, Canada.

Sobhi MA, Li L & Aubertin M. (2016). Numerical investigation of the earth pressure coefficient along the center line of backfilled stopes. *Can. Geotech. J.*, available online.

Swan G & Brummer RK. (2001) Backfill design for deep, Underhand drift-and-fill mining. 7th International Symposium on Mining with Backfill. SME.

Take W & Valsangkar A. (2001) Earth pressures on unyielding retaining walls of narrow backfill width. *Canadian Geotechnical Journal*, 38(6), 1220-1230.

Terzaghi K. (1936a) The Shearing resistance of saturated soils. First International Conference on Soil Mechanics, 1, 54-56.

Terzaghi K. (1936b) Stress distribution in dry and in saturated sand above a yielding trap-door. *Proc. Intern. Conf. Soil Mechanics*, Cambridge, Mass., 1, 307-311.

Terzaghi K. (1943) *Theoretical soil mechanics*. John Weily& Sons, New York.

Tesarik DR, Seymour JB & Yanske TR. (2009) Long-term stability of a backfilled room-and-pillar test section at the Buick Mine, Missouri, USA. *International Journal of Rock Mechanics and Mining Sciences*, 46(7), 1182-1196.

Thibodeau D. (1989) In situ determination of high density alluvial sand fill. *Innovations in Mining Backfill Technology: 4th International Symposium*, Montreal.

Thomas EG. (1979) *Fill Technology in Underground Metalliferous Mines*. *International Academic Services Limited*, Kingston, Ontario, Canada.

Thompson BD, Bawden WF & Grabinsky MW. (2011a) In situ monitoring of cemented paste backfill pressure to increase backfilling efficiency. *CIM Journal*, 2(4), 1-10.

Thompson BD, Bawden WF & Grabinsky MW. (2011b) In situ pressures in cemented paste backfill - a review of fieldwork from three mines. *14th International Seminar on Paste and Thickened Tailings*, Perth, Australia.

Thompson BD, Bawden WF, Isagon I & Grabinsky MW. (2013) Increasing paste and hydraulic backfilling efficiency through instrumentation. *23rd World Mining Congress*. Montreal: CIM.

Thompson BD, Grabinsky MW & Bawden WF. (2012) In situ measurements of cemented paste backfill at Cayeli Mine, *Canadian Geotechnical Journal*, 49(7), 755-772.

Thompson BD, Grabinsky MW, Counter DB & Bawden WF. (2009) In situ measurements of cemented paste backfill in long-hole stopes. *3rd CANUS Rock Mechanics Symposium*. Toronto, 199.

Thompson BD, Hunt T, Malek F, Grabinsky MW & Bawden WF. (2014a) In situ behaviour of cemented hydraulic and paste backfills and the use of instrumentation in optimising efficiency. In *Mine Fill 2014*, Y Potvin & AG Grice (eds), ACG, Perth, Australia.

Thompson BD, Simon D, Grabinsky MW, Counter DB & Bawden WF. (2014b) Constrained thermal expansion as a causal mechanism for in situ pressure in cemented paste and hydraulic backfilled stopes. In *Mine Fill 2014*, Y Potvin & AG Grice (eds), ACG, Perth, Australia.

Ting CH, Sivakugan N, Read W & Shukla SK. (2014) Analytical expression for vertical stress within an inclined mine stope with non-parallel walls. *Geotech. Geol. Eng.*, 32, 577-586.

Ting CH, Shukla S & Sivakugan N. (2011) Arching in soils applied to inclined mine stopes. *International Journal of Geomechanics*. 29-35.

Ting CH, Sivakugan N & Shukla SK. (2012) Laboratory simulation of the stresses within inclined stopes. *Geotech. Test. J.*, 35(2), 1-15.

Traves WH & Isaacs LT. (1991) Three-dimensional modelling of fill drainage in mine stopes. *Transactions of the Institution of Mining and Metallurgy*, Section A: Mining Industry, 100, A66-A72.

Walske ML, McWilliam H, Doherty J & Fourie A. (2016) Influence of curing temperature and stress conditions on mechanical properties of cementing paste backfill. *Canadian Geotechnical Journal*, 53(1), 148-161.

Widisinghe S, Sivakugan N & Wang VZ. (2013) Laboratory investigations of arching in backfilled mine stopes. *Advances in Geotechnical Infrastructure*, 741-746.

Winch C. (1999) Geotechnical characteristics and stability of paste backfill at BHP Cannington Mine, *B. E. Hons Thesis*, James Cook University, Townsville, Australia.

Yang (2015) Investigation of the hydro-mechanical behavior of backfill in mine stopes and barricade drifts. *Pre-doctoral Report* (unpublished), Polytechnique Montréal, Canada.

Yang PY & Li L. (2014) A 3D analytical solution for the short-term stress distribution in backfilled stopes and on barricades. *67th Canadian Geotechnical Conference*, Regina, SK, Canada.

Yang PY & Li L. (2015) Investigation of the short-term stress distribution in stopes and drifts backfilled with cemented paste backfill. *International Journal of Mining Science and Technology*, 25(5), 721-728.

Yang PY & Li L. (2016) Evolution of water table and pore water pressure in stopes with submerged hydraulic fill. *International Journal of Geomechanics*. Accepted with changes in October 2016. This article is presented in Chapter 3.

Yang PY, Brochu-Baekelmans M, Li L & Aubertin M. (2014) An improved solution for sizing barricades made of waste rock to retain cemented paste backfill. *67th Canadian Geotechnical Conference*, Regina, SK, Canada.

Yang PY, Li L, Aubertin M, Brochu-Baekelmans M & Ouellet S. (2016a) Stability analyses of waste rock barricades designed to retain paste backfill. *International Journal of Geomechanics*, doi: 10.1061/(ASCE)GM.1943-5622.0000740, 04016079. This article is presented in Chapter 4.

Yang PY, Li L & Aubertin M. (2016b) A new solution to assess the required strength of mine backfill with a vertical exposure. *International Journal of Geomechanics*. Submitted in September 2016. This article is presented in Chapter 5.

Yang PY, Li L & Aubertin M. (2016c) A comprehensive numerical analysis of stress ratios in vertical backfilled openings. *International Journal of Geomechanics*. Submitted in November 2016. This article is presented in Chapter 6.

Yang PY, Li L, Aubertin M & Tiwari A. (2016d) An investigation of the relationships between K_0, ϕ' and ν for granular materials. To be submitted. Main results are presented in Appendix A.

Yu TR. (1989) Some factors relating to the stability of consolidated rockfill at Kidd Creek. In *Innovations in Mining Backfill Technology*, Hassani et al. (eds), Balkema, Rotterdam, 279-286.

Yu TR, & Counter DB. (1983) Backfill practice and technology at Kidd Creek Mines. *CIM Bulletin*, 76(856), 56-65.

Yumlu M & Guresci M. (2007) Paste backfill bulkhead monitoring - A case study from Inmet's Cayeli mine. *9th International Symposium in Mining with Backfill*, CIM, Montreal, Canada.

Zhang Q, Zhang JX, Huang YL & Ju F. (2012) Backfilling technology and strata behaviors in fully mechanized coal mining working face. *Int J Min Sci Technol*, 22(2), 151-157.

Zhang JX, Li BY, Zhou N & Zhang Q. (2016) Application of solid backfilling to reduce hard-roof caving and longwall coal face burst potential. *International Journal of Rock Mechanics and Mining Sciences*, 88, 197-205.

Zhu ZM. (2002) Analysis of mine backfill behaviour and stability. *Ph.D. Thesis*, McGill University, Montreal, Canada.

Zou DH & Nadarajah N. (2006) Optimizing backfill design for ground support and cost saving. *41st US Rock Mechanics Symp.: 50 Years of Rock Mechanics*, ARMA, Alexandria.

APPENDIX A – AN INVESTIGATION OF THE RELATIONSHIPS BETWEEN K_0, ϕ' AND ν FOR GRANULAR MATERIALS

A1. INTRODUCTION

The coefficient of earth pressure at-rest, K_0, is a key parameter that is frequently used in geotechnical engineering. It is usually defined as the ratio between the horizontal and vertical effective stresses ($K_0 = \sigma'_h/\sigma'_v$) in a semi-infinite soil mass, under conditions where uniform vertical loading does not produce lateral strain (e.g., Terzaghi et al. 1996; Craig 2004; Aysen 2005; Sivakugan & Das 2009). The value of the coefficient of earth pressure at-rest K_0 mainly depends on the type of the soil, its density, stress history, and plasticity characteristics (Bishop 1958; Terzaghi et al. 1996; Michalowski 2005).

In practice, the value of K_0 is rarely measured. It is usually obtained from a simple relationship with the internal friction angle ϕ' proposed by Jaky (1944, 1948) or, more rarely, from the theoretical relationship with Poisson's ratio ν. This duality leads to the assumption that the internal friction angle ϕ' and Poisson's ratio ν could be, in some ways, related to each other, so that a unique (and consistent) value of coefficient K_0 is obtained from the two approaches. Although this view is not necessarily shared by all (e.g., Talesnick 2012), it seems quite relevant to investigate this aspect given the impact that this may have on the analysis of various types of problems such as the simulated stress state in mining backfilled stopes (e.g., Falaknaz et al. 2015; Jahanbakhshzadeh 2016).

In the following, the two main approaches for defining K_0 are briefly recalled. A simple correlation between the internal friction angle ϕ' and Poisson's ratio ν (at small strains), based on K_0, is then proposed. The validity of this correlation is evaluated using a large number of experimental results taken from the literature on granular materials. The data are used to evaluate both ϕ' and ν from conventional triaxial compression (CTC) tests performed on sands and rockfills. The assessment also includes a comparison of the K_0 values predicted by the two basic equations based on ϕ' and ν.

A2. THE EARTH PRESSURE COEFFICIENT AT-REST K_0

Jaky's equation

Jaky (1944) analyzed the state of stress within a free-standing pile of loose granular material with sides inclined at the angle of repose. This angle of repose α is often considered equal to the internal friction angle under the loosest soil state (ϕ_0'). Jaky (1944) analyzed the stress state along the centerline of the pile model, for an at-rest condition (i.e., K_0 state). Based on several simplifying assumptions, Jaky (1944) proposed the following expressions for the vertical (effective) stress $\sigma'_v = \sigma'_1$ (major principal stress) and horizontal stress $\sigma'_h = \sigma'_3$ (minor principal stress) acting along the centerline of the pile model:

$$\sigma'_1 = \gamma z \tag{A.1a}$$

$$\sigma'_3 = \gamma z(1-\sin\phi')\frac{1+\frac{2}{3}\sin\phi'}{1+\sin\phi'} \tag{A.1b}$$

where γ (kN/m^3) is the soil unit weight; z (m) is the vertical distance from the top to the calculation point along the centerline. In this equation, it was assumed that $\phi' = \phi_0'$ as it was developed for loose soils.

The coefficient of earth pressure at-rest K_0 is thus given by

$$(K_0)_{\phi'} = \frac{\sigma'_h}{\sigma'_v} = \frac{\sigma'_3}{\sigma'_1} = (1-\sin\phi')\frac{1+\frac{2}{3}\sin\phi'}{1+\sin\phi'} \tag{A.2}$$

For soils with ϕ' values between 20° and 45°, Jaky (1944) approximated the second term on the right-hand side of equation (A.2) to be 0.9 to obtain

$$(K_0)_{\phi'} = 0.9(1-\sin\phi') \tag{A.3}$$

Equations (A.1) - (A.3) have been developed for granular materials in a very loose state, when $\alpha = \phi_0' = \phi'$, but this condition is rarely encountered in practice. Later, without much explanation, Jaky (1948) gave the following modified expression for K_0, based on the peak internal friction angle, $\phi' = \phi_p'$ (instead of the loose state value):

$$(K_0)_{\phi'} = 1-\sin\phi' \tag{A.4}$$

Figure A-1 shows the variation of K_0 with the internal friction angle ϕ', obtained by these three equations. The commonly used expression (equation (A.4)) is thus an approximation of the original one (equation (A.2)); it leads to somewhat higher values of K_0 for $\phi' > 0°$.

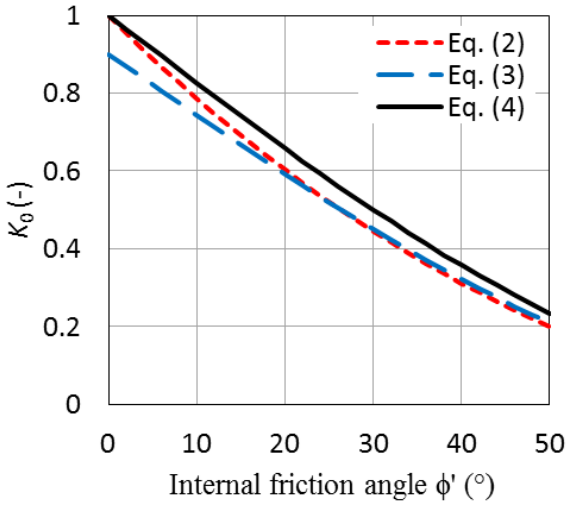

Figure A-1: The variation of K_0 with internal friction angle, obtained by the different expressions proposed by Jaky (1944, 1948)

Equation (A.4) indicates that the value of K_0 tends to increase with a decrease of ϕ', up to $K_0 = 1$ when there is no friction (i.e., $\sigma'_h = \sigma'_v$, for $\phi' = 0$). The latter corresponds to the behavior of incompressible fluids, and it is commonly applied to the response of saturated fine grained (clay) soils under unconsolidated-undrained (UU) conditions (e.g., Lambe & Whitman 1979).

Equation (A.4) was later shown experimentally to be applicable to sands of various densities (e.g., Bishop & Eldin 1953; Hendron 1963; Al-Hussaini & Townsend 1975; Mesri & Hayat 1993) and to normally consolidated clays (e.g., Brooker & Ireland 1965; Ladd et al. 1977; Mayne & Kulhawy 1982; Feda 2013). Equation (A.4) has also been extended to over-consolidated soils (e.g., Hendron 1963; Schmidt 1966; Alpan 1967; Brooker & Ireland 1965; Daramola 1980; Mayne & Kulhawy 1982; Sherif et al. 1984; Kulhawy 2005; Das 2010b; Holtz et al. 2011; Feda 2013).

Equation (A.4) is often considered non-rigorous, in part because it relates a yielding/failure strength parameter, ϕ', to an at-rest (stable) state parameter, K_0 (e.g., Mesri & Hayat 1993; Michalowski & Park 2004; Michalowski 2005; Wanatowski & Chu 2007; Federico et al. 2009; Talesnick 2012). Despite these reservations, it remains widely used in practice.

K_0 based on Poisson's ratio

The Poisson's ratio v was originally defined as a material constant and applied to linear elastic behavior (mainly for metals) (e.g., Bower 2009). As soils rarely behave elastically, it

could be argued that a more appropriate term would be "principal strains ratio" (PSR) for their deformation characteristics (see below). For the sake of simplicity however, the authors are using the commonly used terminology, i.e., Poisson's ratio, when analyzing the multiaxial deformation characteristics of granular materials.

The value of the coefficient of earth pressure at-rest K_0 can be theoretically related to Poisson's ratio v, based on the following well-known Hooke's law (within a semi-infinite isotropic mass):

$$\varepsilon_1 = \frac{1}{E}\left(\sigma'_1 - 2v\sigma'_3\right) \tag{A.5a}$$

$$\varepsilon_3 = \frac{1}{E}\left[\sigma'_3\left(1-v\right) - v\sigma'_1\right] \tag{A.5b}$$

where ε_1 and ε_3 are the major (vertical) and minor (horizontal) principal strains, respectively; E is Young's modulus.

Under an at-rest state, the horizontal (lateral) strain due to an increase of the vertical stress is nil ($\varepsilon_3 = 0$), as straining can only occur vertically in the semi-infinite medium. When equation (A.5b) is equal to zero, the value of K_0 can be expressed as follows (e.g., Tschebotarioff 1973; Blight 1986; Bardet 1997; Aysen 2005; McCarthy 2007; Das 2010a; Talesnick 2012; Briaud 2013):

$$\left(K_0\right)_v = \frac{\sigma'_3}{\sigma'_1} = \frac{\sigma'_h}{\sigma'_v} = \frac{v}{1-v} \tag{A.6}$$

It is however generally recognized that this relationship is difficult to apply in the case of soils because determining the value of v is challenging and often ambiguous. This limitation may largely explain why Jaky's expression (equation (A.4)) is commonly preferred in geotechnique to define the value of K_0.

A3. PROPOSED CORRELATION BETWEEN ϕ' AND v

The two main relationships available to obtain the value of K_0 (equations (A.4) and (A.6)) suggest that the values of ϕ' and v should be related, so that a unique (consistent) K_0 is obtained from these two equations (which are sometimes considered "equivalent"; e.g., Dysli 2001; McCarthy 2007; Blight 2010). This leads to the following relationship (Duncan & Bursey 2013; Falaknaz 2014):

$$\nu = \frac{1 - \sin\phi'}{2 - \sin\phi'} \tag{A.7}$$

It could be argued that this equation should be applied systematically when an elasto-plastic model is used (in numerical simulations for instance) so a single (unique) value of K_0 is obtained (e.g., Falaknaz et al. 2015; Jahanbakhshzadeh 2016).

A somewhat similar expression has been proposed by Duncan et al. (1991), based on the same premises (as for equation (A.7)) combined with other (empirical) considerations:

$$\nu = \frac{1 - 3/4\sin\phi'}{2 - \sin\phi'} \tag{A.8}$$

The following simple expression can thus be obtained from equations (A.7) and (A.8):

$$\nu = \frac{1 - \lambda\sin\phi'}{2 - \sin\phi'} \tag{A.9}$$

where λ is a material parameter. Equation (A.9) is proposed here to establish the relationship between the internal friction angle ϕ' and Poisson's ratio v. As special cases, when $\lambda = 1$ or 0.75, equation (A.9) reduces to equation (A.7) or (A.8), respectively.

In the following sections, the authors present the approach used to assess the validity of equation (A.9) and the corresponding value of λ. This process can be challenging, in a large part due to the uncertainty regarding the determination of Poisson's ratio. The analysis and results shown below nonetheless indicate that the proposed relationship is applicable to relatively loose granular materials having a contractive behavior.

A4. ANALYSIS OF CONVENTIONAL TRIAXIAL COMPRESSION TESTS (CTC) RESULTS

As stated above, the direct determination of Poisson's ratio of soils often raises some issues (e.g., Lambe & Whitman 1979; Yokota & Konno 1980; Aysen 2005; Briaud 2013; Suwal & Kuwano 2013). Their shear (failure) strength is more commonly evaluated. Many experimental results will be used in the following to determine ϕ' and v, and investigate the correlation between these two parameters.

Source and interpretation of data

Figure A-2 schematically shows typical deviatoric stress-axial strain-volume strain relationships for a granular material under a constant confining pressure (σ'_3) during a CTC test. It is seen that the axial strain ε_1 - deviatoric stress (σ'_1-σ'_3) relationship is nonlinear almost from the onset. The maximum deviatoric stress corresponds to the peak strength. Specimens of relatively loose granular materials undergo volumetric contraction during the initial stage of deviatoric loading, followed by a constant volume response or a phase of dilation with further shearing. Theses stress-strain curves depend on the confining stress σ'_3.

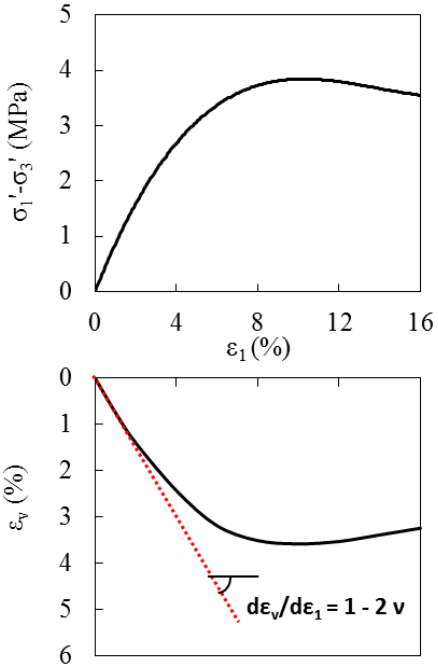

Figure A-2: Schematic illustration of deviatoric stress-axial strain-volumetric strain relationships measured on a granular material submitted to CTC tests

As the response of granular materials is generally non-linear, stress dependent, and inelastic (e.g., Hall & Gordon 1964; Marsal 1967; Marschi et al. 1972; Charles & Watts 1980; Lambe & Heartz 1988; Araei 2014; Honkanadavar et al. 2014), it is essential to define the method to obtain the two parameters of interest (ϕ' and ν).

Experimental results (taken from various sources) are analyzed to determine the values of ϕ' and ν for 7 types of sands and 20 types of rockfill materials submitted to CTC tests. For the Poisson's ratio, the focus is put on the initial stage of loading when the specimens undergo volumetric contraction. The main characteristics of these tests are summarized in Table A-1. All

the tests were performed under CD (consolidated, drained) conditions. Materials identification is based on the abbreviations (given in Table A-1) in the following. The methods applied to determine the values of ϕ' and v from CTC tests are specifically described in the following.

Table A-1. Characteristics of the sands and rockfills submitted to CTC tests

Sands or Rockfills	Abbreviation	σ'_3 (kPa)	d_{max} (mm)	C_U	G_s	e_0	D^*H (cm)	CT	Source
Compacted sand	CS	392, 961, 1933, 2953, 3924	NA	NA	2.7	~0.5	5.5/12.7	NA	Hirschfeld & Poulos 1964
Ham river sand	HRS	690, 3450, 6831	NA	NA	NA	NA	3.8/7.6	ISO	Bishop et al. 1965
Basalt	B	491, 981, 2453	200	19	2.78	0.3	113/250	ISO	Marsal 1967
Silica sand	SS3	98, 294, 490	NA	NA	NA	0.67	3.6/8.6	ISO	Duncan & Chang 1970
Argillite	A1	207, 966, 2898, 4485	50.8	NA	2.62	0.45	30.5/76.2	ISO	Marachi et al. 1972
Argillite	A2		152.4	NA	2.62	0.45	91.4/228.6		
Argillite	A3		11.4	NA	2.62	0.45	7.1/17.8		
San Francisco Basalt	SFB		50.8	NA	2.87	0.43	30.5/76.2		
Graywacke sand stone	GSS	49, 98, 196, 343, 589	NA	NA	2.69	NA	30/60	ISO	Ansari & Chandra 1986
Toyoura sand	TS1	98	0.16	1.46	2.64	0.907	7/15, 7/18	NA	Goto & Tatsuoka 1988
Toyoura sand	TS2	196, 588, 1470, 2940, 4900, 9800	NA	1.48	2.65	~0.75	NA	ISO	Kitamura & Haruyama 1988

Table A-1. Characteristics of the sands and rockfills submitted to CTC tests (cont'd)

Sands or Rockfills	Abbreviation	σ'_3 (kPa)	d_{max} (mm)	C_U	G_s	e_0	D^*H (cm)	CT	Source
Sandy silt	SS1	98, 392	NA	NA	NA	NA	20/40	NA	Mochizuki et al. 1988
Seto sand	SS2		2	3.1	2.557	0.566			
Micaceous sandstone and quartzite	MSQ	200, 400, 600, 800	50	NA	NA	NA	38.1/813	NA	Varadarajan et al. 2003, 2006
Limestone	LS4	300, 600, 900, 1200	25	NA	NA	NA			
Alluvium rockfill	ARF	350, 700, 1100, 1400	80	NA	NA	NA	38.1/813, 50/60		
Blasting rockfill	BRF	300, 600, 900, 1200	80	NA	NA	NA			
Granite	G	800, 1600	60	NA	NA	NA	30/60	NA	Cheng et al. 2010
Coarse grained soil	CGS	100, 200, 400	60	15.5	NA	NA	30/60	NA	Qin et al. 2010
Volcanic and limestone	VLS	200, 600, 1000, 1500	NA	NA	NA	NA	30/60	NA	Araei 2014
Limestone	LS5		NA	NA	NA	NA			
Limestone	LS1	400, 800, 1200	25	NA	2.66	NA	38.1/813	ISO	Honkanadavar et al. 2014
Limestone	LS2		50	NA	2.66	NA			
Limestone	LS3		80	NA	2.66	NA			
Metamorphic gneiss	MG		25	NA	2.73	NA			
Riverbed rockfill	RRF	200, 400, 600, 800	4.75	NA	NA	NA			Honkanadavar & Sharma 2014
Quarried rockfill	QRF								

σ'_3 = confining pressure; d_{max} = maximum particle size; C_U = coefficient of uniformity; G_s = specific gravity; e_0 = initial void ratio; D = specimen diameter; H = specimen height; CT = consolidation type; ISO = isotropically consolidated; NA = not available.

Determination of ϕ'

The typical stress-strain response of granular soils submitted to CTC tests indicate that for a given axial strain (ε_1), the deviatoric stress (σ'_1-σ'_3) and its peak value tend to increase with the confining pressures (σ'_3). A curve fitting technique has been applied to obtain the values of ϕ' (= ϕ_p') from the peak values of σ'_1-σ'_3, based on the Mohr-Coulomb criterion. The best fitting straight lines are forced to pass through the origin in the principal stress plane (i.e., no cohesion, $c' = 0$) for all the granular materials investigated here.

For the relatively loose granular materials considered here, the internal friction angle ϕ' (= ϕ_p') is often equal (or very close) to the constant volume (ultimate) internal friction angle (i.e., $\phi' = \phi_p' = \phi'_{cv}$; e.g., Craig 2004).

Determination of ν

The Poisson's ratio ν of a specimen (assumed to be isotropic) subjected to a CTC test can be obtained by rearranging equations (A.5a) and (A.5b) for incremental loading (e.g., Lambe & Whitman 1979; Watabe et al. 2003):

$$\nu = \frac{d\varepsilon_3 d\sigma'_1 - d\varepsilon_1 d\sigma'_3}{2d\varepsilon_3 d\sigma'_3 - d\varepsilon_1 \left(d\sigma'_1 + d\sigma'_3\right)} \tag{A.11}$$

where $d\varepsilon_1$ and $d\varepsilon_3$ are the vertical and horizontal strains variations (increments), respectively.

The confining pressure usually remains constant during deviatoric loading with a CTC test, so $d\sigma'_3 = 0$ in equation (A.11). The Poisson's ratio can thus be obtained from the negative value of the ratio between $d\varepsilon_3$ and $d\varepsilon_1$ (e.g., Lambe & Whitman 1979; Hoque & Tatsuoka 1998; Watabe et al. 2003; Suwal & Kuwano 2013):

$$\nu = -\frac{d\varepsilon_3}{d\varepsilon_1} \tag{A.12}$$

When $d\varepsilon_3$ is not directly measured, the lateral strain variation can be obtained from the measured axial $d\varepsilon_1$ and volumetric $d\varepsilon_v$ strain increments:

$$d\varepsilon_3 = \frac{d\varepsilon_v - d\varepsilon_1}{2} \tag{A.13}$$

Introducing equation (A.13) into equation (A.12) leads to the following expression (e.g., Duncan & Chang 1970; Bardet 1997; Magnan & Mestat 1997):

$$\nu = \frac{1 - d\varepsilon_v / d\varepsilon_1}{2} \tag{A.14}$$

Equation (A.14) has been used here to determine the values of Poisson's ratio from CTC tests results at relatively low strains.

For all the materials considered here, the stress-strain curves are analyzed for relatively low confining pressures (see below) using first the data points at very small strains (≤ 2%). The corresponding Poisson's ratio (expressed as $\nu_{2\%}$) is determined from the slope (i.e., $d\varepsilon_v/d\varepsilon_1$) of the best fit line (e.g., the dash lines shown in Fig. A-2) based on equation (A.14). The same approach is applied to the values of the Poisson's ratio at a larger (but still small) strain $\varepsilon_1 \leq 4\%$ ($\nu_{4\%}$). Both values are given in Table A-2.

A5. RESULTS AND ANALYSIS

Table A-2 gives the values of the internal friction angle ϕ' (= ϕ_p') and Poisson's ratio ν at very low ($\varepsilon_1 \leq 2\%$) and low ($\varepsilon_1 \leq 4\%$) strains (with the corresponding K_0, see below), based on the tests results identified in Table A-1, for granular materials with a contractive behavior. The specific intervals of axial strain ε_1 used to define ν (for $\varepsilon_1 \leq 2\%$ and $\varepsilon_1 \leq 4\%$) are also presented in Table A-2.

It is observed from this table that the value of ϕ' varies from about 30° to 45° for rockfills and 25° to 38° for sands; these are in the typical ranges for such types of materials (e.g., Budhu 2000; Duncan & Wright 2005; Das 2010a; Briaud 2013).

For rockfills, the value of Poisson's ratio typically varies from about 0.23 to 0.37 (average value of 0.30) for very low strains ($\varepsilon_1 \leq 2\%$) and from about 0.24 to 0.38 (average value of 0.32) for low strains ($\varepsilon_1 \leq 4\%$). For sands, the value of $\nu_{2\%}$ typically ranges between about 0.15 and 0.38 with an average value of 0.28 and $\nu_{4\%}$ between about 0.23 and 0.38 with an average value of 0.31. These ranges are fairly close to the typical range of Poisson's ratio, from 0.2 to 0.35, for loose sands reported by Hunt (1986) and Das (2010a). Briaud (2013) also reported values of the Poisson's ratio, which are between 0.2 to 0.4 for loose sands and from 0.2 to 0.35 for loose gravels. The results determined here are thus deemed representative of these granular materials.

Table A-2. Values of the internal friction angle and Poisson's ratio at very low ($\varepsilon_1 \leq 2\%$) and low ($\varepsilon_1 \leq 4\%$) strains, obtained from CTC tests results on granular materials, with the corresponding K_0 (see Table A-1)

Material identification (symbol)	ϕ_p' (°)	K_0 based on ϕ_p' (Eq. A.4)	$\nu_{2\%}$	K_0 based on $\nu_{2\%}$ (Eq. A.6)	ε_1 interval for $\nu_{2\%}$ (%)	$\nu_{4\%}$	K_0 based on $\nu_{4\%}$ (Eq. A.6)	ε_1 interval for $\nu_{4\%}$ (%)
B	37.76	0.388	0.251	0.335	1~2	0.304	0.436	1~4
G	43.61	0.310	0.240	0.315	0~1.8	0.240	0.315	0~1.8
A1	36.96	0.399	0.250	0.333	0~1.5	0.250	0.333	0~1.5
A2	36.10	0.411	0.232	0.302	0~1	0.305	0.438	0~2.3
A3	38.60	0.376	0.307	0.443	0.2~0.8	0.362	0.567	0.2~1.4
SFB	37.98	0.385	0.320	0.470	0.5~1.7	0.320	0.470	0.5~1.7
GSS	41.30	0.340	0.302	0.432	0.3~1.5	0.316	0.462	0.3~2
LS1	37.13*	0.396	0.282	0.393	0~1	0.328	0.489	0~2
LS2	38.37*	0.379	0.279	0.387	0~1	0.327	0.486	0~2
LS3	39.76*	0.360	0.234	0.306	0~1	0.294	0.417	0~2
MG	43.35*	0.314	0.254	0.340	0~1	0.307	0.444	0~2
RRF	36.30*	0.408	0.327	0.486	0~1	0.341	0.517	0~1.5
QRF	47.50*	0.263	0.325	0.481	0~1	0.327	0.485	0~2
MSQ	35.30*	0.422	0.312	0.453	0~1	0.333	0.500	0~1.5
LS4	42.90*	0.319	0.346	0.528	0~1	0.352	0.544	0~1.5
ARF	35.40*	0.421	0.287	0.403	0~1	0.316	0.462	0~3
BRF	30.60*	0.491	0.311	0.452	0~2	0.347	0.532	0~3
VLS	38.37	0.379	0.357	0.556	0~0.3	0.381	0.616	0~1
LS5	39.11	0.369	0.332	0.498	0~0.6	0.343	0.522	0~1.2
CGS	36.98	0.398	0.369	0.585	0~0.5	0.374	0.597	0~0.9
CS	38.36	0.38	0.245	0.325	0~1.7	0.277	0.382	0~3.5
TS1	34.38	0.44	0.260	0.351	0~0.4	0.350	0.537	0~1.5
HRS	30.37	0.49	0.269	0.367	0~1.5	0.284	0.396	0~2
TS2	25.73	0.566	0.376	0.603	0~0.7	0.376	0.603	0~0.7
SS1	34.87	0.43	0.150	0.176	0~1.4	0.225	0.290	0~3.2
SS2	35.60	0.42	0.313	0.457	0~1	0.345	0.527	0~2
SS3	30.40*	0.49	0.341	0.517	0.5~1	0.341	0.517	0.5~1

* = available from the source.

Relationship between ϕ' and v at very small strains

Figure A-3 illustrates the relationships between $v_{2\%}$ and ϕ' (= ϕ_p') obtained from equation (A.9) and the CTC testing results (identified in Table A-1) for 20 rockfills (Fig. A-3a) and 7 sands (Fig. A-3b). It is shown that fairly well defined correlations exist between the values of $v_{2\%}$ and ϕ' for these granular materials. Fig. A-3a shows that the values of $v_{2\%}$ obtained from equation (A.9) with λ = 0.75 (equation (A.8)) and with λ = 1.15 appears to give the upper and lower bounds for rockfills. It is also seen from Fig. A-3b that experimental results fall in the range given by equation (A.9) with λ = 1.35 and λ = 0.75 (equation (A.8)) for sands. May be more importantly, the analysis indicates that most experimental data are fairly close to equation (A.9) with λ equal to unity (or equation (A.7), from Jaky) for both types of materials, with an average value of λ = 0.94 for rockfills (Fig. A-3a) and with λ = 1 for sands (Fig. A-3b).

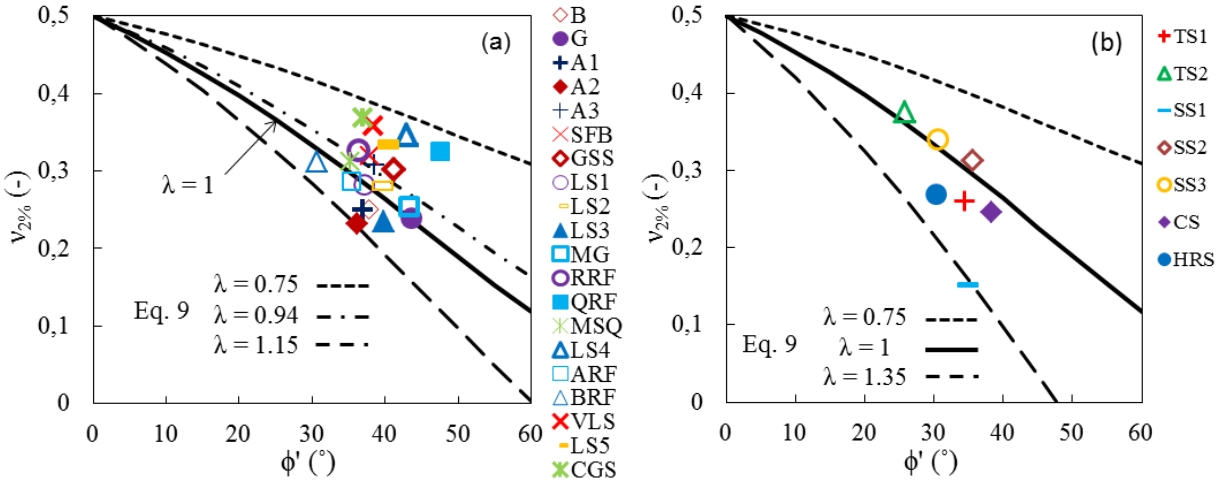

Figure A-3: Variations of $v_{2\%}$ with ϕ' (= ϕ_p') for (a) rockfills and (b) sands (materials characteristics and testing conditions given in Table A-1)

Figure A-4 shows the values of $v_{4\%}$ as a function of ϕ' (= ϕ_p') obtained from equations (A.7) - (A.9) applied to the testing results identified in Table A-1 (for granular materials). It is seen that the values of $v_{4\%}$ are generally larger than $v_{2\%}$. Samples tend to show a more pronounced lateral expansion with higher axial strains, which increases the values of Poisson's ratio (i.e., v increases with ε_1; Lambe & Whittman 1979).

There also appears to be fairly well defined relationships between the values of $v_{4\%}$ and ϕ' for both rockfills and sands. For the former, it is seen from Fig. A-4a that most experimental data fall in the range given by equation (A.9) with λ = 1 (equation (A.7)) and λ = 0.75 (equation (A.8)). Equation (A.9) with λ = 0.87 appears to give a best fit for rockfills. For the latter, Fig. A-4b shows that the values of $v_{4\%}$ obtained from equation (A.9) with λ = 0.75 (equation (A.8)) and with λ = 1.25 appears to give the upper and lower bounds; most of the experimental results are close to equation (A.9) with λ = 1 (equation A.7) for sands.

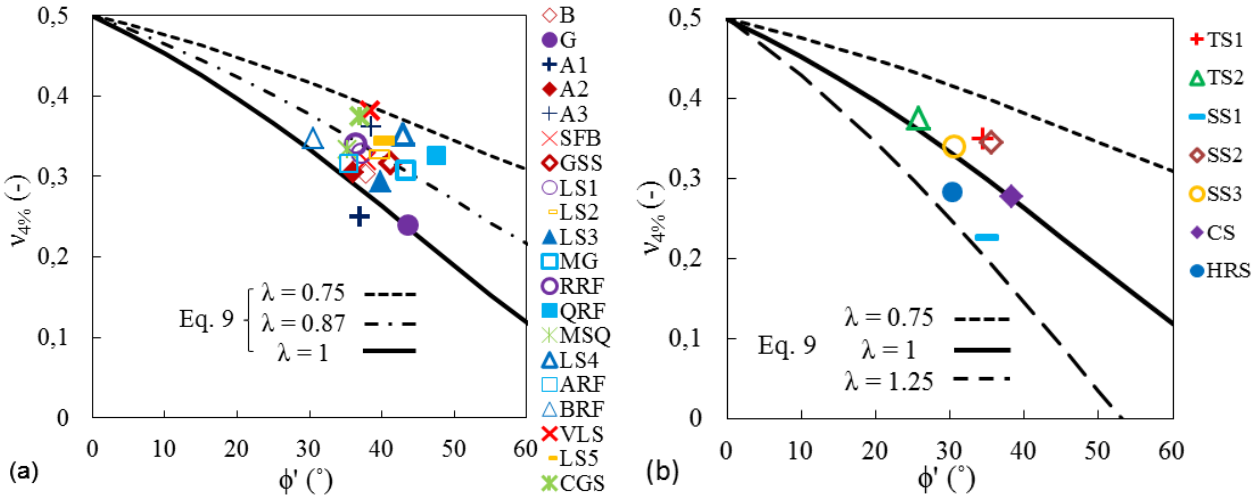

Figure A-4: Variations of $v_{4\%}$ with ϕ' (= ϕ_p') for (a) rockfills and (b) sands (materials characteristics and testing conditions given in Table A-1)

K_0 based on ϕ' and v

Figure A-5 illustrates the comparisons of K_0 values calculated with equation (A.4) using the internal friction angle ϕ' (= ϕ_p') and equation (A.6) using $v_{2\%}$, based on the results from CTC tests performed on 20 types of rockfills (Fig. A-5a) and 7 types of sands (Fig. A-5b). It is seen from Fig. 5a that most experimental data for rockfills correlate well with equation (A.9) with λ = 0.94 (i.e., close to λ = 1); the values of $v_{2\%}$ obtained from equation (A.9) with λ = 0.75 (equation (A.8)) and with λ = 1.15 provide the upper and lower bounds. Fig. A-5b shows that for sands, most experimental results are close to equation (A.9) with λ = 1 (equation (A.7)), and bounded by the relationships given by λ = 0.75 (equation (A.8)) and λ = 1.35.

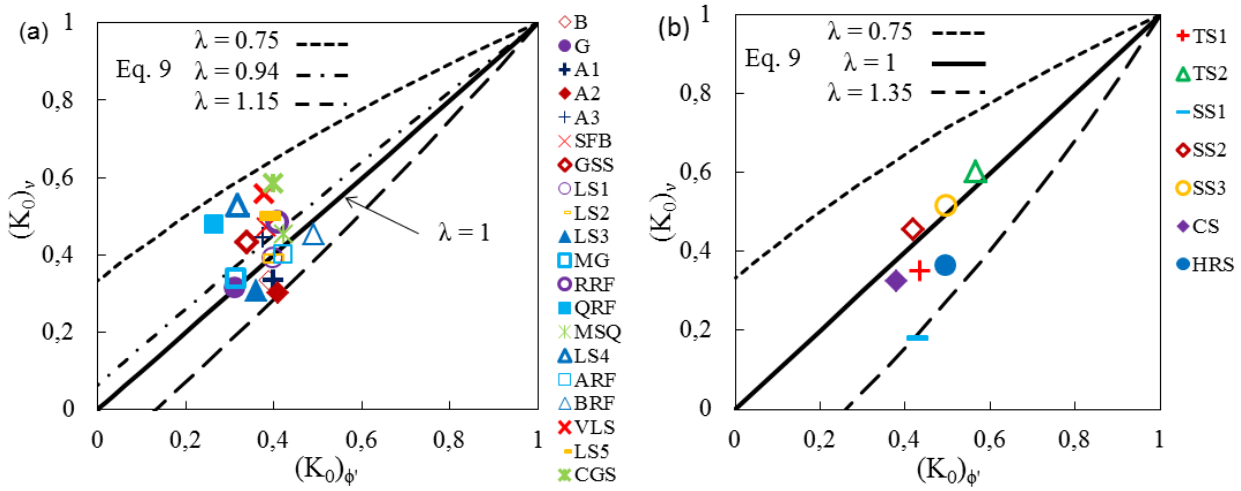

Figure A-5: Evaluation of the K_0 values based on ϕ' (= ϕ_p') and $\nu_{2\%}$ for different (a) rockfills and (b) sands (materials characteristics and testing conditions given in Table A-1)

Figure A-6 shows the comparisons of K_0 values estimated from equation (A.4) based on the internal friction angle ϕ' (= ϕ_p') and equation (A.6) with the Poisson's ratio at larger strain $\nu_{4\%}$. Fig. A-6a indicates that the values of $(K_0)_{\phi'}$ are lower than those obtained from the $\nu_{4\%}$ for most rockfills (see Fig. A-5a). Almost all the experimental data on rockfills fall in the range given by equation (A.9) with λ = 1 (equation (A.7)) and λ = 0.75 (equation (A.8)). A best fit is obtained for λ = 0.87. The experimental results on sands shown in Fig. A-6b are quite close to equation (A.9) with λ = 1 and bounded by λ = 0.75 (equation (A.8)) and λ = 1.25.

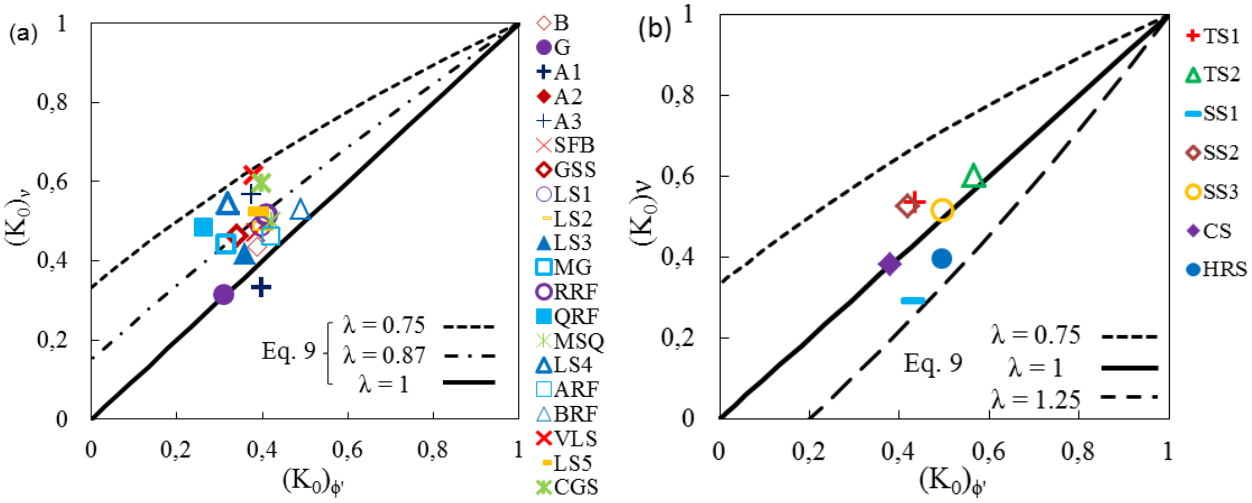

Figure A-6: Evaluation of the K_0 values based on ϕ' (= ϕ_p') and $\nu_{4\%}$ for different (a) rockfills and (b) sands (materials characteristics and testing conditions given in Table A-1)

Despite the normal scattering expected for soil behavior, there thus appears to be a well-defined relationship between the two approaches for defining K_0, and thus between the internal friction angle ϕ' and Poisson's ratio ν at very low and low strains.

A6. DISCUSSION

It was postulated here that the values of ϕ' and ν should be related to ensure a unique (consistent) definition of K_0. The correlation between ϕ' and ν should be applied systematically in numerical analyses, as it may affect the simulated outcomes for various types of problems such as the stress state in mining backfilled stopes (e.g., Falaknaz et al. 2015; Jahanbakhshzadeh 2016).

A simple relationship is proposed for this purpose. Conventional triaxial compression (CTC) tests results performed on 20 types of rockfills and 7 types of sands, reported in the literature, have been analyzed for this purpose. These results cover a fairly wide range of characteristics, so these can be considered representative of many granular materials encountered in geotechnical engineering. The analyses presented above strongly suggest that the proposed relationship (equation (A.9)) is valid for relating the peak internal friction angle and the Poisson's ratio at very low ($\varepsilon_1 \leq 2\%$) and low strains ($\varepsilon_1 \leq 4\%$), for relatively loose materials with a contractive behavior.

Despite the encouraging outcomes, it should be kept in mind that the analysis (including the tests results and data interpretation) is based on a number of simplifying assumptions. For instance, it is assumed (as is commonly done) that the stress state and strains are uniform in the tested samples. In reality, this may not be entirely the case, so the methods used to obtain the Poisson's ratio and (to a lesser extent) the internal friction angle from the tests results can be approximate (and somewhat imprecise). More direct measurements would be required to obtain more accurate and reliable values.

Although most soils do not behave linear-elastically, "elastic" parameters (such as Young's modulus and Poisson's ratio) have sometimes been determined from the initial stage of loading (at low strains) based on CTC tests results (e.g., Lambe & Whitman 1979; Duncan & Chang 1970; Samieh 1995; Bardet 1997; Magnan & Mestat 1997; Varadarajan et al. 2003; Honkanadavar & Sharma 2014; Honkanadavar et al. 2014). The approach taken here is thus in line with earlier treatment of testing results, and suffers from the same limitations.

At a given small axial strain ε_1, the values of the Poisson's ratio determined from CTC tests can vary with the imposed confining pressure σ'_3 (e.g., Yokota & Konno 1980; Bates 1989; Kumar & Madhusudhan 2010; Suwal & Kuwano 2013). In a CTC test, higher confining pressures would normally lead to denser soil specimens (with a lower void ratio). Soils submitted to relatively low σ_3 are deemed closer to a normally consolidated state at relatively shallow depth. Therefore, the Poisson ratio was defined here from tests with relatively small σ'_3. The value of σ'_3 used here to define the Poisson ratio ranges from 49 to 800 kPa for rockfills and from 98 to 690 kPa for sands (see Table A-1).

If the best fit line in σ'_1-σ'_3 plane was not forced to pass through the origin (nonzero cohesion), the values of ϕ' would be slightly smaller than those based on cohesionless materials (assumed above). However, the difference in the K_0 values obtained from the two methods is insignificant.

It should also be recalled that the assessment of K_0 was based only on the relationships presented above. No direct measurement of K_0 has been considered here. It is thus assumed that these relationships give an adequate evaluation of the at-rest earth pressure coefficient for normally consolidated and relatively loose granular soils; this assumption is supported by the results of various investigations on Jaky's equation (e.g., Brooker & Ireland 1965; Al-Hussaini & Townsend 1975; Ladd et al. 1977; Mayne & Kulhawy 1982; Mesri & Hayat 1993).

A7. CONCLUSIONS

The results presented above tends to confirm that a well-defined correlation (equation (A.9)) can be established between the internal friction angle ϕ' and Poisson's ration v (through K_0), based on values of ϕ' and v estimated from the CTC tests results on 20 types of rockfills and 7 types of sands (reported in the literature). The corresponding values of K_0 based on the theoretical relationship with ϕ' and v are also compared.

The analysis strongly suggests that the proposed correlation (equation (A.9)) is valid for relating the peak internal friction angle and the Poisson's ratio at very low ($\varepsilon_1 \leq 2\%$) and low strains ($\varepsilon_1 \leq 4\%$), for relatively loose materials with a contractive behavior. The optimum value of λ may be somewhat dependent on the type of material. Nonetheless, applying equation (A.9) with $\lambda = 1$ (equation (A.7)) can be (and should be) done systematically when an elasto-plastic model is used in numerical simulations so a single (unique) value of K_0 is obtained.

The analysis of the CTC tests results specifically shows that the peak ϕ' varies from about 30° to 45° for rockfills and 25° to 38° for sands. For rockfills, the value of Poisson's ratio typically falls in the range of about 0.23 to 0.37 (average value of 0.30) for very low strains ($\varepsilon_1 \leq$ 2%) and about 0.24 to 0.38 (average value of 0.32) for low strains ($\varepsilon_1 \leq 4\%$). For sands, the value of $v_{2\%}$ typically varies from about 0.15 to 0.38 with an average value of 0.28 and $v_{4\%}$ from about 0.23 to 0.38 with an average value of 0.31.

NOTATION

K_0 coefficient of earth pressure at-rest

ϕ' effective internal friction angle

v Poisson's ratio

σ'_h horizontal effective stress

σ'_v vertical effective stress

α angle of repose

ϕ_0' effective internal friction angle under the loosest state

σ'_1 major effective principal stress

σ'_3 minor effective principal stress (confining pressure)

γ unit weight

z vertical distance from the top to the calculation point along the centerline

$(K_0)_{\phi'}$ coefficient of earth pressure at-rest based on Jaky's equation

ϕ_p' peak effective internal friction angle

ε_1 major (vertical) principal strain

ε_3 minor (horizontal) principal strain

E Young's modulus

$(K_0)_v$ coefficient of earth pressure at-rest based on Poisson's ratio

λ material parameter

ε_v volumetric strain

d_{max} maximum particle size

C_U coefficient of uniformity

G_s specific gravity

e_0 initial void ratio

D specimen diameter

H specimen height

c' effective cohesion

ϕ'_{cv} constant volume (ultimate) internal friction angle

$d\varepsilon_1$ vertical strain variation (increment)

$d\varepsilon_3$ horizontal strain variation (increment)

$d\varepsilon_v$ volumetric strain variation (increment)

$v_{2\%}$ Poisson's ratio at very small strains ($\leq 2\%$)

$v_{4\%}$ Poisson's ratio at small strains ($\leq 4\%$)

A8. REFERENCES

Al-Hussaini, M. & Townsend, F. (1975). Stress deformation of sand under K_0 conditions. In *Proceedings 5th panamerican conference on soil mech and found Eng.* **1**, pp. 129-136. Buenos Aires, Argentina.

Alpan, I. (1967). The empirical evaluation of the coefficient K_0 and K_{0r}. *Soils and Foundations*. *Japanese Society of Soil Mechanics and Foundation Engineering* **7**, No. 1, 31-40.

Ansari, K. S. & Chandra, S. (1986). How ought one to determine soil parameters to be used in the design of earth and rockfill dams. In *Proceedings of Indian geotechnical conference* **2**, pp. 1-6. New Delhi, India.

Araei, A. A. (2014). Artificial neural networks for modeling drained monotonic behavior of rockfill materials. *International Journal of Geomechanics* **14**, No. 3, 04014005.

Aysen, A. (2005). *Soil mechanics: basic concepts and engineering applications*. CRC Press.

Bates, C. R. (1989). Dynamic soil property measurements during triaxial testing. *Géotechnique* **39**, No. 4, 721-726.

Bishop, A. W. (1958). Test requirements for measuring the coefficient of earth pressure at-rest. In *Proceedings of Brussels conference on earth pressure problems.* pp. 2-14. Brussels, Belgium.

Bishop, A. W. & Eldin, G. (1953). The effect of stress history on the relationship between ϕ and porosity in sand. In *Proceedings of the third international conference on soil mechanics and foundation engineering*, pp. 100-105. Switzerland.

Bishop, A. W., Webb, D. L. & Skinner, A. E. (1965). Triaxial tests on soil at elevated cell pressures. In *Proceedings of the international conference of soil mechanics* **1**, pp. 170-174. Montréal, Canada.

Blight, G. E. (1986). Pressure exerted by materials stored in silos. Part I: Coarse materials. *Géotechnique* **36**, No. 1, 33-46.

Blight, G. E. (2010). *Geotechnical engineering for mine waste storage facilities*. Taylor & Francis, London.

Bower, A. F. (2009). *Applied mechanics of solids*. CRC press.

Briaud, J. L. (2013). *Geotechnical engineering: unsaturated and saturated soils*. John Wiley and Sons.

Brooker, E. W. & Ireland, H. O. (1965). Earth pressures at-rest related to stress history. *Canadian Geotechnical Journal* **2**, No.1, 1-15.

Budhu, M. (2000). *Soil mechanics and foundations*. John Wiley & Sons.

Charles, J. A. & Watts, K. S. (1980). The influence of confining pressure on the shear strength of compacted rockfill. *Géotechnique* **30**, No. 4, 353-367.

Cheng, Z. L., Zuo, Y. Z., Ding, H. S., Jiang, J. S., & Kong, X. Y. (2010). Wetting characteristics of coarse-grained materials. *Chinese Journal of Geotechnical Engineering* **32**, No. 2, 243-247.

Craig, R. F. (2004). *Craig's soil mechanics*. CRC Press.

Daramola, O. (1980). On estimating K_0 for overconsolidated granular soils. *Géotechnique* **30**, No. 3, 310-313.

Das, B. M. (2010a). *Geotechnical engineering handbook*. J. Ross Publishing.

Das, B. M. (2010b). *Principles of geotechnical engineering*. Cengage Learning.

Duncan, J. M. & Chang, C. Y. (1970). Nonlinear analysis of stress and strain in soils. *Journal of the Soil Mechanics and Foundations Division* **96**, No. 5, 1629-1653.

Duncan, J. M. & Wright, S. G. (2005). *Soil strength and slope stability*. John Wiley & Sons.

Duncan, J. M., & Bursey, A. (2013). Soil modulus correlations. In *Foundation engineering in the face of uncertainty: Honoring Fred H. Kulhawy*, 321-336. ASCE.

Duncan, J. M., Williams, G. W., Sehn, A. L. & Seed, R. B. (1991). Estimation earth pressures due to compaction. *Journal of Geotechnical Engineering* **117**, No. 12, 1833-1847.

Dysli, M. (2001). *Recherche bibliographique et synthèse des corrélations entre les caractéristiques des sols*. Ecole Polytechnique Fédéral de Lausanne-Laboratoire de mécanique des sols.

Falaknaz, N. (2014). *Analysis of the geomechanical behavior of two adjacent backfilled stopes based on two and three dimensional numerical simulations*. PhD thesis, Polytechnique Montréal, Canada.

Falaknaz, N., Aubertin, M. & Li, L. (2015). Numerical investigation of the geomechanical response of adjacent backfilled stopes. *Canadian Geotechnical Journal* **52**, No. 10, 1507-1525.

Jahanbakhshzadeh, A. (2016). *Analyse du comportement géomécanique des remblais miniers dans des 467 excavations souterraines inclinées*. PhD thesis, Polytechnique Montréal.

Feda, J. (2013). *Stress in subsoil and methods of final settlement calculation*. Elsevier.

Federico, A., Elia, G., Hamza, M., Shahien, M. & El-Mossallamy, Y. (2009). At-rest earth pressure coefficient and Poisson's ratio in normally consolidated soils. In *Proceedings of the 17th international conference on soil mechanics and geotechnical engineering: The academia and practice of geotechnical engineering*, Alexandria, Egypt, IOS Press.

Goto, S. & Tatsuoka, F. (1988). Effects of end conditions on triaxial compressive strength for cohesionless soil. In *Proceedings of Symposium on Advanced triaxial testing of soil and rock* (eds R. T. Donaghe, R. C. Chaney & M. L. Silver), ASTM International, pp. 692-705. Louisville, USA.

Hall, E. B. & Gordon, B. B. (1964). Triaxial testing with large-scale high pressure equipment. In *Proceedings of Symposium on Laboratory shear testing of soils*. ASTM International. Ottawa, Canada.

Hendron, Jr. A. J. (1963). *The behavior of sand in one-dimensional compression*. PhD thesis, Illinois Univ, Urbana.

Hirschfeld, R. C. & Poulos, S. J. (1963). High-pressure triaxial tests on a compacted sand and an undisturbed silt. In *Proceedings of Symposium on Laboratory shear testing of soils*. pp. 329-41. Ottawa, Canada.

Holtz, R. D., Kovacs, W. D. & Sheahan, T. C. (2011). *An introduction to geotechnical engineering*. Pearson Education Limited.

Honkanadavar, N. P. & Sharma, K. G. (2014). Testing and modeling the behavior of riverbed and blasted quarried rockfill materials. *International Journal of Geomechanics* **14**, No. 6, 04014028.

Honkanadavar, N. P., Kumar, N. & Ratnam, M. (2014). Modeling the behaviour of alluvial and blasted quarried rockfill materials. *Geotechnical and Geological Engineering* **32**, No. 4, 1001-1015.

Hoque, E. & Tatsuoka, F. (1998). Anisotropy in elastic deformation of granular materials. *Soils and Foundations* **38**, No. 1, 163-179.

Hunt, R. (1986). *Geotechnical engineering techniques and practices*. McGraw Hill, New York.

Jaky, J. (1944). The coefficient of earth pressure at-rest. *Journal of the Society of Hungarian Architects and Engineers* **78**, No. 22, 355-358.

Jaky, J. (1948). Pressure in silos. In *Proceedings of the 2nd international conference on soil mechanics and foundation engineering* **1**, pp. 103-107. Rotterdam, Netherlands.

Kitamura, R. & Haruyama, M. (1988). Compression and shear deformation of soil under wide-ranging confining pressure. In *Proceedings of Symposium on Advanced triaxial testing of soil and rock* (eds R. T. Donaghe, R. C. Chaney & M. L. Silver), pp. 501-511, ASTM International. Louisville, USA.

Kumar, J. & Madhusudhan, B. N. (2010). Effects of relative density and confining pressure on Poisson ratio from bender and extender elements tests. *Géotechnique* **60**, No. 7, 561–567.

Kulhawy, F. H. (2005). Estimation of soil properties for foundation design. *Notes for a short course sponsored by the ASCE Seattle Section Geotechnical Group*.

Ladd, C. C., Foott, R., Ishihara, K., Schlosser, F. & Poulos, H. G. (1977). Stress-deformation and strength characteristics. In *Proceedings of 9th international conference on soil mechanics and foundation engineering* **2**, 421-494.

Lambe, T. W. & Whitman, R. V. (1979). *Soil mechanics*. Massachusetts institute of technology.

Lambe, P. C. & Heartz, W. T. (1988). Consolidated drained triaxial testing of piedmont residual soil. In *Proceedings of Symposium on Advanced triaxial testing of soil and rock* (eds R. T. Donaghe, R. C. Chaney, and M. L. Silver), pp. 311-320, ASTM International. Louisville, USA.

Magnan, J. P. & Mestat, P. (1997). *Lois de comportement et modélisation des sols*. Ed. Techniques Ingénieur.

Marachi, N. D., Chan, C. K. & Seed, H. B. (1972). Evaluation of properties of rockfill materials. *Journal of the Soil Mechanics and Foundations Division* **97**, No. SM1, 95-114.

Marsal, R. J. (1967). Large-scale testing of rockfill materials. *Journal of the Soil Mechanics and Foundations Division* **93**, No. 2, 27-43.

Mayne, P. W. & Kulhawy, F. H. (1982). K_0-OCR relationships in soil. *Journal of the Geotechnical Engineering Division* **108**, No. 6, 851-872.

Mesri, G. & Hayat, T. M. (1993). The coefficient of earth pressure at-rest. *Canadian Geotechnical Journal* **30**, No. 4 647-666.

McCarthy, D. F. (2007). *Essentials of soil mechanics and foundations: Basic geotechnics*. Prentice Hall.

Michalowski, R. L. (2005). Coefficient of earth pressure at-rest. *Journal of Geotechnical and Geoenvironmental Engineering* **131**, No. 11, 1429-1433.

Michalowski, R. L. & Park, N. (2004). Admissible stress fields and arching in piles of sand. *Géotechnique* **54**, No. 8, 529-538.

Mochizuki, A., Mikasa, M. & Takahashi, S. (1988). A new independent principal stress control apparatus. In *Proceedings of Symposium on Advanced triaxial testing of soil and rock* (eds R. T. Donaghe, R. C. Chaney & M. L. Silver), pp. 844-858, ASTM International. Louisville, USA.

Qin, S. L., Chen, S. X., Han, Z., & Xu, X. C. (2010). Large-scale triaxial test study of behavior of over coarse-grained soils. *Rock and Soil Mechanics* **31**, supplement No. 2, 189-193.

Samieh, A. M. (1995). *Behavioural characteristics and constitutive modelling of Athabasca tar sand at low effective stresses*. PhD thesis, Department of Civil Engineering, University of Calgary, Canada.

Sherif, M. A., Fang, Y. S., and Sherif, R. I. (1984). K_a and K_o behind rotating and non-yielding walls. *Journal of Geotechnical Engineering* **110**, No. 1, 41-56.

Sivakugan, N. & Das, B. M. (2009). *Geotechnical engineering: a practical problem solving approach.* J. Ross Publishing.

Suwal, L. P. & Kuwano, R. (2013). Statically and Dynamically Measured Poisson's Ratio of Granular Soils on Triaxial Laboratory Specimens. *Geotechnical Testing Journal* **36**, No. 4, 493-505.

Talesnick, M. L. (2012). A different approach and result to the measurement of K_o of granular soils. *Géotechnique* **62**, No. 11, 1041-1045.

Terzaghi, K., Peck, R. B. & Mesri, G. (1996). *Soil mechanics in engineering practice*. John Wiley and Sons.

Tschebotarioff, G. P. (1973). *Foundations: retaining and earth structures: the art of design and construction and its scientific basis in soil mechanics*. McGraw-Hill, New York.

Varadarajan, A., Sharma, K. G., Venkatachalam, K. & Gupta, A. K. (2003). Testing and modeling two rockfill materials. *Journal of Geotechnical and Geoenvironmental Engineering* **129**, No. 3, 206-218.

Varadarajan, A., Sharma, K. G., Abbas, S. M. & Dhawan, A. K. (2006). Constitutive model for rockfill materials and determination of material constants. *International Journal of Geomechanics* **6**, No. 4, 226-237.

Wanatowski, D. & Chu, J. (2007). K_0 of sand measured by a plane-strain apparatus. *Canadian Geotechnical Journal* **44**, No. 8, 1006-1012.

Watabe, Y., Tanaka, M., Tanaka, H. & Tsuchida, T. (2003). K_0-consolidation in a triaxial cell and evaluation of in-situ K_0 for marine clays with various characteristics. *Soils and Foundations* **43**, No. 1, 1-20.

Yokota, K. & Konno, M. (1980). Dynamic Poisson's ratio of soil. In *Proceedings 7th world conf. earthquake Eng.* **3**, pp. 475-478. Istanbul, Turkey.

APPENDIX B – VALIDATION OF SEEP/W USING VARIABLE-HEAD PERMEABILITY TEST

The variable-head permeability test simulated by Chapuis (2009) is first reproduced using the code SEEP/W (GEO-SLOPE 2010). Such model is then extended to simulate the permeability test in a column with a pond on the top surface of the specimen. The validity of these numerical models is verified by the existing analytical solution.

B1 Variable-head permeability test

Fig. B-1 illustrates the axisymmetric model of the typical variable-head permeability test built with SEEP/W. The burette is simulated by "reservoir elements" (Chapuis 2009) that are modeled as unsaturated/saturated material using the hydraulic functions shown in Fig. 3-4. On this figure, the elevation of the water table (h_1) is 1.2 m and the total head at the base of specimen (h_2) is 0.5 m. The water table can drop to an elevation of 0.5 m in the burette. The initial difference in the total head (Δh) between the top and base of the specimen is $\Delta h_0 = 0.7$ m.

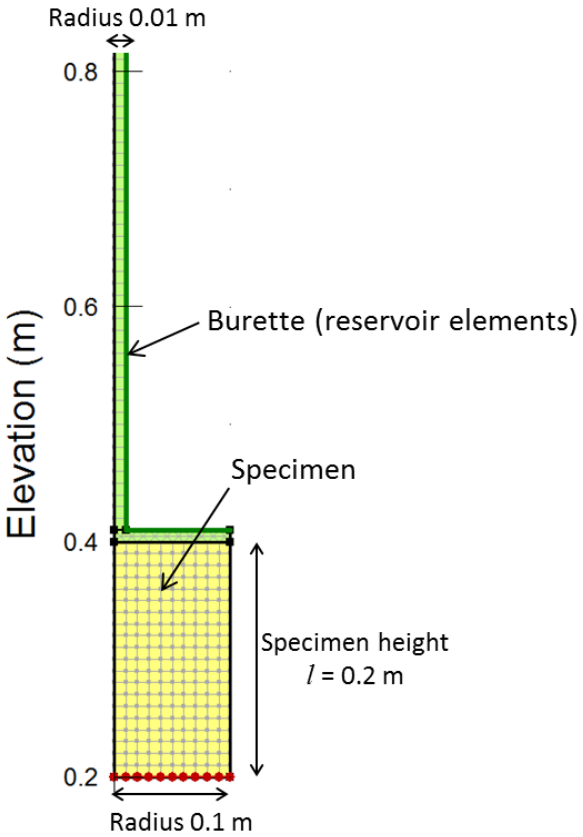

Figure B-1: Axisymmetric SEEP/W model of a typical variable-head permeability test

At any intermediate time t (s), the difference in the total head (Δh) between the top and base of the specimen Δh_t can be expressed as:

$$\Delta h_t = \Delta h_0 \exp\left(\frac{-kAt}{al}\right) \quad \text{(B.1)}$$

where Δh_0 = 0.7 m in this case, k (m/s) is the saturated hydraulic conductivity of the specimen, l is the height of the specimen and equals 0.2 m, A and a (m^2) are the cross-section areas of the specimen cylinder and burette, respectively.

The saturated hydraulic conductivity k of the specimen used by Chapuis (2009) is 1e-05 m/s. Other parameters such as the saturated volumetric water content wc and the coefficient of volume compressibility m_v were not given. The parameter m_v (kPa^{-1}) is defined by the slope of the water retention curve in the positive range (saturated condition) and it describes how much the saturated soil will swell or shrink as the pore water pressure varies. For soils, the m_v value is usually small. It is known that the m_v value of the specimen may affect the simulated outcomes.

In the following, sensitivity and parametric analyses will be performed to investigate the effect of the mesh size and parameters wc and m_v on the numerical outcomes.

Effect of mesh size

Fig. B-2 shows that the simulations using mesh size 0.05 m would be sufficient to yield stable numerical results. Chapuis (2009) has suggested an element size of 0.01 or 0.02 m for the reservoir elements for this problem. The mesh size of 0.01 m is thus used in the following.

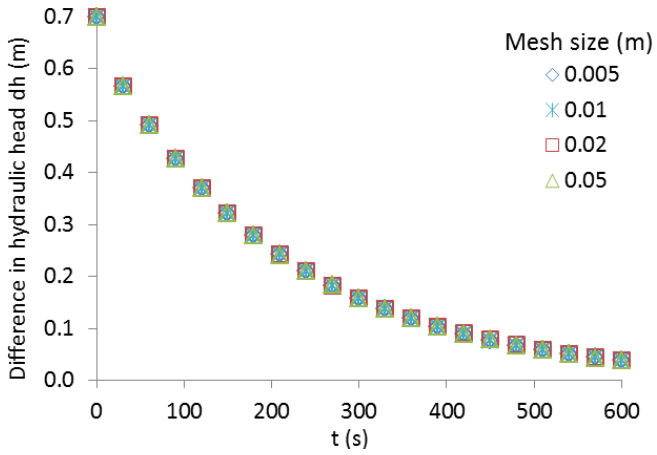

Figure B-2: The difference of the hydraulic head between top and base of the specimen in the variable-head permeability test for different mesh sizes

Effect of saturated water content wc

The results shown in Fig. B-3 indicate that the saturated volumetric water content *wc* (from 0 to 1) has no influence on the simulated outcomes. This is due probably to the fact that the specimen is always saturated during the infiltration.

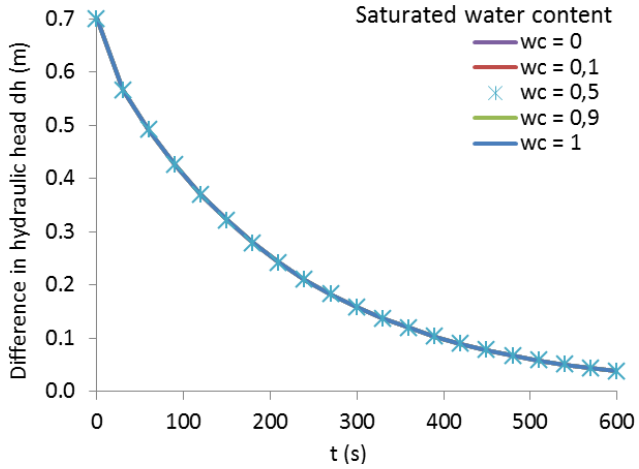

Figure B-3: The difference of the hydraulic head between top and base of the specimen in the variable-head permeability test for different values of *wc*

Effect of m_v of the specimen and burette

Fig. B-4 illustrates that the numerical results may be largely affected by the value of m_v of the specimen. The calculations done with $m_v \leq$ 1e-04 kPa^{-1} converge and correlate well with the analytical solution (Eq. B.1). The optimal m_v value of the specimen is thus taken as 1e-04 kPa^{-1}.

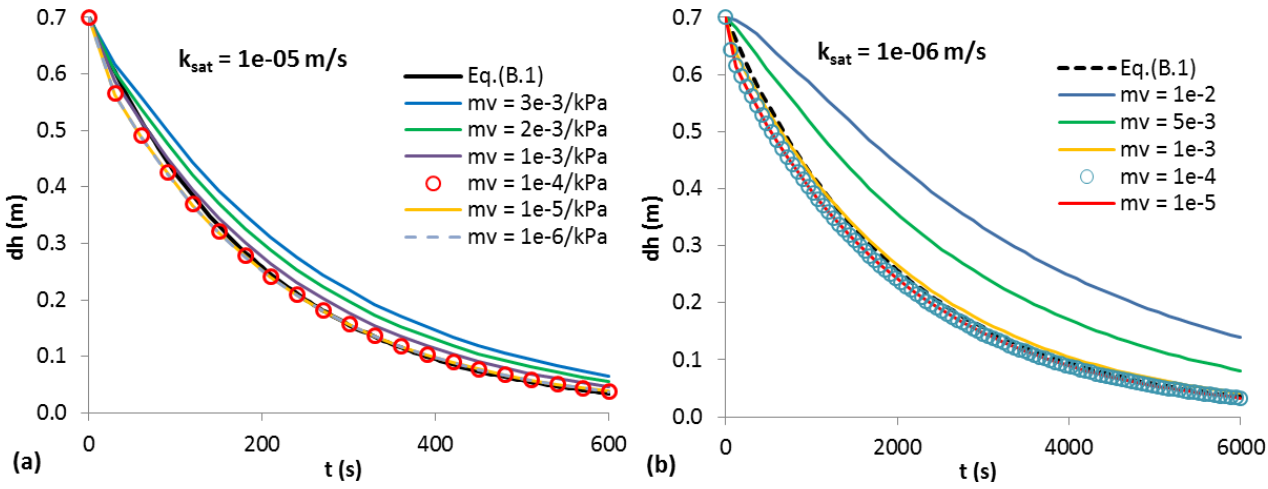

Figure B-4: The difference of the hydraulic head between top and base of the specimen in the variable-head permeability test for different values of m_v of specimen

Fig. B-5 shows the dependence of the numerical simulations on the value of m_v of the burette (reservoir elements). It is seen that the numerical results obtained with $m_v \leq$ 1e-03 kPa^{-1} converge. The value of m_v of the reservoir elements is thus taken as 0 kPa^{-1} (see also the slope of the water retention curve in the positive pore pressure range shown in Fig. 3-4a).

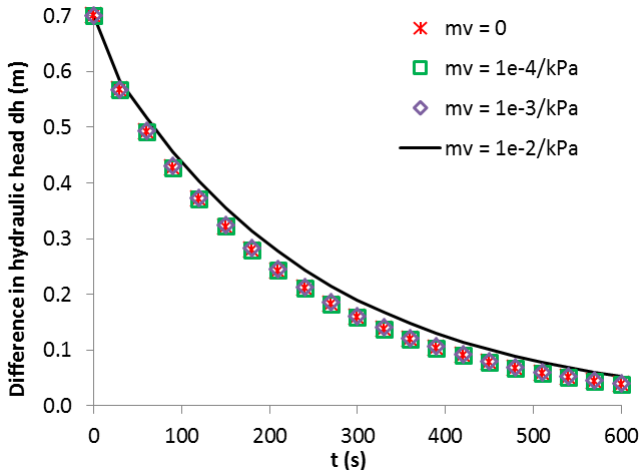

Figure B-5: The difference of the hydraulic head between top and base of the specimen in the variable-head permeability test for different values of m_v of burette

B2 Permeability test in a column with a pond

The burette of the variable-head permeability test shown in Fig. B-1 is expanded to have the same radius as the specimen cylinder, as illustrated in Fig. B-6. Such model represents the permeability test in a column with a pond on the top surface of the specimen.

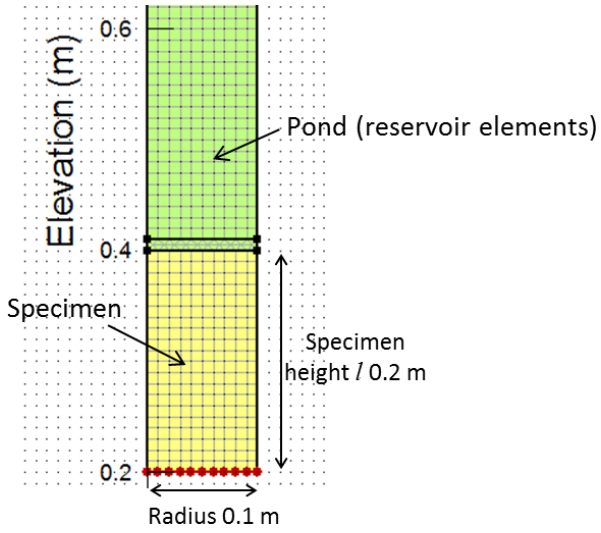

Figure B-6: Axisymmetric SEEP/W model of the variable-head permeability test

Fig. B-6 illustrates that the numerical results (obtained with the mesh size of 0.01 m, $m_{v,\ specimen}$ = 1e-04 kPa^{-1}, $m_{v,\ burette}$ = 0 kPa^{-1}) correlate well with the analytical solution (Eq. B.1).

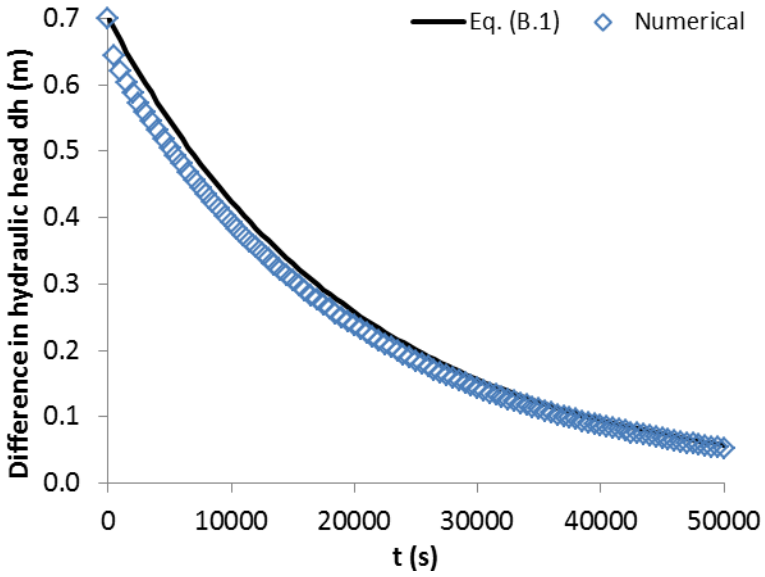

Figure B-7: The difference of the hydraulic head between top and base of the specimen in the column permeability test

APPENDIX C – VALIDATION OF CODES FLAC AND FLAC^{3D}

The problem of a cylindrical hole in an infinite linear elastic or Mohr-Coulomb medium is used to validate the codes FLAC and FLAC^{3D} (Itasca 2011, 2013). Figs. C-1a and C-2a illustrate the 2D and 3D physical models and their boundary conditions. The corresponding numerical models built with FLAC and FLAC^{3D} are shown in Figs. C-1b and C-2b, respectively. The radius of the hole (excavation) is 1 m. P_0 is the stress applied at the boundaries and also represents the in-situ stress in the rock mass. The radial grid ratio between adjacent grids is 1.1 (Figs. C-1b and C-2b).

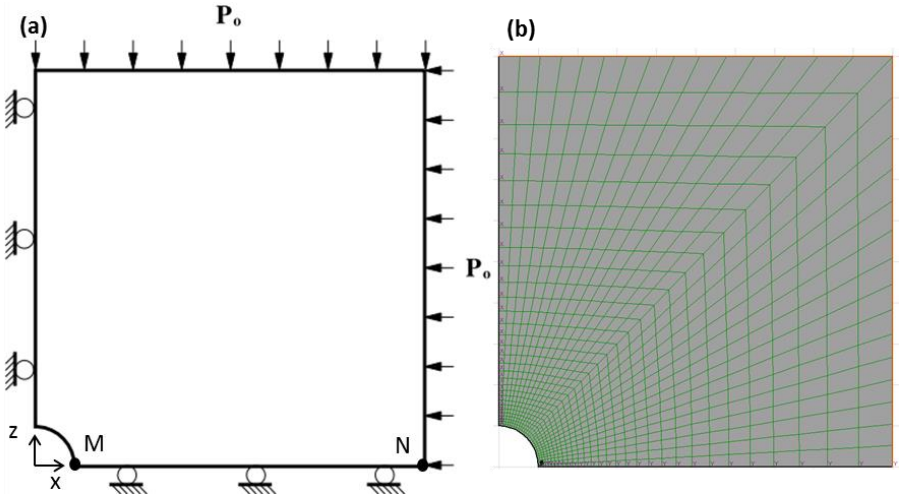

Figure C-1: 2D quarter symmetric (a) physical model and (b) numerical model of the cylindrical hole in an infinite medium

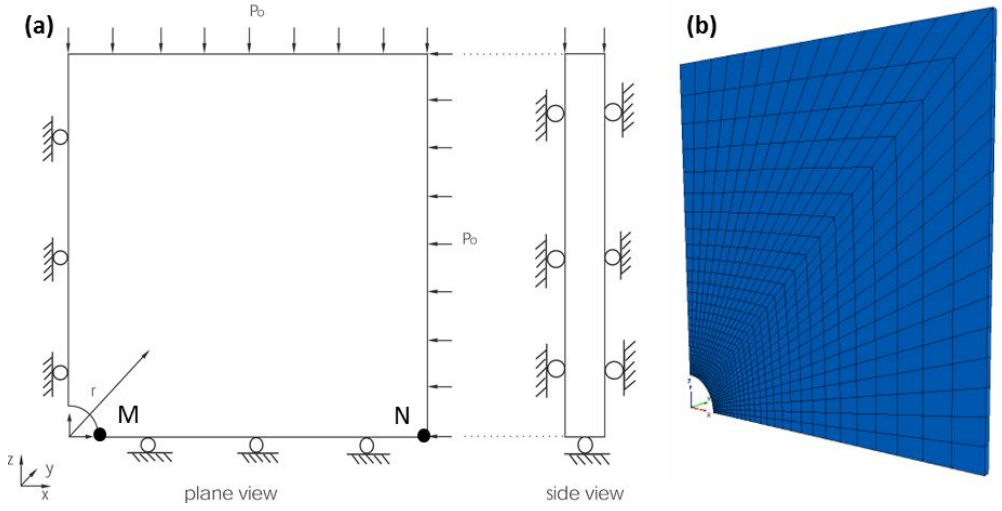

Figure C-2: 3D quarter symmetric (a) physical model and (b) numerical model of the cylindrical hole in an infinite medium

The dependence of stress and displacement on various parameters is investigated, including the mesh size, domain *D*, large and small strain, modulus *E*, cohesion *c*, tensile strength T_0 and third dimension *y*. The values of the internal friction angle ϕ' and Poisson's ratio ν of the rock mass are taken as independent variables. The focus is placed on the simulations conducted with non-associated flow (i.e., dilatation angle $\psi = 0°$). The density of the rock mass is 2500 kg/m^3. Small-strain calculations are used unless specified. Other parameters used for various cases are given in Table C-1.

Table C-1: Various parameters used in simulations performed with FLAC or FLAC^{3D}

Case	Domain (m)			E (MPa)	c (kPa)	T_0 (GPa)	ψ (°)	ϕ' (°)	ν	P_0 (MPa)
	x	z	y							
1^{MC}	10	10	0.2^{1}	6780	3450	10	0	30	0.21	30
2^{MC}	**Variable**		0.2^{1}	6780	3450	10	0	30	0.21	30
3^{MC}	10	10	**Variable[1]**	6780	3450	10	0	30	0.21	30
4^{MC}	10	10	**0.2***	6780	3450	10	0	30	0.21	30
5^{MC}	10	10	0.2^{1}	6780	3450	10	**30**	30	0.21	30
6^{MC}	10	10	0.2^{1}	6780	3450	**0**	0	30	0.21	30
7^{MC}	10	10	0.2^{1}	**100**	3450	0	0	30	0.21	30
8^{MC}	10	10	**Variable[1]**	**100**	3450	0	0	30	0.21	30
9^{MC}	30	30	0.2^{1}	6780	**1000**	0	0	30	0.21	30
10^{MC}	30	30	**Variable[1]**	6780	**1000**	0	0	30	0.21	30
11^{MC}	30	30	**0.2***	6780	1000	0	0	30	0.21	30
12^{MC}	10	10	0.2^{1}	**100**	**17000**	0	0	30	0.21	30
13^{LE}	10	10	0.2^{1}	**100**	-	-	-	30	0.21	30
14^{MC}	30	30	-	**Variable**	**10**	0	0	**40**	**0.3**	**0.13**
15^{MC}	30	30	-	**100**	**Variable**	0	0	**40**	**0.3**	**0.13**

Notes: *y* is the third dimension and only applicable to FLAC^{3D}; [1]: there is only 1 grid in y direction; *: uniform grid, i.e., the mesh size in y direction is the same as that of the directions of *x* and *z*; [MC]: Mohr-Coulomb; [LE]: linear elastic.

In the following, the stress (radial and tangential) and displacement profiles along the line MN and the displacement of point M (Figs. C-1a and C-2a) are presented to illustrate the effect of various parameters for different mesh sizes and domains. The rock mass with competent and reduced properties (including waste rock) are considered. The simulated stress and displacement are validated using analytical solutions proposed by Salencon (1969).

C1 Competent rock mass

Fig. C-3 shows that the radial and tangential stresses along line MN obtained from FLAC tend to converge when the mesh size is reduced to 0.1 × 0.1 m. The mesh size indicates the size of the element at the inner boundary of the rock mass. The radial ratio between adjacent meshes is 1.1.

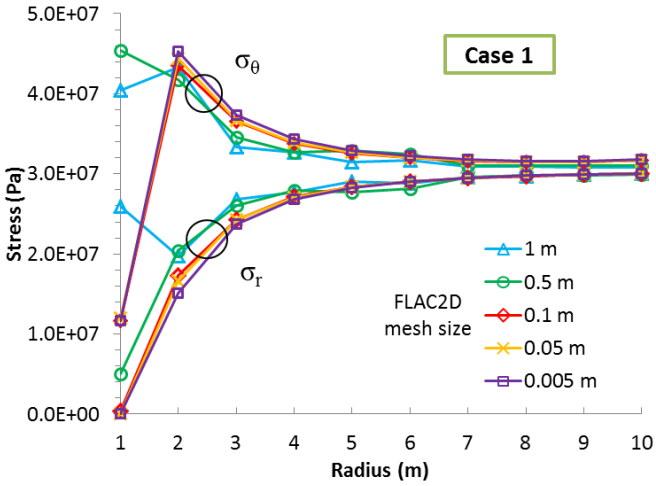

Figure C-3: Distribution of radial and tangential stresses along line MN for different mesh sizes

The mesh size of 0.1 × 0.1 m is used in the models built with FLAC^{3D}. Fig. C-4 illustrates that the (radial and tangential) stress and (radial) displacement profiles along line MN obtained from FLAC^{3D} generally correlate well with the theoretical solutions of Salencon (1969). However, Fig. C-4b shows that there are small discrepancies for the displacement near the boundaries (at points M and N) obtained from two approaches. The displacement on the boundaries is of particular interest and will be further assessed in the following.

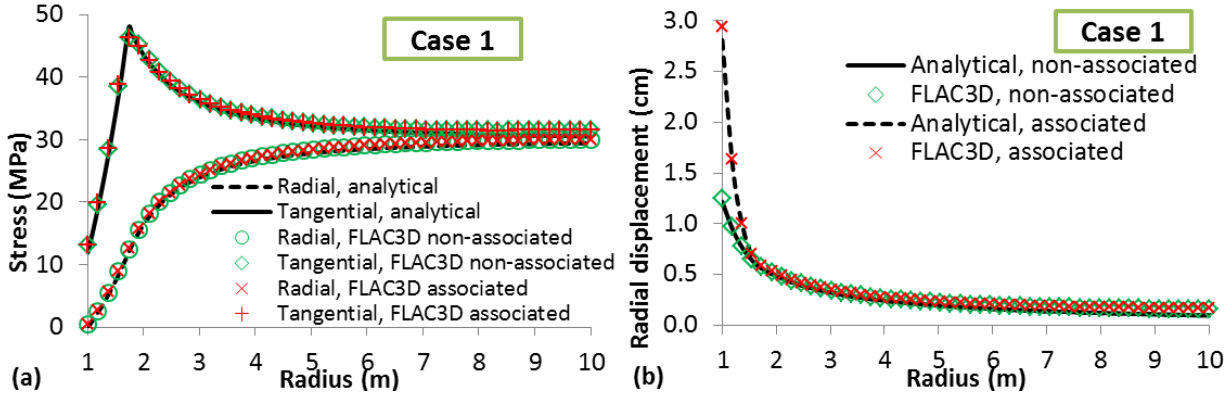

Figure C-4: Distribution of (a) stress (radial and tangential) and (b) radial displacement along the line MN

Fig. C-5 shows that the radial displacement at the point M tends to be stable when the mesh size decreases to about 0.05 m. But the radial displacement obtained with FLAC^{3D} continues to slightly increase when the element size goes below 0.01 m. In general, the displacement obtained with FLAC^{3D} and FLAC are very similar.

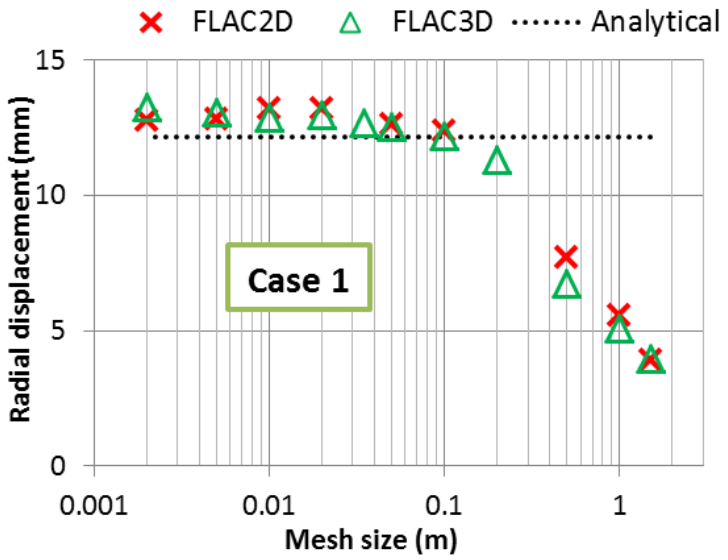

Figure C-5: Radial displacement at the point M for different mesh sizes (Case 1 in Table C-1)

Effect of domain

Fig. C-6 illustrates that the domain of 10 m is sufficient for the simulations conducted with the competent rock mass. Fig. C-6b shows that the radial displacement at the point M tends to converge better for larger domains when the mesh size is below 0.01m.

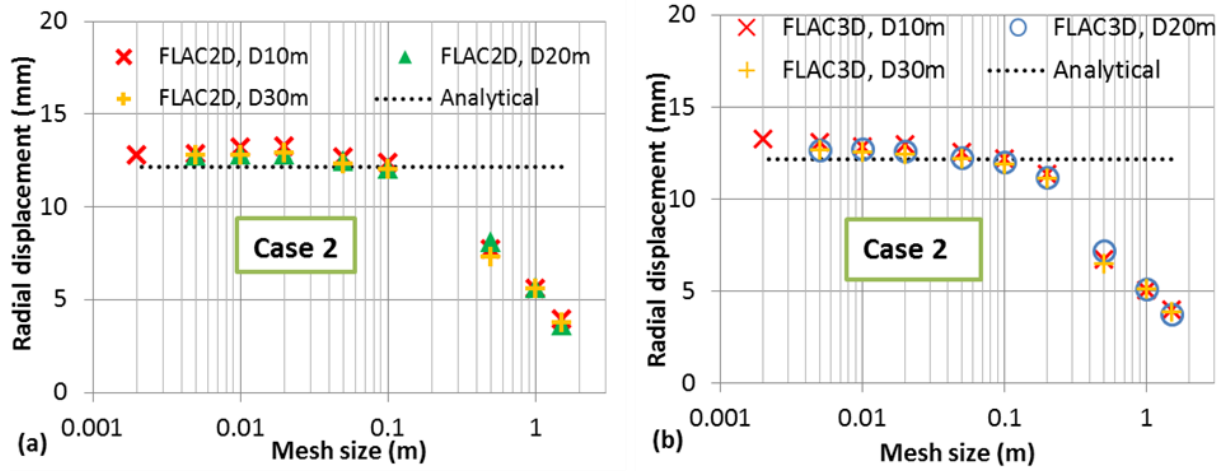

Figure C-6: Radial displacement at the point M for different mesh sizes (Case 2 in Table C-1)

Effect of the third dimension

Fig. C-7 illustrates that the length of third dimension and its grid type (1 grid or uniform grid, see notes of Table C-1) has little effect on the numerical results.

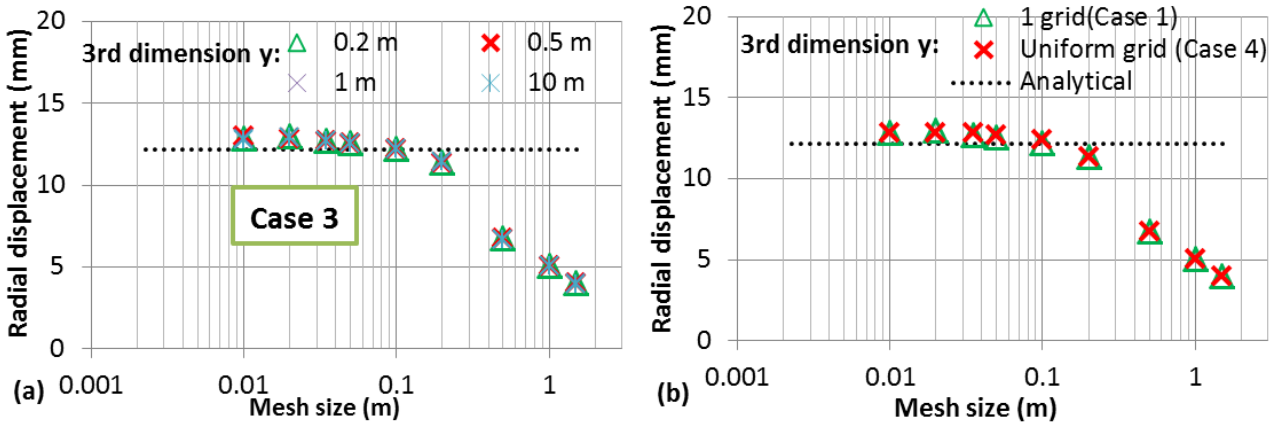

Figure C-7: Radial displacement at the point M for different mesh sizes (Cases 1, 3 and 4 in Table C-1)

Associated flow

Fig. C-8 shows that the radial displacement at the point M obtained with FLAC^{3D} tends to converge when the element size is decreased to about 0.05 m, but it slightly increases when the mesh size goes below 0.01 m. This is similar to the cases of non-associated flow.

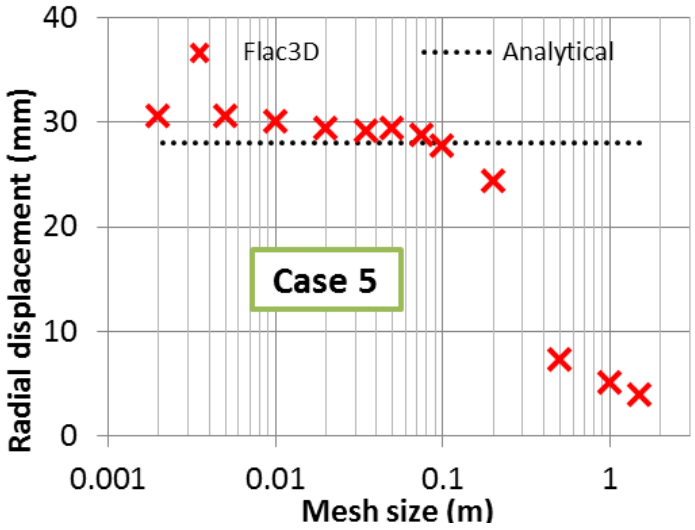

Figure C-8: Radial displacement at the point M obtained with associated flow for different mesh sizes (Case 5 in Table C-1)

Effect of tensile strength

Fig. C-9 illustrates that there is little difference between the results obtained with small and large strain calculations for the competent rock mass. It is also seen that the tensile strength of the rock mass has no effect on the simulated displacement, due to the compressive manner of this problem.

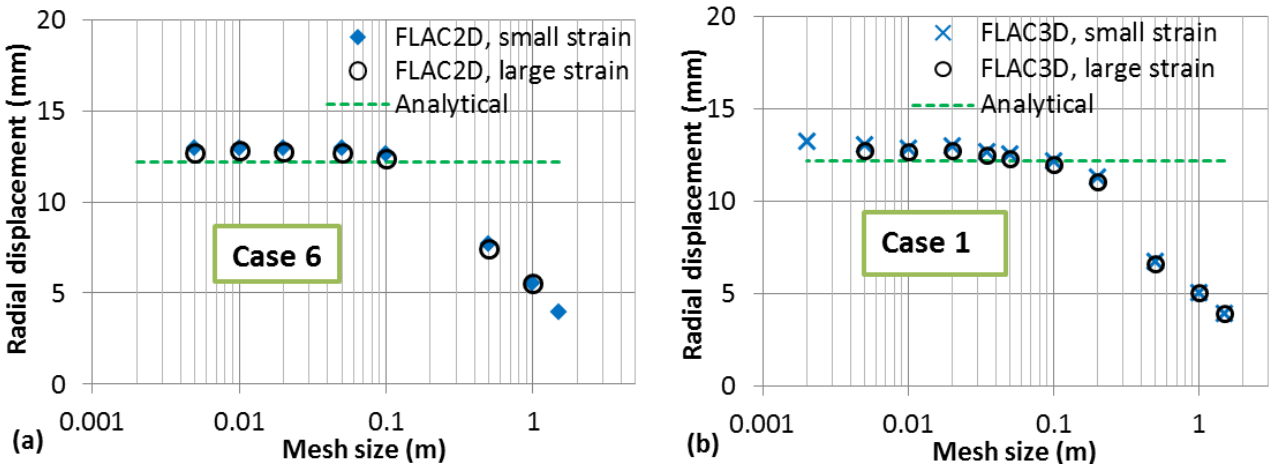

Figure C-9: Radial displacement at the point M for different mesh sizes (Cases 1 and 6 in Table C-1)

C2 Rock mass with reduced properties

Effect of modulus

Fig. C-10 shows that the calculations made with large strain are not stable when the modulus of the rock mass is reduced to 100 MPa for the given in-situ stress condition. For large stain, bad geometry occurs when mesh size is less than 0.2m.

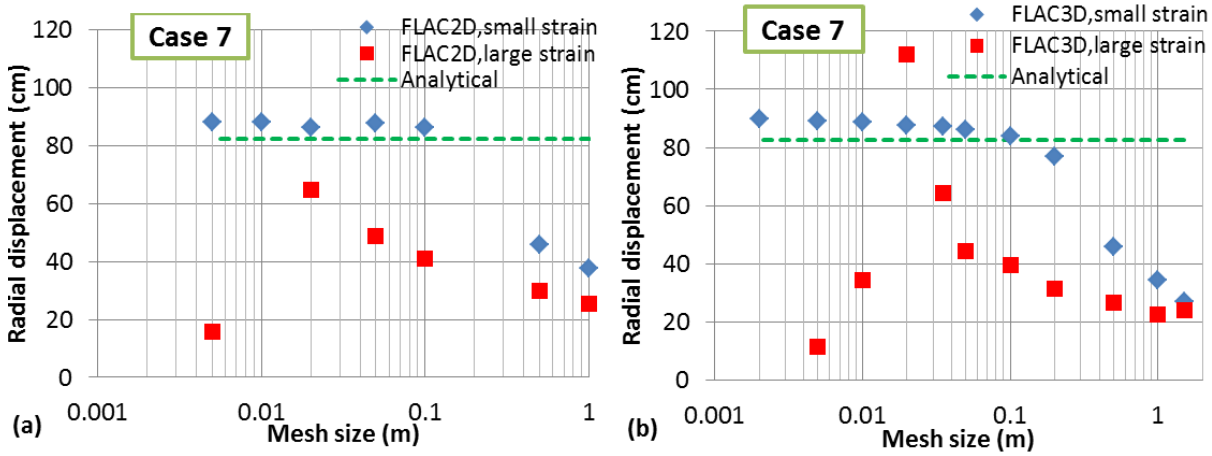

Figure C-10: Radial displacement at the point M for different mesh sizes (Case 7 in Table C-1)

Fig. C-11 illustrates that the length of third dimension (with 1 grid) has little effect on the simulated displacement when the modulus of the rock mass is reduced to 100 MPa.

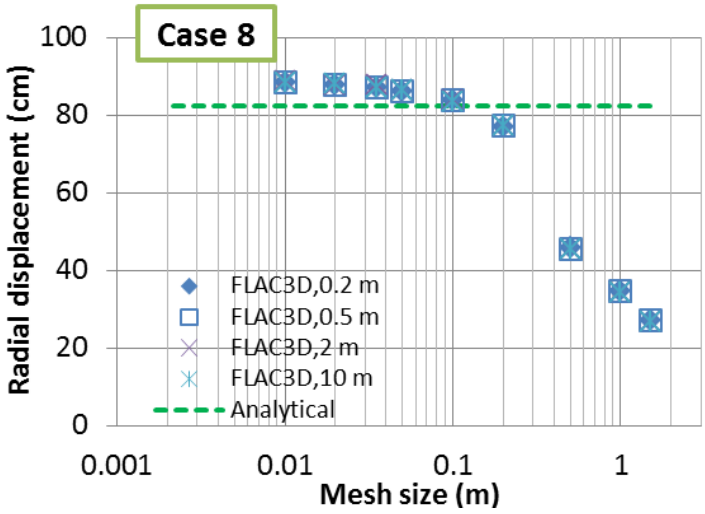

Figure C-11: Radial displacement at the point M for different mesh sizes (Case 8 in Table C-1)

Effect of cohesion

Fig. C-12 shows that the calculations become unstable as mesh size decreases for reduced c = 1 MPa under the given in-situ stress condition.

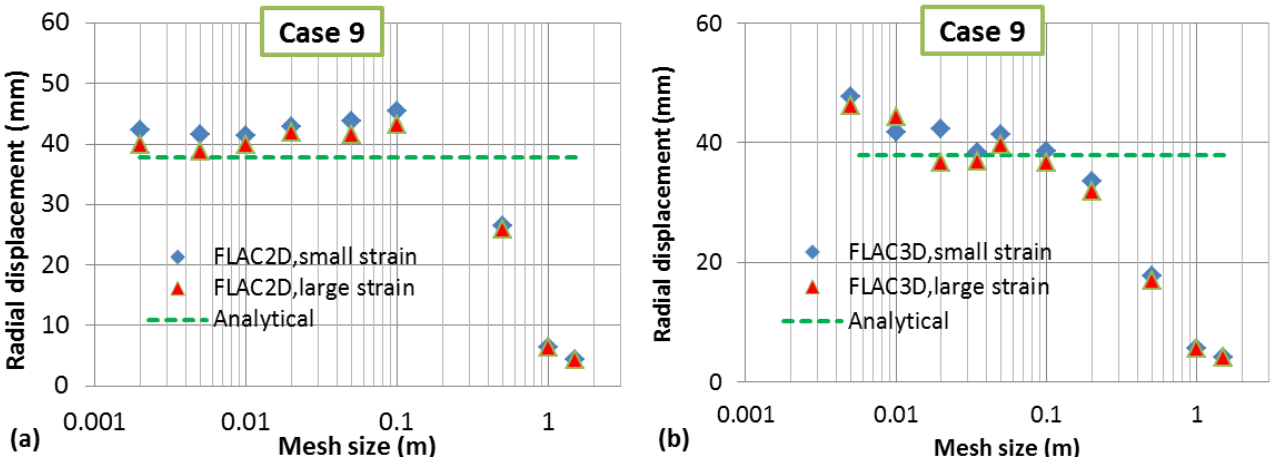

Figure C-12: Radial displacement at the point M for different mesh sizes (Case 9 in Table C-1)

Fig. C-13 illustrates that the length of third dimension and its grid type (1 grid or uniform grid, see notes of Table C-1) may influence the simulated displacement at the point M, for reduced c = 1 MPa under the given in-situ stress condition.

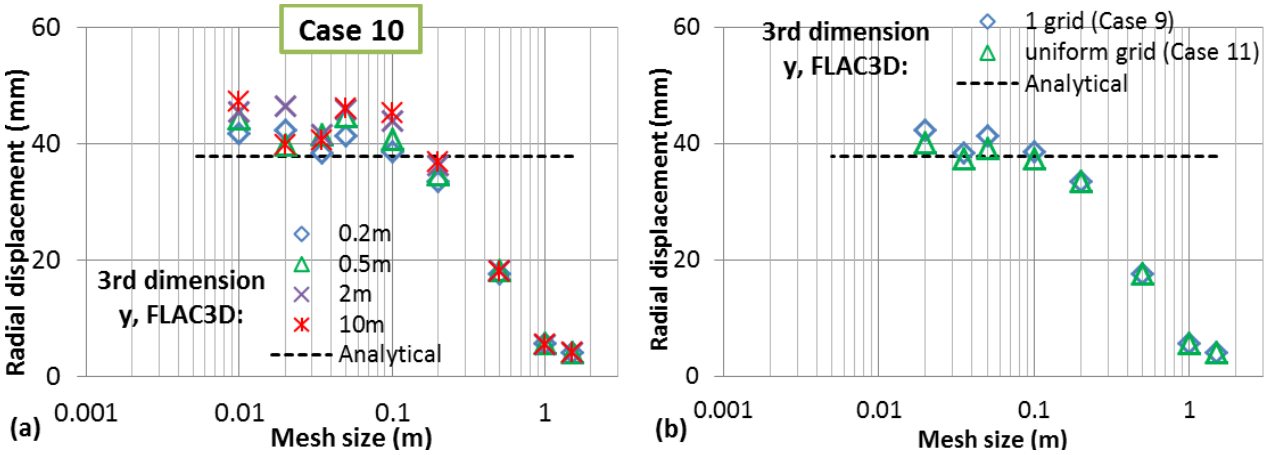

Figure C-13: Radial displacement at the point M for different mesh sizes (Cases 9, 10 and 11 in Table C-1)

Constitutive model

When the cohesion of the rock mass is increased to 17 MPa, it is seen from Fig. C-14 that the stresses and displacement obtained with the Mohr-Coulomb (MC) criterion become very similar to those of the linear elastic (LE) model.

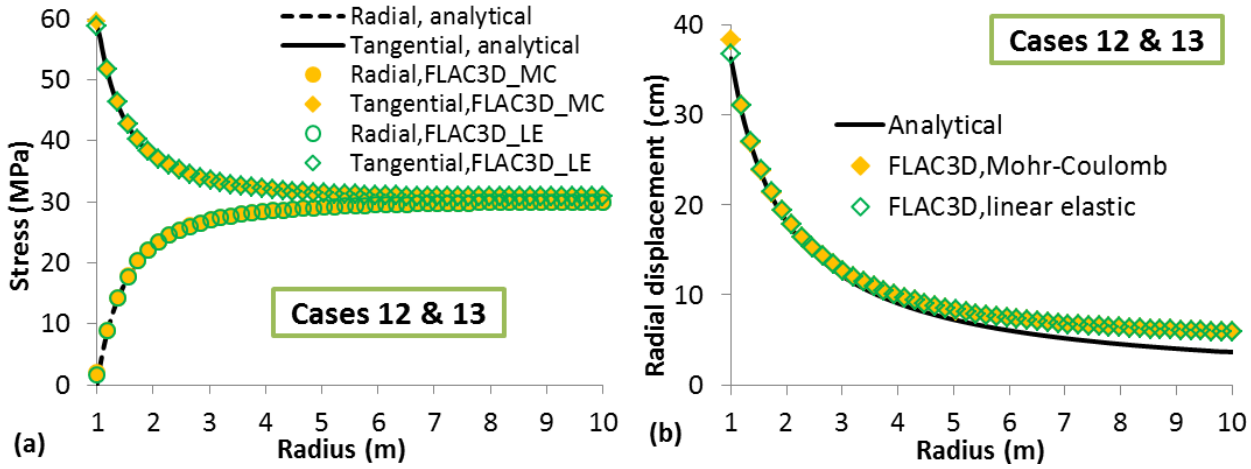

Figure C-14: Distribution of (a) stress (radial and tangential) and (b) radial displacement along the line MN (Cases 12 and 13 in Table C-1)

Fig. C-15 shows that the calculations made with large strain obtained from both MC and LE models are unstable (with bad geometry) for the reduced modulus 100 MPa.

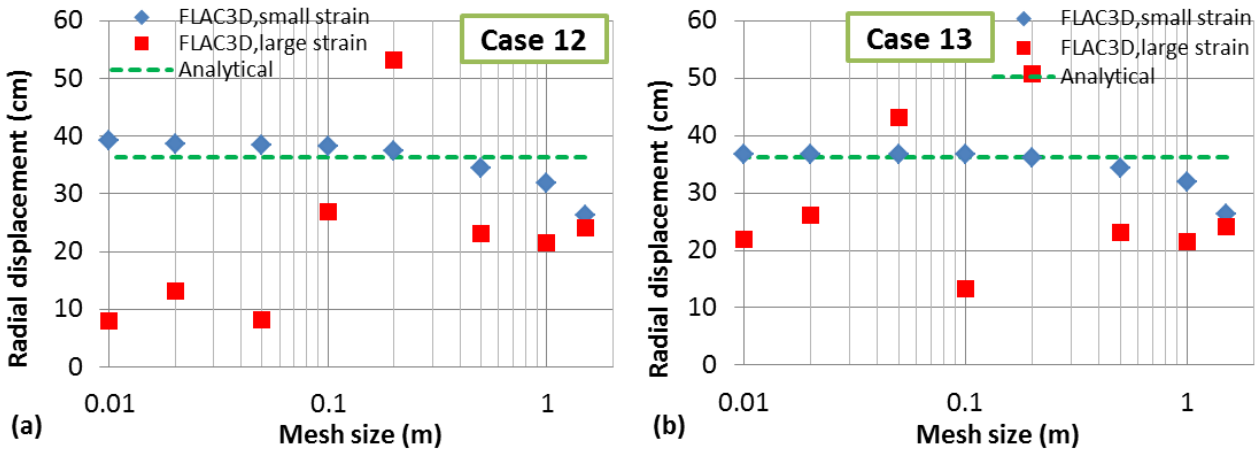

Figure C-15: Radial displacement at the point M for different mesh sizes (Cases 12 and 13 in Table C-1)

C3 Rock mass with properties similar to waste rock

The properties of the rock mass are changed to that of waste rock in Cases 14 and 15. Accordingly, the in-situ stress is reduced from 30 MPa to 130 kPa in these two cases (see Table C-1). Fig. C-16a shows that the results obtained with both small and large strain correlate well and converge for the modulus E = 100 MPa and cohesion c = 10 kPa.

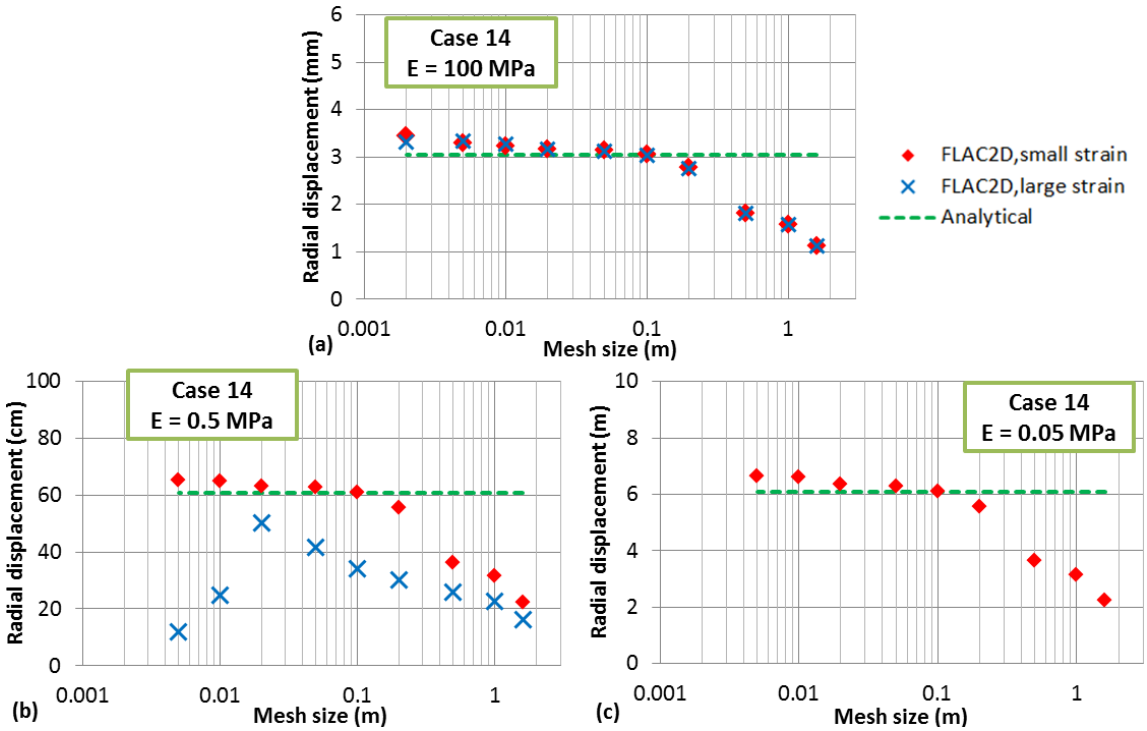

Figure C-16: Radial displacement at the point M for different mesh sizes (Case 14 in Table C-1)

The calculations made with large strain become unstable when the modulus of the waste rock goes below 0.5 MPa for the same in-situ stress condition (Figs. C-16b and C-16c).

When the cohesion of the waste rock is 10 kPa, Fig. C-17a illustrates that the simulated displacement at point M tends to somewhat converge as the mesh size is decreased. However, it is seen from Figs. C-17b and C-17c that when the cohesion is zero or 0.1 kPa, the numerical results become unstable for both small and large strain calculations.

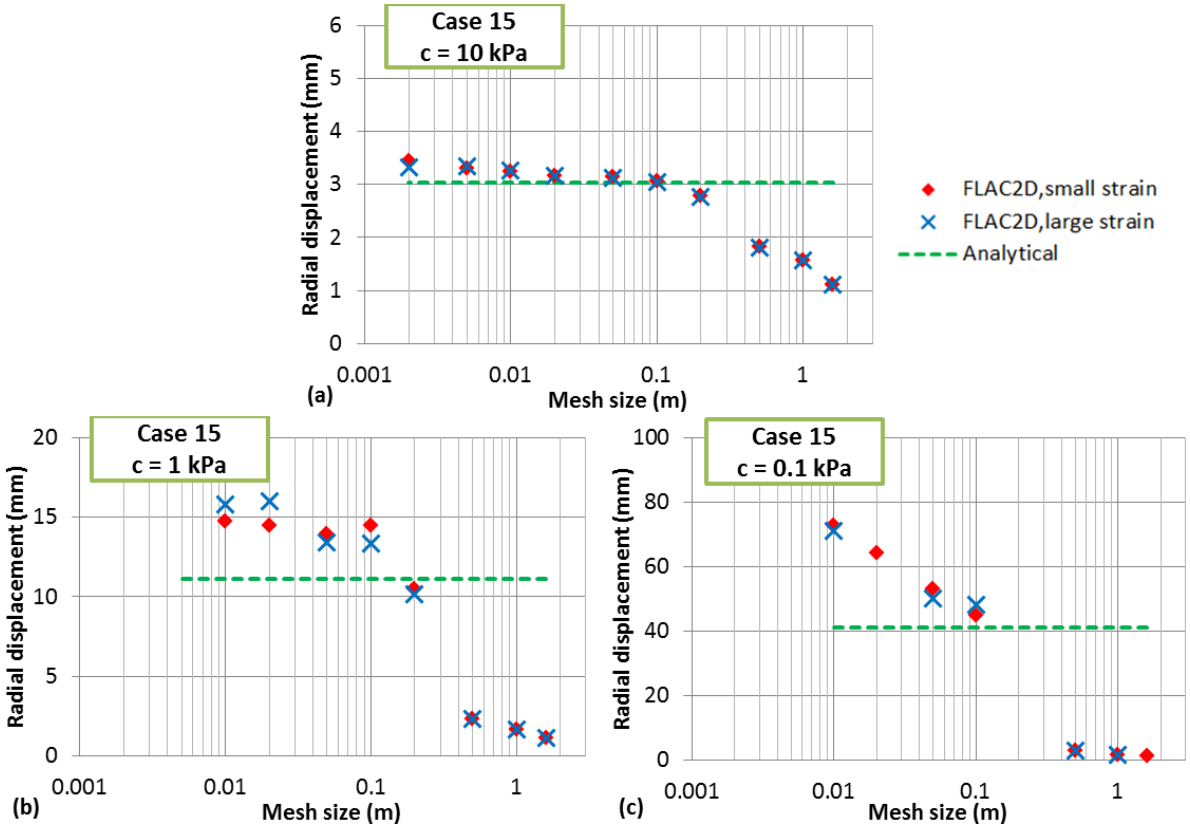

Figure C-17: Radial displacement at the point M for different mesh sizes (Case 15 in Table C-1)

APPENDIX D – SENSITIVITY ANALYSES RELATED TO CHAPTER 3

This section presents the sensitivity analyses related to the numerical results (using SEEP/W; GEO-SLOPE 2010) presented in Chapter 3. In the following, the dependence of the numerical outcomes on the mesh size, time step and start time of calculation is illustrated. The geometric and mechanical properties for each case are given in Table 3-1.

D1 Effect of mesh size of the backfill and pond

The optimal mesh of the pond and backfill is taken uniformly as 0.1 m based on the results shown in Figs. D-1 and D-2.

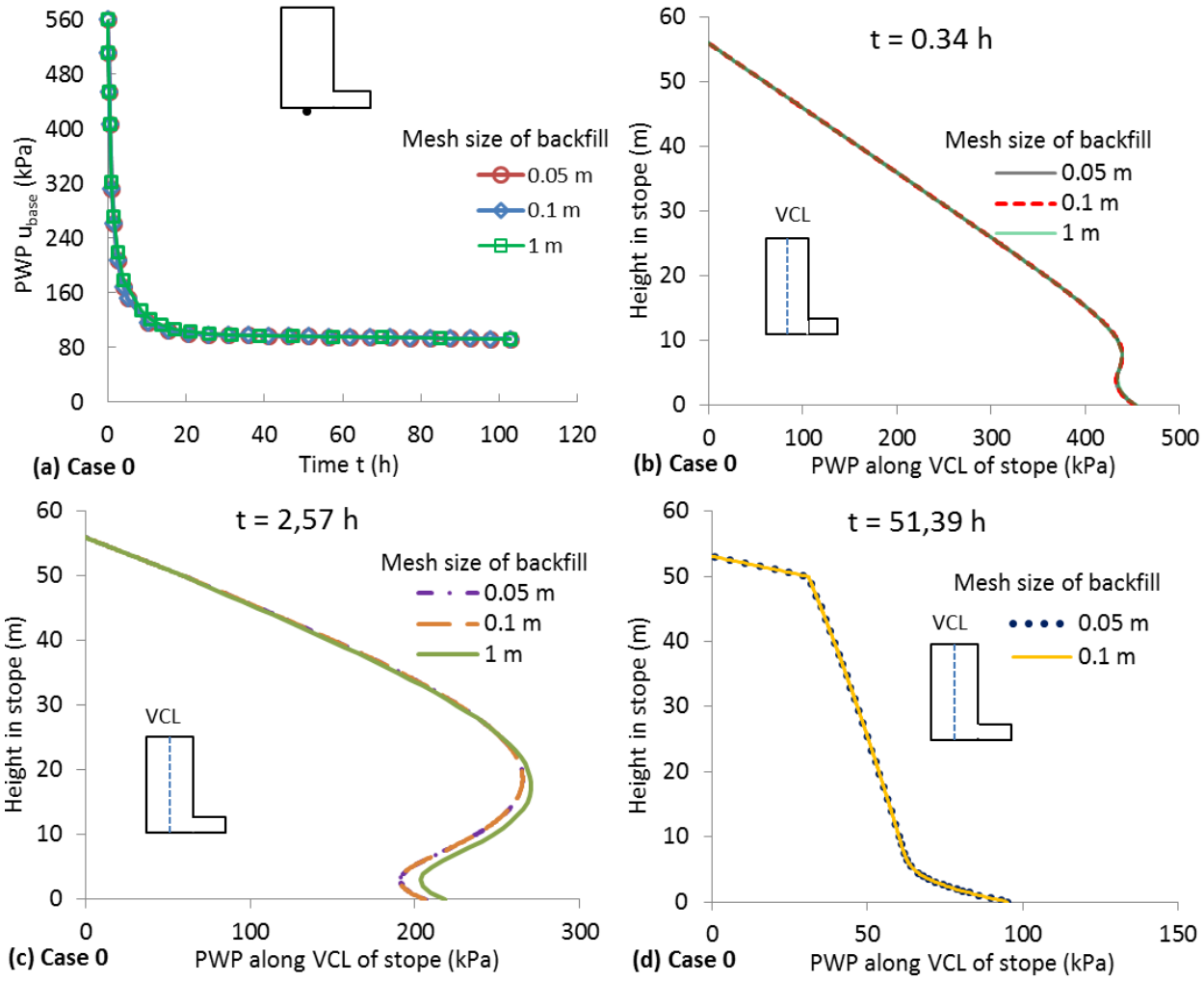

Figure D-1: (a) Evolution of PWP at stope base u_{base} and (b, c and d) distributions of PWP along the VCL of stope at different times, for different mesh sizes of backfill; the mesh size of the pond is 0.1 m (Case 0, Table 3-1)

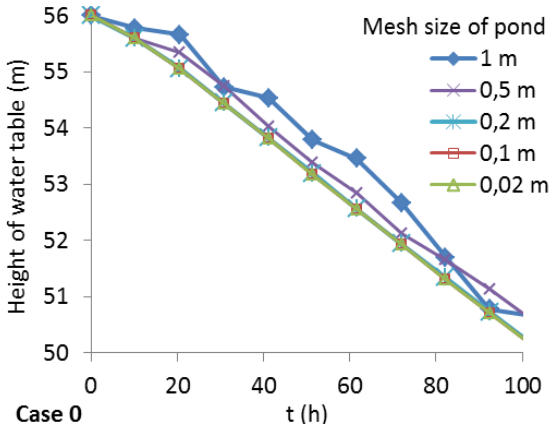

Figure D-2: Evolution of the water table height *H* with time *t* for different mesh sizes of the pond; the mesh size of backfill is 1 m (Case 0, Table 3-1)

In the following, the mesh size of the pond and backfill is taken uniformly as 0.1 m.

D2 Effect of time step

Figs. D-3 to D-5 illustrate that the effect of time step on the results is insignificant.

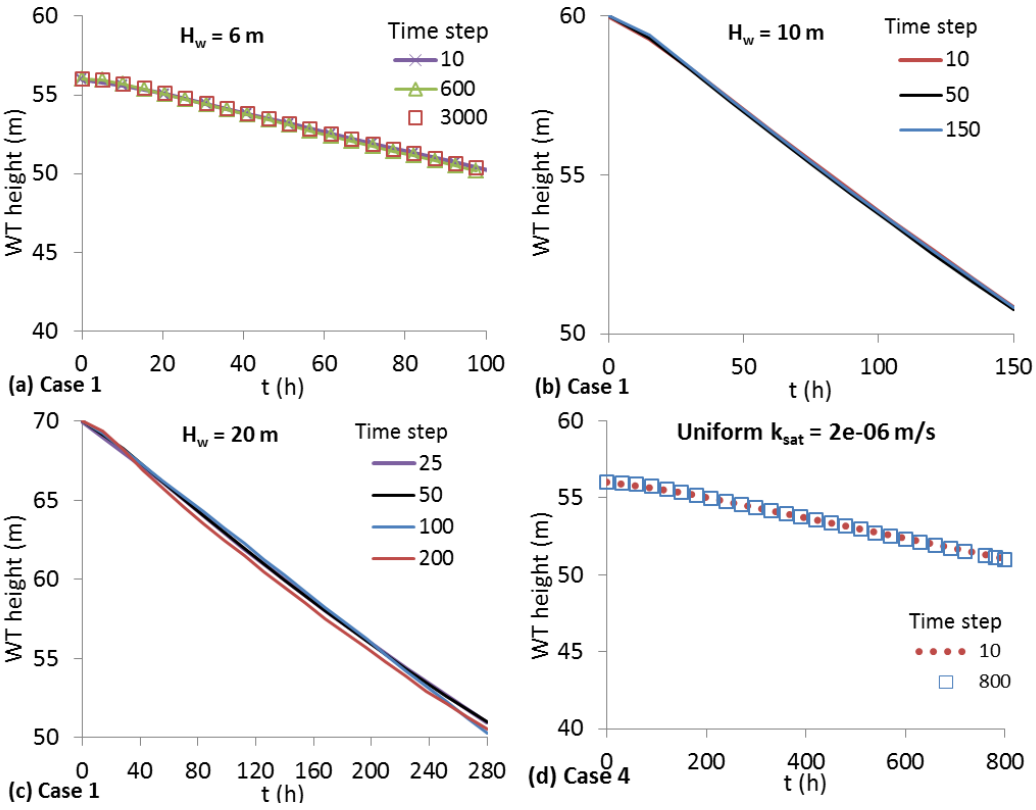

Figure D-3: Evolution of the water table height *H* with time *t* for different time steps (Cases 1 and 4, Table 3-1)

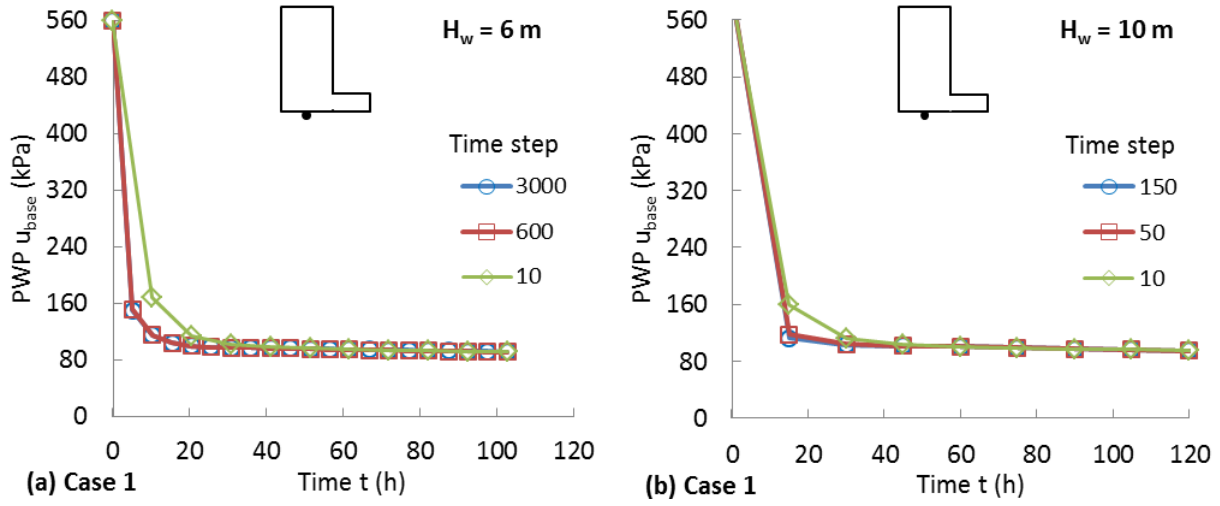

Figure D-4: Evolution of PWP at stope base u_{base}, for different time steps (Case 1, Table 3-1)

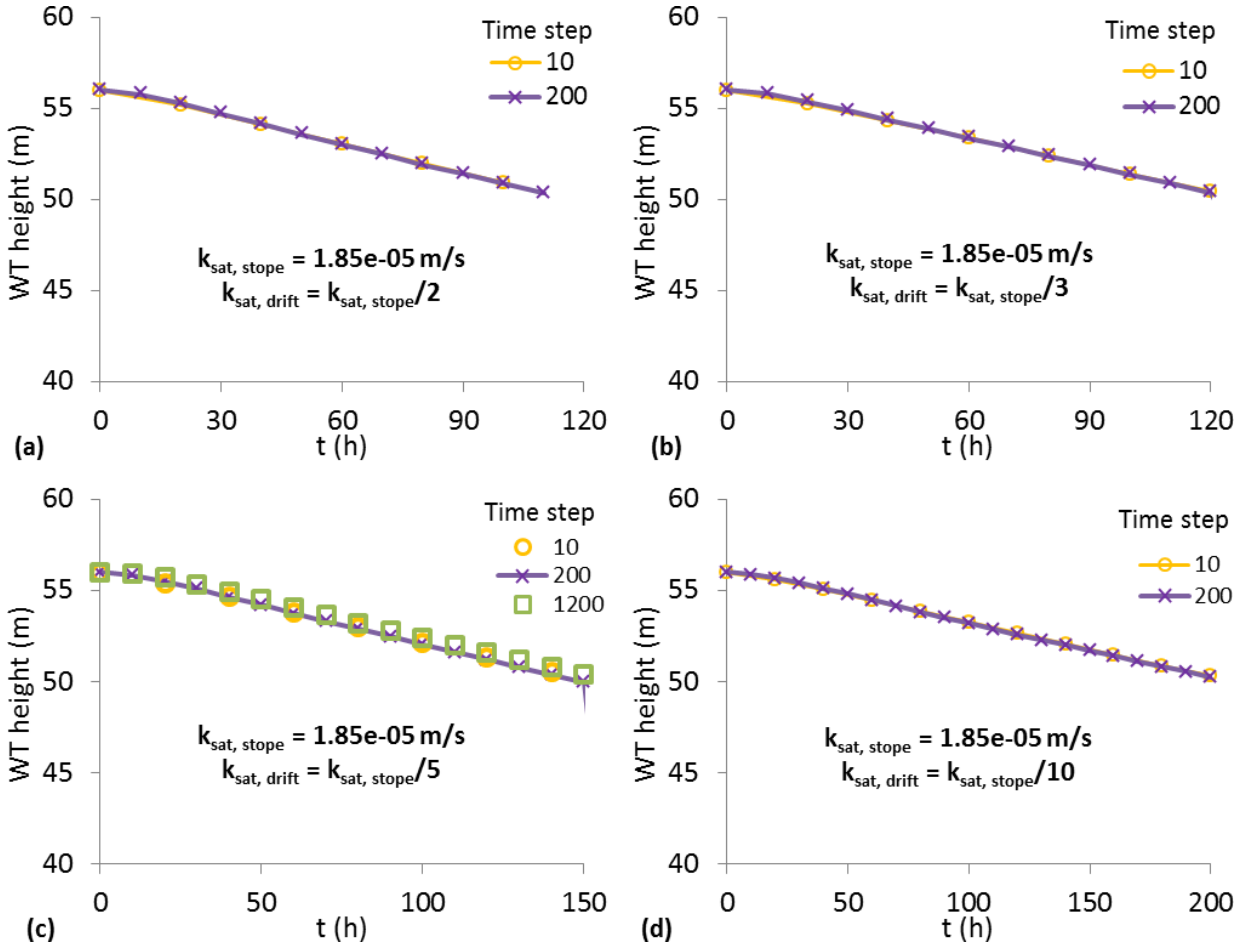

Figure D-5: Evolution of water table height with time *t* for different time steps (Case 5, Table 3-1)

D3 Effect of start time of calculation

Fig. D-6 shows that the calculations starting at 0 and 2nd second give almost identical results.

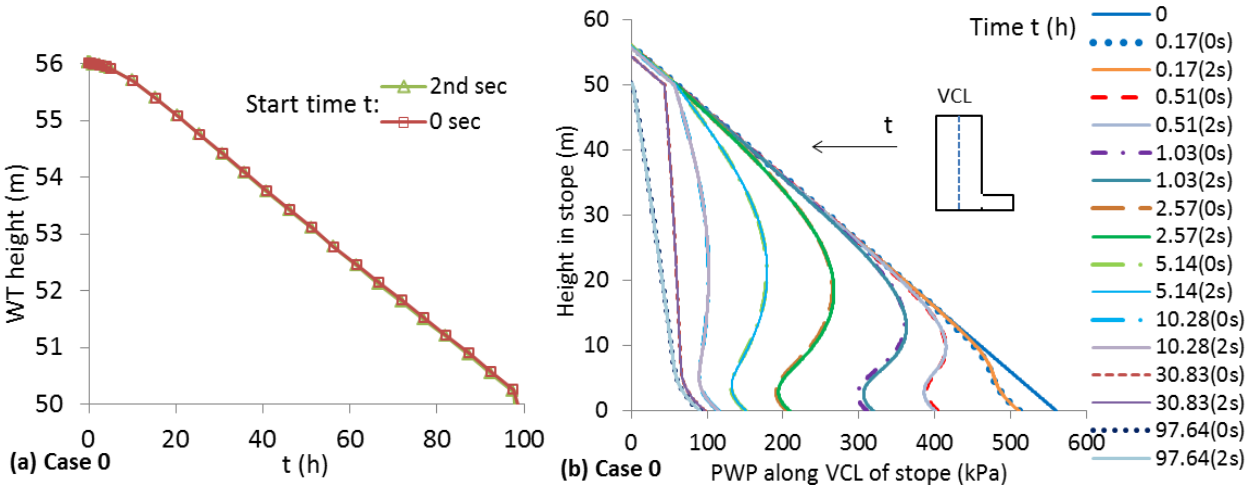

Figure D-6: (a) Evolution of the water table height with time *t* and (b) distributions of PWP along the VCL of stope at different times, for different start time of calculations (Case 0, Table 3-1)

APPENDIX E – SENSITIVITY AND PARAMERIC ANALYSES RELATED TO CHAPTER 4

This section presents the sensitivity and parametric analyses related to the numerical simulations conducted using FLAC (Itasca 2011) presented in Chapter 4. In the following, the effect of mesh size and cohesion on the displacement of waste rock barricade is first illustrated. Complementary results regarding instability criterion for defining the failure of waste rock barricade are also presented. The values of the internal friction angle ϕ' and Poisson's ratio ν of the waste rock are independent.

E1 Effect of mesh size from 2.5 to 0.025 m

Fig. F-1 shows the schematic model of the waste rock barricade used for the sensitivity and parametric analyses. The mesh size is reduced from 2.5 to 0.025 m (at the barricade top) to find the optimal mesh size. Numerical results shown in this section are obtained with the backfill (plug) height H = 9 m, barricade height H_d = 5 m, slope angles $\alpha_1 = \alpha_2$ = 37°, unit weight γ_{wr} = 19.62 kN/m^3, Young's modulus E = 100 MPa, Poisson's ratio ν = 0.3 and effective friction angle ϕ' = 40°.

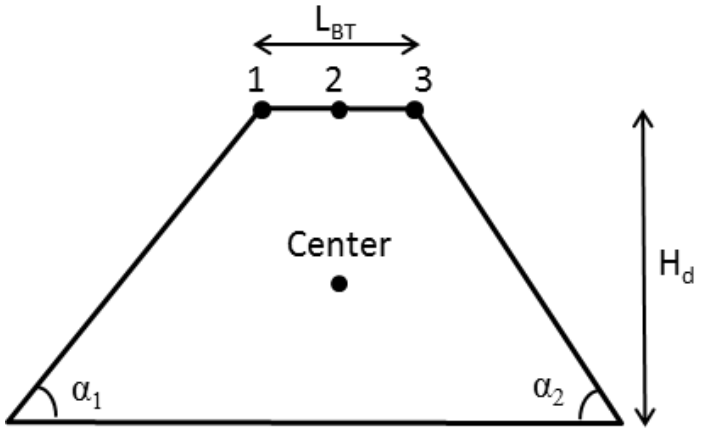

Figure E-1: Schematic view of the model of the waste rock barricade

c = 0 kPa

Figs. E-2 to E-4 illustrate that when the cohesion c of backfill is zero, the simulated displacement on the top surface of barricade (points 1, 2 and 3 in Fig. E-1) cannot converge as the mesh become finer. Fig. E-5 shows that the simulated displacement at the center of barricade becomes stable when the mesh size is reduced to 0.1 × 0.1 m.

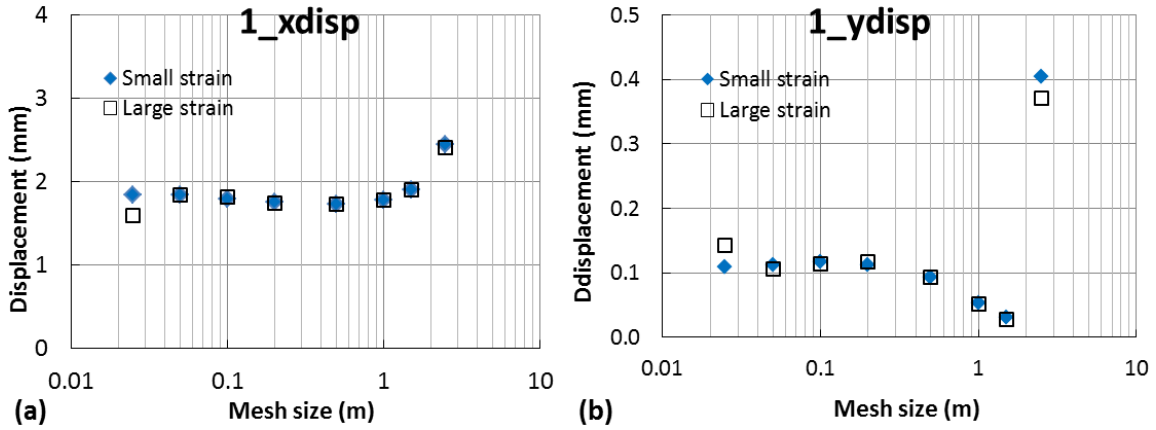

Figure E-2: (a) X-displacement and (b) Y-displacement at the point 1 (in Fig. E-1) of barricade for different mesh sizes obtained with ***c* = 0 kPa**

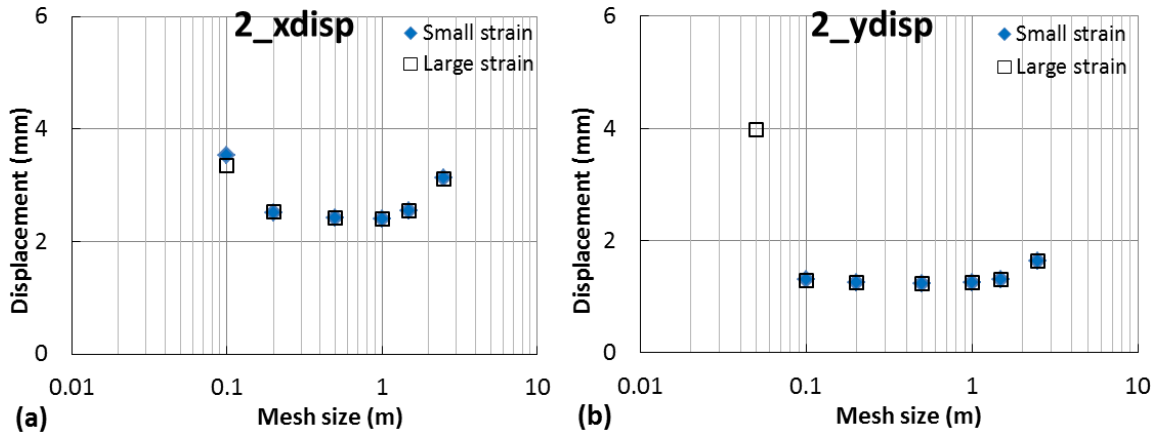

Figure E-3: (a) X-displacement and (b) Y-displacement at the point 2 (in Fig. E-1) of barricade for different mesh sizes obtained with ***c* = 0 kPa**

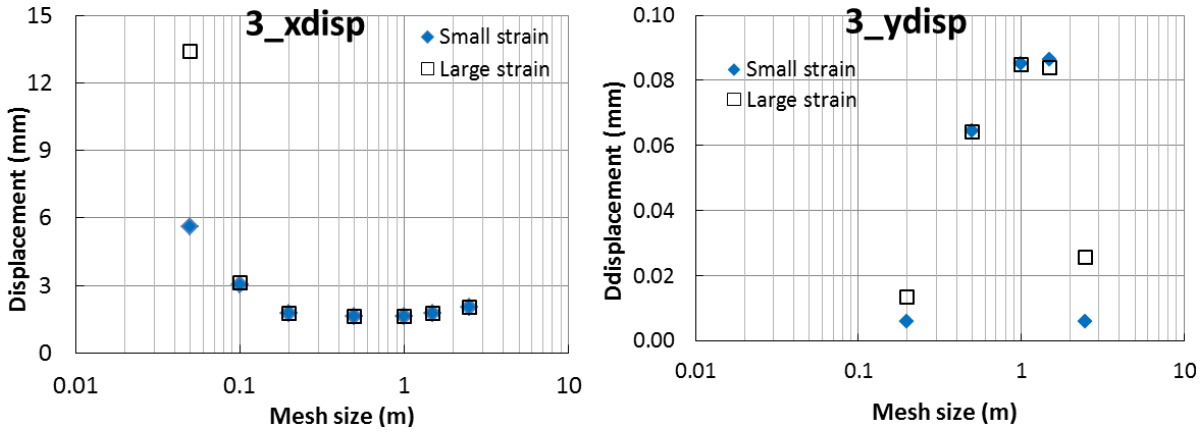

Figure E-4: (a) X-displacement and (b) Y-displacement at the point 3 (in Fig. E-1) of barricade for different mesh sizes obtained with ***c* = 0 kPa**

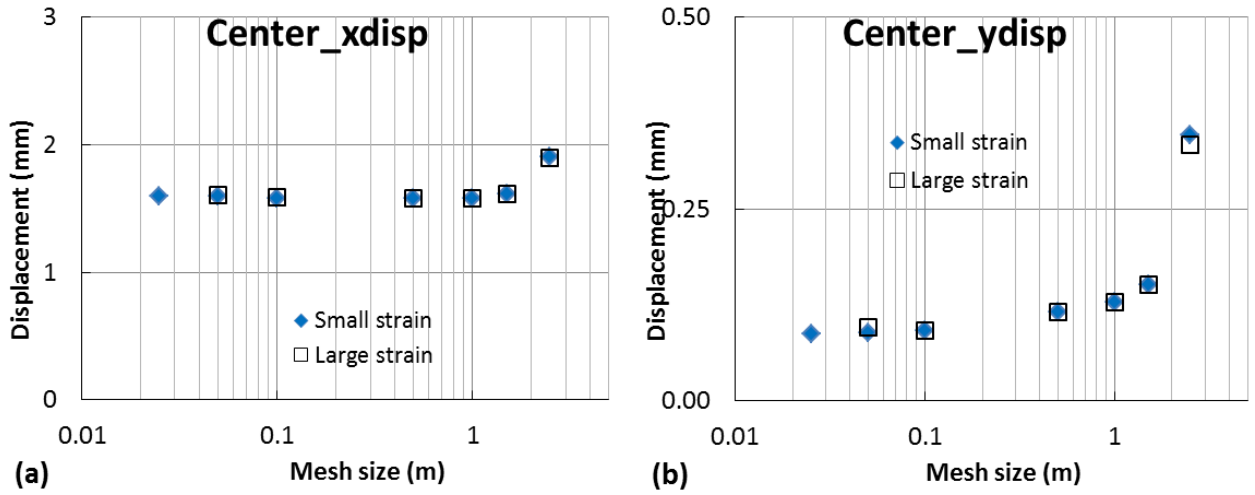

Figure E-5: (a) X-displacement and (b) Y-displacement at the center point C (in Fig. E-1) of barricade for different mesh sizes obtained with ***c* = 0 kPa**

c = 0.1 kPa

When the cohesion of backfill is 0.1 kPa, Fig. E-6 illustrates that the simulated displacement of point 1 (in Fig. E-1) at the barricade top tends to converge as the mesh size is decreased to 0.1 × 0.1 m. Figs. E-7 and E-8 show that the simulated displacement of points 2 and 3 (in Fig. E-1) at the barricade top cannot converge as the mesh become finer.

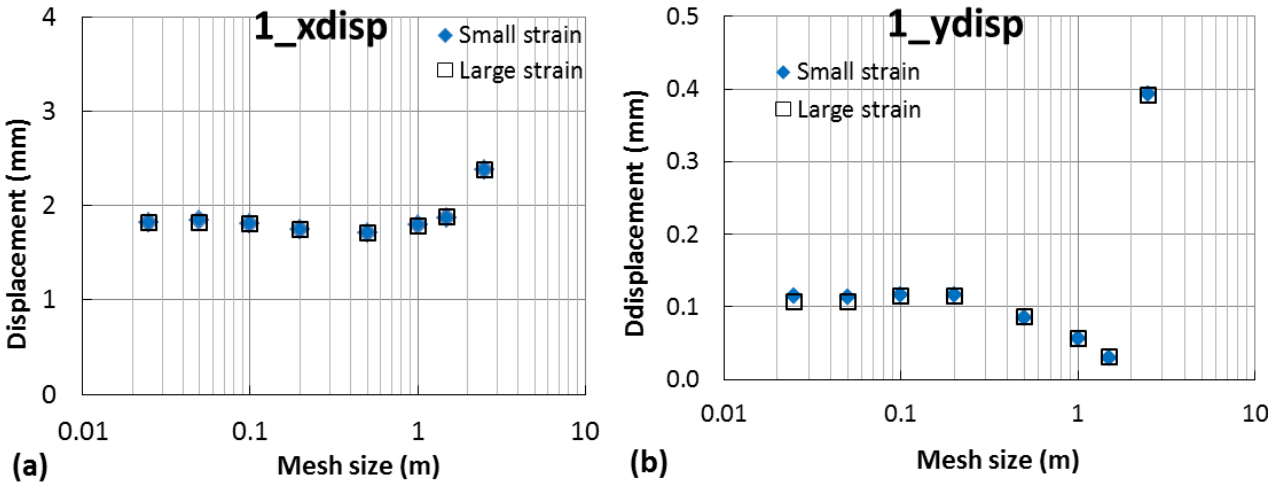

Figure E-6: (a) X-displacement and (b) Y-displacement at the point 1 (in Fig. E-1) of barricade for different mesh sizes obtained with ***c* = 0.1 kPa**

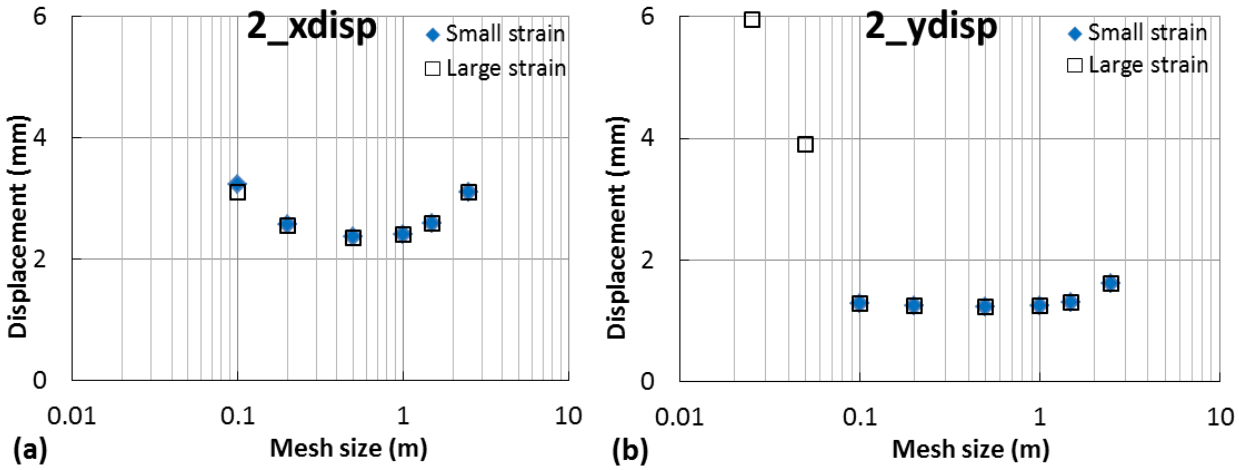

Figure E-7: (a) X-displacement and (b) Y-displacement at the point 2 (in Fig. E-1) of barricade for different mesh sizes obtained with ***c* = 0.1 kPa**

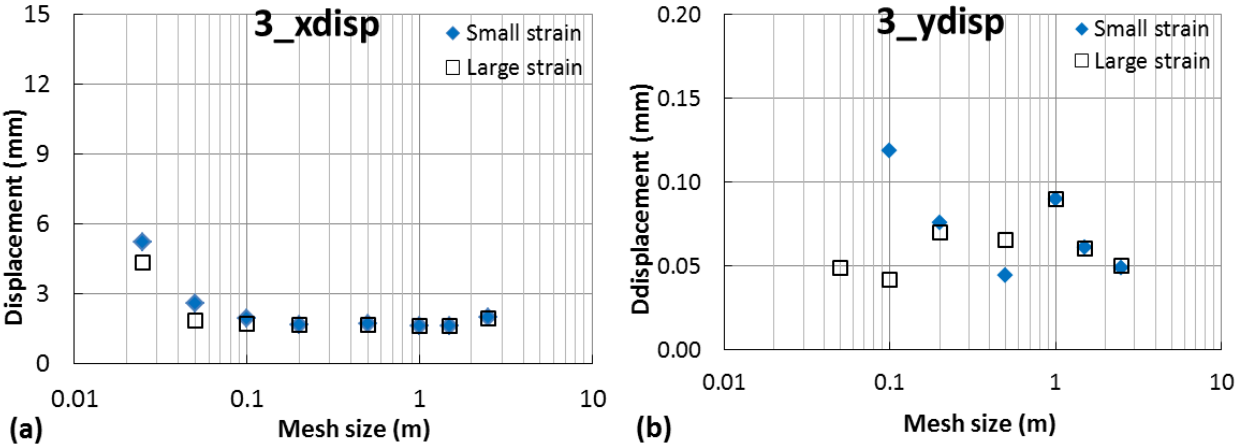

Figure E-8: (a) X-displacement and (b) Y-displacement at the point 3 (in Fig. E-1) of barricade for different mesh sizes obtained with ***c* = 0.1 kPa**

c = 10 kPa

When the backfill cohesion is 10 kPa, Figs. E-9 to E-11 illustrate that the simulated displacement of points 1, 2 and 3 (in Fig. E-1) at the barricade top all converges at the mesh size 0.1 × 0.1 m.

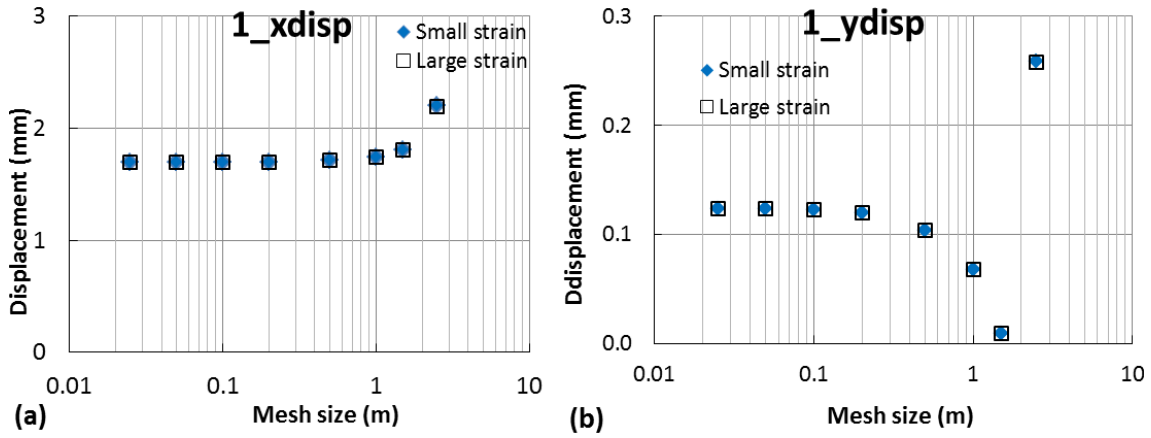

Figure E-9: (a) X-displacement and (b) Y-displacement at the point 1 (in Fig. E-1) of barricade for different mesh sizes obtained with ***c* = 10 kPa**

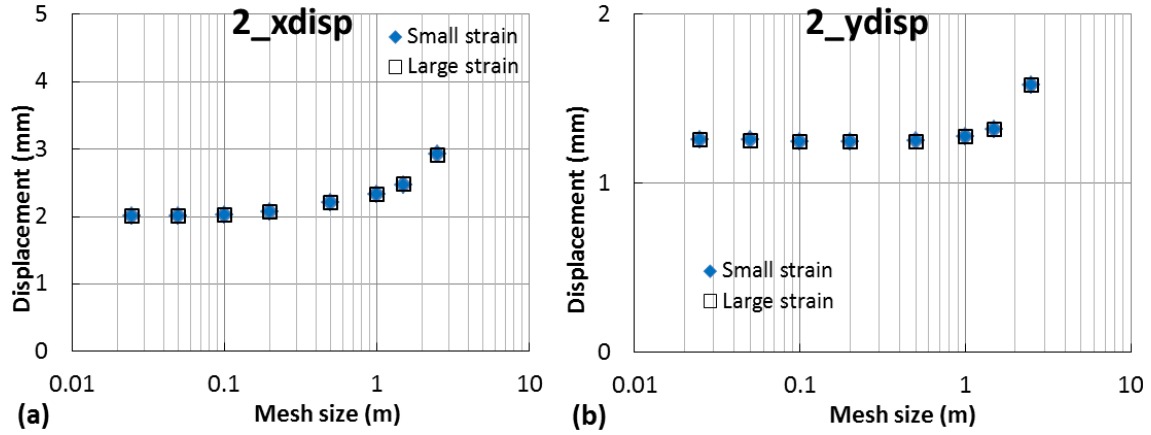

Figure E-10: (a) X-displacement and (b) Y-displacement at the point 2 (in Fig. E-1) of barricade for different mesh sizes obtained with ***c* = 10 kPa**

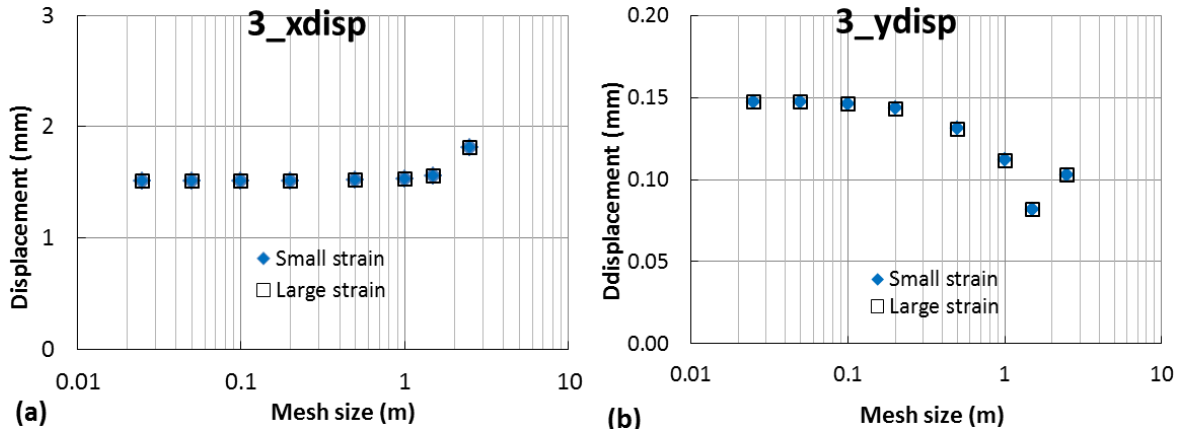

Figure E-11: (a) X-displacement and (b) Y-displacement at the point 3 (in Fig. E-1) of barricade for different mesh sizes obtained with ***c* = 10 kPa**

E2 Instability criterion

In the following, the optimal mesh of 0.1 × 0.1 m (at the barricade top) is used. Numerical results presented in this section are obtained with the backfill (plug) height H = 9 m, barricade height H_d = 5 m, slope angles $\alpha_1 = \alpha_2$ = 37°, unit weight γ_{wr} = 19.62 kN/m^3, Young's modulus E = 100 MPa, Poisson's ratio v = 0.3, **cohesion c = 0 kPa** and effective friction angle ϕ' = 40°.

The X-displacement of the point 2 (in Fig. E-1) is monitored when reducing the top length L_{BT} of the barricade to find the critical L_{BT}.

δ = 30°

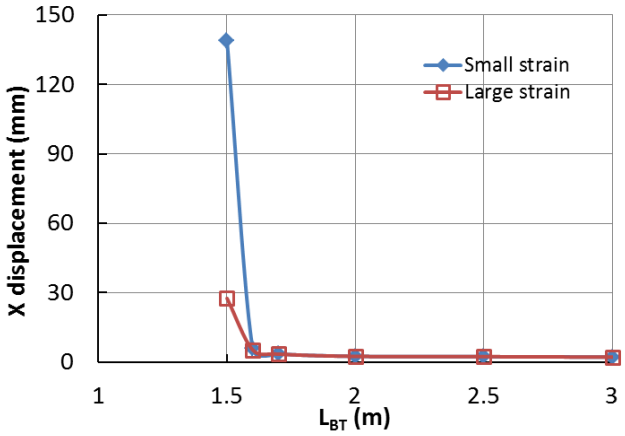

Figure E-12: Variation of the horizontal displacement at the point 2 (in Fig. E-1) as a function of the barricade top length L_{BT} with δ = **30°**

δ = 40°

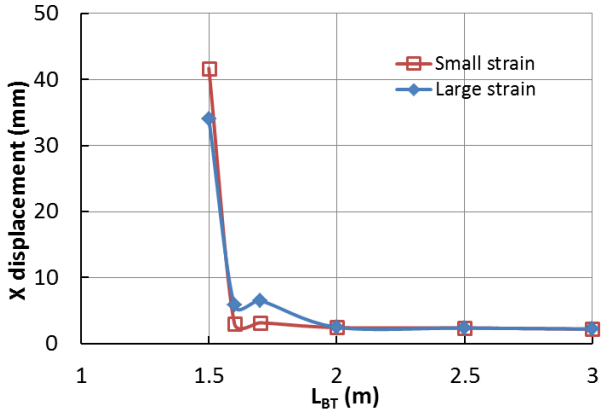

Figure E-13: Variation of the horizontal displacement at the point 2 (in Fig. E-1) as a function of the barricade top length L_{BT} with δ = **40°**

E3 Conclusions

- When the backfill cohesion is zero, the simulated displacement inside the barricade tends to converge as mesh becomes finer, while that at the barricade top cannot converge;
- A nonzero value of backfill cohesion (for instance c = 10 kPa) is required to yield converged displacement at the barricade top as mesh becomes finer;
- The instability criterion can be sued to find the critical barricade top length to judge the failure of the waste rock barricade;
- The instability criterion applies when the backfill cohesion is zero;
- The barricade failure defined by the modelling with large strain and small strain is very similar.

APPENDIX F – SENSITIVITY AND PARAMERIC ANALYSES RELATED TO CHAPTER 5

This section presents the sensitivity and parametric analyses related to the numerical results obtained with FLAC^{3D} (Itasca 2013) presented in Chapter 5. In the following, the effect of backfill modulus, cohesion and tensile strength for different mesh sizes on the stress state and displacement of side-exposed backfill is first presented. Complementary results of instability criterion for defining the failure of exposed cemented fill are also illustrated. The values of the internal friction angle ϕ' and Poisson's ratio v of the backfill are related through Eq. (A.9) in Appendix A.

F1 Effect of mesh size from 2 to 0.2 m

Fig. F-1 schematically illustrates the model of the exposed cemented fill used for analyzing the optimal mesh size. The backfill exposure is performed by freeing the restraints on the open face. The cemented fill is exposed in one step unless specified. Numerical results shown in this section are obtained with H = 40 m, B = 10 m, L = 8 m, ϕ' = 35°, v = 0.3 and γ = 18 kN/m^3.

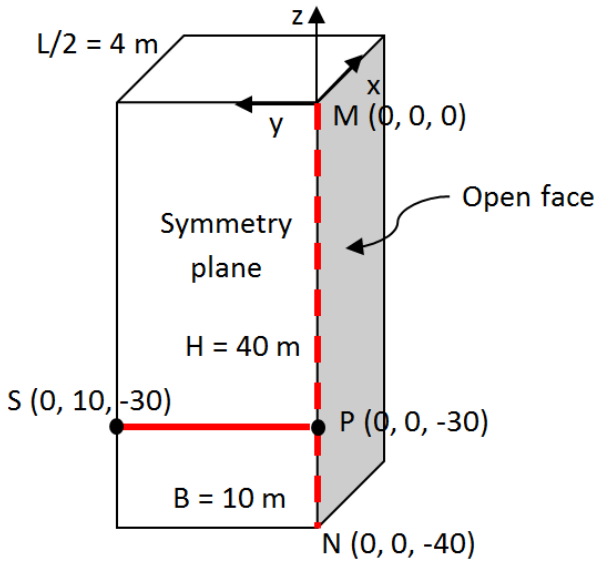

Figure F-1: Schematic view of the model of the exposed cemented fill

E = 300 MPa, c = 30 kPa, T_0 = 0 kPa

Figs. F-2 to F-7 show that when the tension cut-off T_0 of backfill is zero or 3 kPa, the numerical results become somewhat stable at mesh size 0.5 × 0.5 m, except for the displacement on the

open face. A hump of vertical stress S_{zz} is observed in Fig. F-3b when the mesh size is 0.2 m and it disappears when the backfill cohesion is increased (see below).

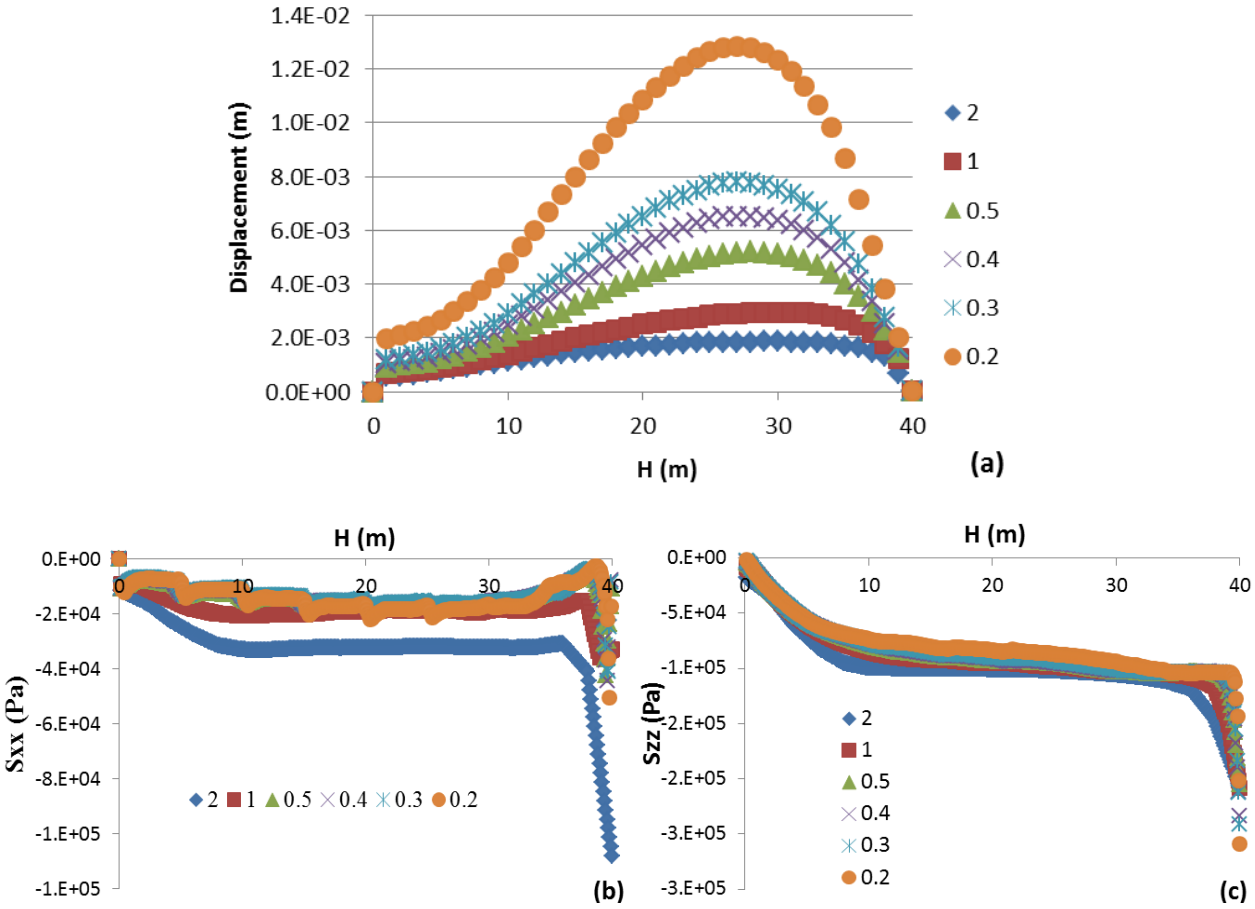

Figure F-2: (a) Displacement (b) S_{xx} and (c) S_{zz} profiles along the line MN (in Fig. F-1) on the open face for different mesh sizes (m) obtained with ***E* = 300 MPa, *c* = 30 kPa and T_0 = 0 kPa**

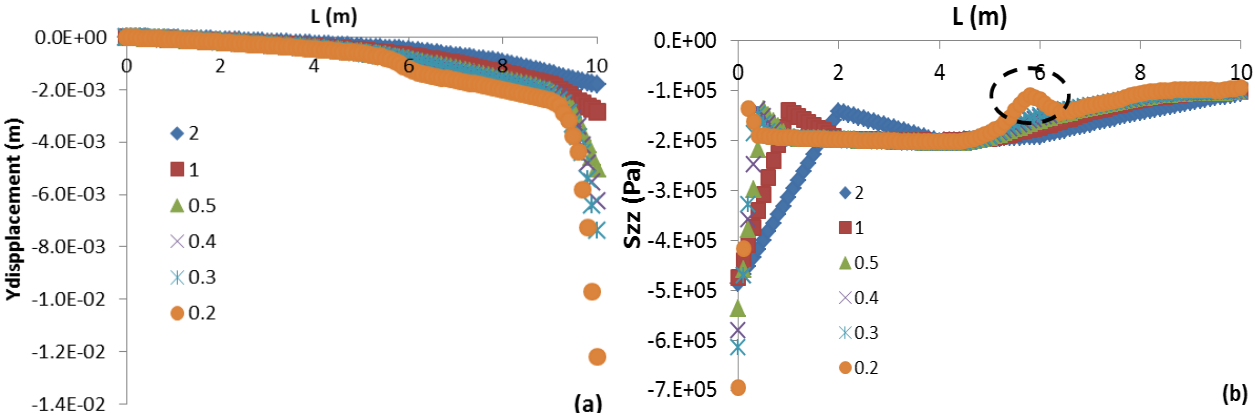

Figure F-3: (a) Y-displacement and (b) S_{zz} profiles along the line SP (in Fig. F-1) for different mesh sizes (m) obtained with ***E* = 300 MPa, *c* = 30 kPa and T_0 = 0 kPa**

E = 300 MPa, c = 30 kPa, T_0 = 3 kPa

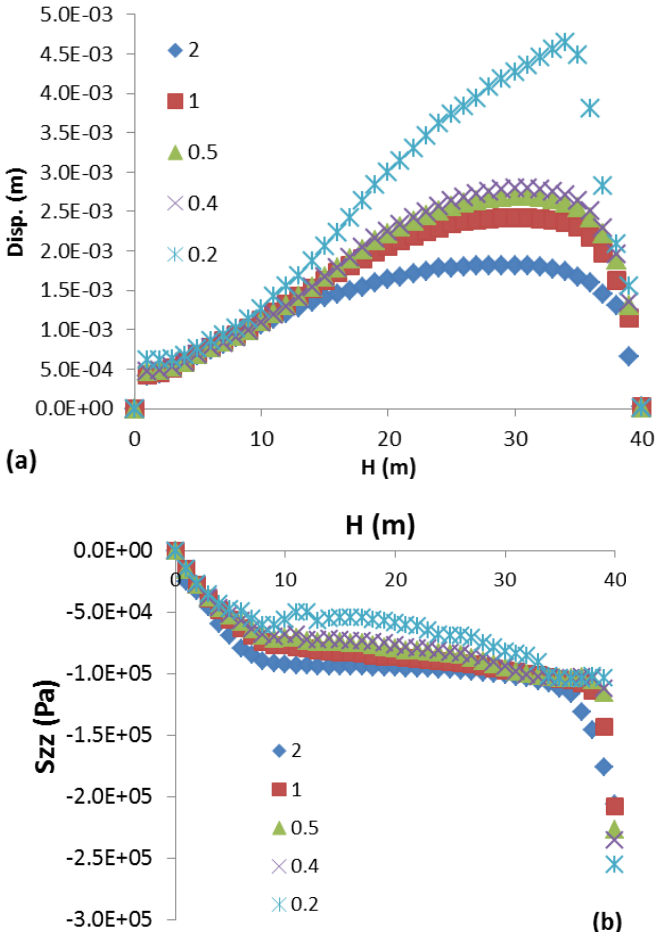

Figure F-4: (a) Displacement and (b) S_{zz} profiles along the line MN (in Fig. F-1) on the open face for different mesh sizes (m) obtained with ***E* = 300 MPa, *c* = 30 kPa and T_0 = 3 kPa**

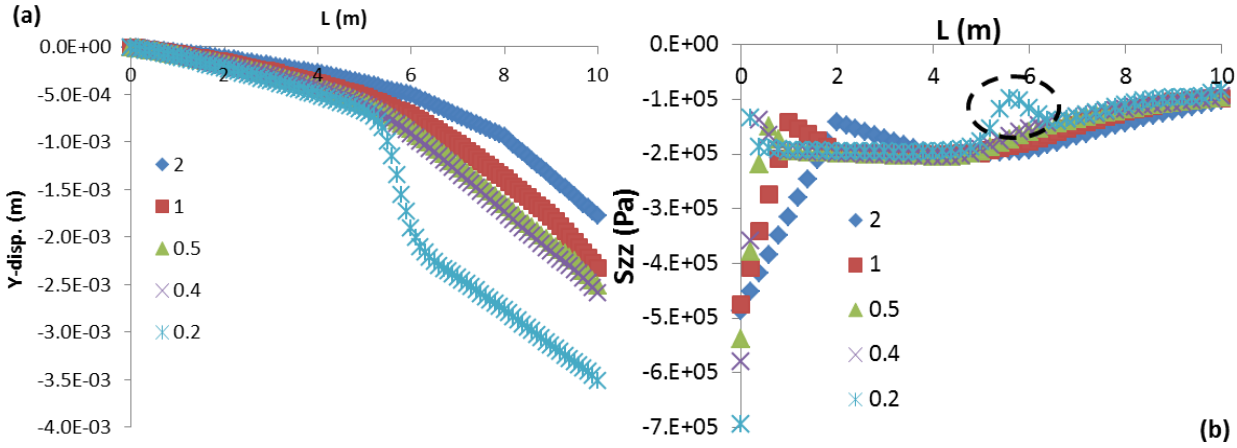

Figure F-5: (a) Y-displacement and (b) S_{zz} profiles along the line SP (in Fig. F-1) for different mesh sizes (m) obtained with ***E* = 300 MPa, *c* = 30 kPa and T_0 = 3 kPa**

E = 300 MPa, c = 50 kPa, T_0 = 0 kPa

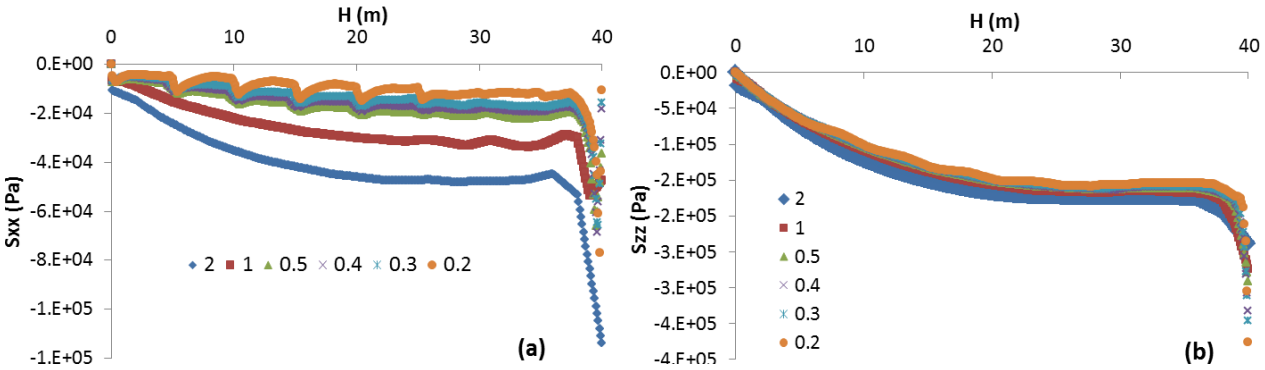

Figure F-6: (a) S_{xx} and (b) S_{zz} profiles along the line MN (in Fig. F-1) on the open face for different mesh sizes (m) obtained with ***E* = 300 MPa, *c* = 50 kPa and T_0 = 0 kPa**

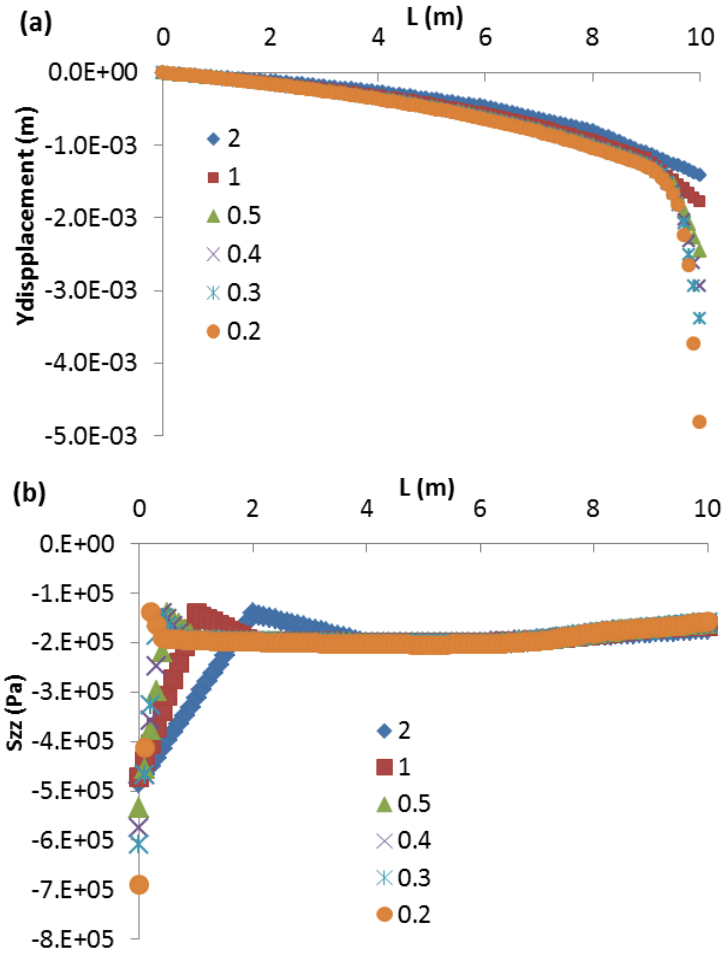

Figure F-7: (a) Y-displacement and (b) S_{zz} profiles along the line SP (in Fig. F-1) for different mesh sizes (m) obtained with ***E* = 300 MPa, *c* = 50 kPa and T_0 = 0 kPa**

$\underline{E = 300 \text{ MPa}, c = 50 \text{ kPa}, T_0 = 5\text{kPa}}$

Figs. F-8 to F-10 illustrate that when the tension cut-off T_0 of backfill is 5 kPa, the numerical results, including the displacement on the open face, become stable at mesh size 0.5 × 0.5 m.

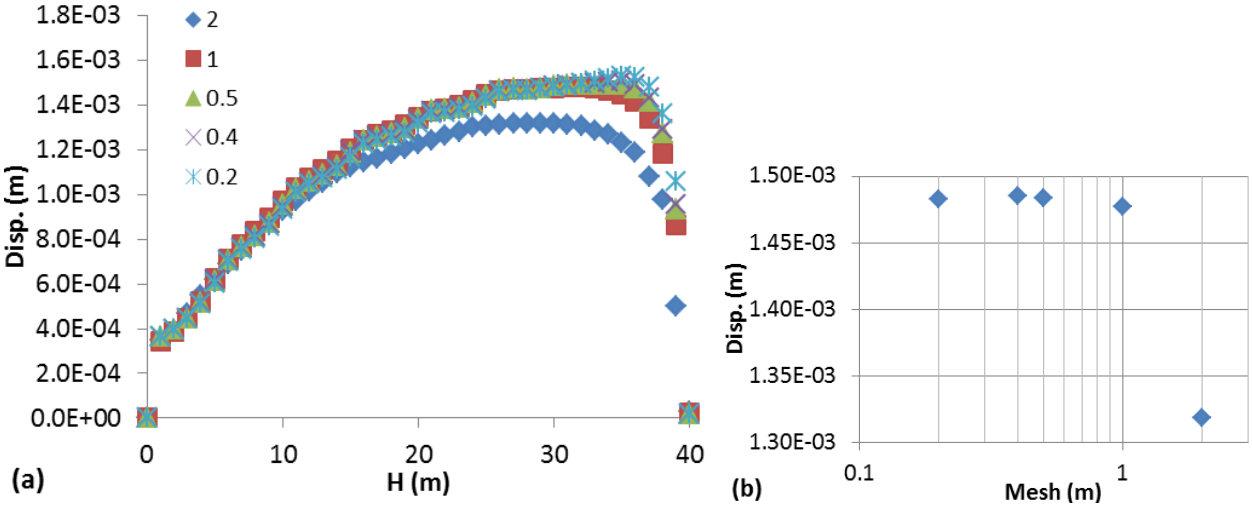

Figure F-8: Displacement (a) profiles along the line MN and (b) of point P (in Fig. F-1) on the open face for different mesh sizes (m) obtained with ***E* = 300 MPa, *c* = 50 kPa and T_0 = 5 kPa**

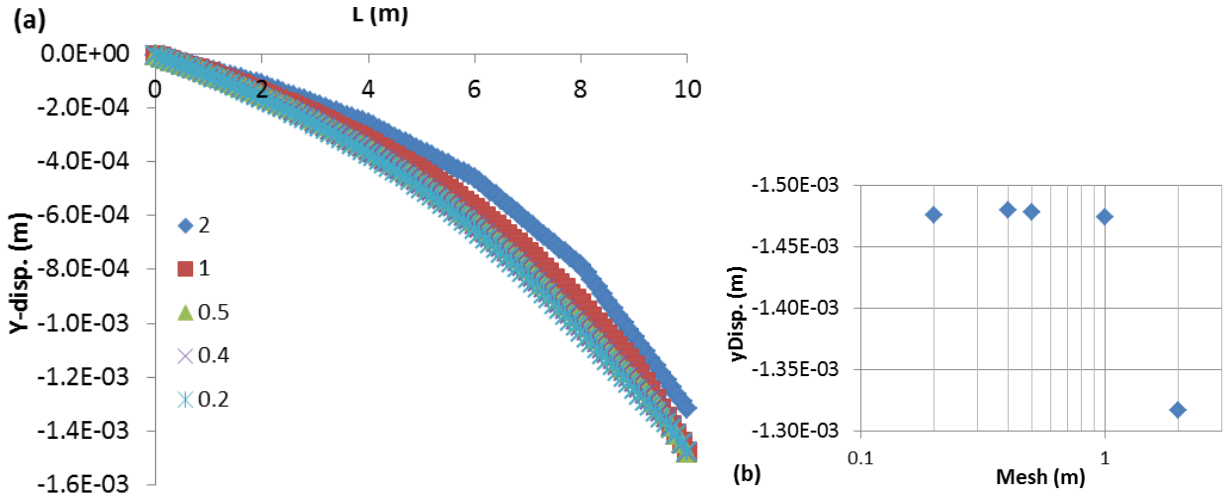

Figure F-9: Displacement (a) profiles along the line SP and (b) of point P (in Fig. F-1) for different mesh sizes (m) obtained with ***E* = 300 MPa, *c* = 50 kPa and T_0 = 5 kPa**

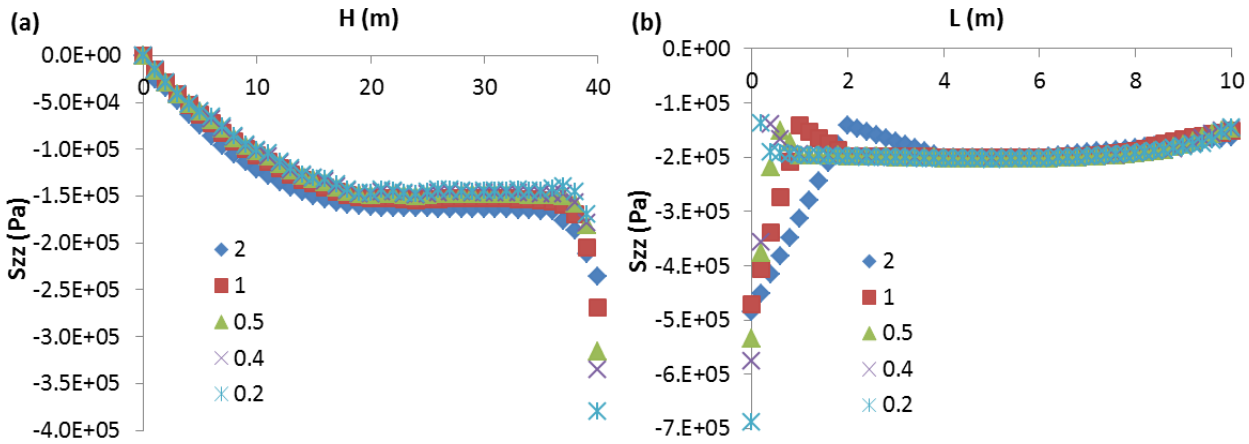

Figure F-10: S_{zz} profiles along (a) the line MN and (b) the line SP (in Fig. F-1) for different mesh sizes (m) obtained with ***E* = 300 MPa, *c* = 50 kPa and T_0 = 5 kPa**

<u>*E* = 300 MPa, *c* = 500 kPa, T_0 = 0 kPa</u>

Figs. F-11 and F-12 show that when the tension cut-off T_0 of backfill is zero, the displacement on the open face is not stable as the mesh becomes finer (from 2 to 0.2 m) even for very high backfill cohesion and modulus.

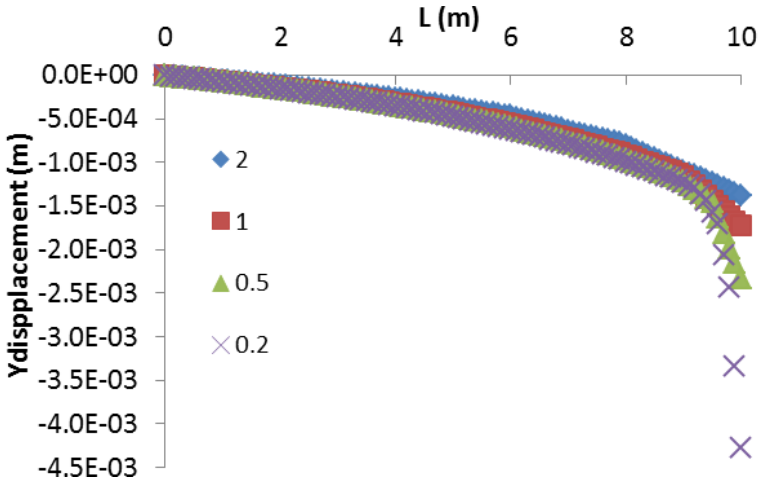

Figure F-11: Y-displacement profiles along the line SP (in Fig. F-1) for different mesh sizes obtained with ***E* = 300 MPa, *c* = 500 kPa and T_0 = 0 kPa**

E = 1 GPa, c = 500 kPa, T_0 = 0 kPa

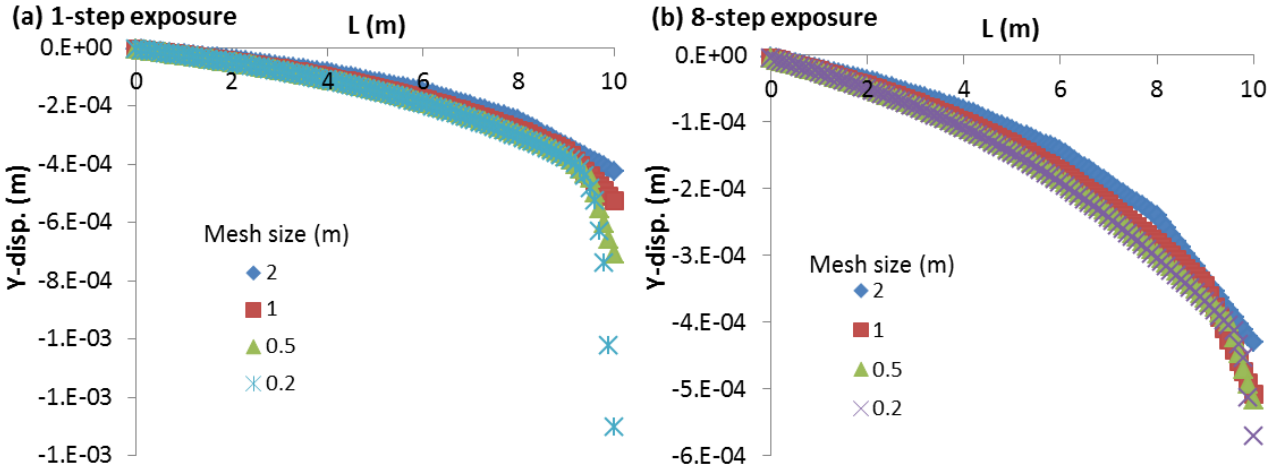

Figure F-12: Y-displacement profiles along the line SP (in Fig. F-1) for different mesh sizes obtained with ***E* = 1 GPa, *c* = 500 kPa and T_0 = 0 kPa**

E = 1 GPa, c = 500 kPa, T_0 = 10 kPa

Figs. F-13 and F-14 illustrate that when the tension cut-off T_0 of backfill is 10 KPa, the numerical results, including the displacement on the open face, become stable at mesh size 0.5 × 0.5 m.

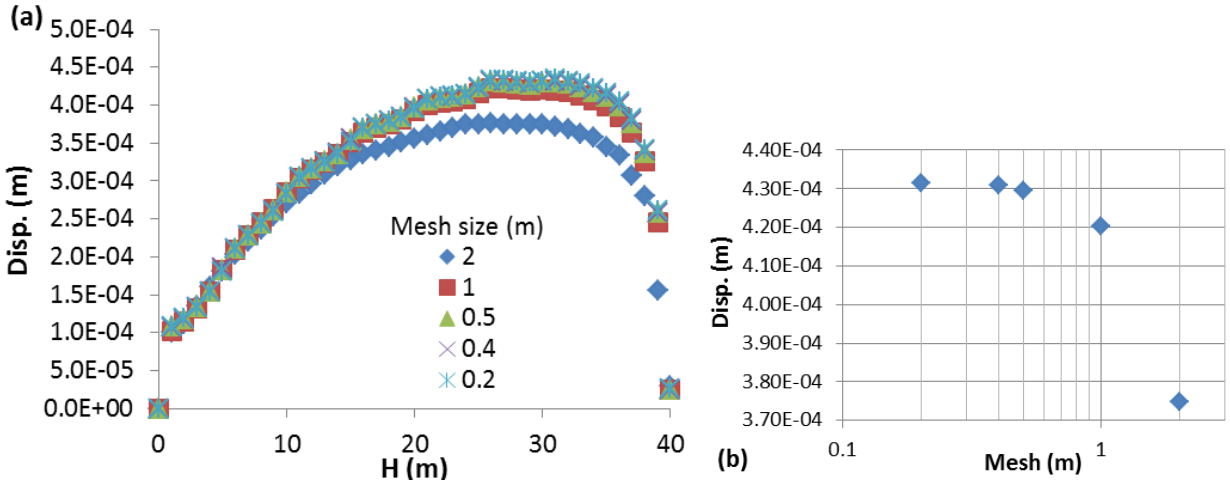

Figure F-13: Displacement (a) profiles along the line MN and (b) of point P (in Fig. F-1) for different mesh sizes (m) obtained with ***E* = 1 GPa, *c* = 500 kPa and T_0 = 10 kPa**

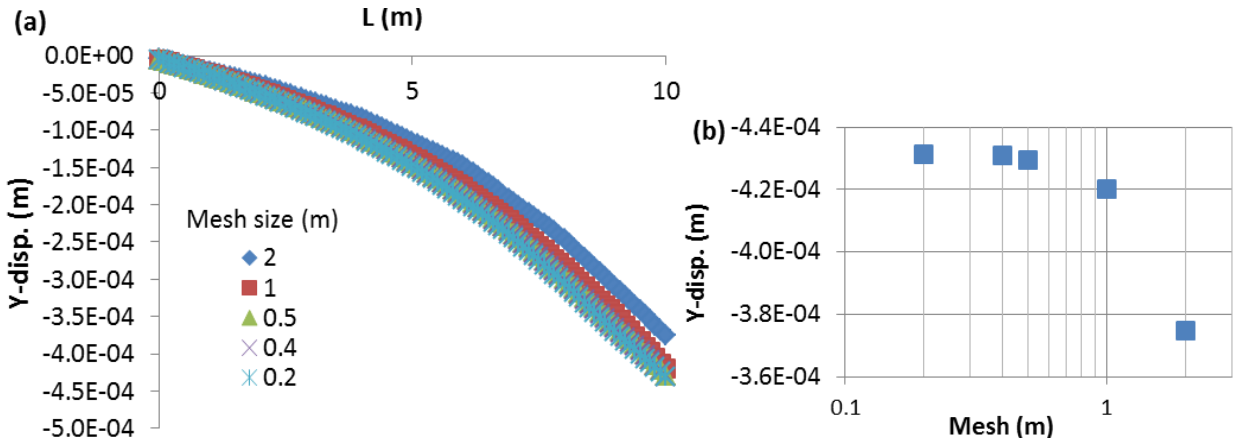

Figure F-14: Displacement (a) profiles along the line SP and (b) of point P (in Fig. F-1) for different mesh sizes obtained with ***E* = 1 GPa, *c* = 500 kPa and T_0 = 10 kPa**

The optimal mesh size is 0.5 × 0.5 m for exposed cemented fill.

F2 Instability criterion

In the following, the optimal mesh of 0.5 × 0.5 m is used for backfill. The numerical results are obtained with ϕ' = 35°, ν = 0.3, γ = 18 kN/m^3 and E = 300 MPa.

The displacement of Point (0 0 -30) (in Fig. 5-2) is monitored when reducing the backfill cohesion to find the critical backfill cohesion.

T_0 = 0 kPa

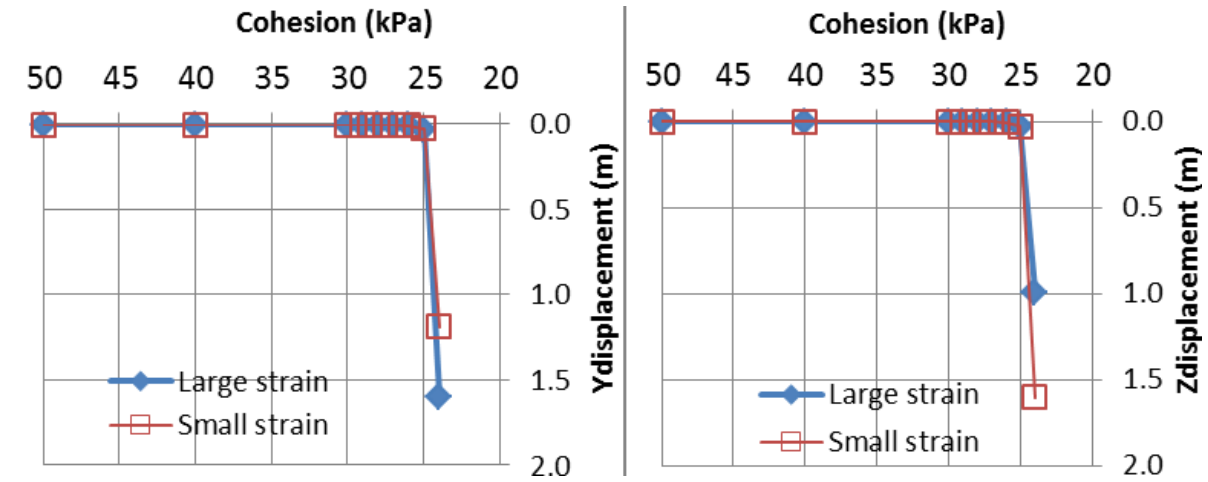

Figure F-15: Displacement of Point (0 0 -30) (in Fig. 5-2) for different values of fill cohesion *c* with **T_0 = 0 kPa,** H = 45 m, B = 6 m and L = 9 m

$\underline{T_0 = c/10}$

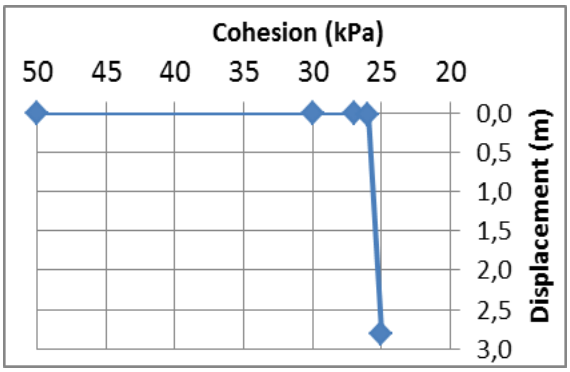

Figure F-16: Displacement of Point (0 0 -30) (in Fig. 5-2) for different values of fill cohesion *c* with $\boldsymbol{T_0 = c/10}$, H = 45 m, B = 6 m and L = 9 m

The displacement of Line MN (in Fig. 5-2) is also monitored while reducing the backfill cohesion to find the critical fill cohesion.

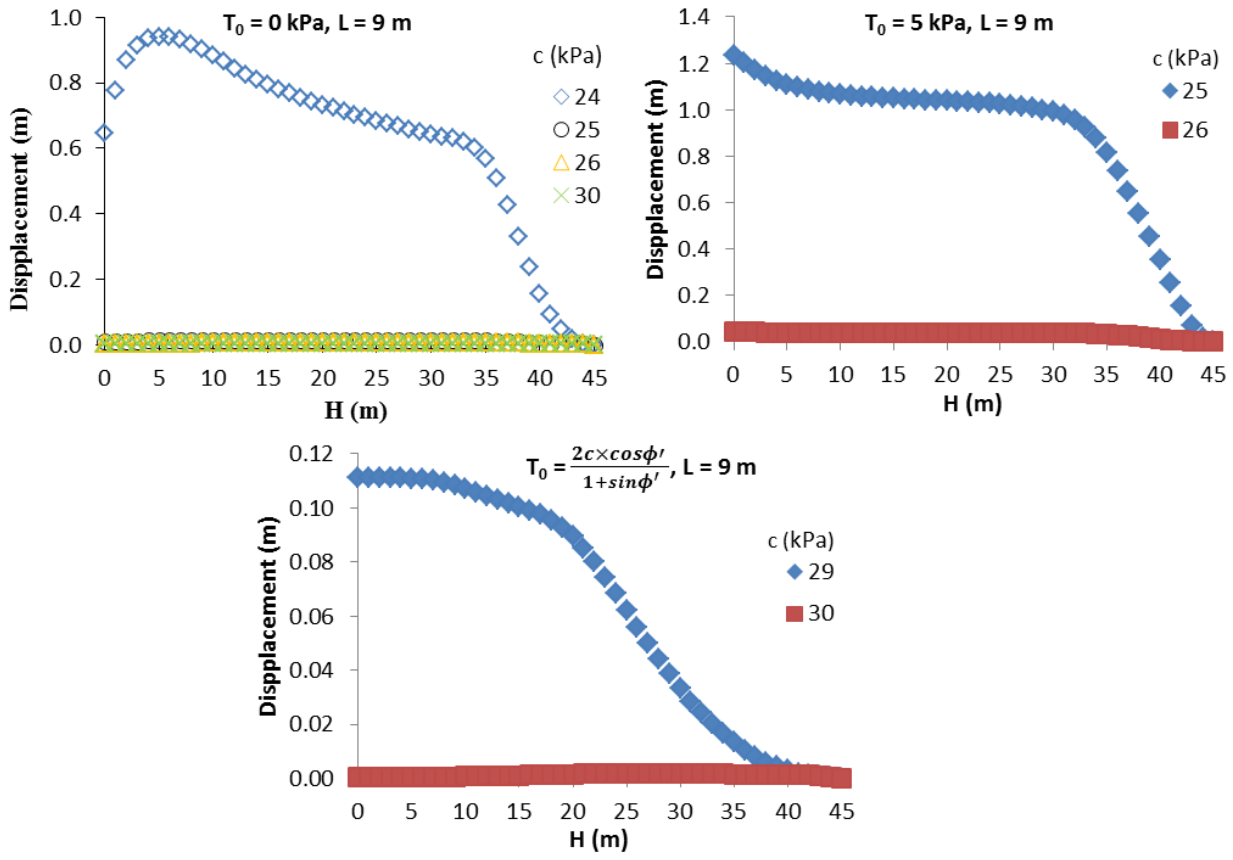

Figure F-17: Displacement profiles along the line MN (in Fig. 5-2) for different values of fill cohesion *c* with H = 45 m, B = 6 m and L = 9 m

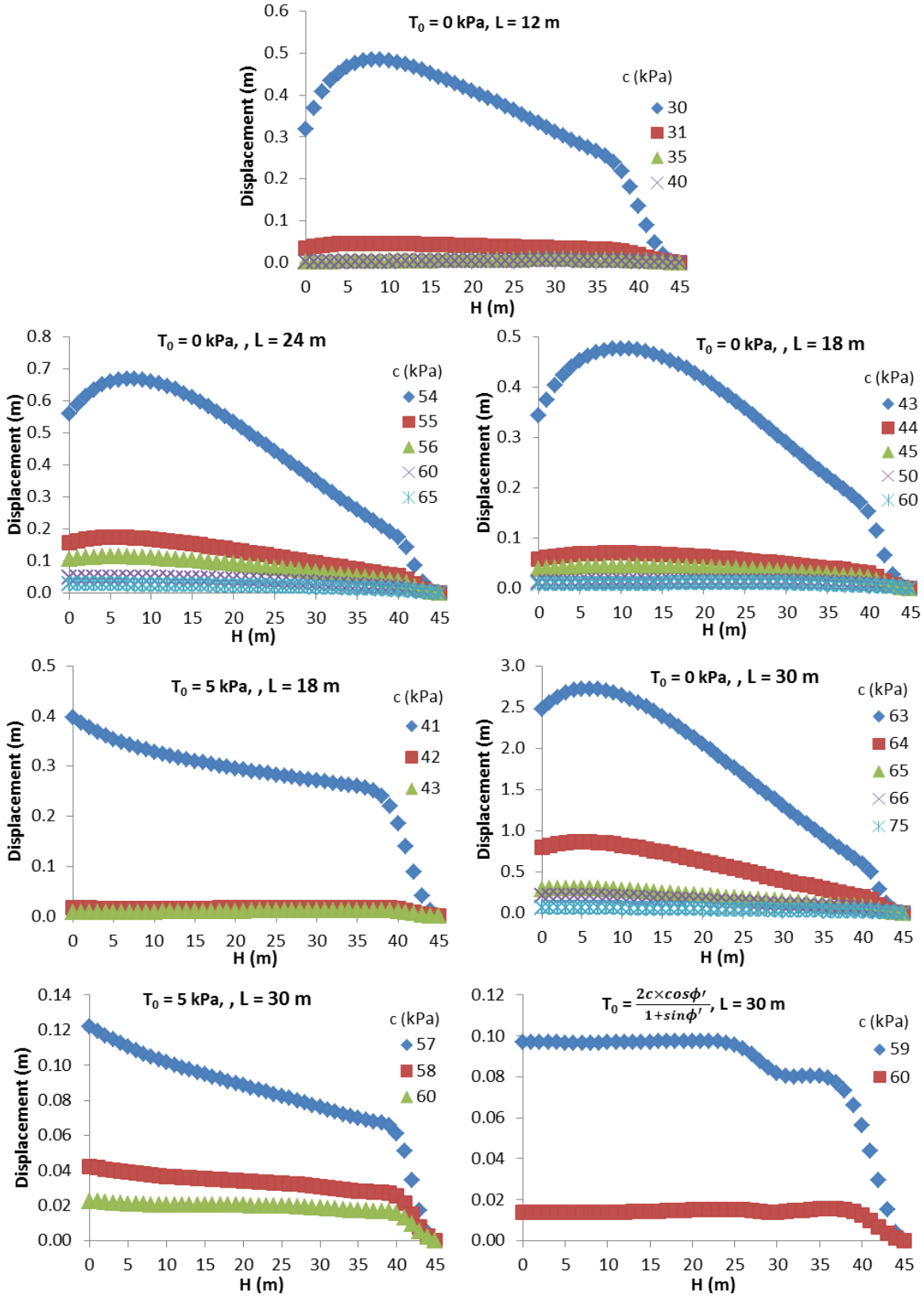

Figure F-18: Displacement profiles along the line MN (in Fig. 5-2) for different values of fill cohesion c with H = 45 m and B = 6 m

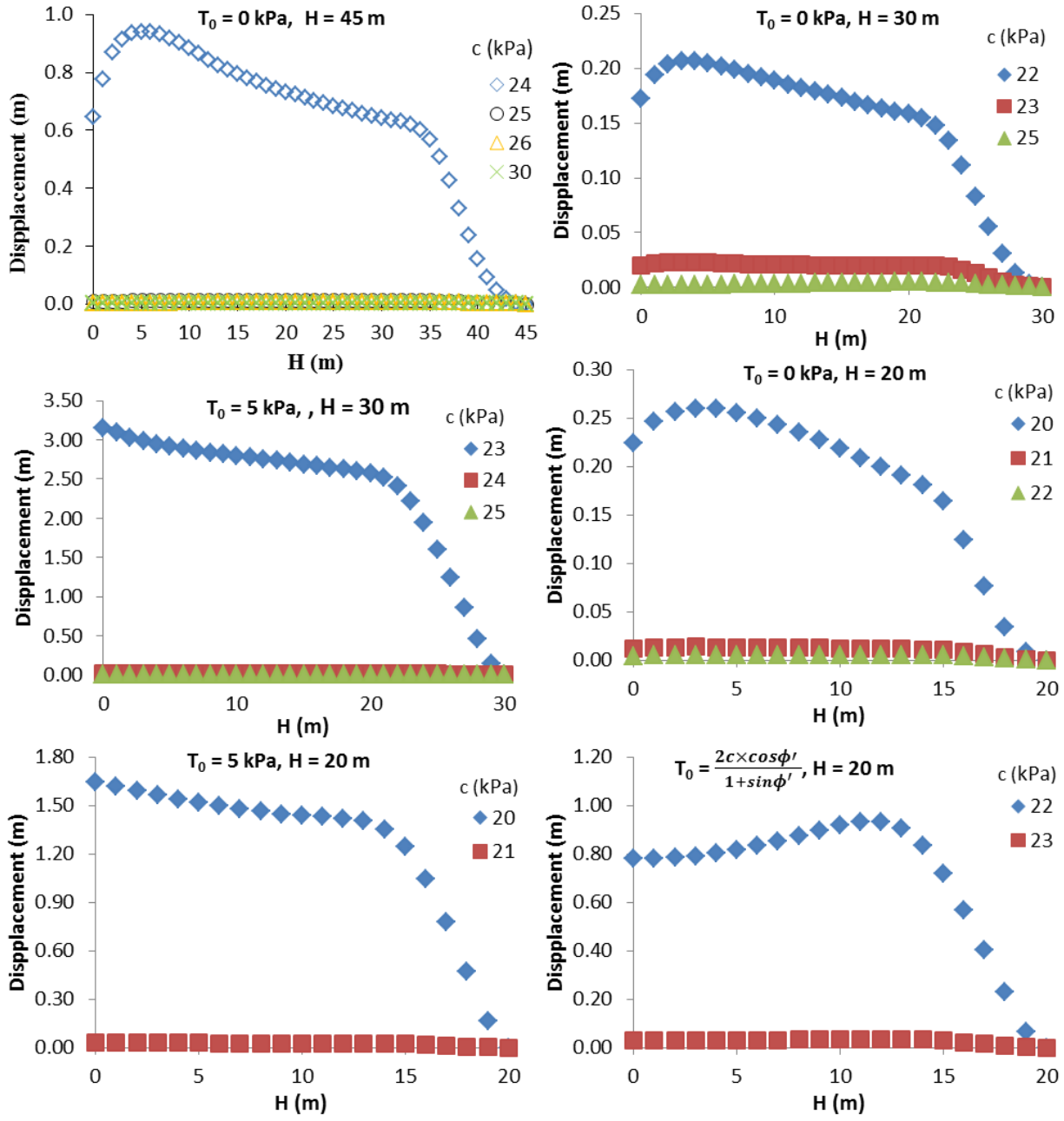

Figure F-19: Displacement profiles along the line MN (in Fig. 5-2) for different values of fill cohesion c with B = 6 m and L = 9 m

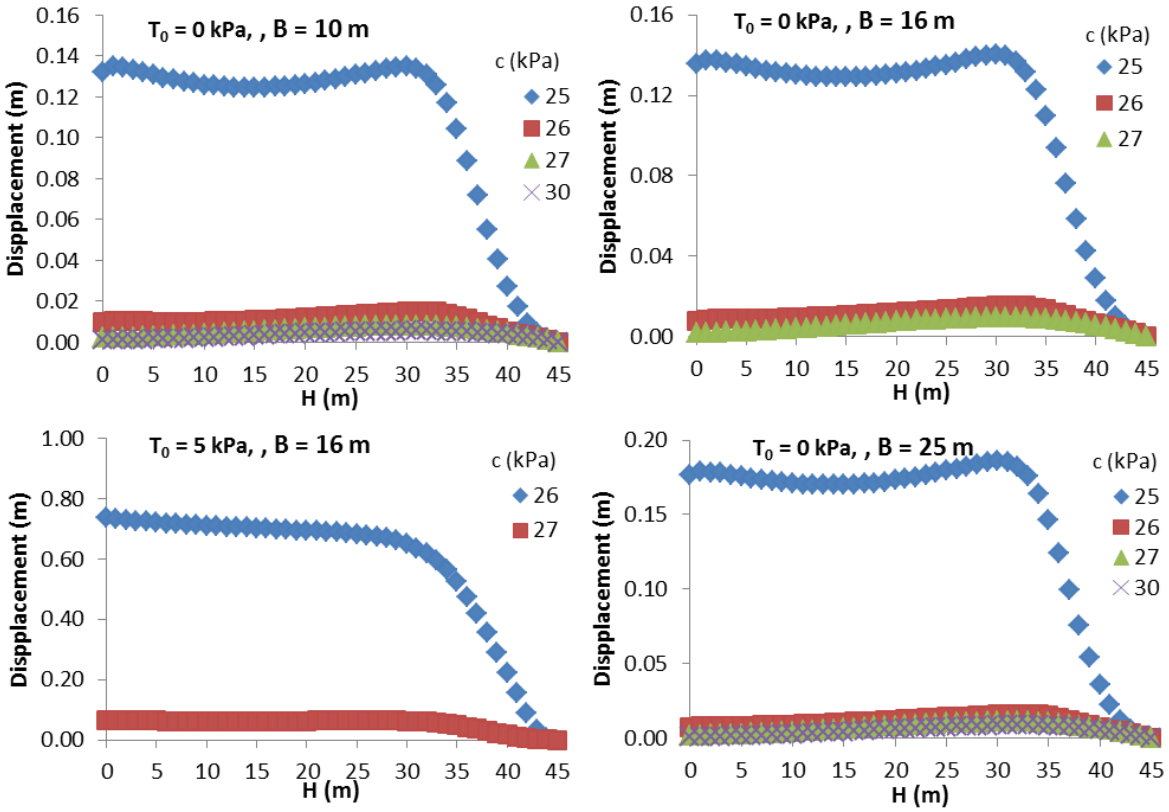

Figure F-20: Displacement profiles along the line MN (in Fig. 5-2) for different values of fill cohesion c with H = 45 m and L = 9 m

F3 Conclusions

- When the tension cut-off T_0 of backfill is zero or too small (for instance T_0 = 3 kPa), the displacement and stress on the open face of backfill cannot converge as the mesh becomes finer (from 2 to 0.2 m), even for very high modulus and cohesion of backfill;
- When the tension cut-off T_0 of backfill is a finite value (for instance T_0 = 5 or 10 kPa), the numerical results become stable at the optimal mesh size (0.5 × 0.5 m) for exposed backfill;
- The results obtained with large strain and small strain are almost identical for stable cemented (nonzero cohesion) fill upon exposure. Once failure occurs, the calculations of small strain cannot converge, while that of large strain give very large displacement after twisted meshes;
- The instability criterion can be sued to find a critical value of fill cohesion to define the failure of the exposed cemented fill;
- The instability criterion is also applicable to cases of zero tension cut-off of backfill.

APPENDIX G – SENSITIVITY AND PARAMERIC ANALYSES RELATED TO CHAPTER 6

This section presents the sensitivity and parametric analyses related to the numerical simulations conducted using FLAC (Itasca 2011) presented in Chapter 6. The effect of mesh size and thickness of filling layer on stress state and the resulting stress ratios (K and K_{ps}) is illustrated. The values of the internal friction angle ϕ' and Poisson's ratio ν of the backfill are related through Eq. (A.9) (in Appendix A) in cases of related parameters.

G1 Effect of mesh size

Based on the numerical results shown in Figs. G-1 and G-2, quadrilateral elements of 0.2 × 0.2 m is regarded as the optimal mesh size for backfill.

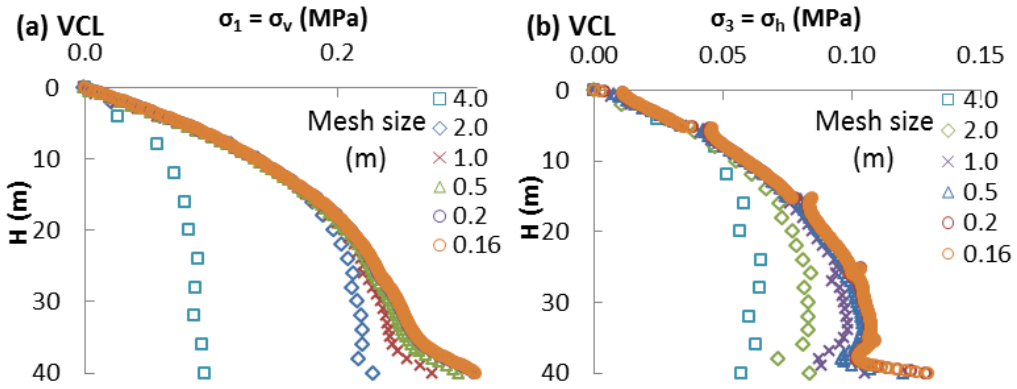

Figure G-1: (a) Vertical and (b) horizontal stress distributions along the VCL of backfilled openings for different mesh sizes with related ν = 0.3 and ϕ' = 35° (Case 3' in Table 6-1)

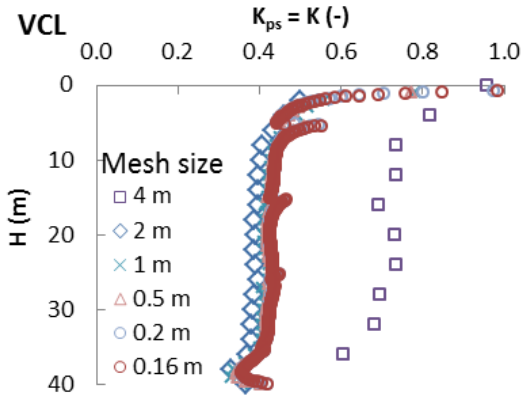

Figure G-2: Vertical profiles of K (= K_{ps}) along the VCL of backfilled openings obtained with stresses shown in Fig. G-1

G2 Effect of thickness of filling layer

The optimal mesh of 0.2 × 0.2 m is used for backfill.

For the independent values of v and ϕ' of backfill, Figs. G-3 and G-4 show that the thickness of filling layer (from 5 to 0.2 m/layer) has little effect on the stress state and the resultant earth pressure coefficient.

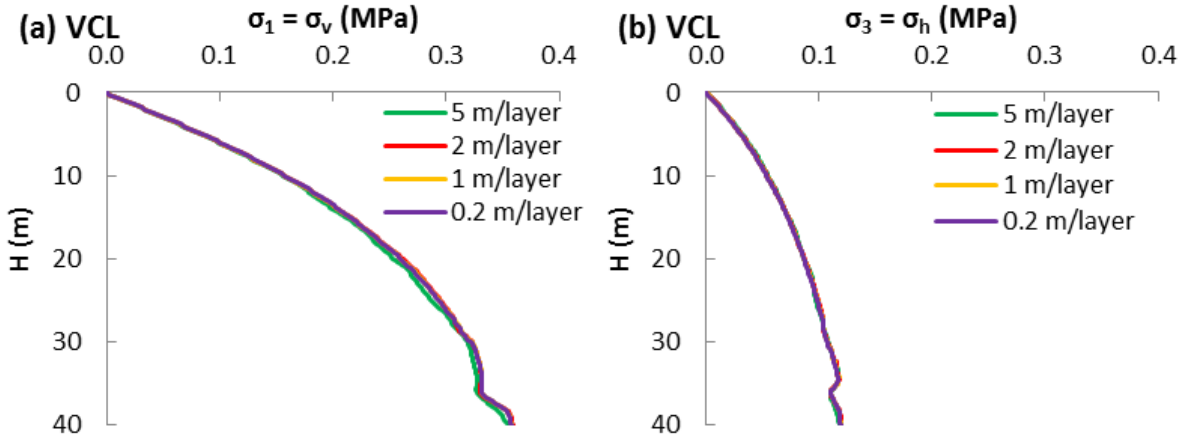

Figure G-3: (a) Vertical and (b) horizontal stress distributions along the VCL of backfilled openings for different thickness of filling layer for independent v = 0.2 and ϕ' = 30° (Case 0 in Table 6-1)

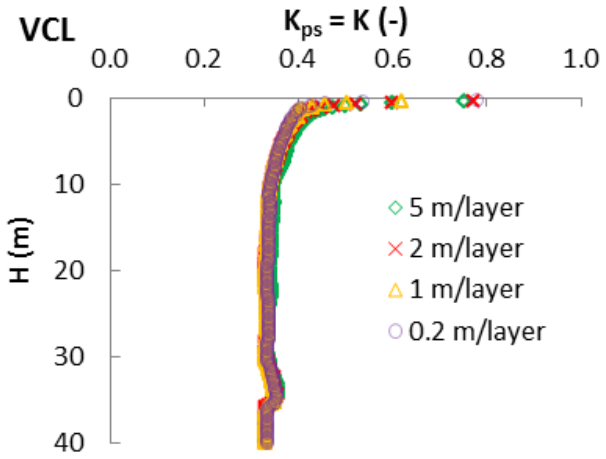

Figure G-4: Vertical profiles of K (= K_{ps}) along the VCL of backfilled openings obtained with stresses shown in Fig. G-3

For the related values of v and ϕ' of backfill, Figs. G-5 illustrates that the thickness of filling layer (from 5 to 0.5 m/layer) has little effect on the vertical stress (Fig. G-5a), while the

horizontal stress becomes stable and almost superposed once the filling layer is below 1 m/layer (Fig. G-5b). Accordingly, Fig. G-6 depicts that the resulting stress ratios becomes stable when the thickness of filling layer is smaller than 1 m/layer. Therefore, 1 m/layer is used to minimize the effect of layer thickness on the stress state and stress ratios.

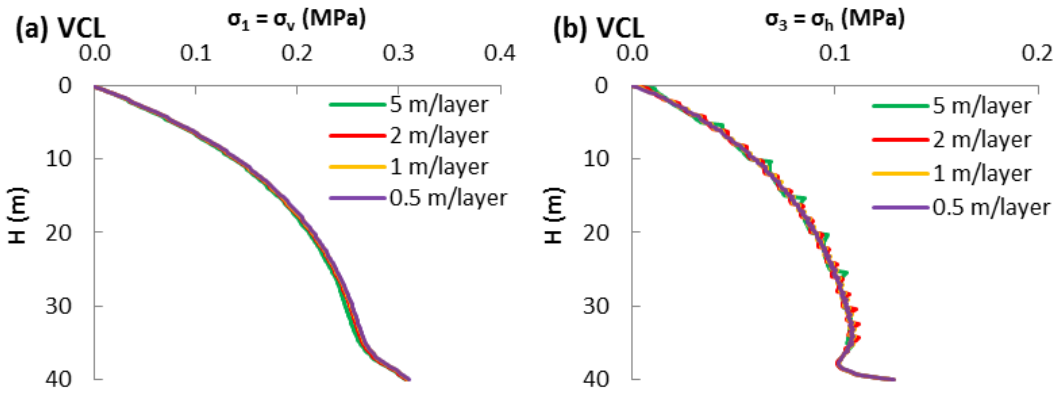

Figure G-5: (a) Vertical and (b) horizontal stress distributions along the VCL of backfilled openings for different thickness of filling layer for related ν = 0.3 and ϕ' = 35° (Case 3' in Table 6-1)

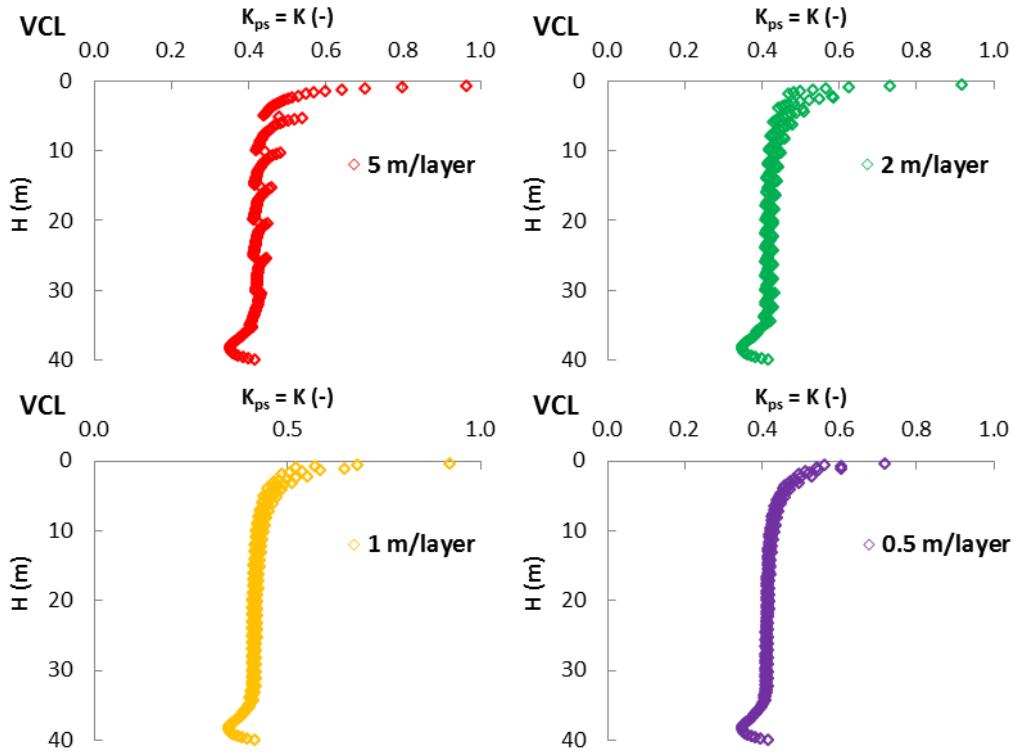

Figure G-6: Vertical profiles of K (= K_{ps}) along the VCL of backfilled openings obtained with stresses shown in Fig. G-5

APPENDIX H – ADDITIONAL RESULTS RELATED TO CHAPTER 6

This section presents the complementary results to Chapter 6. In Section H1, simulated stresses in backfilled openings used for calculating the stress ratios (K_{ps} and K) of various cases shown in Chapter 6 are presented. The effect of interface angle δ (= ϕ' to 0) on the stress ratio is illustrated in Section H2 and on the stress state in backfilled openings is shown in Section H3. The geometric and mechanical properties of the backfill-stope system are given in Table 6-1.

H1 Stress distribution along the opening height in backfilled openings

H1.1 Independent ϕ' and ν

Effect of opening width B (Case 1 in Table 6-1)

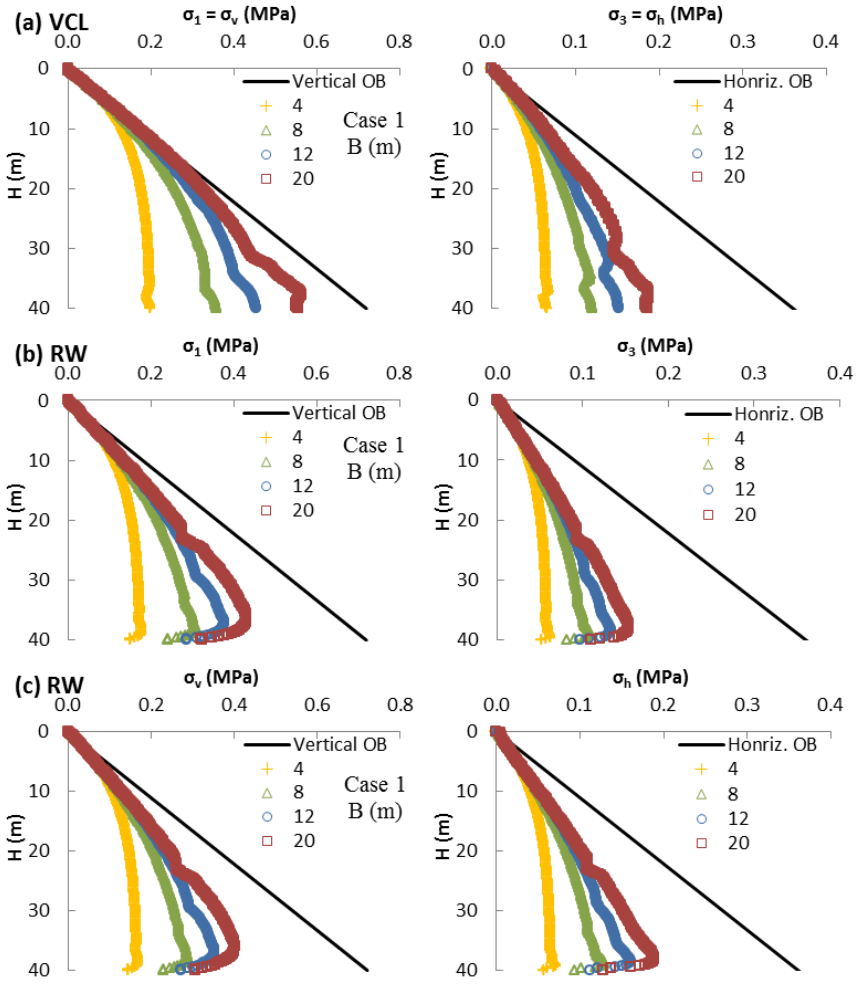

Figure H-1: Stress distributions along the VCL (a) and near the RW (b and c) as a function of opening width B for independent ν and ϕ' (Case 1 in Table 6-1)

Effect of backfill modulus *E* (Case 2 in Table 6-1)

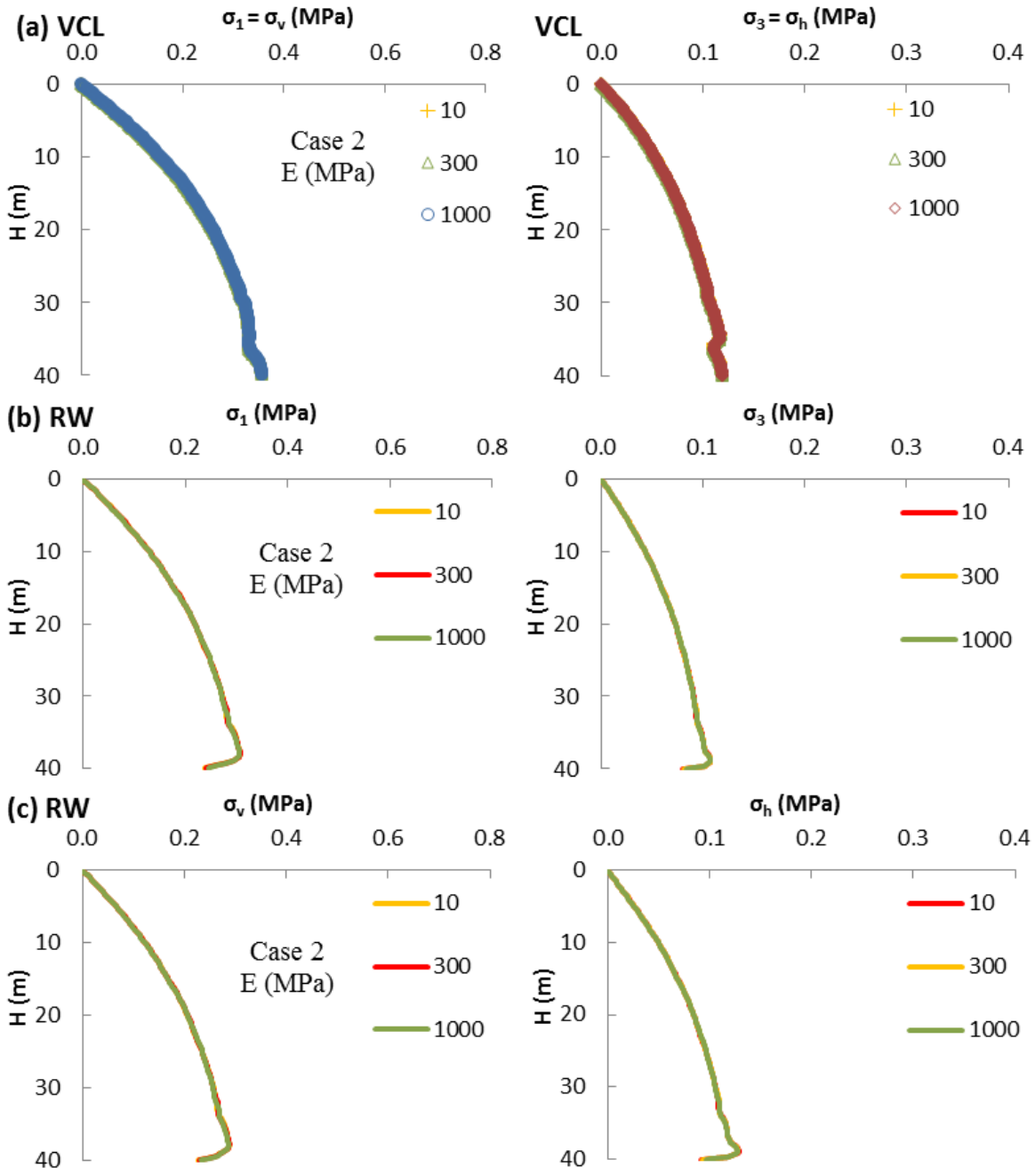

Figure H-2: Stress distributions along the VCL (a) and near the RW (b and c) as a function of backfill modulus *E* for independent *v* and ϕ' (Case 2 in Table 6-1)

Effect of internal friction angle of backfill ϕ' (Case 3 in Table 6-1)

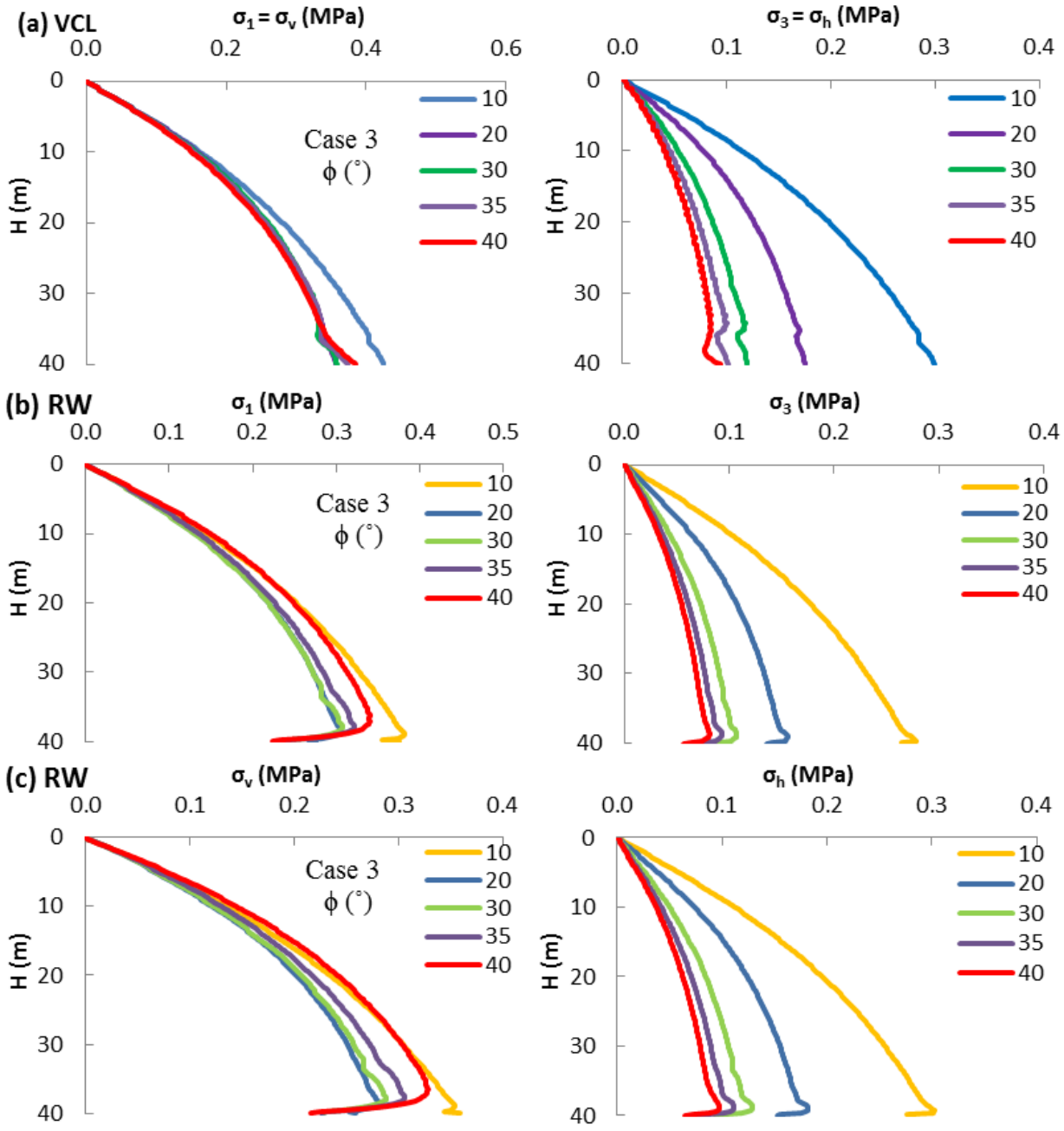

Figure H-3: Stress distributions along the VCL (a) and near the RW (b and c) as a function of ϕ' for constant ν = 0.2 (Case 3 in Table 6-1)

Effect of Poisson's ratio of backfill *v* (Case 4 in Table 6-1)

Fig. H-4 illustrates the stress distributions along the opening height for Case 4. Fig. H-4a shows that both vertical σ'_v and horizontal σ'_h stresses along the VCL are almost insensitive to the change of v value from 0.001 to 0.2. This leads to nearly constant values of K_{ps} (= K) along the VCL that can be represented by K_a for $0.001 \leq v \leq 0.2$ (Fig. 6-8a) for independent v and ϕ'. When v value changes from 0.2 to 0.4, Fig. H-4a shows that the σ'_h slightly increases and the σ'_v decreases, leading to increased K value along the VCL (Fig. 6-8a).

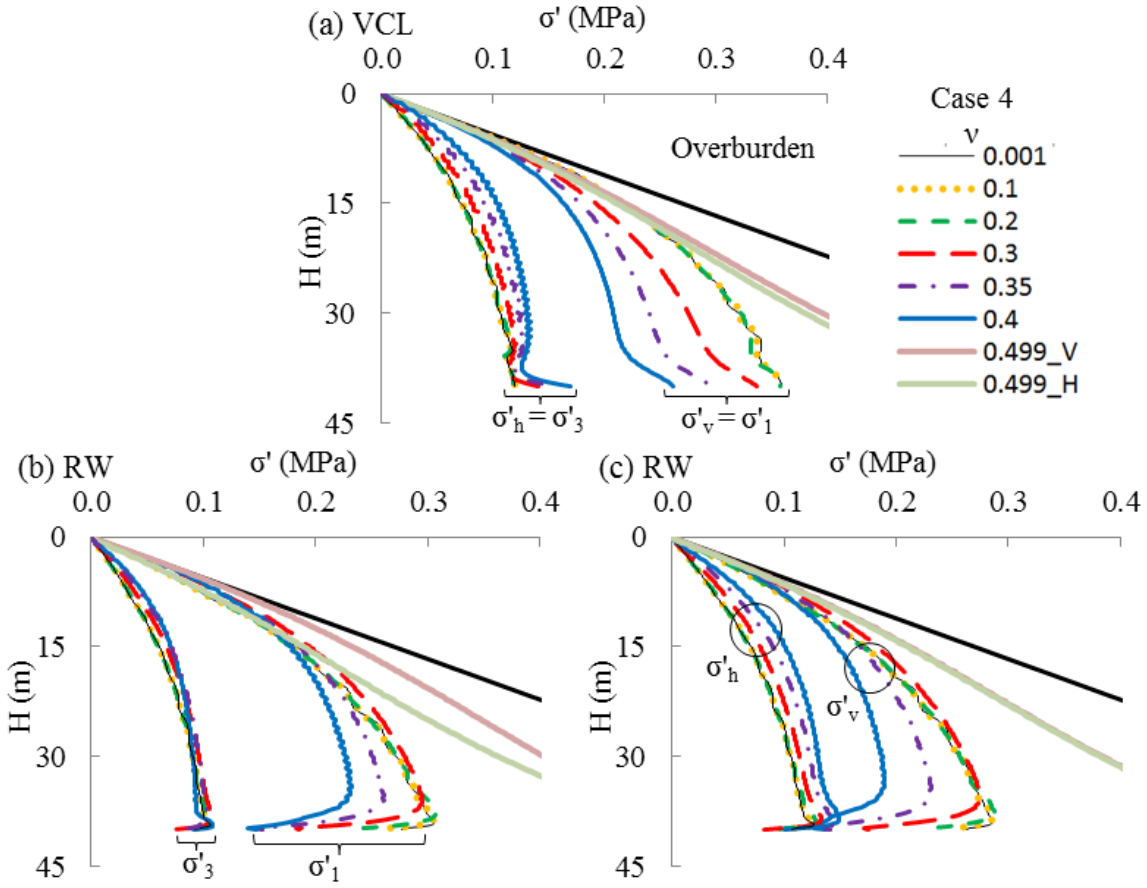

Figure H-4: Stress distributions along the VCL (a) and near the RW (b and c) for different v values when disconnected with ϕ' (Case 4 in Table 6-1)

Near the RW, it has been shown above that the K_{ps} values are almost constant and match K_a for $v \leq 0.3$ (Fig. 6-8b). This is due to the nearly unchanged principal stresses near the RW for $v \leq 0.3$, as shown in Fig. H-4b. Similar tendencies for the σ'_v and σ'_h near walls observed in Fig. H-4c indicate that the K values would remain nearly constant for $v \leq 0.3$ (Fig. 6-8c).

H1.2 Related ϕ' and v

The values of the internal friction angle ϕ' and Poisson's ratio v of the backfill are related through Eq. (A.9) in Appendix A.

Effect of opening width *B* (Case 1' in Table 6-1)

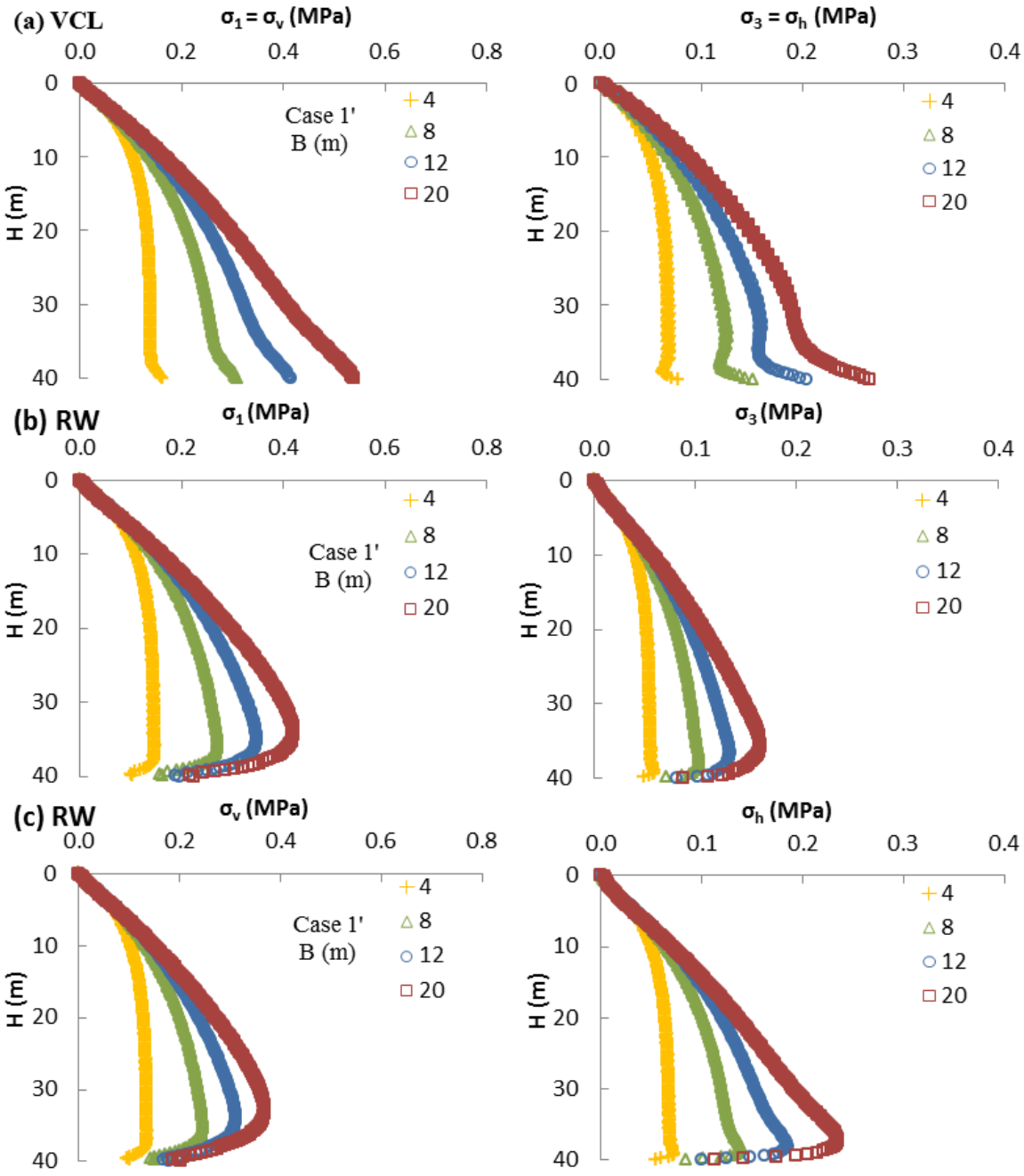

Figure H-5: Stress distributions along the VCL (a) and near the RW (b and c) as a function of opening width *B* for related v and ϕ' (Case 1' in Table 6-1)

Effect of backfill modulus *E* (Case 2' in Table 6-1)

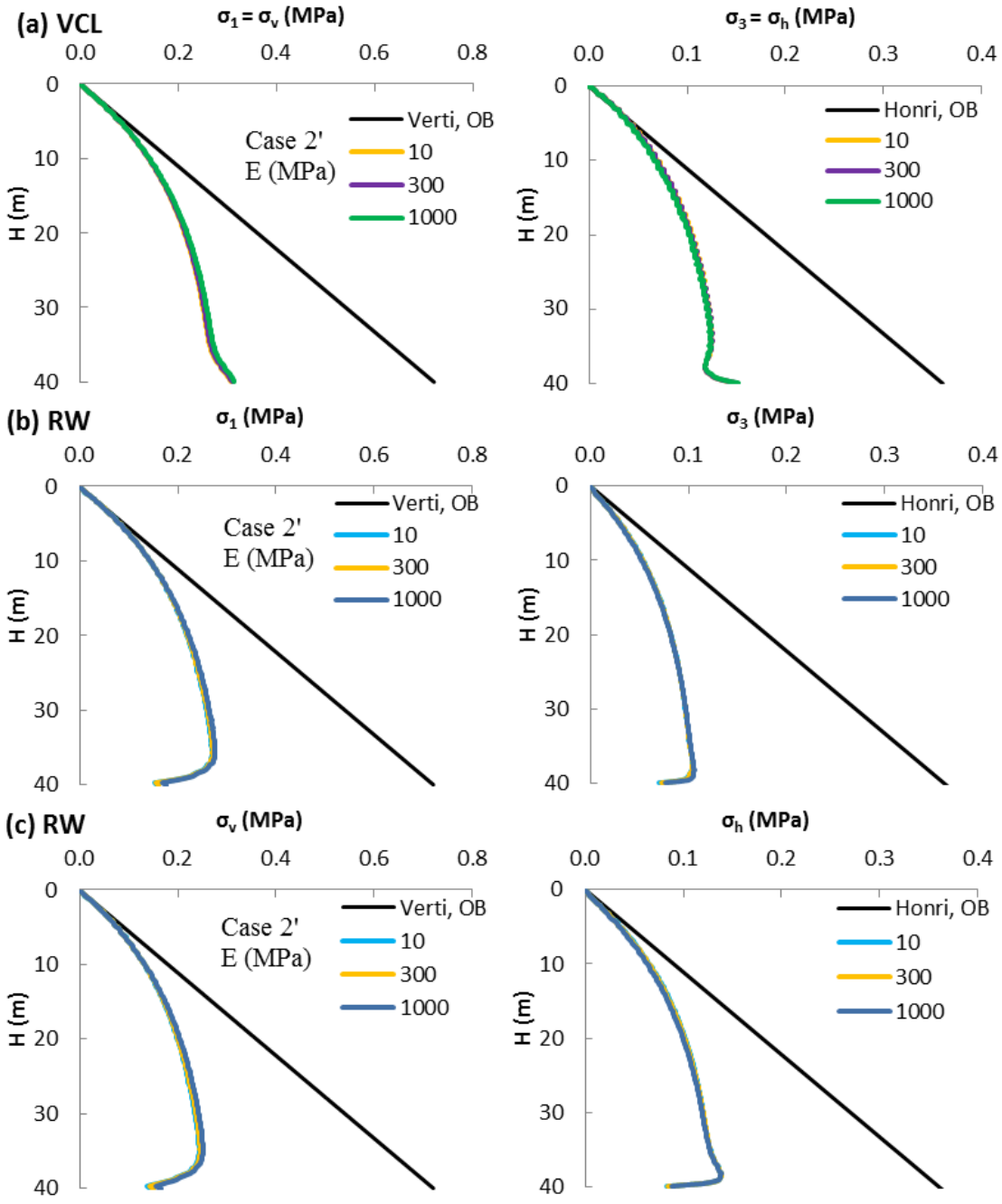

Figure H-6: Stress distributions along the VCL (a) and near the RW (b and c) as a function of backfill modulus *E* for related values of *v* and ϕ' (Case 2' in Table 6-1)

Effect of ϕ' and v for backfill (Case 3' in Table 6-1)

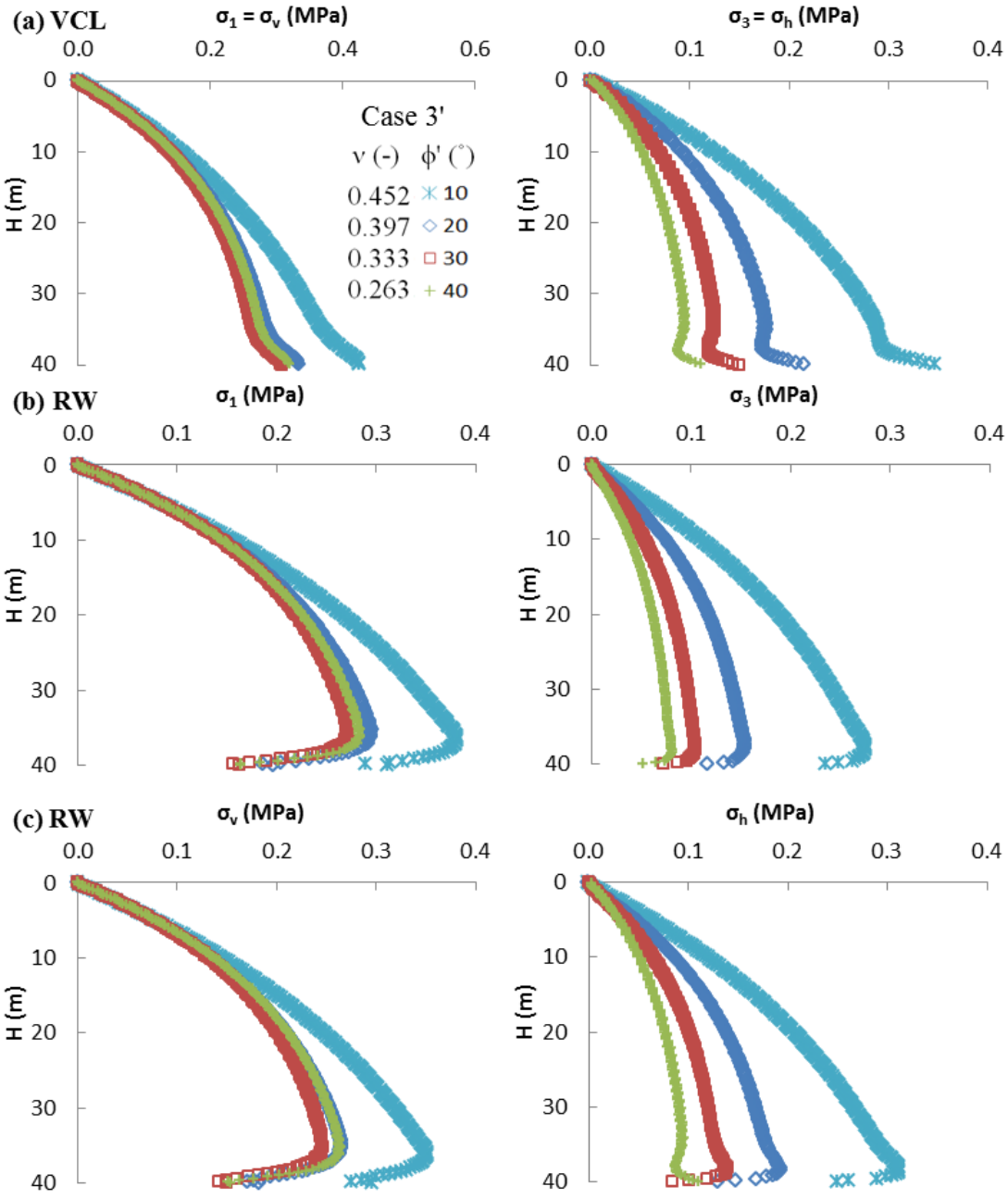

Figure H-7: Stress distributions along the VCL (a) and near the RW (b and c) for different ϕ' values related to v values (Case 3' in Table 6-1)

Fig. H-8 shows the vertical profiles of K_{ps} and K located from the VCL to the RW for related v and ϕ' (Case 0' in Table 1). The values of K_{ps} along the stope height change gradually from K_0 near the stope center to a value close to K_a near stope walls (Fig. H-8a). Fig. H-8b illustrates that the values of K along the stope height remains close to K_0 across the stope width.

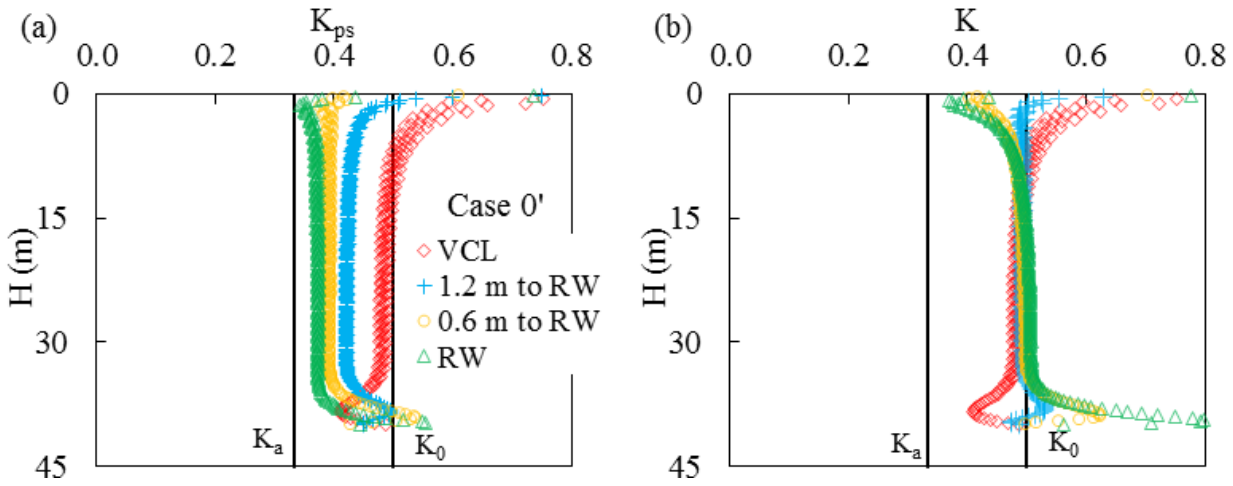

Figure H-8: Vertical profiles of (a) K_{ps} and (b) K from the VCL to RW in backfilled stopes for related values of v and ϕ' (Case 0' in Table 6-1)

H2. Stress ratios (K_{ps} and K) obtained from modelling with interface elements

H2.1 Independent ϕ' and v

Effect of opening width B

$\delta = \phi' = 30°$: Results are very similar to that obtained without interfaces (Case 1)

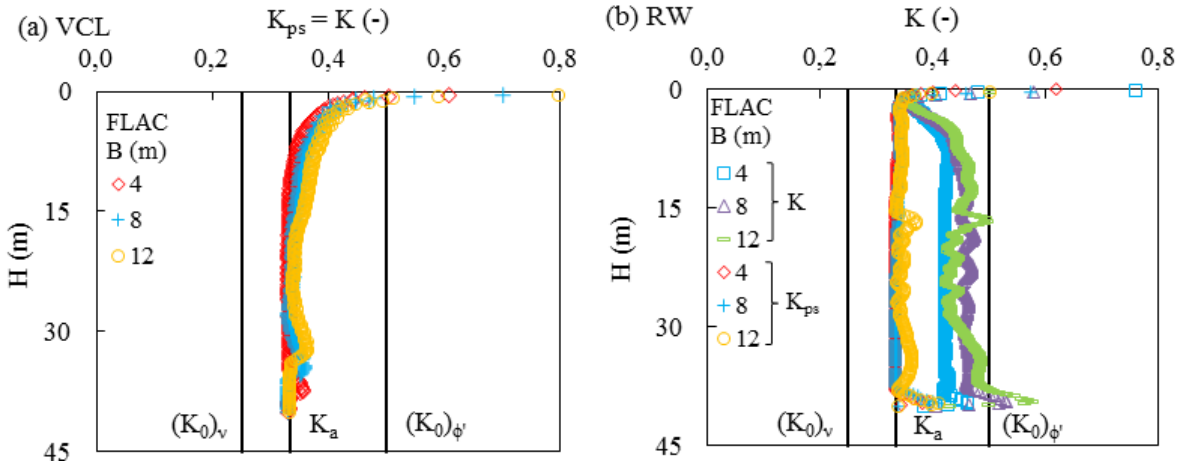

Figure H-9: Vertical profiles of K and K_{ps} (a) along the VCL and (b) near the RW as a function of B for $\delta = \phi'$ independent of v

$\underline{\delta = 2/3\phi' = 20°}$

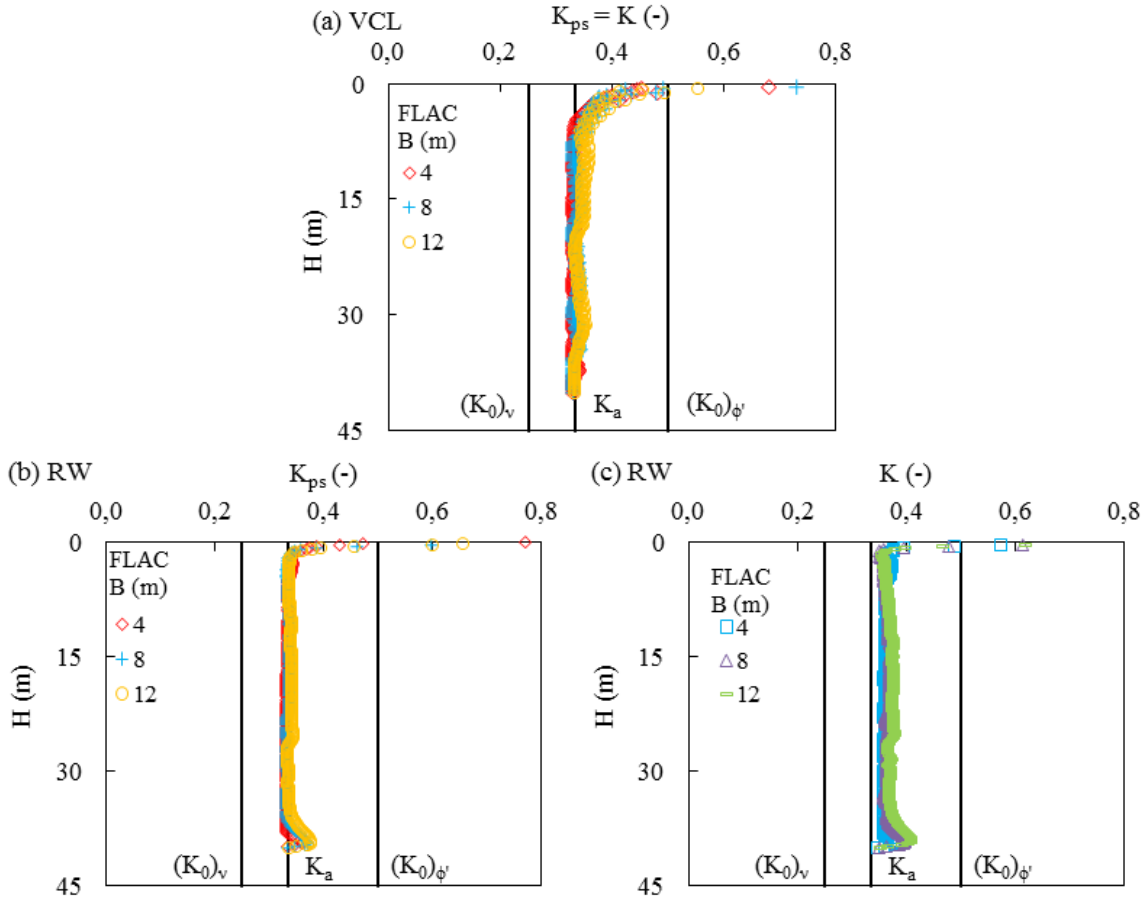

Figure H-10: Vertical profiles of K and K_{ps} (a) along the VCL and (b and c) near the RW as a function of B for $\delta = 2/3\phi'$ independent of v

$\delta = 1/3\phi' = 10°$

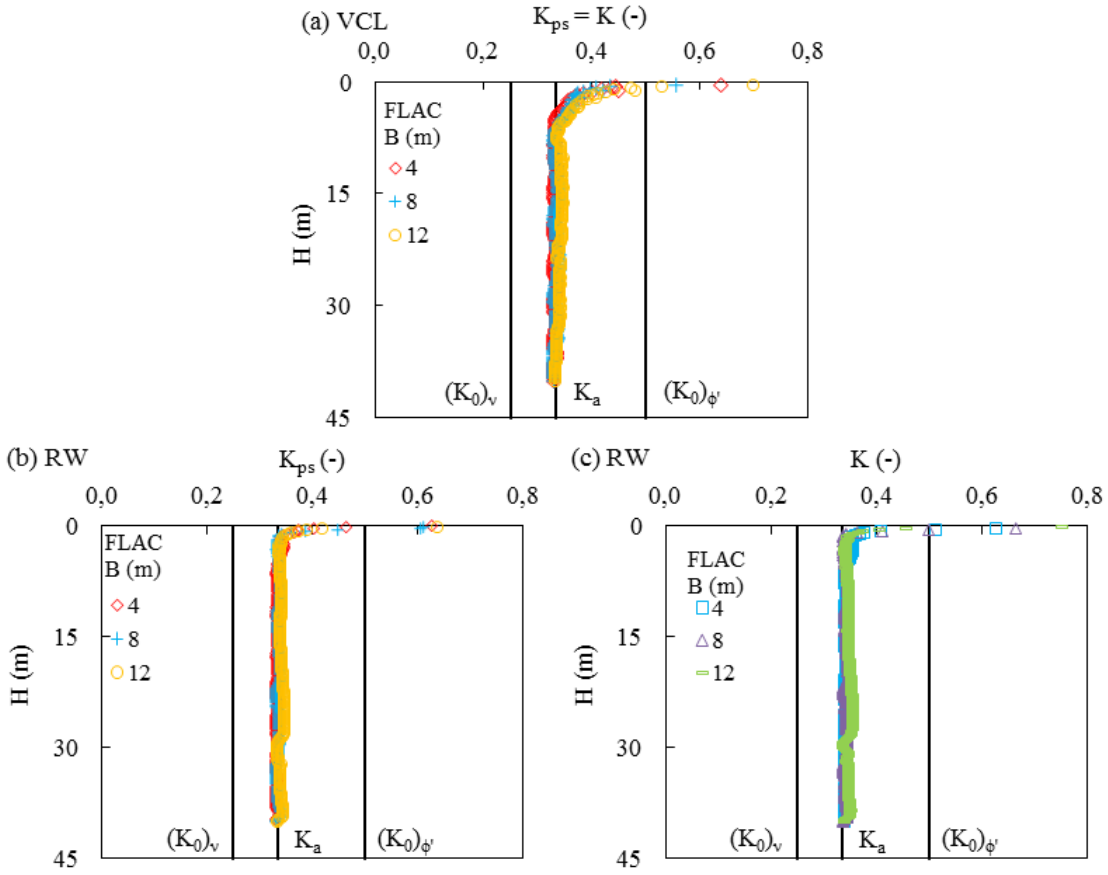

Figure H-11: Vertical profiles of K and K_{ps} (a) along the VCL and (b and c) near the RW as a function of B for $\delta = 1/3\phi'$ independent of v

$\delta = 0°$

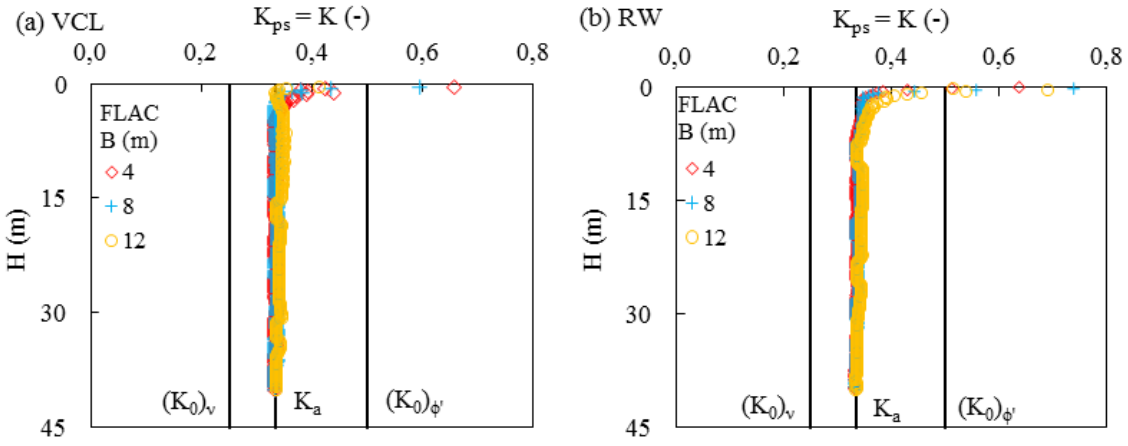

Figure H-12: Vertical profiles of K and K_{ps} (a) along the VCL and (b) near the RW as a function of B with $\delta = 0$ for independent v and ϕ'

Effect of backfill modulus *E*

$\delta = \phi' = 30°$: Results are very similar to that obtained without interfaces (Case 2)

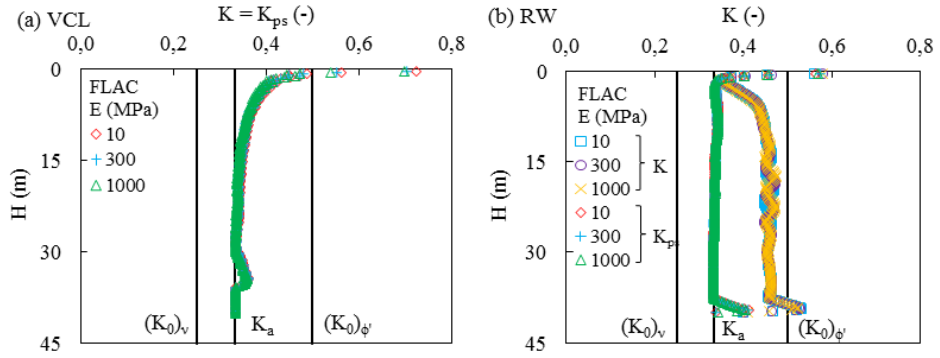

Figure H-13: Vertical profiles of K and K_{ps} (a) along the VCL and (b) near the RW as a function of E for $\delta = \phi'$ independent of v

$\delta = 2/3\phi' = 20°$

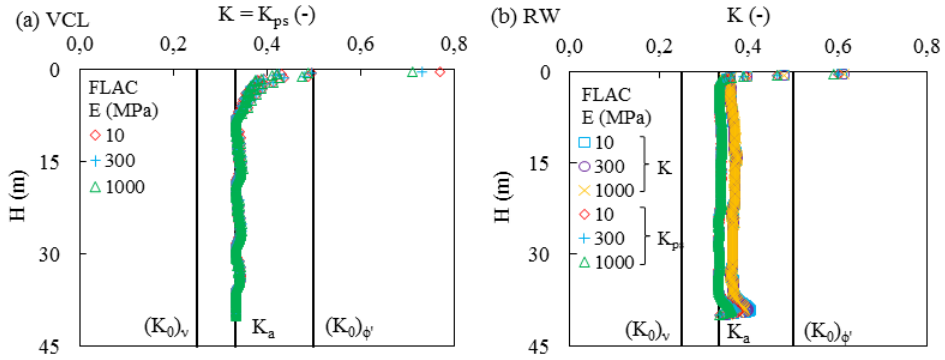

Figure H-14: Vertical profiles of K and K_{ps} (a) along the VCL and (b) near the RW as a function of E for $\delta = 2/3\phi'$ independent of v

$\delta = 1/3\phi' = 10°$

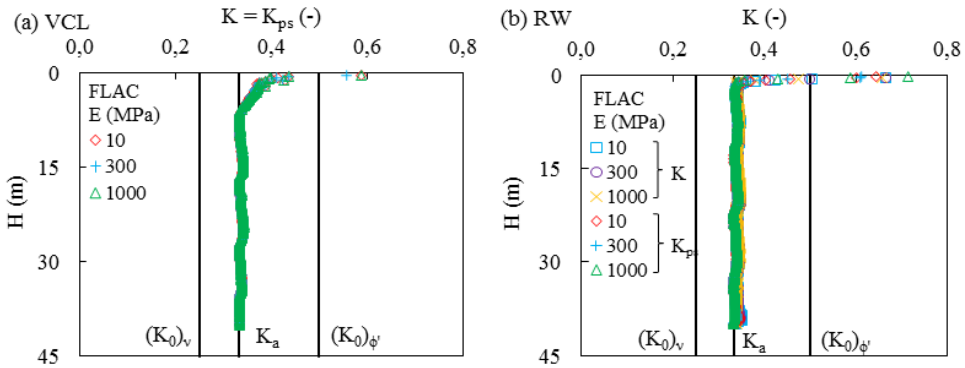

Figure H-15: Vertical profiles of K and K_{ps} (a) along the VCL and (b) near the RW as a function of E for $\delta = 1/3\phi'$ independent of v

$\underline{\delta = 0°}$

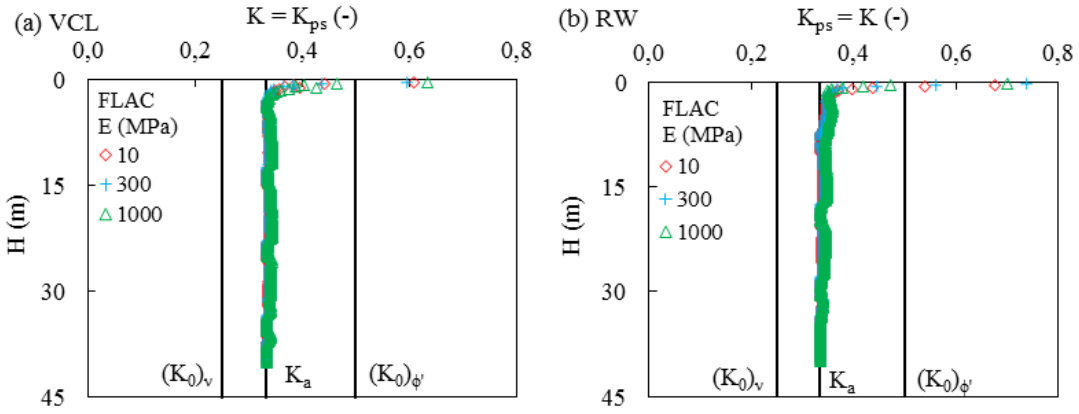

Figure H-16: Vertical profiles of K and K_{ps} (a) along the VCL and (b) near the RW as a function of E with $\delta = 0$ for independent v and ϕ'

Effect of internal friction angle of backfill ϕ'

$\underline{\delta = \phi'}$: Results are very similar to that obtained without interfaces (Case 3)

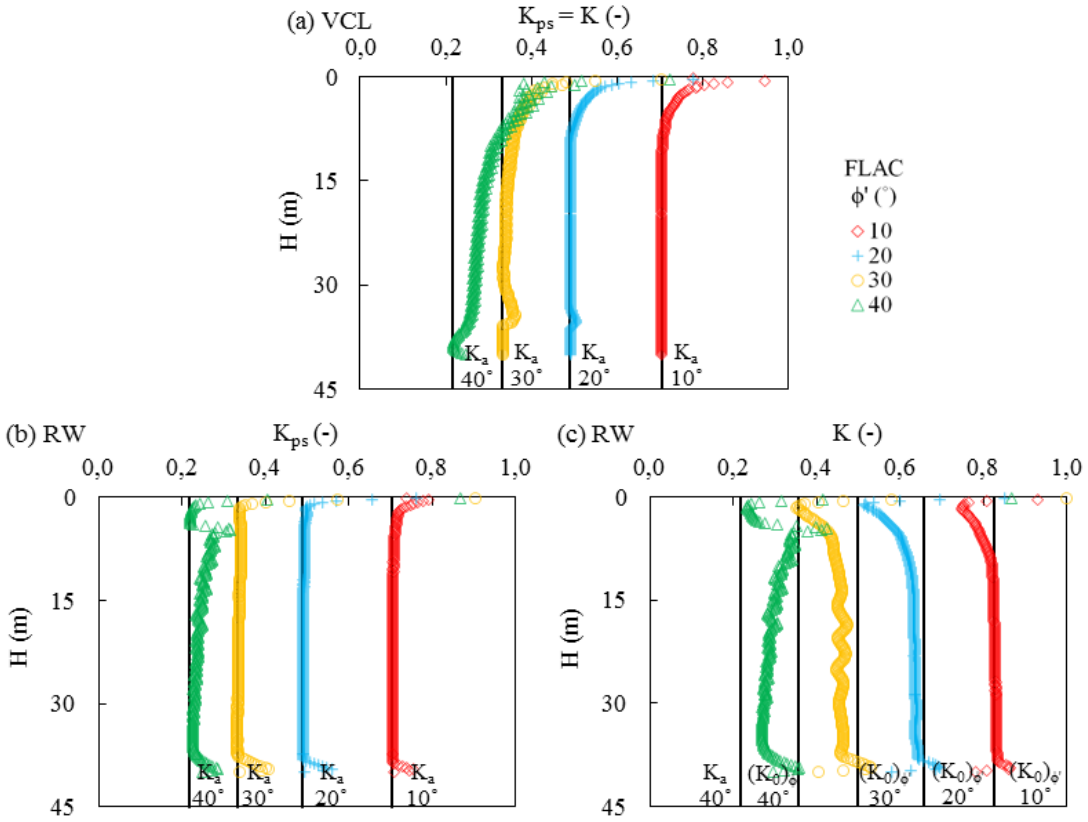

Figure H-17: Vertical profiles of K and K_{ps} (a) along the VCL and (b and c) near the RW as a function of ϕ' (independent of v) for $\delta = \phi'$

$\underline{\delta = 2/3\phi'}$

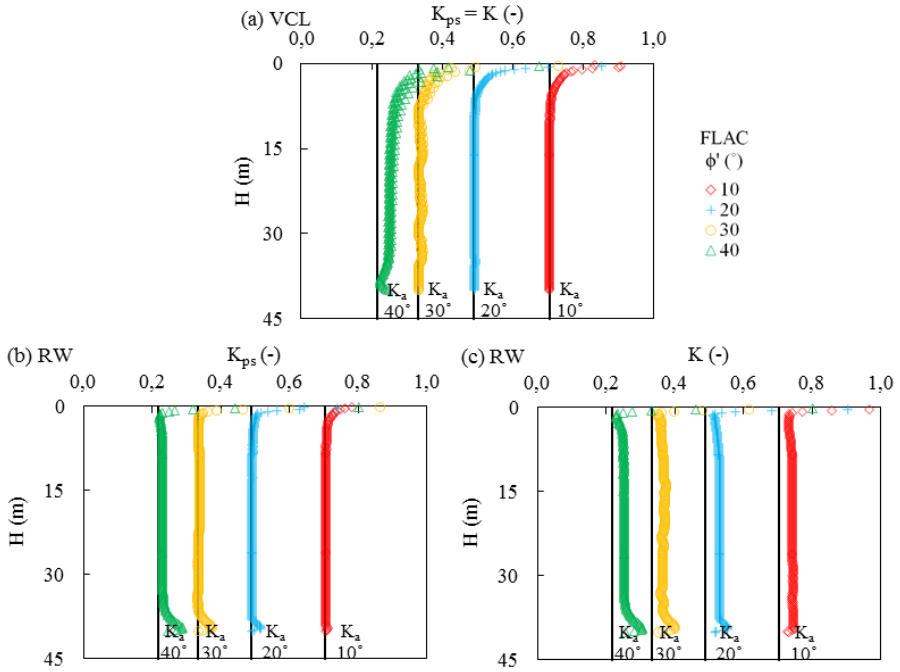

Figure H-18: Vertical profiles of K and K_{ps} (a) along the VCL and (b and c) near the RW as a function of ϕ' (independent of v) for $\delta = 2/3\phi'$

$\underline{\delta = 1/3\phi'}$

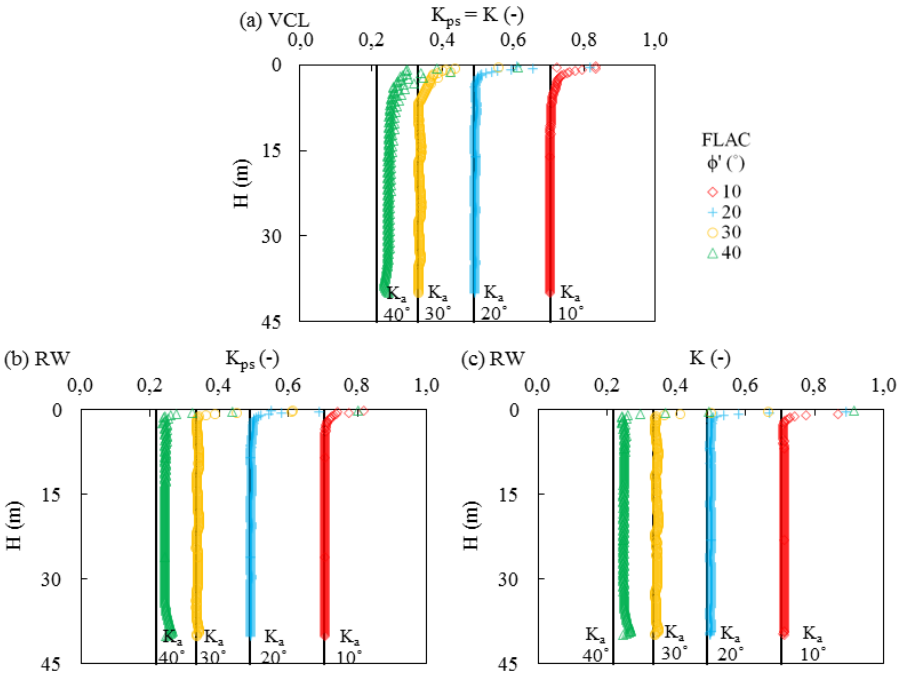

Figure H-19: Vertical profiles of K and K_{ps} (a) along the VCL and (b and c) near the RW as a function of ϕ' (independent of v) for $\delta = 1/3\phi'$

$\underline{\delta = 0°}$

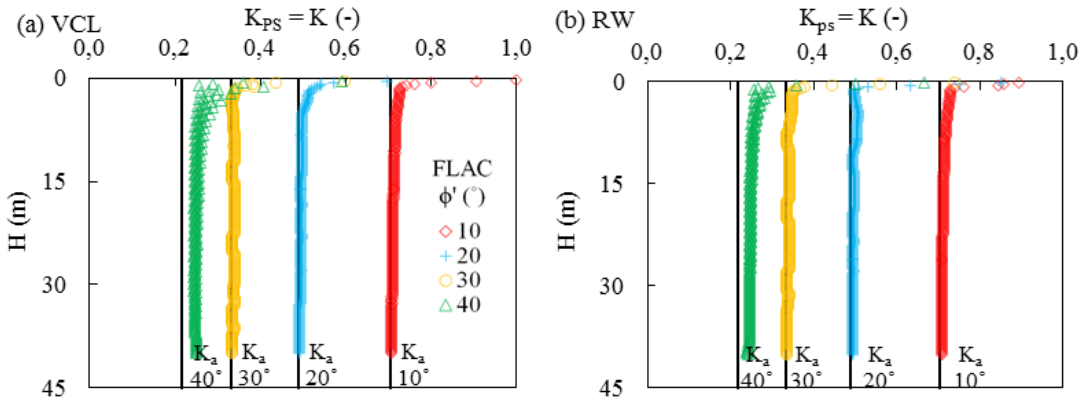

Figure H-20: Vertical profiles of K and K_{ps} (a) along the VCL and (b) near the RW as a function of ϕ' (independent of ν) for $\delta = 0$

Effect of Poisson's ratio of backfill ν

$\underline{\delta = \phi' = 30°:}$ Results are very similar to that obtained without interfaces (Case 4)

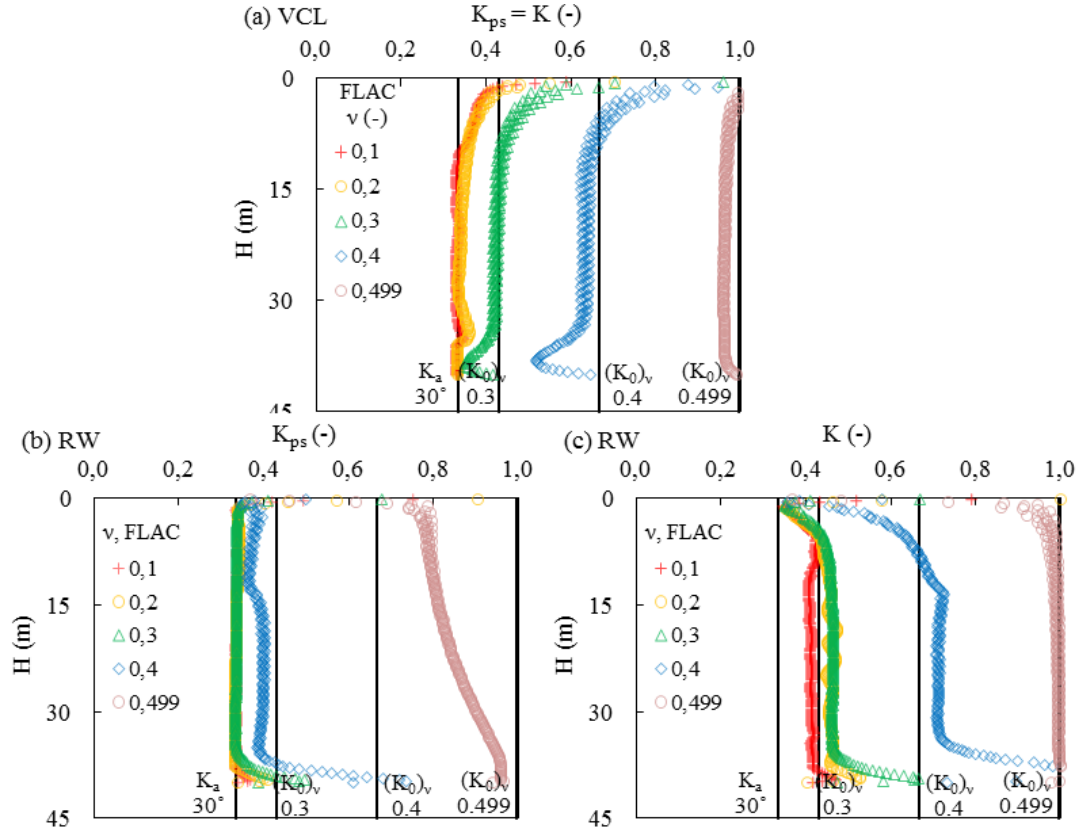

Figure H-21: Vertical profiles of K and K_{ps} (a) along the VCL and (b and c) near the RW as a function of ν (independent of ϕ') for $\delta = \phi'$

$\delta = 2/3\phi' = 20°$

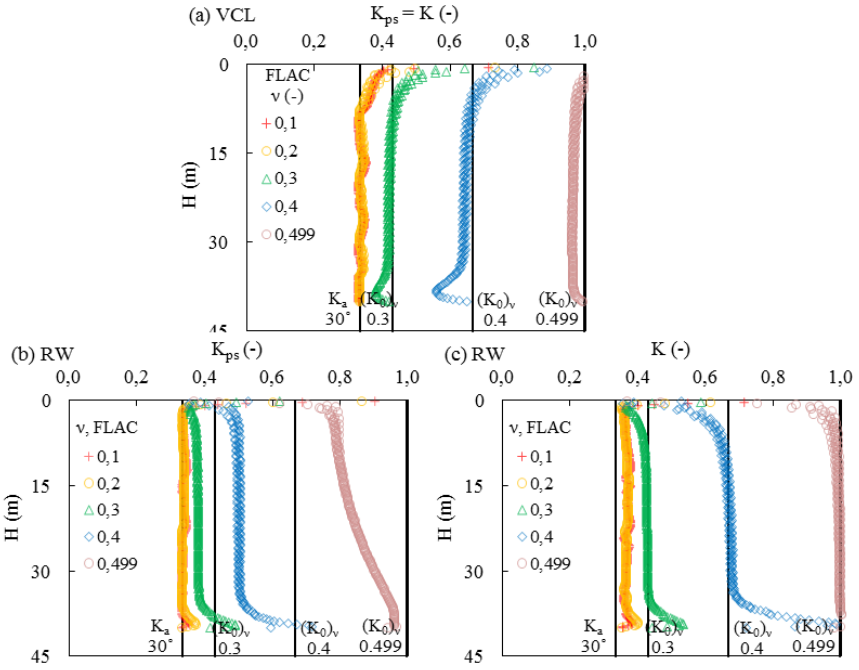

Figure H-22: Vertical profiles of K and K_{ps} (a) along the VCL and (b and c) near the RW as a function of ν (independent of ϕ') for $\delta = 2/3\phi'$

$\delta = 1/3\phi' = 10°$

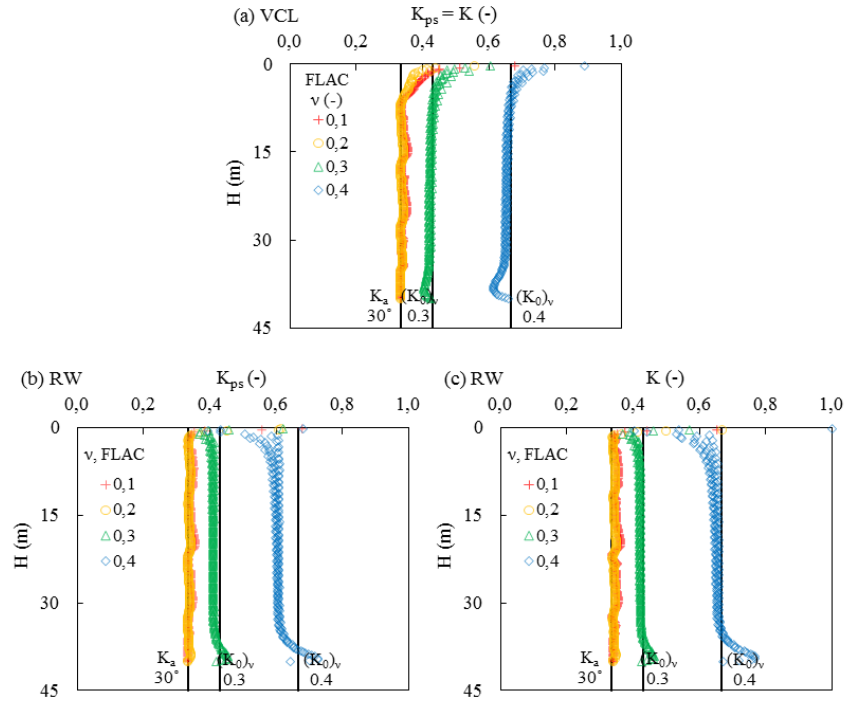

Figure H-23: Vertical profiles of K and K_{ps} (a) along the VCL and (b and c) near the RW as a function of ν (independent of ϕ') for $\delta = 1/3\phi'$

$\delta = 0°$

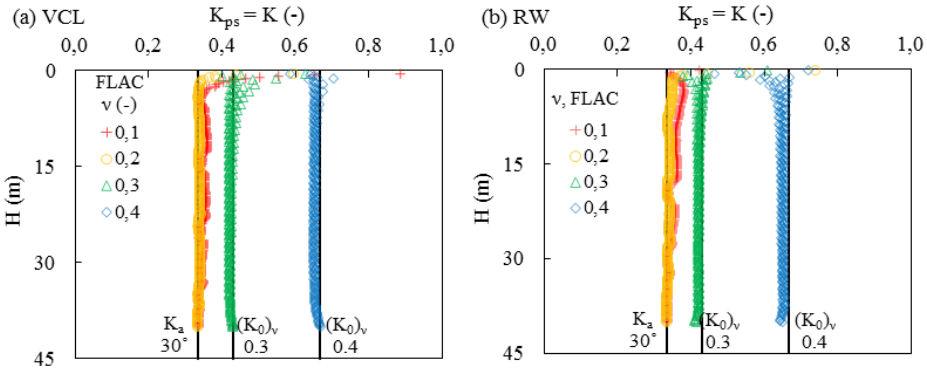

Figure H-24: Vertical profiles of K and K_{ps} (a) along the VCL and (b) near the RW as a function of v (independent of ϕ') for $\delta = 0$

H2.2 Related ϕ' and v

The values of the internal friction angle ϕ' and Poisson's ratio v of the backfill are related through Eq. (A.9) in Appendix A.

Effect of opening width B

$\delta = \phi' = 30°$: Results are very similar to that obtained without interfaces (Case 1')

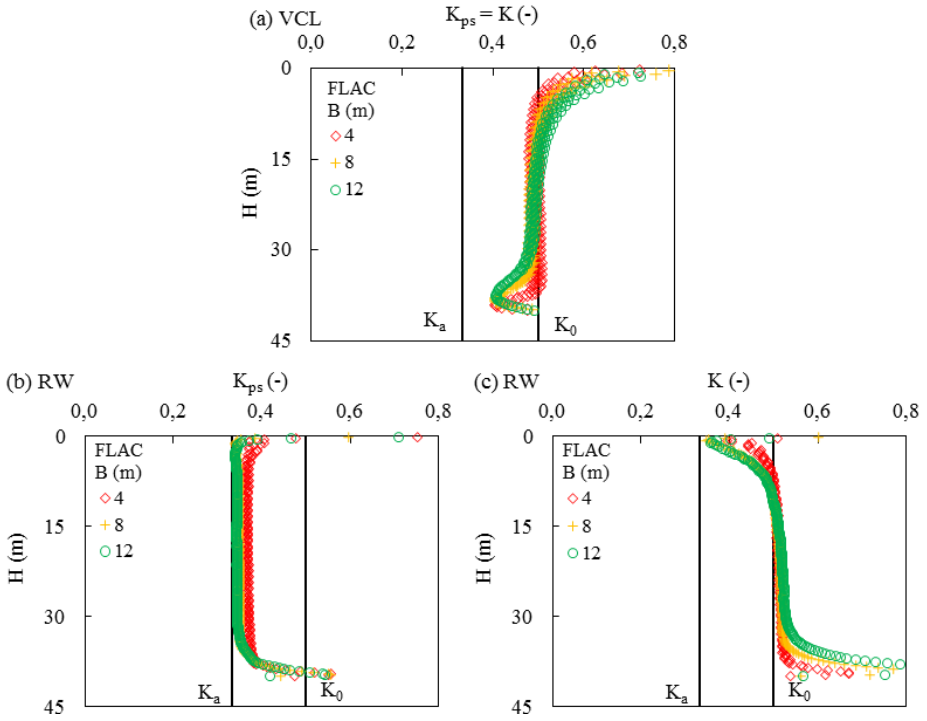

Figure H-25: Vertical profiles of K and K_{ps} (a) along the VCL and (b) near the RW as a function of B for $\delta = \phi'$ related with v

$\delta = 2/3\phi' = 20°$

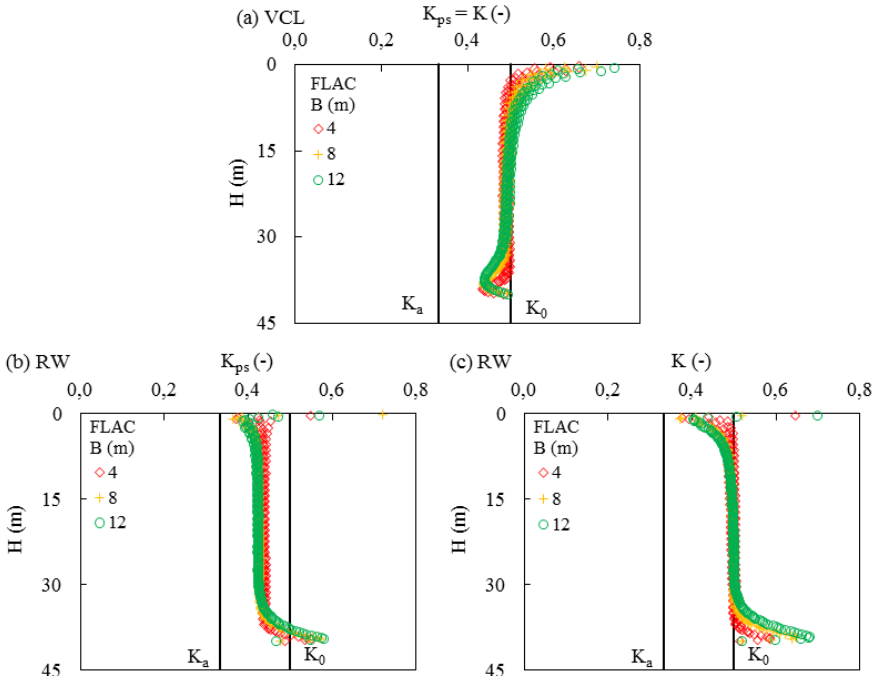

Figure H-26: Vertical profiles of K and K_{ps} (a) along the VCL and (b and c) near the RW as a function of B for $\delta = 2/3\phi'$ related with v

$\delta = 1/3\phi' = 10°$

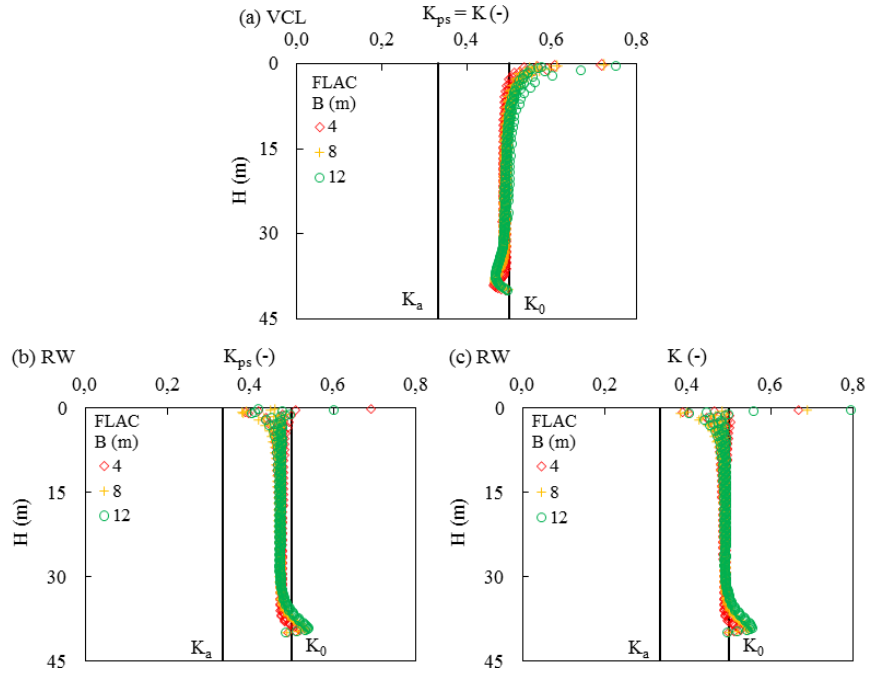

Figure H-27: Vertical profiles of K and K_{ps} (a) along the VCL and (b and c) near the RW as a function of B for $\delta = 1/3\phi'$ related with v

$\delta = 0°$

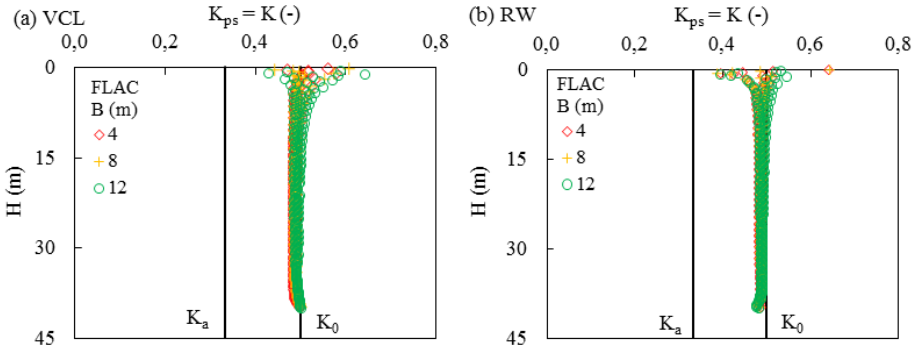

Figure H-28: Vertical profiles of K and K_{ps} (a) along the VCL and (b) near the RW as a function of B with $\delta = 0$ for related v and ϕ'

Effect of backfill modulus E

$\delta = \phi' = 30°$: Results are very similar to that obtained without interfaces (Case 2')

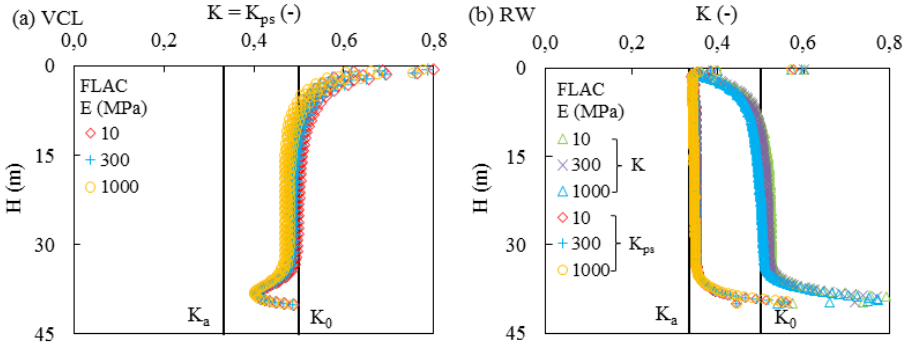

Figure H-29: Vertical profiles of K and K_{ps} (a) along the VCL and (b) near the RW as a function of E for $\delta = \phi'$ related with v

$\delta = 2/3\phi' = 20°$

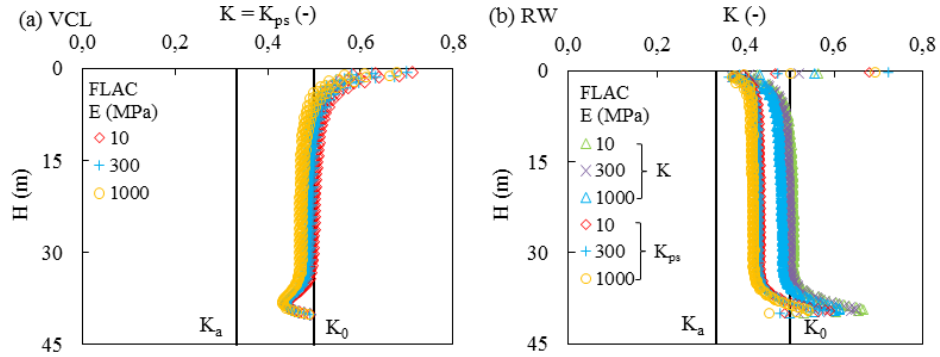

Figure H-30: Vertical profiles of K and K_{ps} (a) along the VCL and (b) near the RW as a function of E for $\delta = 2/3\phi'$ related with v

$\delta = 1/3\phi' = 10°$

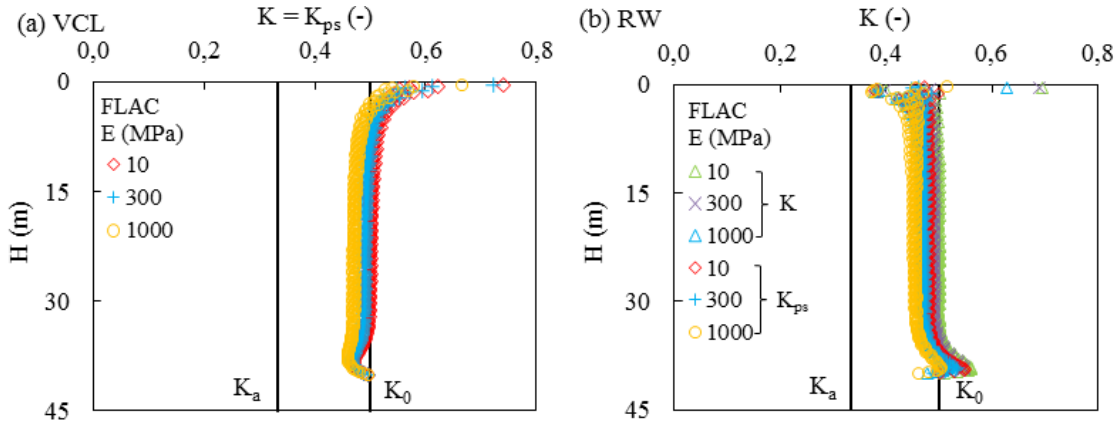

Figure H-31: Vertical profiles of K and K_{ps} (a) along the VCL and (b) near the RW as a function of E for $\delta = 1/3\phi'$ related with v

$\delta = 0°$

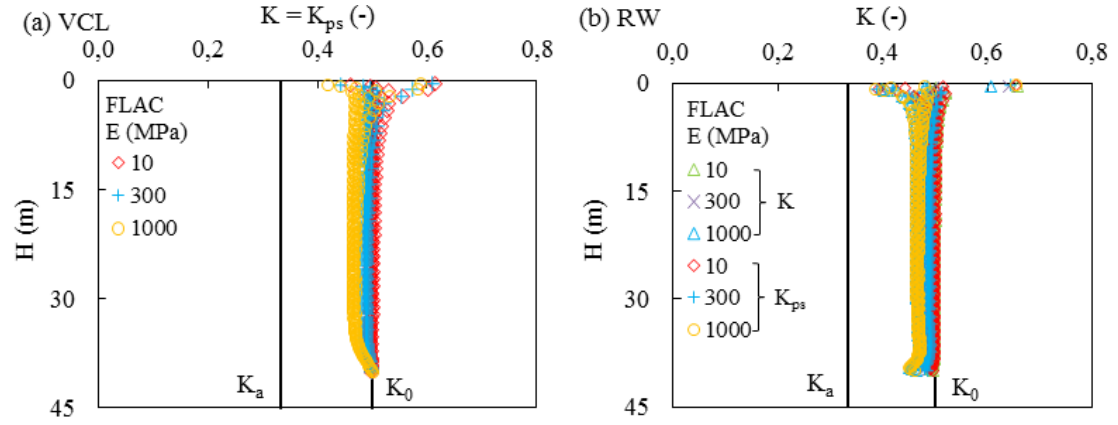

Figure H-32: Vertical profiles of K and K_{ps} (a) along the VCL and (b) near the RW as a function of E with $\delta = 0$ for related v and ϕ'

Effect of ϕ' and v for backfill

$\delta = \phi'$: Results are very similar to that obtained without interfaces (Case 3')

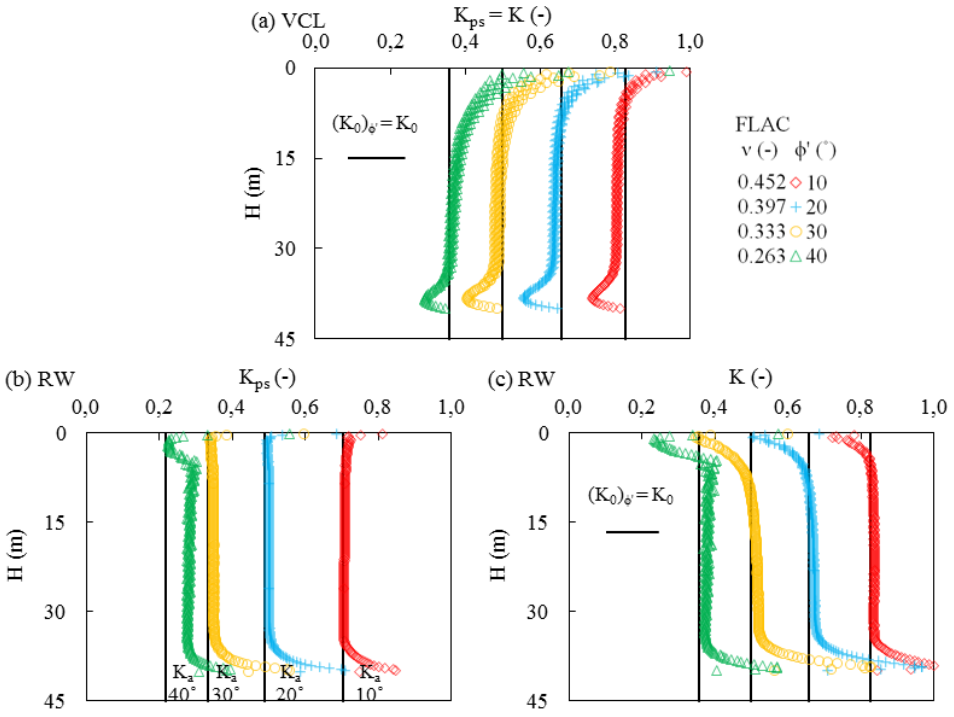

Figure H-33: Vertical profiles of K and K_{ps} (a) along the VCL and (b and c) near the RW as a function of ϕ' (related with ν) for $\delta = \phi'$

$\underline{\delta = 2/3\phi'}$

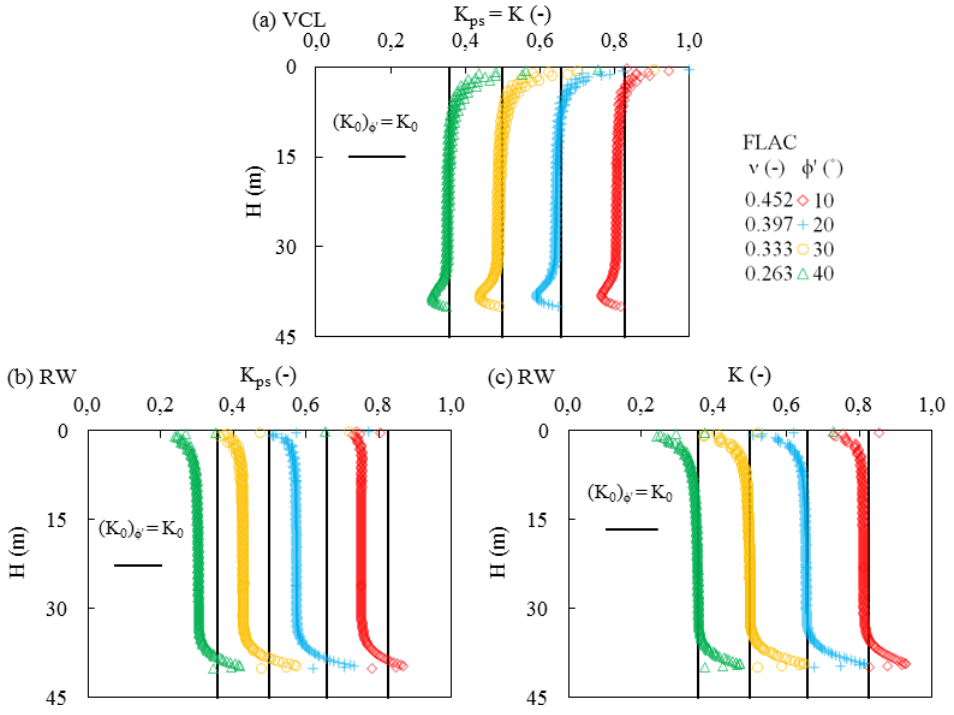

Figure H-34: Vertical profiles of K and K_{ps} (a) along the VCL and (b and c) near the RW as a function of ϕ' (related with ν) for $\delta = 2/3\phi'$

$\delta = 1/3\phi'$

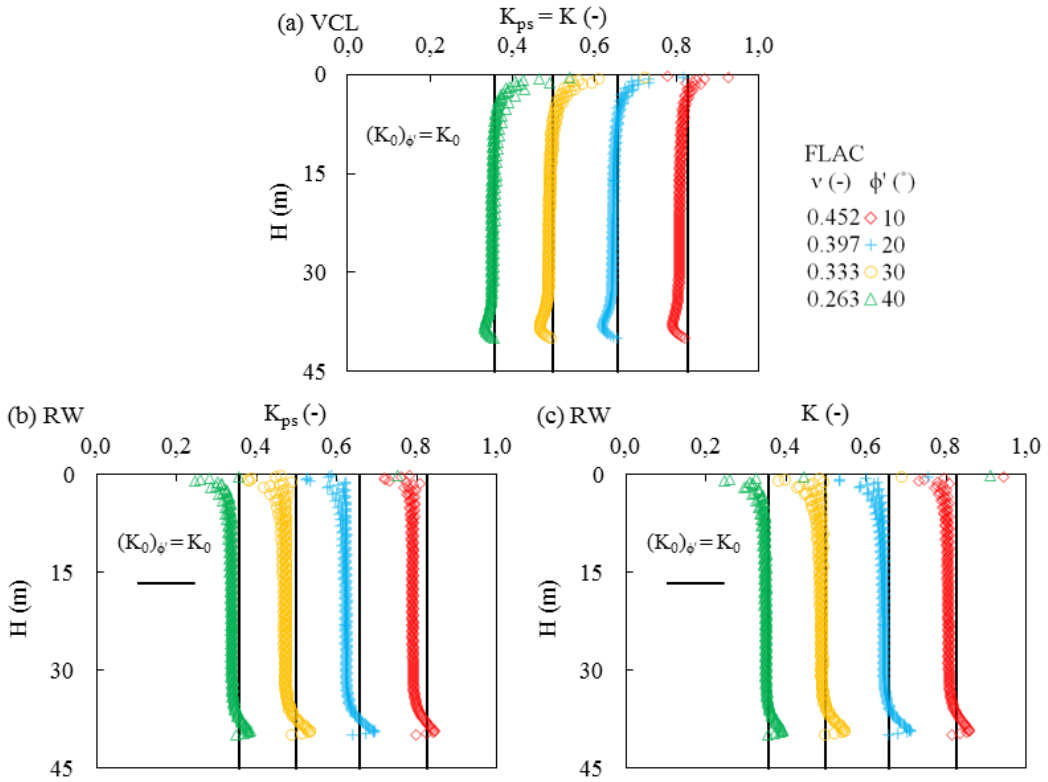

Figure H-35: Vertical profiles of K and K_{ps} (a) along the VCL and (b and c) near the RW as a function of ϕ' (related with ν) for $\delta = 1/3\phi'$

$\delta = 0°$

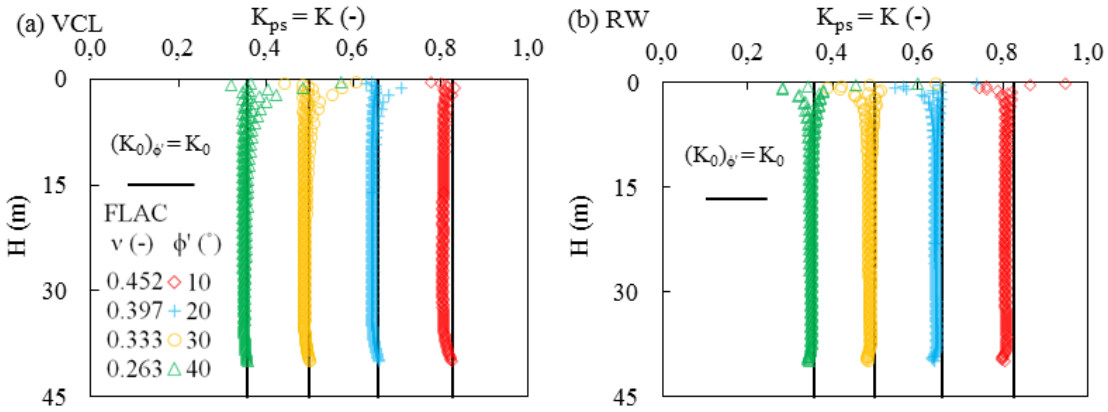

Figure H-36: Vertical profiles of K and K_{ps} (a) along the VCL and (b) near the RW as a function of ϕ' (related with ν) for $\delta = 0$

H3. Effect of interface roughness on the stress state in backfilled openings

Fig. H-37 illustrates the stress distributions along the VCL (Fig. H-37a) and near the RW (Figs. H-37b and H-37c) in a backfilled stope for Case 5 (v = 0.2; with interfaces) and Case 0 (without interfaces) when v and ϕ' are independent. The vertical and horizontal (based on Rankine's K_a) stresses due to overburden (OB) are also shown. For a rough rock surface ($\delta' = \phi'$), Fig. H-37a shows that the stresses along the VCL obtained from both cases can be quite close. It is seen from Fig. H-37b that the principal stresses near walls obtained from simulations with interfaces are lower than that without interfaces. Accordingly, the principal stress ratios (K_{ps}) near stope center and walls obtained from both cases are close to K_a for independent v and ϕ' (Table 6-2).

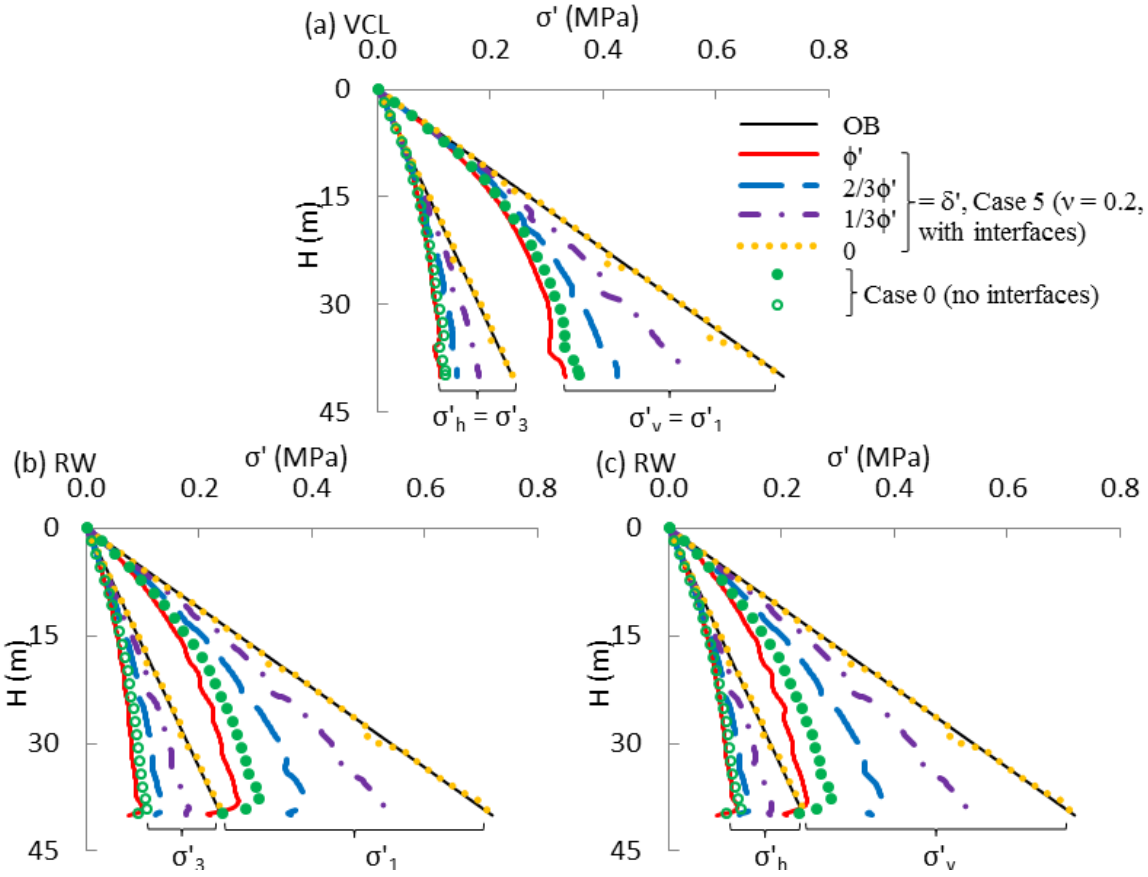

Figure H-37: Stress distributions along the VCL (a) and near the RW (b and c) for Case 5 with v = 0.2 (with interfaces) and Case 0 (without interfaces); values of v and ϕ' are disconnected

Fig. H-37c depicts that vertical stresses near walls obtained from modelling with interfaces are lower than that without interfaces while horizontal stresses remain similar. This leads to a slight increase in K value (from about 0.4 to 0.5) near walls in the cases with interfaces.

Fig. H-37 also shows that for less rough interfaces ($\delta' = 2/3\phi'$ and $1/3\phi'$), the stresses increase due to decreased arching and can be underestimated by simulations conducted without interfaces. The stresses are seen to be almost superposed with OB for frictionless interfaces ($\delta' = 0$).

Fig. H-38 presents the stress profiles along the VCL (Fig. H-38a) and near the RW (Figs. H-38b and H-38c) in a backfilled stope for Case 4' ($\phi' = 30^\circ$ and $\nu = 0.333$; with interfaces) and Case 0' (without interfaces) for related ν and ϕ'. The vertical and horizontal (based on Jaky's K_0) stresses due to overburden (OB) are also plotted. For a rough rock surface ($\delta' = \phi'$), it is seen that the stresses near the stope center and walls obtained from simulations with or without interfaces are very similar. For both cases, the coefficient K_{ps} along the VCL is close to K_0; near the walls, the ratio K_{ps} is close to K_a while the K value can be estimated by K_0 (Table 6-2). Again, Fig. H-38 shows that for less rough interfaces ($\delta' = 2/3\phi'$ and $1/3\phi'$), the stresses increase due to reduced arching and can be under predicted by simulations conducted without interfaces. It is also seen that the numerical results perfectly match OB weight in the case of frictionless interfaces ($\delta' = 0$).

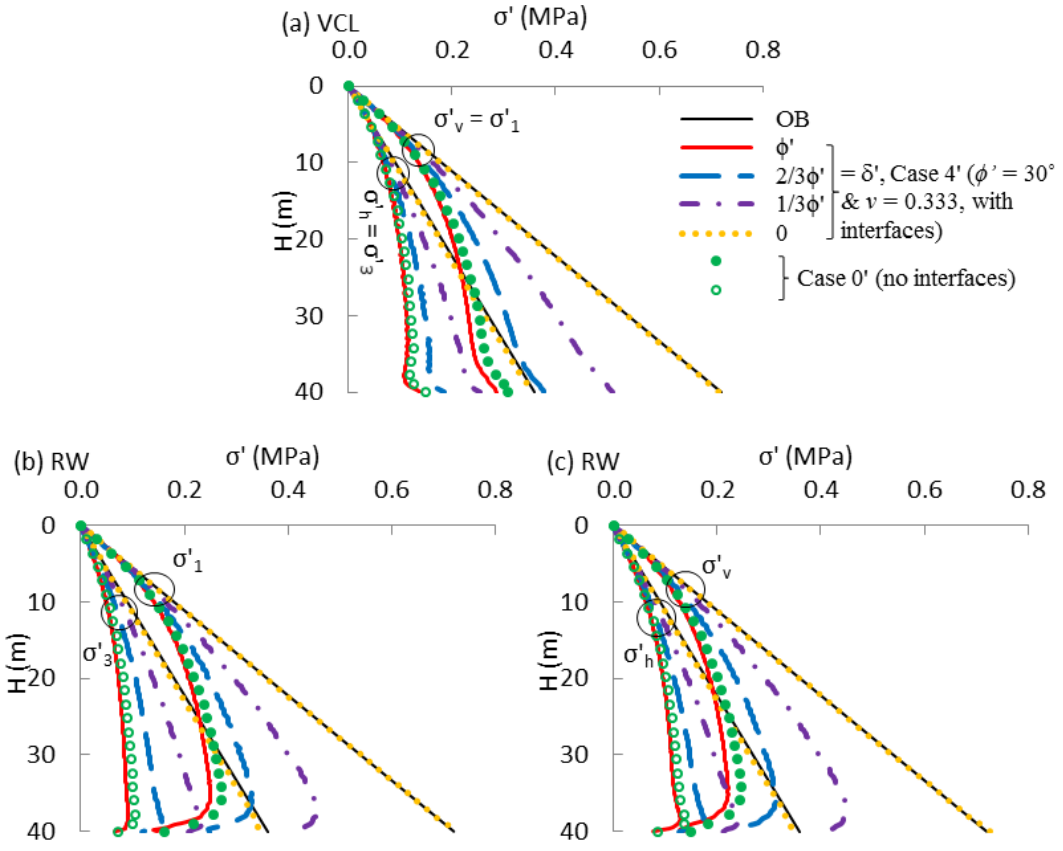

Figure H-38: Stress distributions along the VCL (a) and near the RW (b and c) for Case 4' (related $\phi' = 30^\circ$ and $\nu = 0.333$, with interfaces) and Case 0' (without interfaces)